Continent-wide climate impacts on bumblebees *pp. 125 & 177*

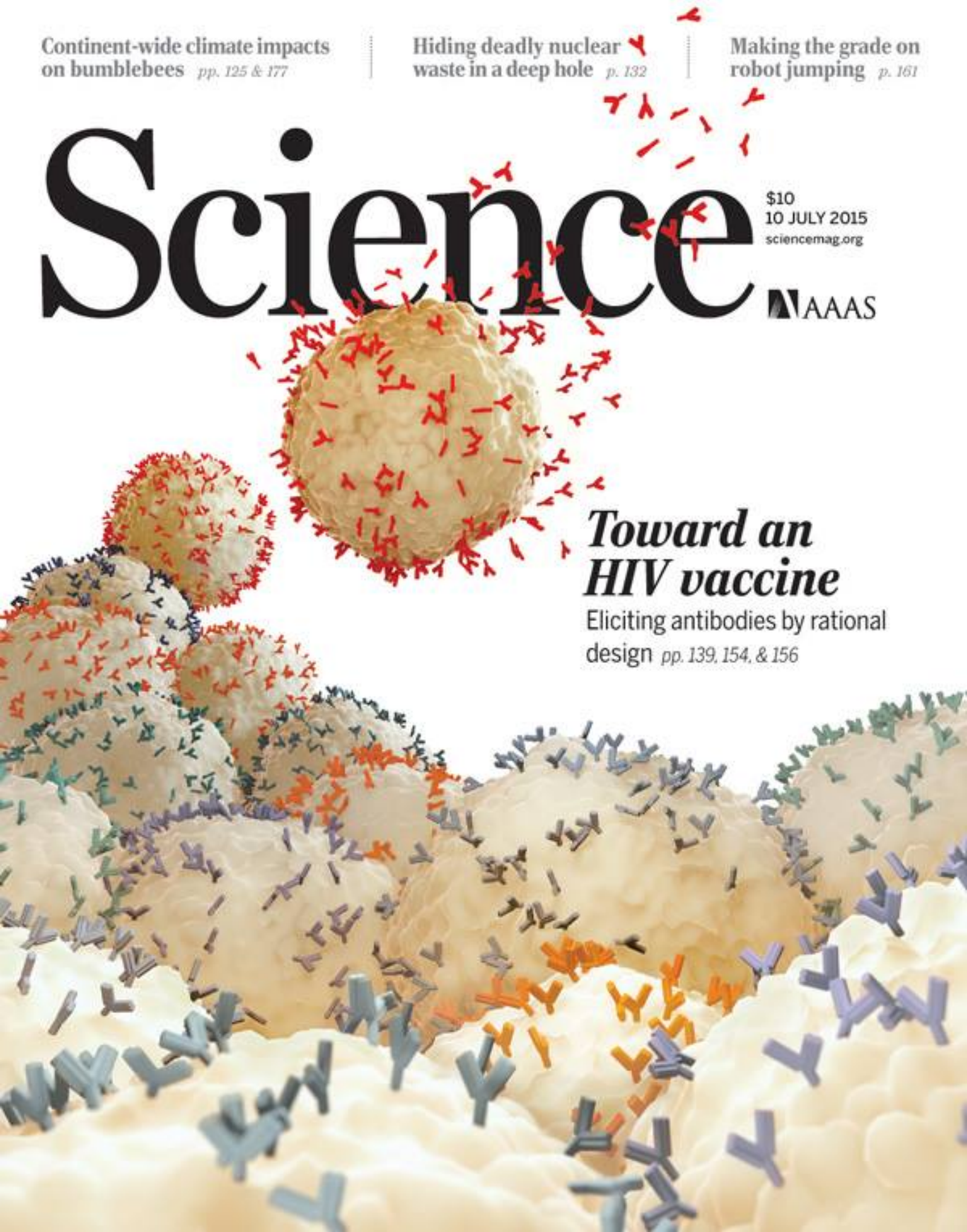
Hiding deadly nuclear waste in a deep hole *p. 132*

Making the grade on robot jumping *p. 161*

Science

$10
10 JULY 2015
sciencemag.org

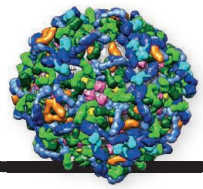
AAAS



Toward an HIV vaccine

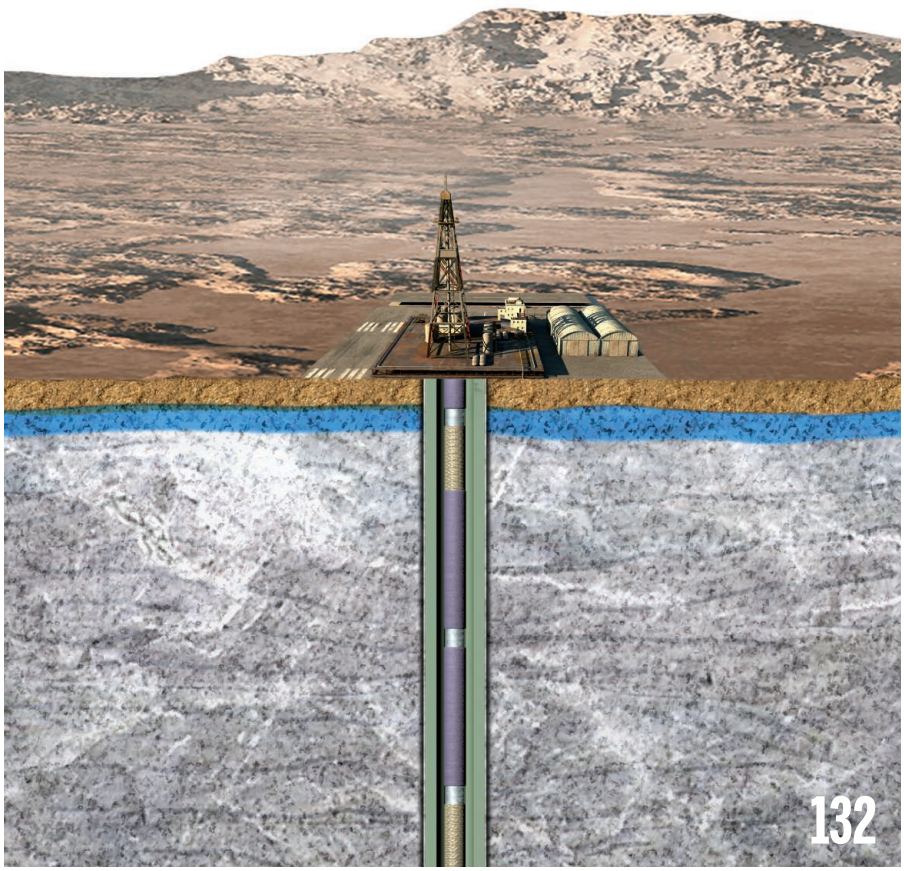
Eliciting antibodies by rational design *pp. 139, 154, & 156*

CONTENTS



142 Vesicle coats

10 JULY 2015 • VOLUME 349 • ISSUE 6244



132

NEWS

IN BRIEF

122 Roundup of the week's news

IN DEPTH

125 **SCIENTISTS DREAD GREEK EXIT FROM THE EURO**
Decisive 'No' to bailout could lead to a rupture with Europe and endanger key funding *By E. Stokstad*

126 **BUMBLEBEES AREN'T KEEPING UP WITH A WARMING PLANET**
Pollinators retreat from the south, but don't move north *By C. Carswell*

127 **PLAN TO DROP GOALS FOR WOMEN ROILS JAPANESE SCIENCE**
Change stirs debate about how to remedy underrepresentation of women *By D. Normile*

128 **TARGETING COPPER TO TREAT BREAST CANCER**
Business obstacles threaten to delay the phase III trial of a copper-depleting drug *By K. Garber*

129 **Cancer's copper connections** *By K. Garber*

130 **PLUTO CAPS ONE MAN'S ODYSSEY**
NASA veteran Tom Krimigis has been on missions to all of the sun's planets, and beyond *By E. Hand*

131 **U.S. TO REVIEW AGRICULTURAL BIOTECH REGULATIONS**
New gene-editing methods challenge old framework *By K. Servick*

FEATURES

132 **DEEP SLEEP**
Boreholes drilled into Earth's crust get a fresh look for nuclear disposal *By W. Cornwall*

135 **Rolling out a welcome mat for waste** *By W. Cornwall*

INSIGHTS

PERSPECTIVES

136 **150 YEARS OF MAXWELL'S EQUATIONS**
Powerful tools are available for the manipulation of electromagnetic fields *By N. Engheta*

138 **WATER, BOUND AND MOBILE**
Isotopic data help to resolve global hydrologic fluxes *By J. R. Brooks*
▸ REPORT P. 175

139 **THE MODERN ERA OF HIV-1 VACCINE DEVELOPMENT**
Current vaccine designs are on the path to eliciting antibodies that neutralize HIV-1 *By J. R. Mascola*
▸ RESEARCH ARTICLES PP. 154 & 156; REPORT P. 191

141 **INTELLECTUALS AND THE RISE OF THE MODERN ECONOMY**
Well-educated elites enabled scientific and technological creativity during the Industrial Revolution *By J. Mokyr*

142 **COPI GETS A FANCY NEW COAT**
An interconnected scaffolding of proteins bends the membrane to form vesicles *By A. J. Noble and S. M. Stagg*
▸ REPORT P. 195

144 **MANAGING MINING OF THE DEEP SEABED**
Contracts are being granted, but protections are lagging *By L. M. Wedding* et al.

BOOKS *ET AL.*

146 **SPIRALS IN TIME**
By H. Scales, reviewed by C. Kemp

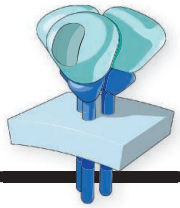
147 **THE ETHICS POLICE?**
By R. L. Klitzman, reviewed by L. F. Ross

LETTERS

148 **MEETING OF THE MINDS: SEND YOUR STORIES**
By J. F. Albaugh et al.

Science Staff 118
New Products 200
Science Careers 201

Published by AAAS



139, 154 & 156
HIV-1's trimeric envelope glycoprotein



187
Structure of a sterol sensor

148 ONLINE BUZZ RECOMMENDING WOMEN

149 REVIEWING EINSTEIN
By D. Kennefick and M. Blume

149 TECHNICAL COMMENT ABSTRACTS

RESEARCH

IN BRIEF

150 From *Science* and other journals

REVIEW

153 SEA-LEVEL RISE
Sea-level rise due to polar ice-sheet mass loss during past warm periods
A. Dutton et al.
REVIEW SUMMARY; FOR FULL TEXT: dx.doi.org/10.1126/science.aaa4019

RESEARCH ARTICLES

154 HIV-1 VACCINES
HIV-1 neutralizing antibodies induced by native-like envelope trimers *R. W. Sanders* et al.
RESEARCH ARTICLE SUMMARY; FOR FULL TEXT: dx.doi.org/10.1126/science.aac4223
▸ PERSPECTIVE P. 139; RESEARCH ARTICLE P. 156; REPORT P. 191

155 IMMUNOLOGY
An interactive reference framework for modeling a dynamic immune system
M. H. Spitzer et al.
RESEARCH ARTICLE SUMMARY; FOR FULL TEXT: dx.doi.org/10.1126/science.1259425



CREDIT: ANTONY LONG

156 HIV-1 VACCINES
Priming a broadly neutralizing antibody response to HIV-1 using a germline-targeting immunogen *J. G. Jardine* et al.
▸ PERSPECTIVE P. 139; RESEARCH ARTICLE P. 154; REPORT P. 191

REPORTS

161 SOFT ROBOTICS
A 3D-printed, functionally graded soft robot powered by combustion *N. W. Bartlett* et al.

165 APPLIED PHYSICS
Mid-infrared plasmonic biosensing with graphene *D. Rodrigo* et al.

168 GALAXY EVOLUTION
An over-massive black hole in a typical star-forming galaxy, 2 billion years after the Big Bang *B. Trakhtenbrot* et al.

171 ANIMAL PHYSIOLOGY
Exceptionally low daily energy expenditure in the bamboo-eating giant panda *Y. Nie* et al.

175 WATER RESOURCES
Hydrologic connectivity constrains partitioning of global terrestrial water fluxes *S. P. Good* et al.
▸ PERSPECTIVE P. 138

177 CLIMATE CHANGE
Climate change impacts on bumblebees converge across continents *J. T. Kerr* et al.

180 PLACE CELLS
Autoassociative dynamics in the generation of sequences of hippocampal place cells *B. E. Pfeiffer and D. J. Foster*

184 NEURONAL MODELING
Single-trial spike trains in parietal cortex reveal discrete steps during decision-making *K. W. Latimer* et al.

187 PROTEIN STRUCTURE
Crystal structure of a mycobacterial Insig homolog provides insight into how these sensors monitor sterol levels
R. Ren et al.

191 HIV-1 ENVELOPE
Effect of the cytoplasmic domain on antigenic characteristics of HIV-1 envelope glycoprotein
J. Chen et al.
▸ PERSPECTIVE P. 139; RESEARCH ARTICLES PP. 154 & 156

195 VESICULAR TRANSPORT
A structure of the COPI coat and the role of coat proteins in membrane vesicle assembly
S. O. Dodonova et al.
▸ PERSPECTIVE P. 142

DEPARTMENTS

121 EDITORIAL
Engaging new scientific horizons
By Marcia McNutt and Alan Stern

206 WORKING LIFE
Getting noticed is half the battle
By Eleftherios P. Diamandis

ON THE COVER



A goal in HIV research is to design a vaccine that will protect against the rapidly mutating virus. Such a vaccine would elicit B cells to produce broadly neutralizing antibodies with a high affinity for the HIV envelope protein. Pictured here are B cells displaying colored antibodies; B cells in the foreground express unmutated antibodies of varying specificities. Over time, the right mutations take place to create the lineage of the sought-after antibody (lineage depicted by orange-red gradient, with the unmutated ancestor depicted in orange). This happens in some HIV patients naturally, but now scientists have immunized animals with engineered immunogens that prime a first step on the antibody mutation pathway. See pages 139, 154, and 156. *Illustration: Valerie Altounian*/Science

SCIENCE (ISSN 0036-8075) is published weekly on Friday, except the last week in December, by the American Association for the Advancement of Science, 1200 New York Avenue, NW, Washington, DC 20005. Periodicals mail postage (publication No. 484460) paid at Washington, DC, and additional mailing offices.

Copyright © 2015 by the American Association for the Advancement of Science. The title SCIENCE is a registered trademark of the AAAS.

Domestic individual membership and subscription (51 issues): $153 ($74 allocated to subscription). Domestic institutional subscription (51 issues): $1282; Foreign postage extra: Mexico, Caribbean (surface mail) $55; other countries (air assist delivery) $85. First class, airmail, student, and emeritus rates on request. Canadian rates with GST available upon request, GST #1254 88122. Publications Mail Agreement Number 1069624. **Printed in the U.S.A.**
Change of address: Allow 4 weeks, giving old and new addresses and 8-digit account number. **Postmaster:** Send change of address to AAAS, P.O. Box 96178, Washington, DC 20090–6178. **Single-copy sales:** $10.00 current issue, $15.00 back issue prepaid includes surface postage; bulk rates on request.

Authorization to photocopy material for internal or personal use under circumstances not falling within the fair use provisions of the Copyright Act is granted by AAAS to libraries and other users registered with the Copyright Clearance Center (CCC) Transactional Reporting Service, provided that $30.00 per article is paid directly to CCC, 222 Rosewood Drive, Danvers, MA 01923. The identification code for *Science* is 0036-8075. *Science* is indexed in the *Reader's Guide to Periodical Literature* and in several specialized indexes.

Published by AAAS

Science
AAAS
1200 New York Avenue, NW, Washington, DC 20005
Bateman House, 82-88 Hills Road, Cambridge, UK CB2 1LQ

Editor-in-Chief Marcia McNutt
Executive Editor Monica M. Bradford **News Editor** Tim Appenzeller
Managing Editor, Research Journals Katrina L. Kelner
Deputy Editors Barbara R. Jasny, Andrew M. Sugden(UK), Valda J. Vinson, Jake S. Yeston

Research and Insights

SR. EDITORS Caroline Ash(UK), Gilbert J. Chin, Lisa D. Chong, Julia Fahrenkamp-Uppenbrink(UK), Pamela J. Hines, Stella M. Hurtley(UK), Paula A. Kiberstis, Marc S. Lavine(Canada), Kristen L. Mueller, Ian S. Osborne(UK), Beverly A. Purnell, L. Bryan Ray, Guy Riddihough, H. Jesse Smith, Jelena Stajic, Peter Stern(UK), Phillip D. Szuromi, Brad Wible, Nicholas S. Wigginton, Laura M. Zahn **ASSOCIATE EDITORS** Brent Grocholski, Keith T. Smith, Sacha Vignieri **ASSOCIATE BOOK REVIEW EDITOR** Valerie B. Thompson **ASSOCIATE LETTERS EDITOR** Jennifer Sills **CHIEF CONTENT PRODUCTION EDITOR** Cara Tate **SR. CONTENT PRODUCTION EDITORS** Harry Jach **CONTENT PRODUCTION EDITORS** Jeffrey E. Cook, Chris Filiatreau, Cynthia Howe, Lauren Kmec, Barbara P. Ordway, Catherine Wolner **SR. EDITORIAL COORDINATORS** Carolyn Kyle, Beverly Shields **EDITORIAL COORDINATORS** Ramatoulaye Diop, Joi S. Granger, Lisa Johnson, Anita Wynn **PUBLICATIONS ASSISTANTS** Aneera Dobbins, Jeffrey Hearn, Dona Mathieu, Le-Toya Mayne Flood, Shannon McMahon, Scott Miller, Jerry Richardson, Rachel Roberts(UK), Alice Whaley(UK), Brian White **EXECUTIVE ASSISTANT** Anna Bashkirova **ADMINISTRATIVE SUPPORT** Janet Clements(UK), Lizanne Newton(UK), Maryrose Madrid, Laura-Nadine Schuhmacher (UK, Intern), Alix Welch (Intern), John Wood(UK)

News

NEWS MANAGING EDITOR John Travis **INTERNATIONAL EDITOR** Richard Stone **DEPUTY NEWS EDITORS** Daniel Clery(UK), Robert Coontz, Elizabeth Culotta, David Grimm, David Malakoff, Leslie Roberts **CONTRIBUING EDITOR** Martin Enserink(Europe) **SR. CORRESPONDENTS** Jeffrey Mervis, Elizabeth Pennisi **NEWS WRITERS** Adrian Cho, Jon Cohen, Jennifer Couzin-Frankel, Carolyn Gramling, Eric Hand, Jocelyn Kaiser, Catherine Matacic, Kelly Servick, Robert F. Service, Erik Stokstad(Cambridge, UK), Emily Underwood **INTERNS** Emily Conover, Emily DeMarco, Annick Laurent, Laura Olivieri, Juan David Romero **CONTRIBUTING CORRESPONDENTS** Michael Balter(Paris), John Bohannon, Ann Gibbons, Mara Hvistendahl, Sam Kean, Richard A. Kerr, Eli Kintisch, Kai Kupferschmidt(Berlin), Andrew Lawler, Christina Larson(Beijing), Mitch Leslie, Charles C. Mann, Eliot Marshall, Virginia Morell, Dennis Normile(Tokyo), Heather Pringle, Tania Rabesandratana(London), Gretchen Vogel(Berlin), Lizzie Wade(Mexico City) **CAREERS** Jim Austin(Editor), Donisha Adams, Rachel Bernstein **COPY EDITORS** Kara Estelle (Chief), Julia Cole, Jennifer Levin **ADMINISTRATIVE SUPPORT** Jessica Williams

Executive Publisher Rush D. Holt
Publisher Kent R. Anderson **Chief Digital Media Officer** Rob Covey

BUSINESS OPERATIONS AND PORTFOLIO MANAGEMENT DIRECTOR Sarah Whalen **BUSINESS SYSTEMS AND FINANCIAL ANALYSIS DIRECTOR** Randy Yi **MANAGER OF FULFILLMENT SYSTEMS** Neal Hawkins **SYSTEMS ANALYST** Nicole Mehmedovich **ASSISTANT DIRECTOR, BUSINESS OPERATIONS** Eric Knott **MANAGER, BUSINESS OPERATIONS** Jessica Tierney **BUSINESS ANALYSTS** Cory Lipman, Cooper Tilton, Celeste Troxler **FINANCIAL ANALYST** Robert Clark **RIGHTS AND PERMISSIONS ASSISTANT DIRECTOR** Emilie David **PERMISSIONS ASSOCIATE** Elizabeth Sandler **RIGHTS, CONTRACTS, AND LICENSING ASSOCIATE** Lili Kiser

MARKETING DIRECTOR Ian King **MARKETING MANAGER** Julianne Wielga **MARKETING ASSOCIATE** Elizabeth Sattler **SR. MARKETING EXECUTIVE** Jennifer Reeves **SR. ART ASSOCIATE, PROJECT MANAGER** Tzeitel Sorrosa **ART ASSOCIATE** Seil Lee **JR. ART ASSOCIATE** Kim Huynh **ASSISTANT COMMERCIAL EDITOR** Selby Frame **MARKETING PROJECT MANAGER** Angelissa McArthur **PROGRAM DIRECTOR, AAAS MEMBER CENTRAL** Peggy Mihelich **FULFILLMENT SYSTEMS AND OPERATIONS** membership@aaas.org **MANAGER, MEMBER SERVICES** Pat Butler **SPECIALISTS** LaToya Casteel, Terrance Morrison, Latasha Russell **MANAGER, DATA ENTRY** Mickie Napoleoni **DATA ENTRY SPECIALISTS** JJ Regan, Brenden Aquilino, Fiona Giblin

DIRECTOR, SITE LICENSING Tom Ryan **DIRECTOR, CORPORATE RELATIONS** Eileen Bernadette Moran **SR. PUBLISHER RELATIONS SPECIALIST** Kiki Forsythe **PUBLISHER RELATIONS MANAGER** Catherine Holland **PUBLISHER RELATIONS, EASTERN REGION** Keith Layson **PUBLISHER RELATIONS, WESTERN REGION** Ryan Rexroth **SALES RESEARCH COORDINATOR** Aiesha Marshall **MANAGER, SITE LICENSE OPERATIONS** Iquo Edim **SENIOR PRODUCTION SPECIALIST** Robert Koepke **SENIOR OPERATIONS ANALYST** Lana Guz **FULFILLMENT ANALYST** Judy Lillibridge **ASSOCIATE DIRECTOR, MARKETING** Christina Schlecht **MARKETING ASSOCIATES** Thomas Landreth, Isa Sesay-Bah

DIRECTOR OF WEB TECHNOLOGIES Ahmed Khadr **SR. DEVELOPER** Chris Coleman **DEVELOPERS** Dan Berger, Jimmy Marks **SR. PROJECT MANAGER** Trista Smith **SYSTEMS ENGINEER** Luke Johnson

CREATIVE DIRECTOR, MULTIMEDIA Martyn Green **DIRECTOR OF ANALYTICS** Enrique Gonzales **SR. WEB PRODUCER** Sarah Crespi **WEB PRODUCER** Alison Crawford **VIDEO PRODUCER** Nguyen Nguyen **SOCIAL MEDIA PRODUCER** Meghna Sachdev

DIRECTOR OF OPERATIONS PRINT AND ONLINE Lizabeth Harman **DIGITAL/PRINT STRATEGY MANAGER** Jason Hillman **QUALITY TECHNICAL MANAGER** Marcus Spiegler **DIGITAL PRODUCTION MANAGER** Lisa Stanford **ASSISTANT MANAGER DIGITAL/PRINT** Rebecca Doshi **DIGITAL MEDIA SPECIALIST** Tara Kelly **SENIOR CONTENT SPECIALISTS** Steve Forrester, Antoinette Hodal, Lori Murphy, Anthony Rosen **CONTENT SPECIALISTS** Jacob Hedrick, Kimberley Oster

DESIGN DIRECTOR Beth Rakouskas **DESIGN EDITOR** Marcy Atarod **SENIOR SCIENTIFIC ILLUSTRATORS** Chris Bickel, Katharine Sutliff **SCIENTIFIC ILLUSTRATOR** Valerie Altounian **SENIOR ART ASSOCIATES** Holly Bishop, Preston Huey **SENIOR DESIGNER** Garvin Grullón **DESIGNER** Chrystal Smith **SENIOR PHOTO EDITOR** William Douthitt **PHOTO EDITORS** Leslie Blizard, Christy Steele

DIRECTOR, GLOBAL COLLABORATION, CUSTOM PUBLICATIONS, ADVERTISING Bill Moran **EDITOR, CUSTOM PUBLISHING** Sean Sanders: 202-326-6430 **ASSISTANT EDITOR, CUSTOM PUBLISHING** Tianna Hicklin: 202-326-6463 **ADVERTISING MARKETING MANAGER** Justin Sawyers: 202-326-7061 science_advertising@aaas.org **ADVERTISING MARKETING ASSOCIATE** Javia Flemmings **ADVERTISING SUPPORT MANAGER** Karen Foote: 202-326-6740 **ADVERTISING PRODUCTION OPERATIONS MANAGER** Deborah Tompkins **SR. PRODUCTION SPECIALIST/GRAPHIC DESIGNER** Amy Hardcastle **PRODUCTION SPECIALIST** Yuse Lajiminmuhip **SR. TRAFFIC ASSOCIATE** Christine Hall **SALES COORDINATOR** Shirley Young **ASSOCIATE DIRECTOR, COLLABORATION, CUSTOM PUBLICATIONS/CHINA/TAIWAN/KOREA/SINGAPORE** Ruolei Wu: +86-186 0822 9345, rwu@aaas.org **COLLABORATION/ CUSTOM PUBLICATIONS/JAPAN** Adarsh Sandhu + 81532-81-5142 asandhu@aaas.org **EAST COAST/E. CANADA** Laurie Faraday: 508-747-9395, FAX 617-507-8189 **WEST COAST/W. CANADA** Lynne Stickrod: 415-931-9782, FAX 415-520-6940 **MIDWEST** Jeffrey Dembski: 847-498-4520 x3005, Steven Loerch: 847-498-4520 x3006 **UK EUROPE/ASIA** Roger Goncalves: TEL/FAX +41 43 243 1358 **JAPAN** Katsuyoshi Fukamizu(Tokyo): +81-3-3219-5777 kfukamizu@aaas.org **CHINA/TAIWAN** Ruolei Wu: +86-186 0822 9345, rwu@aaas.org

WORLDWIDE ASSOCIATE DIRECTOR OF SCIENCE CAREERS Tracy Holmes: +44 (0) 1223 326525, FAX +44 (0) 1223 326532 tholmes@science-int.co.uk **CLASSIFIED** advertise@sciencecareers.org **U.S. SALES** Tina Burks: 202-326-6577, Nancy Toema: 202-326-6578 **SALES ADMINISTRATOR** Marci Gallun **EUROPE/ROW SALES** Axel Gesatzki, Sarah Lelarge **SALES ASSISTANT** Kelly Grace **JAPAN** Hiroyuki Mashiki(Kyoto): +81-75-823-1109 hmashiki@aaas.org **CHINA/TAIWAN** Ruolei Wu: +86-186 0082 9345 rwu@aaas.org **MARKETING MANAGER** Allison Pritchard **MARKETING ASSOCIATE** Aimee Aponte

AAAS BOARD OF DIRECTORS RETIRING PRESIDENT, CHAIR Gerald R. Fink **PRESIDENT** Geraldine (Geri) Richmond **PRESIDENT-ELECT** Barbara A. Schaal **TREASURER** David Evans Shaw **CHIEF EXECUTIVE OFFICER** Rush D. Holt **BOARD** Bonnie L. Bassler, May R. Berenbaum, Carlos J. Bustamante, Stephen P.A. Fodor, Claire M. Fraser, Michael S. Gazzaniga, Laura H. Greene, Elizabeth Loftus, Mercedes Pascual

SUBSCRIPTION SERVICES For change of address, missing issues, new orders and renewals, and payment questions: 866-434-AAAS (2227) or 202-326-6417, FAX 202-842-1065. Mailing addresses: AAAS, P.O. Box 96178, Washington, DC 20090-6178 or AAAS Member Services, 1200 New York Avenue, NW, Washington, DC 20005

INSTITUTIONAL SITE LICENSES 202-326-6755 **REPRINTS:** Author Inquiries 800-635-7181 **COMMERCIAL INQUIRIES** 803-359-4578 **PERMISSIONS** 202-326-6765, permissions@aaas.org **AAAS Member Services** 202-326-6417 or http://membercentral.aaas.org/discounts

Science serves as a forum for discussion of important issues related to the advancement of science by publishing material on which a consensus has been reached as well as including the presentation of minority of conflicting points of view. Accordingly, all articles published in *Science*—including editorials, news and comment, and books reviews—are signed and reflect the individual views of the authors and not official points of view adopted by AAAS or the institutions with which the authors are affiliated.

INFORMATION FOR AUTHORS See pages 678 and 679 of the 6 February 2015 issue or access www.sciencemag.org/about/authors

SENIOR EDITORIAL BOARD

Robert H. Grubbs, *California Institute of Technology,* **Gary King,** *Harvard University*
Susan M. Rosenberg, *Baylor College of Medicine,* **Ali Shilatifard,** *Northwestern University*
Feinberg School of Medicine, **Michael S. Turner**, *U. of Chicago*

BOARD OF REVIEWING EDITORS (Statistics board members indicated with **(S)**)

Adriano Aguzzi, *U. Hospital Zürich*
Takuzo Aida, *U. of Tokyo*
Leslie Aiello, *Wenner-Gren Foundation*
Judith Allen, *U. of Edinburgh*
Sonia Altizer, *U. of Georgia*
Sebastian Amigorena, *Institut Curie*
Kathryn Anderson, *Memorial Sloan-Kettering Cancer Center*
Meinrat O. Andreae, *Max-Planck Inst. Mainz*
Paola Arlotta, *Harvard U.*
Johan Auwerx, *EPFL*
David Awschalom, *U. of Chicago*
Jordi Bascompte, *Estación Biológica de Doñana CSIC*
Facundo Batista, *London Research Inst.*
Ray H. Baughman, *U. of Texas, Dallas*
David Baum, *U. of Wisconsin*
Carlo Beenakker, *Leiden U.*
Kamran Behnia, *ESPCI-ParisTech*
Yasmine Belkaid, *NIAID, NIH*
Philip Benfey, *Duke U.*
Stephen J. Benkovic, *Penn State U.*
May Berenbaum, *U. of Illinois*
Gabriele Bergers, *U. of California, San Francisco*
Bradley Bernstein, *Massachusettes General Hospital*
Peer Bork, *EMBL*
Bernard Bourdon, *Ecole Normale Supérieure de Lyon*
Chris Bowler, *École Normale Supérieure*
Ian Boyd, *U. of St. Andrews*
Emily Brodsky, *U. of California, Santa Cruz*
Ron Brookmeyer, *U. of California Los Angeles* **(S)**
Christian Büchel, *U. Hamburg-Eppendorf*
Joseph A. Burns, *Cornell U.*
Gyorgy Buzsaki, *New York U. School of Medicine*
Blanche Capel, *Duke U.*
Mats Carlsson, *U. of Oslo*
David Clapham, *Children's Hospital Boston*
David Clary, *U. of Oxford*
Joel Cohen, *Rockefeller U., Columbia U.*
James Collins, *Boston U.*
Robert Cook-Deegan, *Duke U.*
Alan Cowman, *Walter & Eliza Hall Inst.*
Robert H. Crabtree, *Yale U.*
Roberta Croce, *Vrije Universiteit*
Janet Currie, *Princeton U.*
Jeff L. Dangl, *U. of North Carolina*
Tom Daniel, *U. of Washington*
Frans de Waal, *Emory U.*
Stanislas Dehaene, *Collège de France*
Robert Desimone, *MIT*
Claude Desplan, *New York U.*
Ap Dijksterhuis, *Radboud U. of Nijmegen*
Dennis Discher, *U. of Pennsylvania*
Gerald W. Dorn II, *Washington U. School of Medicine*
Jennifer A. Doudna, *U. of California, Berkeley*
Bruce Dunn, *U. of California, Los Angeles*
Christopher Dye, *WHO*
Todd Ehlers, *U. of Tuebingen*
David Ehrhardt, *Carnegie Inst. of Washington*
Tim Elston, *U. of North Carolina at Chapel Hill*
Gerhard Ertl, *Fritz-Haber-Institut, Berlin*
Barry Everitt, *U. of Cambridge*
Ernst Fehr, *U. of Zurich*
Anne C. Ferguson-Smith, *U. of Cambridge*
Michael Feuer, *The George Washington U.*
Toren Finkel, *NHLBI, NIH*
Kate Fitzgerald, *U. of Massachusetts*
Peter Fratzl, *Max-Planck Inst.*
Elaine Fuchs, *Rockefeller U.*
Daniel Geschwind, *UCLA*
Andrew Gewirth, *U. of Illinois*
Karl-Heinz Glassmeier, *TU Braunschweig*
Ramon Gonzalez, *Rice U.*
Julia R. Greer, *Caltech*
Elizabeth Grove, *U. of Chicago*
Nicolas Gruber, *ETH Zurich*
Kip Guy, *St. Jude's Children's Research Hospital*
Taekjip Ha, *U. of Illinois at Urbana-Champaign*
Christian Haass, *Ludwig Maximilians U.*
Steven Hahn, *Fred Hutchinson Cancer Research Center*
Michael Hasselmo, *Boston U.*
Martin Heimann, *Max-Planck Inst. Jena*
Yka Helariutta, *U. of Cambridge*
James A. Hendler, *Rensselaer Polytechnic Inst.*
Janet G. Hering, *Swiss Fed. Inst. of Aquatic Science & Technology*
Kai-Uwe Hinrichs, *U. of Bremen*
Kei Hirose, *Tokyo Inst. of Technology*
David Hodell, *U. of Cambridge*
David Holden, *Imperial College*
Lora Hooper, *UT Southwestern Medical Ctr. at Dallas*
Raymond Huey, *U. of Washington*
Steven Jacobsen, *U. of California, Los Angeles*
Kai Johnsson, *EPFL Lausanne*
Peter Jonas, *Inst. of Science & Technology (IST) Austria*
Matt Kaeberlein, *U. of Washington*
William Kaelin Jr., *Dana-Farber Cancer Inst.*
Daniel Kahne, *Harvard U.*
Daniel Kammen, *U. of California, Berkeley*
Masashi Kawasaki, *U. of Tokyo*
V. Narry Kim, *Seoul National U.*
Joel Kingsolver, *U. of North Carolina at Chapel Hill*
Robert Kingston, *Harvard Medical School*
Etienne Koechlin, *Ecole Normale Supérieure*
Alexander Kolodkin, *Johns Hopkins U.*
Alberto R. Kornblihtt, *U. of Buenos Aires*
Leonid Kruglyak, *UCLA*
Thomas Langer, *U. of Cologne*
Mitchell A. Lazar, *U. of Pennsylvania*
David Lazer, *Harvard U.*
Thomas Lecuit, *IBDM*
Virginia Lee, *U. of Pennsylvania*
Stanley Lemon, *U. of North Carolina at Chapel Hill*
Ottoline Leyser, *Cambridge U.*
Marcia C. Linn, *U. of California, Berkeley*
Jianguo Liu, *Michigan State U.*
Luis Liz-Marzan, *CIC biomaGUNE*
Jonathan Losos, *Harvard U.*
Ke Lu, *Chinese Acad. of Sciences*
Christian Lüscher, *U. of Geneva*
Laura Machesky, *CRUK Beatson Inst. for Cancer Research*
Anne Magurran, *U. of St. Andrews*
Oscar Marin, *CSIC & U. Miguel Hernández*
Charles Marshall, *U. of California, Berkeley*
C. Robertson McClung, *Dartmouth College*
Graham Medley, *U. of Warwick*
Tom Misteli, *NCI*
Yasushi Miyashita, *U. of Tokyo*
Mary Ann Moran, *U. of Georgia*
Richard Morris, *U. of Edinburgh*
Alison Motsinger-Reif, *NC State U.* **(S)**
Sean Munro, *MRC Lab. of Molecular Biology*
Thomas Murray, *The Hastings Center*
James Nelson, *Stanford U. School of Med.*
Daniel Neumark, *U. of California, Berkeley*
Kitty Nijmeijer, *U. of Twente*
Pär Nordlund, *Karolinska Inst.*
Helga Nowotny, *European Research Advisory Board*
Ben Olken, *MIT*
Joe Orenstein, *U. of California Berkeley & Lawrence Berkeley National Lab*
Harry Orr, *U. of Minnesota*
Andrew Oswald, *U. of Warwick*
Steve Palumbi, *Stanford U.*
Jane Parker, *Max-Planck Inst. of Plant Breeding Research*
Giovanni Parmigiani, *Dana-Farber Cancer Inst.* **(S)**
Donald R. Paul, *U. of Texas, Austin*
John H. J. Petrini, *Memorial Sloan-Kettering Cancer Center*
Joshua Plotkin, *U. of Pennsylvania*
Albert Polman, *FOM Institute AMOLF*
Philippe Poulin, *CNRS*
Jonathan Pritchard, *Stanford U.*
David Randall, *Colorado State U.*
Colin Renfrew, *U. of Cambridge*
Felix Rey, *Institut Pasteur*
Trevor Robbins, *U. of Cambridge*
Jim Roberts, *Fred Hutchinson Cancer Research Ctr.*
Barbara A. Romanowicz, *U. of California,Berkeley*
Jens Rostrup-Nielsen, *Haldor Topsoe*
Mike Ryan, *U. of Texas, Austin*
Mitinori Saitou, *Kyoto U.*
Shimon Sakaguchi, *Kyoto U.*
Miquel Salmeron, *Lawrence Berkeley National Lab*
Jürgen Sandkühler, *Medical U. of Vienna*
Alexander Schier, *Harvard U.*
Randy Seeley, *U. of Cincinnati*
Vladimir Shalaev, *Purdue U.*
Robert Siliciano, *Johns Hopkins School of Medicine*
Denis Simon, *Arizona State U.*
Alison Smith, *John Innes Centre*
Richard Smith, *U. of North Carolina* **(S)**
John Speakman, *U. of Aberdeen*
Allan C. Spradling, *Carnegie Institution of Washington*
Jonathan Sprent, *Garvan Inst. of Medical Research*
Eric Steig, *U. of Washington*
Paula Stephan, *Georgia State U. and National Bureau of Economic Research*
Molly Stevens, *Imperial College London*
V. S. Subrahmanian, *U. of Maryland*
Ira Tabas, *Columbia U.*
Sarah Teichmann, *Cambridge U.*
John Thomas, *North Carolina State U.*
Shubha Tole, *Tata Institute of Fundamental Research*
Christopher Tyler-Smith, *The Wellcome Trust Sanger Inst.*
Herbert Virgin, *Washington U.*
Bert Vogelstein, *Johns Hopkins U.*
Cynthia Volkert, *U. of Göttingen*
Douglas Wallace, *Dalhousie U.*
David Wallach, *Weizmann Inst. of Science*
Ian Walmsley, *U. of Oxford*
Jane-Ling Wang, *U. of California, Davis*
David A. Wardle, *Swedish U. of Agric. Sciences*
David Waxman, *Fudan U.*
Jonathan Weissman, *U. of California, San Francisco*
Chris Wikle, *U. of Missouri* **(S)**
Ian A. Wilson, *The Scripps Res. Inst.* **(S)**
Timothy D. Wilson, *U. of Virginia*
Rosemary Wyse, *Johns Hopkins U.*
Jan Zaanen, *Leiden U.*
Kenneth Zaret, *U. of Pennsylvania School of Medicine*
Jonathan Zehr, *U. of California, Santa Cruz*
Len Zon, *Children's Hospital Boston*
Maria Zuber, *MIT*

BOOK REVIEW BOARD

David Bloom, *Harvard U.,* **Samuel Bowring,** *MIT,* **Angela Creager,** *Princeton U.,*
Richard Shweder, *U. of Chicago,* **Ed Wasserman,** *DuPont*

Published by AAAS

EDITORIAL

Engaging new scientific horizons

Next week, the New Horizons spacecraft will reconnoiter Pluto and its system of moons on the ragged edge of our planetary system. It may then fly by icy bodies in the Kuiper Belt, more than a billion kilometers beyond Neptune's orbit. These will become the farthest worlds ever explored, ushering in a new era of discovery. Although information from previous planetary probes has helped scientists understand the origin of the inner rocky planets (Mercury, Venus, Earth, and Mars) and the gas giants (Jupiter, Saturn, Uranus, and Neptune), as well as their moons, this will be the first opportunity to undertake a close-up study of the dwarf planets that are so common beyond Neptune.



" 'This is a moment...to share the passion for discovery that drives each of us to explore.' "

The U.S. National Aeronautics and Space Administration (NASA) launched New Horizons in January 2006 after 5 years of development at a cost of $723 million. The spacecraft carries seven scientific instruments to probe the surface properties, geology, interior makeup, and atmospheres of these planetary bodies. It is the first journey of science and exploration to venture to the outer reaches of our planetary system since the Voyager explorations of Uranus and Neptune in the late 1980s.

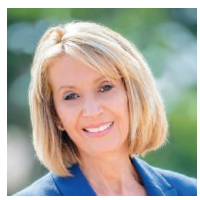
Exploration is fundamental to the human spirit. The promise of wonders unimagined from New Horizons has reawakened public and media interest that is rarely seen in science these days but is reminiscent of the early days of space exploration. Some of this attention is no doubt because little Pluto and its system of moons are distant enigmas; some because of the mysteries that beckon from the Kuiper Belt; and some because a distant space voyage of pure exploration has not happened in so long—since the 1980s—and another is not even in the planning stage by any space agency.

All of this presents an important opportunity to catalyze broader support for education in science, technology, engineering, and mathematics (STEM) fields, engage the public in informal science learning, motivate young people to pursue STEM careers, and ignite general excitement about the capacity to still make big discoveries. Efforts by the New Horizons project to educate and encourage young people to pursue STEM careers range from providing pre-college lesson plans and hosting teacher workshops, to promoting a "Pluto-Palooza" campaign at museums, science centers, planetariums, and other facilities during the Pluto flyby. It will be the first planetary mission in NASA history to carry a scientific instrument built by students.

Paleontologist and Drexel University professor Kenneth Lacovara recently remarked (to A. Stern) of New Horizons, "This is a moment for every scientist to be reminded of and to share the passion for discovery that drives each of us to explore." Indeed, all who believe that our horizons will never be limited as long as we continue to explore should spread the word about New Horizons. By doing so, enthusiasm about the mission can be translated into support for future projects that capture public imagination for doing exploratory science across numerous frontiers—from plumbing the ocean depths, to examining the diversity within the human microbiome, to space missions involving humans and robots on faraway worlds. What other projects within the next decade can raise a level of excitement that spurs waves of popular interest in the research enterprise and in research careers? There will be many, if we sow the seeds now.

With sufficient public engagement in New Horizons and a thirst for more discoveries, New Horizons need not be the last voyage of space discovery, but rather the first to explore the Kuiper Belt. But that will take some effort. Excitement about exploration is infectious. Let's point more attention to the exploration that New Horizons will undertake in July and enlist some new supporters in the thrill of scientific discovery.

– **Marcia McNutt and Alan Stern**



Marcia McNutt is Editor-in-Chief of the Science *family of journals.*



Alan Stern is the principal investigator of the New Horizons mission and a vice president at the Southwest Research Institute, Boulder, CO. E-mail: alan@boulder.swri.edu

PHOTOS: (TOP RIGHT) STACEY PENTLAND PHOTOGRAPHY; (BOTTOM RIGHT) RAYNA TEDFORD; (INSET) © NASA/JHU APL/SWRI/STEVE GRIBBEN

Downloaded from www.sciencemag.org on July 10, 2015

10.1126/science.aac8477

Published by AAAS

NEWS

$18,700,000,000

Settlement amount, announced last week, of claims by the federal government and five states against oil giant BP for the 2010 Gulf of Mexico oil spill. At least one-half of the amount will go to ecological restoration and research.

IN BRIEF

Catastrophic floods caused by pollution



Floodwaters surging through Sichuan province in 2013 produced deadly landslides.

In just 5 days in July 2013, enough rain fell in China's Sichuan province to produce the country's worst flooding in 50 years. Rivers burst their banks and poured through city streets, washing away homes, factories, and bridges. Some 200 people died and another 300,000 were displaced. Atmospheric scientist Jiwen Fan of the Pacific Northwest National Laboratory in Richland, Washington, wondered what role air pollution played in the disaster. Smog is "notorious" in Sichuan, Fan says; mountains surrounding the province trap emissions from big cities like Chongqing and Chengdu. So Fan and her colleagues designed computer models of the atmospheric conditions before the flood. They found that the contaminated air reduced sunlight reaching the basin, and instead trapped more heat higher up in the atmosphere. That led to altered atmospheric circulation patterns and redistributed precipitation: Instead of rain clouds forming over the basin during the day, the rain fell at higher intensity the following night in the nearby mountains, they reported this month in *Geophysical Research Letters*.

AROUND THE WORLD

Report pans WHO Ebola response

GENEVA, SWITZERLAND | The World Health Organization (WHO) bungled its response to the Ebola epidemic in West Africa last year, an independent six-member panel writes in a report released on 7 July. The group, led by Dame Barbara Stocking, the former chief executive of Oxfam in the United Kingdom, says there were "significant und unjustifiable delays" in WHO's response, and the agency's communication was "unable to gain command over the narrative of the outbreak." It also criticizes WHO member states for unwarranted restrictions on travel. The report suggests wide-ranging reforms, including the establishment of a new Centre for Emergency Preparedness and Response within WHO, and says countries' members fees should go up by 5%. http://scim.ag/Ebolareport

Earthquake lawsuits get the OK

OKLAHOMA CITY | Lawsuits in Oklahoma against oil and gas companies accused of inducing earthquakes can go ahead, following an Oklahoma Supreme Court decision on 30 June. The state has seen a drastic rise in small earthquakes in recent years, and scientific studies have linked them to the injection of wastewater from oil and gas operations. The court decision says that two lawsuits, stemming from a magnitude-5.7 earthquake in 2011 in Prague, Oklahoma, should proceed through the court system, potentially making industry vulnerable to class action lawsuits. Industry attorneys had



Oklahoma has seen a dramatic rise in small quakes.

PHOTOS: (TOP TO BOTTOM) © AP/CORBIS; © EYE35.PIX/ALAMY

Downloaded from www.sciencemag.org on July 10, 2015

Published by AAAS

argued that the cases should be adjudicated by the Oklahoma Corporation Commission, the state body tasked with regulating oil and gas operations.

Scouts seek EC science advisers

BRUSSELS | The European Commission has asked a trio of scouts to help fill the void left by the former chief scientific adviser (CSA), a role the commission controversially removed when it took office in November. The scouts will be tasked with finding scientists for a seven-strong "high-level group" of advisers, one of the key elements of the commission's new science advice system. The trio consists of chemist David King, a former U.K. CSA; law professor Rianne Letschert of the International Victimology Institute Tilburg in the Netherlands; and António Vitorino, president of the Jacques Delors Institute, a European policy think tank. The commission aims to have the group up and running by early October, a spokesperson says. **http://scim.ag/ECscouts**

NEWSMAKERS

McNutt tapped to lead NAS

Geophysicist **Marcia McNutt**, who has served as editor-in-chief of the *Science* family of journals since 2013, was nominated this week to stand for election as the next president of the National Academy of Sciences (NAS). If elected, as expected, McNutt would become the first woman to head the U.S. government's premier science advisory organization, which was founded in 1863. McNutt is slated to take the helm at NAS on 1 July 2016, when current president Ralph J. Cicerone ends his second term. Prior to joining *Science*, McNutt was head of the U.S. Geological Survey, and was president and chief executive officer of the Monterey Bay Aquarium Research Institute. She plans to remain at the helm of the *Science* journals until she formally takes the NAS post.

Scientist jailed for faking data

A former AIDS researcher at Iowa State University in Ames was sentenced to more than 4.5 years in prison last week and ordered to repay more than $7 million to the U.S. National Institutes of Health in a rare case of a scientist receiving prison time for faking data. **Dong-Pyou Han** was found to have tampered with rabbit blood to alter the results of an AIDS vaccine study. In December 2013, Han agreed to a 3-year ban on federal funding after an investigation by the U.S. Office of Research Integrity. But Han's case also caught the eye of Senator Charles Grassley (R–IA), who protested that the penalty seemed "very light"—and prosecutors apparently agreed. Han pleaded guilty to two felony counts of making false statements, joining a tiny number of U.S.-based researchers sentenced to prison for misconduct.



PHOTO: © PRISMA BILDAGENTUR AG/ALAMY

Fate of U.S. red wolves uncertain

The U.S. Fish and Wildlife Service (FWS) is pondering the fate of a group of 50 to 75 red wolves (*Canis rufus*, pictured), on a North Carolina peninsula, the only population left in the wild. Red wolves were nearly hunted to extinction in the 20th century. Biologists established a captive breeding population and began releasing wolves in North Carolina in 1987. Although the long-term threat is hybridization with coyotes, wolves were also being shot by coyote hunters. After a court-ordered ban on coyote hunting, locals protested and the North Carolina Wildlife Resources Commission demanded that FWS reconsider the wolf recovery program. FWS said last week that it must learn more, and will spend the rest of the year evaluating recovery efforts and conducting research on the species—including questions such as whether it can survive outside of zoos, and whether it is really a distinct species—and won't release any more animals into the wild for the time being. **http://scim.ag/_redwolf**

Three Q's

Biological oceanographer **Mark Abbott** will be the next president and director of the Woods Hole Oceanographic Institution (WHOI) in Massachusetts. Abbott, dean of the College of Earth, Ocean, and Atmospheric Sciences at Oregon State University, Corvallis, since 2001, takes

Published by AAAS

WHOI's helm amid choppy seas for the ocean sciences: A National Research Council (NRC) report in January found that the tough budget climate will necessitate significant spending cuts to major ocean infrastructure such as the Ocean Observatories Initiative (OOI), in which WHOI plays a large role.
http://scim.ag/AbbottWHOI

Q: How will the NRC's report affect WHOI?
A: [The survey] did identify a real dilemma: What is the appropriate balance between community-supported infrastructure and individual success? OOI suffered a bit by not having the data out there, and as the community begins to see what it can achieve scientifically people will be more positive. Infrastructure without the science is not of much use.

Q: What challenges and opportunities does WHOI face?
A: The biggest challenge is how we move science forward in an era of tight federal budgets. [WHOI is] an organization driven by individual success … but it's not just a collection of entrepreneurs. I see opportunities to restrengthen links to the Navy, and to rethink and rebuild traditional relationships with the National Science Foundation, NOAA, and others. [WHOI's] Center for Marine Robotics offers exciting opportunities to engage with the high-tech sector.

Q: Is autonomous sampling the future of ocean science?
A: [Physical oceanographer] Walter Munk [called] the first century of modern ocean science the century of undersampling. We can't get out there enough. Autonomous sensors and vehicles are going to play a key role. There is a revolution underway. We can start to think about sampling and understanding the ocean on the same scales at which we sample and understand the atmosphere.



Why *The Joy of Life* has lost its shine

When Henri Matisse's *Le bonheur de vivre* (*The Joy of Life*, pictured) debuted in 1906, its shockingly bright colors—including abundant amounts of cadmium sulfide (CdS)–based yellow—caused a stir at Paris's Salon des Indépendents. But the vivid colors have since faded. In 2006, scientists using portable x-ray fluorescence found CdS pigments in all the regions of the painting with fading, flaking, and other degradation effects. Now, a new study in *Applied Physics A* by scientists working at the European Synchrotron in Grenoble, France, digs deeper into the degradation mechanisms. The team tested tiny samples of damaged paint with techniques including x-ray diffraction, x-ray absorption spectroscopy, x-ray fluorescence, and infrared microscopy. The culprit? Light. The water-insoluble CdS pigment, they found, is vulnerable to light-induced oxidation that turns it into water-soluble—and colorless—cadmium sulfate. And many other masterpieces are at risk of fading, they note—the pigment was widely used by other Impressionist and Post-Impressionist artists, including Vincent Van Gogh.

UCAR head leaving post

Thomas Bogdan, president of the University Corporation for Atmospheric Research (UCAR), a federally funded laboratory based in Boulder, Colorado, is leaving the organization. Last week, UCAR's Board of Trustees announced its intention to terminate Bogdan's 5-year contract after 3.5 years. UCAR drew criticism earlier this year when it lost a key weather forecasting contract with the U.S. Air Force, one of the main supporters of its Weather Research and Forecasting (WRF) model. WRF, supported through partnerships with organizations including the Air Force, the National Weather Service, and the Navy, is the primary weather forecasting model in the United States. Effective in 2016, the Air Force plans to instead adopt a model created by the U.K. Met Office to improve forecasting abilities and lower costs.

BY THE NUMBERS

The U.S. National Institutes of Health plans to analyze genetic information from 1 million people for a study on individual genetic variability, part of the Precision Medicine Initiative. A recent survey of 2601 people to help guide the study found the following:

74%
want their genetic results from the study returned to them

43%
are willing to have "their information and research results available on the Internet to anyone," if anonymized

58%
believe research participants should help decide what to do with study results

IMAGE: *THE JOY OF LIFE*. 1905-06 (OIL ON CANVAS), MATISSE, HENRI (1869-1954)/THE BARNES FOUNDATION, PHILADELPHIA, PENNSYLVANIA, USA/© 2015 SUCCESSION H. MATISSE/DACS, LONDON/BRIDGEMAN IMAGES

Published by AAAS



Anti-austerity voters celebrate the outcome of the referendum in front of the Parliament building in Athens.

CREDITS: (PHOTO) MARKO DJURICA/REUTERS; (DATA) JRC/*ERAWATCH*

EUROPE

Scientists dread Greek exit from the euro

Decisive "no" to bailout could lead to a rupture with Europe and endanger key funding

By **Erik Stokstad**

A tumultuous week has left Greek scientists in an even greater state of uncertainty about the future of research in their debt-ridden country. On 5 July, Greek voters rejected the terms of a bailout package proposed by E.U. negotiators. As *Science* went to press, banks were closed and the economy was grinding to a halt, but what the decisive "no" vote would mean for the country's place in Europe was still very unclear.

The scientific community's greatest fear is a Greek departure from Europe's common currency, the euro, or even the European Union itself. The latter is a particularly devastating prospect, many say, because it would imperil E.U. funds and collaborations that help keep Greek science alive.

"It would be a catastrophe for the next years and the next generations," says Nikolaos Stavrakakis, an applied mathematician at the National Technical University of Athens. "I feel horrible. I'm really worried about science," says Achilleas Mitsos, an economist and science policy expert at the University of the Aegean, Mytilene, and a former director-general for research at the European Commission. "But I'm worried about my country, more than anything else."

Costas Fotakis, Greece's vice minister for research and innovation, sought to downplay concerns in an interview with *Science* before Sunday's referendum. The Greek government has no intention of leaving the common currency zone, Fotakis said, and "even in the hypothetical case that Greece decides to leave the eurozone, Greece will be able to apply for E.U. grants as an E.U. member."

Like most other people in Greece, scientists have suffered under the austerity-driven cuts to government budgets—and so has their ability to work. University salaries have been cut by more than 40% since 2010, and research centers have seen their government support slashed by more than half. Some centers have not received any government funding at all this year.

As a result, some institutes have a cash crunch. The Biomedical Sciences Research Center "Alexander Fleming" (BSRC Fleming) in Vari owes the electrical company €130,000, largely for the energy-intensive animal care facility that can house more than 15,000 mice, says the center's director, Babis Savakis, who has until the end of the month to pay the bill.

The closure of Greek banks last week has added to the troubles. The government has delayed a membership payment to CERN, for example, because of the bank closure, and academic access to many international online journals was cut off because the government has failed to provide funds for subscriptions. With the banks shut, BSRC Fleming can't buy research supplies, says Savakis, who has asked the government for an exemption to unfreeze its accounts. "It's a dismal situation," he says. Researchers at the Hellenic Centre for Marine Research (HCMR) in Anavyssos postponed field work because they were afraid they wouldn't be able to withdraw enough cash for travel expenses that can't be paid by credit card. "At the moment, it's planning for next week only," says HCMR ichthyologist Maria Stoumboudi.

€1.34 billion
Total expenditure on R&D in Greece in 2012

15.8 percent
E.U. contribution to Greek R&D spending in 2012

Sunday's referendum could portend greater hardships. The bailout terms that Greek voters rejected—set by the International Monetary Fund, the European Union, and the European Central Bank—were part of an offer that no longer stands. Many observers viewed the vote instead as a referendum on whether Greece should stay in the eurozone.

A "Grexit"—for which there is no precedent or even a legal pathway—could lead to financial chaos, a difficult transition back to Greece's former currency, the drachma, and further government austerity. Worse, some experts have argued that Greece would have to leave the European Union as well, putting E.U. funding at stake.

Downloaded from www.sciencemag.org on July 10, 2015

Published by AAAS

E.U. money plays an important role in Greece's modest science endeavor; according to the commission's Joint Research Center, the union paid for 15.8% of Greece's total R&D spending in 2012, far more than is typical for a country in the Europen Union. So-called structural funds, aimed at developing Europe's economically weaker regions, have provided the bulk of stable support to research institutes in Greece. (For BSRC Fleming, losing access to structural funds could mean halting 60% of its research and laying off 75 of its 155 employees, Savakis says.)

Another large slice of Greece's funding has come from Horizon 2020, a 7-year E.U. research funding program, and its predecessor, the Seventh Framework Programme, in which Greek researchers fared quite well. "We are deeply integrated into the European system," says Nektarios Tavernarakis, director of the Institute of Molecular Biology and Biotechnology in Heraklion. "These links would be severed."

As a non-E.U. member, Greece might have the option to buy into Horizon 2020 as an "associated country," as Norway, Turkey, Israel, and nine other countries have done. But it would have to find the money somewhere. The commission declined to answer questions about the referendum's potential impact on E.U. funding for Greek research. "Sorry, but we won't enter into such speculations," a spokesperson for the Directorate-General for Research and Innovation says.

Early this week, there was still some hope that a new deal could stave off a Grexit. The surprise resignation on Monday of Greek Finance Minister Yanis Varoufakis, a thorn in the side of E.U. officials, "could be a signal that the Greek side is ready to make serious proposals and accept the consequences," Mitsos says.

Even if Greece leaves the eurozone, there is no reason it would have to leave the European Union and forgo Horizon 2020 grants and structural funds, says Fotakis, the vice minister. But a return to the drachma would make foreign supplies and equipment more expensive, he admits. It would also exacerbate the brain drain from Greece, says Peter Tindemans, a science policy expert and the secretary general of Euroscience, a lobby group based in Strasbourg, France. "I'm pretty sure it would be another push for Greek scientists to leave the country."

Fotakis says he hopes to help the scientific community by cutting bureaucracy, for example by simplifying rules for the use of structural funds. He also envisions centers of excellence that will attract and retain young researchers—although money will remain a problem. "How can I ask for funds," Fotakis says, "when you have people sleeping in the streets or digging in the rubbish?" ■



The two-spotted bumblebee, found in eastern North America, is one of about 250 bumblebee species worldwide.

PHOTO: © 68/ED RESCHKE/OCEAN/CORBIS

CLIMATE CHANGE

Bumblebees aren't keeping up with a warming planet

Pollinators retreat from south, but don't move north

By **Cally Carswell**

As the climate changes, plants and animals are on the move. So far, many are redistributing in a similar pattern: As habitat that was once too cold warms up, species are expanding their ranges toward the poles, whereas boundaries closer to the equator have remained more static.

Bumblebees, however, appear to be a disturbing exception, according to a study on p. 177 of this issue. A comprehensive look at dozens of species, it finds that many North American and European bumblebees are failing to "track" warming by colonizing new habitats north of their historic range. Simultaneously, they are disappearing from the southern portions of their range.

"Climate change is crushing [bumblebee] species in a vice," says ecologist Jeremy Kerr of the University of Ottawa in Canada, the study's lead author. The findings underscore the importance of conserving the habitat the insects currently persist in, says Rich Hatfield, a biologist with the Xerces Society for Insect Conservation in Portland, Oregon, who was not involved in the study. Where bumblebees vanish, the wild plants and crops they pollinate could also suffer.

To see how global climate change is affecting the bees, the researchers amassed a data set consisting of some 423,000 observations, dating back to 1901, of 67 bumblebee species in North America and Europe. Then they mapped large-scale changes in the species' territories and in their "thermal ranges"—the warmest and coolest places the bees live. They also built statistical models to test whether any range shifts were best explained by climate change, or whether two other factors—changes in land cover and the use of pesticides such as neonicotinoids, which have been implicated in smaller-scale bee declines—also played a key role.

Overall, they found that some bumblebees have retreated as many as 300 kilometers from the southern edge of their historic ranges since 1974. The rusty patched bumblebee (*Bombus affinis*), for instance, has disappeared from parts of the southeastern United States. Southern species are also retreating to higher elevations, shifting upward by an average of about 300 meters over the same time period. Meanwhile, few species have expanded their northern territories. And it turned out that climate change was the only factor that had a meaningful impact on the large-scale range shifts. (Data on pesticide use were available only in the United States, however, and the study did not examine whether populations were growing or shrinking.)

Published by AAAS

One clue to the importance of climate: Bumblebee ranges began shrinking "even before the neonicotinoid pesticides came into play in the 1980s," says ecologist and coauthor Alana Pindar, a postdoctoral fellow at the University of Guelph in Canada. She says the retreat from southern territories is "a huge loss for bumblebee distributions" and happened surprisingly quickly. The researchers believe the retreat—and the move to higher elevations—may reflect the fact that bumblebees evolved in cooler climates than many other insects that haven't yet lost ground, and so are especially sensitive to warming temperatures.

More mysterious is their failure to push north. "What we can infer is that temperature in the northern latitudes is not what's limiting their spread," says Ignasi Bartomeus, a researcher at Spain's Estación Biológica de Doñana in Seville, who was not involved in the study. Differences in daylight or food could hamper a march north, or bumblebee populations may simply be too slow-growing to quickly expand. Many bumblebees form small colonies, Kerr explains, limiting their ability to spread quickly. In contrast, species with high population growth rates are "more likely to be able to establish a new colony that represents a measurable difference in geographic range." He notes that one outlier in the study, the buff-tailed bumblebee (*Bombus terrestris*), one of Europe's most common species, is known for its reproductive success and has moved north. The species "is kind of like the dandelion of the bumblebee world," he says.

So far, says Bartomeus, the most common bumblebee species seem to be the most resilient. But "we have a lot of losers," he cautions, including species that have specialized habitat requirements. And climate change could further strain species already struggling with dwindling habitat and other pressures, Kerr says. "We're hitting these animals with everything," he says. "There's no way you can nail a bee with neonicotinoids, invasive pathogens, and climate change and come out with a happy bee."

The loss of bee species could carry consequences for ecosystems and people. For instance, "plants that like their pollinators to be pretty loyal" could see declines in reproduction, says ecologist Laura Burkle of Montana State University, Bozeman. And given that wild bees help pollinate many crops, "we play with these things at our peril," Kerr says. "The human enterprise is the top floor in a really big scaffold. What we're doing is reaching out and knocking out the supports." ■

Cally Carswell is a freelance journalist in Santa Fe.

DATA SOURCE: MINISTRY OF EDUCATION, CULTURE, SPORTS, SCIENCE AND TECHNOLOGY

WOMEN IN SCIENCE

Plan to drop goals for women roils Japanese science

Change stirs debate about how to remedy underrepresentation of women

By **Dennis Normile**, *in Tokyo*

Japan Prime Minister Shinzō Abe repeatedly has said he intends "to create a society in which women shine." Now, female researchers are wondering if they are included in his vision. Japan's top science advisory panel has issued a draft 5-year national research plan that drops longstanding numerical targets for boosting the number of women in scientific fields, sparking concerns about the nation's commitment to reshaping the male-dominated sector.

The draft, unveiled on 28 May by Japan's Council for Science, Technology and Innovation (CSTI), has prompted debate over whether the targets—which have been in place for nearly a decade—are the best way to foster change. "Previous targets have not had as much impact as we would like," says Yuko Harayama, a political scientist and executive member of CSTI. "We need to analyze why." But dropping the targets is not the right response, says Hisako Ohtsubo, a molecular biologist at Nihon University, Funabashi, near Tokyo. "Without numerical targets we're afraid progress could stall," she says. Last week, Ohtsubo and several colleagues started lobbying CSTI and other government officials to add targets and additional supportive measures to the final plan, which is due by the end of the year and takes effect next April.

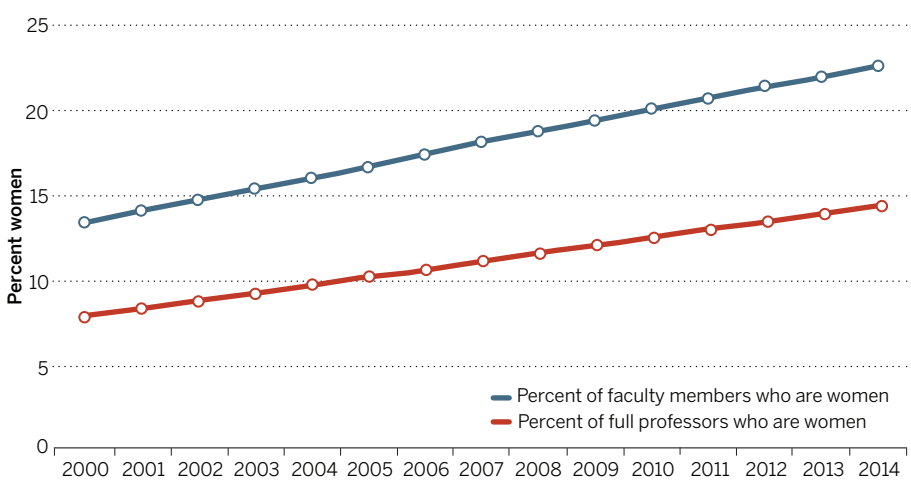
> ***"Targets have not had as much impact as we would like."***
>
> **Yuko Harayama**, Council for Science, Technology and Innovation

Japan continues to lag in recruiting women into its academic and scientific workforce, especially at top research universities. Nagoya University leads the way, with women holding 14.5% of all faculty positions as of May 2013. Tokyo and Kyoto universities, considered Japan's top schools, were at 11% and 10.6%, respectively. The average for Japan's 86 national universities is 14.1%, excluding teaching assistants, according to the Japan Association of National Universities (the student body is about 30% female).

Those numbers are "are very low" compared with other developed countries, says cancer biologist Michinari Hamaguchi, Nagoya University president from

Stuck on the first rung

In Japan, women have made up a growing percentage of total faculty members but a smaller proportion is being promoted to full professorships.



Downloaded from www.sciencemag.org on July 10, 2015

Published by AAAS

2009 until this past March. Women are 36% of total faculty in the United States, 44% in the United Kingdom, 36% in Germany, and 33% in France, according to a study by science policy experts Sotaro Shibayama of the University of Tokyo, and Aldo Geuna of the University of Turin in Italy.

To help close the gap, since 2006 Japan's 5-year plans for science and technology have included numerical goals for female recruitment. The plan adopted in 2006, for instance, called for women to make up 25% of the researchers recruited into the overall scientific workforce by 2011. It also set goals for specific fields, including 30% in health, 30% in agriculture, 20% in the natural sciences, and 15% in engineering. The current plan, adopted in 2011, upped the overall recruitment goal to 30%. And in 2013, the government's Gender Equality Bureau urged that the 30% goal apply to university presidencies and other leadership positions, not just the rank and file. The target date is 2020, but so far, Japan is not on track to meet these goals.

The new draft plan, for the years 2016 through 2020, drops gender targets in favor of so-far unspecified strategies to advance women. That approach alarms some advocates. Ohtsubo, for one, says "numerical targets are definitely necessary" for advancing women. She and a number of colleagues are also pushing to expand other supportive measures. For example, earlier plans have encouraged funding agencies to create grants for women who rejoin the workforce after raising children and to relax age limits for young investigator grants, so as not to disadvantage women who take time out for maternity leave.

> ***"Without numerical targets we're afraid progress could stall."***
> **Hisako Ohtsubo**, Nihon University

Advocates point to some institutions as a model. At Nagoya University, Hamaguchi created a scheme to recruit one or two promising female principal investigators each year without regard to their specialty, putting them on track to fill faculty positions as older professors retire. A mentoring program encourages senior female faculty to share tips with newcomers, and the university organizes leadership seminars to prepare women for higher positions. It also keeps its day care center open for particularly long hours, and helps provide care for sick kids. The center even sends taxis to pick up children from nearby schools.

Supporting women "had a snowball effect," Hamaguchi says. In 2006, for example, Nagoya's graduate biology department had just one female professor and one female teaching assistant. Now, 18 of the department's 75 faculty members are women. "The university's affirmative actions led to a natural increase in women faculty," says Narie Sasaki, a molecular cell biologist who helped craft some of the initiatives.

Hamaguchi and others worry that a lack of similar support elsewhere is contributing to a female brain drain. Women make up close to 60% of the Japanese citizens working in Western countries as students, teachers, and researchers, according to a Ministry of Foreign Affairs survey. And anecdotes suggest that the overseas female Japanese scientists are among the cream of the crop. Over the past decade, for instance, the Howard Hughes Medical Institute (HHMI) has awarded its prestigious grants to just three Japanese scientists working in the United States, and all are women.

That might be a statistical fluke, says one of the HHMI scholars, plant biologist Keiko Torii of the University of Washington in Seattle. But she thinks Japan does need "some strong government initiative ... to promote women in science as well as help them and their husbands balance families and careers."

CSTI's Harayama, who spent a decade on the faculty of Tohoku University in Sendai, shares those concerns. But she worries that overemphasizing numerical targets might lead to institutions simply filling slots with women without addressing the many other issues that can hold them back.

Harayama notes that CSTI is sponsoring studies examining how and why women choose certain career paths. One preliminary result is that young women who excel in science are gravitating toward fields such as health care and teaching, which provide credentials—such as teaching certificates or medical licenses—that offer a passport back into the workforce after time off raising children. "Young women are being very pragmatic in choosing career paths," she says.

Harayama also suspects many women avoid leadership positions because they don't find the prospect of working within Japan's male-dominated, opaque decision-making hierarchies very attractive. "We need changes in the establishment," she says.

How the final plan might encourage those changes won't be clear until later this year. But Harayama predicts it will include "more concrete actions" to create an academic community in which more women scientists can shine. ■

BIOMEDICINE

Targeting copper to treat breast cancer

Business obstacles threaten to delay the phase III trial of a copper-depleting drug

By **Ken Garber**

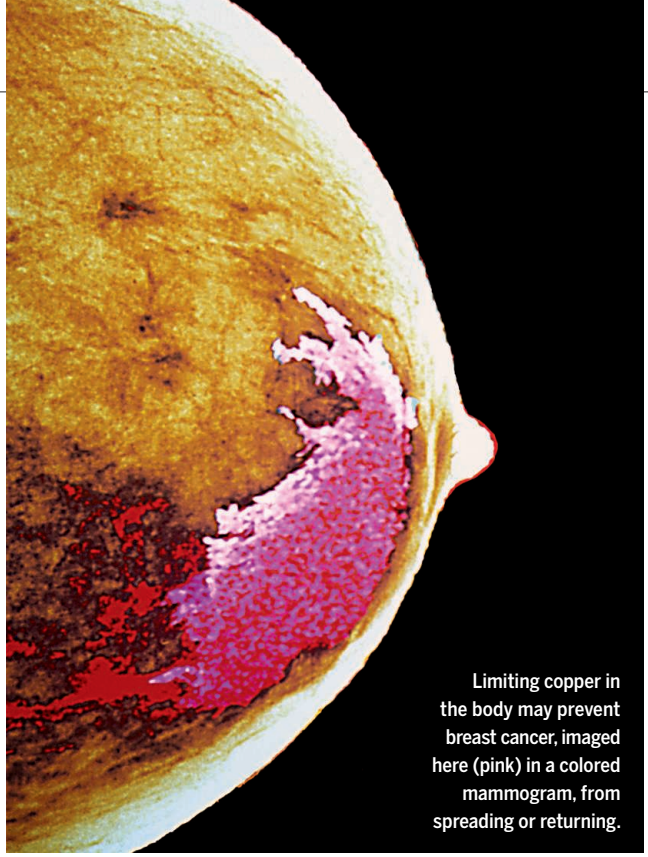
In 2007, a woman facing an almost certain death sentence took a chance on a drug that needed a second chance itself. The woman had stage IV breast cancer that had spread to her liver. Chemotherapy had eliminated her primary tumor, and surgeons had removed the liver metastases, leaving her in a status called "no evidence of disease" (NED). But oncologists cannot eliminate microscopic distant metastases—and this woman had the "triple negative" subclass of breast cancer, which is particularly aggressive and prone to bouncing back. Patients like her usually relapse within a year, with death following swiftly.

So, as part of a 2-year clinical trial of advanced breast cancer patients, the woman began taking a drug that mops up copper, thought to play a role in tumor growth (*Science*, 15 January 2010, p. 331). The drug, tetrathiomolybdate (TM), had already failed a series of previous cancer clinical trials, but this new trial has since been extended several times and there is still no sign of cancer in the woman after 8 years.

The full trial results are equally striking, as Weill Cornell Medical College (WCMC) oncology fellow Eleni Nackos reported last month at the annual meeting of the American Society of Clinical Oncology (ASCO). At a median follow-up of nearly 5 years, 62 other women in the 75-patient TM trial also had no detectable cancer. Among them were 12 of the 15 other women with stage IV triple negative breast cancer, whose typical median survival is months, with NED status only a temporary reprieve.

Though these are extremely small numbers and the study had no placebo arm, University of Chicago oncologist Olufunmilayo Olopade says she was "blown away" by the data presented at ASCO. "What was so compelling about this study was that they were looking [at] women who were at high risk of recurrence," she adds.

Published by AAAS



Limiting copper in the body may prevent breast cancer, imaged here (pink) in a colored mammogram, from spreading or returning.

PHOTO: EPHYR / SCIENCE SOURCE

Yet the promise of copper depletion appears tarnished—not by clinical results but by corporate strategy. WCMC oncologist Linda Vahdat, who led the trial, now wants to proceed with a larger, phase III trial of TM for triple negative breast cancer. But the rights to treating cancer with TM are held by a Swedish biotech company that is developing the drug instead for Wilson disease, a rare inherited disease of copper accumulation. The company, Wilson Therapeutics, has no immediate plans to test TM in cancer patients, its CEO acknowledges, and for now will not sublicense the drug.

TM, easily synthesized in the lab, has a long history as a copper chelator—a compound that binds and inactivates ionic copper. In veterinary medicine, it cures copper poisoning in sheep, which are very sensitive to copper in their food. Around 1990, George Brewer, a University of Michigan (UM) physician and geneticist, began testing TM in people with Wilson disease.

The cancer connection emerged after work by several research teams showed that copper boosts angiogenesis, the creation of new blood vessels, which solid tumors need to grow and metastasize. Brewer, with colleagues at UM, gave TM to female mice genetically engineered to develop breast tumors. None of the treated animals became cancerous, whereas more than half of control mice did. Under a microscope, says Brewer, he could see dormant, precancerous cells in the treated mice "just sitting there, not growing because they couldn't develop a blood supply."

The mouse work led to a series of human trials of TM in various types of cancers, with disappointing results. Instead of abandoning the drug, Brewer concluded that that copper depletion would be more effective against the microtumors that seed metastases, which differ biologically from the primary tumor. He tried to convince a biotech company, Attenuon, to use TM to prevent recurrence in cancer patients in remission, but the company instead enrolled people with bulk tumors. These trials, too, failed.

Meanwhile, aware of the UM mouse work and studies linking copper to angiogenesis and metastasis, Vahdat organized the current phase II trial. Like Brewer, she concluded that the drug was best deployed in people at risk of recurrence, and she raised money for the small trial from private foundations and cancer nonprofits.

At ASCO, Nackos reported that the drug reduced copper in patients' blood by about half, with few serious side effects. That may have triggered several antitumor mechanisms (see sidebar). For example, TM treatment lowered the number of bone marrow–derived, angiogenesis-promoting cells in blood, probably because copper is needed to activate growth factors important to those cells. TM's "real value is to prevent metastasis," Vahdat says. "And that's by changing the tumor microenvironment … It's a totally different way to treat cancer."

To mount a phase III trial, Vahdat sought Wilson Therapeutics' version of TM because it only needs to be taken once a day. Wilson will provide it at cost, but the company will not fund the trial. And Vahdat's recent application for a $10 million grant from a U.S. Department of Defense program devoted to breast cancer was rejected.

Wilson Therapeutics CEO Jonas Hansson says he has closely followed Vahdat's phase II trial, which he calls "promising." His company is now reviewing all the literature on TM and cancer. "We are in the evaluation phase," Hansson says. "We just can't give these rights [to TM] away, because we ourselves want to understand it first."

The impasse with Wilson had left Vahdat increasingly frustrated. "They have laserlike focus on Wilson's disease, because that's what their investors have invested in," she says. "But they are interested in cancer, and I think ultimately when the timing is right for them, that they will look into it. It's just that I'm ready and raring to go right now." ■

Ken Garber is a writer based in Ann Arbor, Michigan.

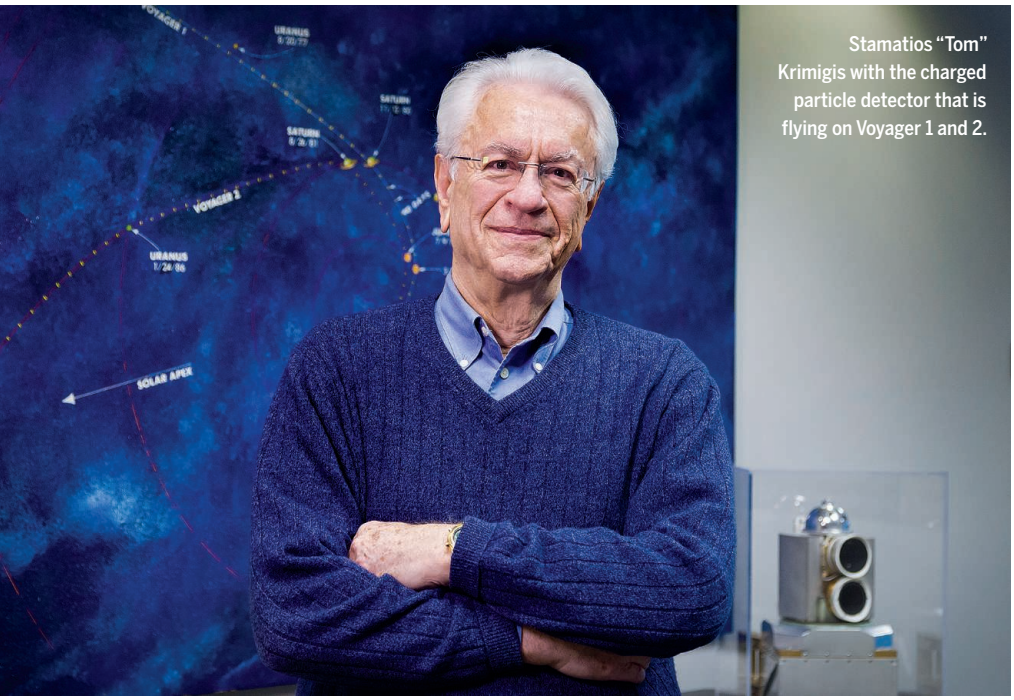
Cancer's copper connections

Dozens of human enzymes incorporate or utilize copper, taking advantage of the metal's readiness to donate or accept electrons to catalyze key biochemical reactions. Tumors, however, may be especially dependent on the metal.

Copper, for example, promotes angiogenesis, the growth of blood vessels that can feed an expanding tumor, and depleting it may keep cancer in check (see main story, p. 128). Nancy Hynes at the Friedrich Miescher Institute in Basel, Switzerland, also reported in 2014 in *Science Signaling* that copper binds and activates the enzyme Memo, which enables tumor cells to move independently and thus metastasize. And in 2014, a Duke University group reported in *Nature* that copper is required for signaling by the mutant BRAF protein, which drives half of melanomas and many other cancers. Duke has recently launched a phase I clinical trial that combines an anticopper drug with a BRAF inhibitor in melanoma patients.

Yet another role for the metal emerged when Janine Erler at the University of Copenhagen found that a copper-containing enzyme called lysyl oxidase-like 2 creates a collagen scaffold for cancer cells to occupy as they spread. In a clinical trial of a copper chelator in breast cancer patients, the enzyme's level fell. "All of these mechanisms might be at play," says pharmacologist Donita Brady of the Duke group. "And maybe what we'll find is that particular cancer types are more susceptible to particular copper-dependent processes." —*K.G.*

Published by AAAS



Stamatios "Tom" Krimigis with the charged particle detector that is flying on Voyager 1 and 2.

PLANETARY SCIENCE

Pluto caps one man's odyssey

NASA veteran Tom Krimigis has been on missions to all of the sun's planets, and beyond

By **Eric Hand**

Ermis, *Aphrodite*, *Aris*, *Días*, *Kronos*, *Ouranos*, *Poseidon*, *Pluton*. Growing up near the beach on the Greek island of Chios, Stamatios "Tom" Krimigis would look for wandering planets in the night sky. "How could I anticipate at the time that I would be one of humanity's representatives [to those bodies]?" asks Krimigis, the former head of the space department at Johns Hopkins University's Applied Physics Laboratory (APL) in Laurel, Maryland. On 14 July, when the New Horizons spacecraft swoops past Pluto, he will become the only person to have visited them all, instrumentally speaking. "It's the stuff dreams are made of."

The Pluto flyby will cap a remarkable half-century of planetary reconnaissance, 50 years to the day after Mariner 4 flew past Mars and returned the first image from another planet. Krimigis, an expert in planetary magnetospheres, had a hand in both missions, as well as in visits to all the other worlds in the solar system. "Timing is certainly critical," says Ed Stone, the project scientist for Voyager, the grand tour of the outer planets that accounted for half of Krimigis's tally. "He's obviously had the right ideas to propose to NASA, time after time."

Born in 1938 in Greece, Krimigis came to the United States at the age of 18 to enroll at the University of Minnesota. The launch of Sputnik in 1957 galvanized him, and many others of his generation, to study physics and space science. After college, he went to the University of Iowa to work for James Van Allen, who had been principal investigator on Explorer 1—the United States' first satellite. It detected the first traces of the belts of protons and electrons, trapped by Earth's magnetic field, that bear Van Allen's name. In 1963, Krimigis recalls, Van Allen asked him a question that was to shape his career: "He said, 'How would you like to be a co-investigator on the first mission to Mars?'"

Scientists wondered whether radiation belts like Earth's existed around other planets. Van Allen was principal investigator for Mariner 4's trapped-radiation detector, designed to answer that question for Mars. The detectors were essentially Geiger counters, which detect the tiny jolts of ionizing radiation but cannot distinguish between x-rays, protons, and electrons. Krimigis's job was to add a solid-state detector that could tell them apart by measuring the energy of incoming particles. "I finally got the thing working about a month before we launched it," he says.

When Mariner 4 flew past Mars on 14 July 1965, Krimigis and Van Allen watched for jitters on a stripchart recorder needle as their data came down at 8.33 bits per second. The needle barely moved: There were no radiation belts at Mars. The first picture was disappointing, too, with none of the hoped-for canals of lore. "It looked like a crater on the moon!" Krimigis remembers. A few years later, Van Allen and Krimigis sent a particle detector to Venus on Mariner 5; no radiation belts turned up there, either.

By the time of the payload selection for the twin Voyager spacecraft in the early 1970s, Krimigis, still focused on charged particles, was ready to compete against Van Allen with an instrument proposal of his own. "The prodigal son was going up against his mentor, and he had a whole team of us young guys," says Louis Lanzerotti, a space physicist at the New Jersey Institute of Technology in Newark, who joined Krimigis on his winning Low Energy Charged Particle (LECP) experiment, designed to detect nuclei of elements heavier than hydrogen or helium.

In 1979, when Voyager 1 and Voyager 2 passed by Jupiter, Krimigis's detectors picked up sulfur and oxygen ions whipped up by the giant planet's powerful magnetic fields. Later, scientists discovered that these elements originated in the volcanoes on Jupiter's moon Io. The two probes went on to Saturn, where they found oxygen ions, fed by the watery geysers of the moon Enceladus. Then, Voyager 2 swung by Uranus and Neptune, and discovered simple belts of protons and electrons.

Krimigis's instruments also explored deep space. The LECP has a scanning motor that sweeps through a near circle and

Planetary pilgrim

Decades of NASA spacecraft have taken Krimigis's instruments on a Grand Tour of the solar system.

MISSION	LAUNCH YEAR	TARGET
Mariner 4	1964	Mars
Mariner 5	1967	Venus
Voyager	1977	Jupiter, Saturn, Uranus, Neptune
MESSENGER	2004	Mercury
New Horizons	2006	Pluto

PHOTO: JOHNS HOPKINS UNIVERSITY APPLIED PHYSICS LABORATORY

Downloaded from www.sciencemag.org on July 10, 2015

Published by AAAS

measures particles from different directions. The motor—still working today after 6.5 million pivots—helped Voyager 1 scientists improvise measurements of the solar wind when a dedicated instrument failed.

It took a while for Krimigis to notch Mercury onto his planetary belt. He missed out on the payload for Mariner 10, which flew past Mercury twice in 1974. Scientists on that mission claimed to find protons—perhaps a small radiation belt trapped by Mercury's magnetic field. But in 2011, APL's MESSENGER mission arrived at Mercury with an innovative particle detector Krimigis had helped design, able to determine the charge and speed of incoming ions with unprecedented precision. It found no protons, only short-lived belts of electrons that the nearby sun's powerful magnetic field disrupts almost as soon as they form.

Now, finally, comes Pluto's visit by New Horizons, a mission that Krimigis helped usher into existence while space department head at APL. He recruited its principal investigator, Alan Stern (*Science*, 26 June, p. 1414), and lobbied Congress to keep the mission afloat in the early 2000s. The charged-particle detector on New Horizons, PEPSSI, is a descendant of the one flown on MESSENGER. Pluto has a thin, wispy atmosphere and probably lacks a magnetic field, so Krimigis isn't expecting to find much more than a few stray protons and electrons. But he's prepared to be surprised: "It's not what you think you're going to find, but the things you don't expect," he says. The New Horizons encounter will return 5000 times as much data as Mariner 4 did at Mars, Stern says.

Norman Ness, a veteran of 21 NASA missions and an emeritus researcher at the University of Delaware in Newark, has nearly as many trophies as Krimigis. In addition to leading a magnetic experiment on Voyager (which netted him the giant planets), he was a principal investigator on Mariner 10, which flew past Venus on its way to Mercury, and a co-investigator on the Mars Global Surveyor. But Ness says he doesn't put much stock in the tallies. "I have never looked upon that as a metric to worry about," he says.

In any case, Krimigis isn't done yet. He's waiting for the telltale signs that Voyager 2 has left the solar system, as Voyager 1 did in 2012, and is preparing for his next project: a turn inward, toward the sun. He is a co-investigator for an ion-measuring instrument on Solar Probe Plus, scheduled to launch in 2018 and fly within the sun's wispy, scorching atmosphere, the corona. Krimigis has been involved in planning the mission since the late 1970s. "My lifelong dream project had always been the solar probe," he says. "It's the first mission to a star." ■

PHOTO: GLOFISH

SCIENCE POLICY

U.S. to review agricultural biotech regulations

New gene-editing methods challenge old framework

By **Kelly Servick**

The White House is ready to modernize the rules that govern inventions in agricultural biotechnology, it announced last week. The multiyear review process should clarify the roles of the agencies now involved in determining the safety of genetically altered plants and animals: the Food and Drug Administration (FDA), the U.S. Department of Agriculture (USDA), and the Environmental Protection Agency (EPA). Another goal: to update the regulatory process in light of precise gene-editing methods, such as CRISPR, which may not require the same review as traditional genetic engineering.

Many researchers and entrepreneurs who have struggled to navigate the current system welcome the planned review. "It's long overdue, certainly," says Peggy Lemaux, a plant biologist at the University of California, Berkeley. Uncertainty about safety and regulatory requirements has kept many academics and small companies from developing new products, she says.



Ornamental fish carrying fluorescent genes were commercialized without federal review.

The federal framework for reviewing agricultural biotech products was laid out in 1986 and updated in 1992—2 years before the slow-ripening Flavr Savr tomato became the first genetically modified (GM) food to hit the market. Since then, new gene-modification strategies have emerged, Lemaux says. "People in 1986 and 1992 didn't have a clue that anything like gene editing would happen."

The outdated framework has resulted in some puzzling regulatory paths, says Todd Kuiken, of the Synthetic Biology Project at the Woodrow Wilson International Center for Scholars, a Washington, D.C.–based think tank. For example, a GM sterile mosquito developed by Oxitec to reduce the spread of dengue fever qualifies as an animal drug, and is currently under review at FDA's Center for Veterinary Medicine.

Meanwhile, commercially sold houseplants that glow thanks to a firefly gene weren't reviewed by either EPA or USDA, in part because their modification didn't rely on agrobacterium—a plant pathogen that was the workhorse of gene transfer when the rules were developed. That lack of regulation "raised a lot of eyebrows," Kuiken says. "It just seemed that there was no one in charge."

The new White House initiative creates a working group of officials from the three agencies to help clarify who is in charge of a given product. Within a year, that group will update the current regulatory framework and develop a long-term strategy to ensure agency evaluations use sound science. How, or even whether, to review products created by CRISPR and similar methods is likely to be a high-profile issue. Rather than introducing whole genes at multiple, unpredictable locations, as earlier methods do, these new techniques can change precise points in the genome, which some argue reduces safety concerns. "There's such a range of modifications that you can create," says Daniel Voytas, a molecular geneticist at the University of Minnesota, Twin Cities, and chief scientific officer at the agricultural biotech Calyxt.

USDA determined that Calyxt's potatoes and soybeans, engineered for longer storage and healthier oil using a CRISPR alternative called TALENs, fall outside its authority for GM plants. But Voytas hopes the White House review will provide clarity on other gene-editing efforts. He wonders, for example, whether editing the genome of a cultivated plant so it has the gene variant of a wild relative—mimicking the result of traditional plant breeding—would require USDA review.

Another responsibility of the new working group: developing a plan for periodic "horizon-scanning" to detect new biotech breakthroughs long before they reach a regulator's desk. ■

Published by AAAS

FEATURES

DEEP SLEEP

Boreholes drilled into Earth's crust get a fresh look for nuclear waste disposal

By **Warren Cornwall**

One of the world's biggest radioactive headaches sits in an aging cinderblock building in the desert near Hanford, Washington, at the bottom of a pool of water that glows with an eerie blue light. The nearly 2000 half-meter-long steel cylinders are filled with highly radioactive cesium and strontium, leftover from making plutonium for nuclear weapons. The waste has been described as the most lethal single source of radiation in the United States, after the core of an active nuclear reactor. It could cause a catastrophe if the pool were breached by an unexpectedly severe earthquake, according to the U.S. Department of Energy (DOE), the waste's owner.

For decades, the federal government has been floundering over what to do with the cylinders. They're too hot to be easily housed with other waste. And the government's quest to create a single permanent burial ground for all the nation's high-level nuclear waste, from both military and civilian activities, is in disarray (see sidebar, p. 135).

Now, a deceptively simple-sounding solution is emerging: Stick the cylinders in a very deep hole. The approach, known as deep borehole disposal, involves punching a 43-centimeter-wide hole 5 kilometers into hard rock in Earth's crust. Engineers would then fill the deepest 2 kilometers with waste canisters, plug up the rest with concrete and clay, and leave the waste to quietly decay.

The idea has been around for decades, but not long ago scientists had all but abandoned it. Over the past 5 years, however, as improved drilling technologies converged with the political and technical woes bedeviling other nuclear waste solutions, boreholes have regained their allure. DOE has gone from spending almost nothing on borehole research to planning a full-scale field test, costing at least $80 million. And earlier this year U.S. Energy Secretary Ernest Moniz gave boreholes a dash of publicity during a major speech, mentioning them as a promising way to deal with the cesium and strontium waste at DOE's Hanford Site nuclear complex.

Boreholes have "been plan B and just missed the boat for years," says nuclear engineer Michael Driscoll, a retired professor from the Massachusetts Institute of Technology (MIT) in Cambridge and one of the concept's leading advocates. "Maybe now is the time."

Many nuclear waste veterans, however, are skeptical. The technical challenges are daunting, they argue, and boreholes won't end political opposition to building new nuclear waste facilities. "The borehole thing to me is a red herring," says attorney Geoff Fettus of the Natural Resources Defense Council (NRDC) in Washington, D.C., which supports underground disposal in a shallower mine, but has sued DOE over now abandoned plans to bury the waste inside Nevada's Yucca Mountain.

Still, even some doubters say that given the current deadlock over nuclear waste, boreholes deserve a second look, at least for those troublesome cylinders at Hanford.

U.S. high-level nuclear waste

70,000
metric tons of civilian waste stored at 75 sites

13,000
metric tons of military waste stored at five sites

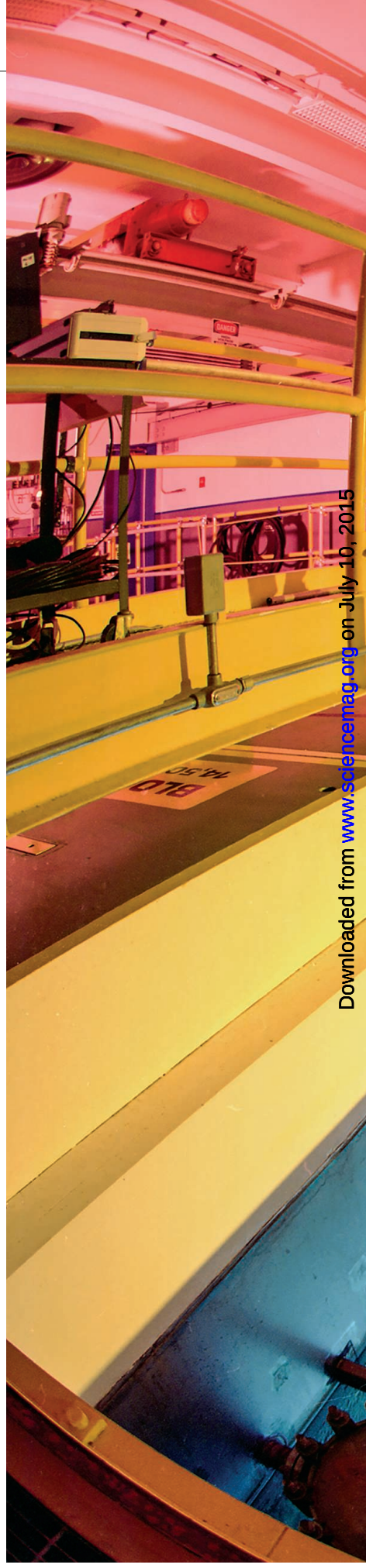


PHOTO: U.S. DEPARTMENT OF ENERGY

Downloaded from www.sciencemag.org on July 10, 2015

Published by AAAS



Borehole advocates say cesium and strontium waste stored at the Hanford site in Washington State could go deep underground.

"If we can move forward with disposing of some of the DOE waste, that's a good thing," says geoscientist Allison Macfarlane, director of the Center for International Science and Technology Policy at George Washington University in Washington, D.C., and a former chair of the U.S. Nuclear Regulatory Commission. "We have to make some progress somewhere."

IF ONE PERSON deserves credit for helping revive U.S. borehole research, it's Driscoll, the retired MIT engineer. Now 80, he has spent more than 25 years quietly exploring the potential for depositing radioactive waste deep in granite bedrock.

Driscoll wasn't the first to pursue the idea; since the 1950s, boreholes have vied with other nuclear waste disposal options, ranging from the improbable (shoot it into outer space or melt it into an ice sheet) to the mundane (stash it in a shallow mine). Ironically, by the time Driscoll got interested in boreholes, U.S. policymakers thought they had settled the issue. In 1987, after years of fierce debate, Congress approved legislation creating a national repository for high-level nuclear waste in a mine carved into Yucca Mountain, roughly 110 kilometers northwest of Las Vegas, Nevada. With that decision, U.S. funding for borehole research largely evaporated.

Driscoll wasn't deterred. Boreholes, he thought, had some potential advantages over a single big facility. For example, they could spread the burden of storing waste that no one wanted, because suitable rock is found across the United States. So even as engineers began to plan the Yucca Mountain repository, Driscoll and a handful of graduate students kept churning out papers delving into borehole costs and technical feasibility.

In one scenario they explored, spent fuel rods are placed in slender canisters that are strung together like sausage links, then lowered into the hole. Even very radioactive material would be safe, advocates say, if placed in the right kind of deep rock: ancient crystalline granite with few cracks that might allow radioactive materials to seep into groundwater or reach the surface. The surrounding rock and the salty water would dissipate heat generated by the waste. And the top 3 kilometers of each hole would be plugged with a layer cake of cement, gravel, and bentonite clay, which swells when wet. The nation's entire cache of high-level waste could fit into 700 to 950 boreholes, at a cost of $40 million per hole (not counting transportation), according to recent estimates by scientists at DOE's Sandia National Laboratories in Albuquerque, New Mexico, who have worked with Driscoll.

Boreholes got their first big break in 2010,

Published by AAAS

when the Obama administration announced that it was abandoning Yucca Mountain after years of delays and resistance from state politicians. The government began looking for other options. That year, Sandia made its first big investment: $734,000 to study how fluid and radioactive particles might behave in a borehole, and how best to seal it. In 2012, a presidential commission added its recommendation for more studies.

Soon after, Moniz became energy secretary. Moniz, a former colleague of Driscoll's at MIT, had already heard his sales pitch about boreholes. In 2003, the two men served together on a study panel that endorsed "aggressively" studying the technology.

This past March, a White House policy shift opened the door further. Moniz announced that the Obama administration would abandon previous plans to put all high-level waste in one spot and instead would seek separate sites for disposing of commercial nuclear waste—about 85% of the total—and military waste. Moniz called some of the defense waste, including Hanford's radioactive cylinders, "ideal candidates for deep borehole disposal."

CESIUM-137 AND STRONTIUM-90 are the hot potatoes of the nuclear waste world, packing a powerful radioactive punch in a relatively short half-life of 30 years. At Hanford, there's barely enough to fill the back of a pickup truck. Yet it contains more than 100 million curies of radiation, roughly one-tenth the radiation in the core of a large nuclear reactor. And it produces enough heat to power more than 200 homes.

To prevent the tubes from causing trouble, they sit under about 4 meters of water in what resembles a giant swimming pool, emanating a blue glow known as Cherenkov radiation as high-energy particles slam into the water. The 1974 building housing the pool is past its 30-year life span, according to DOE's inspector general. Bombarded by radiation, the pool's concrete walls are significantly weakened in places. Some of the tubes have failed and been stuck inside larger containers. In a review of DOE facilities conducted after the 2011 disaster at Japan's Fukushima Daiichi Nuclear Power Station, the department's Office of Environmental Management concluded that the Hanford pool had the highest risk of catastrophic failure of any DOE facility, for example in a massive earthquake, according to a report from the department's inspector general. DOE says it plans to move the pool waste into dry casks for safer storage, but it hasn't said when.

"It's an urgent situation and a huge safety risk," says Tom Carpenter, executive director of the watchdog group Hanford Challenge in Seattle, Washington, which has been critical of DOE's efforts to secure the waste.

Borehole advocates point out that the Hanford tubes are less than 7 centimeters in diameter, narrow enough to fit down a hole without extensive repackaging. All could fit into a single shaft. Other military waste could also go down a borehole, advocates add. One candidate is plutonium that DOE has extracted from dismantled nuclear weapons. Most of it is currently stored as softball-sized metal spheres at a DOE facility in Texas. In contrast to Hanford's cesium and strontium, the plutonium is fairly cool, but extremely long-lived, with a half-life of 24,000 years. DOE is considering other options for the plutonium, including turning it into fuel for nuclear reactors or combining it with other nuclear waste and burying it. But boreholes could be an effective way to put it far out of the reach of anyone trying to lay their hands on bomb-making material.

Yet borehole disposal is not as straightforward as it might seem. The Nuclear Waste Technical Review Board, an independent panel that advises DOE, notes a litany of potential problems: No one has drilled holes this big 5 kilometers into solid rock. If a hole isn't smooth and straight, a liner could be hard to install, and waste containers could get stuck. It's tricky to see flaws like fractures in rock 5 kilometers down. Once waste is buried, it would be hard to get it back (an option federal regulations now require). And meth-

A rocky tomb for the most dangerous waste

Boreholes envisioned for holding highly radioactive waste would be far deeper than proposed or existing underground disposal. In one version, waste canisters would sit in the lowest part of the hole (right, inset). The upper 3 kilometers would be sealed with layers of clay, rocks, and cement.

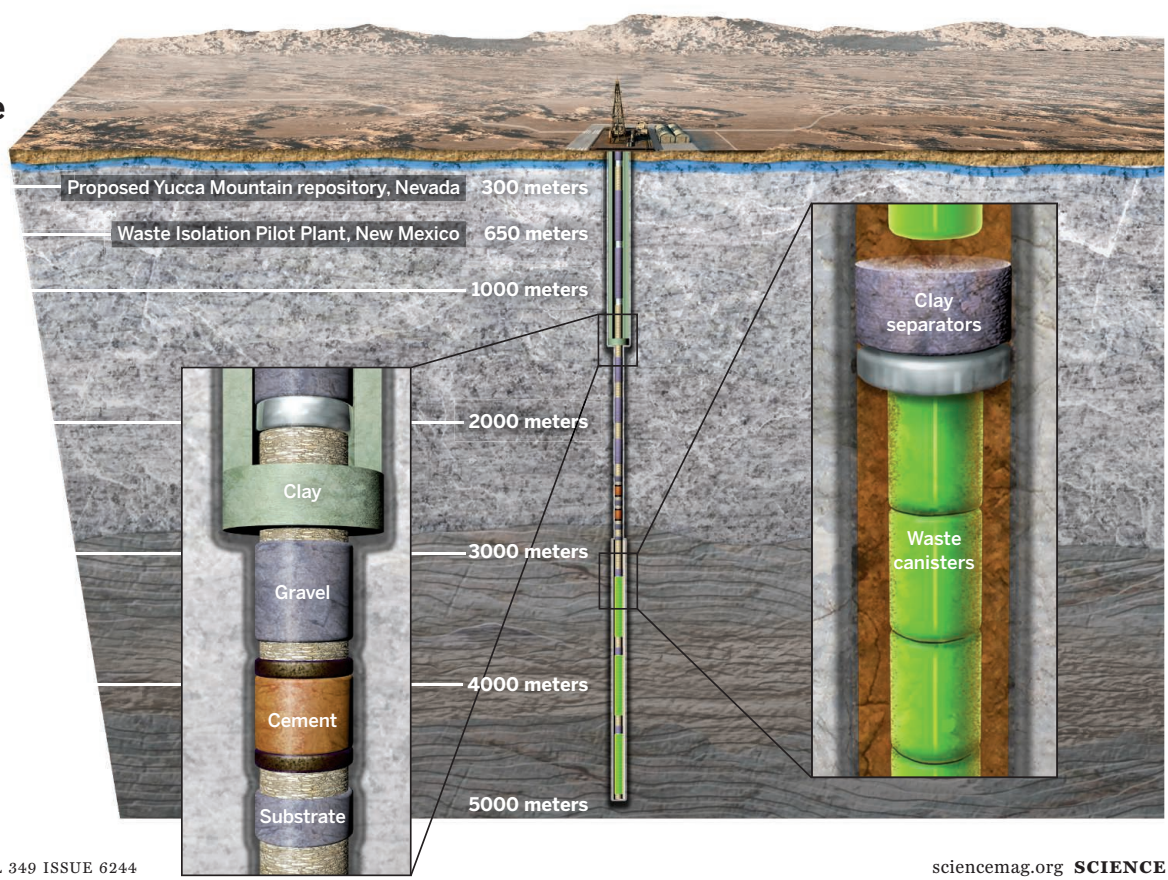


ILLUSTRATION: NICOLLE R. FULLER

Published by AAAS

ods for plugging the holes haven't been sufficiently tested. "These are all pretty daunting technical challenges," says the board's chair, geologist Rod Ewing, of Stanford University in Palo Alto, California.

Even if those technical problems are surmounted, boreholes might solve only a fraction of the nation's waste problem. That's because much of the high-level waste simply wouldn't fit down a hole without extensive repackaging. "Due to the physical dimensions of much of the used nuclear fuel, it is not presently considered to be as good of a candidate [for borehole disposal] as the smaller waste forms," said William Boyle, director of DOE's Office of Used Nuclear Fuel Disposition Research and Development, in a statement to *Science*. Spent fuel rods from commercial power reactors, for instance, are often bundled into casks that are about 2 meters across.

Then there's the same problem that dogged Yucca Mountain: the politics of finding a place to drill the holes. "Let's just assume [boreholes] could work better than anybody ever imagined," says Fettus, the NRDC attorney. "You still wouldn't solve the nut that everyone has been unable to solve": persuading state and local governments to take on waste from across the nation.

DESPITE THESE CHALLENGES, Sandia scientists are moving forward with a 5-year plan to drill one or more 5-kilometer-deep boreholes. Pat Brady, a Sandia geochemist helping plan the tests, is optimistic. "There's a lot of institutional experience with drilling holes in the ground," he says.

The drilling technology is better than ever, he says. Drillers have gained valuable experience boring deep holes into hard rock for geothermal energy, and improved rigs can more easily and accurately drill deep, straight holes. The Sandia team is currently looking for a U.S. site for the first test hole, with a plan to start drilling in the fall of 2016.

Besides seeing if they can cost-effectively drill a hole that's deep and wide enough, they also want to test methods for determining whether the rock is solid and whether any water near the bottom of the hole is connected to shallow groundwater. Then they will lower a model waste canister down the hole to see if it gets stuck.

Other nations with nuclear waste, including China, are watching. But, for now, the United States is the only country getting ready to drill. "Nobody else has stepped forward," says Geoff Freeze, a nuclear engineer at Sandia who is overseeing the U.S. experiment. "It kind of fell to us." ■

Warren Cornwall is a freelance journalist in Bellingham, Washington.

PHOTO: U.S. DEPARTMENT OF ENERGY

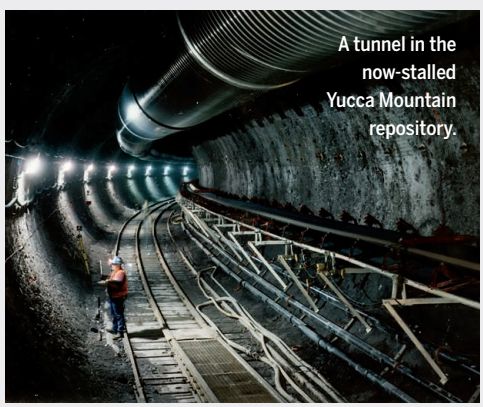
Rolling out a welcome mat for waste

By **Warren Cornwall**

Five years ago, the United States abandoned its decades-long effort to find a permanent home for its growing cache of high-level nuclear waste. That opened the way for alternative schemes, such as burying some waste in deep boreholes (see main story, p. 132). And, in a surprising twist, the move has launched a bidding war between landlords eager to house the waste.

In recent months, communities in the pan-flat desert where New Mexico's southeast corner pokes against Texas have declared their desire to temporarily store spent fuel from nuclear power plants. Long known for oil derricks and cattle drives, the region "is remote, it's dry, and it has people who are willing to consider something people in other parts of the country aren't willing to consider," says Bill Jones, an attorney in Austin and a founder of AFCI Texas, one of at least three companies angling to site a new waste facility in the area.

Facing stiff opposition from Nevada politicians and others, President Barack Obama announced in 2010 that his administration was abandoning a plan to build a single repository deep beneath the state's Yucca Mountain. Now, federal officials are considering creating a temporary storage site for commercial waste (about 85% of the total), while hunting for separate permanent disposal sites for military and commercial waste. They are focusing on working with states and communities that, unlike Nevada, actually want the waste.



A tunnel in the now-stalled Yucca Mountain repository.

The desert borderland is already a hotbed of nuclear entrepreneurship. The New Mexico side hosts the federal Waste Isolation Pilot Plant near Carlsbad, which started taking lower level waste—mostly plutonium-contaminated clothes and tools—in 1999. (It has been temporarily closed since 2014 as the result of a container leak.) Not far away is a $4 billion factory that enriches uranium for nuclear power plants, opened in 2010 by an arm of Urenco, a U.K.-based company. In nearby Texas is the country's largest private nuclear waste dump, opened in 2012 by the Dallas-based company Waste Control Specialists (WCS). The sprawling 5600-hectare compound takes low-level commercial waste from Texas and 34 other states.

Now, there's a cross-border duel over getting some of the country's 70,000 metric tons of spent nuclear fuel. This past February, WCS announced that it is seeking a license from the U.S. Nuclear Regulatory Commission to temporarily house approximately half the current stock. In April, an alliance of local governments in New Mexico's Eddy and Lea counties unveiled a competing plan.

Both proposals have won endorsements from key state politicians. But not everyone likes the idea. New Mexico's two U.S. senators, for instance, say they won't back a temporary storage site until the federal government has a plan for disposing of the waste for good. And environmentalists warn of being permanently saddled. "Since there's no [permanent] disposal site, interim could essentially be forever," says Don Hancock, director of the nuclear waste program at the Southwest Research and Information Center, a nonprofit based in Albuquerque, New Mexico.

Meanwhile, some in Congress want to restart the Yucca Mountain project in Nevada, encouraged in part by the impending retirement of Senator Harry Reid (D–NV), long a powerful and implacable foe. But definitive action on Yucca Mountain, or any other permanent burial site, could be years away. Meanwhile, down on the Texas–New Mexico border, WCS says it could start taking spent fuel by 2020. ■

Published by AAAS

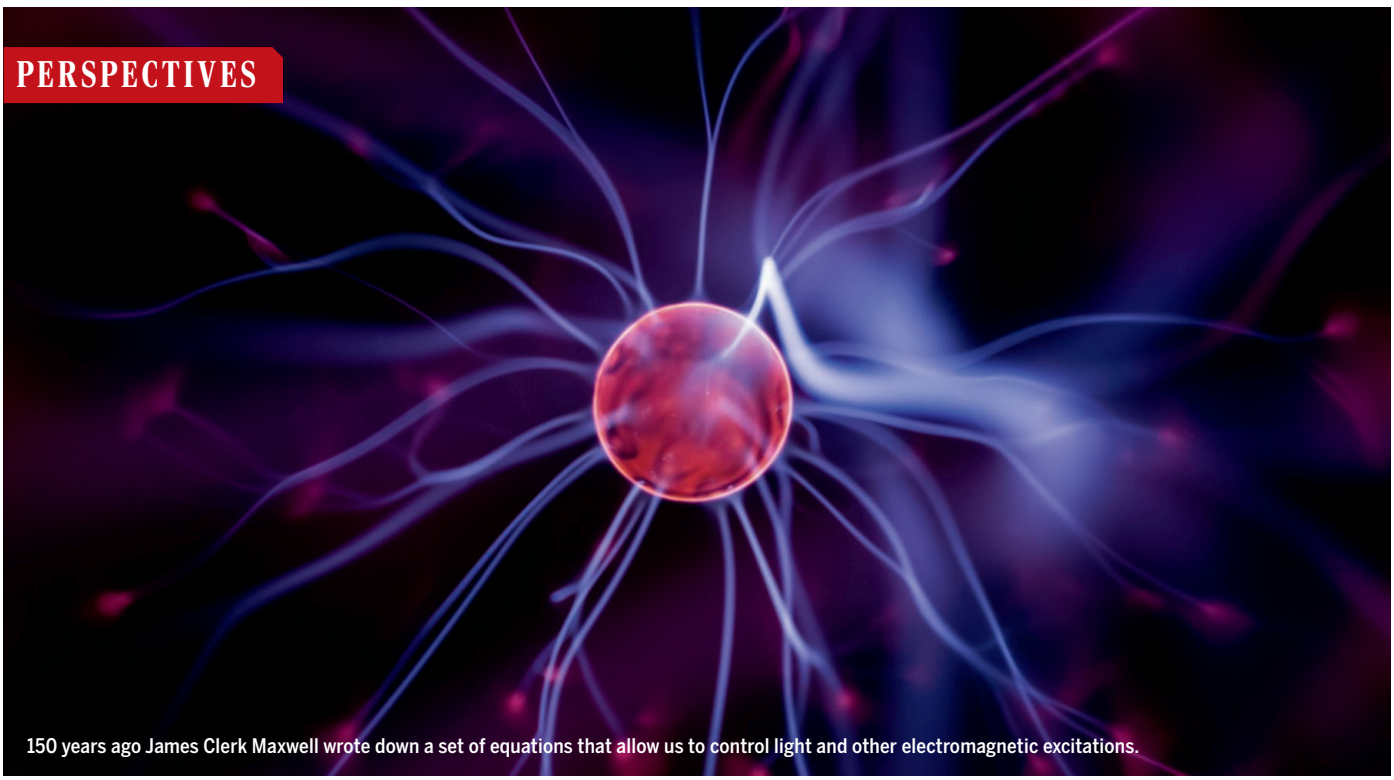
INSIGHTS

How to foster scientific creativity *p. 141* ▸

Precautionary policy for mining the deep seabed *p. 144*



PERSPECTIVES



150 years ago James Clerk Maxwell wrote down a set of equations that allow us to control light and other electromagnetic excitations.

OPTICS

150 years of Maxwell's equations

Powerful tools are available for the manipulation of electromagnetic fields

By **Nader Engheta**

On page 499 of his 1865 paper (*1*), James Clerk Maxwell wrote, "The agreement of the results seems to show that light and magnetism are affections of the same substance, and that light is an electromagnetic disturbance propagated through the field according to electromagnetic laws." With that knowledge, he changed the world forever. In the span of 150 years since his celebrated paper, numerous scientific discoveries and technological innovations have originated from Maxwell's equations. Electromagnetic and optical waves can be manipulated, tailored, and controlled by means of materials, and consequently, during the past one and a half centuries, materials science and engineering has always played the key roles in taming these waves for the purpose of inventing new functional devices. Early examples include radio-frequency antennas, lenses and mirrors, microwave waveguides, optical fibers, and telegraph transmission lines, to name just a few. Recent developments in nanoscience and nanotechnology, materials science and technology, and condensed matter physics has made it possible to conceive materials and structures with atomic-level controllability and with unprecedented properties not otherwise present in naturally available materials. These developments have opened doors to numerous opportunities to shape and sculpt light at the nano-, micro- and mesoscales in a desired fashion.

Ushering photons into desired paths requires the design of structures with proper inhomogeneity in material parameters such as permittivity and/or permeability. A good example of such photon traffic control can be achieved with defects within photonic crystals (*2*), where periodic arrays of permittivity variations with photonic band gaps analogous to the electronic band structures for electrons, provide paths for light to propagate (see the figure, panel A). Although bending light has been traditionally done by reflection and refraction of rays through surfaces based on Snell's law, the advent of metamaterials and metasurfaces is now supplying us with transformation optics (*3*) and generalization of Snell's law (*4*, *5*) for tailoring fields at subwavelength scales, opening up possibilities for exciting scenarios such as cloaking, light concentration, optical illusion, and flat photonics. Another paradigm for manipulation of light at the nanoscale is achieved

IMAGE: DUBASSY/THINKSTOCK

Downloaded from www.sciencemag.org on July 10, 2015

Published by AAAS

by optical metatronics (*6*), in which deeply subwavelength structures function as "lumped" optical circuit elements (analogous to the resistor, inductor, and capacitor elements in electronics). This unifying circuit paradigm furnishes "common alphabets" between electronics and photonics, allowing transfer of ideas and designs between these two fields. Collections of nanoparticles, when properly designed and suitably juxtaposed, form optical nanocircuits with unprecedented capability of information processing at subwavelength regions (see the figure, panel B). One can then envision designing materials that tailor light-matter interaction in order to perform optical signal processing at the nanoscale, e.g., performing mathematical operations such as differentiation and integration as light passes through such materials and structures (*7*). Perhaps the notion of doing math with light in materials might also be extended to solving equations with light if properly designed nanostructures could be used.

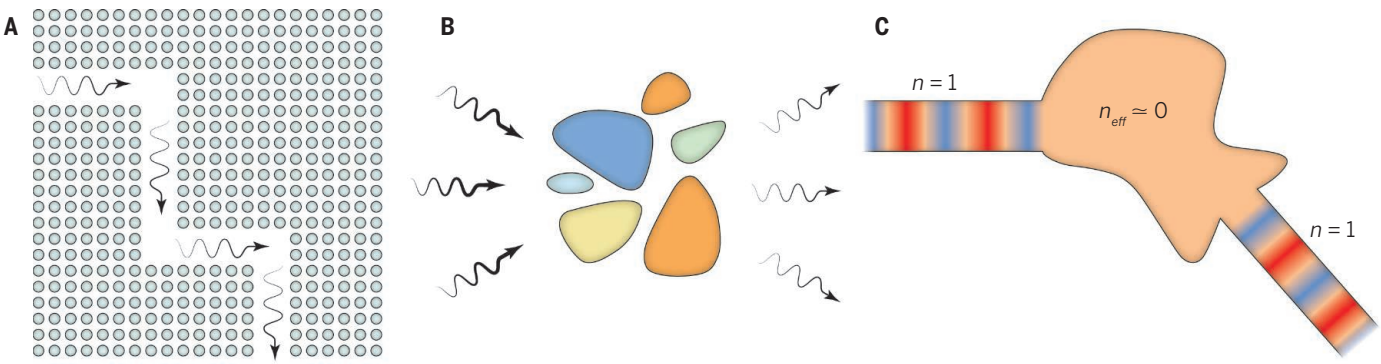
The ability to synthesize materials with desired parameters now offers opportunities to take manipulating the Maxwell equations to the "extreme." For example, two-dimensional materials such as the graphene have brought previously unimaginable possibilities to photonics.

The propagation of highly confined electromagnetic surface waves in the form of surface plasmon polaritons along the graphene sheet has been demonstrated (*8*, *9*), which makes it possible to envision optical devices just one atom thick. Other low-dimensional materials such as hexagonal boron nitride (hBN) and molybdenum disulfide (MoS_2) are also attracting attention as new platforms for manipulating light. Another extreme scenario is highly confined concentration of light using plasmonic nanoantennas (*10*). Antennas, which have been traditionally used to convert the confined electromagnetic energy in subwavelength regions into the far-field radiation, have been instrumental in the development of numerous fields, such as wireless communications and satellite technology. Shrinking conventional radio frequency antennas into the nanophotonics arena raises the possibility of using suitably designed metallic nanostructures to concentrate light in deeply subwavelength volumes with high field intensity. This has opened new frontiers in detection, sensing, and emission control, such as nanoantenna-enhanced surface-enhanced Raman spectroscopy, and engineering spontaneous emission of quantum dots (*11*).

Adding nonreciprocity to the optics of nanoantennas by using magnetized magneto-optical materials results in phenomena such as near-field optical energy rotation. These effects would be enhanced due to the plasmonic resonance of such nanoantennas and the high intensity of optical fields in their vicinity. This can be a basis for nonreciprocal optical devices, such as circulators, at the nanoscale. As a final example of extreme manipulation of waves, metamaterials with effective parameters near zero bring an entirely new set of mechanisms for tailoring fields and waves (*12*). As relative permittivity and/or relative permeability attain near-zero values in a properly designed metamaterial, the effective refractive index approaches zero, causing the effective wavelength to become very large for the operating frequency. Therefore, the phase of steady-state signals within such a structure is spatially uniform, implying that the structure appears to be subwavelength electromagnetically regardless of its shape and size.

For example, two waveguides linked by a near-zero effective-index junction would operate as though they were connected directly to each other (see the figure, panel C). This may have important implication in both classical and quantum optics, in which the distance between two points (two observers, two emitters, or an observer and an emitter), although they may be physically far apart, would behave as if they were close together. This effect will present interesting possibilities for long-range collective emission, quantum entanglement, and cavity quantum electrodynamics, involving such extreme structures.

James Clerk Maxwell could not have imagined that 150 years later his predicted electromagnetic waves would be manipulated in numerous manners due to developments in science and technology. One would wonder where our world would have been without his ingenious and elegant equations. ■



Manipulating electromagnetic fields and waves. (**A**) Photonic crystals as a platform for photon traffic control. (**B**) Optical metatronics, i.e., a collection of nanostructures with properly selected shapes, sizes, and materials, as lumped circuit elements for manipulating and processing optical fields and waves at subwavelength scales. (**C**) "Extreme" metamaterials with near-zero effective refractive index, providing a spatially uniform phase in a bounded region of space that functions as an "electromagnetic point" connecting two distant ports (*12*).

University of Pennsylvania, Department of Electrical and Systems Engineering, Philadelphia, PA 19104, USA.
E-mail: engheta@ee.upenn.edu

REFERENCES AND NOTES

1. J. C. Maxwell, *Philos. Trans. R. Soc. Lond.* **155**, 499 (1865).
2. E. Yablonovitch, *Phys. Rev. Lett.* **58**, 2059 (1987).
3. J. B. Pendry, D. Schurig, D. R. Smith, *Science* **312**, 1780 (2006).
4. N. Yu *et al.*, *Science* **334**, 333 (2011).
5. X. Ni, N. K. Emani, A. V. Kildishev, A. Boltasseva, V. M. Shalaev, *Science* **335**, 427 (2012).
6. N. Engheta, *Science* **317**, 1698 (2007).
7. A. Silva *et al.*, *Science* **343**, 160 (2014).
8. Z. Fei *et al.*, *Nature* **487**, 82 (2012).
9. J. Chen *et al.*, *Nature* **487**, 77 (2012).
10. M. Agio, A. Alù, *Optical Antennas* (Cambridge Univ. Press, Cambridge, 2013).
11. Y. C. Jun, R. Pala, M. Brongersma, *J. Phys. Chem. C* **114**, 7269 (2010).
12. A. M. Mahmoud, N. Engheta, *Nat. Commun.* **5**, 5638 (2014).

ACKNOWLEDGMENTS

This work is supported in part by the U.S. Air Force Office of Scientific Research (AFOSR) Multidisciplinary University Research Initiatives (MURI) grant numbers FA-9550-12-1-0488 and FA9550-14-1-0389.

10.1126/science.aaa7224

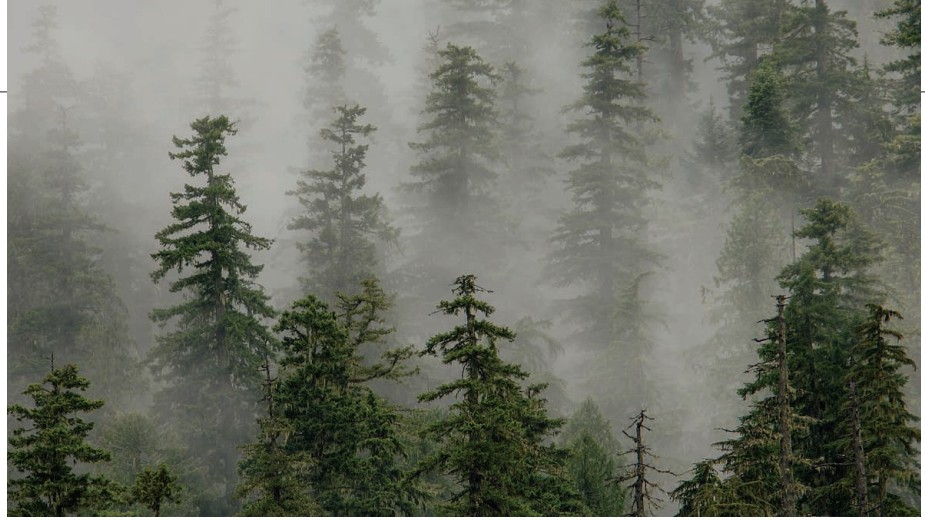
Published by AAAS

HYDROLOGY

Water, bound and mobile

Isotopic data help to resolve global hydrologic fluxes

By **J. Renée Brooks**



Transpiration and evaporation, intermingled. This old-growth Douglas fir forest in Oregon, USA, illustrates how intermingled transpiration and evaporation complicate measurement of the separate fluxes.

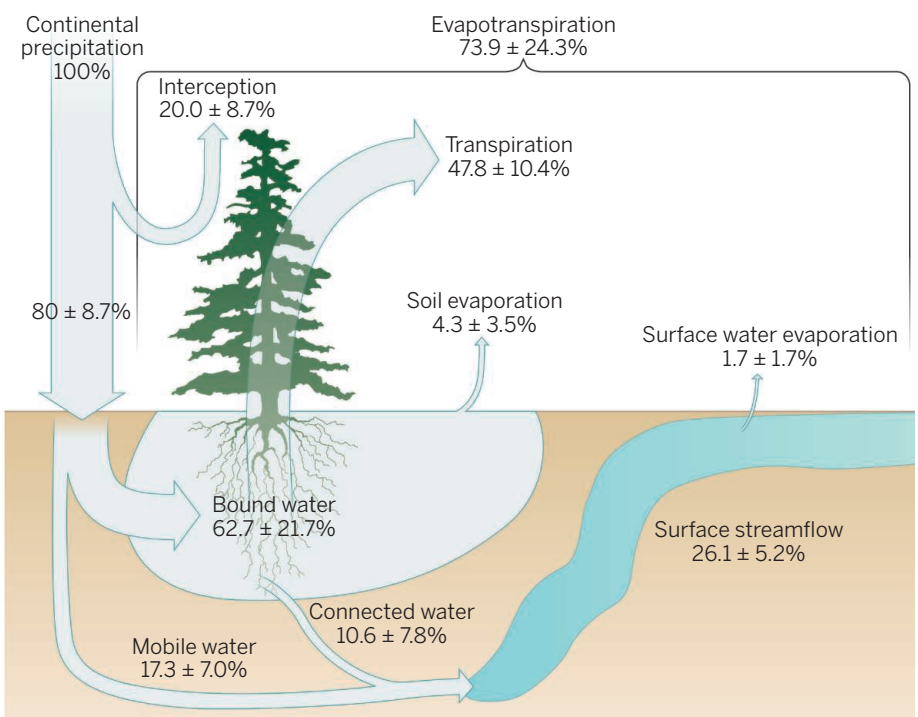
How much water is exchanged between the atmosphere and the land and ocean surfaces every year? The answer is important for developing accurate models of Earth's water cycle both now and in a warmer future climate. Good *et al.* recently reported high-resolution data on hydrogen water isotopes from the Tropospheric Emissions Spectrometer (TES) aboard NASA's Aura satellite (*1*). On page 175 of this issue, Good, Noone, and Bowen (*2*) use these data to estimate global values for plant transpiration, streamflow, and evaporation from various sources.

The authors estimate the mean global value for plant transpiration (the water that moves from the soil through plants to the atmosphere) to be 48% of continental precipitation. A further 26% of continental precipitation returns to the oceans as streamflow (see the figure). The remainder is evaporation from the following components: precipitation intercepted by plant canopies (20%), soil water (4.3%), and surface water (1.7%). Separately measuring the amount of transpired water and evaporated water is methodologically challenging (see the photo). Most commonly, evaporation and transpiration are measured as one water flux leaving the land surface (evapotranspiration). Good *et al.* estimate the proportion of water transpired to be 64% of total evapotranspiration, which is comparable to the median value of 61% from the limited field data sets available (*3*).

Resolving the global transpiration flux is critical to constraining global carbon cycle models because carbon uptake by photosynthesis in terrestrial plants (gross primary productivity, GPP) is directly related to water lost through transpiration. Quantifying GPP globally is challenging (*4*) because GPP can only be measured directly at the leaf level. By adding water isotopic constraints to models of global hydrologic fluxes, Good *et al.* dramatically narrow the potential range of transpiration/evapotranspiration, and thus the range for GPP. Using the simple assumption that, on average, plants lose ~300 water molecules for every CO_2 molecule captured by photosynthesis, their transpiration estimate (55,000 km^3/year) equates to a GPP of ~120 Pg C/year, which is similar to modeled estimates (*4*–*6*). Future work will likely resolve these fluxes simultaneously by integrating the hydrologic isotopic data with the global isotopic tracers of CO_2 measured by NOAA's Global Greenhouse Gas Reference Network.

To model the hydrologic fluxes from the global water isotope budget, Good *et al.* restrict the degree of mixing between water bound by the soil (where evaporation and transpiration occur) and mobile soil water (which ends up in surface water returning to the ocean). They define hydrologic connectivity between bound and mobile water as the proportion of surface water that has interacted with soil-bound water and has thereby acquired some isotopic signature from soil evaporation.

In their Monte Carlo simulations, 38 ± 28% of surface waters mixed with soil-bound water, which translates to 10 ± 8% of continental precipitation (see the figure). This decoupling was necessary in their model because their earlier work (*1*) pointed to differences in the hydrogen isotope composition between the global evapotranspiration flux (–40.0 per mil) and global runoff to the ocean (–77.3 per mil). In the current study, Good *et al.* could only simulate this isotopic difference by disconnecting bound and mobile



Global hydrologic fluxes. Good *et al.* use global water isotope data to resolve the world's hydrologic fluxes. Connected water is the fraction of bound water that drains into the mobile water pool, a factor that was critical to resolving their model.

SCHEMATIC: P. HUEY/*SCIENCE*; PHOTO (TOP): THOMAS IRACI

Western Ecology Division, National Health and Environmental Effects Laboratory, Office of Research and Development, U.S. Environmental Protection Agency, Corvallis, OR 97333, USA. E-mail: brooks.reneej@epa.gov

Downloaded from www.sciencemag.org on July 10, 2015

Published by AAAS

pools to some extent. This leads to their startling finding that most water flowing within streams to the ocean has not interacted with soil-bound water used by plants.

These results demonstrate the importance of bound and mobile water. Hydrologists have long recognized that water flows rapidly in preferential flowpaths and slowly through the soil matrix; however, they assumed that new water entering the soil displaces older resident water, pushing it farther along to the stream (*7*). On the basis of isotopic evidence, I and others (*8*) proposed that water contained in small pores in the soil matrix was isolated from fast water flowpaths. For a small watershed in the Pacific Northwest, USA, we observed that stream and soil water were isotopically distinct and hypothesized that hydrologic separation between these water pools was responsible. Goldsmith *et al.* (*9*) have reported similar results in a seasonally dry tropical montane cloud forest in central Veracruz, Mexico. Good *et al.*'s simulations indicate that hydrologic separation of bound and mobile water must be a widespread phenomenon.

Hydrologic fluxes through soils transport nutrients and other contaminants to surface waters, causing billions of dollars in damage to downstream ecosystems (*10*). Given that bound water contains higher nutrient concentrations than does mobile water, knowing how bound and mobile water interact could help to manage and predict fluxes of pollutants. However, current conceptual models for runoff generation and biogeochemical fluxes will require substantial revisions to include this ecohydrologic separation of bound and mobile water (*11*). Indeed, McDonnell (*7*) emphasized that investigating how, where, and when ecohydrologic separation occurs is one of the great challenges of hydrology. The magnitude of and mechanisms behind ecohydrologic separation are likely to be spatially and temporally diverse. Nonetheless, Good *et al.*'s study indicates the importance of ecohydrologic separation on hydrologic fluxes at the global scale, further illustrating the need for understanding how mobile water interacts with bound soil water. ■

REFERENCES

1. S. P. Good, D. Noone, N. Kurita, M. Benetti, G. J. Bowen, *Geophys. Res. Lett.* 10.1002/2015GL064117 (2015).
2. S. P. Good, D. Noone, G. Bowen, *Science* **349**, 175 (2015).
3. W. H. Schlesinger, S. Jasechko, *Agric. For. Meteorol.* **189–190**, 115 (2014).
4. L. R. Welp *et al*, *Nature* **477**, 579 (2011).
5. M. Jung *et al*, *J. Geophys. Res.* **116**, G00J07 (2011).
6. C. J. Still *et al*., *Global Biogeochem. Cycles* **17**, 6-1 (2003).
7. J. J. McDonnell, *WIREs Water* **1**, 323 (2014).
8. J. R. Brooks *et al*., *Nat. Geosci.* **3**, 100 (2010).
9. G. R. Goldsmith *et al*., *Ecohydrology* **5**, 779 (2012).
10. D. J. Sobota *et al*., *Environ. Res. Lett.* **10**, 025006 (2015).
11. F. M. Phillips, *Nat. Geosci.* **3**, 77–78 (2010).

10.1126/science.aac4742

HIV

The modern era of HIV-1 vaccine development

Current vaccine designs are on the path to eliciting antibodies that neutralize HIV-1

By **John R. Mascola**

More than 30 years after the discovery of HIV-1, where are we in our quest to develop a vaccine that could prevent human infections and help stem the global HIV-1 pandemic? The truth is, unfortunately, that we are not yet close. Even at the laboratory bench, we do not have a vaccine that can induce cross-reactive neutralizing antibodies—the type of response likely needed to provide high-level protective immunity (*1*, *2*). This goal of inducing neutralizing antibodies has proved especially intractable and remains a focus of HIV-1 vaccine researchers. A major culprit in this story is the structurally complex surface envelope glycoprotein (Env) that mediates entry of HIV-1 into host cells (*3*). On pages 154, 191, and 156 of this issue, Sanders *et al.* (*4*), Chen *et al.* (*5*), and Jardine *et al.* (*6*), respectively, and another study (*7*), provide new insights into the nature of the HIV-1 Env trimer, its potential use as a vaccine, and how the humoral immune system generates antibodies with the necessary characteristics to neutralize HIV-1.

Env is composed of three identical precursor glycoprotein molecules (gp160) that are cleaved into a surface component (gp120) and a membrane component (gp41), which noncovalently associate to form the entry-competent Env trimer—also called the viral spike. HIV-1 Env resists neutralization by a combination of remarkable antigenic diversity and concealing critical epitopes via its quaternary structure and heavy glycosylation. Moreover, antibodies must undergo extensive evolution (somatic hypermutation) to gain the ability to recognize the native trimer and block HIV-1 infection (*1*, *8*) (see the figure).

Shortly after the discovery of HIV-1, the viral genes for gp160 and gp120 were cloned and encoded into viral vaccine vectors or expressed as recombinant protein vaccines. However, these envelope vaccines did not elicit broadly reactive neutralizing antibodies, and gp120 protein vaccines failed to protect against HIV-1 infection in human efficacy trials (*2*). The RV144 vaccine trial, which used a pox virus prime and gp120 boost, showed a modest 31% protective efficacy (*2*). There is now a sense of why these vaccines were suboptimal, and how to address the problem. A key concept is that much of the antigenic surface of a monomeric gp120 molecule is buried within trimeric Env, and thus, most antibodies elicited by gp120 do not bind the functional viral spike (*3*). The solution to this problem is conceptually simple—express the native Env trimer as a vaccine immunogen. Technically, this is a challenge, partly because the noncovalent interactions between gp120 and gp41 do not allow for trimer stability outside the context of the viral membrane.

Sanders *et al.* solved this problem by engineering a protein with specific disulfide bonds to hold gp120 and gp41 together called BG505 SOSIP; BG505 is the strain of virus used to make the protein, SOS refers to the disulfide bond, and IP is a specific mutation of gp41 required for SOSIP trimer stability (*9*). The authors have now used BG505 SOSIP to immunize rabbits and monkeys. To a casual reader, their results would seem disappointing: The vaccine elicited neutralizing antibodies to the autologous virus (matching the vaccine), and not to heterologous viruses. Because HIV-1 is genetically diverse, this trimer has certainly not solved the HIV-1 vaccine problem. The key question is whether these results are a first step on a pathway to generate more cross-reactive responses. Some of these next steps are already underway, including development of alternative strains and platforms to make additional trimers (*10*) and the ability to further stabilize the trimer to potentially improve its immunogenicity (*11*). In this regard, Chen *et al.* report the ability to produce near-homoge-

> ***"...where are we in our quest to...stem the global HIV-1 pandemic?"***

Vaccine Research Center, National Institute of Allergy and Infectious Diseases, National Institutes of Health, Bethesda, MD 20892, USA. E-mail: jmascola@mail.nih.gov

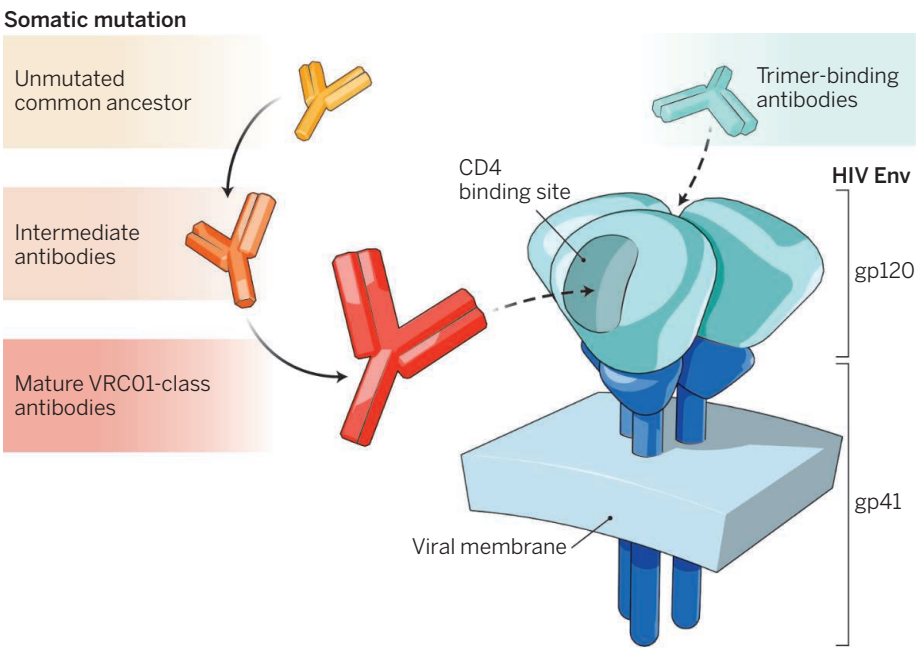
Published by AAAS

neous native Env trimers on the cell surface of stably transfected cell lines. Interestingly, they demonstrate that alterations made to the intracytoplasmic region of gp41, something that is routinely done when soluble gp140 proteins are expressed, can adversely affect trimer conformation and antigenicity.

Although native trimers provide a major new tool for HIV-1 vaccine research and development, there is still the problem that high levels of somatic mutation, and in some cases preferential immunoglobulin variable gene usage, are required for effective neutralization. Antibodies to the CD4 binding site on gp120 are of particular interest because they bind to a functionally conserved region on the virus. A major category of such antibodies, called the VRC01 class, can neutralize HIV-1 by mimicking the interaction of the cellular receptor CD4 with gp120. Importantly, VRC01-class antibodies are found in multiple HIV-1–infected donors and, hence, appear to represent a reproducible solution to targeting a vulnerable site on the HIV-1 trimer (*12*). All VRC01-class antibodies have two key immunological characteristics: They derive from the same heavy-chain variable gene allele, VH1-2*02, and they have a short (five amino acid) CDR3 region of the light chain—needed to avoid clashes with parts of the Env trimer.

To study how the immune system pairs this unusual short light chain with the VH1-2*02–derived heavy chain, Jardine *et al.* and Dosenovic *et al.* (*7*) generated transgenic mice that express the full human heavy chain of a VRC01-class antibody. Antibody-producing B cells from these mice preferentially express the human VH1-2*02–derived heavy chain, but importantly, the murine light chain repertoire is intact. Jardine *et al.* generated mice that expressed the near-germline (i.e., unmutated) heavy chain of the VRC01 antibody and then immunized the mice with a modified gp120 protein specifically engineered to engage this antibody. Notably, less than 0.1% of mouse light chains have the required characteristics to produce an appropriate VRC01-class neutralizing antibody. Yet, over 90% of vaccine elicited B cells targeting the CD4 binding site region that contained the appropriate five–amino acid light chain. The results are illuminating—they suggest that with appropriate antigenic stimulation, the rare immunoglobulin gene rearrangements required to produce neutralizing antibodies are efficiently produced. Importantly, the antibodies generated were unable to neutralize HIV-1—they were early VRC01 precursor antibodies that would likely require further somatic mutation to display effective virus neutralization.

Dosenovic *et al.* engineered mice to express the germline-reverted VRC01-class antibody called 3BNC60, and immunized these mice with engineered variants of gp120. They demonstrate the generation of some 3BNC60 precursor antibodies—but again without neutralizing activity. However, in transgenic mice expressing the mature 3BNC60 heavy chain, immunization with the BG505 SOSIP trimer produced measurable amounts of serum neutralization by VRC01-class antibodies. Antigen-specific B cells were cloned, and the antibodies they produced contained the expected mature 3BNC60 heavy chain and the necessary five–amino acid CDR3 light-chain motif. Overall, the results of Jardine *et al.* and Dosenovic *et al.* show the proficiency of the humoral immune system in pairing rare light chains with the appropriate heavy chain to produce effective antibodies.



Stimulating antibody lineages. The ability to express the native HIV-1 Env trimer as a recombinant protein is a major step forward for vaccine development. Through somatic mutation, an antibody lineage evolves from its unmutated common ancestor, through a series of intermediates, to a mature form that can neutralize the virus. Current vaccine designs, such as the BG505 SOSIP and engineered gp120 variants, appear to stimulate intermediate antibodies.

How do these four studies advance the potential for an effective HIV-1 vaccine? As a first step, they show that we can now immunize with authentic native trimer proteins—and thus, there is a greater potential to generate antibodies that will recognize the functional viral spike and neutralize the virus. Single trimer proteins are just a first step, but they should provide the necessary framework from which to design more effective vaccine immunogens. The studies also demonstrate proof of concept that HIV-1 Env immunogens can be modified, based on our knowledge of structure and immune recognition, and that such immunogens can efficiently engage the appropriate naïve B cells.

Based on our understanding of the circumstances that lead to the generation of broadly neutralizing antibodies in HIV-1–infected individuals (*13*, *14*), success achieved through immunization will likely require various sequential immunogens and iterative human trials. Whether specifically engineered smaller portions of Env, or the full trimer—or perhaps both—will be needed for driving difficult-to-induce B cell lineages should be determined in these immunization trials. We now have novel vaccine immunogens along with an understanding of immune pathways leading to effective antibodies, and the technologic tools to study the B cell response in detail. It may be reasonable to conclude that we have finally entered the modern era of HIV-1 vaccinology. ■

REFERENCES AND NOTES

1. F. Klein *et al.*, *Science* **341**, 1199 (2013).
2. L. E. McCoy, R. A. Weiss, *J. Exp. Med.* **210**, 209 (2013).
3. J. P. Julien *et al.*, *Immunol. Rev.* **250**, 180 (2012).
4. R. W. Sanders *et al.*, *Science* **349**, aac4223 (2015).
5. J. Chen *et al.*, *Science* **349**, 191 (2015).
6. J. G. Jardine *et al.*, *Science* **349**, 156 (2015).
7. P. Dosenovic *et al.*, *Cell* **161**, 1505 (2015).
8. J. R. Mascola, B. F. Haynes, *Immunol. Rev.* **254**, 225 (2013).
9. R. W. Sanders *et al.*, *PLOS Pathog.* **9**, e1003618 (2013).
10. S. K. Sharma *et al.*, *Cell Rep.* **11**, 539 (2015).
11. Y. D. Kwon *et al.*, *Nat. Struct. Mol. Biol.*, 10.1038/nsmb.3051 (2015).
12. T. Zhou *et al.*, *Cell* **161**, 1280 (2015).
13. H. X. Liao *et al.*, *Nature* **496**, 469 (2013).
14. N. A. Doria-Rose *et al.*, *Nature* **509**, 55 (2014).

ACKNOWLEDGMENTS

I thank J. Stuckey for help with the figure sketch.

10.1126/science.aac7800

ILLUSTRATION: V. ALTOUNIAN/*SCIENCE*

Published by AAAS

ECONOMICS

Intellectuals and the rise of the modern economy

Well-educated elites enabled scientific and technological creativity during the Industrial Revolution

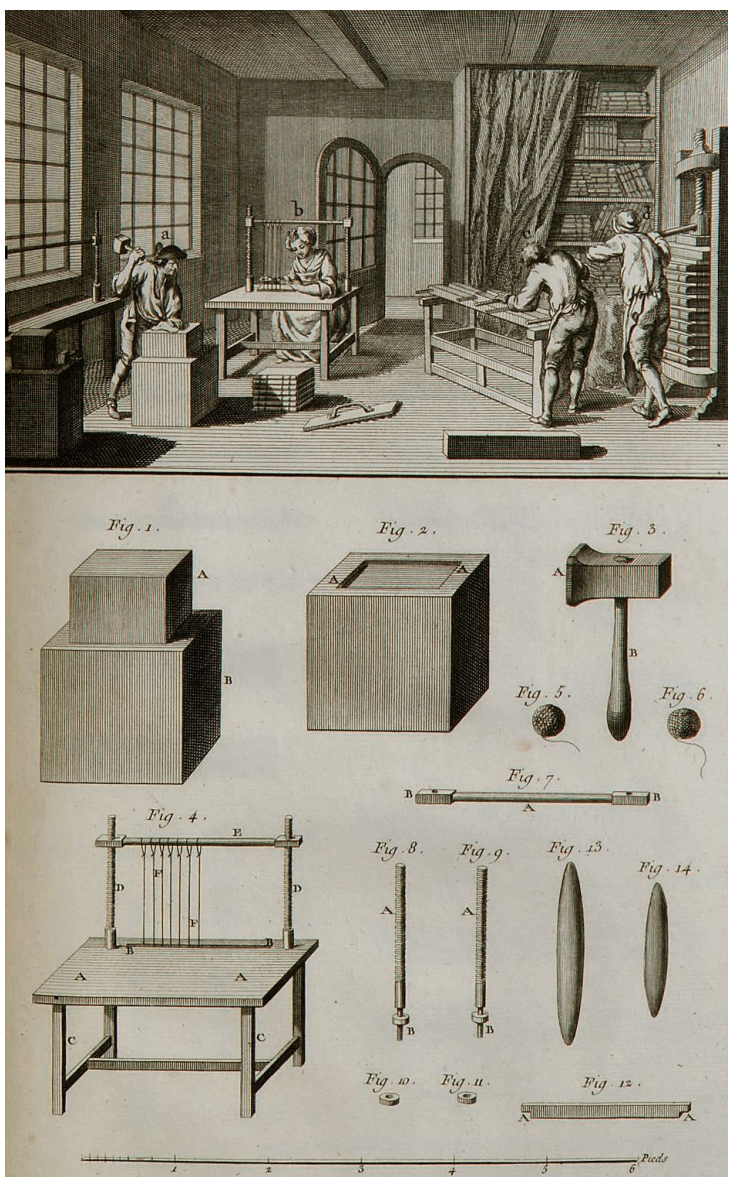
By **Joel Mokyr**

For many decades, economists dismissed culture as irrelevant to most questions in economic growth. However, in the past decade they have rediscovered its importance in the emergence of the Great Enrichment (the rapid and unprecedented process of economic growth since 1850) (*1*–*3*). In retrospect, this development seems inevitable. Once it was accepted that institutions are a powerful factor in explaining differences in national per-capita income today (*4*), culture—in the sense of the beliefs and values on which institutions were founded—could not be far behind. In a recent paper, Squicciarini and Voigtländer (*5*) provide further support for this idea by showing how culture affected the rise of the modern economy.

But whose culture matters here? Was it popular culture, the beliefs of the great masses, and the growth of general literacy and mass education? The answer is not simple. The Industrial Revolution of the late 18th century and the continuing waves of economic growth that followed it were largely driven by inventions and the science on which they increasingly relied. In the Victorian age, many authors tended to explain the advent of the Industrial Revolution by the actions of a few great inventors such as Watt and Arkwright and great scientists such as Galileo and Newton. In the 20th century, scholars (many of them influenced by Marx) reacted to such hero worship by seeing the sources of ingenuity as impersonal deep forces and denying single individuals any agency at all. Tolstoy famously advocated in *War and Peace* that "To study the laws of history we must completely change the subject of our observation, must leave aside kings, ministers, and generals, and study the common, infinitesimally small elements by which the masses are moved" (*6*). In this view, individuals matter little; if Henry Bessemer had not invented the converter that made cheap steel possible, someone else would have.

That said, what explains truly transformative technological ideas such as steam power, gas lighting, smallpox vaccination, the transistor, and antibiotics? Single individuals may have mattered less than their worshippers suppose, but it is hard to deny that in the 18th century, the segment of the population that generated and created new technology and new science was a very thin slice indeed. Technological improvements leading to a rise in living standards were created by people who were either educated and learned or extremely skilled and resourceful—and of course quite a few who were both. Some scientists were also brilliant instrument makers, such as the great Alessandro Volta, or inventive engineers with good connections to the scientific community, such as James Watt and John Smeaton.

Pathbreaking advances were adapted to production by a second tier of tweakers and implementers (*7*). However, that still meant a small minority of the population—a few thousand at most—who challenged conventional wisdom and created the new techniques and machines that made the modern age. No one put it better than the prescient scientist and master instrument maker Robert Hooke, who noted in 1666 that "There hath not been wanting in all ages and places great numbers of men whose genius and constitution hath inclined them to delight in the inquiry into the nature and causes of things, and from those inquiries to produce somewhat of use to themselves or mankind. ... But this newfound world



Fostering scientific creativity. A page from an 18th-century encyclopedia (*15*) illustrates the tools used in book binding. Squicciarini and Voigtländer argue that the relative numbers of subscribers to such works predict the subsequent rate of economic development. Thus, small, well-educated elites were—and arguably still are—crucial for scientific and technological creativity.

ILLUSTRATION: BEQUEST OF MARIANNE KHUNER/METROPOLITAN MUSEUM OF ART

Department of Economics, Northwestern University, Evanston, IL 60208, USA. E-mail: j-mokyr@northwestern.edu

Downloaded from www.sciencemag.org on July 10, 2015

Published by AAAS

must be conquered by a Cortesian army, well Disciplined and regulated, though their numbers be but small" (*8*).

A more formal representation of this idea is to consider the distribution of human capital in society. Typically economists such as Richard Easterlin have regarded human capital as a precondition for economic growth and examined various measures of it, such as overall literacy rates or the mean (or median) number of school years completed. There are good reasons for this approach, but historical data suggest that focusing on the entire labor force is more appropriate for explaining the adoption and diffusion of existing technology rather than the generation of new knowledge (*9*). What matters for the latter are those in the right-hand tail of the distribution: a small number of exceptional people who can think creatively and have the cutting-edge knowledge and training to carry cutting-edge technology to the operational stage (*10*, *11*).

"...in the 18th century, the segment of the population that generated and created new technology and new science was a very thin slice indeed."

Squicciarini and Voigtländer (*5*) have put this proposition to an imaginative test. They reason that high-quality individuals generated economic progress in two ways. First, they were able to make the new blueprints work and scale them up. Second, they continuously improved those techniques by small adjustments and adaptations. These individuals were the key actors in economic progress. Squicciarini and Voigtländer measure the number of such intellectuals from an unexpected source: the relative number of people who subscribed to the *Grande Encyclopédie*, published in France in 1777–1778. About 7000 French intellectuals bought subscriptions to this heterodox and progressive work, often regarded as the epitome of Enlightenment thought.

Squicciarini and Voigtländer argue that these subscribers represented a practical intelligentsia: After all, the encyclopedia contained practical information and descriptions of techniques in use at the time (see the image), in addition to liberal philosophy. They then show that the relative number of subscribers in French cities predicts the subsequent rate of economic development in French cities after the process of industrialization, using the new technology, took off in the late 18th century. Moreover, the average level of human capital, as measured by literacy rates, mattered little in the early stages of industrialization. In other words, by itself, the number of people able to read was not important for growth. What mattered was the elite: the number of well-educated people who read sophisticated texts.

How precisely the reading of such texts affected inventive and entrepreneurial activity is, of course, still a mystery. It stands to reason that both are related to unobservable characteristics such as curiosity, scientific creativity, access to cutting-edge knowledge, and a desire to increase economic efficiency.

Does this finding have implications for our own time? Modern research has suggested that the benefits of education for economic growth are far from obvious (*12*, *13*). The total stock of human capital is not a sufficient statistic for explaining the growth rate of an economy; in addition, we need to know the composition of the human capital (highly educated versus more widespread education) and how close the economy is to the world technology frontier (*14*). For economies that are at the technological frontier, investing in the education of the best and the brightest may be as important as raising the mean of the entire distribution. For the rest of the world, which imitates and adopts rather than invents, investing in mass education is still the best strategy for economic growth. ■

REFERENCES

1. G. Tabellini, *J. Eur. Econ. Assoc.* **6**, 255 (2008).
2. D, McCloskey, *The Bourgeois Virtues: Ethics for an Age of Commerce* (Univ. of Chicago Press, Chicago, 2006).
3. E. Spolaore, R. Wacziarg, *J. Econ. Lit.* **51**, 325 (2013).
4. D. C. North, *Institutions, Institutional Change, and Economic Performance* (Cambridge Univ. Press, Cambridge, 1990).
5. M. P. Squicciarini, N. Voigtländer, Working Paper 20219, National Bureau of Economic Research (2014); www.nber.org/papers/w20219.
6. L. Tolstoy, *War and Peace*, chap. 11.01; see http://genius.com/Leo-tolstoy-war-and-peace-chap-1101-annotated.
7. R. R. Meisenzahl, J. Mokyr, in *The Rate and Direction of Innovation*, S. Stern, J. Lerner, Eds. (Univ. of Chicago Press, Chicago, 2012), pp. 443–479.
8. R. Hooke, *Royal Society Classified Papers* xx.50, fol. 94 (1666).
9. S. O. Becker, E. Hornung, L. Woessmann, *Am. Econ. J. Macroecon.* **3**, 92 (2011).
10. J. Mokyr, *The Gifts of Athena* (Princeton Univ. Press, Princeton, NJ, 2002).
11. J. Mokyr, *The Enlightened Economy: An Economic History of Britain, 1700–1850* (Yale Univ. Press, New York, 2010).
12. L. Pritchett, *World Bank Econ. Rev.* **15**, 367 (2001).
13. W. Easterly, *The Elusive Quest for Growth* (MIT Press, Cambridge, MA, 2001).
14. P. Aghion, P. Howitt, *The Economics of Growth* (MIT Press, Cambridge, MA, 2009).
15. *Encyclopedie Dictionnaire Raisonne des Sciences, des Arts et des Métiers* (Briasson, Paris, 1751–1765).

10.1126/science.aac6520

STRUCTURAL BIOLOGY

COPI gets a fancy new coat

An interconnected scaffolding of proteins bends the membrane to form vesicles

By **Alex J. Noble**[1] *and* **Scott M. Stagg**[2,3]

A defining characteristic of eukaryotic cells is their numerous membrane-bound compartments, including the endoplasmic reticulum (ER), Golgi apparatus, and other organelles. Proteins and lipids are transported between these compartments and the cell surface by vesicles about 100 nm in diameter. Three canonical protein coat complexes facilitate the formation of these small vesicular carriers: the clathrin coat, coat protein 1 (COPI), and coat protein 2 (COPII) complexes. The COPII coat mediates vesicle formation at the ER for transport to the Golgi; the COPI coat forms vesicles at the cis-Golgi for transport to the ER; and clathrin has a dual role, forming vesicles at the trans-Golgi for transport to the plasma membrane and forming vesicles at the plasma membrane for endocytosis. Each of these coat complexes is composed of numerous proteins that bind to membrane, recognize cargo proteins, bend the parent membranes into a bud, and pinch the buds off into vesicles (*1*). On page 195 of this issue, Dodonova *et al.* (*2*) have created an atomic model of the COPI coat by using cryogenic electron tomography (cryo-ET) combined with labeling and cross-linking mass spectrometry. Their model gives new insights into the mechanisms by which the COPI proteins assemble into highly interconnected scaffoldings and work together to bend membrane.

Individual proteins in the three different coat protein complexes share similar folds and are proposed to be distant evolutionary relatives (*3*). Despite these similarities, the coats have evolved different functional mechanisms. The basic assembly unit for the COPI coat is called coatomer (*4*), which consists of a heteroheptameric complex of α-, β-, β′-, γ-, δ-, ε-, and ζ-COP proteins. These are simultaneously recruited to the membrane during the vesiculation process (*5*). This contrasts with clathrin and COPII, the subunits

Published by AAAS

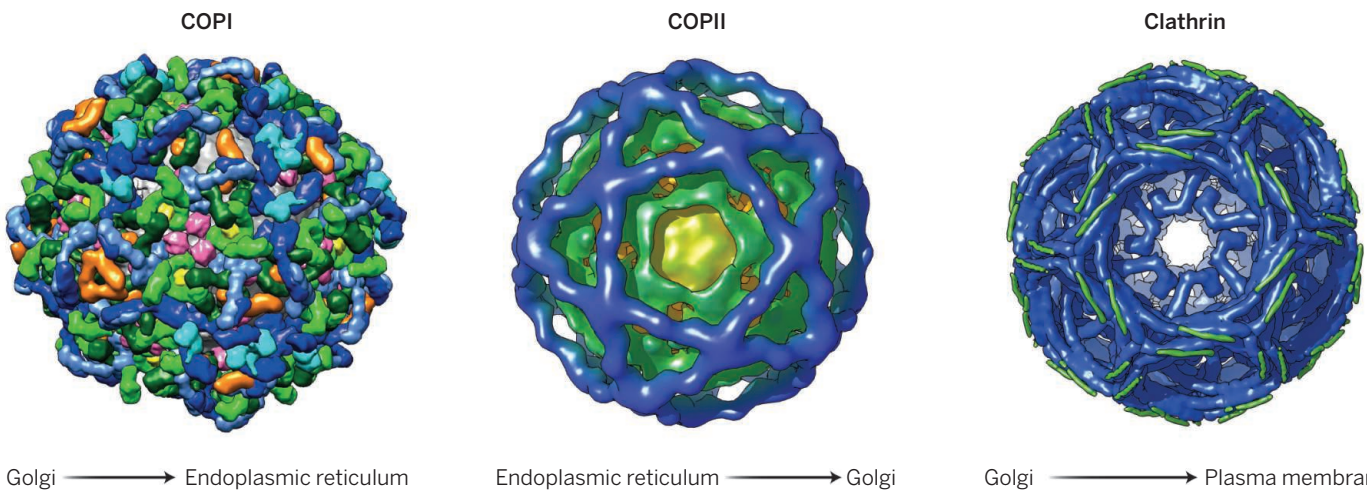
of which are recruited sequentially (*6*). The structure determined by Dodonova *et al.* explains the basis for the en bloc recruitment of the COPI proteins. In contrast to COPII and clathrin, which form discrete adapter and cage layers, the COPI proteins combine both of those functions into one unit and together form a highly interconnected network (see the figure) where a given COPI assembly unit, the triad can make up to four different contacts with neighboring triads.

The lack of discrete adapter and cage layers for COPI is surprising given that the coat was previously shown to have two stable subassemblies: α-β′-ε-COP, which is structurally similar to the cage component of clathrin and COPII coats, and γ-ζ-β-δ-COP, which is structurally similar to the adapter protein 1 (AP1) and AP2 complexes in clathrin (*7*). In the case of the COPI coat, however, instead of forming discrete adapter and cage layers, the α-β′-ε-COP subcomplexes are nestled down close to the membrane next to the γ-ζ-β-δ-COP subcomplexes to form a triad. Another interesting comparison can be made between the clathrin adapters and γ-ζ-β-δ-COP. AP1 and AP2 form two conformations: a closed cytosolic version (*8*) and a putative membrane-bound open form (*9*). The γ-ζ-β-δ-COP subcomplex is topologically equivalent to the open form of AP1, but in contrast to AP1, it forms a "hyper-open" conformation. The COPI structure raises the interesting question of whether AP1 and AP2 similarly have a "hyper-open" conformation when bound to membrane and conversely whether γ-ζ-β-δ-COP has open and closed forms. Moreover, it remains to be determined what specific roles these conformations play in the respective coat functions.

The structure determined by Dodonova *et al.* also helps to explain the mechanism by which the COPI coat generates membrane curvature. One of the COPI proteins, Arf1, has an amphipathic α helix that is buried in the outer leaflet of the COPI vesicle. A mathematical model has been proposed that quantifies the degree of membrane bending induced by inserting an α helix into one leaflet of a membrane bilayer (*10*). Based on the observed sparse distribution of the Arf1 proteins and the mathematical model, the authors propose that Arf1 alone is insufficient to bend membrane to the required curvature for vesicle formation, and that the remaining curvature must be generated by the rest of the coat. A remaining question is whether the coat physically squeezes the membrane or locally induces curvature at a given triad, then clusters the locally deformed regions into a coherent vesicle by assembling them into a coat. Additionally, it is unknown how different cargoes affect membrane curvature in vivo.

The COPI coat structure almost completely covers the membrane surface, leaving little room for cargo with large cytosolic domains. It is unclear how such a cargo protein could be fitted into the COPI coat structure without altering the coat geometry in some way. Future studies will determine whether cargo can direct coat remodeling or if it is accommodated by some other mechanism. One unique aspect of the COPI structure is the linkages between the triads in the full COPI coats. Four different linkages are described, but unlike most biomolecular complexes that assemble via a small number of discrete connections, the linkages in the COPI coat occur over a range of contact areas. Why is this so? One possibility is that the proto-COPI coat evolved the four different linkages to expand the repertoire of geometries that the coat can accommodate and thus adapt to the secretory needs of the cell.

It is worth noting that the study by Dododnova *et al.* represents a technical tour de force. By combining high-resolution cryo-ET, cross-linking mass spectrometry, differential nanogold labeling, and directed Monte Carlo searches, the authors were able to localize individual crystal structures into the triad density map. Only a handful of structures have been determined to better than 15 Å by cryo-ET, and even with such resolution, it is difficult to unambiguously dock crystal structures into the density maps. The combination of high-resolution cryo-ET and biochemical characterization is a powerful approach for determining the structures of complicated multisubunit molecular assemblies. This approach should be useful in future studies for determining the structures of other macromolecular complexes in the cell. ■



Coat architecture. Three different coat protein complexes are involved in vesicle trafficking in the cell. Clathrin [Protein Data Bank accession code PDB-1XI4 (*11*)], COPII [Electron Microscopy Data Bank accession code EMD-1511 (*12*)], and COPI [EMD-2985, EMD-2986, EMD-2987, EMD-2988, EMD-2989, and PDB-5A1U, PDB-5A1V, PDB-5A1W, PDB-5A1X, PDB-5A1Y (*2*)] are shown.

[1]*Department of Physics, Florida State University, 77 Chieftan Way, Tallahassee, FL 32306, USA.* [2]*Department of Chemistry and Biochemistry, Florida State University, 95 Chieftain Way, Tallahassee, FL 32306, USA.* [3]*Institute of Molecular Biophysics, Florida State University, 91 Chieftan Way, Tallahassee, FL 32306, USA. E-mail: sstagg@fsu.edu*

REFERENCES

1. M. Faini *et al.*, *Trends Cell Biol.* **23**, 279 (2013).
2. S. O. Dodonova *et al.*, *Science* **349**, 195 (2015).
3. D. Devos *et al.*, *PLOS Biol.* **2**, e380 (2004).
4. M. G. Waters *et al.*, *Nature* **349**, 248 (1991).
5. S. Hara-Kuge *et al.*, *J. Cell Biol.* **124**, 883 (1994).
6. K. Matsuoka *et al.*, *Cell* **93**, 263 (1998).
7. M. Lowe, T. E. Kreis, *J. Biol. Chem.* **270**, 31364 (1995).
8. E. E. Heldwein *et al.*, *Proc. Natl. Acad. Sci. U.S.A.* **101**, 14108 (2004).
9. L. P. Jackson *et al.*, *Cell* **141**, 1220 (2010).
10. F. Campelo *et al.*, *Biophys. J.* **95**, 2325 (2008).
11. A. Fotin *et al.*, *Nature* **432**, 573 (2004).
12. S. M. Stagg *et al.*, *Cell* **134**, 474 (2008).

10.1126/science.aac6537

Published by AAAS

OCEANS

Managing mining of the deep seabed

Contracts are being granted, but protections are lagging

By L. M. Wedding,[1] S. M. Reiter,[1,2] C. R. Smith,[3*] K. M. Gjerde,[4,5] J. N. Kittinger,[1,6] A. M. Friedlander,[7,8] S. D. Gaines,[9] M. R. Clark,[10] A. M. Thurnherr,[11] S. M. Hardy,[12] L. B. Crowder[1]

POLICY

Interest in mining the deep seabed is not new; however, recent technological advances and increasing global demand for metals and rare-earth elements may make it economically viable in the near future (*1*). Since 2001, the International Seabed Authority (ISA) has granted 26 contracts (18 in the last 4 years) to explore for minerals on the deep seabed, encompassing ~1 million km^2 in the Pacific, Atlantic, and Indian Oceans in areas beyond national jurisdiction (*2*). However, as fragile habitat structures and extremely slow recovery rates leave diverse deep-sea communities vulnerable to physical disturbances such as those caused by mining (*3*), the current regulatory framework could be improved. We offer recommendations to support the application of a precautionary approach when the ISA meets later this July.

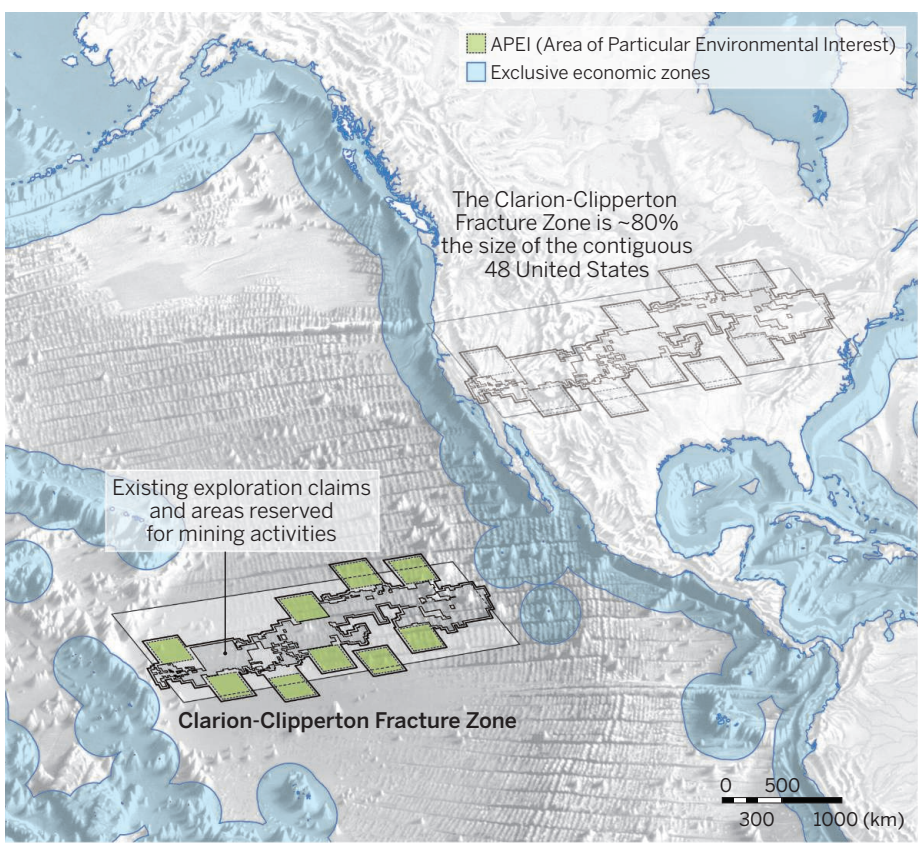
Deep-sea benthic ecosystems are globally important reservoirs of biodiversity and endemism that provide important ecosystem services (e.g., carbon sequestration and nutrient cycling) (*4*, *5*) and include diverse habitats (e.g., soft-sediment abyssal plains, hydrothermal vents, seamounts, continental slopes, and submarine canyons) (*6*). The deep seabed also harbors substantial, untapped mineral resources (e.g., polymetallic nodules containing nickel, copper, cobalt, and lithium; massive sulfides containing copper and gold; and seamount crusts containing cobalt, manganese, and rare-earth minerals) (*1*, *7*). The challenge ahead is to find ways to permit initial exploration, and ultimately commercial exploitation, of seabed minerals while sustaining the ecosystems that surround them.

The seabed outside of national jurisdictions [called the "Area" in the United Nations Convention on the Law of the Sea (UNCLOS)] is legally part of the "common heritage of mankind" and is not subject to direct claims by sovereign states (*8*). The common-heritage principle imposes a kind of trusteeship obligation on the ISA, created under UNCLOS in 1994, and its member states, wherein "the interests of future generations have to be respected in making use of the international commons"; those interests include both resource exploitation and environmental protection (*9*).

At its July 2015 session, the ISA, for the first time, will consider a draft regulatory framework to manage exploitation of these seabed resources consistent with the common heritage principle. In addition, the current regulatory framework for seabed mineral exploration could be improved. The ISA could develop a process to establish regional environmental management plans as part of the framework for governing both exploration and exploitation of deep seabed minerals, that includes a network of no-mining areas among other measures to protect the marine environment.

PIONEERING PRECAUTION IN THE ABYSSAL PACIFIC. Efforts focused on the Clarion-Clipperton Fracture Zone (CCZ) in the abyssal Pacific provide a useful model (see the map). The CCZ has the largest known concentrations of high-grade polymetallic nodules, with potentially great commercial value (*7*). The scale of impacts that would be associated with nodule mining in the CCZ may affect 100s to 1000s of km^2 per mining operation per year (*3*). In 2007, an international workshop brought together expert representatives from ISA and the scientific and international ocean law communities to develop design principles and recommendations for a network of marine protected areas (MPAs) in the CCZ off-limits to mining, to be considered by the ISA as part of a regional environmental management plan. The workshop used a recent assessment of biodiversity, species ranges, and gene flow in the CCZ to develop recommendations honoring existing mining exploration claims while incorporating accepted principles of ecosystem management (see the map).

MPA networks support a precautionary approach for managing ecosystems where



Region targeted for nodule mining in the abyssal Pacific. The vast extent of mining exploration claims and areas reserved for mining in the CCZ in the abyssal Pacific Ocean.

ILLUSTRATION: (IMAGE) STUDIO GANG ARCHITECTS; (BASE MAP) HEINRICH BERANN © 2015 NATIONAL GEOGRAPHIC CREATIVE; (MAP DATA SETS) INTERNATIONAL SEABED AUTHORITY

Downloaded from www.sciencemag.org on July 10, 2015

Published by AAAS

data are limited (e.g., in the deep sea) by preserving replicated portions of diverse habitats and associated biodiversity and ecosystem function (*10*), in situations where exploitation may cause serious, unpredictable, and potentially irreversible damage. The efficacy of individual MPAs to protect biodiversity and critical habitats has been well documented in the marine environment, and MPA networks further safeguard against uncertainty and promote ecosystem connectivity in the face of environmental degradation. Recent studies have demonstrated that the effectiveness of MPA networks is greater than the sum of the effects of individual MPAs (*11*).

In 2012, the ISA pioneered a precautionary approach in the CCZ when it provisionally adopted the deep seabed's first environmental management plan that included Areas of Particular Environmental Interest (APEIs), a modified version of the recommended MPA network from the 2007 workshop (*12*, *13*). The design principles used in developing the APEIs included (i) compatibility with the existing legal framework of the ISA for managing seabed mining and protecting the marine environment. (ii) minimizing socioeconomic impacts by honoring existing exploration claims; (iii) maintaining sustainable, intact, and healthy marine populations; (iv) accounting for regional ecological gradients; (v) protecting a full range of habitat types; (vi) creating buffer zones to protect against external anthropogenic threats (e.g., mining plumes); and (vii) establishing straight-line boundaries to facilitate rapid recognition and compliance (*12*).

The regional environmental management plan designated no-mining areas (i.e., APEIs) that are provisionally in place only for the CCZ (and only for 3 years, subject to review at the July 2015 ISA session) (*14*). Meanwhile, the ISA continues to grant exploration contracts for large areas of other deep-sea habitats in the Indian, Atlantic, and Pacific Oceans.

THE COMMON HERITAGE OF MANKIND. At the upcoming July session, the ISA can continue to apply a precautionary approach by tailoring the MPA network design principles established for the CCZ to other deep-sea habitats in which exploration claims will be granted. Networks of MPAs will be most effective if their location and spatial extent are established before additional mining exploration claims are granted that may compromise ISA's ability to site these networks in the most effective locations. This lesson was learned in the CCZ planning process, because existing and emerging exploration contracts required substantial modifications to the spatial location of the science-based recommendations for the proposed MPA network. Preexisting or new exploration claims (up to ~75,000 km^2 for nodules) can erode the effectiveness of protected-area networks by preempting protection of critical habitats and by limiting population connectivity by causing excessive spacing between MPAs. We thus recommend that the ISA consider suspending further approval of exploration contracts (and not approve exploitation contracts) until MPA networks are designed and implemented for each targeted region.

The ISA has the power and the opportunity to use the CCZ network design principles when it develops the regulatory framework for mineral exploitation in deep seabed areas beyond national jurisdiction. The scientific information applied in the CCZ was characteristic of this abyssal plain region, and yet the CCZ plan development process may serve as a general model for the ISA. First, the ISA could convene workshops, where scientific experts use the CCZ and other MPA design principles to develop tailored plans for MPA networks in other deep-sea regions targeted for mining (e.g., the Mid-Atlantic Ridge, Indian Ocean, and Western Pacific). Second, the ISA could then organize meetings of all stakeholders to recommend necessary revisions to the draft plans developed by the science workshops, balancing trade-offs between mining interests and environmental protection. Third, the ISA could then embed these newly tailored MPA network designs into environmental management plans for the other regions of the deep seabed targeted for mining.

"The science of establishing MPA networks and minimizing human impacts is relatively new for deep-sea mining."

The science of establishing MPA networks and minimizing human impacts is relatively new for deep-sea mining. However, given the uncertainty in the spatial and temporal scales and the intensity of mining impacts, combined with high biodiversity and extremely slow recovery rates of many communities and habitats in the deep sea, a precautionary approach using MPAs is warranted. As deep-sea protected areas are implemented, research will be necessary to evaluate their efficacy and to adaptively manage these networks as new science emerges regarding the intensity and scale of mining disturbance.

The ISA has a unique mandate to act on behalf of humankind to manage mining of deep-sea resources in the area beyond national jurisdiction. The ISA is thus responsible for applying the precautionary principle in providing appropriate and timely environmental protection of deep-sea ecosystems in regions potentially affected by mining (*15*). A carefully designed regulatory framework, including provisions for MPA networks embedded in regional environmental management plans, can reduce uncertainty about future mining activities and protect existing mining claims and economic investments, all while safeguarding deep-sea biodiversity and ecosystem function at relevant geographic scales. Although this endeavor will be challenging, the time is now to assure appropriate environmental protection in the context of mineral resource development in the deep sea. ■

[1]Center for Ocean Solutions, Stanford University, Palo Alto, CA, USA. [2]Monterey Bay Aquarium, Monterey, CA, USA. [3]Department of Oceanography, University of Hawaii at Manoa, HI, USA. [4]Middlebury Institute for International Studies, Monterey, CA, USA. [5]Wycliffe Management, Warsaw, Poland. [6]Conservation International, Honolulu, HI, USA. [7]Pristine Seas, National Geographic Society, Washington, DC, USA. [8]Fisheries Ecology Research Lab, Department of Biology, University of Hawaii at Manoa, HI, USA. [9]Department of Ecology, Evolution, and Marine Biology, University of California, Santa Barbara, CA, USA. [10]National Institute of Water and Atmospheric Research, Wellington, New Zealand. [11]Lamont-Doherty Earth Observatory, Columbia University, New York, NY, USA. [12]School of Fisheries and Ocean Sciences, University of Alaska—Fairbanks, AK, USA. *Corresponding author. E-mail: craigsmi@hawaii.edu

REFERENCES AND NOTES

1. J. Halfar, R. M. Fujita, *Mar. Policy* **26**, 103 (2002).
2. J.-P. Lévy, *The International Seabed Authority: 20 Years* (ISA, Kingston, Jamaica, 2014), 69 pp.
3. C. R. Smith, L. A. Levin, A. Koslow, P. A. Tyler, A. G. Glover, in *Aquatic Ecosystems: Trends and Global Prospects*, N. Polunin, Ed. (Cambridge Univ. Press, Cambridge, 2008).
4. A. R. Thurber *et al.*, *Biogeosciences* **11**, 3941 (2014).
5. K. J. Mengerink *et al.*, *Science* **344**, 696 (2014).
6. E. Ramirez-Llodra *et al.*, *Biogeosciences* **7**, 2851 (2010).
7. Y. Beaudoin *et al.*, *Environ. Dev.* **12**, 50 (2014).
8. UNCLOS, part XI, arts. 133–150 (1982).
9. R. Wolfrum, "Common heritage of mankind," in Max Planck Encyclopedia of Public International Law Online, R. Wolfrum, Ed. (Oxford Univ. Press, Oxford, 2009).
10. S. D. Gaines, S. E. Lester, K. Grorud-Colvert, C. Costello, R. Pollnac, *Proc. Natl. Acad. Sci. U.S.A.* **107**, 18251 (2010).
11. K. Grorud-Colvert *et al.*, *PLOS ONE* **9**, e102298 (2014).
12. L. M. Wedding *et al.*, *Proc. Biol. Sci.* **280**, 20131684 (2013).
13. M. Lodge *et al.*, *Mar. Policy* **49**, 66 (2014).
14. ISA Decision of the Council relating to an environmental management plan for the Clarion-Clipperton Zone, no. 2, ISBA Doc. 18/C/22, 26 July 2012.
15. Seabed Disputes Chamber of the International Tribunal for the Law of the Sea, Case no. 17 (2011); https://www.itlos.org/index.php?id=109.

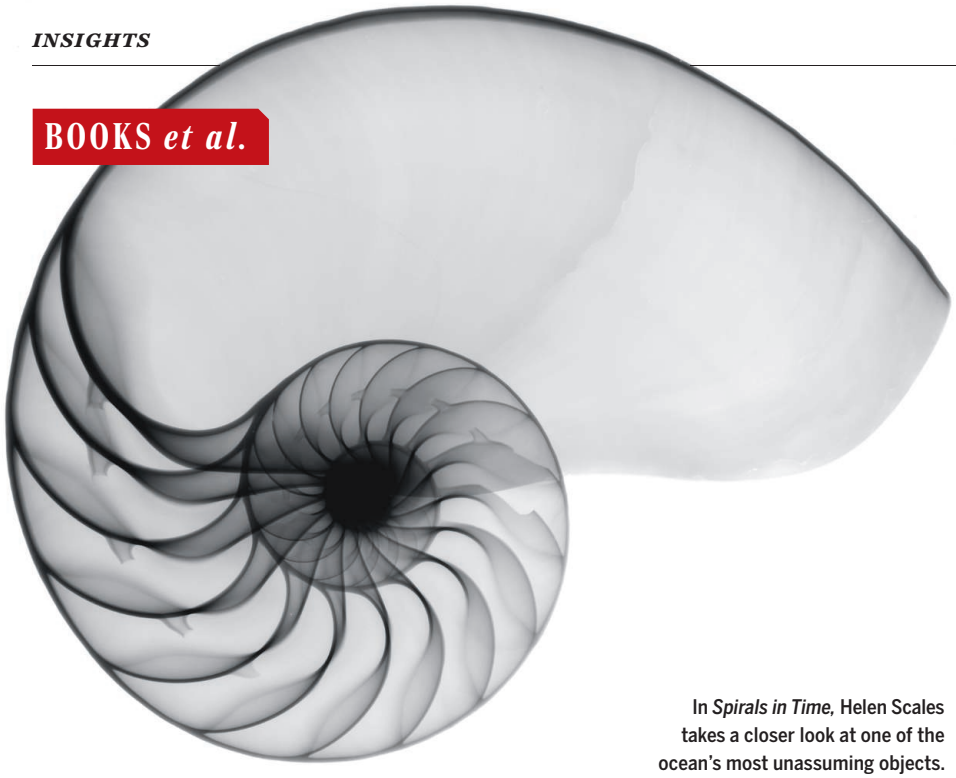
ACKNOWLEDGMENTS

The workshop to develop APEIs in the CCZ was supported by a Pew Fellowship in Marine Conservation (to C. S.), as well as by the Sloan Foundation through CeDAMar (Census of the Diversity of Abyssal Marine Life) and CenSeam (Global Census of Marine Life on Seamounts), the J.M. Kaplan Fund, and the ISA. The authors thank H. Walecka (University of California, Santa Barbara) for support in manuscript preparation and the graduate students in the Middlebury Institute of International Studies at Monterey (MIIS) February to March 2015 deep-sea mining workshop. Center for Ocean Solutions supported the development of this manuscript. K.M.G. has been supported by European Union Framework Programme 7 MIDAS project, contract number 603418. C.R.S. receives support from Seabed Resources Development Limited.

10.1126/science.aac6647

Published by AAAS

BOOKS *et al.*



In *Spirals in Time*, Helen Scales takes a closer look at one of the ocean's most unassuming objects.

MARINE ECOLOGY

Beachcomber's delight

The hidden mysteries and human history of seashells

By **Christopher Kemp**

A few years ago, while researching a natural history of ambergris (*1*, *2*), I spent every spare moment on the coastline of New Zealand, scouring the high tide line for what is, essentially, a pathological secretion of hardened sperm whale dung. I never found any. But, every time I returned home from the shoreline, my pockets were filled with wet shells. In some locations, the *Maoricolpus roseus*—a delicately tapered turret shell—were so numerous that each receding tide left an inch-deep drift of them on the sand. Later, in the wide bay of Revere Beach, near Boston, Massachusetts, I collected empty moonsnail shells larger than golf balls. I still have them.

While reading Helen Scales's *Spirals in Time*, I thought of my shells again. Digging them from a drawer, I picked a single violet-colored turret shell from the bag and followed its whorls with renewed interest. Scales, a marine biologist and author of *Poseidon's Steed: The Story of Seahorses, from Myth to Reality*, takes us on a fascinating journey into the strange and captivating world of mollusks.

Together, mollusks make up an enormously diverse phylum of organisms—an estimated 85,000 known species, with thousands more waiting in the ocean, and in museum collections, to be described. They are found, as Scales tells us, inland too: like *Cornu aspersum*, the familiar land snail that inhabits English gardens, and certain species of the *Plectosoma* genus, found only on limestone karsts in Malaysia. *Plectosoma* have strangely convoluted shells designed to outwit predators, which, upon entering the shell, are unable to locate its inhabitant.

Shells of every kind have always occupied a meaningful place in human history. Their earliest appearance in the human record dates back 125,000 years to a site in northeastern Morocco: dog whelks decorated with ochre, pierced with holes, and likely worn as jewelry. Much later, the money cowrie, a little ovate shell with a crimped edge, became the currency of the African slave trade. Money cowries are unassuming shells. They look like gnocchi. But in 1770, 150,000 of them were sufficient to enslave a human being.

On her travels, Scales takes us to the Mumbles, on the Gower peninsula in Wales, to observe the reseeding of a long-disappeared oyster fishery, which fell to overfishing and pollution. We follow as she visits a women's oyster farming collective in the mangrove roots of The Gambia, a program that has empowered the women involved, in the face of rampant gender discrimination, and to Taranto, an island in the Tyrrhenian Sea, near Italy, to investigate sea silk, a mysterious textile harvested from the noble pen shell. Along the way, we learn numerous facts: how mollusks make their shells; how oysters mate; and why, currently at least, most shells spiral to the right. (The gene that controls spiraling in snail shells is the same gene that controls asymmetry in humans, as exemplified by the left-sided placement of the heart in the chest.)

Carefully researched and entertaining throughout, *Spirals in Time* is never dull. My only criticism, and it is a gentle one, is that such a visual subject is accompanied by so few images. The art of Aaron John Gregory graces the cover of the book and appears occasionally throughout. But it is not enough.

At one point, Scales writes of an efficient wood-devouring mollusk named the shipworm: "Admittedly, they are wormlike in appearance, but at one end they have an unmistakable pair of shells revealing their true identity—a type of clam." In fact, the shipworm has sent entire fleets to the ocean floor, filled with bore holes like wheels of Swiss cheese. But no matter how hard I bent my brain to the task, I simply could not imagine what a shipworm looks like. It began to overwhelm me in the way that small things sometimes can.

Eventually, on Google, I found enough photographs of shipworms to satisfy my curiosity. A short time later, I was diverted again: I spent a whole hour watching YouTube videos of naked hermit crabs selecting new shells to inhabit. This cannot be considered a shortcoming of the book. In the end, it is the strength of a work like this. Scales's book is so relentlessly interesting, you will have to prop it open on a laptop as I did—a keystroke away from images of shipworms, mating oysters, and every other strange, shell-clad inhabitant of the oceans.

The reviewer is at the Department of Translational Science and Molecular Medicine, Michigan State University, Grand Rapids, MI 49503, USA. E-mail: cjkemp@gmail.com

Spirals in Time
The Secret Life and Curious Afterlife of Seashells
Helen Scales
Bloomsbury Sigma, 2015.
312 pp.



REFERENCES AND NOTES

1. C. Kemp, *Floating Gold: A Natural (and Unnatural) History of Ambergris* (University of Chicago Press, Chicago, 2012).
2. S. DeRuiter, *Science* **337**, 296–297 (2012).

10.1126/science.aac5988

PHOTO: BERT MYERS/SCIENCE SOURCE

Downloaded from www.sciencemag.org on July 10, 2015

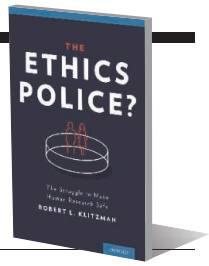
Published by AAAS

RESEARCH ETHICS

The safety dance

A researcher takes aim at the committees charged with protecting human subjects

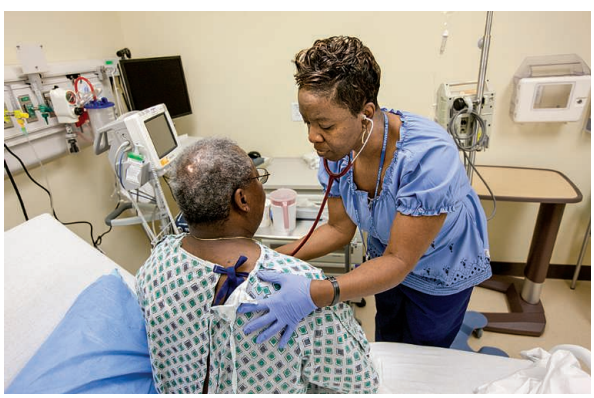
By **Lainie Friedman Ross**



The Ethics Police? The Struggle to Make Human Research Safe
Robert L. Klitzman
Oxford University Press, 2015. 432 pp.

Robert Klitzman opens *The Ethics Police* with a personal anecdote about his father's death. He describes how, in his father's final weeks, the physician offers his father chemotherapy that he admits is a "bit of an experiment." Klitzman, a newly minted physician himself, encourages his father to try the treatment. The drugs succeed in normalizing his father's blood count, but the side effects kill him. Klitzman claims the physician used the infamous adage "The experiment worked, but the patient died" to explain the outcome. The story is sad, and Klitzman clearly struggles with the role he feels he played in his father's decision.

The Ethics Police examines problems in what we in the United States call institutional review boards (IRBs), known globally as research ethics committees. IRBs are committees charged with protecting the rights and welfare of research participants. They are the mechanism by which the goal of advancing science is balanced with society's responsibility to protect the human participants on or with whom the research is performed.



Institutional review boards come under fire for placing seemingly unnecessary and arbitrary burdens on researchers in *The Ethics Police*.

The problem is that no matter what problems exist in IRBs, fixing them would not have saved Klitzman's dad. The physician, we learn, offered an informal experiment—to try some medicines approved for other conditions in what is known as "off label" prescribing. Such experiments are not considered "research" and are thus beyond the domain of the IRB.

Had Klitzman's dad been offered enrollment in a clinical trial using the same drugs, the experiment would have fallen under IRB jurisdiction, and the physician would have had to provide a more comprehensive description of the risks, benefits, and alternatives. The same decision may have been made, the same outcome may have sadly occurred, but Klitzman's dad would have had greater protection if only because other physician-colleagues would have been aware of what was being offered, the consent process would have been more thorough, and Klitzman's father would have been informed that he could withdraw at any time.

Despite the fact that his father's treatment was beyond IRB review, this experience colors Klitzman's views on the current state of human subject protections. His dissatisfaction is compounded by his frustration with the obstacles he has experienced in getting approval for the research he planned to conduct for this book. Most would categorize the proposed interview format as being of minimal risk to the participants and approve it in an expedited fashion. Instead, Klitzman's proposal was subjected to full IRB review. This may not be surprising, given that the reviewers were potential participants.

Klitzman's overall thesis is right: IRBs are flawed. He is one of many voices criticizing the inconsistencies across IRBs and their seemingly subjective interpretations of the federal regulations written to protect human subjects. He astutely points out that IRB members may not appreciate the costs of requesting protocol changes, particularly when these changes go beyond the regulations' requirements. Such changes can lead to differences between sites that make research comparisons more complex. One important insight he gleans from his research is that IRB members justify this variability on the grounds of "local knowledge." In practice, however, this leaves researchers vulnerable to the idiosyncrasies of individual IRB members. Klitzman supports a more centralized review process, although he concedes that this is not a panacea for all that is wrong with the system.

Klitzman convincingly shows that IRBs underestimate the actual authority they have. He argues for the need for checks and balances, pointing out that many researchers perceive no appeals process when their IRB requests protocol or consent changes. However, he also notes that "these interviews taught me that committees frequently make suggestions or express concerns that are negotiable, not incontestable" and that many of the IRB personnel he spoke with were amenable to reconsideration. Klitzman persuasively shows that IRBs need to be more transparent.

Although wary of the authority of IRBs, Klitzman concedes that some expansion beyond current regulatory protections may be needed. He criticizes the regulations' exclusive focus on individual harms, arguing that ignoring group harms can lead IRBs to approve research that may exacerbate health disparities. He also critiques the fact that IRBs tend to focus on nitpicky changes to consent forms, while failing to monitor the consent process. (However, as he acknowledges, there is no regulatory requirement or funding for this type of oversight, and this would signify further expansion of the authority of IRBs.)

The book is well written and accessible to a broad audience, but those who have served on IRBs will find it lacking. Klitzman defensively objects to those who discount his research by claiming that "only studies that directly observe IRBs are relevant." I don't discount his keen insights, although I believe the book would have been strengthened if he had observed committees in action. Consider the analogy of a baseball commentator who interviews all the players, coaches, umpires, and fans but has never watched the sport being played. His comments may miss some important complexities and nuances of the game. Likewise, this is true when one is trying to understand the IRB system.

10.1126/science.aac4236

The reviewer is at the MacLean Center for Clinical Medical Ethics, University of Chicago, Chicago, IL 60637, USA. E-mail: lross@uchicago.edu

PHOTO: © BROOKS KRAFT/CORBIS

Downloaded from www.sciencemag.org on July 10, 2015

Published by AAAS

LETTERS

Edited by **Jennifer Sills**

Meeting of the minds: Send your stories

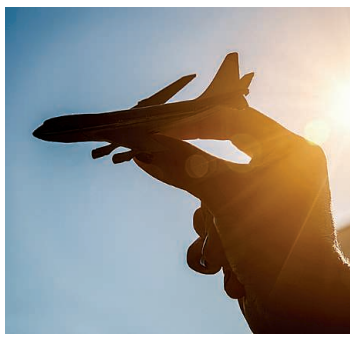
THE PATH FROM Gila monster venom to the diabetes medication Exenatide runs through an American Diabetes Association meeting in 1996. There, Department of Veterans Affairs researcher, endocrinologist, and Golden Goose Award winner Dr. John Eng presented results on how a compound in Gila monster venom affects insulin production, catching the attention of a small biotechnology company, Amylin Pharmaceuticals. After receiving U.S. Food and Drug Administration approval in 2005, the resulting drug Exenatide is now used by millions of people to manage Type 2 diabetes.

The story of Dr. Eng and Amylin is just one of many—spanning all science and technology disciplines—that exemplify the important role of conferences in advancing science, developing the next generation of scientific talent, and bringing new technologies and potential cures to the benefit of society.

In 2012, the White House Office of Management and Budget instituted new government-wide regulations (*1*) that substantially cut spending on conference participation and travel and require the senior leadership to review agency-wide conference costs that exceed $100,000, with more stringent requirements for costs in excess of $500,000. At current prices for travel and lodging, this would cover the cost of only a few hundred attendees, whereas the Departments of Defense and Energy each employ over 100,000 scientists and engineers either directly or as contractors. The U.S. Congress has further limited travel to international conferences to 50 employees per agency for most agencies. In response, federal agencies have developed costly tracking and approval systems, and approvals now often require more than a dozen signatures.

Under these new restrictive regulations, members of the scientific community employed by federal agencies have been subject to approval processes that have ballooned from weeks to as much as 9 months, and some scientists and engineers are now choosing not to request travel at all. The Government Accountability Office (*2*) and White House Office of Science and Technology Policy (*3*) have shown that this has led to reductions in conference participation among these colleagues, to the detriment of science as a whole.

This is why we and our colleagues in the science and technology community recently wrote a letter to the U.S. Congress expressing our deep concerns about the stifling impacts of these policies on science and engineering, and encouraging them to act (*4*). The letter was signed by more than 100 organizations and institutions that collectively represent and support millions of scientists, engineers, and mathematicians.



We hear from policy-makers in Congress and regulators at federal agencies that current problems stem, in part, from a lack of understanding of why scientific and technical conferences are important parts of the work of each and every member of our community, not fancy junkets. So today, we and our colleagues are reaching out to ask for your help.

Tell us about a collaboration that started at a conference and led to an exciting new discovery, or how an interaction at a conference was critical to your career as a young scientist or engineer. Because current regulations affect federal employees and contractors most, we especially encourage stories that involve collaborations with colleagues at national labs or research institutes. Submit your experiences at www.aaas.org/yourstory (*5*).

James F. Albaugh,[1]* Joseph R. Haywood,[2] James A. Jefferies,[3] Toyohiko Yatagai[4]

[1]President, American Institute of Aeronautics and Astronautics, Reston, VA 20191, USA. [2]President, Federation of American Societies for Experimental Biology, Bethesda, MD 20814, USA. [3]President,

ONLINE BUZZ

Recommending women

In her Editorial "Give women an even chance" (8 May, p. 611), Marcia McNutt urges those writing recommendations to search their letters for biased descriptions of women, such as "nice," "humble," and "able to balance research and parenthood." In the comments section, some readers lauded McNutt's warnings, whereas others felt they were misguided. Excerpts from their comments are below. Read the full comments, and add your own, at http://comments.sciencemag.org/content/10.1126/science.aac4767.

A selection of your thoughts:

...It is so striking how the expectations for women differ from those for men, and can so easily place them at a disadvantage in the science career pipeline.

Mary Ann McCabe

...Thank you for pointing out that this bias is held equally by women and men. We can hardly expect men to understand the importance of shedding this bias if women do not.

Lorraine Albritton

...it would be a simple thing to translate "nice," for example, to more grant-relevant language such as "is a good mentor in the lab, finds the time to assist others, and elevates the work of those around her."

Amanda Siegel

...we should acknowledge that bias cuts both ways. An overemphasis on brilliance, creativity, hard work, insightfulness, and leadership, at the expense of humility, kindness, and friendliness, will select for a distinct personality in the next generation of scientists (a personality that I'm not certain I would want to associate with)....

Felix Vajdos

...It is unrealistic to expect referees to write unbiased letters of recommendation. It is up to committees to use such letters carefully.

Maria Hötzel

Downloaded from www.sciencemag.org on July 10, 2015

PHOTO: © LEONARDO PATRIZI/ISTOCKPHOTO.COM

Published by AAAS

IEEE-USA, Washington, DC 20036, USA. [4]President, SPIE, Bellingham, WA 98227-0010, USA.

*Corresponding author. E-mail: communications@aiaa.org

REFERENCES AND NOTES

1. Executive Office of the President, Office of Management and Budget M-12-12, "Promoting Efficient Spending to Support Agency Operations" (www.whitehouse.gov/sites/default/files/omb/memoranda/2012/m-12-12.pdf).
2. U.S. Government Accountability Office, "Defense science and technology: Further DOD and DOE actions needed to provide timely conference decisions and analyze risks from changes in participation," *GAO Highlights* (2015); www.gao.gov/assets/670/668845.pdf.
3. L. Rein, "How the federal travel crackdown hits scientists especially hard," *Washington Post*, 25 March 2015; www.washingtonpost.com/blogs/federal-eye/wp/2015/03/25/the-white-house-asked-federal-scientists-how-bad-its-crackdown-on-travel-is-the-answer-bad/.
4. Letter to Senate Appropriations Committee (www.aaas.org/sites/default/files/SApprops%20S%26T%20Conference%20Travel%20Letter.pdf).
5. AAAS, publisher of *Science*, led the above-referenced letter to the U.S. Congress and is also hosting the story collection.

Reviewing Einstein

THE NEWS ARTICLE "Einstein eschews peer review" (E. Conover, special issue on General Relativity, 6 March, p. 1092) told the story of Einstein's withdrawal of a paper from the *Physical Review* in 1936 after he received a critical anonymous review. As an update to the story recently noted (*1*), one of us (D.K.) has written extensively on the subject. Here, we provide more information about how Howard Percy Robertson was identified.

As of the mid-1990s, the editors of the *Physical Review* did not have records old enough to provide information about the referee's identity. Einstein himself provided a clue: He acknowledged the helpful advice of Robertson in the published version of the paper. Robertson's documents at the Caltech archive (*2*) include a letter written by Robertson to John T. Tate Sr., the then-editor of *Physical Review*, which strongly suggested that Robertson was the referee (though naturally, Robertson did not reveal as much to Einstein).

In 2005, M.B., then editor-in-chief of the American Physical Society, realized the significance for Einstein scholars of a recently discovered early log book of the *Physical Review*. The log book included records on all papers submitted to the journal in the 1930s, including confirmation that Robertson was the referee of Einstein and Rosen's 1936 submission. The information could be made public because, after 69 years, none of those involved were still living. New materials have since been deposited in Robertson's Caltech archive, including the entire exchange between Robertson and Tate (*2*, *3*).

***Daniel Kennefick*[1]** and *Martin Blume*[2]**

[1]Department of Physics, University of Arkansas, Fayetteville, AR 72701, USA. [2]CMPMS Department, Brookhaven National Laboratory, Upton, NY 11973-5000, USA.

*Corresponding author. E-mail: danielk@uark.edu

REFERENCES AND NOTES

1. The update states, "Research by Daniel Kennefick of the University of Arkansas uncovered the historical events detailed in this anecdote. You can read the whole story in his article in the September 2005 issue of *Physics Today* http://scitation.aip.org/content/aip/magazine/physicstoday/article/58/9/10.1063/1.2117822
2. H. P. Robertson papers, Caltech archives, box 7, folders 12 and 13; finding aid available at www.oac.cdlib.org/findaid/ark:/13030/kt3s2026qn/dsc/#c02-1.2.10.2.2.
3. D. Kennefick, *Traveling at the Speed of Thought: Einstein and the Quest for Gravitational Waves* (Princeton Univ. Press, Princeton, NJ, 2007).

TECHNICAL COMMENT ABSTRACTS

Comment on "Asymmetric syntheses of sceptrin and massadine and evidence for biosynthetic enantiodivergence"

David H. Sherman, Sachiko Tsukamoto, Robert M. Williams

Ma *et al.* (Reports, 10 October 2014, p. 219) report asymmetric syntheses of sceptrin and massadine and, through a stereochemical reassignment, claim to "uncover enantiodivergence as a new biosynthetic paradigm for natural products." We challenge and clarify this claim with relevant examples from the literature of this well-known phenomenon of enantiodivergent congener biosynthesis within the same producing organism.

Full text at http://dx.doi.org/10.1126/science.aaa9349

Response to Comment on "Asymmetric syntheses of sceptrin and massadine and evidence for biosynthetic enantiodivergence"

Zhiqiang Ma, Xiaolei Wang, Xiao Wang, Rodrigo A. Rodriguez, Curtis E. Moore, Shuanhu Gao, Xianghui Tan, Yuyong Ma, Arnold L. Rheingold, Phil S. Baran, Chuo Chen

Sherman *et al.* commented on the precedence of enantiodivergence, listing a number of congeneric natural products with opposite chirality. However, these "congeners" are not derived from enantiodivergent biosyntheses. Instead, they are antipodes arising from separate enantiomeric biosyntheses. A distinct feature of the biosynthesis of the cyclic pyrrole-imidazole dimers is the production of antipodal congeners without the corresponding enantiomers.

Full text at http://dx.doi.org/10.1126/science.aaa9626

Published by AAAS

TECHNICAL COMMENT

ORGANIC SYNTHESIS

Comment on "Asymmetric syntheses of sceptrin and massadine and evidence for biosynthetic enantiodivergence"

David H. Sherman,[1] Sachiko Tsukamoto,[2] Robert M. Williams[3,4]*

Ma *et al*. (Reports, 10 October 2014, p. 219) report asymmetric syntheses of sceptrin and massadine and, through a stereochemical reassignment, claim to "uncover enantiodivergence as a new biosynthetic paradigm for natural products." We challenge and clarify this claim with relevant examples from the literature of this well-known phenomenon of enantiodivergent congener biosynthesis within the same producing organism.

Ma *et al*. reported impressive syntheses of the bis-guanidine alkaloids sceptrin and massadine (*1*). Examination of the absolute configurations of the synthetic and natural materials revealed that sceptrin and massadine, versus ageliferin, have mismatched chirality. The authors conclude that they "uncover enantiodivergence as a new biosynthetic paradigm for natural products" and "Although enantiomeric biosynthesis that produces both enantiomers of a natural product has been reported [(*2*)], enantiodivergent biosynthesis that produces opposite enantiomers of natural products as congeners described herein is unknown." Unfortunately, these statements overlook a substantial body of literature unambiguously demonstrating that this phenomena is well known. The authors' work is another affirmation that nature has evolved enantiodivergent biogeneses leading to new secondary metabolic diversity. The biogenesis postulated (Fig. 1) accommodates the reassigned stereochemistry, providing a working hypothesis for experimental verification (*1*). Although congeneric metabolites with opposite chirality have been confirmed through this work, the details of the biosynthetic pathways to these alkaloids remain unknown.

Numerous examples of enantiodivergent biosynthesis producing congeners of opposite absolute stereochemistry and distinct framework connectivity within the same producing organism are well known (*2*); a nonexhaustive list is shown in Fig. 2 (*3*–*15*). Little is known about the intricate genetic, biocatalytic, and mechanistic details of how enantiomeric, or pseudo-enantiomeric metabolites, are constructed. Co-isolated congeners in the same, as well as distinct, oxidation states—presumably derived from the same pathway or via parallel pathways—are evident, including the biogenesis postulated by Ma (*1*). Pseudo-enantiomeric congeners encompass disparate families of metabolites, including polyketides, terpenes, alkaloids, and amino acid derivatives. Pseudo-enantiomeric diastereomeric congeners (*2*, *10*, *11*), as well as instances of natural products sharing structural cores of opposite absolute stereochemistry, but differing in substitution patterns and oxidation states, are known (Fig. 2). Lignans, derived by the homodimerization of cinnamic alcohol units in plants, are particularly relevant, with (+)-syringaresinol and (−)-lariciresinol from *Dirca occidentalis* and *Wikstroemia elliptica* being salient examples.

In a particularly interesting system, Shen and others (*14*) demonstrated that nonactin and congeners are biosynthesized in *Streptomyces griseus* by a pair of enantiospecific pathways, which construct (+)- and (−)-nonactic acid, as well as both enantiomers of the higher congeners homononactic acid and bishomononactic acid. The macrotetrolides are assembled from these apparently biochemically compartmentalized, enantiomeric fragments (Fig. 3).

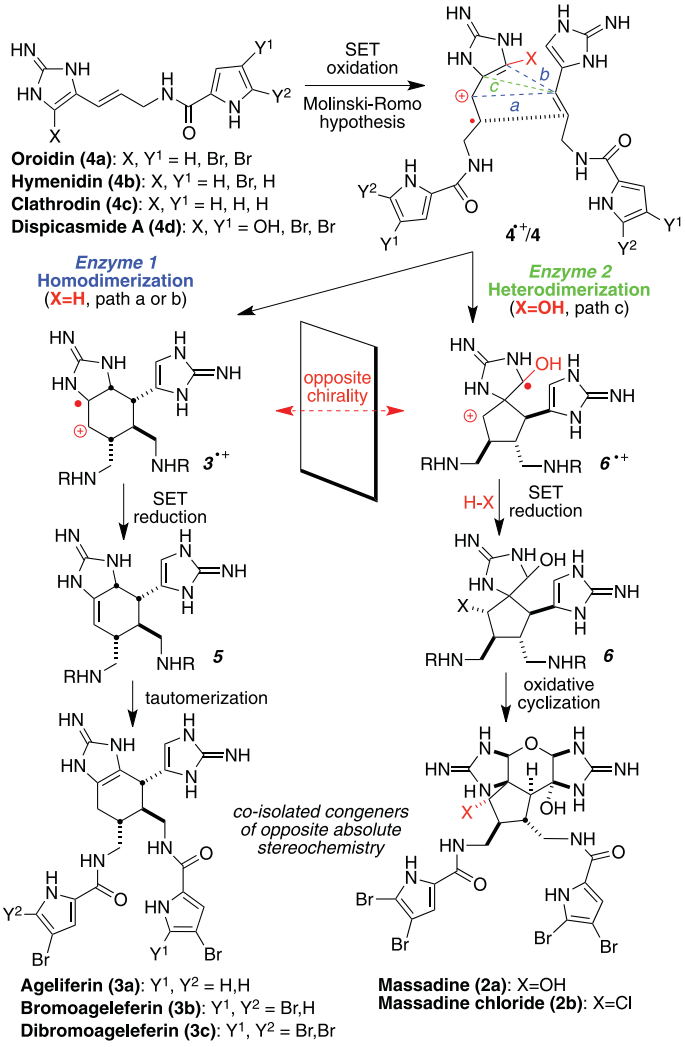


Fig. 1. Proposed enantiodivergent biogenesis. Reassignment of natural product stereochemistry formed the basis upon which Ma *et al*. postulate the biosynthesis of the massadines and ageliferins (*1*).

[1]Life Sciences Institute and Departments of Medicinal Chemistry, Microbiology and Immunology, and Chemistry, University of Michigan, Ann Arbor, MI 48109, USA. [2]Graduate School of Pharmaceutical Sciences, Kumamoto University, 5-1 Oe-honmachi, Kumamoto 862-0973, Japan. [3]Department of Chemistry, Colorado State University, Fort Collins, CO 80523, USA. [4]The University of Colorado Cancer Center, Aurora, CO 80045, USA.
*Corresponding author. E-mail: robert.williams@colostate.edu

Downloaded from www.sciencemag.org on July 10, 2015

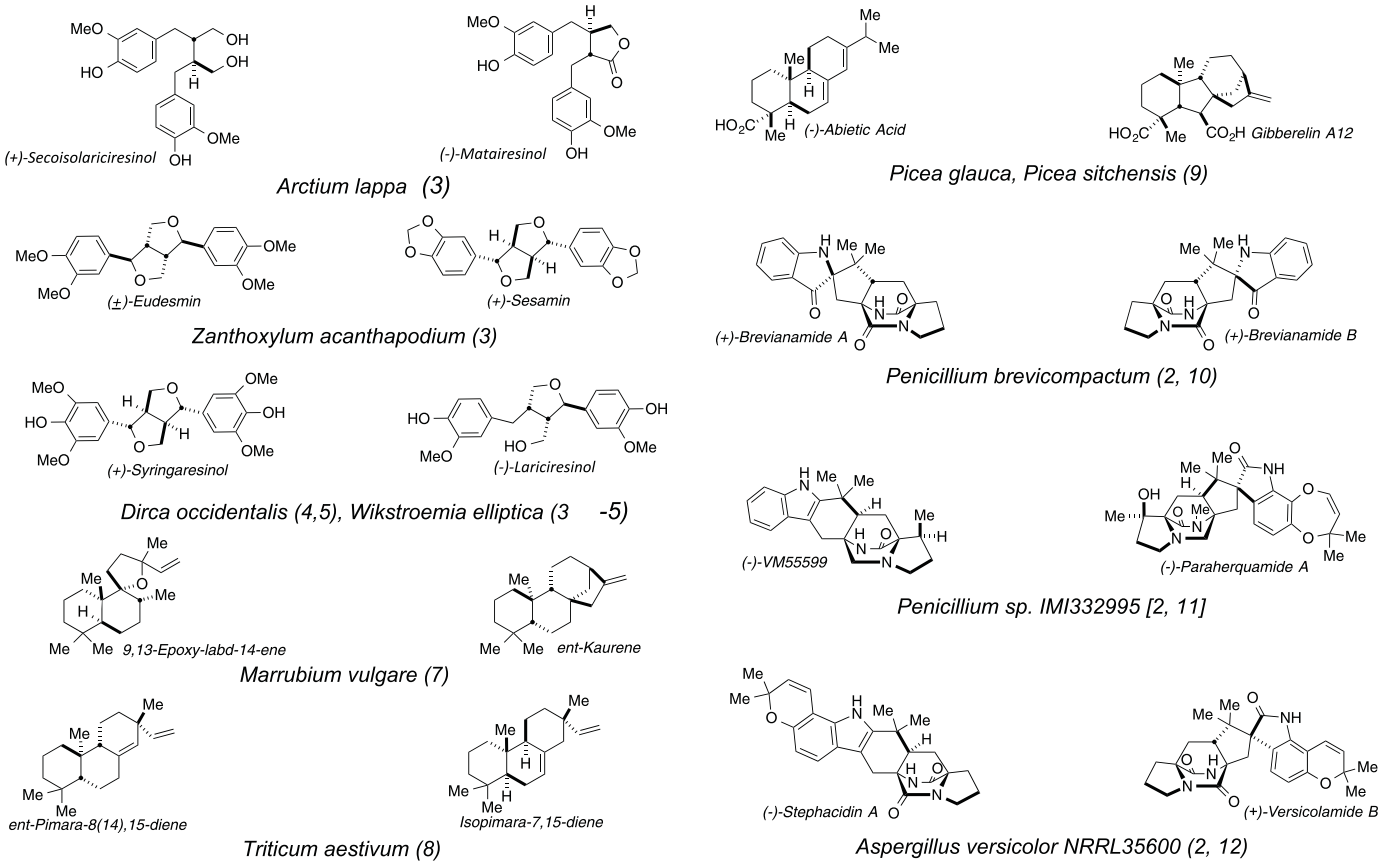


Fig. 2. Pseudo-enantiomeric natural product congeners co-isolated from the same producing organism.

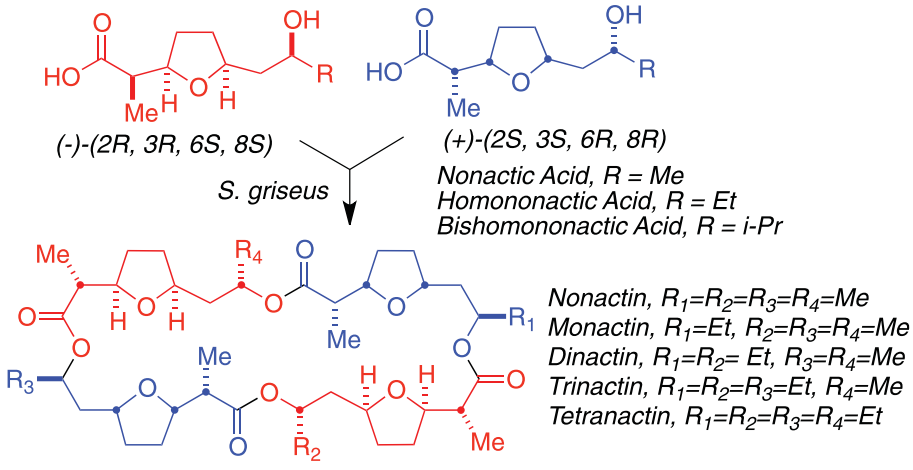


Fig. 3. Macrotetrolide biosynthesis. Enantiodivergent biosynthesis of monomer units and assembly of the macrotetrolides (*13*).

Plant terpenoids, such as copalyl pyrophosphate (CPP) derivatives, constitute various families of co-isolable pseudo-enantiomeric congeners, with *ent*-kaurene and 9,13-epoxy-labd-14-ene from *Marrubium vulgare* and the production of (–)-abietic acid and the ubiquitous plant hormone gibberellin A12 from spruce trees (*Picea glauca* and *P. sitchensis*) being illustrative. It is well known that higher plants produce both enantiomers of CPP, the core substrates from which numerous terpenoid congeners of opposite absolute stereochemistry arise (*7*–*10*). Indeed, many terpene cyclases have been documented to produce racemic or partially racemic metabolites (*2*), demonstrating a further mechanism whereby nature diversifies secondary metabolite stereochemistry. Selective catabolism or tailoring of one enantiomer of a biosynthetic racemate (i.e., by an enantiospecific oxidase or reductase) is another strategy for the coproduction of pseudo-enantiomeric congeners and may also be one means by which partially racemic natural products, as well as pseudo-enantiomeric congeners, might arise.

Fungal prenylated indole alkaloids, such as brevianamides A and B, constitute another example of pseudo-enantiomeric diasteromeric congeners from the same biosynthetic pathway with structural cores of opposite absolute configuration (*12*). Related examples are *Penicillium* sp. congeners (–)-VM*55599* and paraherquamide A (*13*) and the co-isolated congeners (+)-versicolamide B and (–)-stephacidin A in *Aspergillus versicolor* (*13*).

In several instances, enantiodivergent gene clusters that direct congener secondary metabolite biosynthesis appear in disparate organisms of distinct genus types and are not restricted to speciation. Evolutionary selection pressure must be the obligatory driving force for the diversification of secondary metabolite structure and stereochemistry, with enantiodivergence being among the palette of nature's tools. As more natural products are identified from the vast reservoir of as-yet-undiscovered organisms on earth, it is tantalizing to ponder the adaptive importance of the evolution, conservation of genes, and apparent distribution of genes between organisms that diversify secondary metabolites structurally and stereochemically.

Although little is understood regarding genetic and biochemical mechanisms that control enantioselectivity in pathways generating enantiodivergent congeners, preliminary information is emerging (*7*–*9*, *14*–*16*). For example, genome sequencing, gene cluster mining, and annotation of enzymes specifying the biosynthesis of (–)-stephacidin A and (+)-versicolamide B reveal high amino acid sequence identity (79 to 88%) between every structural pathway protein (*16*). Here, enantiodivergence is clearly a result of orthologous divergent, rather than paralogous convergent evolutionary processes. That nature clearly interrogates stereochemical diversity in the context of structural diversity is firmly established, and many more examples are anticipated. The interesting pyrrole-imidazole alkaloids (*1*) provide a provocative working hypothesis from which to investigate the putative existence of yet another striking example of enantiodivergent congener biosynthesis. The claim to having discovered enantiodivergent congener biosynthesis must be tempered in the context of a substantial body of published evidence dating back four decades.

REFERENCES AND NOTES

1. Z. Ma *et al*., *Science* **346**, 219–224 (2014).
2. J. Finefield, D. H. Sherman, M. Kreitman, R. M. Williams, *Angew. Chem. Int. Ed.* **51**, 4802 (2012).
3. S. Suzuki, T. Umezawa, M. Shimada, *Biosci. Biotechnol. Biochem.* **66**, 1262–1269 (2002).
4. T. Umezawa, T. Okunishi, M. Shimada, *Wood Res.* **84**, 62–75 (1997).
5. M. M. Badawi, S. S. Handa, A. D. Kinghorn, G. A. Cordell, N. R. Farnsworth, *J. Pharm. Sci.* **72**, 1285–1287 (1983).
6. T. Okunishi, T. Umezawa, M. Shimada, *J. Wood Sci.* **46**, 234–242 (2000).
7. P. Zerbe *et al*., *Plant J.* **79**, 914–927 (2014).
8. K. Zhou *et al*., *Phytochemistry* **84**, 47–55 (2012).
9. C. I. Keeling *et al*., *Plant Physiol.* **152**, 1197–1208 (2010).
10. A. J. Birch, R. A. Russell, *Tetrahedron* **28**, 2999–3008 (1972).
11. The absolute stereochemistry of (+)-brevianamide B was later reassigned to that shown; see references cited in (*2*).
12. S. E. Blanchflower, R. M. Banks, J. R. Everett, C. Reading, *J. Antibiot.* **46**, 1355–1363 (1993).
13. T. J. Greshock *et al*., *Angew. Chem. Int. Ed.* **47**, 3573–3577 (2008).
14. H. J. Kwon *et al*., *Science* **297**, 1327–1330 (2002).
15. W. C. Smith, L. Xiang, B. Shen, *Antimicrob. Agents Chemother.* **44**, 1809–1817 (2000).
16. S. Li *et al*., *Med. Chem. Comm.* **3**, 987–996 (2012).

ACKNOWLEDGMENTS

We are grateful to the National Institutes of Health for financial support (CA70375 to R.M.W. and D.H.S.). We thank J. Finefield for assistance in preparing the manuscript and B. Shen, J. Bohlmann, R. Croteau, and R. Peters for helpful discussions. We confirm no competing financial interests.

16 February 2015; accepted 5 May 2015
10.1126/science.aaa9349

TECHNICAL RESPONSE

ORGANIC SYNTHESIS

Response to Comment on "Asymmetric syntheses of sceptrin and massadine and evidence for biosynthetic enantiodivergence"

Zhiqiang Ma,[1]* Xiaolei Wang,[1]* Xiao Wang,[1] Rodrigo A. Rodriguez,[2] Curtis E. Moore,[3] Shuanhu Gao,[1] Xianghui Tan,[1] Yuyong Ma,[1] Arnold L. Rheingold,[3] Phil S. Baran,[2] Chuo Chen[1]†

Sherman *et al*. commented on the precedence of enantiodivergence, listing a number of congeneric natural products with opposite chirality. However, these "congeners" are not derived from enantiodivergent biosyntheses. Instead, they are antipodes arising from separate enantiomeric biosyntheses. A distinct feature of the biosynthesis of the cyclic pyrrole-imidazole dimers is the production of antipodal congeners without the corresponding enantiomers.

We found that cyclic pyrrole-imidazole dimers exist in nature as two sets of enantiomers (*1*). Unlike other natural products, all the [3+2] dimers exist in one enantiomeric form, whereas all the [2+2] and [4+2] dimers have the opposite chirality. Although the biosynthetic pathways of these alkaloids have not been genetically characterized, emerging evidence suggests that they are assembled from two molecules of pyrrole-imidazole monomers through single-electron transfer (SET)–promoted cycloaddition reactions (*2*). The [2+2] and [4+2] cycloaddition reactions of **1** give **2** and **3** that are antipodal to the [3+2] cycloadduct **4** (Fig. 1A). This "enantiodivergent" biosynthesis should not be confused with the "enantiomeric" biosynthesis that generates enantiomers—for example, (+)- and (−)-linalyl diphosphate (**6**) from geranyl diphosphate (**5**) (Fig. 1B) (*3*). The two enantiomers of limonene (**7**) and carvone (**8**) can further be produced from **6** through stereoselective cyclization and oxidation reactions.

We agree with Sherman *et al*. (*4*) that the world of natural products is full of enantiomeric diversity, although most natural products are produced in only one enantiomeric form. The terpene class of molecules, in particular, has long been recognized to exist with a wide variety of optical purities. Sherman and Williams, together with Finefield and Kreitman, have reviewed this topic in (*3*), which we cited in (*1*). We note that enantiomeric biosynthesis has also been referred to as enantiodivergent biosynthesis at times, and there are no clear definitions for these terms. Within the scope of this discussion, we use "enantiodivergent" biosynthesis only when the enantiodetermining step (eds) bifurcates in both absolute stereochemistry and framework connectivity. For an eds that generates enantiomers, we apply the term "enantiomeric" biosynthesis.

Sherman *et al*. commented that numerous examples of enantiodivergent biosynthesis exist. However, their list of antipodal congeners represents additional cases of enantiomeric biosynthesis. For example, (+)-secoisolariciresinol and (−)-matairesinol are presented as antipodal congeners, but the opposite enantiomers (−)-secoisolariciresinol and (+)-matairesinol also exist in nature (*3*). Matairesinol actually comes from secoisolariciresinol through enantiospecific oxidation by NAD-dependent secoisolariciresinol dehydrogenase (*5*). Likewise, additional "antipodal congeners" in fig. 2 in (*4*) are mostly antipodes arising from two separate enantiomeric biosyntheses instead of divergent bond formation with opposite facial selectivity. The enantiomers of (+)-sesamin, (+)-syringaresinol, (−)-laricresinol, *ent*-kaurene, *ent*-pimara-8(14),15-diene, isopimara-7,15-diene, (−)-abietic acid, (−)- stephacidin A, and (+)-versicolamide B can all be found in nature

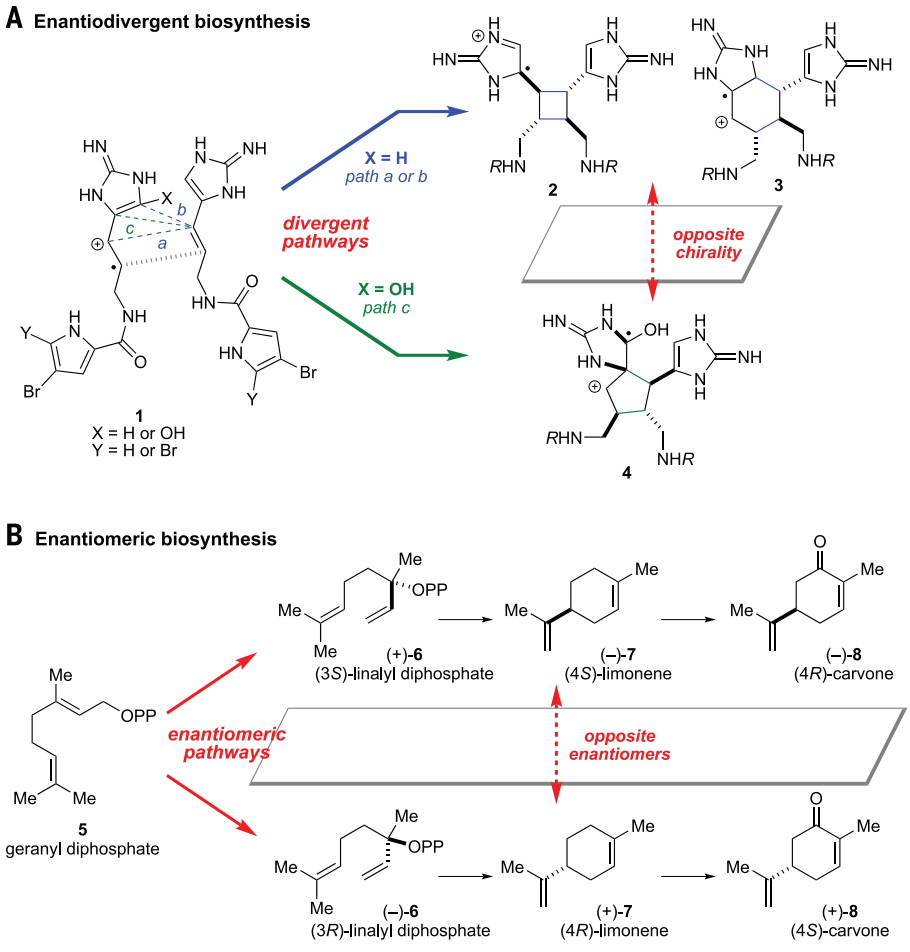


Fig. 1. Enantiodivergent versus enantiomeric biosyntheses. Enantiodivergent biosynthesis (**A**) leads to the formation of antipodal congeners, whereas enantiomeric biosynthesis (**B**) produces enantiomers.

[1]Department of Biochemistry, The University of Texas Southwestern Medical Center, Dallas, TX 75390, USA. [2]Department of Chemistry, The Scripps Research Institute, La Jolla, CA 92037, USA. [3]Department of Chemistry and Biochemistry, University of California San Diego, La Jolla, CA 92093, USA.
*These authors contributed equally to this work.
†Corresponding author. E-mail: chuo.chen@utsouthwestern.edu

Downloaded from www.sciencemag.org on July 10, 2015

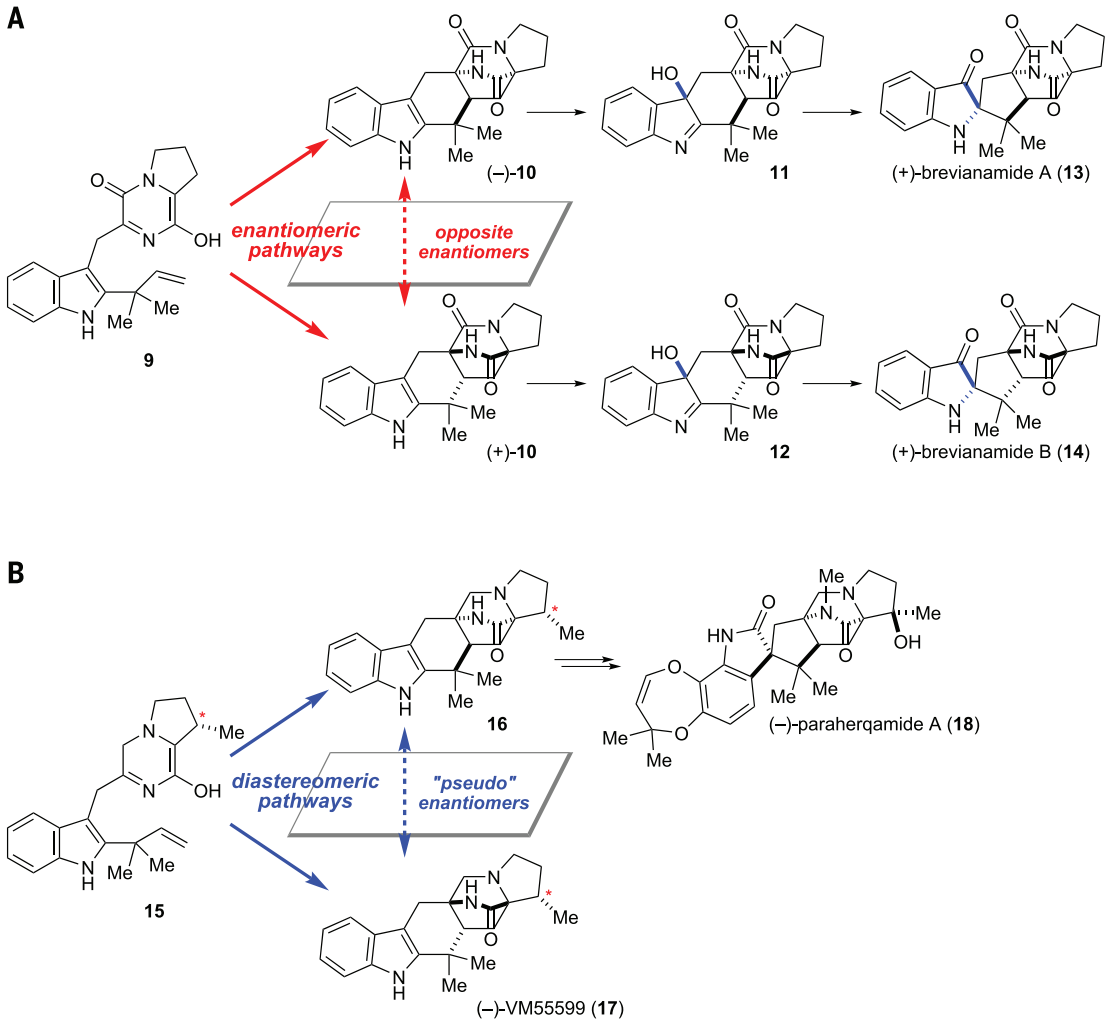


Fig. 2. Biosynthetic pathways for the reverse prenylated indole alkaloids. (**A**) Brevianamides A and B arise from enantiomeric biosynthesis. (**B**) Paraherquamide A and VM55599 arise from diastereomeric biosynthesis.

(*3*, *6*–*8*). As to nonactin, the biosynthetic eds is the formation of (+)- and (–)-nonactic acid (*3*).

The reverse prenylated indole alkaloids are intriguing fungal metabolites that nicely showcase the molecular complexity and diversity of natural products. Their syntheses and biosyntheses have been studied by Williams and others extensively (*9*). Brevianamides A and B should also arise from enantiomeric biosynthesis because the eds is the Diels-Alder reaction of the achiral precursor **9** to give (–)- and (+)-**10** (Fig. 2A) (*10*). These biosynthetic intermediates are then oxidized from the same face of the indole to give diastereomers **11** and **12**. Subsequent stereospecific rearrangement gives brevianamides A (**13**) and B (**14**), correspondingly. Similarly, VM55599 (**17**) and paraherquamide A (**18**) arise from diastereomeric Diels-Alder reactions of the chiral precursor **15**, which is assembled from L-tryptophan, L-isoleucine, and isoprenyl diphosphate (Fig. 2B) (*11*). Feeding experiments support the notion that **16** is a biosynthetic intermediate of **18**.

In closing, it is fascinating that biosynthetic eds can generate opposite enantiomers of natural products. It is even more perplexing that the biosynthetic eds of the cyclic pyrrole-imidazole dimers generates antipodal congeners. We have examined all the reports of the isolation of cyclic pyrrole-imidazole dimers. To date, all optically characterized [3+2] dimers are uniformly antipodal to the [2+2] and [4+2] dimers, regardless of the species and geographic location of the producing sponges. This mismatched chiral relationship is different from the enantiomeric relationship previously described.

REFERENCES AND NOTES

1. Z. Ma *et al.*, *Science* **346**, 219–224 (2014).
2. E. P. Stout, Y.-G. Wang, D. Romo, T. F. Molinski, *Angew. Chem. Int. Ed.* **51**, 4877–4881 (2012).
3. J. M. Finefield, D. H. Sherman, M. Kreitman, R. M. Williams, *Angew. Chem. Int. Ed.* **51**, 4802–4836 (2012).
4. D. H. Sherman, S. Tsukamoto, R. M. Williams, *Science* **349**, 149 (2015).
5. Z.-Q. Xia, M. A. Costa, H. C. Pélissier, L. B. Davin, N. G. Lewis, *J. Biol. Chem.* **276**, 12614–12623 (2001).
6. H. Kenmoku, M. Tanaka, K. Ogiyama, N. Kato, T. Sassa, *Biosci. Biotechnol. Biochem.* **68**, 1574–1577 (2004).
7. V. N. Aiyar, T. R. Seshadri, *Curr. Sci.* **41**, 839–840 (1972).
8. T. Lu, D. Vargas, S. G. Franzblau, N. H. Fischer, *Phytochemistry* **38**, 451–456 (1995).
9. R. M. Williams, R. J. Cox, *Acc. Chem. Res.* **36**, 127–139 (2003).
10. J. Baldas, A. J. Birch, R. A. Russell, *J. Chem. Soc., Perkin Trans. 1* 50–52 (1974).
11. J. F. Sanz-Cervera, R. M. Williams, *J. Am. Chem. Soc.* **124**, 2556–2559 (2002).

ACKNOWLEDGMENTS

Financial support was provided by NIH (NIGMS R01-GM079554 and R01-GM073949), the Welch Foundation (I-1596), and The University of Texas Southwestern Medical Center.

10.1126/science.aaa9626

RESEARCH

Bumblebees are failing to move northward in a warming world

Kerr et al., *p. 177*



IN *SCIENCE* JOURNALS

Edited by **Stella Hurtley**



Pandas live life in a metabolic slow zone

ANIMAL PHYSIOLOGY

Laid-back bamboo eater

Pandas are members of the order Carnivora but are entirely herbivorous, living almost exclusively on bamboo. Unlike most other herbivorous species, however, their digestive tract has not evolved the long twists and turns that facilitate the slower digestion necessary for cellulose-rich plants. Nie *et al*. measured energy expenditure in both wild and captive pandas, which was extremely low, relative to other mammals. The pandas' thyroid hormone levels are also a fraction of the mammalian norm. — SNV

Science, this issue p. 171

PROTEIN STRUCTURE

Structure of a sterol sensor

The aberrant accumulation of sterols contributes to heart attack and stroke. Two proteins embedded in the membrane of the endoplasmic reticulum, Insig-1 and Insig-2, are key players in the cellular pathway that regulates cellular sterol levels. Ren *et al*. report the structure of a mycobacterial homolog of Insig. The structure, together with biochemical experiments, suggests how Insig interacts with other components of the sterol regulatory pathway. — VV

Science, this issue p. 187

ALZHEIMER'S DISEASE

Protecting neurons from amyloid β

In the developing nervous system, the secreted protein Reelin helps to guide migrating neurons to their correct destination. In the adult nervous system, Reelin enhances synaptic plasticity and protects isolated neurons from amyloid β toxicity. Accumulation of amyloid β causes the neurodegeneration characteristic of Alzheimer's disease. To avoid the developmental defects associated with Reelin deficiency, Lane-Donovan *et al*. generated mice with an inducible knockout of Reelin. Mice that lacked Reelin as adults showed defects in synaptic plasticity, learning, and memory in response to amyloid β accumulation. Thus, Reelin can protect against amyloid β neurotoxicity in vivo. — WW

Sci. Signal. **8**, ra67 (2015).

GALAXY EVOLUTION

Black hole out of kilter with theory

It is believed that black holes and their host galaxies coevolve, with the feedback from the black hole inducing star formation. Such a scenario requires certain timing and mass constraints for the black hole and the star-forming gas. Trakhtenbrot *et al*. looked at high–red shift galaxies, when the universe was only about 2 billion years old. They found a black hole that developed to maturity much earlier than would be expected and was about 10% of the total galactic mass—much more than expected. Moreover, star formation continued after it would have been expected to stop. — ISO

Science, this issue p. 168

WATER RESOURCES

Continental global water filter

Mobile surface waters and soil waters are relatively disconnected on a global scale. Water on land is eventually lost by surface runoff into the oceans or is ultimately sent back to the atmosphere through evapotranspiration processes. Good *et al*. determined that 65% of continental water evaporation is from soils, which includes water taken up and transpired by plants (see the Perspective by Brooks). Although just a small fraction of global surface waters pass through soils, individual stream ecosystems may be affected by water quality changes in nearby soils. — NW

Science, this issue p. 175; see also p. 138

Downloaded from www.sciencemag.org on July 10, 2015

PHOTOS: (TOP TO BOTTOM) ANTAGAIN/ISTOCKPHOTO; © OLGA KHOROSHUNOVA/ALAMY

Published by AAAS

VESICULAR TRANSPORT

A coat of many components

The formation of coated trafficking vesicles is among the most fundamental of cellular processes. COP1 transport vesicles are involved in retrograde membrane trafficking in the Golgi apparatus and endoplasmic reticulum. Dodonova *et al*. applied cryo–electron tomography to determine the structure of the COPI coat in its fully assembled form on budded vesicles (see the Perspective by Noble and Stagg). They combined structural data with cross-linking mass spectrometry to generate a complete molecular model. The model suggests a mechanism of coat assembly in which coat proteins cluster via flexible interactions instead of forming a protein cage on the membrane. — SMH

Science, this issue p. 195; see also p. 142

SOFT ROBOTICS

Making jack jump efficiently

In the future, soft-bodied robots may be able to squeeze into tight spaces or work in environments where they could be crushed. However, it is hard to ensure efficient power transmission in a soft-bodied device. One promising solution is to use explosions to drive the robot, using efficient weight-to-power energy sources. Using three-dimensional printing to fuse together multiple materials, Bartlett *et al*. built a combustion-powered robot. The robot has a rigid core that transitions to a soft exterior. They produced an efficient jumping robot in which the gradations in the hardness of the body materials also improved robustness. — MSL

Science, this issue p. 161



Jumping robots in action

PHOTOS: (LEFT TO RIGHT) BARTLETT *ET AL*.; H. T.-K. VU *ET AL*., *ELIFE* (9 JUNE 2015) © 2015 ELIFE SCIENCES PUBLICATIONS, LTD.

PLUTONIUM

"Missing magnetism" puzzle solved

To explain plutonium's complex structural properties, conventional band structure theories typically invoke magnetism, in stark contrast with experiment. Janoschek *et al*. used neutron spectroscopy and found that the magnetism in plutonium is not "missing" but dynamic: the fingerprint of an electronic ground state that is a quantum-mechanical admixture of localized and itinerant electronic configurations. This finding provides a natural explanation for plutonium's complex structural, magnetic, and electronic properties. — ZHK

Sci. Adv. 10.1126. sciadv.1500188 (2015).

NEURONAL MODELING

A better way to explain neuronal activity

A brain region called the lateral intraparietal (LIP) area is involved in primate decision-making. The dominant model to explain neuronal firing in LIP assumes that neurons slowly accumulate sensory evidence in favor of one choice or another. Latimer *et al*. hypothesized that neurons instead exhibit rapid steps or jumps in their firing rate, reflecting discrete changes in the animal's decision state. They recorded from LIP neurons in macaque monkeys performing a motion-discrimination task. LIP spike trains in most cells involved discrete stepping dynamics rather than slow evidence integration dynamics. — PRS

Science, this issue p. 184

IN OTHER JOURNALS

Edited by **Kristen Mueller** *and* **Jesse Smith**



Protonephridia of the planarian excretory system

DEVELOPMENT

Planaria have model kidneys

Individuals with polycystic kidney disease (PKD) develop fluid-filled cysts in their nephrons that interfere with kidney function. Looking for a suitable invertebrate model of PKD, Vu *et al*. discovered that the excretory system of planarian flatworms is a good model for normal and diseased human kidneys. The planarian protonephridia shares structural similarities with the subsegments of the vertebrate nephron, and both organisms use cilia-driven ultrafiltration and filtrate modification. Moreover, mutating planarian orthologs of human genes resulted in phenotypes and pathologies similar to those seen in human PKD. — BAP

eLife 10.7554/eLife.07405 (2015).

INFLUENZA

Geometry and virus evolution

An influenza pandemic is only a couple of mutations away. Or is it? Meyer and Wilke analyzed how the hemagglutinin protein of the H3 subtype of influenza has evolved, to learn how mutation allows this virus to escape host immune surveillance. This method combines sequencing data with data on protein structure and present and past antigenic sites (that is, sites recognized by antibodies) on hemagglutinin. Surprisingly, antigenic information revealed little, but the geometrical changes wrought by mutations in the host cell receptor-binding site did. This analysis indicates that mutation in sites that we understand to be antigenic may not influence how influenza evolves as much as previously assumed. — CA

PLOS Pathol. **11**, e1004940 (2015).

CANCER THERAPY

(Mis)matching tumors to immunotherapy

Despite the amazing success stories seen in some patients receiving cancer

Published by AAAS

ALSO IN *SCIENCE* JOURNALS

Edited by **Stella Hurtley**

SEA-LEVEL RISE

Warming climate, melting ice, rising seas

We know that the sea level will rise as climate warms. Nevertheless, accurate projections of how much sea-level rise will occur are difficult to make based solely on modern observations. Determining how ice sheets and sea level have varied in past warm periods can help us better understand how sensitive ice sheets are to higher temperatures. Dutton *et al*. review recent interdisciplinary progress in understanding this issue, based on data from four different warm intervals over the past 3 million years. Their synthesis provides a clear picture of the progress we have made and the hurdles that still exist. — HJS

Science, this issue p. 153

HIV-1 VACCINES

Steps in the right direction

HIV-1 mutates rapidly, making it difficult to design a vaccine that will protect people against all of the virus' iterations. A potential successful vaccine design might protect by eliciting broadly neutralizing antibodies (bNAbs), which target specific regions on HIV-1's trimeric envelope glycoprotein (Env) (see the Perspective by Mascola). Jardine *et al.* used mice engineered to express germline-reverted heavy chains of a particular bNAb and immunized them with an Env-based immunogen designed to bind to precursors of that bNAb. Sanders *et al*. compared rabbits and monkeys immunized with Env trimers that adopt a native-like conformation. In both cases, immunized animals produced antibodies that shared similarities with bNAbs. Boosting these animals with other immunogens may drive these antibodies to further mutate into the long-sought bNAbs. Chen *et al*. report that retaining the cytoplasmic domain of Env proteins may be important to attract bNAbs. Removing the cytoplasmic domain may distract the immune response and instead generate antibodies that target epitopes on Env that would not lead to protection. — KLM

Science, this issue p. 139, p. 154, p. 156; see also p. 191

IMMUNOLOGY

Single-cell measurements map immunity

Multiple characteristics of individual cells define cell types and their physiological states. Spitzer *et al*. quantitated the abundance of 39 different cell surface proteins or transcription factors on individual cells of the mouse immune system. They used these measurements to create a map that clustered similar individual cells into groups corresponding to cell type and function. Their extensible experimental platform will allow the inclusion of other data types and data from independent laboratories. — LBR

Science, this issue p. 155

APPLIED PHYSICS

Graphene-based biosensors

The mid-infrared (mid-IR) range is particularly well suited for biosensing because it encompasses the molecular vibrations that identify the biochemical building blocks of life, such as proteins, lipids, and DNA. However, the resulting optical signal is extremely weak and often requires complex techniques to enhance the biological detection. Rodrigo *et al*. present a graphene-based biosensor that they dynamically tuned over a broad spectral range through electrical gating. The authors selectively probed protein molecules at different mid-IR frequencies using a single device. — ISO

Science, this issue p. 165

ECONOMICS

The heroes of the Industrial Revolution

Did a few great inventors and scientists drive the Industrial Revolution, or would it have happened regardless of such brilliant individuals? In a Perspective, Mokyr argues that the truth probably lies in the middle. Only a small minority of the population was involved in creating and adapting the new techniques and machines that would revolutionize the economy. A recent study estimates the size of these educated elites in French cities from the subscribers to the *Grande Encyclopédie*. The more subscribers there were in a city, the faster was the subsequent process of industrialization. Modern societies aiming to foster scientific and technological creativity may thus need to do more than raise the levels of mass education. — JFU

Science, this issue p. 141

PLACE CELLS

Memory storage in neural networks

Neuronal networks can store and retrieve discrete memories, but often fail to retrieve stored sequences. This is because error decreases over time for a static attractor, but builds up drastically over time if patterns are not trained to retrieve themselves but to retrieve the next item in a sequence. Pfeiffer and Foster studied brain activity in awake but immobile rats. Recording simultaneously from a large number of place cells in the hippocampal formation, they found that internally generated sequences alternated between periods of hovering in place while being strengthened, and periods of abrupt transition to a new place. — PRS

Science, this issue p. 180

CLIMATE CHANGE

Bucking the trend

Responses to climate change have been observed across many species. There is a general trend for species to shift their ranges poleward or up in elevation. Not all species, however, can make such shifts, and these species might experience more rapid declines. Kerr *et al*. looked at data on bumblebees across North America and Europe over the past 110 years. Bumblebees have not shifted northward and are experiencing shrinking distributions in the southern ends of their range. Such failures to shift may be because of their origins in a cooler climate, and suggest an elevated susceptibility to rapid climate change. — SNV

Science, this issue p. 177

LUNG DISEASE

Calming the cytokine storm

The innate immune response is poised to act quickly in the face of pathogenic invaders. However, this priming can incite a cytokine storm: excessive production of inflammatory cytokines that harm the host. Coon *et al*. now report that HECTD2, a ubiquitin E3 ligase, can degrade the anti-inflammatory protein PIAS1, enhancing this inflammatory effect. People with a polymorphism in the *HECTD2* gene exhibit lower inflammation and are protected from acute respiratory distress syndrome. Moreover, a small-molecule inhibitor of HECTD2 reduced lung inflammation in mice. These observations pinpoint HECTD2 as a therapeutic target for inflammation-induced lung injury. — ACC

Sci. Transl. Med. **7**, 295ra109 (2015).

Published by AAAS

REVIEW SUMMARY

SEA-LEVEL RISE

Sea-level rise due to polar ice-sheet mass loss during past warm periods

A. Dutton,* A. E. Carlson, A. J. Long, G. A. Milne, P. U. Clark, R. DeConto, B. P. Horton, S. Rahmstorf, M. E. Raymo

BACKGROUND: Although thermal expansion of seawater and melting of mountain glaciers have dominated global mean sea level (GMSL) rise over the last century, mass loss from the Greenland and Antarctic ice sheets is expected to exceed other contributions to GMSL rise under future warming. To better constrain polar ice-sheet response to warmer temperatures, we draw on evidence from interglacial periods in the geologic record that experienced warmer polar temperatures and higher GMSLs than present. Coastal records of sea level from these previous warm periods demonstrate geographic variability because of the influence of several geophysical processes that operate across a range of magnitudes and time scales. Inferring GMSL and ice-volume changes from these reconstructions is nontrivial and generally requires the use of geophysical models.

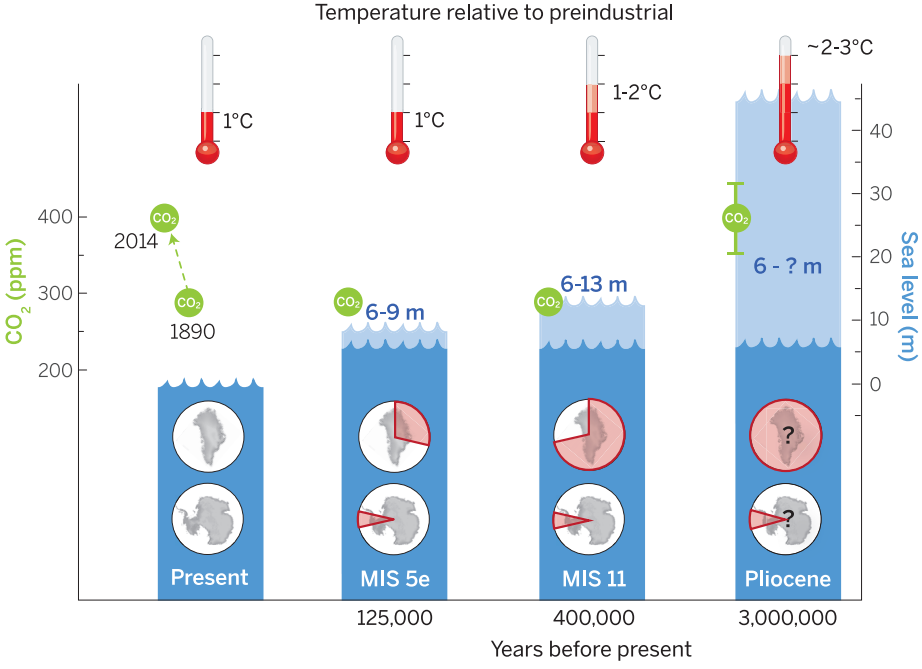
ON OUR WEB SITE

Read the full article at http://dx.doi.org/10.1126/science.aaa4019

ADVANCES: Interdisciplinary studies of geologic archives have ushered in a new era of deciphering magnitudes, rates, and sources of sea-level rise. Advances in our understanding of polar ice-sheet response to warmer climates have been made through an increase in the number and geographic distribution of sea-level reconstructions, better ice-sheet constraints, and the recognition that several geophysical processes cause spatially complex patterns in sea level. In particular, accounting for glacial isostatic processes helps to decipher spatial variability in coastal sea-level records and has reconciled a number of site-specific sea-level reconstructions for warm periods that have occurred within the past several hundred thousand years. This enables us to infer that during recent interglacial periods, small increases in global mean temperature and just a few degrees of polar warming relative to the preindustrial period resulted in ≥6 m of GMSL rise. Mantle-driven dynamic topography introduces large uncertainties on longer time scales, affecting reconstructions for time periods such as the Pliocene (~3 million years ago), when atmospheric CO_2 was ~400 parts per million (ppm), similar to that of the present. Both modeling and field evidence suggest that polar ice sheets were smaller during this time period, but because dynamic topography can cause tens of meters of vertical displacement at Earth's surface on million-year time scales and uncertainty in model predictions of this signal are large, it is currently not possible to make a precise estimate of peak GMSL during the Pliocene.

OUTLOOK: Our present climate is warming to a level associated with significant polar ice-sheet loss in the past, but a number of challenges remain to further constrain ice-sheet sensitivity to climate change using paleo–sea level records. Improving our understanding of rates of GMSL rise due to polar ice-mass loss is perhaps the most societally relevant information the paleorecord can provide, yet robust estimates of rates of GMSL rise associated with polar ice-sheet retreat and/or collapse remain a weakness in existing sea-level reconstructions. Improving existing magnitudes, rates, and sources of GMSL rise will require a better (global) distribution of sea-level reconstructions with high temporal resolution and precise elevations and should include sites close to present and former ice sheets. Translating such sea-level data into a robust GMSL signal demands integration with geophysical models, which in turn can be tested through improved spatial and temporal sampling of coastal records.

Further development is needed to refine estimates of past sea level from geochemical proxies. In particular, paired oxygen isotope and Mg/Ca data are currently unable to provide confident, quantitative estimates of peak sea level during these past warm periods. In some GMSL reconstructions, polar ice-sheet retreat is inferred from the total GMSL budget, but identifying the specific ice-sheet sources is currently hindered by limited field evidence at high latitudes. Given the paucity of such data, emerging geochemical and geophysical techniques show promise for identifying the sectors of the ice sheets that were most vulnerable to collapse in the past and perhaps will be again in the future. ■



Peak global mean temperature, atmospheric CO_2, maximum global mean sea level (GMSL), and source(s) of meltwater. Light blue shading indicates uncertainty of GMSL maximum. Red pie charts over Greenland and Antarctica denote fraction (not location) of ice retreat.

The list of author affiliations is available in the full article online.
*Corresponding author. E-mail: adutton@ufl.edu
Cite this paper as A. Dutton *et al.*, *Science* 349, aaa4019 (2015). DOI: 10.1126/science.aaa4019

Downloaded from www.sciencemag.org on July 10, 2015

REVIEW

SEA-LEVEL RISE

Sea-level rise due to polar ice-sheet mass loss during past warm periods

A. Dutton,[1]* A. E. Carlson,[2] A. J. Long,[3] G. A. Milne,[4] P. U. Clark,[2] R. DeConto,[5] B. P. Horton,[6,7] S. Rahmstorf,[8] M. E. Raymo[9]

Interdisciplinary studies of geologic archives have ushered in a new era of deciphering magnitudes, rates, and sources of sea-level rise from polar ice-sheet loss during past warm periods. Accounting for glacial isostatic processes helps to reconcile spatial variability in peak sea level during marine isotope stages 5e and 11, when the global mean reached 6 to 9 meters and 6 to 13 meters higher than present, respectively. Dynamic topography introduces large uncertainties on longer time scales, precluding robust sea-level estimates for intervals such as the Pliocene. Present climate is warming to a level associated with significant polar ice-sheet loss in the past. Here, we outline advances and challenges involved in constraining ice-sheet sensitivity to climate change with use of paleo–sea level records.

Global mean sea level (GMSL) has risen over the past century, largely in response to global warming (~0.19 m rise in GMSL between 1901 and 2010) (*1*). The response to global warming includes thermal expansion of ocean water as well as mass loss from glaciers and ice sheets, all of which increase the volume of water in the ocean and cause the sea level to rise. Recent GMSL rise has been dominated by thermal expansion and glacier loss, which collectively explain ~75% of the observed rise since 1971 (*1*). The contribution from mass loss from the Greenland (GrIS) and Antarctic (AIS) ice sheets has increased since the early 1990s, composing ~19% of the total observed rise in GMSL between 1993 and 2010 (*1*), and is expected to exceed other contributions under future sustained warming [e.g., (*2*)]. Estimates from short, recent time periods—though not as robust as analyses of longer records because of the dominance of interannual variability—suggest that polar ice-sheet loss may now compose as much as ~40% of the total observed rise in GMSL between 2003 and 2008 (*3*, *4*).

These same processes contributed to higher-than-present sea levels in the past when global mean temperature was warmer than the preindustrial period (before 1750). However, because mountain glaciers and thermal expansion can only explain ~1 to 1.5 m of GMSL rise for the 1° to 3°C warming associated with these periods (*5*, *6*), evidence for former GMSL exceeding this amount requires a contribution from the GrIS and/or AIS. Understanding how polar ice sheets lost mass and contributed to sea-level rise during past warm periods can provide insights into their sensitivity to climate change, as well as constrain process-based models used to project ice-sheet response to future climate change.

Many studies have used data and/or models to determine the sensitivity of ice sheets to changes in temperature or atmospheric CO_2 over long time scales (*2*, *7*–*12*). Given the recent increases in greenhouse gases (GHGs) and global mean temperature, the present ice sheets are out of equilibrium with the climate, raising important questions regarding their potential future contribution to sea-level rise: (i) What is the equilibrium sea-level rise for a given warming scenario? (ii) How quickly will the GrIS and the AIS respond to present and future radiative forcing and associated warming, and what will be the accompanying rates of sea-level change? (iii) What are the source regions of the ice-mass loss, a factor that will strongly influence the geographic pattern of future sea-level change (*1*, *2*, *13*)?

To address these questions, we examine how our understanding of ice-sheet response during past warm periods is evolving through the progressive integration of several disciplines. In particular, we consider observational evidence of paleo–sea levels and ice-sheet reconstructions with climate, ice-sheet, and solid Earth models. For each time period, we identify key geophysical signals that must be quantitatively estimated and removed from relative sea level (RSL; refers to the local height of sea level) records in order to infer past changes in GMSL (Box 1). Last, we review the state of knowledge regarding the magnitudes, rates, and sources of sea-level rise during several of the most prominent interglacial peaks of the last three million years, including the mid-Pliocene warm period [MPWP, ~3 million years ago (Ma)], marine isotope stage (MIS) 11 [~400 thousand years ago (ka)], and MIS 5e (~125 ka) (Fig. 1).

Mid-Pliocene warm period (~3.2 to 3.0 Ma)

The MPWP comprises a series of orbitally paced [41–thousand year (ky)] climate cycles associated with atmospheric CO_2 in the range of 350 to 450 parts per million (ppm) (*14*, *15*). Peak global mean temperatures derived from general circulation model simulations average 1.9° to 3.6°C warmer than preindustrial (*16*). Some Arctic temperature reconstructions indicate warming of 8°C or more, whereas some Southern Ocean records suggest warming of 1° to 3°C (*17*). However, these temperature estimates are uncertain and, in some cases, may not correlate precisely to the MPWP time interval. Both modeling and field evidence suggest that polar ice sheets were smaller during the MPWP, but constraints on the magnitude of GMSL maxima during the warm extremes as inferred from RSL reconstructions are highly uncertain (*18*).

In the Southern Hemisphere, the West Antarctic Ice Sheet (WAIS) experienced multiple retreat and advance phases during the Pliocene (*19*). Studies of ice-rafted debris (IRD) suggest that portions of the East Antarctic Ice Sheet (EAIS) experienced retreat during parts of the early to middle Pliocene (*20*), apparently paced by precessional (23-ky) cycles (*21*). In the Northern Hemisphere, there are no firm observational constraints on changes in the size of the MPWP GrIS. Ice-sheet models, on the other hand, simulate retreat in both Greenland (*22*) and Antarctica (*12*) in response to imposed Pliocene climate forcing, raising GMSL by ~7 m and ~6 m, respectively.

Many early studies of Pliocene coastal records considered Earth to be rigid and inferred a uniform GMSL rise across a wide range of elevations [+15 to 60 m; see table 1 in (*18*)]. Some studies attempted to correct individual RSL records for the influence of local tectonics or subsidence (*23*–*27*). More recently, Raymo *et al.* (*18*) corrected Pliocene RSL observations for the effects of glacial isostatic adjustment (GIA), but the global variability in the elevation of observed shorelines remains substantial, ranging over tens of meters. This is thought to be due to the influence of mantle-driven dynamic topography (Box 1), as well as to uncertainties in the elevation and the age of shoreline features (*18*, *28*, *29*). Improvements in model parameters for GIA and dynamic topography and in dating of coastal records are needed to better constrain estimates of Pliocene sea level from coastal records.

The amplitude of negative excursions in benthic oxygen isotope ($\delta^{18}O$) records during the MPWP [~0.4 per mil (‰) relative to the Holocene] (Fig. 1) may imply higher GMSL than today, but extracting the ice-volume signal from the $\delta^{18}O$ calcite record remains a challenge. Typical analytical errors in $\delta^{18}O$ measurements translate to large uncertainties in sea level (~±10 m). Moreover, inferring ice volume requires that the

[1]Department of Geological Sciences, University of Florida, Gainesville, FL 32611, USA. [2]College of Earth, Ocean, and Atmospheric Sciences, Oregon State University, Corvallis, OR 97331, USA. [3]Department of Geography, Durham University, Durham, UK. [4]Department of Earth Sciences, University of Ottawa, Ottawa, Canada. [5]Department of Geosciences, University of Massachusetts, Amherst, MA 01003, USA. [6]Department of Marine and Coastal Sciences, Rutgers University, New Brunswick, NJ 08901, USA. [7]Earth Observatory of Singapore, Nanyang Technological University, Singapore, 639798. [8]Potsdam Institute for Climate Impact Research, Potsdam, Germany. [9]Lamont-Doherty Earth Observatory, Columbia University, Palisades, NY 10964, USA.
*Corresponding author. E-mail: adutton@ufl.edu

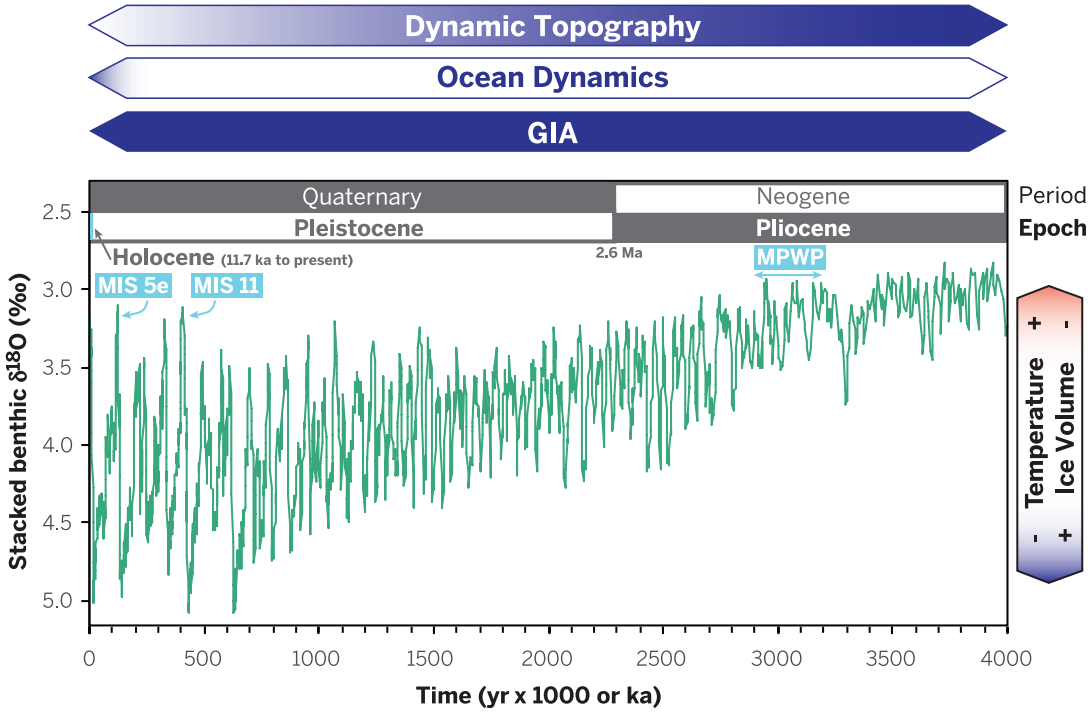


Fig. 1. Stacked benthic $\delta^{18}O$ with time periods discussed in text. Benthic $\delta^{18}O$ [green curve–LR04 (*32*)] provides a combined signal of ice volume and temperature deep into the geologic past (*106*). Physical processes that contribute to RSL signals are depicted as blue bars. The length of the blue bar indicates timespan over which the process is active; shading denotes time interval where the process can have the most significant influence on RSL reconstructions. For example, the rates of dynamic topography are slow enough that it generally is only a significant factor for reconstructing older paleoshorelines, as denoted by shading. GIA can dominate spatial variability in RSL across all of these time scales.

contribution of seawater temperature and hydrography to the benthic $\delta^{18}O$ signal is known. The Mg/Ca of the benthic calcite record can be used to isolate the temperature portion of the corresponding $\delta^{18}O$ signal, but uncertainties in calibration (*30*, *31*), carbonate ion saturation (*32*), diagenesis of calcite (*33*), and long-term seawater Mg/Ca variability (*34*) are significant. Until these effects are better understood and able to be isolated, the $\delta^{18}O$ proxy records will continue to be plagued by uncertainties as large as the signal we are seeking. In light of these considerations, the Miller *et al.* (*24*) peak GMSL estimate of 21 ± 10 m at the end of the MPWP (~2.95 Ma) that is based on evidence from non–GIA-corrected coastal records, benthic $\delta^{18}O$ (*35*), and paired $\delta^{18}O$-Mg/Ca records probably carries more uncertainty than the quoted range.

MIS 11 (~424,000 to 395,000 years ago)

MIS 11 was an unusually long interglacial period (~30 ky) with a highly uncertain global average temperature [estimates range from slightly cooler than MIS 5e (see below) (*36*, *37*) up to ~2°C warmer than preindustrial (*38*)] and atmospheric CO_2 peaking at 286 ppm (similar to preindustrial values) (*39*). Limited proxy data indicate Arctic summer maximum air and sea surface temperatures reaching up to 4° and 9°C warmer, respectively, than peaks attained during the Holocene or MIS 5e (*40*, *41*). Antarctic ice-core analyses indicate temperatures ~2.6°C warmer than preindustrial (*42*). Climate models forced by insolation and GHG concentrations during MIS 11, however, simulate only slightly warmer global mean temperatures (~0.1°C) than for the Holocene (*38*, *43*). Hence, if the limited proxy data are correct in implying enhanced warmth in the polar regions, the underlying cause of the warmer climates is unresolved.

Reconstructions of MIS 11 GMSL suggest that it was higher than present. Several records document at least partial retreat of the GrIS during MIS 11, suggesting that it contributed to higher GMSL. Pollen in marine records offshore of southeast Greenland indicates the development of spruce forest over parts of now-ice-covered regions (*44*). Likewise, biomolecules from the base of the Dye-3 ice core indicate a forested southern Greenland that could be from MIS 11, although the age of these molecules is uncertain (*45*). A cessation of ice-sheet-eroded sediment discharge and IRD suggests ice-margin retreat from the southern Greenland coast (*46*), whereas continued IRD deposition in the northeast demonstrates the persistence of marine-terminating ice over northeastern Greenland (*47*). Comparison of these constraints with ice-sheet models suggests that the GrIS could have contributed 4.5 to 6 m to GMSL rise above present (*46*). Higher GMSL estimates thus require an Antarctic contribution, but few geologic constraints on AIS history exist for MIS 11 (*48*).

Early work on interpreting MIS 11 coastal records assumed a geographically uniform GMSL change, with sea-level estimates ranging from –3 (*49*) to +20 m (*50*). If the records are all the same age, the large range may largely reflect geographic variability in the RSL signal associated with GIA and dynamic topography (Box 1 and Fig. 2). For example, when corrected for GIA, MIS 11 RSL in the Bermuda and Bahamas regions (~20 m above present) suggests a peak GMSL of only 6 to 13 m above present (*51*), a level that would require loss of the GrIS and/or sectors of the AIS. This estimate is consistent with the 8- to 11.5-m estimate based on paleoshorelines in South Africa that have been corrected for GIA effects and local tectonic motion (*52*, *53*). Overall, multiple lines of evidence seem to agree that GMSL was 6 to 13 m higher near the end of MIS 11.

By comparison, paired $\delta^{18}O$-Mg/Ca measurements of benthic foraminifera suggest GMSL during MIS 11 in excess of 50 ± ~20 m above present (*31*, *54*), although, as with the MPWP reconstructions, the uncertainties on these estimates may be much larger. On the other hand, the Red Sea planktic $\delta^{18}O$ record suggests that RSL reached just above present (1 ± 12 m at 2σ) (*55*, *56*). Additional contributions from GIA and possibly also from dynamic topography to the sill depth of the Red Sea over the last several hundred ky that are not captured in the present reconstruction could impart additional uncertainties. The large uncertainty and the lack of agreement associated with all of these $\delta^{18}O$-based records point to the difficulty in using them to tightly constrain peak GMSL during previous warm periods.

MIS 5e (~129,000 to 116,000 years ago)

We consider the time interval of MIS 5e when GMSL was above present (~129 to 116 ka) (*8*, *57*). Relative to the preindustrial period, model simulations indicate little global average temperature change during MIS 5e, whereas proxy data imply ~1°C of warming, but with possible spatial and temporal sampling biases (*58*). Greenland temperatures peaked between ~5° to 8°C above preindustrial (*59*, *60*), and Antarctic temperatures were ~3° to 5°C warmer (*42*).

Shorelines that developed during the MIS 5e sea-level highstand are the best-preserved and most geographically widespread record of a higher-than-present GMSL during a previous warm period. Recent global compilations of RSL data combined with GIA modeling indicate that peak GMSL was higher than the previous long-standing estimate (4 to 6 m), in the range of ~6 to 9 m

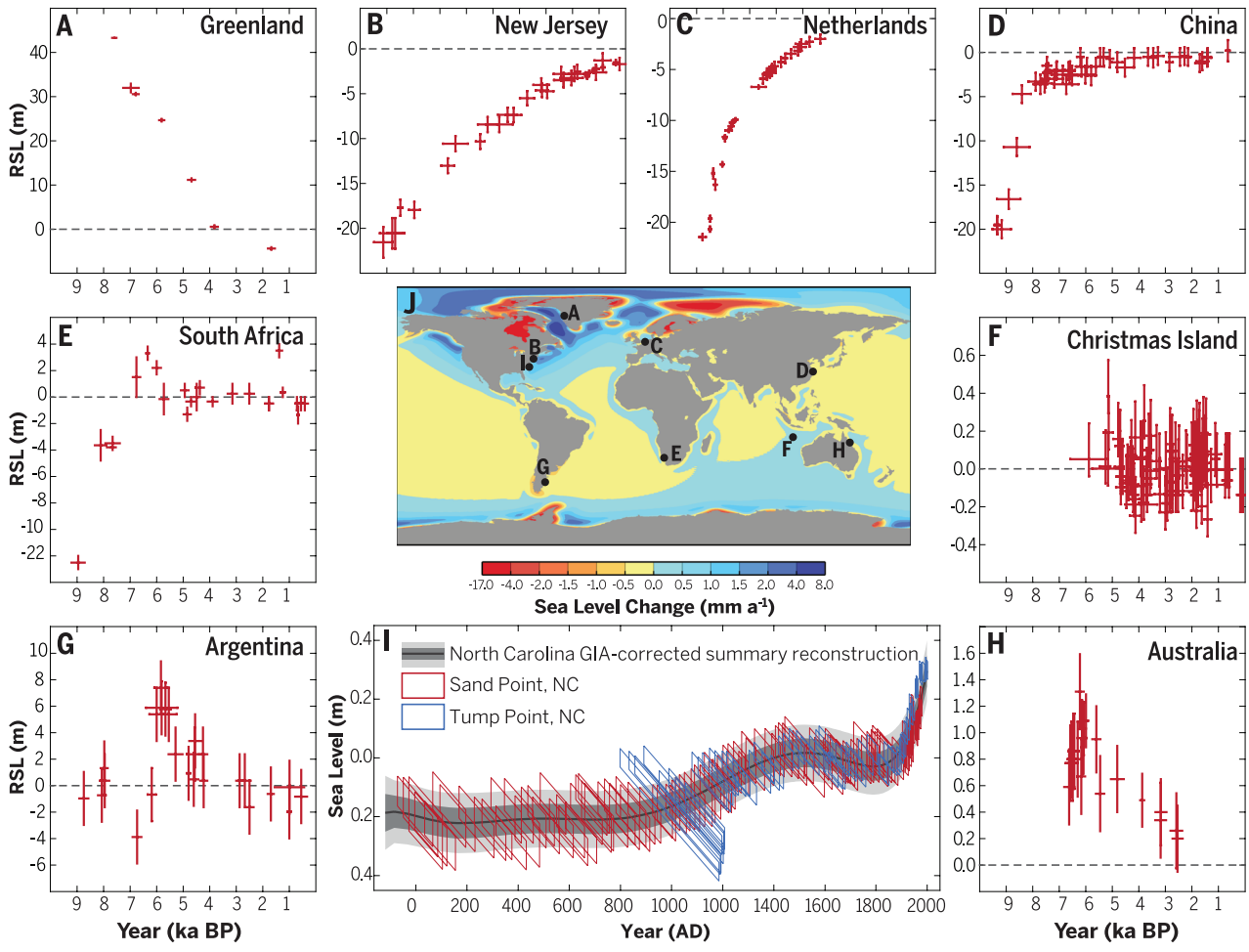


Fig. 2. Selected Holocene RSL reconstructions. Elevations and interpretation of sea-level index points (including errors) have not been amended from the original publication. Radiocarbon ages were converted to calibrated dates where necessary, shown as calibrated years before present × 1000 (ka BP). (**A** to **I**) Site locations and data sources are listed in table S1. (I) GIA-adjusted sea level at North Carolina relative to a preindustrial average for 1400 to 1800 CE. Center panel (J) shows rates of present sea-level change resulting from GIA, based on ICE-5G (*125*) and the VM2 Earth model with a 90-km-thick lithosphere.

above present (*61*, *62*), in agreement with site-specific, GIA-corrected coastal records in the Seychelles at 7.6 ± 1.7 m (*63*) and in Western Australia at 9 m (no uncertainty reported) (*64*) above present (Fig. 3). The Red Sea planktic $\delta^{18}O$ record places peak RSL values during MIS 5e at 6.7 ± 3.4 m (maximum probability with 95% probability envelope) (*65*). Detailed GIA corrections for the temporal evolution of the hydraulic geometry of the Red Sea during MIS 5e are not applied to this planktic $\delta^{18}O$ record and could change the peak value by a few meters (*66*). Paired benthic $\delta^{18}O$-Mg/Ca data (*31*, *54*) reflect high uncertainty and poor agreement for peak GMSL when compared with the coastal records (Fig. 4).

The 3-m uncertainty range in peak GMSL derived from coastal records (i.e., ~6 to 9 m) presents a challenge when assessing relative GrIS and AIS contributions. Ice-core and marine records show that the GrIS was smaller than present during MIS 5e, with substantial (but not complete) retreat of the southern sector at the same time as peak GMSL ~122 to 119 ka (*60*, *67*). Recent modeling studies suggest that total GrIS mass loss was between 0.6 to 3.5 m (Fig. 3 and references therein). With thermal expansion and melting of mountain glaciers contributing up to ~1-m rise (*5*, *68*), an additional contribution is required from the AIS to explain peak GMSL during MIS 5e. However, direct evidence for AIS retreat at this time is lacking, with only some poorly dated records that suggest that WAIS retreated during some previous interglacial periods, including possibly MIS 5e (*69*).

The primary means of establishing an accurate and precise chronology for MIS 5e sea level is through U-Th dating of fossil corals that lived near the sea surface. Existing chronologies suggest regional differences in the timing of peak MIS 5e RSL. In some cases, this reflects variable diagenesis that causes open-system conditions in the corals with respect to U and Th isotopes [e.g., (*70*)]. However, differences in timing may also be real and reflect the spatially variable influence of GIA (*61*). Most studies suggest that peak GMSL occurred sometime after ~125 ka, usually in the range of ~122 to 119 ka (*64*, *71*–*74*), but the timing of AIS versus GrIS contributions to maximum GMSL remains unresolved.

Differences in RSL reconstructions from site to site yield a range of interpretations about the evolution of GMSL during the MIS 5e highstand, including (i) a stable sea level (*57*), (ii) two peaks separated by an ephemeral drop in sea level (*72*, *73*), (iii) a stable sea level followed by a rapid sea-level rise (*64*, *71*), and (iv) three to four peaks in sea level reflecting repeated sea-level oscillations (*74*, *75*). As yet, no consensus exists regarding this suite of scenarios, but robust sedimentary evidence from multiple coastal sites argues for at least one and possibly several meter-scale sea-level oscillations during the course of the highstand [e.g., (*64*, *71*–*73*, *76*)]. These data suggest

dynamic behavior of polar ice sheets at a time when global mean temperature was similar to present. It is not clear whether such variability was driven by one unstable ice-sheet sector or by differences in the phasing of ice-mass changes in multiple ice-sheet sectors across the duration of MIS 5e.

Estimated rates of sea-level change associated with these oscillations range from 1 to 7 m ky^{-1} (*74*, *75*, *77*). Resolving rates on shorter time scales is hindered by the precision of the dating and RSL reconstruction methods. Even the m ky^{-1} rates listed above are highly uncertain if one incorporates a full consideration of observational errors. For example, MIS 5e reefs in the Bahamas have uncertainties in coral paleowater depths of >5 m (based on the assumed depth range of *Acropora palmata*) or more (for the *Montastrea* sp. and *Diploria* sp.), which are similar in magnitude to the inferred change in sea level (4 to 6 m) (*72*, *74*). As another example, meter-scale RSL fluctuations during the MIS 5e highstand inferred from the Red Sea planktic $\delta^{18}O$ record are not replicated between the two cores used in the analysis and the variability largely falls within the reported uncertainty, so it is not possible to reject the null hypothesis that RSL was stable based on this record (*75*). Thus, despite the clear sedimentary evidence for sea-level variability in during MIS 5e, associated rates of GMSL change remain poorly resolved.

The Holocene (11,700 years ago to present)

Global mean temperatures during the Holocene have ranged from ~0.75°C warmer (from ~9.5 to 5.5 ka) than preindustrial temperatures (*78*) to preindustrial levels (*79*). Although this temperature reconstruction is relatively well constrained by proxy data, models simulate a warming trend through the Holocene, which may be an indication of uncertainty in the reconstructions, the models, or both (*80*).

The Holocene has the most abundant and highly resolved RSL reconstructions in comparison to previous interglacial periods (Fig. 2). In addition, the history of ice-sheet retreat is relatively well constrained, particularly in the Northern Hemisphere. Detailed sea-level reconstructions from the past few millennia are important for constraining the natural variability in sea level and providing context for evaluating current and future change (*1*, *81*).

GMSL was ~60 m lower than present at the beginning of the Holocene, largely because of the remaining Scandinavian and Laurentide ice sheets as well as a greater-than-present AIS volume. Rates of GMSL rise slowed by ~7 ka after the final deglaciation of the Laurentide Ice Sheet—from ~15 m ky^{-1} between ~11.4 to 8.2 ka to ~1 m ky^{-1} or less for the remainder of the preindustrial Holocene (*82*). Only a few meters of ice-sheet loss occurred between ~7 and ~2 ka (*82*, *83*), which is thought to be dominated by loss from the AIS (*84*, *85*). Field data and ice-sheet models suggest that the GrIS was smaller than present during the early to middle Holocene thermal optimum (9.5 to 5.5 ka) (*86*, *87*) and began to re-advance during the cooler Neoglacial period (<5 ka), reaching its maximum extent in many places during the Little Ice Age and causing a GMSL lowering of <0.2 m (*88*).

Over the past ~7 ky, RSL has fallen in many near-field areas that were formerly covered by major ice sheets because of glacial isostatic rebound (Fig. 2A), whereas RSL in intermediate- and far-field regions reflects changes in GMSL, proglacial forebulge collapse, and hydro-isostatic loading (*89*, *90*), with deltaic regions being further influenced by compaction (Fig. 2, B to D). Equatorial and Southern Hemisphere RSL reconstructions record a mid-Holocene highstand at ~6 ka of a few decimeters to several meters (*91*, *92*) (Fig. 2, E to H) that is a consequence of the GIA effect known as equatorial siphoning (*89*, *90*).

Sea-level reconstructions from salt marshes bordering the North Atlantic region reveal regional decimeter-scale variability on multidecadal to millennial time scales over the past ~2 ky (*81*, *93*) (Fig. 2I) that reflect ice-sheet loss and coupled atmosphere-ocean variability (*94*). Late-Holocene ice-margin reconstructions for the AIS suggest little change (*84*, *85*, *95*), whereas those for the GrIS suggest general advance (*86*–*88*). The clearest signal in geological and long tide gauge records is the transition from low rates of change during the last ~2 ky (order of tenths of mm $year^{-1}$) to modern rates (order of mm $year^{-1}$) in the late 19th to early 20th centuries, although the spatial manifestation of this change is variable (*1*, *81*).

Discussion and future challenges

Recent interdisciplinary studies on sea-level and ice-sheet change during previous warm periods confirm that there is a strong sensitivity of polar ice-sheet mass loss (and associated sea-level rise) to higher insolation forcing and polar temperatures with similar or higher GHG forcing (Fig. 4). This understanding of polar ice-sheet response to climate change has improved considerably through an increase in the number and geographic distribution of RSL reconstructions, better ice-sheet constraints, and the recognition that several geophysical processes cause spatially complex patterns across time scales spanning tens to millions of years (Figs. 1 and 2). Spatial variability in Holocene RSL from GIA has long been recognized (*89*), but widely disparate estimates of the magnitude of GMSL change associated with any given previous warm period have only recently been documented as similarly reflecting the

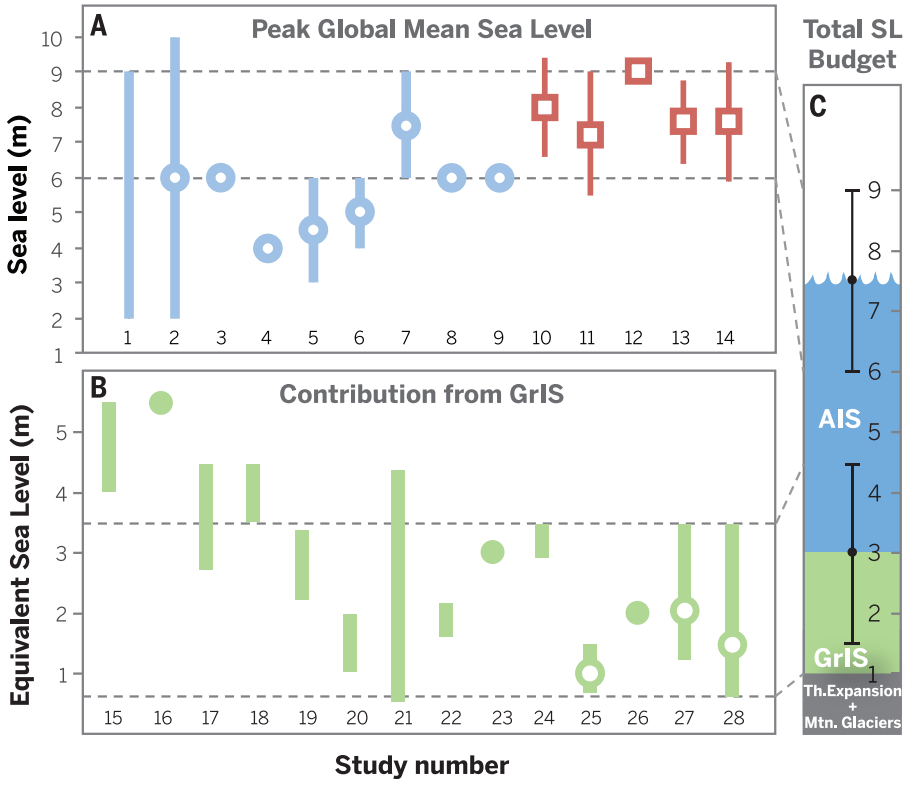


Fig. 3. Compilation of MIS 5e reconstructions for peak GMSL, GrIS contribution, and best estimate of the total sea level budget. Estimates of (**A**) peak MIS 5e GMSL and (**B**) meltwater contribution from the GrIS shown in chronological order of time of publication from left to right. Ranges indicated by vertical bars; point estimates and best estimates within ranges shown as circles. GIA-corrected records are shown in red squares. Horizontal dashed lines denote range of agreement between recent studies. (**C**) Total sea-level budget of MIS 5e, shown with estimated uncertainty for each component. One meter is attributed to thermal expansion and loss of mountain glaciers (gray shading). As the estimate of GrIS (green shading) has decreased, the overall peak GMSL estimate has grown, leading to increased confidence of a more substantial contribution from the AIS (blue shading). Data sources are listed in table S2.

spatial variability in RSL resulting from GIA and dynamic topography (e.g., see MIS 5e estimates in Fig. 3).

Despite the many advances in our understanding of GMSL during past warm periods, a number of challenges remain. Foremost among these is the need to continue to improve the accuracy and precision of the age and elevation of RSL indicators. In particular, now that we recognize that time-dependent GIA effects will affect the elevation of shorelines depending on whether they formed early or late in the interglacial period, improving chronologies to resolve the timing of observations during RSL highstands becomes all that much more critical to inferring the GMSL signal (*51*, *61*). Although the precision of U-Th dating has improved, complications related to open-system diagenesis and former seawater U-isotope composition continue to limit precision and accuracy of marine carbonate U-Th ages [see review by (*96*)].

Translating site-specific data into a global context requires better constraints on the properties of the solid Earth that strongly influence RSL on long time scales, especially the viscosity and density structure of the mantle. Increased spatial and temporal density of past RSL and ice-sheet margins will improve ice and Earth models, whereas use of three-dimensional (3D) GIA models may improve predictions in areas where lateral heterogeneities are important (*97*).

Determining equilibrium GMSL for different forcing scenarios with use of paleodata requires consideration of factors beyond understanding the peak value of GMSL, polar (or global) temperature, or atmospheric CO_2 during a given time period. Given lags in the climate system, simple correlation between such climate parameters can be misleading because the extremes may not be synchronous over a 10-ky-long interglacial period. Peak temperatures attained during previous warm periods may also be dependent on the length of the interglacial period (*41*, *46*), suggesting that warm periods lasting several ky may not represent equilibrium conditions for the climate-cryosphere system. Moreover, ice sheets in different hemispheres may not respond in phase.

In the case of MIS 11 and 5e, warm climates and higher GMSL resulted largely from orbital forcing that changes the intensity of solar insolation at high latitudes. Insolation forcing is quite different from the relatively uniform global forcing of increased atmospheric CO_2 that will influence future sea levels. Furthermore, regional sea and air temperatures exert the most direct influence on mass loss from a polar ice sheet, suggesting that past global mean temperature may not be the best predictor for past GMSL. More detailed regional climate reconstructions thus represent an additional target to improve understanding of the climatic forcing required for specific ice-sheet response scenarios. Improved chronological frameworks are also required that can directly relate sea-level and climate reconstructions, particularly to facilitate comparisons between reconstructions that rely on radiometric versus orbitally tuned chronologies.

In the following, we summarize our current understanding of magnitudes, rates, and sources of sea-level change during warm periods and their associated uncertainties and conclude with the recommendation to develop comprehensive databases that will be required to optimally capture the temporal and spatial variability of past high sea levels and their sources.

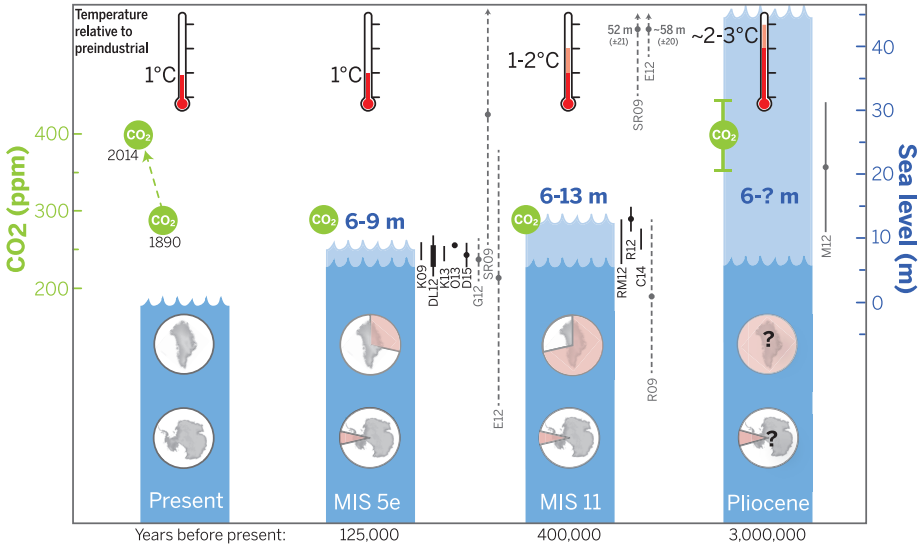


Fig. 4. Peak global mean temperature, atmospheric CO_2, maximum GMSL, and source(s) of meltwater. Light blue shading indicates uncertainty of sea-level maximum. Black vertical lines represent GMSL reconstructions from combined field observations and GIA modeling; gray dashed lines are $\delta^{18}O$-based reconstructions. Red pie charts over Greenland and Antarctica denote fraction (not location) of ice retreat. Although the peaks in temperature, CO_2, and sea level within each time period may not be synchronous and ice sheets are sensitive to factors not depicted here, significantly higher sea levels were attained during MIS 5e and 11 when atmospheric CO_2 forcing was significantly lower than present. See tables S3 and S4 for data and sources.

Magnitudes of GMSL rise

The best agreement in the magnitude of peak GMSL is between multiple GIA-corrected coastal records for MIS 5e and 11, but the uncertainty introduced from the combined influence of GIA and dynamic topography going farther back in time presently precludes us from placing a firm estimate on GMSL during the MPWP interglacial peaks. Given the constraints from existing data and models of MPWP temperatures and ice-sheet reconstructions combined with the evidence for stronger GHG forcing, we hypothesize that MPWP sea levels would have exceeded those attained during MIS 11 and 5e. This provides a lower bound of +6 m with the distinct potential for higher GMSL, particularly if the GrIS, WAIS, and EAIS experienced simultaneous mass loss. This hypothesis should be tested in the context of additional data and modeling constraints.

In comparison to GIA-corrected coastal records, paired $\delta^{18}O$-Mg/Ca records have greater uncertainty and in several cases have poor accuracy, suggesting that the current state of these geochemical methods makes them unable to provide confident, quantitative estimates of peak GMSL during these periods (Fig. 4). The planktic $\delta^{18}O$ from the Red Sea (*15*, *75*, *84*) is an innovative approach to overcoming some of the limitations of the benthic $\delta^{18}O$ or paired $\delta^{18}O$-Mg/Ca methods and remains one of the most valuable, semi-continuous records of sea-level change across century to millennial time scales. However, it carries uncertainties that are common to both the coastal reconstructions (such as GIA corrections) as well as the other $\delta^{18}O$-based reconstructions, some of which will magnify farther back in time. Targeted GIA modeling of the Red Sea basin, in particular to derive isostatic corrections for the Hanish Sill during these interglacial highstands, would be a valuable undertaking toward the use of this reconstruction to interpret GMSL.

Rates of GMSL rise

Rates of sea-level change for previous warm periods when sea level was higher than present range from highly uncertain to completely unconstrained depending on the time period, yet this is perhaps the most societally relevant information the paleorecord can provide for predicting and adapting to future sea-level change. MIS 5e holds the greatest potential for information on past rates of sea-level change in a world with higher GMSL. Although MIS 5e sea-level oscillations appear abrupt in the sedimentary record, uncertainties in dating and interpretation of RSL markers have prevented precise quantification of this abruptness beyond an indication that GMSL rose (and fell) one to several meters over one to a few ky [e.g., (*74*)]. Hence, deriving rates of interest on societal time scales (cm $year^{-1}$, m $century^{-1}$), such as can be achieved in Holocene reconstructions, remains a primary challenge.

Box 1. Methods of reconstructing past sea level and ice volume.

***Sea-level reconstructions*:** In our analysis of sea-level reconstructions, we consider two categories separately: those that are derived from $\delta^{18}O$ of marine carbonates (hereafter termed $\delta^{18}O$-proxy records) and those based on direct observational evidence of sea level or shoreline elevation (hereafter termed coastal records).

There are three types of $\delta^{18}O$-proxy records used to estimate former GMSL: (i) benthic $\delta^{18}O$, which comprises a combined signal of temperature and global ice volume (*106*); (ii) benthic or planktic $\delta^{18}O$ in foraminifera or ostracods, paired with a proxy that can independently constrain the temperature component embedded in this signal (*31*, *54*); and (iii) planktic $\delta^{18}O$ from evaporative marginal seas, which is transformed into a RSL signal by using hydraulic models that constrain the salinity of surface waters as a function of sea level [e.g., (*56*)]. Each of these geochemical approaches entails certain assumptions and uncertainties, and we note that in the case of isolated basins, such as the Red Sea or Mediterranean (*56*, *107*), additional corrections and assumptions about regional hydrology, relative humidity, and tectonic stability and isostatic response of the sill depth must also be made in addition to assumptions about how sea surface temperature changed.

Coastal records of former sea level reflect RSL rather than GMSL. Each RSL record has uncertainties in its age and elevation that are primarily a function of the dating technique(s) and the nature of the geologic archive, respectively. Coastal records include geomorphological features, shallow-water corals, and salt-marsh records that directly track the elevation of RSL through time. To associate changes in RSL to GMSL, one must quantify and correct for geophysical processes (described below) that may contribute significantly to RSL at the site (Fig. 1). GIA is arguably the most important of these processes because it can influence the present-day elevation of sea-level indicators from any time period in the past. Additional processes operate on more specific space and time scales and thus only become important at those particular scales of analysis (Fig. 1). For example, interannual to multidecadal ocean-atmosphere interactions, such as the North Atlantic Oscillation or the Pacific Decadal Oscillation, can cause RSL fluctuations of up to several decimeters. Such processes are important when interpreting highly resolved reconstructions, such as those from instrumental records or from late-Holocene geologic archives. On the other hand, dynamic topography resulting from flow in Earth's mantle can dominate the RSL signal over time scales of millions of years and produce high-amplitude (meter- to multimeter-scale) variability.

***Glacial isostatic adjustment*:** The water mass transfer between the ice sheets and oceans during glacial-interglacial cycles causes changes in Earth's shape, gravity field, and rotation that create a distinct spatial pattern to RSL across the globe (*108*) (Fig. 2). These GIA processes dominate the spatial variability in sea-level change over millennial time scales during the Quaternary and are also a significant (several mm $year^{-1}$) background component to recent (historical) sea-level change (Fig. 2). GIA is also an important contributor to RSL for older time periods, in part because of the fact that solid Earth is continuing to isostatically adjust to the most recent deglaciation (*18*).

GIA models are primarily driven by an a priori ice model that defines the volume and geographic extent of grounded ice through time, which is then used to solve for the elevation of the shorelines and the changes in the height of the ocean floor and sea surface—the latter being affected by changes in gravity. The ice model is constrained by field evidence on the timing, thickness, and geographic extent of ice, as well as by constraints from observations of the elevation of RSL through time from sites close to ("near-field") and far from ("far-field") the former ice sheets [e.g., (*109*–*111*)]. The other key component of GIA models is an Earth model that is defined by layer thicknesses, viscosity, elasticity, and density of Earth's interior, which in turn dictate the way in which Earth's surface responds and deforms to the assumed ice-load history. Typically, global GIA models are run by using a single, laterally homogeneous Earth model. Regional studies are often used to explore variations in the Earth model that provide a better fit to data in that area. More recently, 3D GIA models have been applied to examine the influence of lateral Earth structure on RSL changes [e.g., (*97*, *112*)].

GIA models typically simulate global patterns in RSL change because of ice melting over relatively short time scales (10s to 100s of years). In this case, the solid Earth response is dominantly elastic, and so accurately defining the viscosity structure, a primary source of GIA model uncertainty, becomes less important. Because the elastic properties of Earth are relatively well defined from seismic investigations, the computed RSL response can be accurately interpreted in terms of melt-source location. In other words, the spatial pattern of RSL change can be used to "fingerprint" melt sources, hence the use of the term "sea-level fingerprinting" for this application. This technique has been applied to rapid melting events in the geological record (*102*, *105*), 20th century sea-level change (*113*, *114*), and regional projections of future change (*13*, *115*).

***Dynamic topography*:** Lateral motion of Earth's tectonic plates (lithosphere) is due to buoyancy-driven viscous flow of the mantle that can also lead to vertical motion of Earth's surface through plate convergence and consequent lithospheric deformation (e.g., orogenesis). However, the same viscous flow of the mantle also results in normal stresses at the solid Earth-ocean/atmosphere interface, which can produce a vertical deflection of this interface of up to a few km in amplitude (*116*–*118*). This component of Earth's topography is associated with convectively supported vertical stresses and is termed "dynamic topography." (The same term is also used in oceanography to describe undulations in the sea surface associated with flow within the ocean.) As the distribution of density structure within the mantle evolves with time, so does the surface dynamic topography, resulting in significant changes in both local RSL and GMSL on time scales of 1 to 100 Ma (*119*–*121*). Vertical motion associated with dynamic topography also results in lateral stresses that can cause significant crustal deformation and thus additional vertical motion at Earth's surface (*122*, *123*). This additional component of vertical motion has yet to be considered in calculations of dynamic topography applied to sea-level studies.

Numerical models of mantle flow [e.g., (*124*)] are used to compute dynamic topography and predict how it evolves with time. The two primary inputs to these models are a 3D density anomaly field to drive the simulation of material flow in the mantle, as well as a radial viscosity profile that governs the rate of flow at a given depth in the mantle. The 3D density field is estimated from seismic models of Earth's internal velocity structure, which reflects both thermal and chemical variations within the mantle. The scaling from seismic velocity structure to density structure is not straightforward because it involves assumptions regarding the cause of seismic velocity variations [thermal, chemical, or both (*119*, *120*)]. It is this uncertainty in defining the input density structure, as well as our relatively poor knowledge of Earth's viscosity structure, that limits the accuracy of modeled sea-level changes resulting from variations in dynamic topography.

***Ice sheets*:** Ice-sheet reconstructions are informed primarily by direct observations of ice-margin and thickness data and nearby marine sediment and RSL records. IRD and sediment provenance from geochemical analyses in marine cores are particularly useful for extending ice-sheet reconstructions farther back in time beyond the last deglaciation (i.e., >21 ka).

Resolving meter-scale sea-level variability during the MIS 5e highstand will require precise chronologies and stratigraphy of sea-level indicators, as well as improved precision in the vertical uncertainties of RSL indicators. Coastal geomorphological features, although compelling, are difficult to date. Fossil corals can potentially provide robust chronologies, if challenges associated with the interpretation of postdepositional alteration of U-Th isotope measurements can be overcome (*96*). Further, fossil corals are usually associated with significant vertical uncertainties

in their paleowater depth. Future improvements on existing paleowater depth estimates of fossil corals will require integration of paleoenvironmental information, including assemblages of reef biota, and a more quantitative understanding of the depth distribution of modern corals and associated reef biota (*98*).

The rate of GMSL rise–associated Northern Hemisphere ice-sheet retreat during the last deglaciation is often cited as providing an upper bound for potential future GMSL rise [e.g., >4 m century^{-1} during meltwater pulse 1A (MWP-1A) (*99*)]. The nature and forcing of that retreat, however, is expected to be significantly different from that of the warm-climate polar ice sheets and thus not directly analogous. Nevertheless, there are aspects of past sea-level changes during glacial maxima or during deglacial transitions that are relevant to understanding interglacial GMSL change. For example, recent modeling identified a positive feedback involving "saddle collapse" of the Laurentide Ice Sheet melting that is capable of delivering a substantial influx of meltwater as a possible mechanism contributing to MWP-1A (*100*). Saddle collapse between the southern and northern domes of the GrIS may be important for driving smaller-scale, but rapid, GMSL change during warm interglacial periods. Similarly, there is increasing evidence that ocean thermal forcing played an important role in destabilizing late-Pleistocene ice sheets [e.g., (*101*)], similar to what is projected for the future.

Constraining the total volume and geographic extent of grounded ice during the Last Glacial Maximum (LGM), in particular, is an important parameter for GIA model predictions of RSL across all time periods, including the present and past interglacial periods [e.g., (*18*)]. Improved constraints on LGM ice volume will also influence the quantification of GMSL changes based on benthic $\delta^{18}O$ reconstructions as well as paired $\delta^{18}O$-Mg/Ca reconstructions. However, there are presently few far-field sites with RSL histories that can be used to constrain the LGM. We note that an ~120 m-below-present GMSL during the LGM has long been held as conventional wisdom, yet several GIA studies put the estimate in the range of 130 to 134 m below present (fig. S1). Because the total volume and extent of the LGM ice sheets is a sensitive parameter for GIA model predictions, improving our understanding of glacial ice loads will influence our interpretations of rates and magnitudes of interglacial GMSL.

Sources of GMSL rise

Two approaches show great promise for identifying and quantifying the contribution of individual ice sheets that retreated during previous warm periods: geochemical provenance in marine sediments (*20*, *46*, *67*) and sea-level fingerprinting (Box 1) (*102*). Existing evidence points to southern Greenland as the most susceptible sector of the GrIS to warmer-than-present temperatures (*46*, *67*), although some models predict retreat in the north and others in the south. In Antarctica, compelling sedimentary (*19*, *21*) and modeling (*12*, *103*) evidence suggests that repeated retreat-advance cycles of the WAIS occurred during the Pliocene and early Pleistocene, but little direct evidence constrains changes in the AIS during more recent intervals, including MIS 11 and 5e and the Holocene. Marine-based portions of the EAIS may be just as vulnerable as the WAIS and should be equally considered as contributors to past sea-level change (*104*).

Improving our understanding of individual polar ice-sheet contributions to GMSL is a key challenge. An important uncertainty for future projections of the GrIS is the threshold temperature beyond which it undergoes irreversible retreat, with current estimates ranging from 1° to 4°C above preindustrial temperatures (*1*). Improved estimates of GrIS loss for a given local or global temperature increase during past warm periods will thus provide a critical constraint on this threshold. For the AIS, the key challenge involves determining which marine-based sectors are most vulnerable to collapse and identifying the forcing (atmospheric or oceanic) that would trigger such events. Paleoconstraints on past ice-sheet mass loss and forcings will be of particular value for validation of coupled ice sheet-climate models.

Recommendations

Addressing outstanding questions and challenges regarding rates, magnitudes, and sources of past polar ice-sheet loss and resulting sea-level rise will continue to require integration of ice-sheet, sea-level, and solid Earth geophysical studies with good spatial distribution of well-dated RSL records to capture the magnitude of RSL variability across the globe. Such synoptic analyses will need a sufficiently sophisticated cyberinfrastructure to enable data sharing, transparency, and standardization of sea-level and ice-sheet paleodata that are derived from multiple and diverse subdisciplines. Where sufficiently resolved, such data can then be used to identify sources of meltwater through their sea-level fingerprints and refine estimates of GMSL change (*102*, *105*). Near-field records of ice-sheet extent and climate will also be essential in identifying the sources and forcing mechanisms responsible for sea-level change. Most importantly, transcending conventional paradigms of sea-level reconstructions and adopting the concept of geographic variability imparted by dynamic physical processes will continue to lead to significant advances in our understanding of GMSL rise in a warming world.

REFERENCES AND NOTES

1. J. A. Church *et al.*, in *Climate Change 2013: The Physical Science Basis. Contribution of Working Group I to the Fifth Assessment Report of the Intergovernmental Panel on Climate Change*, T. F. Stocker *et al.*, Eds. (Cambridge Univ. Press, Cambridge, 2013), pp. 1137–1216.
2. A. Levermann *et al.*, The multimillennial sea-level commitment of global warming. *Proc. Natl. Acad. Sci. U.S.A.* **110**, 13745–13750 (2013). doi: 10.1073/pnas.1219414110; pmid: 23858443
3. A. Cazenave *et al.*, Sea level budget over 2003–2008: A reevaluation from GRACE space gravimetry, satellite altimetry and Argo. *Global Planet. Change* **65**, 83–88 (2009). doi: 10.1016/j.gloplacha.2008.10.004
4. V. Helm, A. Humbert, H. Miller, Elevation and elevation change of Greenland and Antarctica derived from CryoSat-2. *Cryosphere Discuss.* **8**, 1673–1721 (2014). doi: 10.5194/tcd-8-1673-2014
5. D. G. Vaughan *et al.*, in *Climate Change 2013: The Physical Science Basis. Contribution of Working Group I to the Fifth Assessment Report of the Intergovernmental Panel on Climate Change*, T. F. Stocker *et al.*, Eds. (Cambridge Univ. Press, Cambridge, 2013), pp. 317–382.
6. S. Levitus *et al.*, Global ocean heat content 1995-2008 in light of recently revealed instrumentation problems. *Geophys. Res. Lett.* **36**, L07608 (2009).
7. A. Abe-Ouchi *et al.*, Insolation-driven 100,000-year glacial cycles and hysteresis of ice-sheet volume. *Nature* **500**, 190–193 (2013). doi: 10.1038/nature12374; pmid: 23925242
8. V. Masson-Delmotte *et al.*, in *Climate Change 2013: The Physical Science Basis. Contribution of Working Group I to the Fifth Assessment Report of the Intergovernmental Panel on Climate Change*, T. F. Stocker *et al.*, Eds. (Cambridge Univ. Press, Cambridge, 2013), pp. 383–464.
9. J. Ridley, J. M. Gregory, P. Huybrechts, J. Lowe, Thresholds for irreversible decline of the Greenland ice sheet. *Clim. Dyn.* **35**, 1049–1057 (2009). doi: 10.1007/s00382-009-0646-0
10. J. Hansen, M. Sato, G. Russell, P. Kharecha, Climate sensitivity, sea level and atmospheric carbon dioxide. *Philos. Trans. R. Soc. London Ser. A* **371**, 20120294 (2013). doi: 10.1098/rsta.2012.0294; pmid: 24043864
11. G. L. Foster, E. J. Rohling, Relationship between sea level and climate forcing by CO_2 on geological timescales. *Proc. Natl. Acad. Sci. U.S.A.* **110**, 1209–1214 (2013). doi: 10.1073/pnas.1216073110; pmid: 23292932
12. D. Pollard, R. M. DeConto, Modelling West Antarctic ice sheet growth and collapse through the past five million years. *Nature* **458**, 329–332 (2009). doi: 10.1038/nature07809; pmid: 19295608
13. J. X. Mitrovica, N. Gomez, P. U. Clark, The sea-level fingerprint of West Antarctic collapse. *Science* **323**, 753 (2009). doi: 10.1126/science.1166510; pmid: 19197056
14. M. Pagani, Z. Liu, J. LaRiviere, A. C. Ravelo, High Earth-system climate sensitivity determined from Pliocene carbon dioxide concentrations. *Nat. Geosci.* **3**, 27–30 (2010). doi: 10.1038/ngeo724
15. O. Seki *et al.*, Alkenone and boron-based Pliocene pCO_2 records. *Earth Planet. Sci. Lett.* **292**, 201–211 (2010). doi: 10.1016/j.epsl.2010.01.037
16. A. M. Haywood *et al.*, Large-scale features of Pliocene climate: Results from the Pliocene Model Intercomparison Project. *Clim. Past* **9**, 191–209 (2013). doi: 10.5194/cp-9-191-2013
17. H. J. Dowsett *et al.*, Sea surface temperature of the mid-Piacenzian ocean: A data-model comparison. *Sci. Rep.* **3**, 2013 (2013). doi: 10.1038/srep02013; pmid: 23774736
18. M. E. Raymo, J. X. Mitrovica, M. J. O'Leary, R. M. DeConto, P. J. Hearty, Departures from eustasy in Pliocene sea-level records. *Nat. Geosci.* **4**, 328–332 (2011). doi: 10.1038/ngeo1118
19. T. Naish *et al.*, Obliquity-paced Pliocene West Antarctic ice sheet oscillations. *Nature* **458**, 322–328 (2009). doi: 10.1038/nature07867; pmid: 19295607
20. C. P. Cook *et al.*, Dynamic behaviour of the East Antarctic ice sheet during Pliocene warmth. *Nat. Geosci.* **6**, 765–769 (2013). doi: 10.1038/ngeo1889
21. M. O. Patterson *et al.*, Orbital forcing of the East Antarctic ice sheet during the Pliocene and Early Pleistocene. *Nat. Geosci.* **7**, 841–847 (2014). doi: 10.1038/ngeo2273
22. S. J. Koenig, R. M. DeConto, D. Pollard, Impact of reduced Arctic sea ice on Greenland ice sheet variability in a warmer than present climate. *Geophys. Res. Lett.* **41**, 3933–3942 (2014). doi: 10.1002/2014GL059770
23. H. Dowsett, T. M. Cronin, High eustatic sea level during the middle Pliocene: Evidence from the southeastern US Atlantic Coastal Plain. *Geology* **18**, 435 (1990). doi: 10.1130/0091-7613(1990)018<0435:HESLDT>2.3.CO;2
24. K. Miller *et al.*, High tide of the warm Pliocene: Implications of global sea level for Antarctic deglaciation. *Geology* **40**, 407–410 (2012). doi: 10.1130/G32869.1
25. D. E. Krantz, A chronology of Pliocene sea-level fluctuations: The US Middle Atlantic coastal plain record. *Quat. Sci. Rev.* **10**, 163–174 (1991). doi: 10.1016/0277-3791(91)90016-N
26. T. R. Naish, G. S. Wilson, Constraints on the amplitude of Mid-Pliocene (3.6-2.4Ma) eustatic sea-level fluctuations from the New Zealand shallow-marine sediment record. *Philos. Trans. R. Soc. London Ser. A* **367**, 169–187 (2009). doi: 10.1098/rsta.2008.0223; pmid: 18852088

27. B. R. Wardlaw, T. M. Quinn, The record of Pliocene sea-level change at Enewetak Atoll. *Quat. Sci. Rev.* **10**, 247–258 (1991). doi: 10.1016/0277-3791(91)90023-N
28. D. B. Rowley *et al*., Dynamic topography change of the eastern United States since 3 million years ago. *Science* **340**, 1560–1563 (2013). doi: 10.1126/science.1229180; pmid: 23686342
29. A. Rovere *et al*., The Mid-Pliocene sea-level conundrum: Glacial isostasy, eustasy and dynamic topography. *Earth Planet. Sci. Lett.* **387**, 27 (2014). doi: 10.1016/j.epsl.2013.10.030
30. G. S. Dwyer, M. A. Chandler, Mid-Pliocene sea level and continental ice volume based on coupled benthic Mg/Ca palaeotemperatures and oxygen isotopes. *Philos. Trans. R. Soc. London Ser. A* **367**, 157–168 (2009). doi: 10.1098/rsta.2008.0222; pmid: 18854304
31. S. Sosdian, Y. Rosenthal, Deep-sea temperature and ice volume changes across the Pliocene-Pleistocene climate transitions. *Science* **325**, 306–310 (2009). doi: 10.1126/science.1169938; pmid: 19608915
32. J. Yu, W. S. Broecker, Comment on "Deep-sea temperature and ice volume changes across the Pliocene-Pleistocene climate transitions." *Science* **328**, 1480, author reply 1480 (2010). doi: 10.1126/science.1186544; pmid: 20558688
33. R. Kozdon *et al*., In situ $\delta^{18}O$ and Mg/Ca analyses of diagenetic and planktic foraminiferal calcite preserved in deep-sea record of the Paleocene-Eocene thermal maximum. *Paleoceanography* **28**, 517–528 (2013). doi: 10.1002/palo.20048
34. C. L. O'Brien *et al*., High sea surface temperatures in tropical warm pools during the Pliocene. *Nat. Geosci.* **7**, 606–611 (2014). doi: 10.1038/ngeo2194
35. L. E. Lisiecki, M. E. Raymo, A Pliocene-Pleistocene stack of 57 globally distributed benthic $\delta^{18}O$ records. *Paleoceanography* **20**, PA1003 (2005).
36. N. Lang, E. W. Wolff, Interglacial and glacial variability from the last 800 ka in marine, ice and terrestrial archives. *Clim. Past* **7**, 361–380 (2011). doi: 10.5194/cp-7-361-2011
37. Q. Z. Yin, A. Berger, Insolation and CO_2 contribution to the interglacial climate before and after the Mid-Brunhes Event. *Nat. Geosci.* **3**, 243–246 (2010). doi: 10.1038/ngeo771
38. V. Masson-Delmotte *et al*., EPICA Dome C record of glacial and interglacial intensities. *Quat. Sci. Rev.* **29**, 113–128 (2010). doi: 10.1016/j.quascirev.2009.09.030
39. D. Lüthi *et al*., High-resolution carbon dioxide concentration record 650,000-800,000 years before present. *Nature* **453**, 379–382 (2008). doi: 10.1038/nature06949; pmid: 18480821
40. T. M. Cronin *et al*., A 600-ka Arctic sea-ice record from Mendeleev Ridge based on ostracodes. *Quat. Sci. Rev.* **79**, 157–167 (2013). doi: 10.1016/j.quascirev.2012.12.010
41. M. Melles *et al*., 2.8 million years of Arctic climate change from Lake El'gygytgyn, NE Russia. *Science* **337**, 315–320 (2012). doi: 10.1126/science.1222135; pmid: 22722254
42. J. Jouzel *et al*., Orbital and millennial Antarctic climate variability over the past 800,000 years. *Science* **317**, 793–796 (2007). doi: 10.1126/science.1141038; pmid: 17615306
43. A. J. Coletti, R. M. DeConto, J. Brigham-Grette, M. Melles, A GCM comparison of Plio–Pleistocene interglacial–glacial periods in relation to Lake El'gygytgyn, NE Arctic Russia. *Clim. Past Discuss.* **10**, 3127–3161 (2014). doi: 10.5194/cpd-10-3127-2014
44. A. de Vernal, C. Hillaire-Marcel, Natural variability of Greenland climate, vegetation, and ice volume during the past million years. *Science* **320**, 1622–1625 (2008). doi: 10.1126/science.1153929; pmid: 18566284
45. E. Willerslev *et al*., Ancient biomolecules from deep ice cores reveal a forested southern Greenland. *Science* **317**, 111–114 (2007). doi: 10.1126/science.1141758; pmid: 17615355
46. A. V. Reyes *et al*., South Greenland ice-sheet collapse during Marine Isotope Stage 11. *Nature* **510**, 525–528 (2014). doi: 10.1038/nature13456; pmid: 24965655
47. H. A. Bauch, Interglacial climates and the Atlantic meridional overturning circulation: Is there an Arctic controversy? *Quat. Sci. Rev.* **63**, 1–22 (2013). doi: 10.1016/j.quascirev.2012.11.023
48. R. McKay *et al*., Pleistocene variability of Antarctic Ice Sheet extent in the Ross Embayment. *Quat. Sci. Rev.* **34**, 93–112 (2012). doi: 10.1016/j.quascirev.2011.12.012
49. C. V. Murray-Wallace, Pleistocene coastal stratigraphy, sea-level highstands and neotectonism of the southern Australian passive continental margin? A review. *J. Quat. Sci.* **17**, 469–489 (2002). doi: 10.1002/jqs.717
50. P. J. Hearty, P. Kindler, H. Cheng, R. L. Edwards, A +20 m middle Pleistocene sea-level highstand (Bermuda and the Bahamas) due to partial collapse of Antarctic ice. *Geology* **27**, 375 (1999). doi: 10.1130/0091-7613(1999)027<0375:AMMPSL>2.3.CO;2
51. M. E. Raymo, J. X. Mitrovica, Collapse of polar ice sheets during the stage 11 interglacial. *Nature* **483**, 453–456 (2012). doi: 10.1038/nature10891; pmid: 22419155
52. D. L. Roberts, P. Karkanas, Z. Jacobs, C. W. Marean, R. G. Roberts, Melting ice sheets 400,000 yr ago raised sea level by 13m: Past analogue for future trends. *Earth Planet. Sci. Lett.* **357-358**, 226–237 (2012). doi: 10.1016/j.epsl.2012.09.006
53. F. Chen *et al*., Refining estimates of polar ice volumes during the MIS11 Interglacial using sea level records from South Africa. *J. Clim.* **27**, 8740–8746 (2014). doi: 10.1175/JCLI-D-14-00282.1
54. H. Elderfield *et al*., Evolution of ocean temperature and ice volume through the mid-Pleistocene climate transition. *Science* **337**, 704–709 (2012). doi: 10.1126/science.1221294; pmid: 22879512
55. E. J. Rohling *et al*., Antarctic temperature and global sea level closely coupled over the past five glacial cycles. *Nat. Geosci.* **2**, 500–504 (2009). doi: 10.1038/ngeo557
56. M. Siddall *et al*., Sea-level fluctuations during the last glacial cycle. *Nature* **423**, 853–858 (2003). doi: 10.1038/nature01690; pmid: 12815427
57. C. H. Stirling, T. M. Esat, K. Lambeck, M. T. McCulloch, Timing and duration of the Last Interglacial: Evidence for a restricted interval of widespread coral reef growth. *Earth Planet. Sci. Lett.* **160**, 745–762 (1998). doi: 10.1016/S0012-821X(98)00125-3
58. B. L. Otto-Bliesner *et al*., How warm was the last interglacial? New model-data comparisons. *Philos. Trans. R. Soc. London Ser. A* **371**, 20130097 (2013). doi: 10.1098/rsta.2013.0097; pmid: 24043870
59. CAPE Last Interglacial Project Members, Last Interglacial Arctic warmth confirms polar amplification of climate change. *Quat. Sci. Rev.* **25**, 1383–1400 (2006). doi: 10.1016/j.quascirev.2006.01.033
60. NEEM community members, Eemian interglacial reconstructed from a Greenland folded ice core. *Nature* **493**, 489–494 (2013). doi: 10.1038/nature11789; pmid: 23344358
61. A. Dutton, K. Lambeck, Ice volume and sea level during the last interglacial. *Science* **337**, 216–219 (2012). doi: 10.1126/science.1205749; pmid: 22798610
62. R. E. Kopp, F. J. Simons, J. X. Mitrovica, A. C. Maloof, M. Oppenheimer, Probabilistic assessment of sea level during the last interglacial stage. *Nature* **462**, 863–867 (2009). doi: 10.1038/nature08686; pmid: 20016591
63. A. Dutton, J. M. Webster, D. Zwartz, K. Lambeck, B. Wohlfarth, Tropical tales of polar ice: Evidence of last interglacial polar ice sheet retreat recorded by fossil reefs of the granitic Seychelles islands. *Quat. Sci. Rev.* **107**, 182–196 (2015). doi: 10.1016/j.quascirev.2014.10.025
64. M. J. O'Leary *et al*., Ice sheet collapse following a prolonged period of stable sea level during the last interglacial. *Nat. Geosci.* **6**, 796–800 (2013). doi: 10.1038/ngeo1890
65. K. M. Grant *et al*., Rapid coupling between ice volume and polar temperature over the past 150,000 years. *Nature* **491**, 744–747 (2012). pmid: 23151478
66. K. Lambeck *et al*., Sea level and shoreline reconstructions for the Red Sea: Isostatic and tectonic considerations and implications for hominin migration out of Africa. *Quat. Sci. Rev.* **30**, 3542–3574 (2011). doi: 10.1016/j.quascirev.2011.08.008
67. E. J. Colville *et al*., Sr-Nd-Pb isotope evidence for ice-sheet presence on southern Greenland during the Last Interglacial. *Science* **333**, 620–623 (2011). doi: 10.1126/science.1204673; pmid: 21798947
68. N. P. McKay, J. T. Overpeck, B. L. Otto-Bliesner, The role of ocean thermal expansion in Last Interglacial sea level rise. *Geophys. Res. Lett.* **38**, L14605 (2011). doi: 10.1029/2011GL048280
69. R. P. Scherer *et al*., Pleistocene collapse of the west antarctic ice sheet. *Science* **281**, 82–85 (1998). doi: 10.1126/science.281.5373.82; pmid: 9651249
70. C. D. Gallup, R. L. Edwards, R. G. Johnson, The timing of high sea levels over the past 200,000 years. *Science* **263**, 796–800 (1994). doi: 10.1126/science.263.5148.796; pmid: 17770835
71. P. Blanchon, A. Eisenhauer, J. Fietzke, V. Liebetrau, Rapid sea-level rise and reef back-stepping at the close of the last interglacial highstand. *Nature* **458**, 881–884 (2009). doi: 10.1038/nature07933; pmid: 19370032
72. J. H. Chen, H. A. Curran, B. White, G. J. Wasserburg, Precise chronology of the last interglacial period: ^{234}U-^{230}Th data from fossil coral reefs in the Bahamas. *Geol. Soc. Am. Bull.* **103**, 82–97 (1991). doi: 10.1130/0016-7606(1991)103<0082:PCOTLI>2.3.CO;2
73. P. J. Hearty, J. T. Hollin, A. C. Neumann, M. J. O'Leary, M. T. McCulloch, Global sea-level fluctuations during the Last Interglaciation (MIS 5e). *Quat. Sci. Rev.* **26**, 2090–2112 (2007). doi: 10.1016/j.quascirev.2007.06.019
74. W. G. Thompson, H. A. Curran, M. A. Wilson, B. White, Sea-level and ice-sheet instability during the Last Interglacial: New Bahamas evidence. *Nat. Geosci.* **4**, 684 (2011). doi: 10.1038/ngeo1253
75. E. J. Rohling *et al*., High rates of sea-level rise during the last interglacial period. *Nat. Geosci.* **1**, 38–42 (2008). doi: 10.1038/ngeo.2007.28
76. J.-C. Plazait, J.-L. Reyss, A. Choukri, C. Cazala, Diagenetic rejuvenation of raised coral reefs and precision of dating. The contribution of the Red Sea reefs to the question of reliability of the Uranium-series datings of middle to late Pleistocene key reef-terraces of the world. *Carnets Géol.* **CG2008**, 1 (2008).
77. R. E. Kopp, F. J. Simons, J. X. Mitrovica, A. C. Maloof, M. Oppenheimer, A probabilistic assessment of sea level variations within the last interglacial stage. *Geophys. J. Int.* **193**, 711–716 (2013). doi: 10.1093/gji/ggt029
78. S. A. Marcott, J. D. Shakun, P. U. Clark, A. C. Mix, A reconstruction of regional and global temperature for the past 11,300 years. *Science* **339**, 1198–1201 (2013). doi: 10.1126/science.1228026; pmid: 23471405
79. D. L. Hartmann *et al*., in *Climate Change 2013: The Physical Science Basis. Contribution of Working Group I to the Fifth Assessment Report of the Intergovernmental Panel on Climate Change*, T. F. Stocker *et al*., Eds. (Cambridge Univ. Press, Cambridge, 2013), pp. 159–254.
80. Z. Liu *et al*., The Holocene temperature conundrum. *Proc. Natl. Acad. Sci. U.S.A.* **111**, E3501–E3505 (2014). doi: 10.1073/pnas.1407229111; pmid: 25114253
81. A. C. Kemp *et al*., Climate related sea-level variations over the past two millennia. *Proc. Natl. Acad. Sci. U.S.A.* **108**, 11017–11022 (2011). doi: 10.1073/pnas.1015619108; pmid: 21690367
82. K. Lambeck, H. Rouby, A. Purcell, Y. Sun, M. Sambridge, Sea level and global ice volumes from the Last Glacial Maximum to the Holocene. *Proc. Natl. Acad. Sci. U.S.A.* **111**, 15296–15303 (2014). doi: 10.1073/pnas.1411762111; pmid: 25313072
83. K. Fleming *et al*., Refining the eustatic sea-level curve since the Last Glacial Maximum using far and intermediate-field sites. *Earth Planet. Sci. Lett.* **163**, 327–342 (1998). doi: 10.1016/S0012-821X(98)00198-8
84. M. J. Bentley, The Antarctic palaeo record and its role in improving predictions of future Antarctic Ice Sheet change. *J. Quat. Sci.* **25**, 5–18 (2010). doi: 10.1002/jqs.1287
85. J. O. Stone *et al*., Holocene deglaciation of Marie Byrd Land, West Antarctica. *Science* **299**, 99–102 (2003). doi: 10.1126/science.1077998; pmid: 12511648
86. A. J. Long, S. A. Woodroffe, D. H. Roberts, S. Dawson, Isolation basins, sea-level changes and the Holocene history of the Greenland Ice Sheet. *Quat. Sci. Rev.* **30**, 3748–3768 (2011). doi: 10.1016/j.quascirev.2011.10.013
87. A. E. Carlson *et al*., Earliest Holocene south Greenland ice sheet retreat within its late Holocene extent. *Geophys. Res. Lett.* **41**, 5514–5521 (2014). doi: 10.1002/2014GL060800
88. B. S. Lecavalier *et al*., A model of Greenland ice sheet deglaciation constrained by observations of relative sea level and ice extent. *Quat. Sci. Rev.* **102**, 54–84 (2014). doi: 10.1016/j.quascirev.2014.07.018
89. J. A. Clark, W. E. Farrell, W. R. Peltier, Global changes in postglacial sea level: A numerical calculation. *Quat. Res.* **9**, 265–287 (1978). doi: 10.1016/0033-5894(78)90033-9
90. J. X. Mitrovica, G. A. Milne, On the origin of late Holocene sea-level highstands within equatorial ocean basins. *Quat. Sci. Rev.* **21**, 2179–2190 (2002). doi: 10.1016/S0277-3791(02)00080-X
91. J. S. Compton, Holocene sea-level fluctuations inferred from the evolution of depositional environments of the southern Langebaan Lagoon salt marsh, South Africa. *Holocene* **11**, 395–405 (2001). doi: 10.1191/095968301678302832
92. K. Rostami, W. R. Peltier, A. Mangini, Quaternary marine terraces, sea-level changes and uplift history of Patagonia, Argentina: Comparisons with predictions of the ICE-4G (VM2) model of the global process of glacial isostatic adjustment. *Quat. Sci. Rev.* **19**, 1495–1525 (2000). doi: 10.1016/S0277-3791(00)00075-5

93. A. Long *et al*., Contrasting records of sea-level change in the eastern and western North Atlantic during the last 300 years. *Earth Planet. Sci. Lett.* **388**, 110–122 (2014). doi: 10.1016/j.epsl.2013.11.012
94. R. E. Kopp *et al*., The impact of Greenland melt on local sea levels: A partially coupled analysis of dynamic and static equilibrium effects in idealized water-hosing experiments. *Clim. Change* **103**, 619–625 (2010). doi: 10.1007/s10584-010-9935-1
95. J. S. Johnson *et al*., Rapid thinning of Pine Island Glacier in the early Holocene. *Science* **343**, 999–1001 (2014). doi: 10.1126/science.1247385; pmid: 24557837
96. C. H. Stirling, M. B. Andersen, Uranium-series dating of fossil coral reefs: Extending the sea-level record beyond the last glacial cycle. *Earth Planet. Sci. Lett.* **284**, 269–283 (2009). doi: 10.1016/j.epsl.2009.04.045
97. J. Austermann, J. X. Mitrovica, K. Latychev, G. A. Milne, Barbados based estimate of ice volume at Last Glacial Maximum effected by subducted plate. *Nat. Geosci.* **6**, 553–557 (2013). doi: 10.1038/ngeo1859
98. G. Camoin, J. M. Webster, Coral reef response to Quaternary sea-level and environmental changes: State of the science. *Sedimentology* **62**, 401–428 (2015). doi: 10.1111/sed.12184
99. P. Deschamps *et al*., Ice-sheet collapse and sea-level rise at the Bølling warming 14,600 years ago. *Nature* **483**, 559–564 (2012). doi: 10.1038/nature10902; pmid: 22460900
100. L. J. Gregoire, A. J. Payne, P. J. Valdes, Deglacial rapid sea level rises caused by ice-sheet saddle collapses. *Nature* **487**, 219–222 (2012). doi: 10.1038/nature11257; pmid: 22785319
101. S. A. Marcott *et al*., Ice-shelf collapse from subsurface warming as a trigger for Heinrich events. *Proc. Natl. Acad. Sci. U.S.A.* **108**, 13415–13419 (2011). doi: 10.1073/pnas.1104772108; pmid: 21808034
102. C. Hay *et al*., The sea-level fingerprints of ice-sheet collapse during interglacial periods. *Quat. Sci. Rev.* **87**, 60 (2014). doi: 10.1016/j.quascirev.2013.12.022
103. R. M. DeConto, D. Pollard, D. Kowalewski, Modeling Antarctic ice sheet and climate variations during Marine Isotope Stage 31. *Global Planet. Change* **88-89**, 45–52 (2012). doi: 10.1016/j.gloplacha.2012.03.003
104. M. Mengel, A. Levermann, Ice plug prevents irreversible discharge from East Antarctica. *Nat. Clim. Change* **4**, 451–455 (2014). doi: 10.1038/nclimate2226
105. P. U. Clark, J. X. Mitrovica, G. A. Milne, M. E. Tamisiea, Sea-level fingerprinting as a direct test for the source of global meltwater pulse IA. *Science* **295**, 2438–2441 (2002). pmid: 11896236
106. J. Zachos, M. Pagani, L. Sloan, E. Thomas, K. Billups, Trends, rhythms, and aberrations in global climate 65 Ma to present. *Science* **292**, 686–693 (2001). doi: 10.1126/science.1059412; pmid: 11326091
107. E. J. Rohling *et al*., Sea-level and deep-sea-temperature variability over the past 5.3 million years. *Nature* **508**, 477–482 (2014). doi: 10.1038/nature13230; pmid: 24739960
108. W. E. Farrell, J. A. Clark, On postglacial sea-level. *Geophys. J. R. Astron. Soc.* **46**, 647–667 (1976). doi: 10.1111/j.1365-246X.1976.tb01252.x
109. K. Lambeck, C. Smither, P. Johnston, Sea-level change, glacial rebound and mantle viscosity for northern Europe. *Geophys. J. Int.* **134**, 102–144 (1998). doi: 10.1046/j.1365-246x.1998.00541.x
110. L. Tarasov, A. S. Dyke, R. M. Neal, W. R. Peltier, A data-calibrated distribution of deglacial chronologies for the North American ice complex from glaciological modeling. *Earth Planet. Sci. Lett.* **315-316**, 30–40 (2012). doi: 10.1016/j.epsl.2011.09.010
111. A. M. Tushingham, W. R. Peltier, Ice-3G: A new global model of late Pleistocene deglaciation based upon geophysical predictions of post-glacial relative sea-level change. *J. Geophys. Res.* **96**, 4497 (1991). doi: 10.1029/90JB01583
112. P. Wu, W. Van der Wal, Postglacial sea-levels on a spherical, self-gravitating viscoelastic earth: Effects of lateral viscosity variations in the upper mantle on the inference of viscosity contrasts in the lower mantle. *Earth Planet. Sci. Lett.* **211**, 57–68 (2003). doi: 10.1016/S0012-821X(03)00199-7
113. C. P. Conrad, B. H. Hager, Spatial variations in the rate of sea level rise caused by present-day melting of glaciers and ice sheets. *Geophys. Res. Lett.* **24**, 1503–1506 (1997). doi: 10.1029/97GL01338
114. J. X. Mitrovica, M. E. Tamisiea, J. L. Davis, G. A. Milne, Recent mass balance of polar ice sheets inferred from patterns of global sea-level change. *Nature* **409**, 1026–1029 (2001). doi: 10.1038/35059054; pmid: 11234008
115. J. A. Clark, C. S. Lingle, Future sea-level changes due to West Antarctic ice sheet fluctuations. *Nature* **269**, 206–209 (1977). doi: 10.1038/269206a0
116. M. Gurnis, Rapid continental subsidence following the initiation and evolution of subduction. *Science* **255**, 1556–1558 (1992). doi: 10.1126/science.255.5051.1556; pmid: 17820168
117. D. P. McKenzie, Surface deformation, gravity anomalies and convection. *Geophys. J. R. Astron. Soc.* **48**, 211–238 (1977). doi: 10.1111/j.1365-246X.1977.tb01297.x
118. J. X. Mitrovica, C. Beaumont, G. T. Jarvis, Tilting of continental interiors by the dynamical effects of subduction. *Tectonics* **8**, 1079–1094 (1989). doi: 10.1029/TC008i005p01079
119. C. P. Conrad, L. Husson, Influence of dynamic topography on sea level and its rate of change. *Lithosphere* **1**, 110–120 (2009). doi: 10.1130/L32.1
120. R. Moucha *et al*., Dynamic topography and long-term sea-level variations: There is no such thing as a stable continental platform. *Earth Planet. Sci. Lett.* **271**, 101–108 (2008). doi: 10.1016/j.epsl.2008.03.056
121. R. D. Müller, M. Sdrolias, C. Gaina, B. Steinberger, C. Heine, Long-term sea-level fluctuations driven by ocean basin dynamics. *Science* **319**, 1357–1362 (2008). doi: 10.1126/science.1151540; pmid: 18323446
122. E. A. Neil, G. A. Housemann, Rayleigh-Taylor instability of the upper mantle and its role in intraplate orogeny. *Geophys. J. Int.* **138**, 89–107 (1999). doi: 10.1046/j.1365-246x.1999.00841.x
123. R. N. Pysklywec, C. Beaumont, Intraplate tectonics: Feedback between radioactive thermal weakening and crustal deformation driven by mantle lithosphere instabilitie. *Earth Planet. Sci. Lett.* **221**, 275–292 (2004). doi: 10.1016/S0012-821X(04)00098-6
124. S. Zhong, A. McNamara, E. Tan, L. Moresi, M. Gurnis, A benchmark study on mantle convection in a 3-D spherical shell using CitcomS. *Geochem. Geophys. Geosyst.* **9**, Q10017 (2008). doi: 10.1029/2008GC002048
125. W. R. Peltier, Global glacial isostasy and the surface of the ice-age Earth: The ICE-5G (VM2) Model and GRACE. *Annu. Rev. Earth Planet. Sci.* **32**, 111–149 (2004). doi: 10.1146/annurev.earth.32.082503.144359

ACKNOWLEDGMENTS

This manuscript was developed based on collaborations and discussions that have stemmed from the Paleo Constraints on Sea-Level Rise (PALSEA) and PALSEA2 working group, presently funded by Past Global Changes (PAGES) and International Union for Quaternary Science (INQUA). We thank four anonymous reviewers for comments that helped to improve the manuscript, A. Kemp for assistance with one of the figures, and A. Rovere and B. Honisch for helpful comments. Funding was provided by NSF awards 1155495 to A.D., 1202632 to M.E.R., 1343573 to A.E.C., 0958417 and 1043517 to P.U.C., OCE1458904 to B.P.H., and Natural Environment Research Council (UK) grant NE/I008675/1 to A.J.L.

SUPPLEMENTARY MATERIALS

www.sciencemag.org/content/349/6244/aaa4019/suppl/DC1
Fig. S1
Tables S1 to S5
References (*126*–*170*)

10.1126/science.aaa4019

RESEARCH ARTICLE SUMMARY

HIV-1 VACCINES

HIV-1 neutralizing antibodies induced by native-like envelope trimers

Rogier W. Sanders,* Marit J. van Gils, Ronald Derking, Devin Sok, Thomas J. Ketas, Judith A. Burger, Gabriel Ozorowski, Albert Cupo, Cassandra Simonich, Leslie Goo, Heather Arendt, Helen J. Kim, Jeong Hyun Lee, Pavel Pugach, Melissa Williams, Gargi Debnath, Brian Moldt, Mariëlle J. van Breemen, Gözde Isik, Max Medina-Ramírez, Jaap Willem Back, Wayne C. Koff, Jean-Philippe Julien, Eva G. Rakasz, Michael S. Seaman, Miklos Guttman, Kelly K. Lee, Per Johan Klasse, Celia LaBranche, William R. Schief, Ian A. Wilson, Julie Overbaugh, Dennis R. Burton, Andrew B. Ward, David C. Montefiori, Hansi Dean, John P. Moore*

INTRODUCTION: A major goal of HIV-1 vaccine development is to identify immunogens capable of inducing protective titers of broadly neutralizing antibodies (bNAbs) against circulating, neutralization-resistant (tier 2) viruses. The envelope glycoprotein (Env) trimer on the virus surface is the only bNAb target and accordingly serves as the basis for recombinant protein immunogens intended to induce bNAbs. We have engineered soluble, recombinant trimers based on the BG505 clade A and B41 clade B tier 2 viruses. These proteolytically cleaved and stabilized trimers, designated BG505 and B41 SOSIP.664 gp140, display multiple bNAb epitopes and have antigenic properties that mimic viral Env. High-resolution structures of the BG505 trimers reinforce this perspective. In contrast, other trimer designs (uncleaved gp140) that lack the SOSIP modifications and are based on eliminating the intersubunit proteolytic cleavage site adopt non-native configurations.

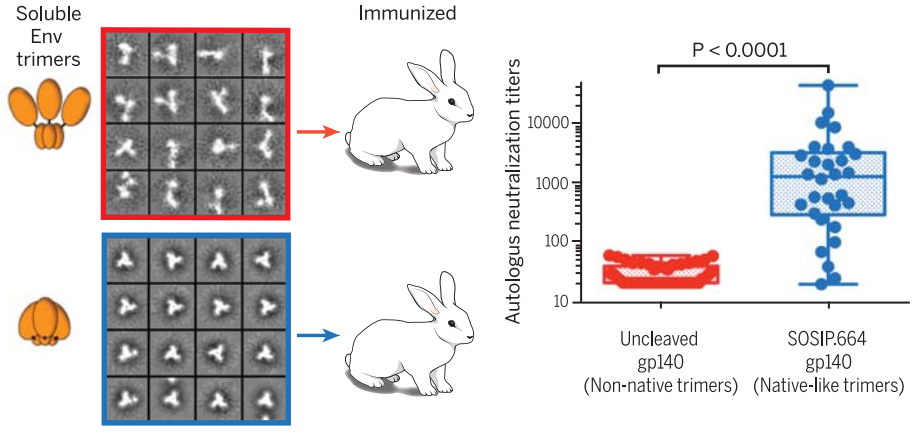
RATIONALE: To determine the NAb response elicited by native-like trimers, we immunized rabbits and macaques with BG505 SOSIP.664 gp140 proteins, and rabbits with their B41 counterparts. For comparison with the BG505 trimers, we also tested gp120 monomers and uncleaved gp140 proteins of the same genotype. We characterized the resulting antibody responses by quantifying their ability to neutralize the autologous tier 2 viruses and multiple heterologous tier 1 (neutralization-sensitive) and tier 2 viruses. We mapped the BG505 NAb responses using various techniques, including a large panel of Env-pseudotyped virus mutants.

RESULTS: BG505 SOSIP.664 trimers consistently induced potent NAbs against the autologous tier 2 virus in rabbits and similar but weaker responses in macaques. Cross-reactive NAbs against the more sensitive tier 1 viruses were also induced in all the immunized animals, but heterologous neutralization of tier 2 viruses was seen only weakly and sporadically. The rabbit responses to B41 SOSIP.664 trimers were qualitatively similar to those seen in the BG505 trimer recipients. The autologous tier 2 NAb titers to both SOSIP.664 trimers were greater than any such responses previously observed using various uncleaved gp140 proteins, including the BG505 version used in this study. The rabbit tier 2 and tier 1 NAb responses to the BG505 SOSIP.664 trimers were uncorrelated. Mapping studies showed the tier 2 NAbs recognized conformational epitopes that differed between animals. In some cases, these NAbs targeted components of the glycan shield previously associated with bNAb epitopes. In contrast, the tier 1 NAbs targeted linear epitopes in the gp120 V3 region.

ON OUR WEB SITE

Read the full article at http://dx.doi.org/10.1126/science.aac4223

CONCLUSIONS: Although an autologous tier 2 NAb response is not sufficient for vaccine protection against HIV-1, it may be a necessary step in various strategies intended to induce bNAbs. Thus, our findings indicate that native-like trimers represent a promising starting point for the further development of recombinant Env immunogens intended to broaden the NAb response. The high-resolution structures of SOSIP.664 trimers allow improvements to be rationally designed. Relevant strategies include the further stabilization of trimer-associated bNAb epitopes while reducing the antigenicity of V3 and other non-neutralizing epitopes that may be distractive; immunizing with longitudinal series of SOSIP.664 trimers from infected individuals who generate bNAbs; using trimer cocktails (e.g., from clades A, B, and C); and priming with trimer variants that trigger desirable germline responses before boosting with wild-type trimers. ■



Autologous tier 2 NAb responses in animals immunized with native-like (SOSIP.664) trimers or non-native uncleaved gp140s. (**Left**) Representative reference-free 2D class averages of negative-stain electron microscopy (EM) images of the uncleaved BG505 gp140 and the native-like BG505 SOSIP.664 trimers. The illustrations (orange) of the two categories of Env protein are based on negative-stain EM. (**Right**) Autologous tier 2 serum NAb titers (IC50) in 50 animals immunized with various uncleaved gp140 proteins, compared to titers in the 30 rabbits given the BG505 or B41 SOSIP.664 trimers described here (see legend of Fig. 2 in the full article for details; $P < 0.0001$, two-tailed Mann-Whitney test).

The list of author affiliations is available in the full article online.
*Corresponding author. E-mail: jpm2003@med.cornell.edu (J.P.M.); rws2002@med.cornell.edu (R.W.S.)
Cite this article as R. W. Sanders *et al.*, *Science* **349**, aac4223 (2015). DOI: 10.1126/science.aac4223

Downloaded from www.sciencemag.org on July 10, 2015

RESEARCH ARTICLE

HIV-1 VACCINES

HIV-1 neutralizing antibodies induced by native-like envelope trimers

Rogier W. Sanders,[1,2]* Marit J. van Gils,[2] Ronald Derking,[2] Devin Sok,[3,4,5] Thomas J. Ketas,[1] Judith A. Burger,[2] Gabriel Ozorowski,[4,5,6] Albert Cupo,[1] Cassandra Simonich,[7] Leslie Goo,[7] Heather Arendt,[8] Helen J. Kim,[4,5,6] Jeong Hyun Lee,[4,5,6] Pavel Pugach,[1] Melissa Williams,[1] Gargi Debnath,[1] Brian Moldt,[3,4,5] Mariëlle J. van Breemen,[2] Gözde Isik,[2] Max Medina-Ramírez,[2] Jaap Willem Back,[9] Wayne C. Koff,[8] Jean-Philippe Julien,[4,5,6] Eva G. Rakasz,[10] Michael S. Seaman,[11,12] Miklos Guttman,[13] Kelly K. Lee,[13] Per Johan Klasse,[1] Celia LaBranche,[14] William R. Schief,[3,4,5,8,12] Ian A. Wilson,[4,5,6,15] Julie Overbaugh,[7] Dennis R. Burton,[3,4,5,12] Andrew B. Ward,[4,5,6] David C. Montefiori,[14] Hansi Dean,[8] John P. Moore[1]*

A challenge for HIV-1 immunogen design is the difficulty of inducing neutralizing antibodies (NAbs) against neutralization-resistant (tier 2) viruses that dominate human transmissions. We show that a soluble recombinant HIV-1 envelope glycoprotein trimer that adopts a native conformation, BG505 SOSIP.664, induced NAbs potently against the sequence-matched tier 2 virus in rabbits and similar but weaker responses in macaques. The trimer also consistently induced cross-reactive NAbs against more sensitive (tier 1) viruses. Tier 2 NAbs recognized conformational epitopes that differed between animals and in some cases overlapped with those recognized by broadly neutralizing antibodies (bNAbs), whereas tier 1 responses targeted linear V3 epitopes. A second trimer, B41 SOSIP.664, also induced a strong autologous tier 2 NAb response in rabbits. Thus, native-like trimers represent a promising starting point for the development of HIV-1 vaccines aimed at inducing bNAbs.

A major goal of HIV-1 vaccine development is to identify immunogens capable of inducing protective titers of broadly neutralizing antibodies (bNAbs) against circulating viruses with a tier 2 or higher resistance profile (*1*). Viruses with these characteristics are the most commonly transmitted strains of HIV-1, and hence they dominate new infections. The humoral immune response of infected individuals creates antibody-mediated selection pressure on the virus, which can generally only persist and be transmitted if it is antibody-resistant. A successful vaccine, then, must be able to induce antibodies that can counter the virus's evolved resistance mechanisms. In addition, the global sequence diversity among HIV-1 strains is so great that vaccine-induced antibodies should target relatively conserved sites and thereby possess breadth of action. A vaccine with the required properties must be based on the envelope glycoprotein (Env), as the gp120-gp41 trimer on the virus surface is the only bNAb target. After two or more years of HIV-1 infection, ~20% of individuals develop bNAbs, which can serve as templates for vaccine design by exposing vulnerabilities in the viral defense mechanisms (*1*). Because bNAbs usually evolve from strain-specific autologous NAbs via multiple cycles of viral escape and antibody affinity maturation [reviewed in (*2*, *3*)], it is unlikely that bNAbs can be raised against any single Env protein of fixed antigenic composition. However, the induction of autologous NAbs to a tier 2 virus would be an excellent starting point for iterative vaccine design (*3*–*6*).

One or more of the bNAb epitopes present on native, virion-associated trimers are also found on various Env-based immunogens, including soluble, monomeric gp120s and multimeric gp140s that contain both the receptor-binding gp120 and fusion-enabling gp41-ectodomain ($gp41_{ECTO}$) subunits. These various forms of Env are all derived from the viral gp160 precursor protein, which is proteolytically cleaved into the gp120 and $gp41_{ECTO}$ subunits when it is processed within the cell and forms membrane-associated trimers. For practical purposes, most Env-based immunogens are made as soluble proteins by eliminating the membrane-spanning domain of gp160 and creating entities known as gp140s. In some cases, the $gp41_{ECTO}$ domain is also removed to make a monomeric gp120 protein. The soluble gp140s oligomerize via interactions between their $gp41_{ECTO}$ components. However, the oligomers are very unstable unless the construct is stabilized, either by eliminating the cleavage site between gp120 and $gp41_{ECTO}$ to make a standard uncleaved gp140 protein, or by introducing specific trimer-stabilizing changes into the properly cleaved form of gp140. We have favored the latter strategy by making stabilized, cleaved trimers that are designated SOSIP.664 gp140s; the SOS term denotes an intermolecular disulfide bond engineered to link the gp120 and $gp41_{ECTO}$ subunits, while IP signifies an Ile^{559} → Pro point substitution that maintains the $gp41_{ECTO}$ components in their pre-fusion form.

Here, we evaluated the immunogenicity of a SOSIP.664 trimer based on the BG505 clade A virus, which was isolated from a 6-week-old infant who later developed a bNAb response within ~2 years of infection (*7*, *8*). We also tested, in less detail, a second SOSIP.664 trimer based on a clade B adult infection founder virus, B41 (*9*). The BG505 and B41 SOSIP.664 trimers display multiple bNAb epitopes but few non-neutralizing Ab (non-NAb) epitopes that may serve as immunological distractions (*9*, *10*). The integrity and native-like appearance of the BG505 SOSIP.664 trimer, including its complex quaternary epitopes, were previously confirmed by high-resolution cryo–electron microscopy (cryo-EM) and x-ray crystallography structures, the first high-resolution depictions of the HIV-1 Env trimer (*11*–*13*). In this study, we conducted animal immunization experiments to determine which NAb specificities can be induced by two different, native-like SOSIP.664 trimer mimics of the native Env spike, and we performed comparisons with gp120 monomers and standard designs of uncleaved gp140 immunogens.

Immunogenicity of BG505 SOSIP.664 trimers in rabbits

The various immunogens tested in this study are depicted schematically in fig. S1A along with their conformations, which are based on negative-stain EM images that are strongly supported by antigenicity and by biophysical and glycan composition data (figs. S2 and S3) (*10*–*20*). Five different experiments were performed, four in rabbits and one in macaques (fig. S1B). In general, the immunization scheme was based on two closely separated initial doses (weeks 0 and 4),

[1]Department of Microbiology and Immunology, Weill Medical College of Cornell University, New York, NY 10065, USA. [2]Department of Medical Microbiology, Academic Medical Center, University of Amsterdam, 1105 AZ Amsterdam, Netherlands. [3]Department of Immunology and Microbial Science, Scripps Research Institute, La Jolla, CA 92037, USA. [4]International AIDS Vaccine Initiative, Neutralizing Antibody Center, and Collaboration for AIDS Vaccine Discovery, Scripps Research Institute, La Jolla, CA 92037, USA. [5]Center for HIV/AIDS Vaccine Immunology and Immunogen Discovery, Scripps Research Institute, La Jolla, CA 92037, USA. [6]Department of Integrative Structural and Computational Biology, Scripps Research Institute, La Jolla, CA 92037, USA. [7]Division of Human Biology, Fred Hutchinson Cancer Research Center, Seattle, WA 98109, USA. [8]International AIDS Vaccine Initiative, New York, NY 10004, USA. [9]Pepscan Therapeutics, 8243RC Lelystad, Netherlands. [10]Wisconsin National Primate Research Center, University of Wisconsin, Madison, WI 53715, USA. [11]Center for Virology and Vaccine Research, Beth Israel Deaconess Medical Center, Harvard Medical School, Boston, MA 02215, USA. [12]Ragon Institute of Massachusetts General Hospital, MIT, and Harvard, Boston, MA 02114, USA. [13]Department of Medicinal Chemistry, University of Washington, Seattle, WA 98195, USA. [14]Department of Surgery, Duke University Medical Center, Durham, NC 27710, USA. [15]Skaggs Institute for Chemical Biology, Scripps Research Institute, La Jolla, CA 92037, USA.
*Corresponding author. E-mail: jpm2003@med.cornell.edu (J.P.M.); rws2002@med.cornell.edu (R.W.S.)

followed by a third dose after a prolonged rest period of usually 16 weeks (*21*).

The first study, in rabbits, compared the immunogenicity of clade A BG505 SOSIP.664 trimers and gp120 monomers, both of which were produced in 293S GnT$^{-/-}$ cells (*10*, *12*, *20*) (fig. S1A). To assess whether trimer glycosylation affected immunogenicity, in rabbit experiment 2 we immunized three groups of rabbits with BG505 SOSIP.664 trimers produced in 293T cells (natural glycosylation), 293S GnT$^{-/-}$ cells [oligomannose-only glycans (*12*, *22*)], or 293S GnT$^{-/-}$ cells followed by EndoH treatment [glycan-depleted (*12*, *23*)]. In rabbit experiment 1, in addition to the BG505 gp120 monomer comparator proteins, we also tested a clade B YU2 uncleaved gp140 protein containing a Foldon trimerization domain that was produced in 293T cells (YU2 gp140-Fd) (*16*). In rabbit experiment 3, we compared BG505 SOSIP.664 trimers with the uncleaved, non-native BG505 sequence-matched WT.SEKS gp140 protein (*14*, *17*). The goal of the comparisons with the YU2 gp140-Fd and BG505 WT.SEKS proteins was to explore whether a native-like trimer conformation is beneficial for immunogenicity. Proteolytic cleavage of gp120 from gp41$_{ECTO}$ is critical for soluble gp140 trimers to maintain native-like structures; standard uncleaved gp140 proteins based on multiple different sequences, including YU2 gp140-Fd and BG505 WT.SEKS, are known to predominantly adopt aberrant, non-native conformations that can be clearly distinguished from the native-like, cleaved SOSIP.664 trimers (*14*–*17*) (fig. S1A). Thus, when viewed by EM, the standard uncleaved gp140s have an irregular and non-native configuration; frequently seen images represent splayed-out, semidissociated gp120 subunits linked by the uncleaved intersubunit strand to a central core comprising the gp41$_{ECTO}$ components (*14*–*17*). In contrast, the BG505 and also B41 SOSIP.664 trimers are consistently regular, trilobed, propeller-shaped structures (*9*, *10*, *14*). Finally, in rabbit experiment 4, we assessed the ability of SOSIP.664 trimers based on the clade B41 genotype and produced in CHO cells (*9*) to induce NAb responses against the autologous tier 2 B41 virus.

The anti-gp120, anti-gp41, and anti-trimer binding antibody titers induced over time by the various Env proteins are summarized in fig. S4. To quantify the NAb responses 2 weeks after the third immunization (i.e., at week 22 or, for some rabbits, week 26), we used the TZM-bl cell assay, which is based on transactivation of a luciferase reporter gene by an infecting virus (Fig. 1 and table S1). We were particularly interested in assessing the NAb response to the autologous (i.e., sequence-matched) BG505.T332N virus, as it has a neutralization-resistant tier 2 phenotype. Although almost all Env protein immunogens (e.g., gp120 monomers, uncleaved gp140s) can raise

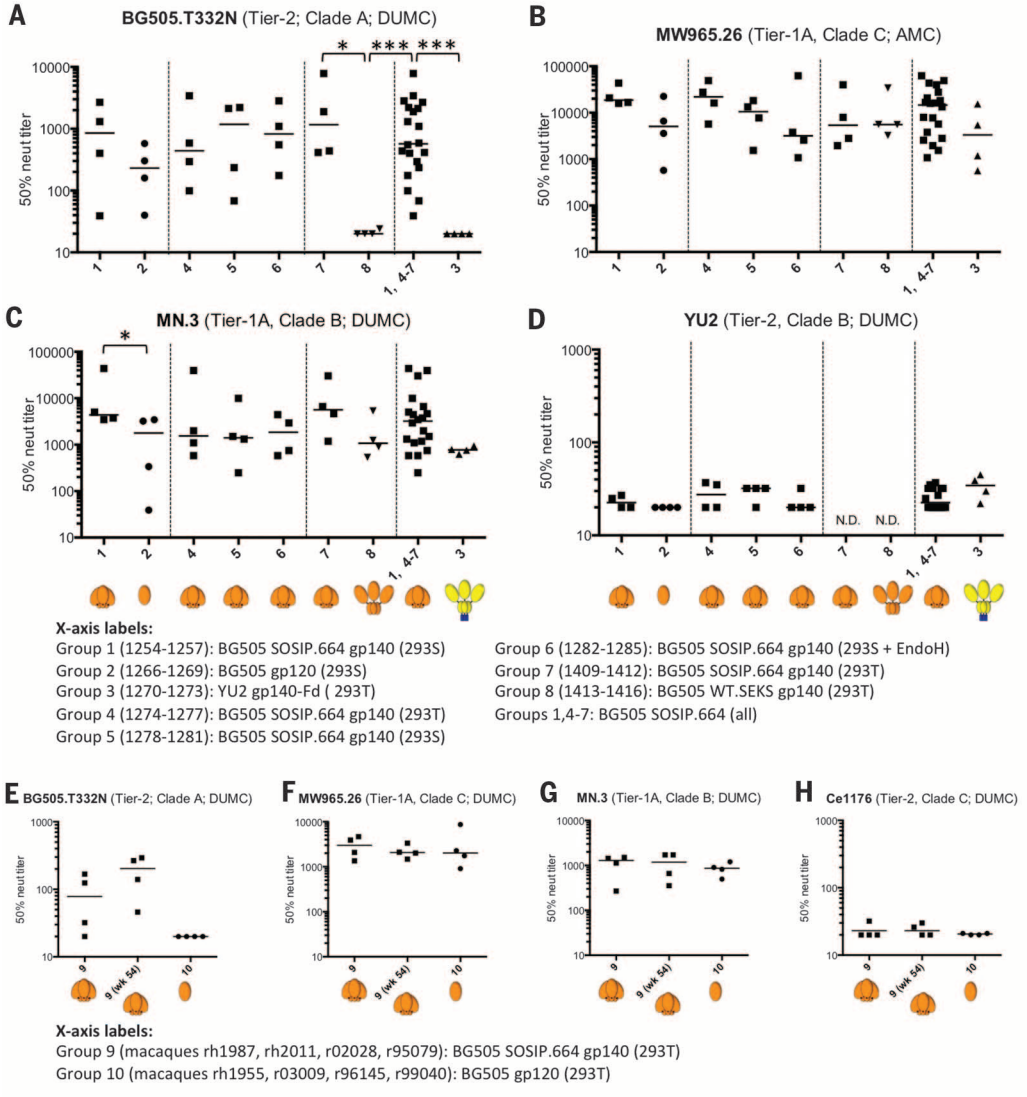


Fig. 1. Induction of autologous tier 2 and heterologous tier 1 NAb responses in rabbits and macaques. (**A** to **D**) Each panel shows the 50% neutralization titers (IC$_{50}$; TZM-bl cell assay) for sera from every immunized rabbit, arranged in the groups outlined in fig. S1. For convenience, all 20 BG505 SOSIP.664 recipient rabbits (groups 1 and 4 to 7) were combined into one group. The dotted lines separate groups that were included in the same immunization experiment. Each panel lists the test virus, its tier classification, and the location of the testing laboratory (*43*) (see Materials and Methods for performance site abbreviations). For additional neutralization data on rabbit sera, see tables S1 and S2. (**E** to **H**) Each panel shows the 50% neutralization titers for individual macaque sera (TZM-bl assay; DUMC) against the specified virus for sera from all eight animals (organized by group) at week 26, and also from the four trimer-immunized animals (group 9) at week 54. The group 10 animals received no further gp120 immunizations after week 24. For additional neutralization data on macaque sera, see table S4. Note that the scales used for the 50% neutralization titers sometimes vary between panels. Negative-stain EM images of the gp140 immunogens are shown in fig. S2 and are the basis for the cartoon depictions shown in brown (BG505 Env) or yellow/blue (YU-2 gp140-Fd). The ISCOMATRIX adjuvant had no detectable adverse effects on the antigenicity of the trimers, assessed by ELISA, or on their appearance in negative-stain EM images (fig. S3). *P < 0.05, ***P < 0.0005 by two-tailed Mann-Whitney test.

NAbs against various neutralization-sensitive tier 1 viruses, the induction of NAbs that are able to counter a tier 2 virus—even an autologous one—has been challenging. Could a native-like trimer do better?

We found that all 20 sera from the BG505 SOSIP.664 trimer-immunized rabbits neutralized the autologous (i.e., sequence-matched) tier 2 virus BG505.T332N (*10*), with titers that ranged from 39 to 7840 (median 570; Fig. 1A). There was no discernible difference in the magnitude of the autologous NAb responses to the three different trimer glycosylation variants (Fig. 1A, groups 4 to 6). Sera from the BG505 gp120 monomer recipients also neutralized the autologous virus, although with a lower median titer of 270 (Fig. 1A, group 2). BG505 gp120 is unusual, as it was selected to bind PG9 and is known to be atypically immunogenic (*24*). It may also be relevant that BG505 gp120 was purified via a bNAb column (in this case 2G12), which may select for more native-like forms of gp120 relative to other methods. The uncleaved BG505 WT.SEKS gp140 induced no NAbs against the autologous BG505.T332N virus (median titer <20) (Fig. 1A, group 8), whereas the uncleaved YU2 gp140-Fd induced NAbs against the autologous, clade-B YU2 virus only weakly (median titer 36) (Fig. 1D, group 3). The difference between the autologous tier 2 NAb responses to the native-like BG505 SOSIP.664 trimer and the non-native WT.SEKS gp140 was significant [$P = 0.029$ for the intra-experiment ($n = 4$ versus $n = 4$) comparison; $P = 0.0002$ when all 20 BG505 SOSIP.664 trimer recipients were included; two-tailed Mann-Whitney test] (Fig. 1A). The poor responses to the WT.SEKS and YU2 proteins are consistent with multiple reports that various uncleaved gp140s are not able to induce NAbs that can neutralize autologous tier 2 viruses consistently in the TZM-bl cell assay (*25*–*29*). The lack of an autologous NAb response to the BG505 WT.SEKS proteins implies that the BG505.T332N virus is not an atypically sensitive tier 2 virus that is vulnerable to any BG505 Env-binding antibodies. The inferiority of WT.SEKS gp140 to gp120 monomers may be because of formation of aberrant intra- and intersubunit disulfide bonds in uncleaved gp140s that create non-native gp120 moieties (*30*, *31*).

We conducted an additional rabbit immunogenicity experiment involving a second native-like trimer, B41 SOSIP.664, based on a clade B tier 2 transmitted/founder virus (fig. S1) (*9*). Eight of 10 animals given these trimers responded by generating an autologous NAb response, with a median titer of 2535 (Fig. 2A). Heterologous tier 1, but not tier 2, NAb responses were induced in all 10 rabbits. Hence the rabbit response to the B41 trimers is qualitatively similar to what was induced by their BG505 counterparts. The median autologous titers against these two versions of fully native-like SOSIP.664 trimers (BG505, 570; B41, 2535; combined group, 1199) exceeded those reported to confer 50% and 80% protection (105 and 329, respectively) in macaque passive-transfer experiments (*32*) (Fig. 2A). Rabbit immunization experiments were conducted several years ago using earlier generations of SOSIP.681 trimers based on the JR-FL and KNH1144 genotypes (*33*, *34*). Autologous tier 2 NAbs were only inconsistently induced in those experiments. However, those trimers, although cleaved, were either not fully native-like (JR-FL) or prone to aggregate formation (KNH1144), which may account for their poor immunogenicity.

To gain an additional perspective on the magnitude of the autologous NAb titers to the BG505 and B41 SOSIP.664 trimers, we compared them with previously reported animal immunization data derived using four uncleaved gp140 proteins based on *env* sequences from the tier 2 viruses 92UG037.8, Q461e2, Q168a2, and CZA97.012 (*25*, *26*) (Fig. 2A). We also included the autologous NAb titers for the YU2 gp140-Fd and BG505 WT.SEKS immunogens shown in Fig. 1A. The four additional uncleaved gp140s were of standard designs that are known or expected to resemble the negative-stain EM images of the uncleaved YU2 gp140-Fd and BG505 WT.SEKS gp140s shown in fig. S2 (*14*, *16*, *19*). The autologous NAb titers induced by the BG505 and B41 SOSIP.664 trimers were greater than the corresponding responses to any other Env protein. When the combined SOSIP.664 trimer groups (median titer 1199, range 20 to 38,598; $n = 30$ rabbits) were compared with the combined

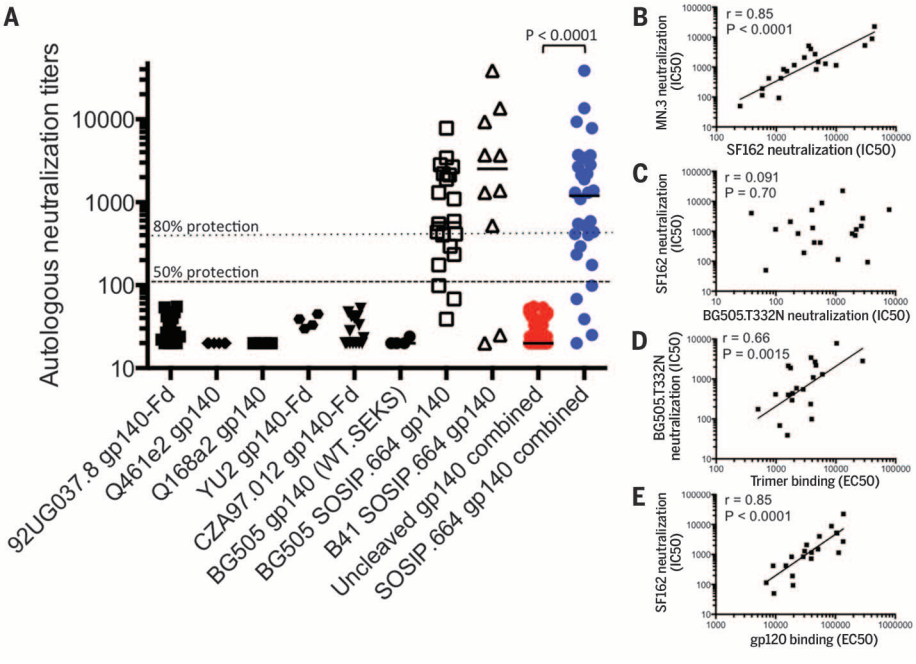


Fig. 2. Comparative depiction of the autologous tier 2 NAb responses elicited in rabbits or guinea pigs by various Env proteins. (**A**) Each data point represents the IC_{50} neutralization titer for serum derived from an individual animal immunized with the stated gp140 protein (some of which incorporated an Fd trimerization domain) when tested in the TZM-bl cell assay against the sequence-matched (i.e., autologous) tier 2 virus. The plotted values are taken from the following papers: 92UG037.8 gp140-Fd [(*25*); $n = 15$], Q461e2 gp140 [(*26*); $n = 6$], Q168a2 gp140 [(*26*); $n = 6$], YU2 gp140-Fd (this paper; $n = 4$; table S1), CZA97.012 gp140-Fd [(*25*); $n = 15$], BG505 gp140 (WT.SEKS; this paper; $n = 4$; table S1), BG505 SOSIP.664 (this paper; $n = 20$; table S1), and B41 SOSIP.664 (this paper; $n = 10$). To minimize the impact of cross-study variables, we restricted the comparison to immunization of small animals (rabbits and guinea pigs), to Env proteins based on tier 2 viruses, and to data generated using the TZM-bl assay under broadly similar conditions. In the rightmost two columns, all the data points for each of the uncleaved gp140s (red symbols) are plotted to allow a statistical comparison with the combined BG505 and B41 SOSIP.664 trimer groups (blue symbols). The difference in the median values is highly significant ($P < 0.0001$ by two-tailed Mann-Whitney test). The dotted and dashed lines denote titers of 105 and 329 that are reported to confer 50% and 80% protection, respectively, to macaques in passive transfer experiments (*32*). (**B** to **E**) Various binding antibody and NAb responses at week 22 (week 26 for experiment 3) from all 20 BG505 trimer-immunized rabbits from experiments 1 to 3 were cross-compared as follows: (B) SF162 NAbs versus MN.3 NAbs; (C) BG505.T332N NAbs versus SF162 NAbs; (D) trimer-binding Abs versus BG505.T332N NAbs; (E) gp120-binding Abs versus SF162 NAbs. The NAb data are the reciprocal of the serum dilution giving 50% inhibition (IC_{50}), the binding Ab data are the reciprocal of the serum dilution giving 50% of the maximum signal in ELISA (EC_{50}). The Spearman *r* and *P* values for the respective correlations are given. Additional correlation analyses as well as details on the statistics are presented in fig. S5.

uncleaved gp140 groups (median titer <20, range <20 to 55; n = 50 animals), the difference was highly significant (P < 0.0001, two-tailed Mann-Whitney test). The magnitude of the difference between the response to the SOSIP.664 trimers and the response to the other Env proteins is so great that immunization protocol variations (such as dosing, schedule, the use of priming vectors, and the identity of the adjuvant) are unlikely to be responsible. Thus, such variables typically influence tier 1 NAb titers by a few multiples but do not make the immunogens capable of inducing autologous tier 2 NAbs.

Sera from BG505 SOSIP.664 trimer-immunized rabbits were usually ineffective against heterologous, neutralization-resistant tier 2 viruses, although we did see some sporadic neutralization at low IC_{50} titers of 30 to 100 (Fig. 1D and tables S1 and S2). The rabbit sera did, however, consistently neutralize more sensitive heterologous tier 1 viruses from different clades, including the ultrasensitive tier 1A viruses MW965.26 (clade C; Fig. 1B), SF162 and MN (both clade B; Fig. 1C and table S1), and the tier 1B viruses BZ167, BaL, 6535.3 (all clade B; table S1), and 93IN905 (clade C; table S1). The TZM-bl assay titers in the 1000s and 100s for the tier 1A and 1B viruses, respectively, are comparable to or greater than titers reported from multiple animal studies of various monomeric gp120 or uncleaved gp140 proteins, as are the negligible titers against heterologous tier 2 viruses (*16*, *25*–*29*, *35*). Overall, the tier 1 NAb responses to the BG505 SOSIP.664, gp120 and WT.SEKS gp140 immunogens were generally similar (Fig. 1, B and C, and table S1). Hence, what distinguishes the native-like SOSIP.664 trimers from the other two Env immunogen designs is not their ability to induce an antibody response per se, but rather the elicitation of a consistent and strong NAb response against the autologous tier 2 virus.

Tier 1 and tier 2 NAb titers do not correlate

To gain an understanding of why the native-like trimers differed from the other Env proteins, we analyzed various aspects of the antibody responses. First, we compared the emergence of heterologous tier 1 (MN, SF162; clade B) and autologous tier 2 (BG505.T332N) NAbs with anti-gp120 and anti-trimer binding antibodies [i.e., enzyme-linked immunosorbent assay (ELISA) titers] in the BG505 SOSIP.664 trimer-immunized rabbits over time (fig. S5, A and B). The trimer-binding responses were initially lower than those to gp120 but became comparable after four immunizations. Autologous tier 2 NAbs were detected only rarely and weakly after two immunizations, but strongly and consistently after three immunizations (fig. S5B). The NAb titers then declined, with kinetics comparable to the binding antibody responses, but were boosted again after the fourth immunization. The tier 1 and autologous tier 2 NAb responses waxed and waned with broadly similar kinetics (fig. S5B).

The NAb titers to the three tier 1 viruses (MN.3, SF162, and MW965.26) induced in the 20 rabbits 2 weeks after the third immunization with BG505 SOSIP.664 trimers strongly correlated with one another (Fig. 2B and fig. S5, C and D). In contrast, the autologous tier 2 titers did not correlate significantly with the heterologous tier 1 titers induced in the same rabbits at the same time (Fig. 2C and fig. S5, E and F). The correlation plots suggest that different NAb specificities mediate the tier 1 and autologous tier 2 responses, as we confirmed experimentally (see below). One implication is that inducing a tier 2 response will not be achieved simply by increasing the titer of tier 1 NAbs, as entirely different antibody specificities and B cell subsets are probably involved.

We also sought associations between NAb and binding antibody titers in the same set of 20 rabbits. The autologous tier 2 NAb titers were correlated with the anti-trimer titers (Fig. 2D; r = 0.66, P = 0.0015), but not with the anti-gp120 titers (fig. S5K). Conversely, the tier 1 NAbs were strongly correlated with the anti-gp120 titers but not at all or only very weakly with the anti-trimer titers (Fig. 2E and fig. S5, H to J, L, and M). The anti-gp120 and anti-trimer titers were not significantly correlated (fig. S5G). The data trends suggest that tier 1 NAb responses are associated with strong binding antibody responses to gp120 monomers. The significant correlation between the BG505.T332N NAb titer and the anti-trimer titer, but not the anti-gp120 titer, again implies that the quaternary structure of a native-like trimer is beneficial for inducing tier 2 NAbs. The non-native WT.SEKS gp140 induced anti-gp120 antibodies efficiently but induced anti-trimer antibodies very poorly (fig. S4, A to C).

Autologous tier 2 and heterologous tier 1 Nabs target different epitopes

We used multiple techniques to gain insights into the various epitopes targeted by the tier 1 and tier 2 NAbs in sera from the BG505 SOSIP.664 trimer-immunized rabbits. First, we performed neutralization assays in the presence of several antigens that could potentially bind and thereby deplete various NAb specificities. These competitors included linear peptides derived from the first, second, and third (V1, V2, and V3) variable loops of Env, a V3-Fc construct, a V1V2 scaffold, a gp41 protein, CD4 binding–defective gp120-D368R monomers and SOSIP.664-D368R trimers, and the resurfaced stabilized core 3 (RSC3) CD4 binding site (CD4bs)–mimetic protein (Table 1). The gp120-D368R monomers and SOSIP.664-D368R trimers absorbed the autologous NAbs comparably and completely, implying that the target epitope(s) are well presented on the isolated gp120 subunit (Table 1 and fig. S6). As residue D368 is a key element of the CD4bs, the inhibitory effect of the two Env-D368R mutants, combined with the lack of effect of the RSC3 protein, implies that the autologous NAbs are unlikely to target the CD4bs directly (Table 1). Truncated gp120-D368R variants lacking the V1, V2, V3, or V1V2 domains were effective competitors for the autologous NAbs, but the variable loop–based peptides or protein constructs and the gp41 proteins were generally inactive (Table 1).

Although the V1/V2 and V3 regions were not generally the targets for autologous NAbs, a noteworthy exception was rabbit 1412. Here, the NAb-depleting effect of the gp120-D368R monomer was completely lost when any of the V1, V2, V1V2, or V3 regions was deleted, but the linear V1, V2, and V3 peptides and the V1V2-scaffold protein were ineffective competitors (Table 1). Hence, the relevant epitope seen by serum 1412 is not present on simple mimics of the V1, V2, and V3 regions (i.e., peptides and scaffolds), but its formation requires that all three variable regions are present on a gp120 monomer or the gp120 subunits of the native trimer.

Peptide serology confirmed that some anti-trimer antibodies recognized the V3 region (fig. S7A). Env trimers undergo conformational transitions that expose V3 both on the virus and on its engineered SOSIP.664 counterparts in vitro (*9*, *10*, *36*). Such "breathing" events are likely to render V3 immunogenic in vaccinated animals. The linear BG505 V3 peptide consistently reduced (by a factor of >10) titers against the tier 1 viruses MN.3, SF162, and MW965.26 when tested against eight sera from trimer-immunized rabbits (fig. S7, B to D) (*35*). This peptide also depleted the tier 1 NAbs induced by the WT.SEKS protein (fig. S7, C and D), consistent with reports that such responses to uncleaved gp140s are typically V3-dominated (*35*, *37*). Deleting the V3 region consistently reduced the ability of the gp120-D368R protein to deplete trimer-induced tier 1 Nabs, but not autologous NAbs (Table 1 and fig. S7, B to D). We conclude that V3 peptide-reactive antibodies raised against the clade-A trimer cross-neutralize tier 1 viruses but do not neutralize the autologous tier 2 virus, which is consistent with the lack of correlation between tier 1 and tier 2 NAb titers (Fig. 2B and fig. S5, C and D) and the resistance of BG505.T332N to V3 monoclonal antibodies (mAbs) that neutralize tier 1 viruses (*10*).

To gain further insight into the autologous NAb response, we tested sera from the nine trimer-immunized rabbits with the highest titers against BG505.T332N against 109 mutants of this virus with single alanine point substitutions of gp120 residues. We sought variants with reduced neutralization sensitivities as a result of sequence changes that affected key epitope(s). The neutralization profile across the virus panel was unique for each serum, showing that the autologous response was different, wholly or in part, in each animal (table S3). The data derived from the mutant panel for all nine rabbits were mapped onto the BG505 SOSIP.664 trimer structure (Fig. 3). Multiple alanine substitutions affected BG505.T332N neutralization. In general, the substitutions with the most impact were clustered at the trimer apex and the gp120 outer domain (OD), including the periphery of the CD4bs, an exception being that serum 1257 was sensitive to the loss of the glycan at C1 residue N88 (Fig. 3, side views). Among individual rabbits, 1274 was affected by mutations in V1, V2, C3, and V5; 1410 by C2, C3, V4, and C5 substitutions; and 1412 by V1, V2, and C5 changes. Among the most frequent

Table 1. Depletion of autologous tier 2 NAbs in sera from rabbits and macaques immunized with BG505 SOSIP.664 trimers or gp120 monomers by a variety of competitor ligands. Sera from 13 BG505 SOSIP.664 trimer-immunized and two BG505 gp120-immunized rabbits, taken 2 weeks after the third immunization (i.e., at week 22 or week 26), as well as sera from two BG505 SOSIP.664 trimer-immunized macaques, taken 2 weeks after the fifth immunization (i.e., week 40), were tested for their ability to neutralize the BG505.T332N virus in the presence of a variety of competitor proteins and peptides, added in excess. The TZM-bl cell assay was conducted at AMC. The data show the relative reduction in neutralization (IC_{50}) in the presence of the specified test reagents; values preceded by > indicate that neutralization was depleted completely (i.e., titer of <20). Empty cells indicate tests not performed.

BG505.T332N pseudovirus			Depletion reagent														
Immunogen	Animal ID	Week	SOSIP.664-D368R	gp120-D368R	gp120-D368R 7C3	gp120-D368R ΔV1	gp120-D368R ΔV2	gp120-D368R ΔV1V2	gp120-D368R ΔV3	gp41	RSC3	V1 peptide	V2 peptide	V3 peptide	V1V2-scaffold	V3-Fc	C1-V1 peptide
BG505	1254	22	3.4		1.7	>3.9	3.1			1.2	1.1			1.4	1.0		1.2
SOSIP.664	1256	22	17.2	>20.7	1.2	25.0	9.6	>20.7	>20.7	0.9	0.7	1.1	1.2	0.8	1.9	1.2	1.9
gp140	1257	22	10.4	>12.0	>28.5	9.9	5.0	>12.0	>12.0	0.5	0.9	1.1	1.6	1.2	1.0		1.0
	1274	22	45.3	>33.7	1.7	54.6	48.9	>33.7	>33.7	0.9	1.0	1.1	1.6	0.5	0.7	1.1	0.9
	1278	22		>14.6	>15.5			>14.6	>14.6	2.0	1.1						0.6
	1279	22		>19.9	>40.6			>19.9	>19.9	0.7	1.4						1.2
	1283	22		>3.8	1.5			>3.8	>3.8	0.7	0.8						1.1
	1284	22	11.4	>8.4	>43.3	24.3	9.2	>8.4	8.0	2.2	1.1	1.3	1.4	0.8	0.7	0.8	0.6
	1285	22	8.4	>4.6	2.7	9.6	8.0	>4.6	>4.6		0.7	1.3	1.8	0.4	0.6		1.3
	1409	26		>22.9	>24.3			>22.9	>22.9	0.9	0.8						1.0
	1410	26		>4.8	>5.7			>4.8	>4.8	0.7	1.2						0.8
	1411	26	>19.3	>78.9	>20.7	18.4	18.4	>78.9	>78.9	1.6	0.9	1.3	2.7	1.8	1.1		1.0
	1412	26	7.0	>7.5	>9.0	0.9	1.4	1.6	1.5	0.8	1.3	1.2	1.2	1.5	1.7		1.2
BG505	1267	22	4.8	3.2	0.8			4.8	4.6	0.8	0.8	2.8	1.0	1.8	1.5		1.2
gp120	1268	22	>22.8	>22.8	2.2			>22.8	21.7	1.2	1.6	1.4	1.2	1.6	1.2		0.7
BG505	rh1987	40		3.3	0.8			3.2	3.2								
SOSIP.664	rh2011	40		>1.3	1.0			>1.3	>1.3								
gp140																	

and largest effects (factor of >5 titer reduction for >5 sera) were changes at L125 (C1); R166 and K168 (V2); P299, R304, and K305 (V3 base); and I420, K421, and Q422 (C4). Autologous NAbs present in seven of nine rabbit sera were sensitive to changes in one or both of the basic R166 and K168 residues in V2 β strand C. These residues are important for forming the epitopes targeted by the bNAbs PG9, PG16, and VRC26 (*6*, *38*), but it is possible they have more distant effects on the conformation of other epitopes.

In rabbit 1412, the autologous response was directed against a conformational epitope involving all three of the V1, V2, and V3 regions and also influenced by N137, N156, and K168 (Table 1, Table 2, and table S3). This sensitivity pattern is akin to a PG9/16-like response, except for the lack of dependency on glycan N160 at the trimer apex. Hence, the autologous NAb response in rabbit 1412 may involve PG9/16-like or VRC26-like antibodies with narrow specificity. The gp120 OD, particularly residues in C3 and C4, was targeted in several rabbits. The depletion experiments with the 7C3 gp120-D368R protein also implicate C3 residues 354 to 363 as direct or indirect influences on the epitope(s) recognized by the autologous NAbs in rabbit sera 1254, 1256, 1274, 1283, and 1285 (Table 1 and Fig. 3). Of note is that BG505.T332N neutralization was adversely affected by mutations that eliminated various OD glycan sites including N185, N301, and N462 (rabbit 1274); N332, N392, and N398 (rabbit 1410); and N137, N156, and N386 (rabbit 1412). We are not aware of the induction of NAbs to glycan-dependent epitopes by gp120 monomers or non-native gp140 proteins.

We used a competition ELISA to study whether the BG505 SOSIP.664, WT.SEKS gp140, or gp120 proteins had induced Abs that could block the trimer binding of various bNAbs (*39*). Several sera from SOSIP.664 or gp120 recipients reduced the binding of CD4bs bNAbs CH103 and VRC01, and also CD4-IgG2, by >50%, whereas sera from WT.SEKS gp140 recipients had no such effect (fig. S8A). The inhibition of CH103 and VRC01 binding correlated with BG505.T332N neutralization, which suggests that at least some serum antibodies mediating the autologous response do so by impeding access to the CD4bs (fig. S8B). However, taken together, the virus mutant data and neutralization-depletion experiments with the RSC3 and gp120-D368R proteins imply that such antibodies do not target the CD4bs directly (Tables 1 and 2). We note that when the PGT135 bNAb binds to its V3 glycan–dependent epitope on the trimer, it reorients other glycans so that they now occlude the CD4bs (*39*, *40*). The PGT135 epitope on the trimer is proximal to residues implicated in the autologous NAb responses for rabbits 1274, 1410, and 1412 (Fig. 3 and fig. S8A). Narrow-specificity NAbs with broadly similar properties to PGT135, including glycan dependency, that indirectly impede access to the CD4bs may be present in some rabbit sera.

The competition ELISA also showed that sera from some trimer-immunized rabbits inhibited the binding of bNAbs 35022 and 3BC315 to their trimer epitopes at the gp120-gp41 interface or gp41, whereas sera from gp120- or WT.SEKS-immunized rabbits did not (fig. S8A). Some autologous NAbs may therefore directly or indirectly occlude epitopes near the bottom of the trimer. Overall, the competition ELISA data confirm that multiple epitopes on the BG505 SOSIP.664 trimer are immunogenic in rabbits, and imply that the trimers were generally more efficient than gp120 and WT.SEKS gp140 proteins at inducing Abs capable of inhibiting bNAb-trimer interactions (fig. S8A).

Comparison with the NAb response induced by the BG505 virus in the infected infant

As our long-term goal is to devise an immunization regimen that can induce bNAbs, we compared the autologous NAb response against the BG505 SOSIP.664 trimers in rabbits with the much broader response that developed in the infant from whom the BG505 virus was isolated (*8*) (see Materials and Methods). The infant's week 14 serum weakly neutralized the BG505 virus, but not BG505.T332N, and completely lacked heterologous neutralization activity even against the tier 1A virus SF162 (Table 3). However, a strong cross-neutralization response against tier 1 and tier 2 viruses, including BG505 and BG505.T332N,

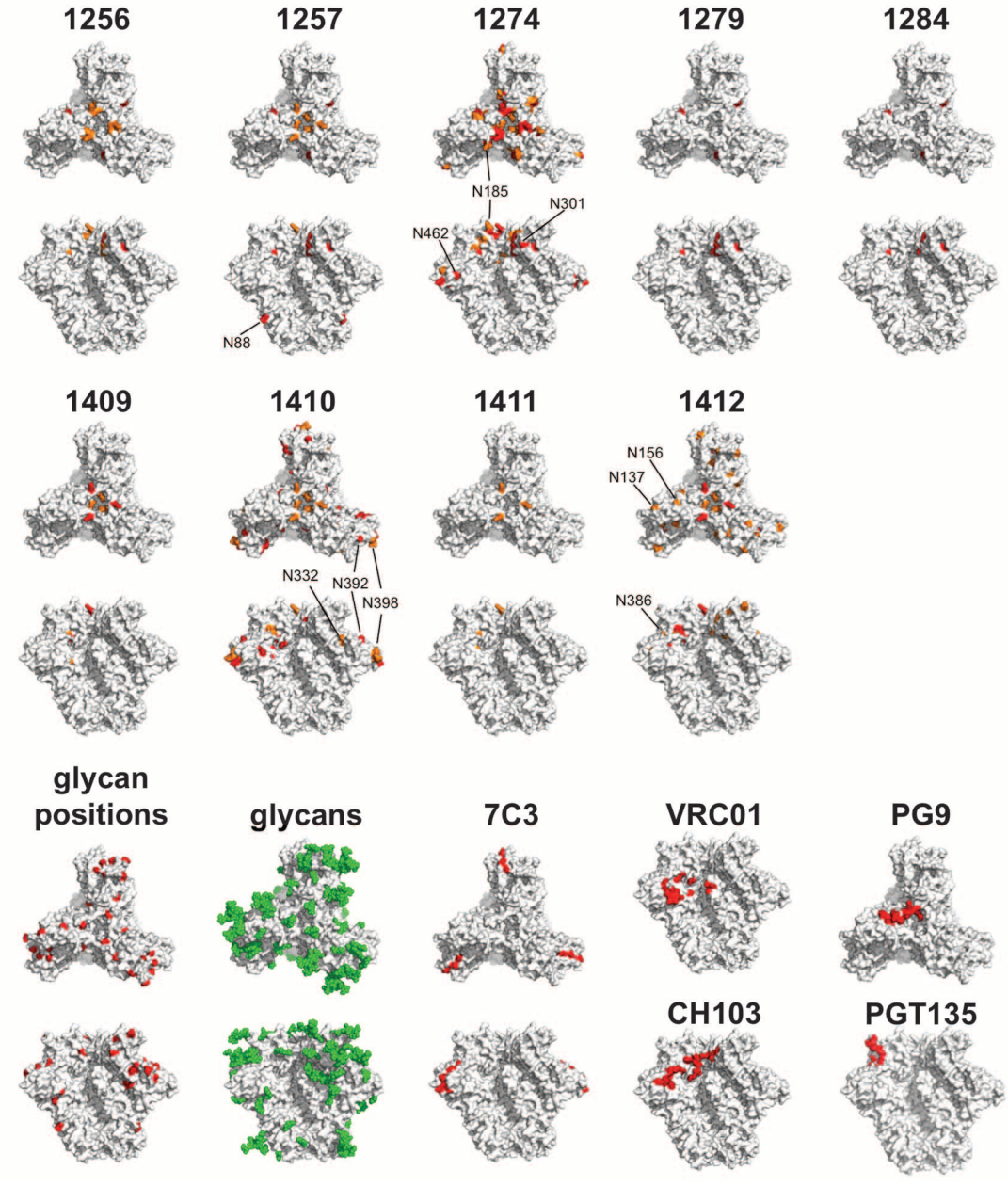


Fig. 3. Autologous tier 2 NAb responses in sera from BG505 SOSIP.664 trimer-immunized rabbits mapped onto the trimer structure. Neutralization data derived when sera from the indicated rabbits were tested against a panel of BG505.T332N virus mutants are shown in table S3. Residues in gp120 where Ala substitutions reduce neutralization by a factor of 5 to 10 and by a factor of >10 are colored orange and red, respectively, on the BG505 SOSIP.664 crystal structure (PDB ID: 4TVP). Each rabbit serum, denoted by a four-digit number, is mapped individually. In each case, the first row is a top view of the trimer, the second row a side view. The glycosylation sites that affect neutralization by rabbit sera 1257, 1274, 1410, and 1412 are labeled. For comparison, the bottom two panels illustrate the positions of glycans (red), the glycans resolved in the crystal structure (green), the seven amino acid substitutions that were under selection pressure in the BG505 infant (7C3, red), and the footprints (within 3 Å) of the bNAbs VRC01 and CH103 (both to the CD4bs), PG9, and PGT135 (all side views, except for PG9, top view).

had developed by month 27. In a direct comparison, week 22 sera from four BG505 SOSIP.664 trimer-immunized rabbits (1256, 1257, 1274, and 1284) neutralized BG505 and BG505.T332N viruses more strongly than the early infant sera, but lacked the neutralization breadth present in the month 27 serum (Table 3). Thus, the recombinant trimers induced NAb responses in rabbits that are similar, but not identical, to the primary infection response of the human infant; autologous NAbs were present in both species.

To guide immunogen design, we studied how BG505 Env sequences evolved in the infant. As expected, the month 27 sequences were highly divergent (9%) from those of week 6. In particular, multiple changes within a 10-residue stretch of C3 (residues 354 to 363) imply a strong selection pressure on this region (fig. S9). The predominant month 27 sequence had seven C3 changes: G354E, Δ356, T357K, I358T, R360I, A362T, and N363K (which removed a glycan site). A gp120-D368R variant containing all seven changes (termed 7C3) was unable to deplete autologous NAbs from sera of five of the 13 test rabbits (numbers 1254, 1256, 1274, 1283, and 1285) but was active against the other eight (Table 1). This variant also did not deplete autologous NAbs from gp120-immunized rabbit sera 1267 and 1268. These findings underscore similarities in how the humoral immune systems of the two species respond to BG505 Env.

Immunogenicity of BG505 SOSIP.664 trimers in rhesus macaques

In a pilot study, we compared the immunogenicity of BG505 SOSIP.664 trimers and gp120 monomers in rhesus macaques (fig. S1). Three of four sera neutralized the autologous BG505.T332N virus at week 26 (median titer, 78), while none of four sera from gp120-immunized animals did so (Fig. 1E and table S4). By week 54, the median autologous titer in the macaques approached that in the rabbits at weeks 22 to 26 (i.e., 203 versus 570) (Fig. 1E and table S4; compare to Fig. 1A). As the anti-gp120 and anti-trimer ELISA titers in the macaques were lower than in the rabbits by a factor of ~5 (fig. S10, A and B; compare to fig. S4A), a stronger adjuvant might be advantageous. NAb titers against tier 1 viruses MW965.26 and MN.3 were similar at the week 26 and week 54 time points and did not differ markedly between trimer and monomer groups at week 26 (Fig. 1, F and G). None of the eight sera neutralized the heterologous tier 2 clade C virus Ce1176 (Fig. 1H).

In the competition ELISA, sera from trimer-immunized macaques induced stronger bNAb-blocking responses than gp120 recipients, including Abs that reduced access of CH103 and VRC01 to the CD4bs and, to a lesser extent, of PGT145 to the trimer apex (fig. S8A). In addition, the BG505 gp120-D368R protein, but not its 7C3 variant, depleted BG505.T332N NAbs from rh1987 sera (Table 1); this finding suggests that, as in some

Table 2. Summary of autologous NAb specificities in sera from rabbits and macaques immunized with BG505 SOSIP.664 trimers or gp120 monomers when analyzed in different assays. The immunogen, producer cell/treatment (i.e., influence on glycosylation profile), and rabbit ID number are listed in the first three columns. The fourth column lists N-linked glycosylation sites that affect autologous BG505.T332N neutralization (factor of >5 decrease in IC_{50}; see table S3). The fifth column lists gp120 domains where substitutions decrease neutralization by a factor of >5 (table S3). The sixth column lists the domains that, when mutated or deleted from the BG505 gp120-D368R protein, impair its neutralization depletion capacity (Table 1). The seventh column lists the bNAbs for which binding to D7324-tagged BG505 SOSIP.664 trimers in ELISA is inhibited by >50% by the test serum (fig. S9). In columns 4 and 5, ND = not done (the serum was not tested against the mutant virus panel). In columns 4, 6, and 7, a blank entry indicates that the assay was performed, but the outcome was uninformative.

Immunogen	Producer cell	Animal ID	Neutralization mutants (glycan)	Neutralization mutants	Neutralization depletion	CD4/bNAb block
BG505	293S	1254	ND	ND	C3	CD4, CH103, PGT151, 35O22, 3BC315
SOSIP.664 gp140	293S	1256		C1, V2, V3, C4	C3	CD4, CH103, VRC01, PGT151, 35O22, 3BC315
	293S	1257	N88	C1, V2, V3, C4		CD4, 35O22, 3BC315
	293T	1274	N185, N301, N462	C1, V2, V3, C3, C4, V5	C3	CH103, VRC01
	293S	1278	ND	ND		CD4, CH103, PGT151, 35O22, 3BC315
	293S	1279		C1, V3, C4		CD4, CH103, VRC01, PGT121, PGT126, PGT151, 35O22, 3BC315
	293S + EndoH	1283	ND	ND	C3	PGT126
	293S + EndoH	1284		C1, V3, C4		CH103, 35O22, 3BC315
	293S + EndoH	1285	ND	ND	C3	VRC01, 35O22, 3BC315
	293T	1409		V2, C4, C5		CH103, VRC01, 3BC315
	293T	1410	N332, N392, N398	V2, C2, V3, C3, V4, C4, C5		CH103, VRC01, 3BC315
	293T	1411		V2, C4, C5		VRC01, 3BC315
	293T	1412	N137, N156, N386	C1, V1, V2, C2, V3, C3, C4, C5	V1, V2, V3	CH103, VRC01, PGT126, 3BC315
BG505	293S	1267	ND	ND	C3	CH103, VRC01
gp120	293S	1268	ND	ND	C3	CD4, CH103, VRC01
BG505	293T	rh1987	ND	ND	C3	CH103, VRC01, PGT126, PGT135
SOSIP.664 gp140	293T	rh2011	ND	ND		CH103, VRC01, PGT145, PGT126, PGT135

Table 3. Comparison of NAb responses induced by BG505 SOSIP.664 trimers in rabbits and by natural infection of an infant with HIV-1 BG505 virus. Sera from rabbits 1256, 1257, 1274, and 1284 after three immunizations (i.e., at week 22) with BG505 SOSIP.664 trimers were compared with sera from infant BG505 taken at week 14 and month 27 after infection. The trimers are based on a sequence derived from the infant at week 6. The TZM-bl cell assay was conducted at FHCRC. The clades and the tier classifications of the test viruses are indicated. The BG505 and BG505.T32N viruses are described in the supplementary materials.

Clade	Tier	Virus isolate	Rabbit 1256 week 22	Rabbit 1257 week 22	Rabbit 1274 week 22	Rabbit 1284 week 22	Human BG505 week 14	Human BG505 month 27
A	2	BG505	581	143	334	113	157	238
A	2	BG505.T332N	773	109	641	169	<100	452
B	1A	SF162	704	1946	106	2362	<100	>3200
A	1B	Q461.D1	<100	202	<100	312	<100	>3200
A	2	Q842.d16	<100	<100	<100	<100	<100	482
A	2	BJ613.E1	<100	<100	<100	<100	<100	<100
A/D	2	BF535.A1	<100	<100	<100	<100	<100	129
B	2	TRO.11	<100	<100	<100	<100	106	262
B	3	THRO4156.18	<100	<100	<100	<100	<100	<100
C	2	QC406.F3	<100	<100	<100	<100	<100	971
C	2	CAP210.E8	<100	<100	<100	<100	<100	590
D	2	QD435.A4	<100	<100	<100	<100	102	548
D	2	QB857.B3	<100	<100	<100	<100	<100	185

rabbits, the C3 region is involved in this autologous response.

Conclusions

Inducing high titers of autologous tier 2 NAbs may be a necessary first step in the elicitation of bNAbs (*3*–*6*). The strong and consistent autologous response to the BG505 and B41 SOSIP.664 trimers reflects their native-like structure, homogeneity, stability, and antigenicity, as well as the immunogenicity of the BG505 virus in the infected infant (*8*, *9*, *12*, *14*, *17*). Taken together, the mapping studies show that multiple specificities contribute to the autologous NAb responses against the BG505 trimers, including antibodies that recognize glycan-influenced epitopes. If a polyspecific response could be achieved in humans, it might provide broader coverage against circulating viruses, but a human vaccine must generate a more broadly neutralizing response than we report here.

The native structure of SOSIP.664 trimers allows candidate immunogens to be rationally redesigned to try to improve immunogenicity. Relevant but not mutually exclusive strategies include (i) introducing sequence changes to increase the stability of the trimer apex and associated bNAb epitopes while reducing the antigenicity of V3 and other non-NAb epitopes that may be immunologic distractions; (ii) immunizing with sequential SOSIP.664 trimers based on later-arising BG505 sequences or cocktails of different trimers (e.g., from clades A, B, and C, etc.) (*9*); or (iii) priming with trimer variants that trigger desirable germline responses (*4*, *5*, *41*, *42*). Overall, our results strongly validate the concept of using native-like trimers and structural information to create an HIV-1 vaccine that induces bNAbs.

Materials and methods

Immunogens and immunizations

The BG505 SOSIP.664 trimers, gp120 monomers, and WT.SEKS uncleaved gp140 proteins were all produced and purified as reported previously (*10*, *14*, *20*). Unless specified, the proteins were expressed in HEK293T cells by transient transfection and purified via a 2G12 mAb affinity column followed by size exclusion chromatography (SEC). Protein purities and properties were comparable to those described elsewhere (*10*, *14*, *20*). BG505 SOSIP.664 trimers were also expressed in HEK293S cells that lack *N*-acetylglucosaminyltransferase I ($GnTI^{-/-}$). The resulting Env proteins bear glycans that are not fully processed and remain in oligomannose form (*22*, *23*). Samples of the 293S cell-derived trimers were treated with the EndoH glycosidase, as previously described, to reduce their total glycan content (*23*). The clade B B41 SOSIP.664 and B41 SOSIP.664-D7324 trimers were produced from stable CHO cell lines that were cultured in 0.5% serum (*9*). The trimers were purified by 2G12 affinity chromatography followed by SEC, as described elsewhere; the extent of V3-clipping was negligible (*9*). The YU2 gp140-Fd protein was made in HEK293T cells under contract for IAVI by G. Stewart-Jones (University of Oxford), as described (*44*).

Rabbit immunizations and blood sampling were carried out under subcontract at Covance (Denver, PA) according to the schedule presented in fig. S1B. Female New Zealand White rabbits (usually 4 per group) were immunized intramuscularly with 30 μg of the various Env proteins (40 μg in experiment 3). The proteins were formulated in 75 Units of ISCOMATRIX, a saponin-based adjuvant obtained from CSL Ltd. (Parkville, Victoria, Australia) (*45*). Macaque immunizations and blood sampling were carried out at the Wisconsin Primate Center according to the schedule in fig. S1B. Rhesus macaques (4 per group) were immunized intramuscularly with 100 μg of BG505 SOSIP.664 or gp120 proteins formulated in 75 units of ISCOMATRIX.

mAbs and human sera

The mAbs used here were provided by the following individuals: CH103 and CH31, B. Haynes (Duke University); VRC01, P. Kwong and J. Mascola (NIH/VRC, Bethesda, MD); NIH45-46, NIH45-46W, 3BNC60, 3BNC117, 12A12, 12A21, M. Nussenzweig (Rockefeller University); various mAbs used for tier classification, S. Zolla-Pazner (New York University School of Medicine). mAbs 2G12 and 2F5 were obtained through the NIH AIDS Reagent Program, Division of AIDS, NIAID, NIH from H. Katinger. The serum samples used for the neutralization sensitivity (i.e., tier) classification of BG505.T332N have been described elsewhere (*46*). Sera obtained from individuals chronically infected with clade-A HIV-1 strains were gifts from B. Haynes and A. McKnight (Barts & London Medical School). mAb ARP3119 used for Western blotting was acquired from the Programme EVA Centre for AIDS Reagents.

BG505 viruses and serum

The BG505 infant was HIV-1 DNA-negative at birth, but DNA-positive 6 weeks later, suggesting that infection occurred within this window (*8*). The sequence of a week 6 clone is the basis of the BG505 SOSIP.664 protein construct, in which a T332N substitution was made to restore bNAb epitopes that require the N332 glycan (*7*, *8*, *10*, *24*). The same change was made to create the BG505. T332N variant of the week 6 BG505 virus (*10*). Serum samples were available from week 6, week 14, and month 27.

ELISA reagents and procedures

The D7324-epitope-tagged version of BG505 SOSIP.664, referred to as SOSIP.664-D7324, and BG505 gp120 with a reconstructed D7324 epitope in C5, were made as described previously (*10*). JR-CSF gp120 was prepared by D. Kubitz at the Scripps Center for Antibody Development and Production (La Jolla, CA) using transient transfection of HEK293F cells, and purified by *Galanthus nivalis* lectin (Vector Labs, Burlingame, CA) affinity chromatography followed by SEC using a Sephacryl S200HR column. Anti-gp120 and anti-trimer ELISAs using the above proteins as antigens were performed as described previously (*10*). The C-terminal His-tagged BG505 SOSIP.664-His trimer was prepared as described previously (*17*, *37*). His-tagged BG505 gp41 (gp41-His) was produced as follows: A His-tagged version of the BG505 IP.664 gp140 protein, which is based on the SOSIP.664 construct but with the SOS disulfide bond omitted (*14*), was expressed in the presence of excess furin in 293F cells. The protein was purified via the His-tag using Ni-NTA chromatography with elution using 250 mM imidazole, followed by three rounds of negative selection using a 2G12 bNAb column to remove any residual gp120 or uncleaved gp140 proteins. The purified gp41 protein bound the gp41-specific non-NAb F240 efficiently, but did not bind 2G12 or VRC01, indicating that contaminant gp120 or gp140 proteins were not present (data not shown). The gp41 protein also did not bind the PGT151 or 3BC315 bNAbs, suggesting that it was not in a pre-fusion conformation (*37*, *47*). Ni-NTA ELISAs using His-tagged trimers and the gp41 protein were performed as described elsewhere (*37*).

For bNAb competition ELISA experiments, rabbit or macaque sera (1:100 dilution) were incubated with D7324-captured BG505 SOSIP.664-D7324 trimers for 1 hour. A biotinylated bNAb was then added at a concentration sufficient to give ~80% of the maximum binding signal, as assessed in a prior titration experiment (i.e., with no competitor present). The bound bNAb was detected using horseradish peroxidase (HRP)-labeled streptavidin. As the PGT151, 35O22, and 3BC315 bNAbs, and also CD4-IgG2, could not be biotinylated without impairing their binding activity (*37*) we detected unlabeled human bNAbs using an HRP-labeled donkey anti-human IgG conjugate that was minimally cross-reactive with rabbit IgG (Jackson Immunoresearch, Westgrove, PA). The latter assay format was unsuitable for macaque sera because the anti-human antibody cross-reacted with macaque IgG. As a result, it was not possible to test the macaque sera for inhibition of PGT151, 35O22, 3BC315, or CD4-IgG2 binding to the trimer.

To analyze the relative titers for serum antibody binding to conformational *vs.* linear epitopes, trimers (0.1 μg/ml) or monomers (0.03 μg/ml) were denatured by heating for 5 min at 99°C in 50 μl of TBS, 10% FCS, 1% SDS, and 50 mM DTT (sodium dodecyl sulfate, SDS; dithiothreitol, DTT). The samples were then diluted by a factor of 140 in TBS and 10% FCS to prevent SDS and DTT from interfering with the ELISA. The use of both SDS and DTT ensures that the Env proteins are fully denatured by heat treatment (*48*). The native or denatured proteins were then used in a D7324-capture ELISA, essentially as described elsewhere (*10*, *48*). The relative reduction of binding to the denatured versus native Env proteins was calculated using the half maximal binding values (EC_{50}).

Neutralization assays

TZM-bl cell neutralization assays using Env-pseudotyped viruses were performed at six sites. For additional information on the assay and all supporting protocols, see www.hiv.lanl.gov/content/nab-reference-strains/html/home.htm. The performance sites were as follows: HMS, Harvard Medical School, and DUMC, Duke University

Medical Center (for methodology see (*49*)); IAVI, International AIDS Vaccine Initiative, Brooklyn, NY (for methodology see (*24*)); AMC, Academic Medical Center, Amsterdam [methodology see (*10*)]; WCMC, Weill Cornell Medical College, New York [methodology see (*50*)]; FHCRC, Fred Hutchinson Cancer Research Center, Seattle, WA [methodology see (*8*)]; TSRI, The Scripps Research Institute [methodology see (*51*)]. The Env-pseudotyped viruses and their tier classifications have been described elsewhere (*8*, *52*–*55*), as have the BG505.T332N and BG505 Env-pseudotyped viruses (*8*, *10*, *24*). The BG505.T332N Env-pseudotyped virus was used except when the test virus is specifically stated to be BG505 (i.e., without the T332N substitution). Also note that the MN Env-pseudotyped virus used at DUMC is designated MN.3. We did not use the A3R5 cell assay because of our concerns that it produces false positive, and hence misleading, detection of NAbs to tier 2 viruses.

Tier categorization of the BG505.T332N and B41 Env-pseudotyped viruses was based on the neutralization sensitivity to a panel of mAbs directed against various epitopes as well as a panel of sera from humans infected with clade A viruses, in comparison with previously tiered viruses (*52*). Data on BG505.T332N sensitivity to another panel of 50 mAbs can be found elsewhere (*10*). For both viruses, the tier classification experiments were performed at DUMC. We constructed a set of BG505.T332N alanine mutants for mapping NAb responses (table S3).

Neutralization depletion experiments

Proteins for neutralization depletion experiments [BG505 gp120-D368R and variants; BG505 SOSIP.664-D368R; RSC3 (*56*)] were expressed transiently in HEK293F cells and purified by 2G12-affinity chromatography. All reagents were based on the BG505 sequence, except for the RSC3 protein. The D368R change was introduced to ensure that the gp120 or SOSIP.664 gp140 proteins do not bind to CD4 on the cell surface and thereby inhibit HIV-1 infection competitively. ELISA experiments confirmed that the D368R substitution strongly reduced the binding of CD4 and several CD4bs bNAbs to BG505 gp120. The gp120-D368R 7C3 reagent contains seven amino acid changes in C3 (G354E, Δ356, T357K, I358T, R360I, A362T, and N363K) based on the month 27 sequences from infant BG505 (fig. S9). Substitutions and deletions were made using the Quickchange mutagenesis kit (Agilent, Santa Clara, CA). The plasmid expressing RSC3 (donated by P. Kwong and J. Mascola, NIH/VRC, Bethesda, MD) has been described elsewhere (*56*). The basis for the design of the BG505 V1V2-scaffold protein has also been described (*57*). The protein was expressed in HEK293S GnTI$^{-/-}$ cells and purified via its C-terminal 6×His tag using Ni-NTA chromatography and $NiCl_2$ elution, followed by SEC on a Superdex 200 column. The theoretical MW of the scaffold, including glycans, is ~25 kD.

BG505-derived peptides with the following sequences were purchased from Genscript (Piscataway, NJ): V1: TNVTNNITDDMRGELKN; V2 (5 overlapping peptides): MTTELRDKKQKVYSL, DKKQKVYSLFYRLDV, YSLFYRLDVVQINEN, LDVVQINENQGNRSN, ENQGNRSNNSNKEYR; V3: TRPNNNTRKSIRIGPGQAFYATGDIIGDIRQAH; C1-V1: VKLTPLCVTLQCTNVTNNITDDMRGELKN.

To characterize the specificities of NAb responses induced in the rabbits, we incubated competitor Env proteins or peptides with appropriately diluted sera (total volume 25 μl) for 1 hour at 37°C. The competitor Env proteins were present at a concentration of 40 μg/ml except for the V1V2-scaffold protein (20 μg/ml). The competitor peptides were also used at 40 μg/ml, except that each individual component of a cocktail of 5 overlapping V2 peptides was present at 20 μg/ml. The Env-pseudotyped virus was then added to the serum-competitor mixture for 1 hour before infection of TZM-bl target cells was initiated. The rest of the assay was carried out as described above and elsewhere (*10*). Neutralization titers were expressed as the reciprocal serum dilution that caused 50% inhibition of virus infection (IC_{50}). The extent of neutralization depletion by the added competitor was expressed as the relative reduction in the IC_{50} value.

Pepscan analysis

15-mer peptides, overlapping by 14 residues, from the BG505 SOSIP.664 as well as the unmodified BG505 gp140 sequences, were synthesized by Fmoc coupling on the solid support of a Pepscan hydrogel (*58*). The peptide libraries were probed with heat-inactivated human sera, at a 1:1000 dilution. After extensive washing, a goat anti-human HRP conjugated secondary antibody was added, followed by color development using 2,2′-azinobis(3-ethylbenzothiazoline-6-sulphonic acid). A charge-coupled device camera was used to quantify the absorbance at 405 nm. For every individual Pepscan dataset, the data were normalized to the average signal intensity derived from the overall analysis.

Negative-stain electron microscopy

The BG505 WT.SEKS, BG505 SOSIP.664, and YU2 gp140-Fd proteins, as well as ISCOMATRIX adjuvant-formulated BG505 SOSIP.664 trimers, were analyzed by negative-stain EM. Samples were prepared for analysis as described (*10*, *14*). Briefly, a 3-μl aliquot containing ~0.01 mg per ml of protein was applied for 5 s onto a carbon-coated 400 Cu mesh grid that had been glow-discharged at 20 mA for 30 s, then negatively stained with 2% (w/v) uranyl formate for 60 s. Data were collected using an FEI Tecnai T12 electron microscope operating at 120 keV, with an electron dose of ~25 $e^-/Å^2$ and a magnification of 52,000× that resulted in a pixel size of 2.05 Å at the specimen plane. Images were acquired with a Tietz TemCam-F416 CMOS camera using a nominal defocus range of 900 to 1300 nm.

Data processing methods were adapted from those used previously (*10*, *14*). Particles were picked automatically using DoG Picker and put into a particle stack using the Appion software package (*59*). Initial, reference-free, two-dimensional (2D) class averages were calculated using particles binned by two via Iterative Multivariate Statistical Analysis (MSA)/Multi-reference Alignment (MRA) and sorted into classes (*60*). Particles corresponding to trimers were selected into a substack and binned by two before another round of reference-free alignment was carried out using Iterative MSA/MRA and Xmipp Clustering and 2D alignment algorithms (*61*).

REFERENCES AND NOTES

1. M. J. van Gils, R. W. Sanders, Broadly neutralizing antibodies against HIV-1: Templates for a vaccine. *Virology* **435**, 46–56 (2013). doi: 10.1016/j.virol.2012.10.004; pmid: 23217615
2. A. P. West Jr. *et al*., Structural insights on the role of antibodies in HIV-1 vaccine and therapy. *Cell* **156**, 633–648 (2014). doi: 10.1016/j.cell.2014.01.052; pmid: 24529371
3. C. A. Derdeyn, P. L. Moore, L. Morris, Development of broadly neutralizing antibodies from autologous neutralizing antibody responses in HIV infection. *Curr. Opin. HIV AIDS* **9**, 210–216 (2014). doi: 10.1097/COH.0000000000000057; pmid: 24662931
4. B. F. Haynes, G. Kelsoe, S. C. Harrison, T. B. Kepler, B-cell-lineage immunogen design in vaccine development with HIV-1 as a case study. *Nat. Biotechnol.* **30**, 423–433 (2012). doi: 10.1038/nbt.2197; pmid: 22565972
5. H.-X. Liao *et al*., Co-evolution of a broadly neutralizing HIV-1 antibody and founder virus. *Nature* **496**, 469–476 (2013). doi: 10.1038/nature12053; pmid: 23552890
6. N. A. Doria-Rose *et al*., Developmental pathway for potent V1V2-directed HIV-neutralizing antibodies. *Nature* **509**, 55–62 (2014). doi: 10.1038/nature13036; pmid: 24590074
7. X. Wu *et al*., Neutralization escape variants of human immunodeficiency virus type 1 are transmitted from mother to infant. *J. Virol.* **80**, 835–844 (2006). doi: 10.1128/JVI.80.2.835-844.2006; pmid: 16378985
8. L. Goo, V. Chohan, R. Nduati, J. Overbaugh, Early development of broadly neutralizing antibodies in HIV-1-infected infants. *Nat. Med.* **20**, 655–658 (2014). doi: 10.1038/nm.3565; pmid: 24859529
9. P. Pugach *et al*., A native-like SOSIP.664 trimer based on an HIV-1 subtype B env gene. *J. Virol.* **89**, 3380–3395 (2015). doi: 10.1128/JVI.03473-14; pmid: 25589637
10. R. W. Sanders *et al*., A next-generation cleaved, soluble HIV-1 Env trimer, BG505 SOSIP.664 gp140, expresses multiple epitopes for broadly neutralizing but not non-neutralizing antibodies. *PLOS Pathog.* **9**, e1003618 (2013). doi: 10.1371/journal.ppat.1003618; pmid: 24068931
11. D. Lyumkis *et al*., Cryo-EM structure of a fully glycosylated soluble cleaved HIV-1 envelope trimer. *Science* **342**, 1484–1490 (2013). doi: 10.1126/science.1245627; pmid: 24179160
12. J.-P. Julien *et al*., Crystal structure of a soluble cleaved HIV-1 envelope trimer. *Science* **342**, 1477–1483 (2013). doi: 10.1126/science.1245625; pmid: 24179159
13. M. Pancera *et al*., Structure and immune recognition of trimeric pre-fusion HIV-1 Env. *Nature* **514**, 455–461 (2014). doi: 10.1038/nature13808; pmid: 25296255
14. R. P. Ringe *et al*., Cleavage strongly influences whether soluble HIV-1 envelope glycoprotein trimers adopt a native-like conformation. *Proc. Natl. Acad. Sci. U.S.A.* **110**, 18256–18261 (2013). doi: 10.1073/pnas.1314351110; pmid: 24145402
15. M. Guttman, K. K. Lee, A functional interaction between gp41 and gp120 is observed for monomeric but not oligomeric, uncleaved HIV-1 Env gp140. *J. Virol.* **87**, 11462–11475 (2013). doi: 10.1128/JVI.01681-13; pmid: 23966389
16. K. Tran *et al*., Vaccine-elicited primate antibodies use a distinct approach to the HIV-1 primary receptor binding site informing vaccine redesign. *Proc. Natl. Acad. Sci. U.S.A.* **111**, E738–E747 (2014). doi: 10.1073/pnas.1319512111; pmid: 24550318
17. A. Yasmeen *et al*., Differential binding of neutralizing and non-neutralizing antibodies to native-like soluble HIV-1 Env trimers, uncleaved Env proteins, and monomeric subunits. *Retrovirology* **11**, 41 (2014). doi: 10.1186/1742-4690-11-41; pmid: 24884783
18. M. Guttman *et al*., CD4-induced activation in a soluble HIV-1 Env trimer. *Structure* **22**, 974–984 (2014). doi: 10.1016/j.str.2014.05.001; pmid: 24931470
19. L. K. Pritchard *et al*., Structural constraints determine the glycosylation of HIV-1 envelope trimers. *Cell Rep.* 10.1016/j.celrep.2015.05.017 (2015). doi: 10.1016/j.celrep.2015.05.017; pmid: 26051934
20. J. P. Julien *et al*., Asymmetric recognition of the HIV-1 trimer by broadly neutralizing antibody PG9. *Proc. Natl. Acad. Sci. U.S.A.* **110**, 4351–4356 (2013).pmid: 23426631

21. J. E. Ledgerwood *et al*., Prime-boost interval matters: A randomized phase 1 study to identify the minimum interval necessary to observe the H5 DNA influenza vaccine priming effect. *J. Infect. Dis.* **208**, 418–422 (2013). doi: 10.1093/infdis/jit180; pmid: 23633407
22. D. Eggink *et al*., Lack of complex N-glycans on HIV-1 envelope glycoproteins preserves protein conformation and entry function. *Virology* **401**, 236–247 (2010). doi: 10.1016/j.virol.2010.02.019; pmid: 20304457
23. R. S. Depetris *et al*., Partial enzymatic deglycosylation preserves the structure of cleaved recombinant HIV-1 envelope glycoprotein trimers. *J. Biol. Chem.* **287**, 24239–24254 (2012). doi: 10.1074/jbc.M112.371898; pmid: 22645128
24. S. Hoffenberg *et al*., Identification of an HIV-1 clade A envelope that exhibits broad antigenicity and neutralization sensitivity and elicits antibodies targeting three distinct epitopes. *J. Virol.* **87**, 5372–5383 (2013). doi: 10.1128/JVI.02827-12; pmid: 23468492
25. J. P. Nkolola *et al*., Breadth of neutralizing antibodies elicited by stable, homogeneous clade A and clade C HIV-1 gp140 envelope trimers in guinea pigs. *J. Virol.* **84**, 3270–3279 (2010). doi: 10.1128/JVI.02252-09; pmid: 20053749
26. C. A. Blish *et al*., Comparative immunogenicity of subtype a Human Immunodeficiency Virus type 1 envelope exhibiting differential exposure of conserved neutralization epitopes. *J. Virol.* **84**, 2573–2584 (2010). doi: 10.1128/JVI.01687-09; pmid: 20015987
27. C. Sundling *et al*., Soluble HIV-1 Env trimers in adjuvant elicit potent and diverse functional B cell responses in primates. *J. Exp. Med.* **207**, 2003–2017 (2010). doi: 10.1084/jem.20100025; pmid: 20679401
28. C. Grundner *et al*., Analysis of the neutralizing antibody response elicited in rabbits by repeated inoculation with trimeric HIV-1 envelope glycoproteins. *Virology* **331**, 33–46 (2005). doi: 10.1016/j.virol.2004.09.022; pmid: 15582651
29. M. N. E. Forsell *et al*., Biochemical and immunogenic characterization of soluble human immunodeficiency virus type 1 envelope glycoprotein trimers expressed by semliki forest virus. *J. Virol.* **79**, 10902–10914 (2005). doi: 10.1128/JVI.79.17.10902-10914.2005; pmid: 16103142
30. E. P. Go, Y. Zhang, S. Menon, H. Desaire, Analysis of the disulfide bond arrangement of the HIV-1 envelope protein CON-S gp140 ΔCFI shows variability in the V1 and V2 regions. *J. Proteome Res.* **10**, 578–591 (2011). doi: 10.1021/pr100764a; pmid: 21114338
31. E. P. Go, D. Hua, H. Desaire, Glycosylation and disulfide bond analysis of transiently and stably expressed clade C HIV-1 gp140 trimers in 293T cells identifies disulfide heterogeneity present in both proteins and differences in O-linked glycosylation. *J. Proteome Res.* **13**, 4012–4027 (2014). doi: 10.1021/pr5003643; pmid: 25026075
32. M. Shingai *et al*., Passive transfer of modest titers of potent and broadly neutralizing anti-HIV monoclonal antibodies block SHIV infection in macaques. *J. Exp. Med.* **211**, 2061–2074 (2014). doi: 10.1084/jem.20132494; pmid: 25155019
33. S. Beddows *et al*., A comparative immunogenicity study in rabbits of disulfide-stabilized, proteolytically cleaved, soluble trimeric human immunodeficiency virus type 1 gp140, trimeric cleavage-defective gp140 and monomeric gp120. *Virology* **360**, 329–340 (2007). doi: 10.1016/j.virol.2006.10.032; pmid: 17126869
34. Y. K. Kang *et al*., Structural and immunogenicity studies of a cleaved, stabilized envelope trimer derived from subtype A HIV-1. *Vaccine* **27**, 5120–5132 (2009). doi: 10.1016/j.vaccine.2009.06.037; pmid: 19567243
35. D. C. Malherbe *et al*., Envelope variants circulating as initial neutralization breadth developed in two HIV-infected subjects stimulate multiclade neutralizing antibodies in rabbits. *J. Virol.* **88**, 12949–12967 (2014). doi: 10.1128/JVI.01812-14; pmid: 25210191
36. J. B. Munro *et al*., Conformational dynamics of single HIV-1 envelope trimers on the surface of native virions. *Science* **346**, 759–763 (2014). doi: 10.1126/science.1254426; pmid: 25298114
37. M. Melchers *et al*., Targeting HIV-1 envelope glycoprotein trimers to B cells by using APRIL improves antibody responses. *J. Virol.* **86**, 2488–2500 (2012). doi: 10.1128/JVI.06259-11; pmid: 22205734
38. R. Ringe, S. Phogat, J. Bhattacharya, Subtle alteration of residues including N-linked glycans in V2 loop modulate HIV-1 neutralization by PG9 and PG16 monoclonal antibodies. *Virology* **426**, 34–41 (2012). doi: 10.1016/j.virol.2012.01.011; pmid: 22314018
39. R. Derking *et al*., Comprehensive antigenic map of a cleaved soluble HIV-1 envelope trimer. *PLOS Pathog.* **11**, e1004767 (2015). doi: 10.1371/journal.ppat.1004767; pmid: 25807248
40. L. Kong *et al*., Supersite of immune vulnerability on the glycosylated face of HIV-1 envelope glycoprotein gp120. *Nat. Struct. Mol. Biol.* **20**, 796–803 (2013). doi: 10.1038/nsmb.2594; pmid: 23708606
41. J. Jardine *et al*., Rational HIV immunogen design to target specific germline B cell receptors. *Science* **340**, 711–716 (2013). doi: 10.1126/science.1234150; pmid: 23539181
42. A. T. McGuire *et al*., Antigen modification regulates competition of broad and narrow neutralizing HIV antibodies. *Science* **346**, 1380–1383 (2014). doi: 10.1126/science.1259206; pmid: 25504724
43. See supplementary materials on *Science* Online.
44. H. Uchtenhagen *et al*., Boosting of HIV-1 neutralizing antibody responses by a distally related retroviral envelope protein. *J. Immunol.* **192**, 5802–5812 (2014). doi: 10.4049/jimmunol.1301898; pmid: 24829409
45. E. Maraskovsky *et al*., Development of prophylactic and therapeutic vaccines using the ISCOMATRIX adjuvant. *Immunol. Cell Biol.* **87**, 371–376 (2009). doi: 10.1038/icb.2009.21; pmid: 19381160
46. P. Hraber *et al*., Prevalence of broadly neutralizing antibody responses during chronic HIV-1 infection. *AIDS* **28**, 163–169 (2014). doi: 10.1097/QAD.0000000000000106; pmid: 24361678
47. C. Blattner *et al*., Structural delineation of a quaternary, cleavage-dependent epitope at the gp41-gp120 interface on intact HIV-1 Env trimers. *Immunity* **40**, 669–680 (2014). doi: 10.1016/j.immuni.2014.04.008; pmid: 24768348
48. J. P. Moore, Q. J. Sattentau, R. Wyatt, J. Sodroski, Probing the structure of the human immunodeficiency virus surface glycoprotein gp120 with a panel of monoclonal antibodies. *J. Virol.* **68**, 469–484 (1994).pmid: 7504741
49. D. C. Montefiori, Measuring HIV neutralization in a luciferase reporter gene assay. *Methods Mol. Biol.* **485**, 395–405 (2009).pmid: 19020839
50. T. J. Ketas, S. Holuigue, K. Matthews, J. P. Moore, P. J. Klasse, Env-glycoprotein heterogeneity as a source of apparent synergy and enhanced cooperativity in inhibition of HIV-1 infection by neutralizing antibodies and entry inhibitors. *Virology* **422**, 22–36 (2012). doi: 10.1016/j.virol.2011.09.019; pmid: 22018634
51. D. Sok *et al*., Recombinant HIV envelope trimer selects for quaternary-dependent antibodies targeting the trimer apex. *Proc. Natl. Acad. Sci. U.S.A.* **111**, 17624–17629 (2014). doi: 10.1073/pnas.1415789111; pmid: 25422458
52. M. S. Seaman *et al*., Tiered categorization of a diverse panel of HIV-1 Env pseudoviruses for assessment of neutralizing antibodies. *J. Virol.* **84**, 1439–1452 (2010). doi: 10.1128/JVI.02108-09; pmid: 19939925
53. M. Li *et al*., Genetic and neutralization properties of subtype C human immunodeficiency virus type 1 molecular env clones from acute and early heterosexually acquired infections in Southern Africa. *J. Virol.* **80**, 11776–11790 (2006). doi: 10.1128/JVI.01730-06; pmid: 16971434
54. A. deCamp *et al*., Global panel of HIV-1 Env reference strains for standardized assessments of vaccine-elicited neutralizing antibodies. *J. Virol.* **88**, 2489–2507 (2014). doi: 10.1128/JVI.02853-13; pmid: 24352443
55. M. D. Simek *et al*., Human immunodeficiency virus type 1 elite neutralizers: Individuals with broad and potent neutralizing activity identified by using a high-throughput neutralization assay together with an analytical selection algorithm. *J. Virol.* **83**, 7337–7348 (2009). doi: 10.1128/JVI.00110-09; pmid: 19439467
56. R. M. Lynch *et al*., The development of CD4 binding site antibodies during HIV-1 infection. *J. Virol.* **86**, 7588–7595 (2012). doi: 10.1128/JVI.00734-12; pmid: 22573869
57. J. S. McLellan *et al*., Structure of HIV-1 gp120 V1/V2 domain with broadly neutralizing antibody PG9. *Nature* **480**, 336–343 (2011). doi: 10.1038/nature10696; pmid: 22113616
58. J. P. M. Langedijk, M. J. Zekveld, M. Ruiter, D. Corti, J. W. Back, Helical peptide arrays for lead identification and interaction site mapping. *Anal. Biochem.* **417**, 149–155 (2011). doi: 10.1016/j.ab.2011.06.002; pmid: 21708118
59. N. R. Voss, C. K. Yoshioka, M. Radermacher, C. S. Potter, B. Carragher, DoG Picker and TiltPicker: Software tools to facilitate particle selection in single particle electron microscopy. *J. Struct. Biol.* **166**, 205–213 (2009). doi: 10.1016/j.jsb.2009.01.004; pmid: 19374019
60. T. Ogura, K. Iwasaki, C. Sato, Topology representing network enables highly accurate classification of protein images taken by cryo electron-microscope without masking. *J. Struct. Biol.* **143**, 185–200 (2003). doi: 10.1016/j.jsb.2003.08.005; pmid: 14572474
61. G. C. Lander *et al*., Appion: An integrated, database-driven pipeline to facilitate EM image processing. *J. Struct. Biol.* **166**, 95–102 (2009). doi: 10.1016/j.jsb.2009.01.002 pmid: 19263523

ACKNOWLEDGMENTS

Supported by NIH grants P01 AI082362, R37 AI036082, R01 AI084817, R01 AI076105, NIAID-NIH Contract HHSN272011000016C, by Scripps CHAVI-ID (UM1 AI100663), by NIH grant P51OD011106, and by Aids Fonds Netherlands grants 2011032 and 2012041. J.-P.J. is a recipient of a Canadian Institutes of Health Research (CIHR) Fellowship. R.W.S. is a recipient of a Vidi grant from the Netherlands Organization for Scientific Research (NWO) and a Starting Investigator Grant from the European Research Council (ERC-StG-2011–280829-SHEV). This work was partially funded by IAVI with the generous support of USAID and the Bill & Melinda Gates Foundation; a full list of IAVI donors is available at www.iavi.org. The contents of this manuscript are the responsibility of the authors and do not necessarily reflect the views of USAID or the U.S. Government. We thank K. Sliepen, J. Korzun, M. Golabek, K. de los Reyes, L. Kong, K. Weisgrau, N. Pomplun, J. Hsueh, K. L. Saye-Francisco, A. Ramos for technical support; S. Schmidt, J. Gorman and N. Doria-Rose for advice; and G. Stewart-Jones, D. Kubitz, P. Kwong, J. Mascola, B. Haynes, A. McKnight, H. Katinger, S. Zolla-Pazner, P. Poignard, and M. Nussenzweig for reagents. The International AIDS Vaccine Initiative has previously filed a patent relating to the BG505 SOSIP.664 trimer: U.S. Provisional Application no. 61/772,739, titled "HIV-1 envelope glycoprotein," with inventors M. Caulfield, A.C., H. D., S. Hoffenberg, C. R. King, P.J.K., A. Marozsan, J.P.M., R.S., A.B.W., I.A.W., and J.-P.J. This does not alter our adherence to all *Science* policies on sharing data and materials.

SUPPLEMENTARY MATERIALS

www.sciencemag.org/content/349/6244/aac4223/suppl/DC1
Figs. S1 to S10
Tables S1 to S4
References (*62*, *63*)

24 April 2015; accepted 5 June 2015
Published online 18 June 2015;
10.1126/science.aac4223

RESEARCH ARTICLE SUMMARY

HIV-1 VACCINES

HIV-1 neutralizing antibodies induced by native-like envelope trimers

Rogier W. Sanders,* Marit J. van Gils, Ronald Derking, Devin Sok, Thomas J. Ketas, Judith A. Burger, Gabriel Ozorowski, Albert Cupo, Cassandra Simonich, Leslie Goo, Heather Arendt, Helen J. Kim, Jeong Hyun Lee, Pavel Pugach, Melissa Williams, Gargi Debnath, Brian Moldt, Mariëlle J. van Breemen, Gözde Isik, Max Medina-Ramírez, Jaap Willem Back, Wayne C. Koff, Jean-Philippe Julien, Eva G. Rakasz, Michael S. Seaman, Miklos Guttman, Kelly K. Lee, Per Johan Klasse, Celia LaBranche, William R. Schief, Ian A. Wilson, Julie Overbaugh, Dennis R. Burton, Andrew B. Ward, David C. Montefiori, Hansi Dean, John P. Moore*

INTRODUCTION: A major goal of HIV-1 vaccine development is to identify immunogens capable of inducing protective titers of broadly neutralizing antibodies (bNAbs) against circulating, neutralization-resistant (tier 2) viruses. The envelope glycoprotein (Env) trimer on the virus surface is the only bNAb target and accordingly serves as the basis for recombinant protein immunogens intended to induce bNAbs. We have engineered soluble, recombinant trimers based on the BG505 clade A and B41 clade B tier 2 viruses. These proteolytically cleaved and stabilized trimers, designated BG505 and B41 SOSIP.664 gp140, display multiple bNAb epitopes and have antigenic properties that mimic viral Env. High-resolution structures of the BG505 trimers reinforce this perspective. In contrast, other trimer designs (uncleaved gp140) that lack the SOSIP modifications and are based on eliminating the intersubunit proteolytic cleavage site adopt non-native configurations.

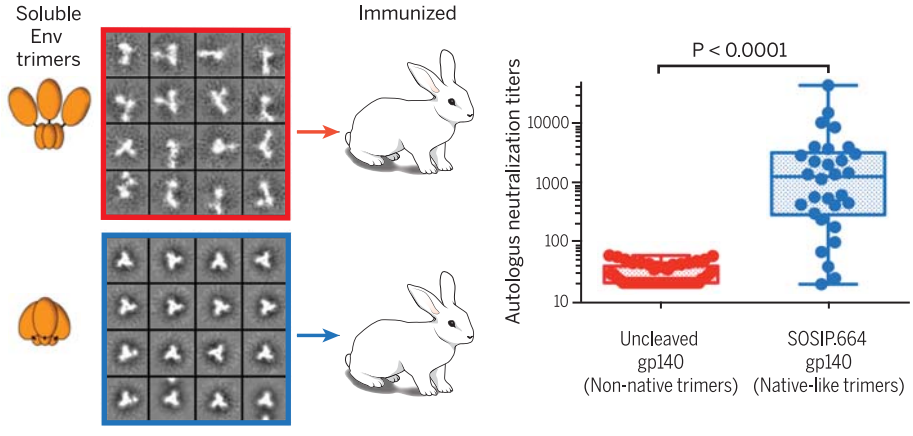
RATIONALE: To determine the NAb response elicited by native-like trimers, we immunized rabbits and macaques with BG505 SOSIP.664 gp140 proteins, and rabbits with their B41 counterparts. For comparison with the BG505 trimers, we also tested gp120 monomers and uncleaved gp140 proteins of the same genotype. We characterized the resulting antibody responses by quantifying their ability to neutralize the autologous tier 2 viruses and multiple heterologous tier 1 (neutralization-sensitive) and tier 2 viruses. We mapped the BG505 NAb responses using various techniques, including a large panel of Env-pseudotyped virus mutants.

RESULTS: BG505 SOSIP.664 trimers consistently induced potent NAbs against the autologous tier 2 virus in rabbits and similar but weaker responses in macaques. Cross-reactive NAbs against the more sensitive tier 1 viruses were also induced in all the immunized animals, but heterologous neutralization of tier 2 viruses was seen only weakly and sporadically. The rabbit responses to B41 SOSIP.664 trimers were qualitatively similar to those seen in the BG505 trimer recipients. The autologous tier 2 NAb titers to both SOSIP.664 trimers were greater than any such responses previously observed using various uncleaved gp140 proteins, including the BG505 version used in this study. The rabbit tier 2 and tier 1 NAb responses to the BG505 SOSIP.664 trimers were uncorrelated. Mapping studies showed the tier 2 NAbs recognized conformational epitopes that differed between animals. In some cases, these NAbs targeted components of the glycan shield previously associated with bNAb epitopes. In contrast, the tier 1 NAbs targeted linear epitopes in the gp120 V3 region.

ON OUR WEB SITE

Read the full article at http://dx.doi.org/10.1126/science.aac4223

CONCLUSIONS: Although an autologous tier 2 NAb response is not sufficient for vaccine protection against HIV-1, it may be a necessary step in various strategies intended to induce bNAbs. Thus, our findings indicate that native-like trimers represent a promising starting point for the further development of recombinant Env immunogens intended to broaden the NAb response. The high-resolution structures of SOSIP.664 trimers allow improvements to be rationally designed. Relevant strategies include the further stabilization of trimer-associated bNAb epitopes while reducing the antigenicity of V3 and other non-neutralizing epitopes that may be distractive; immunizing with longitudinal series of SOSIP.664 trimers from infected individuals who generate bNAbs; using trimer cocktails (e.g., from clades A, B, and C); and priming with trimer variants that trigger desirable germline responses before boosting with wild-type trimers. ■



Autologous tier 2 NAb responses in animals immunized with native-like (SOSIP.664) trimers or non-native uncleaved gp140s. (**Left**) Representative reference-free 2D class averages of negative-stain electron microscopy (EM) images of the uncleaved BG505 gp140 and the native-like BG505 SOSIP.664 trimers. The illustrations (orange) of the two categories of Env protein are based on negative-stain EM. (**Right**) Autologous tier 2 serum NAb titers (IC50) in 50 animals immunized with various uncleaved gp140 proteins, compared to titers in the 30 rabbits given the BG505 or B41 SOSIP.664 trimers described here (see legend of Fig. 2 in the full article for details; $P < 0.0001$, two-tailed Mann-Whitney test).

The list of author affiliations is available in the full article online.
*Corresponding author. E-mail: jpm2003@med.cornell.edu (J.P.M.); rws2002@med.cornell.edu (R.W.S.)
Cite this article as R. W. Sanders *et al.*, *Science* **349**, aac4223 (2015). DOI: 10.1126/science.aac4223

Downloaded from www.sciencemag.org on July 10, 2015

RESEARCH ARTICLE

HIV-1 VACCINES

HIV-1 neutralizing antibodies induced by native-like envelope trimers

Rogier W. Sanders,[1,2]* Marit J. van Gils,[2] Ronald Derking,[2] Devin Sok,[3,4,5] Thomas J. Ketas,[1] Judith A. Burger,[2] Gabriel Ozorowski,[4,5,6] Albert Cupo,[1] Cassandra Simonich,[7] Leslie Goo,[7] Heather Arendt,[8] Helen J. Kim,[4,5,6] Jeong Hyun Lee,[4,5,6] Pavel Pugach,[1] Melissa Williams,[1] Gargi Debnath,[1] Brian Moldt,[3,4,5] Mariëlle J. van Breemen,[2] Gözde Isik,[2] Max Medina-Ramírez,[2] Jaap Willem Back,[9] Wayne C. Koff,[8] Jean-Philippe Julien,[4,5,6] Eva G. Rakasz,[10] Michael S. Seaman,[11,12] Miklos Guttman,[13] Kelly K. Lee,[13] Per Johan Klasse,[1] Celia LaBranche,[14] William R. Schief,[3,4,5,8,12] Ian A. Wilson,[4,5,6,15] Julie Overbaugh,[7] Dennis R. Burton,[3,4,5,12] Andrew B. Ward,[4,5,6] David C. Montefiori,[14] Hansi Dean,[8] John P. Moore[1]*

A challenge for HIV-1 immunogen design is the difficulty of inducing neutralizing antibodies (NAbs) against neutralization-resistant (tier 2) viruses that dominate human transmissions. We show that a soluble recombinant HIV-1 envelope glycoprotein trimer that adopts a native conformation, BG505 SOSIP.664, induced NAbs potently against the sequence-matched tier 2 virus in rabbits and similar but weaker responses in macaques. The trimer also consistently induced cross-reactive NAbs against more sensitive (tier 1) viruses. Tier 2 NAbs recognized conformational epitopes that differed between animals and in some cases overlapped with those recognized by broadly neutralizing antibodies (bNAbs), whereas tier 1 responses targeted linear V3 epitopes. A second trimer, B41 SOSIP.664, also induced a strong autologous tier 2 NAb response in rabbits. Thus, native-like trimers represent a promising starting point for the development of HIV-1 vaccines aimed at inducing bNAbs.

A major goal of HIV-1 vaccine development is to identify immunogens capable of inducing protective titers of broadly neutralizing antibodies (bNAbs) against circulating viruses with a tier 2 or higher resistance profile (*1*). Viruses with these characteristics are the most commonly transmitted strains of HIV-1, and hence they dominate new infections. The humoral immune response of infected individuals creates antibody-mediated selection pressure on the virus, which can generally only persist and be transmitted if it is antibody-resistant. A successful vaccine, then, must be able to induce antibodies that can counter the virus's evolved resistance mechanisms. In addition, the global sequence diversity among HIV-1 strains is so great that vaccine-induced antibodies should target relatively conserved sites and thereby possess breadth of action. A vaccine with the required properties must be based on the envelope glycoprotein (Env), as the gp120-gp41 trimer on the virus surface is the only bNAb target. After two or more years of HIV-1 infection, ~20% of individuals develop bNAbs, which can serve as templates for vaccine design by exposing vulnerabilities in the viral defense mechanisms (*1*). Because bNAbs usually evolve from strain-specific autologous NAbs via multiple cycles of viral escape and antibody affinity maturation [reviewed in (*2*, *3*)], it is unlikely that bNAbs can be raised against any single Env protein of fixed antigenic composition. However, the induction of autologous NAbs to a tier 2 virus would be an excellent starting point for iterative vaccine design (*3*–*6*).

One or more of the bNAb epitopes present on native, virion-associated trimers are also found on various Env-based immunogens, including soluble, monomeric gp120s and multimeric gp140s that contain both the receptor-binding gp120 and fusion-enabling gp41-ectodomain ($gp41_{ECTO}$) subunits. These various forms of Env are all derived from the viral gp160 precursor protein, which is proteolytically cleaved into the gp120 and $gp41_{ECTO}$ subunits when it is processed within the cell and forms membrane-associated trimers. For practical purposes, most Env-based immunogens are made as soluble proteins by eliminating the membrane-spanning domain of gp160 and creating entities known as gp140s. In some cases, the $gp41_{ECTO}$ domain is also removed to make a monomeric gp120 protein. The soluble gp140s oligomerize via interactions between their $gp41_{ECTO}$ components. However, the oligomers are very unstable unless the construct is stabilized, either by eliminating the cleavage site between gp120 and $gp41_{ECTO}$ to make a standard uncleaved gp140 protein, or by introducing specific trimer-stabilizing changes into the properly cleaved form of gp140. We have favored the latter strategy by making stabilized, cleaved trimers that are designated SOSIP.664 gp140s; the SOS term denotes an intermolecular disulfide bond engineered to link the gp120 and $gp41_{ECTO}$ subunits, while IP signifies an Ile^{559} → Pro point substitution that maintains the $gp41_{ECTO}$ components in their pre-fusion form.

Here, we evaluated the immunogenicity of a SOSIP.664 trimer based on the BG505 clade A virus, which was isolated from a 6-week-old infant who later developed a bNAb response within ~2 years of infection (*7*, *8*). We also tested, in less detail, a second SOSIP.664 trimer based on a clade B adult infection founder virus, B41 (*9*). The BG505 and B41 SOSIP.664 trimers display multiple bNAb epitopes but few non-neutralizing Ab (non-NAb) epitopes that may serve as immunological distractions (*9*, *10*). The integrity and native-like appearance of the BG505 SOSIP.664 trimer, including its complex quaternary epitopes, were previously confirmed by high-resolution cryo–electron microscopy (cryo-EM) and x-ray crystallography structures, the first high-resolution depictions of the HIV-1 Env trimer (*11*–*13*). In this study, we conducted animal immunization experiments to determine which NAb specificities can be induced by two different, native-like SOSIP.664 trimer mimics of the native Env spike, and we performed comparisons with gp120 monomers and standard designs of uncleaved gp140 immunogens.

Immunogenicity of BG505 SOSIP.664 trimers in rabbits

The various immunogens tested in this study are depicted schematically in fig. S1A along with their conformations, which are based on negative-stain EM images that are strongly supported by antigenicity and by biophysical and glycan composition data (figs. S2 and S3) (*10*–*20*). Five different experiments were performed, four in rabbits and one in macaques (fig. S1B). In general, the immunization scheme was based on two closely separated initial doses (weeks 0 and 4),

[1]Department of Microbiology and Immunology, Weill Medical College of Cornell University, New York, NY 10065, USA. [2]Department of Medical Microbiology, Academic Medical Center, University of Amsterdam, 1105 AZ Amsterdam, Netherlands. [3]Department of Immunology and Microbial Science, Scripps Research Institute, La Jolla, CA 92037, USA. [4]International AIDS Vaccine Initiative, Neutralizing Antibody Center, and Collaboration for AIDS Vaccine Discovery, Scripps Research Institute, La Jolla, CA 92037, USA. [5]Center for HIV/AIDS Vaccine Immunology and Immunogen Discovery, Scripps Research Institute, La Jolla, CA 92037, USA. [6]Department of Integrative Structural and Computational Biology, Scripps Research Institute, La Jolla, CA 92037, USA. [7]Division of Human Biology, Fred Hutchinson Cancer Research Center, Seattle, WA 98109, USA. [8]International AIDS Vaccine Initiative, New York, NY 10004, USA. [9]Pepscan Therapeutics, 8243RC Lelystad, Netherlands. [10]Wisconsin National Primate Research Center, University of Wisconsin, Madison, WI 53715, USA. [11]Center for Virology and Vaccine Research, Beth Israel Deaconess Medical Center, Harvard Medical School, Boston, MA 02215, USA. [12]Ragon Institute of Massachusetts General Hospital, MIT, and Harvard, Boston, MA 02114, USA. [13]Department of Medicinal Chemistry, University of Washington, Seattle, WA 98195, USA. [14]Department of Surgery, Duke University Medical Center, Durham, NC 27710, USA. [15]Skaggs Institute for Chemical Biology, Scripps Research Institute, La Jolla, CA 92037, USA.
*Corresponding author. E-mail: jpm2003@med.cornell.edu (J.P.M.); rws2002@med.cornell.edu (R.W.S.)

followed by a third dose after a prolonged rest period of usually 16 weeks (*21*).

The first study, in rabbits, compared the immunogenicity of clade A BG505 SOSIP.664 trimers and gp120 monomers, both of which were produced in 293S GnT$^{-/-}$ cells (*10*, *12*, *20*) (fig. S1A). To assess whether trimer glycosylation affected immunogenicity, in rabbit experiment 2 we immunized three groups of rabbits with BG505 SOSIP.664 trimers produced in 293T cells (natural glycosylation), 293S GnT$^{-/-}$ cells [oligomannose-only glycans (*12*, *22*)], or 293S GnT$^{-/-}$ cells followed by EndoH treatment [glycan-depleted (*12*, *23*)]. In rabbit experiment 1, in addition to the BG505 gp120 monomer comparator proteins, we also tested a clade B YU2 uncleaved gp140 protein containing a Foldon trimerization domain that was produced in 293T cells (YU2 gp140-Fd) (*16*). In rabbit experiment 3, we compared BG505 SOSIP.664 trimers with the uncleaved, non-native BG505 sequence-matched WT.SEKS gp140 protein (*14*, *17*). The goal of the comparisons with the YU2 gp140-Fd and BG505 WT.SEKS proteins was to explore whether a native-like trimer conformation is beneficial for immunogenicity. Proteolytic cleavage of gp120 from gp41$_{ECTO}$ is critical for soluble gp140 trimers to maintain native-like structures; standard uncleaved gp140 proteins based on multiple different sequences, including YU2 gp140-Fd and BG505 WT.SEKS, are known to predominantly adopt aberrant, non-native conformations that can be clearly distinguished from the native-like, cleaved SOSIP.664 trimers (*14*–*17*) (fig. S1A). Thus, when viewed by EM, the standard uncleaved gp140s have an irregular and non-native configuration; frequently seen images represent splayed-out, semidissociated gp120 subunits linked by the uncleaved intersubunit strand to a central core comprising the gp41$_{ECTO}$ components (*14*–*17*). In contrast, the BG505 and also B41 SOSIP.664 trimers are consistently regular, trilobed, propeller-shaped structures (*9*, *10*, *14*). Finally, in rabbit experiment 4, we assessed the ability of SOSIP.664 trimers based on the clade B41 genotype and produced in CHO cells (*9*) to induce NAb responses against the autologous tier 2 B41 virus.

The anti-gp120, anti-gp41, and anti-trimer binding antibody titers induced over time by the various Env proteins are summarized in fig. S4. To quantify the NAb responses 2 weeks after the third immunization (i.e., at week 22 or, for some rabbits, week 26), we used the TZM-bl cell assay, which is based on transactivation of a luciferase reporter gene by an infecting virus (Fig. 1 and table S1). We were particularly interested in assessing the NAb response to the autologous (i.e., sequence-matched) BG505.T332N virus, as it has a neutralization-resistant tier 2 phenotype. Although almost all Env protein immunogens (e.g., gp120 monomers, uncleaved gp140s) can raise

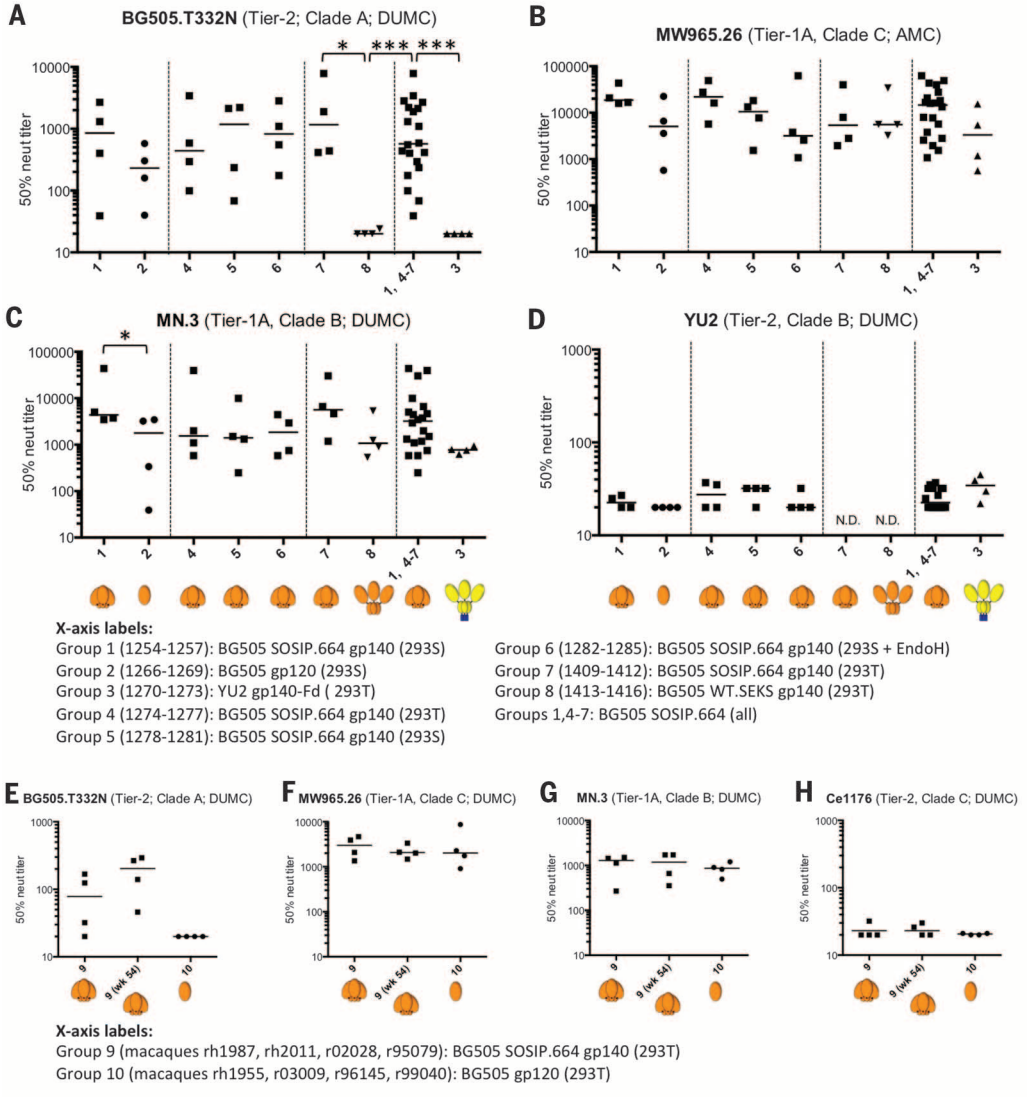


Fig. 1. Induction of autologous tier 2 and heterologous tier 1 NAb responses in rabbits and macaques. (**A** to **D**) Each panel shows the 50% neutralization titers (IC$_{50}$; TZM-bl cell assay) for sera from every immunized rabbit, arranged in the groups outlined in fig. S1. For convenience, all 20 BG505 SOSIP.664 recipient rabbits (groups 1 and 4 to 7) were combined into one group. The dotted lines separate groups that were included in the same immunization experiment. Each panel lists the test virus, its tier classification, and the location of the testing laboratory (*43*) (see Materials and Methods for performance site abbreviations). For additional neutralization data on rabbit sera, see tables S1 and S2. (**E** to **H**) Each panel shows the 50% neutralization titers for individual macaque sera (TZM-bl assay; DUMC) against the specified virus for sera from all eight animals (organized by group) at week 26, and also from the four trimer-immunized animals (group 9) at week 54. The group 10 animals received no further gp120 immunizations after week 24. For additional neutralization data on macaque sera, see table S4. Note that the scales used for the 50% neutralization titers sometimes vary between panels. Negative-stain EM images of the gp140 immunogens are shown in fig. S2 and are the basis for the cartoon depictions shown in brown (BG505 Env) or yellow/blue (YU-2 gp140-Fd). The ISCOMATRIX adjuvant had no detectable adverse effects on the antigenicity of the trimers, assessed by ELISA, or on their appearance in negative-stain EM images (fig. S3). *P < 0.05, ***P < 0.0005 by two-tailed Mann-Whitney test.

NAbs against various neutralization-sensitive tier 1 viruses, the induction of NAbs that are able to counter a tier 2 virus—even an autologous one—has been challenging. Could a native-like trimer do better?

We found that all 20 sera from the BG505 SOSIP.664 trimer-immunized rabbits neutralized the autologous (i.e., sequence-matched) tier 2 virus BG505.T332N (*10*), with titers that ranged from 39 to 7840 (median 570; Fig. 1A). There was no discernible difference in the magnitude of the autologous NAb responses to the three different trimer glycosylation variants (Fig. 1A, groups 4 to 6). Sera from the BG505 gp120 monomer recipients also neutralized the autologous virus, although with a lower median titer of 270 (Fig. 1A, group 2). BG505 gp120 is unusual, as it was selected to bind PG9 and is known to be atypically immunogenic (*24*). It may also be relevant that BG505 gp120 was purified via a bNAb column (in this case 2G12), which may select for more native-like forms of gp120 relative to other methods. The uncleaved BG505 WT.SEKS gp140 induced no NAbs against the autologous BG505.T332N virus (median titer <20) (Fig. 1A, group 8), whereas the uncleaved YU2 gp140-Fd induced NAbs against the autologous, clade-B YU2 virus only weakly (median titer 36) (Fig. 1D, group 3). The difference between the autologous tier 2 NAb responses to the native-like BG505 SOSIP.664 trimer and the non-native WT.SEKS gp140 was significant [$P = 0.029$ for the intra-experiment ($n = 4$ versus $n = 4$) comparison; $P = 0.0002$ when all 20 BG505 SOSIP.664 trimer recipients were included; two-tailed Mann-Whitney test] (Fig. 1A). The poor responses to the WT.SEKS and YU2 proteins are consistent with multiple reports that various uncleaved gp140s are not able to induce NAbs that can neutralize autologous tier 2 viruses consistently in the TZM-bl cell assay (*25*–*29*). The lack of an autologous NAb response to the BG505 WT.SEKS proteins implies that the BG505.T332N virus is not an atypically sensitive tier 2 virus that is vulnerable to any BG505 Env-binding antibodies. The inferiority of WT.SEKS gp140 to gp120 monomers may be because of formation of aberrant intra- and intersubunit disulfide bonds in uncleaved gp140s that create non-native gp120 moieties (*30*, *31*).

We conducted an additional rabbit immunogenicity experiment involving a second native-like trimer, B41 SOSIP.664, based on a clade B tier 2 transmitted/founder virus (fig. S1) (*9*). Eight of 10 animals given these trimers responded by generating an autologous NAb response, with a median titer of 2535 (Fig. 2A). Heterologous tier 1, but not tier 2, NAb responses were induced in all 10 rabbits. Hence the rabbit response to the B41 trimers is qualitatively similar to what was induced by their BG505 counterparts. The median autologous titers against these two versions of fully native-like SOSIP.664 trimers (BG505, 570; B41, 2535; combined group, 1199) exceeded those reported to confer 50% and 80% protection (105 and 329, respectively) in macaque passive-transfer experiments (*32*) (Fig. 2A). Rabbit immunization experiments were conducted several years ago using earlier generations of SOSIP.681 trimers based on the JR-FL and KNH1144 genotypes (*33*, *34*). Autologous tier 2 NAbs were only inconsistently induced in those experiments. However, those trimers, although cleaved, were either not fully native-like (JR-FL) or prone to aggregate formation (KNH1144), which may account for their poor immunogenicity.

To gain an additional perspective on the magnitude of the autologous NAb titers to the BG505 and B41 SOSIP.664 trimers, we compared them with previously reported animal immunization data derived using four uncleaved gp140 proteins based on *env* sequences from the tier 2 viruses 92UG037.8, Q461e2, Q168a2, and CZA97.012 (*25*, *26*) (Fig. 2A). We also included the autologous NAb titers for the YU2 gp140-Fd and BG505 WT.SEKS immunogens shown in Fig. 1A. The four additional uncleaved gp140s were of standard designs that are known or expected to resemble the negative-stain EM images of the uncleaved YU2 gp140-Fd and BG505 WT.SEKS gp140s shown in fig. S2 (*14*, *16*, *19*). The autologous NAb titers induced by the BG505 and B41 SOSIP.664 trimers were greater than the corresponding responses to any other Env protein. When the combined SOSIP.664 trimer groups (median titer 1199, range 20 to 38,598; $n = 30$ rabbits) were compared with the combined

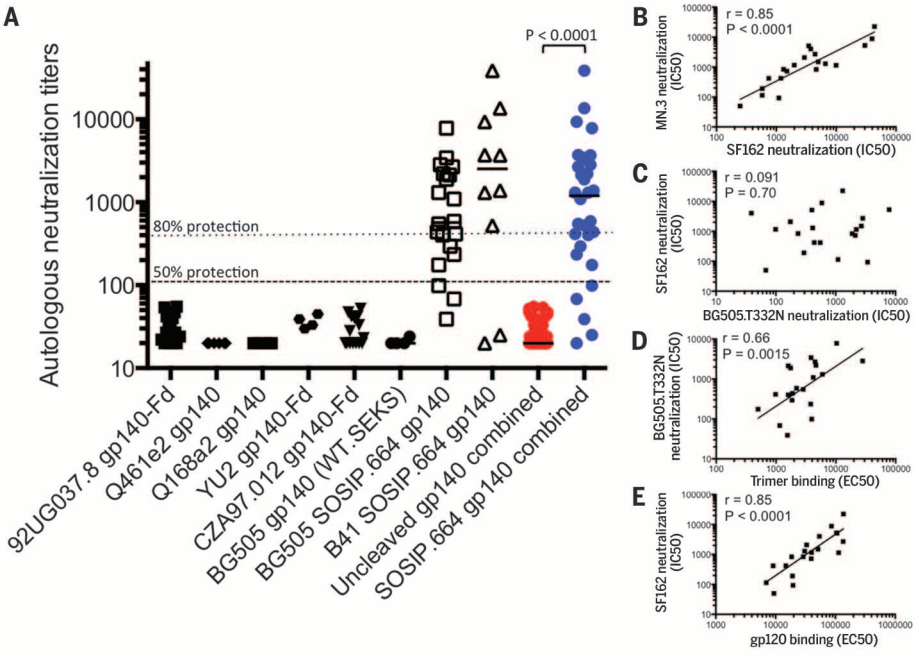


Fig. 2. Comparative depiction of the autologous tier 2 NAb responses elicited in rabbits or guinea pigs by various Env proteins. (**A**) Each data point represents the IC_{50} neutralization titer for serum derived from an individual animal immunized with the stated gp140 protein (some of which incorporated an Fd trimerization domain) when tested in the TZM-bl cell assay against the sequence-matched (i.e., autologous) tier 2 virus. The plotted values are taken from the following papers: 92UG037.8 gp140-Fd [(*25*); $n = 15$], Q461e2 gp140 [(*26*); $n = 6$], Q168a2 gp140 [(*26*); $n = 6$], YU2 gp140-Fd (this paper; $n = 4$; table S1), CZA97.012 gp140-Fd [(*25*); $n = 15$], BG505 gp140 (WT.SEKS; this paper; $n = 4$; table S1), BG505 SOSIP.664 (this paper; $n = 20$; table S1), and B41 SOSIP.664 (this paper; $n = 10$). To minimize the impact of cross-study variables, we restricted the comparison to immunization of small animals (rabbits and guinea pigs), to Env proteins based on tier 2 viruses, and to data generated using the TZM-bl assay under broadly similar conditions. In the rightmost two columns, all the data points for each of the uncleaved gp140s (red symbols) are plotted to allow a statistical comparison with the combined BG505 and B41 SOSIP.664 trimer groups (blue symbols). The difference in the median values is highly significant ($P < 0.0001$ by two-tailed Mann-Whitney test). The dotted and dashed lines denote titers of 105 and 329 that are reported to confer 50% and 80% protection, respectively, to macaques in passive transfer experiments (*32*). (**B** to **E**) Various binding antibody and NAb responses at week 22 (week 26 for experiment 3) from all 20 BG505 trimer-immunized rabbits from experiments 1 to 3 were cross-compared as follows: (B) SF162 NAbs versus MN.3 NAbs; (C) BG505.T332N NAbs versus SF162 NAbs; (D) trimer-binding Abs versus BG505.T332N NAbs; (E) gp120-binding Abs versus SF162 NAbs. The NAb data are the reciprocal of the serum dilution giving 50% inhibition (IC_{50}), the binding Ab data are the reciprocal of the serum dilution giving 50% of the maximum signal in ELISA (EC_{50}). The Spearman *r* and *P* values for the respective correlations are given. Additional correlation analyses as well as details on the statistics are presented in fig. S5.

uncleaved gp140 groups (median titer <20, range <20 to 55; n = 50 animals), the difference was highly significant (P < 0.0001, two-tailed Mann-Whitney test). The magnitude of the difference between the response to the SOSIP.664 trimers and the response to the other Env proteins is so great that immunization protocol variations (such as dosing, schedule, the use of priming vectors, and the identity of the adjuvant) are unlikely to be responsible. Thus, such variables typically influence tier 1 NAb titers by a few multiples but do not make the immunogens capable of inducing autologous tier 2 NAbs.

Sera from BG505 SOSIP.664 trimer-immunized rabbits were usually ineffective against heterologous, neutralization-resistant tier 2 viruses, although we did see some sporadic neutralization at low IC_{50} titers of 30 to 100 (Fig. 1D and tables S1 and S2). The rabbit sera did, however, consistently neutralize more sensitive heterologous tier 1 viruses from different clades, including the ultrasensitive tier 1A viruses MW965.26 (clade C; Fig. 1B), SF162 and MN (both clade B; Fig. 1C and table S1), and the tier 1B viruses BZ167, BaL, 6535.3 (all clade B; table S1), and 93IN905 (clade C; table S1). The TZM-bl assay titers in the 1000s and 100s for the tier 1A and 1B viruses, respectively, are comparable to or greater than titers reported from multiple animal studies of various monomeric gp120 or uncleaved gp140 proteins, as are the negligible titers against heterologous tier 2 viruses (*16*, *25*–*29*, *35*). Overall, the tier 1 NAb responses to the BG505 SOSIP.664, gp120 and WT.SEKS gp140 immunogens were generally similar (Fig. 1, B and C, and table S1). Hence, what distinguishes the native-like SOSIP.664 trimers from the other two Env immunogen designs is not their ability to induce an antibody response per se, but rather the elicitation of a consistent and strong NAb response against the autologous tier 2 virus.

Tier 1 and tier 2 NAb titers do not correlate

To gain an understanding of why the native-like trimers differed from the other Env proteins, we analyzed various aspects of the antibody responses. First, we compared the emergence of heterologous tier 1 (MN, SF162; clade B) and autologous tier 2 (BG505.T332N) NAbs with anti-gp120 and anti-trimer binding antibodies [i.e., enzyme-linked immunosorbent assay (ELISA) titers] in the BG505 SOSIP.664 trimer-immunized rabbits over time (fig. S5, A and B). The trimer-binding responses were initially lower than those to gp120 but became comparable after four immunizations. Autologous tier 2 NAbs were detected only rarely and weakly after two immunizations, but strongly and consistently after three immunizations (fig. S5B). The NAb titers then declined, with kinetics comparable to the binding antibody responses, but were boosted again after the fourth immunization. The tier 1 and autologous tier 2 NAb responses waxed and waned with broadly similar kinetics (fig. S5B).

The NAb titers to the three tier 1 viruses (MN.3, SF162, and MW965.26) induced in the 20 rabbits 2 weeks after the third immunization with BG505 SOSIP.664 trimers strongly correlated with one another (Fig. 2B and fig. S5, C and D). In contrast, the autologous tier 2 titers did not correlate significantly with the heterologous tier 1 titers induced in the same rabbits at the same time (Fig. 2C and fig. S5, E and F). The correlation plots suggest that different NAb specificities mediate the tier 1 and autologous tier 2 responses, as we confirmed experimentally (see below). One implication is that inducing a tier 2 response will not be achieved simply by increasing the titer of tier 1 NAbs, as entirely different antibody specificities and B cell subsets are probably involved.

We also sought associations between NAb and binding antibody titers in the same set of 20 rabbits. The autologous tier 2 NAb titers were correlated with the anti-trimer titers (Fig. 2D; r = 0.66, P = 0.0015), but not with the anti-gp120 titers (fig. S5K). Conversely, the tier 1 NAbs were strongly correlated with the anti-gp120 titers but not at all or only very weakly with the anti-trimer titers (Fig. 2E and fig. S5, H to J, L, and M). The anti-gp120 and anti-trimer titers were not significantly correlated (fig. S5G). The data trends suggest that tier 1 NAb responses are associated with strong binding antibody responses to gp120 monomers. The significant correlation between the BG505.T332N NAb titer and the anti-trimer titer, but not the anti-gp120 titer, again implies that the quaternary structure of a native-like trimer is beneficial for inducing tier 2 NAbs. The non-native WT.SEKS gp140 induced anti-gp120 antibodies efficiently but induced anti-trimer antibodies very poorly (fig. S4, A to C).

Autologous tier 2 and heterologous tier 1 Nabs target different epitopes

We used multiple techniques to gain insights into the various epitopes targeted by the tier 1 and tier 2 NAbs in sera from the BG505 SOSIP.664 trimer-immunized rabbits. First, we performed neutralization assays in the presence of several antigens that could potentially bind and thereby deplete various NAb specificities. These competitors included linear peptides derived from the first, second, and third (V1, V2, and V3) variable loops of Env, a V3-Fc construct, a V1V2 scaffold, a gp41 protein, CD4 binding–defective gp120-D368R monomers and SOSIP.664-D368R trimers, and the resurfaced stabilized core 3 (RSC3) CD4 binding site (CD4bs)–mimetic protein (Table 1). The gp120-D368R monomers and SOSIP.664-D368R trimers absorbed the autologous NAbs comparably and completely, implying that the target epitope(s) are well presented on the isolated gp120 subunit (Table 1 and fig. S6). As residue D368 is a key element of the CD4bs, the inhibitory effect of the two Env-D368R mutants, combined with the lack of effect of the RSC3 protein, implies that the autologous NAbs are unlikely to target the CD4bs directly (Table 1). Truncated gp120-D368R variants lacking the V1, V2, V3, or V1V2 domains were effective competitors for the autologous NAbs, but the variable loop–based peptides or protein constructs and the gp41 proteins were generally inactive (Table 1).

Although the V1/V2 and V3 regions were not generally the targets for autologous NAbs, a noteworthy exception was rabbit 1412. Here, the NAb-depleting effect of the gp120-D368R monomer was completely lost when any of the V1, V2, V1V2, or V3 regions was deleted, but the linear V1, V2, and V3 peptides and the V1V2-scaffold protein were ineffective competitors (Table 1). Hence, the relevant epitope seen by serum 1412 is not present on simple mimics of the V1, V2, and V3 regions (i.e., peptides and scaffolds), but its formation requires that all three variable regions are present on a gp120 monomer or the gp120 subunits of the native trimer.

Peptide serology confirmed that some anti-trimer antibodies recognized the V3 region (fig. S7A). Env trimers undergo conformational transitions that expose V3 both on the virus and on its engineered SOSIP.664 counterparts in vitro (*9*, *10*, *36*). Such "breathing" events are likely to render V3 immunogenic in vaccinated animals. The linear BG505 V3 peptide consistently reduced (by a factor of >10) titers against the tier 1 viruses MN.3, SF162, and MW965.26 when tested against eight sera from trimer-immunized rabbits (fig. S7, B to D) (*35*). This peptide also depleted the tier 1 NAbs induced by the WT.SEKS protein (fig. S7, C and D), consistent with reports that such responses to uncleaved gp140s are typically V3-dominated (*35*, *37*). Deleting the V3 region consistently reduced the ability of the gp120-D368R protein to deplete trimer-induced tier 1 Nabs, but not autologous NAbs (Table 1 and fig. S7, B to D). We conclude that V3 peptide-reactive antibodies raised against the clade-A trimer cross-neutralize tier 1 viruses but do not neutralize the autologous tier 2 virus, which is consistent with the lack of correlation between tier 1 and tier 2 NAb titers (Fig. 2B and fig. S5, C and D) and the resistance of BG505.T332N to V3 monoclonal antibodies (mAbs) that neutralize tier 1 viruses (*10*).

To gain further insight into the autologous NAb response, we tested sera from the nine trimer-immunized rabbits with the highest titers against BG505.T332N against 109 mutants of this virus with single alanine point substitutions of gp120 residues. We sought variants with reduced neutralization sensitivities as a result of sequence changes that affected key epitope(s). The neutralization profile across the virus panel was unique for each serum, showing that the autologous response was different, wholly or in part, in each animal (table S3). The data derived from the mutant panel for all nine rabbits were mapped onto the BG505 SOSIP.664 trimer structure (Fig. 3). Multiple alanine substitutions affected BG505.T332N neutralization. In general, the substitutions with the most impact were clustered at the trimer apex and the gp120 outer domain (OD), including the periphery of the CD4bs, an exception being that serum 1257 was sensitive to the loss of the glycan at C1 residue N88 (Fig. 3, side views). Among individual rabbits, 1274 was affected by mutations in V1, V2, C3, and V5; 1410 by C2, C3, V4, and C5 substitutions; and 1412 by V1, V2, and C5 changes. Among the most frequent

Table 1. Depletion of autologous tier 2 NAbs in sera from rabbits and macaques immunized with BG505 SOSIP.664 trimers or gp120 monomers by a variety of competitor ligands. Sera from 13 BG505 SOSIP.664 trimer-immunized and two BG505 gp120-immunized rabbits, taken 2 weeks after the third immunization (i.e., at week 22 or week 26), as well as sera from two BG505 SOSIP.664 trimer-immunized macaques, taken 2 weeks after the fifth immunization (i.e., week 40), were tested for their ability to neutralize the BG505.T332N virus in the presence of a variety of competitor proteins and peptides, added in excess. The TZM-bl cell assay was conducted at AMC. The data show the relative reduction in neutralization (IC_{50}) in the presence of the specified test reagents; values preceded by > indicate that neutralization was depleted completely (i.e., titer of <20). Empty cells indicate tests not performed.

BG505.T332N pseudovirus			Depletion reagent														
Immunogen	Animal ID	Week	SOSIP.664-D368R	gp120-D368R	gp120-D368R 7C3	gp120-D368R ΔV1	gp120-D368R ΔV2	gp120-D368R ΔV1V2	gp120-D368R ΔV3	gp41	RSC3	V1 peptide	V2 peptide	V3 peptide	V1V2-scaffold	V3-Fc	C1-V1 peptide
BG505	1254	22	3.4		1.7	>3.9	3.1			1.2	1.1			1.4	1.0		1.2
SOSIP.664	1256	22	17.2	>20.7	1.2	25.0	9.6	>20.7	>20.7	0.9	0.7	1.1	1.2	0.8	1.9	1.2	1.9
gp140	1257	22	10.4	>12.0	>28.5	9.9	5.0	>12.0	>12.0	0.5	0.9	1.1	1.6	1.2	1.0		1.0
	1274	22	45.3	>33.7	1.7	54.6	48.9	>33.7	>33.7	0.9	1.0	1.1	1.6	0.5	0.7	1.1	0.9
	1278	22		>14.6	>15.5			>14.6	>14.6	2.0	1.1						0.6
	1279	22		>19.9	>40.6			>19.9	>19.9	0.7	1.4						1.2
	1283	22		>3.8	1.5			>3.8	>3.8	0.7	0.8						1.1
	1284	22	11.4	>8.4	>43.3	24.3	9.2	>8.4	8.0	2.2	1.1	1.3	1.4	0.8	0.7	0.8	0.6
	1285	22	8.4	>4.6	2.7	9.6	8.0	>4.6	>4.6		0.7	1.3	1.8	0.4	0.6		1.3
	1409	26		>22.9	>24.3			>22.9	>22.9	0.9	0.8						1.0
	1410	26		>4.8	>5.7			>4.8	>4.8	0.7	1.2						0.8
	1411	26	>19.3	>78.9	>20.7	18.4	18.4	>78.9	>78.9	1.6	0.9	1.3	2.7	1.8	1.1		1.0
	1412	26	7.0	>7.5	>9.0	0.9	1.4	1.6	1.5	0.8	1.3	1.2	1.2	1.5	1.7		1.2
BG505	1267	22	4.8	3.2	0.8			4.8	4.6	0.8	0.8	2.8	1.0	1.8	1.5		1.2
gp120	1268	22	>22.8	>22.8	2.2			>22.8	21.7	1.2	1.6	1.4	1.2	1.6	1.2		0.7
BG505	rh1987	40		3.3	0.8			3.2	3.2								
SOSIP.664	rh2011	40		>1.3	1.0			>1.3	>1.3								
gp140																	

and largest effects (factor of >5 titer reduction for >5 sera) were changes at L125 (C1); R166 and K168 (V2); P299, R304, and K305 (V3 base); and I420, K421, and Q422 (C4). Autologous NAbs present in seven of nine rabbit sera were sensitive to changes in one or both of the basic R166 and K168 residues in V2 β strand C. These residues are important for forming the epitopes targeted by the bNAbs PG9, PG16, and VRC26 (*6*, *38*), but it is possible they have more distant effects on the conformation of other epitopes.

In rabbit 1412, the autologous response was directed against a conformational epitope involving all three of the V1, V2, and V3 regions and also influenced by N137, N156, and K168 (Table 1, Table 2, and table S3). This sensitivity pattern is akin to a PG9/16-like response, except for the lack of dependency on glycan N160 at the trimer apex. Hence, the autologous NAb response in rabbit 1412 may involve PG9/16-like or VRC26-like antibodies with narrow specificity. The gp120 OD, particularly residues in C3 and C4, was targeted in several rabbits. The depletion experiments with the 7C3 gp120-D368R protein also implicate C3 residues 354 to 363 as direct or indirect influences on the epitope(s) recognized by the autologous NAbs in rabbit sera 1254, 1256, 1274, 1283, and 1285 (Table 1 and Fig. 3). Of note is that BG505.T332N neutralization was adversely affected by mutations that eliminated various OD glycan sites including N185, N301, and N462 (rabbit 1274); N332, N392, and N398 (rabbit 1410); and N137, N156, and N386 (rabbit 1412). We are not aware of the induction of NAbs to glycan-dependent epitopes by gp120 monomers or non-native gp140 proteins.

We used a competition ELISA to study whether the BG505 SOSIP.664, WT.SEKS gp140, or gp120 proteins had induced Abs that could block the trimer binding of various bNAbs (*39*). Several sera from SOSIP.664 or gp120 recipients reduced the binding of CD4bs bNAbs CH103 and VRC01, and also CD4-IgG2, by >50%, whereas sera from WT.SEKS gp140 recipients had no such effect (fig. S8A). The inhibition of CH103 and VRC01 binding correlated with BG505.T332N neutralization, which suggests that at least some serum antibodies mediating the autologous response do so by impeding access to the CD4bs (fig. S8B). However, taken together, the virus mutant data and neutralization-depletion experiments with the RSC3 and gp120-D368R proteins imply that such antibodies do not target the CD4bs directly (Tables 1 and 2). We note that when the PGT135 bNAb binds to its V3 glycan–dependent epitope on the trimer, it reorients other glycans so that they now occlude the CD4bs (*39*, *40*). The PGT135 epitope on the trimer is proximal to residues implicated in the autologous NAb responses for rabbits 1274, 1410, and 1412 (Fig. 3 and fig. S8A). Narrow-specificity NAbs with broadly similar properties to PGT135, including glycan dependency, that indirectly impede access to the CD4bs may be present in some rabbit sera.

The competition ELISA also showed that sera from some trimer-immunized rabbits inhibited the binding of bNAbs 35022 and 3BC315 to their trimer epitopes at the gp120-gp41 interface or gp41, whereas sera from gp120- or WT.SEKS-immunized rabbits did not (fig. S8A). Some autologous NAbs may therefore directly or indirectly occlude epitopes near the bottom of the trimer. Overall, the competition ELISA data confirm that multiple epitopes on the BG505 SOSIP.664 trimer are immunogenic in rabbits, and imply that the trimers were generally more efficient than gp120 and WT.SEKS gp140 proteins at inducing Abs capable of inhibiting bNAb-trimer interactions (fig. S8A).

Comparison with the NAb response induced by the BG505 virus in the infected infant

As our long-term goal is to devise an immunization regimen that can induce bNAbs, we compared the autologous NAb response against the BG505 SOSIP.664 trimers in rabbits with the much broader response that developed in the infant from whom the BG505 virus was isolated (*8*) (see Materials and Methods). The infant's week 14 serum weakly neutralized the BG505 virus, but not BG505.T332N, and completely lacked heterologous neutralization activity even against the tier 1A virus SF162 (Table 3). However, a strong cross-neutralization response against tier 1 and tier 2 viruses, including BG505 and BG505.T332N,

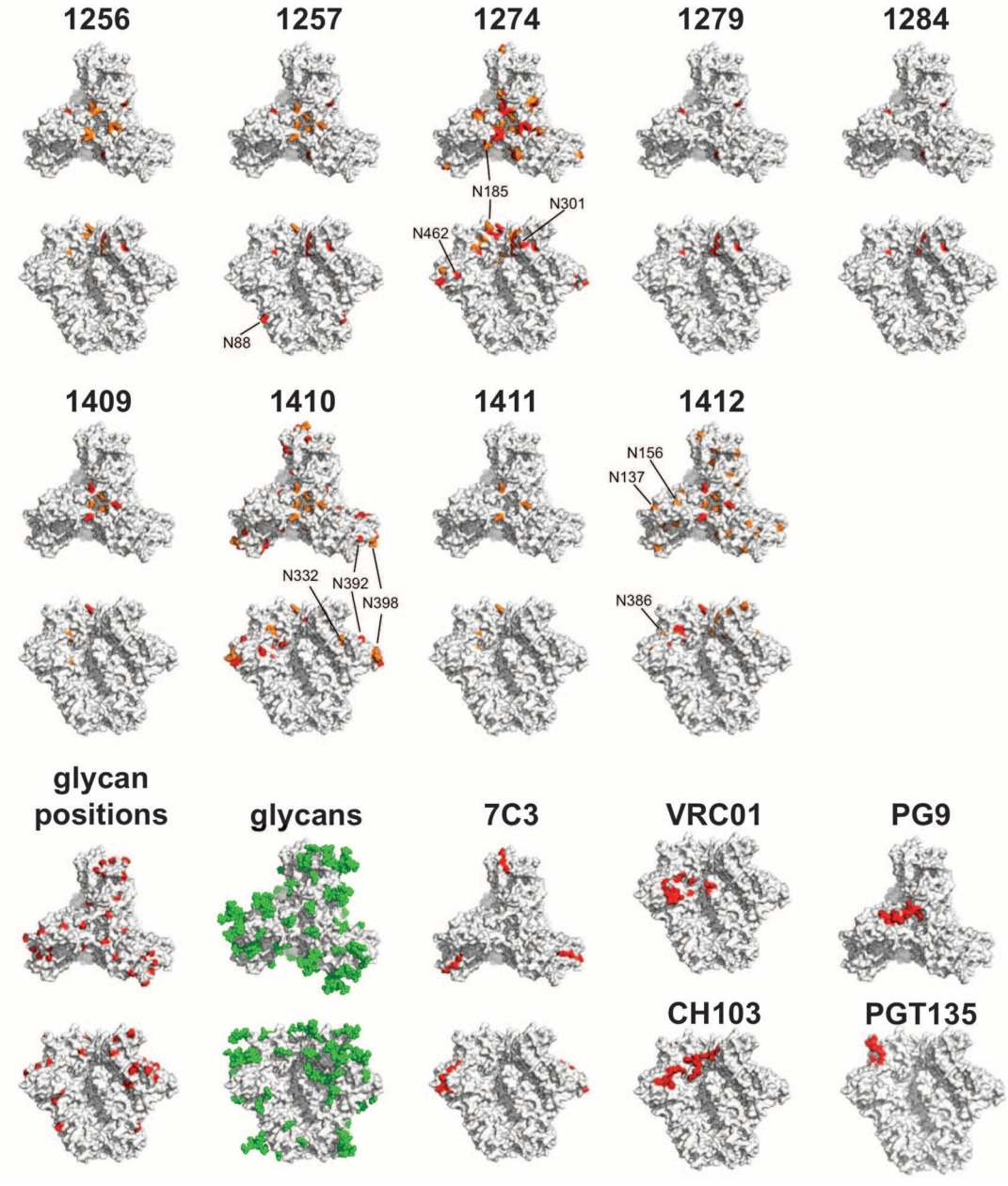


Fig. 3. Autologous tier 2 NAb responses in sera from BG505 SOSIP.664 trimer-immunized rabbits mapped onto the trimer structure. Neutralization data derived when sera from the indicated rabbits were tested against a panel of BG505.T332N virus mutants are shown in table S3. Residues in gp120 where Ala substitutions reduce neutralization by a factor of 5 to 10 and by a factor of >10 are colored orange and red, respectively, on the BG505 SOSIP.664 crystal structure (PDB ID: 4TVP). Each rabbit serum, denoted by a four-digit number, is mapped individually. In each case, the first row is a top view of the trimer, the second row a side view. The glycosylation sites that affect neutralization by rabbit sera 1257, 1274, 1410, and 1412 are labeled. For comparison, the bottom two panels illustrate the positions of glycans (red), the glycans resolved in the crystal structure (green), the seven amino acid substitutions that were under selection pressure in the BG505 infant (7C3, red), and the footprints (within 3 Å) of the bNAbs VRC01 and CH103 (both to the CD4bs), PG9, and PGT135 (all side views, except for PG9, top view).

had developed by month 27. In a direct comparison, week 22 sera from four BG505 SOSIP.664 trimer-immunized rabbits (1256, 1257, 1274, and 1284) neutralized BG505 and BG505.T332N viruses more strongly than the early infant sera, but lacked the neutralization breadth present in the month 27 serum (Table 3). Thus, the recombinant trimers induced NAb responses in rabbits that are similar, but not identical, to the primary infection response of the human infant; autologous NAbs were present in both species.

To guide immunogen design, we studied how BG505 Env sequences evolved in the infant. As expected, the month 27 sequences were highly divergent (9%) from those of week 6. In particular, multiple changes within a 10-residue stretch of C3 (residues 354 to 363) imply a strong selection pressure on this region (fig. S9). The predominant month 27 sequence had seven C3 changes: G354E, Δ356, T357K, I358T, R360I, A362T, and N363K (which removed a glycan site). A gp120-D368R variant containing all seven changes (termed 7C3) was unable to deplete autologous NAbs from sera of five of the 13 test rabbits (numbers 1254, 1256, 1274, 1283, and 1285) but was active against the other eight (Table 1). This variant also did not deplete autologous NAbs from gp120-immunized rabbit sera 1267 and 1268. These findings underscore similarities in how the humoral immune systems of the two species respond to BG505 Env.

Immunogenicity of BG505 SOSIP.664 trimers in rhesus macaques

In a pilot study, we compared the immunogenicity of BG505 SOSIP.664 trimers and gp120 monomers in rhesus macaques (fig. S1). Three of four sera neutralized the autologous BG505.T332N virus at week 26 (median titer, 78), while none of four sera from gp120-immunized animals did so (Fig. 1E and table S4). By week 54, the median autologous titer in the macaques approached that in the rabbits at weeks 22 to 26 (i.e., 203 versus 570) (Fig. 1E and table S4; compare to Fig. 1A). As the anti-gp120 and anti-trimer ELISA titers in the macaques were lower than in the rabbits by a factor of ~5 (fig. S10, A and B; compare to fig. S4A), a stronger adjuvant might be advantageous. NAb titers against tier 1 viruses MW965.26 and MN.3 were similar at the week 26 and week 54 time points and did not differ markedly between trimer and monomer groups at week 26 (Fig. 1, F and G). None of the eight sera neutralized the heterologous tier 2 clade C virus Ce1176 (Fig. 1H).

In the competition ELISA, sera from trimer-immunized macaques induced stronger bNAb-blocking responses than gp120 recipients, including Abs that reduced access of CH103 and VRC01 to the CD4bs and, to a lesser extent, of PGT145 to the trimer apex (fig. S8A). In addition, the BG505 gp120-D368R protein, but not its 7C3 variant, depleted BG505.T332N NAbs from rh1987 sera (Table 1); this finding suggests that, as in some

Table 2. Summary of autologous NAb specificities in sera from rabbits and macaques immunized with BG505 SOSIP.664 trimers or gp120 monomers when analyzed in different assays. The immunogen, producer cell/treatment (i.e., influence on glycosylation profile), and rabbit ID number are listed in the first three columns. The fourth column lists N-linked glycosylation sites that affect autologous BG505.T332N neutralization (factor of >5 decrease in IC_{50}; see table S3). The fifth column lists gp120 domains where substitutions decrease neutralization by a factor of >5 (table S3). The sixth column lists the domains that, when mutated or deleted from the BG505 gp120-D368R protein, impair its neutralization depletion capacity (Table 1). The seventh column lists the bNAbs for which binding to D7324-tagged BG505 SOSIP.664 trimers in ELISA is inhibited by >50% by the test serum (fig. S9). In columns 4 and 5, ND = not done (the serum was not tested against the mutant virus panel). In columns 4, 6, and 7, a blank entry indicates that the assay was performed, but the outcome was uninformative.

Immunogen	Producer cell	Animal ID	Neutralization mutants (glycan)	Neutralization mutants	Neutralization depletion	CD4/bNAb block
BG505	293S	1254	ND	ND	C3	CD4, CH103, PGT151, 35O22, 3BC315
SOSIP.664 gp140	293S	1256		C1, V2, V3, C4	C3	CD4, CH103, VRC01, PGT151, 35O22, 3BC315
	293S	1257	N88	C1, V2, V3, C4		CD4, 35O22, 3BC315
	293T	1274	N185, N301, N462	C1, V2, V3, C3, C4, V5	C3	CH103, VRC01
	293S	1278	ND	ND		CD4, CH103, PGT151, 35O22, 3BC315
	293S	1279		C1, V3, C4		CD4, CH103, VRC01, PGT121, PGT126, PGT151, 35O22, 3BC315
	293S + EndoH	1283	ND	ND	C3	PGT126
	293S + EndoH	1284		C1, V3, C4		CH103, 35O22, 3BC315
	293S + EndoH	1285	ND	ND	C3	VRC01, 35O22, 3BC315
	293T	1409		V2, C4, C5		CH103, VRC01, 3BC315
	293T	1410	N332, N392, N398	V2, C2, V3, C3, V4, C4, C5		CH103, VRC01, 3BC315
	293T	1411		V2, C4, C5		VRC01, 3BC315
	293T	1412	N137, N156, N386	C1, V1, V2, C2, V3, C3, C4, C5	V1, V2, V3	CH103, VRC01, PGT126, 3BC315
BG505	293S	1267	ND	ND	C3	CH103, VRC01
gp120	293S	1268	ND	ND	C3	CD4, CH103, VRC01
BG505	293T	rh1987	ND	ND	C3	CH103, VRC01, PGT126, PGT135
SOSIP.664 gp140	293T	rh2011	ND	ND		CH103, VRC01, PGT145, PGT126, PGT135

Table 3. Comparison of NAb responses induced by BG505 SOSIP.664 trimers in rabbits and by natural infection of an infant with HIV-1 BG505 virus. Sera from rabbits 1256, 1257, 1274, and 1284 after three immunizations (i.e., at week 22) with BG505 SOSIP.664 trimers were compared with sera from infant BG505 taken at week 14 and month 27 after infection. The trimers are based on a sequence derived from the infant at week 6. The TZM-bl cell assay was conducted at FHCRC. The clades and the tier classifications of the test viruses are indicated. The BG505 and BG505.T32N viruses are described in the supplementary materials.

Clade	Tier	Virus isolate	Rabbit 1256 week 22	Rabbit 1257 week 22	Rabbit 1274 week 22	Rabbit 1284 week 22	Human BG505 week 14	Human BG505 month 27
A	2	BG505	581	143	334	113	157	238
A	2	BG505.T332N	773	109	641	169	<100	452
B	1A	SF162	704	1946	106	2362	<100	>3200
A	1B	Q461.D1	<100	202	<100	312	<100	>3200
A	2	Q842.d16	<100	<100	<100	<100	<100	482
A	2	BJ613.E1	<100	<100	<100	<100	<100	<100
A/D	2	BF535.A1	<100	<100	<100	<100	<100	129
B	2	TRO.11	<100	<100	<100	<100	106	262
B	3	THRO4156.18	<100	<100	<100	<100	<100	<100
C	2	QC406.F3	<100	<100	<100	<100	<100	971
C	2	CAP210.E8	<100	<100	<100	<100	<100	590
D	2	QD435.A4	<100	<100	<100	<100	102	548
D	2	QB857.B3	<100	<100	<100	<100	<100	185

rabbits, the C3 region is involved in this autologous response.

Conclusions

Inducing high titers of autologous tier 2 NAbs may be a necessary first step in the elicitation of bNAbs (*3*–*6*). The strong and consistent autologous response to the BG505 and B41 SOSIP.664 trimers reflects their native-like structure, homogeneity, stability, and antigenicity, as well as the immunogenicity of the BG505 virus in the infected infant (*8*, *9*, *12*, *14*, *17*). Taken together, the mapping studies show that multiple specificities contribute to the autologous NAb responses against the BG505 trimers, including antibodies that recognize glycan-influenced epitopes. If a polyspecific response could be achieved in humans, it might provide broader coverage against circulating viruses, but a human vaccine must generate a more broadly neutralizing response than we report here.

The native structure of SOSIP.664 trimers allows candidate immunogens to be rationally redesigned to try to improve immunogenicity. Relevant but not mutually exclusive strategies include (i) introducing sequence changes to increase the stability of the trimer apex and associated bNAb epitopes while reducing the antigenicity of V3 and other non-NAb epitopes that may be immunologic distractions; (ii) immunizing with sequential SOSIP.664 trimers based on later-arising BG505 sequences or cocktails of different trimers (e.g., from clades A, B, and C, etc.) (*9*); or (iii) priming with trimer variants that trigger desirable germline responses (*4*, *5*, *41*, *42*). Overall, our results strongly validate the concept of using native-like trimers and structural information to create an HIV-1 vaccine that induces bNAbs.

Materials and methods

Immunogens and immunizations

The BG505 SOSIP.664 trimers, gp120 monomers, and WT.SEKS uncleaved gp140 proteins were all produced and purified as reported previously (*10*, *14*, *20*). Unless specified, the proteins were expressed in HEK293T cells by transient transfection and purified via a 2G12 mAb affinity column followed by size exclusion chromatography (SEC). Protein purities and properties were comparable to those described elsewhere (*10*, *14*, *20*). BG505 SOSIP.664 trimers were also expressed in HEK293S cells that lack *N*-acetylglucosaminyltransferase I ($GnTI^{-/-}$). The resulting Env proteins bear glycans that are not fully processed and remain in oligomannose form (*22*, *23*). Samples of the 293S cell-derived trimers were treated with the EndoH glycosidase, as previously described, to reduce their total glycan content (*23*). The clade B B41 SOSIP.664 and B41 SOSIP.664-D7324 trimers were produced from stable CHO cell lines that were cultured in 0.5% serum (*9*). The trimers were purified by 2G12 affinity chromatography followed by SEC, as described elsewhere; the extent of V3-clipping was negligible (*9*). The YU2 gp140-Fd protein was made in HEK293T cells under contract for IAVI by G. Stewart-Jones (University of Oxford), as described (*44*).

Rabbit immunizations and blood sampling were carried out under subcontract at Covance (Denver, PA) according to the schedule presented in fig. S1B. Female New Zealand White rabbits (usually 4 per group) were immunized intramuscularly with 30 μg of the various Env proteins (40 μg in experiment 3). The proteins were formulated in 75 Units of ISCOMATRIX, a saponin-based adjuvant obtained from CSL Ltd. (Parkville, Victoria, Australia) (*45*). Macaque immunizations and blood sampling were carried out at the Wisconsin Primate Center according to the schedule in fig. S1B. Rhesus macaques (4 per group) were immunized intramuscularly with 100 μg of BG505 SOSIP.664 or gp120 proteins formulated in 75 units of ISCOMATRIX.

mAbs and human sera

The mAbs used here were provided by the following individuals: CH103 and CH31, B. Haynes (Duke University); VRC01, P. Kwong and J. Mascola (NIH/VRC, Bethesda, MD); NIH45-46, NIH45-46W, 3BNC60, 3BNC117, 12A12, 12A21, M. Nussenzweig (Rockefeller University); various mAbs used for tier classification, S. Zolla-Pazner (New York University School of Medicine). mAbs 2G12 and 2F5 were obtained through the NIH AIDS Reagent Program, Division of AIDS, NIAID, NIH from H. Katinger. The serum samples used for the neutralization sensitivity (i.e., tier) classification of BG505.T332N have been described elsewhere (*46*). Sera obtained from individuals chronically infected with clade-A HIV-1 strains were gifts from B. Haynes and A. McKnight (Barts & London Medical School). mAb ARP3119 used for Western blotting was acquired from the Programme EVA Centre for AIDS Reagents.

BG505 viruses and serum

The BG505 infant was HIV-1 DNA-negative at birth, but DNA-positive 6 weeks later, suggesting that infection occurred within this window (*8*). The sequence of a week 6 clone is the basis of the BG505 SOSIP.664 protein construct, in which a T332N substitution was made to restore bNAb epitopes that require the N332 glycan (*7*, *8*, *10*, *24*). The same change was made to create the BG505. T332N variant of the week 6 BG505 virus (*10*). Serum samples were available from week 6, week 14, and month 27.

ELISA reagents and procedures

The D7324-epitope-tagged version of BG505 SOSIP.664, referred to as SOSIP.664-D7324, and BG505 gp120 with a reconstructed D7324 epitope in C5, were made as described previously (*10*). JR-CSF gp120 was prepared by D. Kubitz at the Scripps Center for Antibody Development and Production (La Jolla, CA) using transient transfection of HEK293F cells, and purified by *Galanthus nivalis* lectin (Vector Labs, Burlingame, CA) affinity chromatography followed by SEC using a Sephacryl S200HR column. Anti-gp120 and anti-trimer ELISAs using the above proteins as antigens were performed as described previously (*10*). The C-terminal His-tagged BG505 SOSIP.664-His trimer was prepared as described previously (*17*, *37*). His-tagged BG505 gp41 (gp41-His) was produced as follows: A His-tagged version of the BG505 IP.664 gp140 protein, which is based on the SOSIP.664 construct but with the SOS disulfide bond omitted (*14*), was expressed in the presence of excess furin in 293F cells. The protein was purified via the His-tag using Ni-NTA chromatography with elution using 250 mM imidazole, followed by three rounds of negative selection using a 2G12 bNAb column to remove any residual gp120 or uncleaved gp140 proteins. The purified gp41 protein bound the gp41-specific non-NAb F240 efficiently, but did not bind 2G12 or VRC01, indicating that contaminant gp120 or gp140 proteins were not present (data not shown). The gp41 protein also did not bind the PGT151 or 3BC315 bNAbs, suggesting that it was not in a pre-fusion conformation (*37*, *47*). Ni-NTA ELISAs using His-tagged trimers and the gp41 protein were performed as described elsewhere (*37*).

For bNAb competition ELISA experiments, rabbit or macaque sera (1:100 dilution) were incubated with D7324-captured BG505 SOSIP.664-D7324 trimers for 1 hour. A biotinylated bNAb was then added at a concentration sufficient to give ~80% of the maximum binding signal, as assessed in a prior titration experiment (i.e., with no competitor present). The bound bNAb was detected using horseradish peroxidase (HRP)-labeled streptavidin. As the PGT151, 35O22, and 3BC315 bNAbs, and also CD4-IgG2, could not be biotinylated without impairing their binding activity (*37*) we detected unlabeled human bNAbs using an HRP-labeled donkey anti-human IgG conjugate that was minimally cross-reactive with rabbit IgG (Jackson Immunoresearch, Westgrove, PA). The latter assay format was unsuitable for macaque sera because the anti-human antibody cross-reacted with macaque IgG. As a result, it was not possible to test the macaque sera for inhibition of PGT151, 35O22, 3BC315, or CD4-IgG2 binding to the trimer.

To analyze the relative titers for serum antibody binding to conformational *vs.* linear epitopes, trimers (0.1 μg/ml) or monomers (0.03 μg/ml) were denatured by heating for 5 min at 99°C in 50 μl of TBS, 10% FCS, 1% SDS, and 50 mM DTT (sodium dodecyl sulfate, SDS; dithiothreitol, DTT). The samples were then diluted by a factor of 140 in TBS and 10% FCS to prevent SDS and DTT from interfering with the ELISA. The use of both SDS and DTT ensures that the Env proteins are fully denatured by heat treatment (*48*). The native or denatured proteins were then used in a D7324-capture ELISA, essentially as described elsewhere (*10*, *48*). The relative reduction of binding to the denatured versus native Env proteins was calculated using the half maximal binding values (EC_{50}).

Neutralization assays

TZM-bl cell neutralization assays using Env-pseudotyped viruses were performed at six sites. For additional information on the assay and all supporting protocols, see www.hiv.lanl.gov/content/nab-reference-strains/html/home.htm. The performance sites were as follows: HMS, Harvard Medical School, and DUMC, Duke University

Medical Center (for methodology see (*49*)); IAVI, International AIDS Vaccine Initiative, Brooklyn, NY (for methodology see (*24*)); AMC, Academic Medical Center, Amsterdam [methodology see (*10*)]; WCMC, Weill Cornell Medical College, New York [methodology see (*50*)]; FHCRC, Fred Hutchinson Cancer Research Center, Seattle, WA [methodology see (*8*)]; TSRI, The Scripps Research Institute [methodology see (*51*)]. The Env-pseudotyped viruses and their tier classifications have been described elsewhere (*8*, *52*–*55*), as have the BG505.T332N and BG505 Env-pseudotyped viruses (*8*, *10*, *24*). The BG505.T332N Env-pseudotyped virus was used except when the test virus is specifically stated to be BG505 (i.e., without the T332N substitution). Also note that the MN Env-pseudotyped virus used at DUMC is designated MN.3. We did not use the A3R5 cell assay because of our concerns that it produces false positive, and hence misleading, detection of NAbs to tier 2 viruses.

Tier categorization of the BG505.T332N and B41 Env-pseudotyped viruses was based on the neutralization sensitivity to a panel of mAbs directed against various epitopes as well as a panel of sera from humans infected with clade A viruses, in comparison with previously tiered viruses (*52*). Data on BG505.T332N sensitivity to another panel of 50 mAbs can be found elsewhere (*10*). For both viruses, the tier classification experiments were performed at DUMC. We constructed a set of BG505.T332N alanine mutants for mapping NAb responses (table S3).

Neutralization depletion experiments

Proteins for neutralization depletion experiments [BG505 gp120-D368R and variants; BG505 SOSIP.664-D368R; RSC3 (*56*)] were expressed transiently in HEK293F cells and purified by 2G12-affinity chromatography. All reagents were based on the BG505 sequence, except for the RSC3 protein. The D368R change was introduced to ensure that the gp120 or SOSIP.664 gp140 proteins do not bind to CD4 on the cell surface and thereby inhibit HIV-1 infection competitively. ELISA experiments confirmed that the D368R substitution strongly reduced the binding of CD4 and several CD4bs bNAbs to BG505 gp120. The gp120-D368R 7C3 reagent contains seven amino acid changes in C3 (G354E, Δ356, T357K, I358T, R360I, A362T, and N363K) based on the month 27 sequences from infant BG505 (fig. S9). Substitutions and deletions were made using the Quickchange mutagenesis kit (Agilent, Santa Clara, CA). The plasmid expressing RSC3 (donated by P. Kwong and J. Mascola, NIH/VRC, Bethesda, MD) has been described elsewhere (*56*). The basis for the design of the BG505 V1V2-scaffold protein has also been described (*57*). The protein was expressed in HEK293S GnTI$^{-/-}$ cells and purified via its C-terminal 6×His tag using Ni-NTA chromatography and $NiCl_2$ elution, followed by SEC on a Superdex 200 column. The theoretical MW of the scaffold, including glycans, is ~25 kD.

BG505-derived peptides with the following sequences were purchased from Genscript (Piscataway, NJ): V1: TNVTNNITDDMRGELKN; V2 (5 overlapping peptides): MTTELRDKKQKVYSL, DKKQKVYSLFYRLDV, YSLFYRLDVVQINEN, LDVVQINENQGNRSN, ENQGNRSNNSNKEYR; V3: TRPNNNTRKSIRIGPGQAFYATGDIIGDIRQAH; C1-V1: VKLTPLCVTLQCTNVTNNITDDMRGELKN.

To characterize the specificities of NAb responses induced in the rabbits, we incubated competitor Env proteins or peptides with appropriately diluted sera (total volume 25 μl) for 1 hour at 37°C. The competitor Env proteins were present at a concentration of 40 μg/ml except for the V1V2-scaffold protein (20 μg/ml). The competitor peptides were also used at 40 μg/ml, except that each individual component of a cocktail of 5 overlapping V2 peptides was present at 20 μg/ml. The Env-pseudotyped virus was then added to the serum-competitor mixture for 1 hour before infection of TZM-bl target cells was initiated. The rest of the assay was carried out as described above and elsewhere (*10*). Neutralization titers were expressed as the reciprocal serum dilution that caused 50% inhibition of virus infection (IC_{50}). The extent of neutralization depletion by the added competitor was expressed as the relative reduction in the IC_{50} value.

Pepscan analysis

15-mer peptides, overlapping by 14 residues, from the BG505 SOSIP.664 as well as the unmodified BG505 gp140 sequences, were synthesized by Fmoc coupling on the solid support of a Pepscan hydrogel (*58*). The peptide libraries were probed with heat-inactivated human sera, at a 1:1000 dilution. After extensive washing, a goat anti-human HRP conjugated secondary antibody was added, followed by color development using 2,2′-azinobis(3-ethylbenzothiazoline-6-sulphonic acid). A charge-coupled device camera was used to quantify the absorbance at 405 nm. For every individual Pepscan dataset, the data were normalized to the average signal intensity derived from the overall analysis.

Negative-stain electron microscopy

The BG505 WT.SEKS, BG505 SOSIP.664, and YU2 gp140-Fd proteins, as well as ISCOMATRIX adjuvant-formulated BG505 SOSIP.664 trimers, were analyzed by negative-stain EM. Samples were prepared for analysis as described (*10*, *14*). Briefly, a 3-μl aliquot containing ~0.01 mg per ml of protein was applied for 5 s onto a carbon-coated 400 Cu mesh grid that had been glow-discharged at 20 mA for 30 s, then negatively stained with 2% (w/v) uranyl formate for 60 s. Data were collected using an FEI Tecnai T12 electron microscope operating at 120 keV, with an electron dose of ~25 $e^-/Å^2$ and a magnification of 52,000× that resulted in a pixel size of 2.05 Å at the specimen plane. Images were acquired with a Tietz TemCam-F416 CMOS camera using a nominal defocus range of 900 to 1300 nm.

Data processing methods were adapted from those used previously (*10*, *14*). Particles were picked automatically using DoG Picker and put into a particle stack using the Appion software package (*59*). Initial, reference-free, two-dimensional (2D) class averages were calculated using particles binned by two via Iterative Multivariate Statistical Analysis (MSA)/Multi-reference Alignment (MRA) and sorted into classes (*60*). Particles corresponding to trimers were selected into a substack and binned by two before another round of reference-free alignment was carried out using Iterative MSA/MRA and Xmipp Clustering and 2D alignment algorithms (*61*).

REFERENCES AND NOTES

1. M. J. van Gils, R. W. Sanders, Broadly neutralizing antibodies against HIV-1: Templates for a vaccine. *Virology* **435**, 46–56 (2013). doi: 10.1016/j.virol.2012.10.004; pmid: 23217615
2. A. P. West Jr. *et al*., Structural insights on the role of antibodies in HIV-1 vaccine and therapy. *Cell* **156**, 633–648 (2014). doi: 10.1016/j.cell.2014.01.052; pmid: 24529371
3. C. A. Derdeyn, P. L. Moore, L. Morris, Development of broadly neutralizing antibodies from autologous neutralizing antibody responses in HIV infection. *Curr. Opin. HIV AIDS* **9**, 210–216 (2014). doi: 10.1097/COH.0000000000000057; pmid: 24662931
4. B. F. Haynes, G. Kelsoe, S. C. Harrison, T. B. Kepler, B-cell-lineage immunogen design in vaccine development with HIV-1 as a case study. *Nat. Biotechnol.* **30**, 423–433 (2012). doi: 10.1038/nbt.2197; pmid: 22565972
5. H.-X. Liao *et al*., Co-evolution of a broadly neutralizing HIV-1 antibody and founder virus. *Nature* **496**, 469–476 (2013). doi: 10.1038/nature12053; pmid: 23552890
6. N. A. Doria-Rose *et al*., Developmental pathway for potent V1V2-directed HIV-neutralizing antibodies. *Nature* **509**, 55–62 (2014). doi: 10.1038/nature13036; pmid: 24590074
7. X. Wu *et al*., Neutralization escape variants of human immunodeficiency virus type 1 are transmitted from mother to infant. *J. Virol.* **80**, 835–844 (2006). doi: 10.1128/JVI.80.2.835-844.2006; pmid: 16378985
8. L. Goo, V. Chohan, R. Nduati, J. Overbaugh, Early development of broadly neutralizing antibodies in HIV-1-infected infants. *Nat. Med.* **20**, 655–658 (2014). doi: 10.1038/nm.3565; pmid: 24859529
9. P. Pugach *et al*., A native-like SOSIP.664 trimer based on an HIV-1 subtype B env gene. *J. Virol.* **89**, 3380–3395 (2015). doi: 10.1128/JVI.03473-14; pmid: 25589637
10. R. W. Sanders *et al*., A next-generation cleaved, soluble HIV-1 Env trimer, BG505 SOSIP.664 gp140, expresses multiple epitopes for broadly neutralizing but not non-neutralizing antibodies. *PLOS Pathog.* **9**, e1003618 (2013). doi: 10.1371/journal.ppat.1003618; pmid: 24068931
11. D. Lyumkis *et al*., Cryo-EM structure of a fully glycosylated soluble cleaved HIV-1 envelope trimer. *Science* **342**, 1484–1490 (2013). doi: 10.1126/science.1245627; pmid: 24179160
12. J.-P. Julien *et al*., Crystal structure of a soluble cleaved HIV-1 envelope trimer. *Science* **342**, 1477–1483 (2013). doi: 10.1126/science.1245625; pmid: 24179159
13. M. Pancera *et al*., Structure and immune recognition of trimeric pre-fusion HIV-1 Env. *Nature* **514**, 455–461 (2014). doi: 10.1038/nature13808; pmid: 25296255
14. R. P. Ringe *et al*., Cleavage strongly influences whether soluble HIV-1 envelope glycoprotein trimers adopt a native-like conformation. *Proc. Natl. Acad. Sci. U.S.A.* **110**, 18256–18261 (2013). doi: 10.1073/pnas.1314351110; pmid: 24145402
15. M. Guttman, K. K. Lee, A functional interaction between gp41 and gp120 is observed for monomeric but not oligomeric, uncleaved HIV-1 Env gp140. *J. Virol.* **87**, 11462–11475 (2013). doi: 10.1128/JVI.01681-13; pmid: 23966389
16. K. Tran *et al*., Vaccine-elicited primate antibodies use a distinct approach to the HIV-1 primary receptor binding site informing vaccine redesign. *Proc. Natl. Acad. Sci. U.S.A.* **111**, E738–E747 (2014). doi: 10.1073/pnas.1319512111; pmid: 24550318
17. A. Yasmeen *et al*., Differential binding of neutralizing and non-neutralizing antibodies to native-like soluble HIV-1 Env trimers, uncleaved Env proteins, and monomeric subunits. *Retrovirology* **11**, 41 (2014). doi: 10.1186/1742-4690-11-41; pmid: 24884783
18. M. Guttman *et al*., CD4-induced activation in a soluble HIV-1 Env trimer. *Structure* **22**, 974–984 (2014). doi: 10.1016/j.str.2014.05.001; pmid: 24931470
19. L. K. Pritchard *et al*., Structural constraints determine the glycosylation of HIV-1 envelope trimers. *Cell Rep.* 10.1016/j.celrep.2015.05.017 (2015). doi: 10.1016/j.celrep.2015.05.017; pmid: 26051934
20. J. P. Julien *et al*., Asymmetric recognition of the HIV-1 trimer by broadly neutralizing antibody PG9. *Proc. Natl. Acad. Sci. U.S.A.* **110**, 4351–4356 (2013).pmid: 23426631

21. J. E. Ledgerwood *et al*., Prime-boost interval matters: A randomized phase 1 study to identify the minimum interval necessary to observe the H5 DNA influenza vaccine priming effect. *J. Infect. Dis.* **208**, 418–422 (2013). doi: 10.1093/infdis/jit180; pmid: 23633407
22. D. Eggink *et al*., Lack of complex N-glycans on HIV-1 envelope glycoproteins preserves protein conformation and entry function. *Virology* **401**, 236–247 (2010). doi: 10.1016/j.virol.2010.02.019; pmid: 20304457
23. R. S. Depetris *et al*., Partial enzymatic deglycosylation preserves the structure of cleaved recombinant HIV-1 envelope glycoprotein trimers. *J. Biol. Chem.* **287**, 24239–24254 (2012). doi: 10.1074/jbc.M112.371898; pmid: 22645128
24. S. Hoffenberg *et al*., Identification of an HIV-1 clade A envelope that exhibits broad antigenicity and neutralization sensitivity and elicits antibodies targeting three distinct epitopes. *J. Virol.* **87**, 5372–5383 (2013). doi: 10.1128/JVI.02827-12; pmid: 23468492
25. J. P. Nkolola *et al*., Breadth of neutralizing antibodies elicited by stable, homogeneous clade A and clade C HIV-1 gp140 envelope trimers in guinea pigs. *J. Virol.* **84**, 3270–3279 (2010). doi: 10.1128/JVI.02252-09; pmid: 20053749
26. C. A. Blish *et al*., Comparative immunogenicity of subtype a Human Immunodeficiency Virus type 1 envelope exhibiting differential exposure of conserved neutralization epitopes. *J. Virol.* **84**, 2573–2584 (2010). doi: 10.1128/JVI.01687-09; pmid: 20015987
27. C. Sundling *et al*., Soluble HIV-1 Env trimers in adjuvant elicit potent and diverse functional B cell responses in primates. *J. Exp. Med.* **207**, 2003–2017 (2010). doi: 10.1084/jem.20100025; pmid: 20679401
28. C. Grundner *et al*., Analysis of the neutralizing antibody response elicited in rabbits by repeated inoculation with trimeric HIV-1 envelope glycoproteins. *Virology* **331**, 33–46 (2005). doi: 10.1016/j.virol.2004.09.022; pmid: 15582651
29. M. N. E. Forsell *et al*., Biochemical and immunogenic characterization of soluble human immunodeficiency virus type 1 envelope glycoprotein trimers expressed by semliki forest virus. *J. Virol.* **79**, 10902–10914 (2005). doi: 10.1128/JVI.79.17.10902-10914.2005; pmid: 16103142
30. E. P. Go, Y. Zhang, S. Menon, H. Desaire, Analysis of the disulfide bond arrangement of the HIV-1 envelope protein CON-S gp140 ΔCFI shows variability in the V1 and V2 regions. *J. Proteome Res.* **10**, 578–591 (2011). doi: 10.1021/pr100764a; pmid: 21114338
31. E. P. Go, D. Hua, H. Desaire, Glycosylation and disulfide bond analysis of transiently and stably expressed clade C HIV-1 gp140 trimers in 293T cells identifies disulfide heterogeneity present in both proteins and differences in O-linked glycosylation. *J. Proteome Res.* **13**, 4012–4027 (2014). doi: 10.1021/pr5003643; pmid: 25026075
32. M. Shingai *et al*., Passive transfer of modest titers of potent and broadly neutralizing anti-HIV monoclonal antibodies block SHIV infection in macaques. *J. Exp. Med.* **211**, 2061–2074 (2014). doi: 10.1084/jem.20132494; pmid: 25155019
33. S. Beddows *et al*., A comparative immunogenicity study in rabbits of disulfide-stabilized, proteolytically cleaved, soluble trimeric human immunodeficiency virus type 1 gp140, trimeric cleavage-defective gp140 and monomeric gp120. *Virology* **360**, 329–340 (2007). doi: 10.1016/j.virol.2006.10.032; pmid: 17126869
34. Y. K. Kang *et al*., Structural and immunogenicity studies of a cleaved, stabilized envelope trimer derived from subtype A HIV-1. *Vaccine* **27**, 5120–5132 (2009). doi: 10.1016/j.vaccine.2009.06.037; pmid: 19567243
35. D. C. Malherbe *et al*., Envelope variants circulating as initial neutralization breadth developed in two HIV-infected subjects stimulate multiclade neutralizing antibodies in rabbits. *J. Virol.* **88**, 12949–12967 (2014). doi: 10.1128/JVI.01812-14; pmid: 25210191
36. J. B. Munro *et al*., Conformational dynamics of single HIV-1 envelope trimers on the surface of native virions. *Science* **346**, 759–763 (2014). doi: 10.1126/science.1254426; pmid: 25298114
37. M. Melchers *et al*., Targeting HIV-1 envelope glycoprotein trimers to B cells by using APRIL improves antibody responses. *J. Virol.* **86**, 2488–2500 (2012). doi: 10.1128/JVI.06259-11; pmid: 22205734
38. R. Ringe, S. Phogat, J. Bhattacharya, Subtle alteration of residues including N-linked glycans in V2 loop modulate HIV-1 neutralization by PG9 and PG16 monoclonal antibodies. *Virology* **426**, 34–41 (2012). doi: 10.1016/j.virol.2012.01.011; pmid: 22314018
39. R. Derking *et al*., Comprehensive antigenic map of a cleaved soluble HIV-1 envelope trimer. *PLOS Pathog.* **11**, e1004767 (2015). doi: 10.1371/journal.ppat.1004767; pmid: 25807248
40. L. Kong *et al*., Supersite of immune vulnerability on the glycosylated face of HIV-1 envelope glycoprotein gp120. *Nat. Struct. Mol. Biol.* **20**, 796–803 (2013). doi: 10.1038/nsmb.2594; pmid: 23708606
41. J. Jardine *et al*., Rational HIV immunogen design to target specific germline B cell receptors. *Science* **340**, 711–716 (2013). doi: 10.1126/science.1234150; pmid: 23539181
42. A. T. McGuire *et al*., Antigen modification regulates competition of broad and narrow neutralizing HIV antibodies. *Science* **346**, 1380–1383 (2014). doi: 10.1126/science.1259206; pmid: 25504724
43. See supplementary materials on *Science* Online.
44. H. Uchtenhagen *et al*., Boosting of HIV-1 neutralizing antibody responses by a distally related retroviral envelope protein. *J. Immunol.* **192**, 5802–5812 (2014). doi: 10.4049/jimmunol.1301898; pmid: 24829409
45. E. Maraskovsky *et al*., Development of prophylactic and therapeutic vaccines using the ISCOMATRIX adjuvant. *Immunol. Cell Biol.* **87**, 371–376 (2009). doi: 10.1038/icb.2009.21; pmid: 19381160
46. P. Hraber *et al*., Prevalence of broadly neutralizing antibody responses during chronic HIV-1 infection. *AIDS* **28**, 163–169 (2014). doi: 10.1097/QAD.0000000000000106; pmid: 24361678
47. C. Blattner *et al*., Structural delineation of a quaternary, cleavage-dependent epitope at the gp41-gp120 interface on intact HIV-1 Env trimers. *Immunity* **40**, 669–680 (2014). doi: 10.1016/j.immuni.2014.04.008; pmid: 24768348
48. J. P. Moore, Q. J. Sattentau, R. Wyatt, J. Sodroski, Probing the structure of the human immunodeficiency virus surface glycoprotein gp120 with a panel of monoclonal antibodies. *J. Virol.* **68**, 469–484 (1994).pmid: 7504741
49. D. C. Montefiori, Measuring HIV neutralization in a luciferase reporter gene assay. *Methods Mol. Biol.* **485**, 395–405 (2009).pmid: 19020839
50. T. J. Ketas, S. Holuigue, K. Matthews, J. P. Moore, P. J. Klasse, Env-glycoprotein heterogeneity as a source of apparent synergy and enhanced cooperativity in inhibition of HIV-1 infection by neutralizing antibodies and entry inhibitors. *Virology* **422**, 22–36 (2012). doi: 10.1016/j.virol.2011.09.019; pmid: 22018634
51. D. Sok *et al*., Recombinant HIV envelope trimer selects for quaternary-dependent antibodies targeting the trimer apex. *Proc. Natl. Acad. Sci. U.S.A.* **111**, 17624–17629 (2014). doi: 10.1073/pnas.1415789111; pmid: 25422458
52. M. S. Seaman *et al*., Tiered categorization of a diverse panel of HIV-1 Env pseudoviruses for assessment of neutralizing antibodies. *J. Virol.* **84**, 1439–1452 (2010). doi: 10.1128/JVI.02108-09; pmid: 19939925
53. M. Li *et al*., Genetic and neutralization properties of subtype C human immunodeficiency virus type 1 molecular env clones from acute and early heterosexually acquired infections in Southern Africa. *J. Virol.* **80**, 11776–11790 (2006). doi: 10.1128/JVI.01730-06; pmid: 16971434
54. A. deCamp *et al*., Global panel of HIV-1 Env reference strains for standardized assessments of vaccine-elicited neutralizing antibodies. *J. Virol.* **88**, 2489–2507 (2014). doi: 10.1128/JVI.02853-13; pmid: 24352443
55. M. D. Simek *et al*., Human immunodeficiency virus type 1 elite neutralizers: Individuals with broad and potent neutralizing activity identified by using a high-throughput neutralization assay together with an analytical selection algorithm. *J. Virol.* **83**, 7337–7348 (2009). doi: 10.1128/JVI.00110-09; pmid: 19439467
56. R. M. Lynch *et al*., The development of CD4 binding site antibodies during HIV-1 infection. *J. Virol.* **86**, 7588–7595 (2012). doi: 10.1128/JVI.00734-12; pmid: 22573869
57. J. S. McLellan *et al*., Structure of HIV-1 gp120 V1/V2 domain with broadly neutralizing antibody PG9. *Nature* **480**, 336–343 (2011). doi: 10.1038/nature10696; pmid: 22113616
58. J. P. M. Langedijk, M. J. Zekveld, M. Ruiter, D. Corti, J. W. Back, Helical peptide arrays for lead identification and interaction site mapping. *Anal. Biochem.* **417**, 149–155 (2011). doi: 10.1016/j.ab.2011.06.002; pmid: 21708118
59. N. R. Voss, C. K. Yoshioka, M. Radermacher, C. S. Potter, B. Carragher, DoG Picker and TiltPicker: Software tools to facilitate particle selection in single particle electron microscopy. *J. Struct. Biol.* **166**, 205–213 (2009). doi: 10.1016/j.jsb.2009.01.004; pmid: 19374019
60. T. Ogura, K. Iwasaki, C. Sato, Topology representing network enables highly accurate classification of protein images taken by cryo electron-microscope without masking. *J. Struct. Biol.* **143**, 185–200 (2003). doi: 10.1016/j.jsb.2003.08.005; pmid: 14572474
61. G. C. Lander *et al*., Appion: An integrated, database-driven pipeline to facilitate EM image processing. *J. Struct. Biol.* **166**, 95–102 (2009). doi: 10.1016/j.jsb.2009.01.002 pmid: 19263523

ACKNOWLEDGMENTS

Supported by NIH grants P01 AI082362, R37 AI036082, R01 AI084817, R01 AI076105, NIAID-NIH Contract HHSN272011000016C, by Scripps CHAVI-ID (UM1 AI100663), by NIH grant P51OD011106, and by Aids Fonds Netherlands grants 2011032 and 2012041. J.-P.J. is a recipient of a Canadian Institutes of Health Research (CIHR) Fellowship. R.W.S. is a recipient of a Vidi grant from the Netherlands Organization for Scientific Research (NWO) and a Starting Investigator Grant from the European Research Council (ERC-StG-2011–280829-SHEV). This work was partially funded by IAVI with the generous support of USAID and the Bill & Melinda Gates Foundation; a full list of IAVI donors is available at www.iavi.org. The contents of this manuscript are the responsibility of the authors and do not necessarily reflect the views of USAID or the U.S. Government. We thank K. Sliepen, J. Korzun, M. Golabek, K. de los Reyes, L. Kong, K. Weisgrau, N. Pomplun, J. Hsueh, K. L. Saye-Francisco, A. Ramos for technical support; S. Schmidt, J. Gorman and N. Doria-Rose for advice; and G. Stewart-Jones, D. Kubitz, P. Kwong, J. Mascola, B. Haynes, A. McKnight, H. Katinger, S. Zolla-Pazner, P. Poignard, and M. Nussenzweig for reagents. The International AIDS Vaccine Initiative has previously filed a patent relating to the BG505 SOSIP.664 trimer: U.S. Provisional Application no. 61/772,739, titled "HIV-1 envelope glycoprotein," with inventors M. Caulfield, A.C., H. D., S. Hoffenberg, C. R. King, P.J.K., A. Marozsan, J.P.M., R.S., A.B.W., I.A.W., and J.-P.J. This does not alter our adherence to all *Science* policies on sharing data and materials.

SUPPLEMENTARY MATERIALS

www.sciencemag.org/content/349/6244/aac4223/suppl/DC1
Figs. S1 to S10
Tables S1 to S4
References (*62*, *63*)

24 April 2015; accepted 5 June 2015
Published online 18 June 2015;
10.1126/science.aac4223

RESEARCH ARTICLE SUMMARY

IMMUNOLOGY

An interactive reference framework for modeling a dynamic immune system

Matthew H. Spitzer,*† Pier Federico Gherardini,* Gabriela K. Fragiadakis, Nupur Bhattacharya, Robert T. Yuan, Andrew N. Hotson, Rachel Finck, Yaron Carmi, Eli R. Zunder, Wendy J. Fantl, Sean C. Bendall, Edgar G. Engleman,‡ Garry P. Nolan†‡

INTRODUCTION: Immune cells constitute an interacting hierarchy that coordinates its activities according to genetic and environmental contexts. This systemically mobile network of cells results in emergent properties that are derived from dynamic cellular interactions. Unlike many solid tissues, where cells of given functions are localized into substructures that can be readily defined, the distribution of phenotypically similar immune cells into various organs complicates discerning any modest differences between them. Over decades of investigation into immune functions during health and disease, research has necessarily focused on understanding the individual cell types within the immune system, and, more recently, toward identifying interacting cells and the messengers they use to communicate.

RATIONALE: Methods of single-cell analysis, such as flow cytometry, have led the effort to enumerate and quantitatively characterize immune cell populations. As research has accelerated, our understanding of immune organization has surpassed the technical limitations of fluorescence-based flow cytometry. With the advent of mass cytometry, which enables measuring significantly more features of individual cells, most known immune cell types can now be identified from within a single experiment. Leveraging this capability, we set out to initiate an immune system reference framework to provide a working definition of immune organization and enable the integration of new data sets.

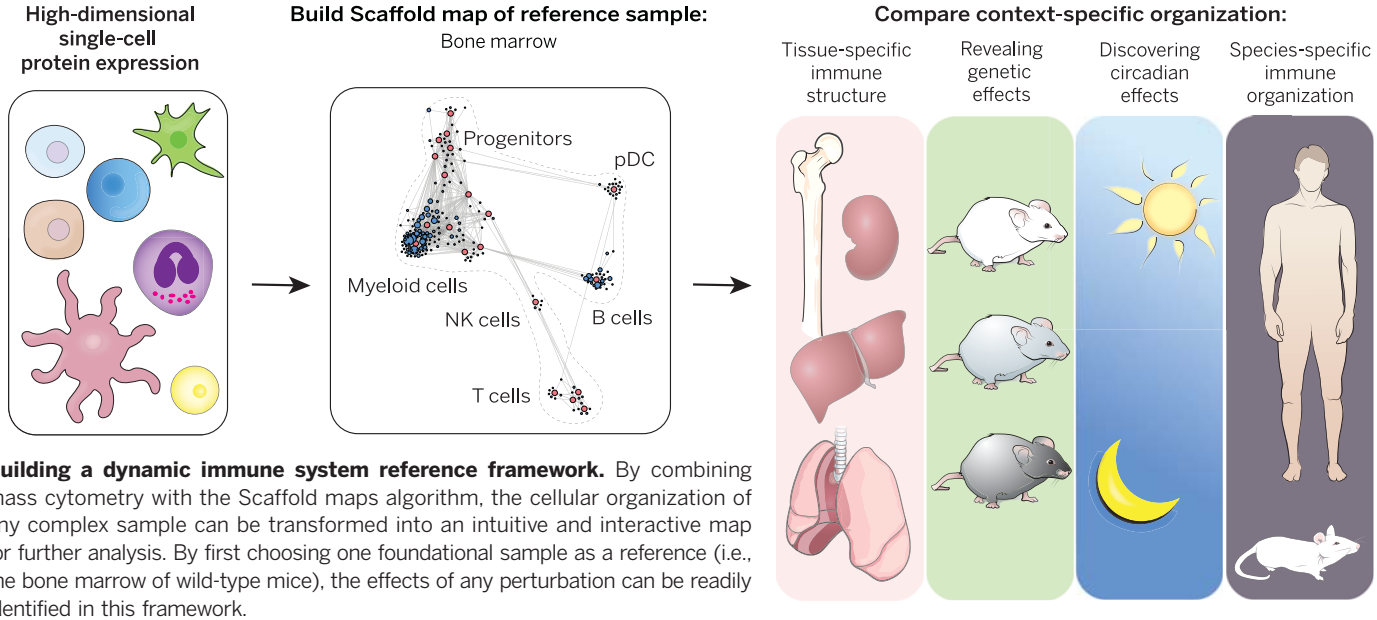
RESULTS: To build a reference framework from mass cytometry data, we developed a novel algorithm to transform the single-cell data into intuitive maps. These Scaffold maps provide a data-driven interpretation of immune organization while also integrating conventional immune cell populations as landmarks to orient the user. By applying Scaffold maps to data from the bone marrow of wild-type C57BL/6 mice, the method reconstructed the organization within this complex developmental organ. Using this sample as a reference point, the unique organization of immune cells within various organs across the body was revealed. The maps recapitulated canonical cellular phenotypes while revealing reproducible, tissue-specific deviations. The approach revealed influences of genetic variation and circadian rhythms on immune structure, permitted direct comparisons of murine and human blood cell phenotypes, and even enabled archival fluorescence-based flow cytometry data to be mapped onto the reference framework.

CONCLUSION: This foundational reference map provides a working definition of systemic immune organization to which new data can be integrated to reveal deviations driven by genetics, environment, or pathology. Beyond providing an analytical framework to understand immune organization from the unified data set generated here, the approaches we describe can serve as a data repository for collating experimental data from the research community, including gene expression and mutational analysis. Efforts that characterize cellular behavior in this open-source approach will continue to improve upon the initiating reference presented here to reveal the inherent structure in biological networks of immunity for clinical benefit. ■

ON OUR WEB SITE

Read the full article at http://dx.doi.org/10.1126/science.1259425

The list of author affiliations is available in the full article online.
*These authors contributed equally to this work.
†Corresponding author. E-mail: gnolan@stanford.edu (G.P.N.); matthew.spitzer@stanford.edu (M.H.S.)
‡These authors contributed equally to this work.
Cite this article as M. H. Spitzer *et al.*, *Science* **349**, 1259425 (2015). DOI: 10.1126/science.1259425



Building a dynamic immune system reference framework. By combining mass cytometry with the Scaffold maps algorithm, the cellular organization of any complex sample can be transformed into an intuitive and interactive map for further analysis. By first choosing one foundational sample as a reference (i.e., the bone marrow of wild-type mice), the effects of any perturbation can be readily identified in this framework.

Downloaded from www.sciencemag.org on July 10, 2015

RESEARCH ARTICLE

IMMUNOLOGY

An interactive reference framework for modeling a dynamic immune system

Matthew H. Spitzer,[1,2,3]*† Pier Federico Gherardini,[1]* Gabriela K. Fragiadakis,[1] Nupur Bhattacharya,[2] Robert T. Yuan,[2,3] Andrew N. Hotson,[1] Rachel Finck,[1] Yaron Carmi,[2] Eli R. Zunder,[1] Wendy J. Fantl,[4] Sean C. Bendall,[2,3] Edgar G. Engleman,[2,3]‡ Garry P. Nolan[1,3]†‡

Immune cells function in an interacting hierarchy that coordinates the activities of various cell types according to genetic and environmental contexts. We developed graphical approaches to construct an extensible immune reference map from mass cytometry data of cells from different organs, incorporating landmark cell populations as flags on the map to compare cells from distinct samples. The maps recapitulated canonical cellular phenotypes and revealed reproducible, tissue-specific deviations. The approach revealed influences of genetic variation and circadian rhythms on immune system structure, enabled direct comparisons of murine and human blood cell phenotypes, and even enabled archival fluorescence-based flow cytometry data to be mapped onto the reference framework. This foundational reference map provides a working definition of systemic immune organization to which new data can be integrated to reveal deviations driven by genetics, environment, or pathology.

The immune system is a systemically mobile network of cells with emergent properties derived from dynamic cellular interactions. Unlike many solid tissues, where cells of given functions are localized into substructures that can be readily defined, the distribution of phenotypically similar immune cells into various organs makes it difficult to discern differences between them. Much research has necessarily focused on understanding the individual cell types within the immune system, and, more recently, toward identifying interacting cells and the messengers they use to communicate. Methods of single-cell analysis, such as flow cytometry, have been at the heart of this effort to enumerate and quantitatively characterize immune cell populations (*1*–*3*). As research has accelerated, the number of markers required to identify cell types and explain detailed mechanisms has surpassed the technical limitations of fluorescence-based flow cytometry (*1*–*4*). Consequently, insights have often been limited because only a few cell subsets could be examined, independent of the immune system as a whole (*5*, *6*).

Although individual immune cell populations have been examined extensively, no comprehensive or standardized reference map of the immune system has been developed, primarily because of the difficulty of data normalization and lack of coexpression measurements that would enable "merging" of results. In other analysis modalities, such as transcript profiling of cell populations, reference standards and minable databases have shown extraordinary utility (*7*–*14*). A comprehensive reference map defining the organization of the immune system at the single-cell level would similarly offer new opportunities for organized data analysis. For example, macrophages exhibit tissue-specific phenotypes (*15*), and adaptive immune responses are influenced by genetics (*16*), but discerning these properties of immune organization required integrating the results of many disparate studies. Even current analytical tools that do provide a systems-level view do not compare new samples to an existing reference framework, making them unsuitable for this objective (*17*, *18*). In contrast, a reference map that is extensible could provide a biomedical foundation for a systematized, dynamic, community-collated resource to guide future analyses and mechanistic studies.

We leveraged mass cytometry, a platform that allows measurement of multiple parameters simultaneously at the single-cell level, to initiate a reference map of the immune system (*19*–*21*). By combining the throughput of flow cytometry with the resolution of mass spectrometry, this hybrid technology enables the simultaneous quantification of 40 parameters in single cells. The use of mass cytometry allows fluorophore reporters to be replaced with isotopically pure, stable heavy metal ions conjugated to antibodies or affinity reagents (*22*). These reporter ions are then quantified by time-of-flight mass spectrometry to provide single-cell measurements, enabling a more detailed characterization of complex cellular systems for a robust reference map.

An analytical framework for a reference map

A useful reference map should enable a data-driven organization of cells and should be flexible enough to accommodate different types of measurements. This would result in a map that has underlying consistency but is also robust enough to allow overlay of new data (or even of archival data from different measurement modalities) according to cell similarities. The approach is meant to provide templates for representing the system as a whole to enable systems-level comparisons, similar to other efforts to compare biological networks (*23*–*28*). Although we provide one template here, the framework is built to enable users to construct individualized or community-organized versions.

Building a reference map requires the ability to overlay data from multiple samples onto one or more foundational reference samples; this ability is not accommodated by algorithms such as SPADE and viSNE, which necessitate incorporating data from all samples at the onset (*17*, *18*). Without this feature, the reference map would not be an extensible solution. Moreover, the reference map ought to incorporate information about millions of individual cells to comprehensively represent the numerous cell types within complex samples, which remains beyond the capacity of other approaches (*18*). The mapping procedure should also enable users to implement one of the many available clustering algorithms or their own subjective definitions to determine cell groupings (*29*). Perhaps most important, positions of landmark cell populations are marked as flags on the map to allow users to compare cells in new samples to cells described in the existing literature (*30*).

Force-directed graphs are a type of graphical model commonly used to spatially organize complex data in an intuitive and flexible manner (*31*). Force-directed graphs also enable a method for grouping cells with similar features in a space that is defined by the molecular features of the individual cells (*32*). Force-directed approaches are based on a set of "forces" that guide data organization into, usually, a two-dimensional (2D) plane (*33*, *34*). Nodes (in this case, groups of cells) that are similar are connected by edges with a length proportional to their resemblance (in our implementation, cosine similarity). These nodes are then spatialized into a graph: All nodes repel one another as if they were the same poles of magnets, but edges pull similar nodes together, acting like springs. We adapted this concept to build a new method to visualize complex cellular samples, termed Scaffold (single-cell analysis by fixed force- and landmark-directed) maps.

Scaffold maps enable a model to be built that incorporates prior knowledge from the literature but also allows the discovery and analysis of unanticipated cell types or behavioral states.

[1]Baxter Laboratory in Stem Cell Biology, Department of Microbiology and Immunology, Stanford University, Stanford, CA 94305, USA. [2]Department of Pathology, Stanford University, Stanford, CA 94305, USA. [3]Program in Immunology, Stanford University, Stanford, CA 94305, USA. [4]Department of Obstetrics and Gynecology, Division of Gynecologic Oncology, Stanford University, Stanford, CA 94305, USA.
*These authors contributed equally to this work. †Corresponding author. E-mail: gnolan@stanford.edu (G.P.N.); matthew.spitzer@stanford.edu (M.H.S.) ‡These authors contributed equally to this work.

Such an extensible map can allow for new data sets to be incorporated and linked to their mechanistic conclusions with references—as do transcriptomics or genomics databases (*7*, *11*, *13*, *14*).

Systematic analysis for an immune reference map

We initiated a prototype high-resolution reference map of the murine immune system by characterizing the expression of 39 cell surface proteins and transcription factors (selected to delineate immune cell types) on more than 3×10^7 single cells from 10 different anatomical locations (fig. S1A, table S1, and Materials and Methods). Single-cell suspensions from the bone marrow, blood, spleen, skin-draining (inguinal) lymph node (SLN), mesenteric lymph node (MLN), thymus, lungs, liver, small intestine, and colon of 12-week-old male C57BL/6, Balb/c, and 129S1/Sv mice were simultaneously processed in replicate. Measurements were done under conditions that limited measuring error (*35*, *36*), and all antibodies were validated to bind target proteins by standard protocols. As such, one antibody cocktail was used for all samples, and cells were bar-coded and pooled by tissue before cell staining to minimize technical variability (Materials and Methods). Single-cell protein expression was quantified using a CyTOF mass cytometer (Fluidigm Corp., South San Francisco, CA). The data for these samples were normalized to account for variability in instrument sensitivity over time (*36*). Cells from each condition were subsequently identified by their bar code and written into a unique flow cytometry standard file for each sample (see acknowledgments for data distribution instructions).

Defining immune organization in the bone marrow

Because the bone marrow contains most developing and mature immune cell types, we used the cells therein to build a foundational map as a point of comparison (Fig. 1A). "Landmark" populations of immune cells commonly recognized in the literature were identified in the bone marrow data of all C57BL/6 replicates by conventional criteria (Fig. 1A and fig. S1B). These populations ranged from hematopoietic stem cells to terminally differentiated lymphocytes and myeloid cells and served as landmarks within the map (visualized by red nodes) to demarcate the location of cell populations of interest (Fig. 1A).

We also took a data-driven approach to group similar cells into "clusters" according to their expression of the measured proteins. Grouping similar cells by clustering allows all of the data to be visualized at once. We therefore performed an unsupervised clustering of the C57BL/6 bone marrow leukocytes from all biological replicates with a modified PAM (partitioning around medioids) algorithm adapted for larger data sets (Fig. 1A and Materials and Methods) (*37*). We chose a number of clusters (200) that we expect exceeds the number of "true" cell populations present in the data. Therefore, we do not expect each cluster to represent a recognized functional cell subset, but rather to overpartition the data to ensure that two populations of distinct natures are not merged through underclustering. We believe this to be an appropriate tradeoff, as the proximity of clusters immediately reveals groups of highly similar cells and thereby provides clarity during visualization. This enables an intuitive browsing of the data rather than relying on clustering to define the "true" number of cell populations, which depends on evolving semantic conventions and understandings of cellular functions. Manual analysis of cell populations by traditional criteria, which we visualized by landmark nodes, remains the standard against which automated clustering algorithms are routinely compared (*29*).

The reference map was built by combining these unsupervised cell clusters (blue nodes) with the manually identified cell populations (red nodes) (Fig. 1A). Cluster sizes were scaled to reflect the relative cell frequencies in these initial maps, although this option can be modified. A force-directed algorithm was applied to the data, attracting cell clusters with similar phenotypes while separating those with dissimilar phenotypes (Fig. 1A). When mapping C57BL/6 bone marrow cells (Fig. 1B), the landmark and unsupervised nodes were arranged (with no manual intervention or organization) into a structure that recapitulated most known developmental relations between these populations (Fig. 1C) (*17*, *20*). For instance, the hematopoietic stem cell (HSC) landmark was situated at the top of the map and linked to progenitors and more mature populations below. Different granulocytes (including neutrophils, eosinophils, basophils, and mast cells) occupied nearby portions of the map. Macrophages and conventional dendritic cells (cDCs) fell adjacent, and the various T cell populations [$CD4^+$, $CD8^+$, NKT (natural killer T), and γδ] grouped together.

Because clusters serve as a means of partitioning the data in this map, the density of clusters also reflected the relative frequencies of immune cells in the bone marrow that correspond to cell types as defined by established criteria (Fig. 1B, inset). For instance, the map exhibited the densest concentration of unsupervised clusters (blue nodes) surrounding the neutrophil, monocyte, and B cell landmarks. Rarer populations, such as dendritic cells, eosinophils, and basophils, were more sparsely represented. The progenitor zone contained cell clusters proximal to every multipotent population identified by established criteria with cell clusters also falling in between them, revealing the transition states between classically defined progenitors. This graph represents the data from all C57BL/6 biological replicates combined, although the data from individual mice consistently demonstrated these trends (fig. S2).

The Scaffold map of the bone marrow thus reflected the expected biological relations between immune cell populations and enabled an unsupervised visualization of its composition and complexity. The profiles of cells in any cluster, or any group of clusters, can also be visualized by conventional histograms. We used this as the initiating reference template and mapped other organs onto this map for comparison.

Mapping immune organization across the body

After determining that Scaffold maps effectively convey the organization of the immune cells present in the bone marrow, we determined how immune cells from other lymphoid organs or the blood might map into this space. By fixing the identity and position of the landmark (red) nodes that represent canonical populations in the bone marrow, we retained a common reference across all samples (Fig. 1A). We performed unsupervised clustering of total leukocytes from each tissue independently, and then overlaid these cell clusters (blue nodes) onto the reference map by allowing them to find their location according to the attractive and repulsive forces described above (Fig. 1A and Fig. 2).

By inspecting the composition of the peripheral blood on the map, it was apparent that the cell populations overlapped with those found in the bone marrow, as was evident by the proximity of unsupervised clusters to the landmarks (Fig. 2A). As expected, the blood did not contain cells localized to the HSC/progenitor portion of the map. Rather, cell clusters associated with landmark nodes of mature cell populations known to predominate in circulating blood at steady state, including granulocytes, monocytes, B cells, T cells, and NKT cells (figs. S3 and S4 and table S2). Because unsupervised cell clusters from the blood were positioned close to landmark populations, there were no substantial unanticipated populations present in the circulation.

In comparison, maps for the secondary lymphoid organs (spleen, SLN, MLN) all exhibited an immune landscape dominated by mature lymphoid cells of the T and B cell lineages (Fig. 2, B to D). Indeed, these populations were also comparable when viewed by conventional 2D dot plots (Fig. 2, B and C, inset). Many of the myeloid cells in these tissues mapped more closely to the macrophage and dendritic cell zones and expressed major histocompatibility complex (MHC) class II, used to present antigens, consistent with the presence of mature antigen-presenting cells (APCs) in these organs (Fig. 2, B to D) (*38*). The clusters from the secondary lymphoid organs also largely mapped near a landmark population, indicating that most cells found in these tissues belong to well-characterized populations. The subtle differences in the cellular organization of these organs become evident thorough investigation of their maps, revealing enrichment in NKT cells, monocytes, macrophages, and cDCs in the spleen relative to frequencies of those cells in lymph nodes [$P < 0.0001$ for each by analysis of variance (ANOVA)]. A higher frequency of macrophages ($P = 0.0006$ by two-sided t test) and lower frequency of cDCs ($P = 0.013$ by two-sided t test) were present in the SLN than in the MLN. An appreciation for the distinct cellular composition of different secondary lymphoid organs provides an opportunity to examine

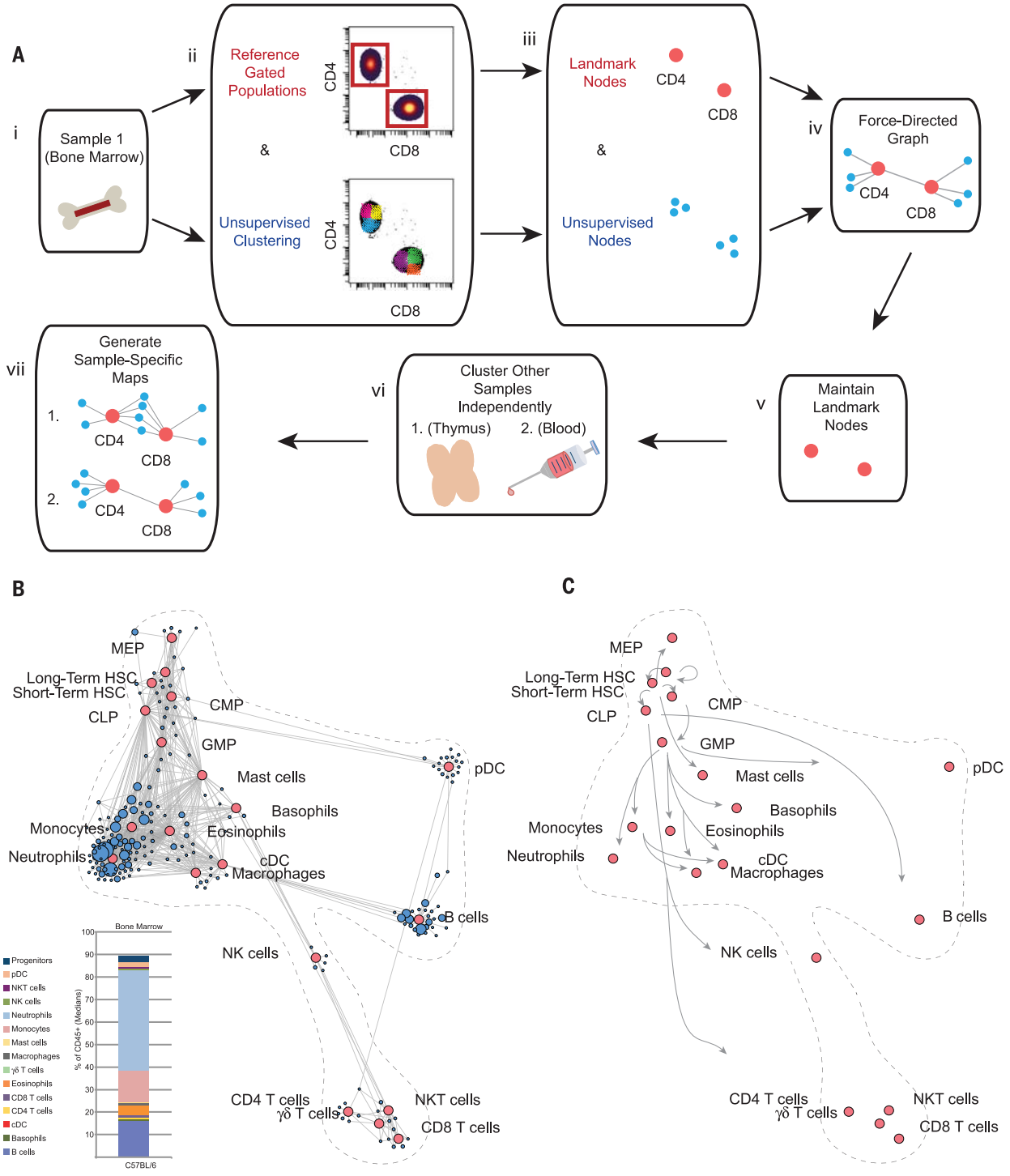


Fig. 1. Scaffold maps reveal immune organization of the bone marrow. (**A**) Schematic of the Scaffold map algorithm. (i) Bone marrow from C57BL/6 mice was chosen as the reference sample. (ii) Leukocytes were grouped according to prior knowledge to define landmark cell populations as reference points on the map. The same leukocytes were subjected to unsupervised clustering to provide an objective view of the tissue composition and organization. An illustration is provided with the two major lineages of mature T cells, which express either CD4 or CD8. (iii, iv) Both landmark populations (red nodes) and unsupervised clusters (blue nodes) were used to generate a force-directed graph in which similar nodes are located close together according to the similarity of their protein expression. Thus, similar nodes fall in proximity to one another while disparate nodes segregate apart from one another. Size of unsupervised clusters denotes the relative number of cells in that grouping. (v) Landmark populations from the bone marrow were fixed in place for subsequent maps to provide points of reference for rapid human interpretation. (vi) Additional samples were each subjected to unsupervised clustering via the same clustering algorithm. (vii) The resulting clusters for each sample were overlaid onto the original landmark nodes to generate tissue-specific Scaffold maps. (**B**) Bone marrow Scaffold map for C57BL/6 mice. Red nodes denote landmark manually gated cell populations; blue nodes represent unsupervised cell clusters from the same data. Inset: median frequencies of cell populations defined by conventional criteria from the bone marrow of C57BL/C mice, $n = 14$. (**C**) Scaffold map showing only the position of the landmark nodes with arrows annotating established maturation relationships in hematopoietic development.

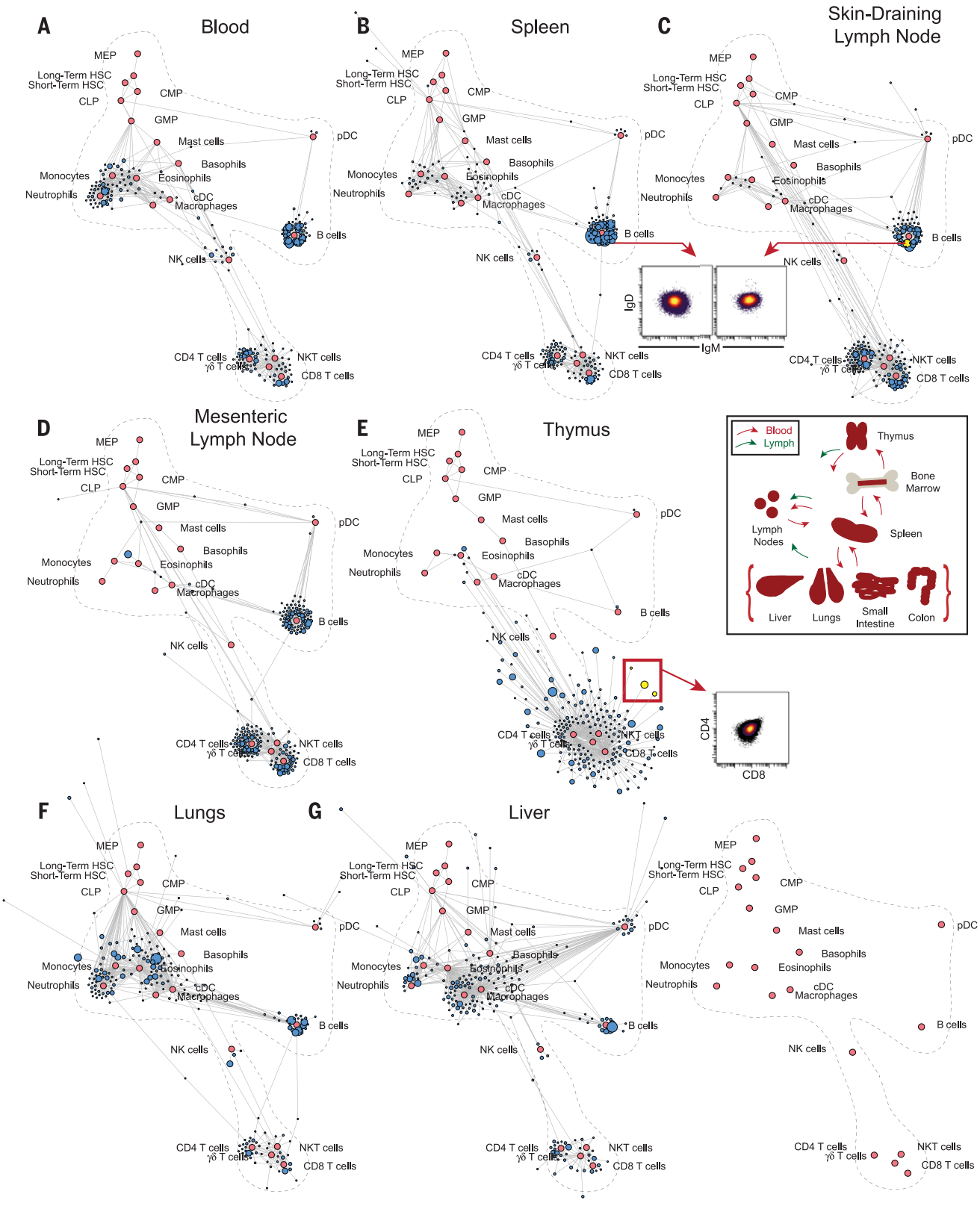


Fig. 2. Mapping systemic immune organization by tissue. Scaffold maps for lymphoid organs and peripheral solid organs from C57BL/6 mice, using bone marrow as the reference sample to define landmark nodes (red): (**A**) blood, (**B**) spleen, (**C**) skin-draining (inguinal) lymph node (SLN), (**D**) mesenteric lymph node (MLN), (**E**) thymus, (**F**) lungs, (**G**) liver; $n = 14$ for each organ. Insets, from top to bottom: Cells comprising B cell clusters from the spleen and SLN were visualized by 2D scatter plot. Immune cell circulation through and within the tissues was characterized by mass cytometry. Cells comprising a deviant thymic T cell population cluster were visualized by 2D scatterplot.

how each cellular environment shapes the immune responses initiated in these locations.

Many of the cell clusters in the thymus radiated far away from the landmarks on the map. Inspection of these clusters indicated that many comprised $CD4^+CD8^+$ double-positive (DP) T cells that were absent from the bone marrow (Fig. 2E, red arrow). As the thymus largely contains developmental T cells, this was expected. However, the increased length of the lines connecting these ubiquitous DP T cell clusters to their nearest landmarks denotes cells that deviate from the characterized reference. We also observed these trends when cell populations from the spleen were used to define landmarks (fig. S5).

Immune cell subsets in peripheral solid organs were compared to the reference map of the bone marrow (Fig. 2, F and G, and fig. S6). The region of the maps representing myeloid cells was, in general, more densely filled (figs. S3 and S4). For instance, cells from the lungs exhibited many clusters distributed among the macrophage, cDC, and eosinophil landmarks, indicating that cells in this tissue were phenotypically distinct from those in bone marrow and even spleen. Alveolar macrophages in the lung expressed the proteins CD11c and Siglec-F, which are canonically markers of cDCs and eosinophils, respectively (Fig. 2F) (*39*). Similarly, the liver map exhibited many clusters connected to the macrophage landmark, although the length of the lines connecting them was longer than those for the macrophages in the bone marrow ($P = 0.0004$ by one-sided Wilcoxon rank sum test; see Materials and Methods), consistent with the unique characteristics of liver macrophages (Kupffer cells) (Fig. 2G) (*40*). Overall, these maps of peripheral solid organs, including the gut (fig. S6), exhibited less fidelity than those of lymphoid organs to the bone marrow reference, indicating that immune cells in these sites are likely distinct in their phenotypes and functions. Several previously uncharacterized cellular phenotypes are listed in table S3. For future studies, cell populations present in any tissue could also be used to define landmarks for organ-specific maps. Moreover, a comparative analysis of immune organization within the gut revealed site-specific characteristics, with significantly lower frequencies of CD4 and CD8 T cells and higher frequencies of macrophages and cDCs in the colon than in the small intestine ($P = 2.8 \times 10^{-15}$, $P = 0.001$, $P = 9.4 \times 10^{-7}$, and $P = 1.0 \times 10^{-5}$, respectively, by one-sided t test; fig. S6). This understanding will inform further investigations of immune responses and pathologies within regions of the gut.

Genetic variation affects immune cell composition and phenotype

We used the reference maps to reveal the impact of genetic diversity on immune cell phenotypes and organization. We generated Scaffold maps of immune cells from two common inbred mouse strains, 129S1/Sv and Balb/c (Fig. 3). Mapping cells from the bone marrow from these animals onto the C57BL/6 reference map revealed that the vast majority of clusters fell close the C57BL/6 landmarks (Fig. 3, A and B). However, certain cell clusters were distinct from those in the C57BL/6 reference. This likely reflects genetic variability, such as the relative lack of T cells in Balb/c mice, which we confirmed by conventional analysis of T cell populations (CD4 T cells, $P = 0.0007$; CD8 T cells, $P = 0.001$; γδ T cells, $P = 2.2 \times 10^{-7}$; NKT cells, $P = 6.2 \times 10^{-8}$ by ANOVA).

Similarly, analysis of the maps for lymphoid organs from these strains demonstrated high fidelity between unsupervised clusters and landmarks, with enrichment for mature lymphocytes. Other cell types in these organs also reflected the underlying genetics, such as pDC and NKT cells, which were overrepresented in the SLN of Balb/c mice ($P = 1.2 \times 10^{-6}$ and $P = 7.5 \times 10^{-8}$, respectively, by ANOVA) (Fig. 3, C and D, fig. S2, and table S2). In contrast, the SLN in C57BL/6 mice contained significantly more cDCs and NKT cells but fewer CD4 T cells than did the SLN from the other strains ($P = 5.0 \times 10^{-5}$, $P = 2.9 \times 10^{-7}$, and $P = 5.5 \times 10^{-10}$, respectively, by ANOVA). Analysis of peripheral solid organs revealed other apparent impacts of genetic variation. In the liver, an unexpected shift in cell density from the macrophage to the cDC landmark was observed only in 129S1/Sv mice. Further investigation of these cells demonstrated differential expression of CD64 and MHC II in liver macrophages from these inbred strains, causing these cells to adopt a phenotype more similar to that of cDCs (Fig. 3, E and F, red arrows). The difference in CD64 staining could be attributable to a polymorphism in the gene expressed by 129S1/Sv mice (*41*). However, this difference in MHC II expression was not observed when comparing macrophages in other solid organs, suggesting that this disparity is specific to the liver.

These results illustrate the ability of Scaffold maps to highlight sample-specific differences in immune cell characteristics. These maps convey a common global structure of immune cell populations along with specific influences of genetic variance.

Circadian influences on immune organization

To investigate circadian immune fluctuations, which can powerfully regulate immune system behavior (*42*, *43*), we obtained organs from C57BL/6 mice in four batches, either in the morning (8 to 9 a.m.; Zeitgeber time 1 to 2) or afternoon (1 to 2 p.m.; Zeitgeber time 6 to 7) of two consecutive days.

Analysis of the maps revealed a number of cell populations that fluctuated according to the time of day. Unexpectedly, these were significantly more pronounced in the peripheral solid organs than in the lymphoid tissues. The lungs displayed clear circadian patterns with remodeling of the ratios for several immune cell populations (Fig. 4A). To validate these findings, we used fluorescence-based flow cytometry to investigate the composition of the lungs in a new cohort of animals. In both analyses, the frequencies of CD8 T cells and B cells were significantly higher in the afternoon than in the morning (Fig. 4B). In contrast, the frequency of macrophages increased in the morning, revealing a compensatory shift in composition from myeloid to lymphoid cells (Fig. 4B). Scaffold maps in which cell populations from the lungs were used as the landmarks additionally recapitulated these results (fig. S7). Further investigation of the macrophage compartment by generating a population-specific, force-directed map revealed differential remodeling of alveolar and interstitial macrophages in a circadian manner (fig. S8A). Validation by conventional criteria corroborated that alveolar macrophages were more prevalent in the morning, whereas interstitial macrophages were increased in frequency in the afternoon (fig. S8, B and C). Thus, reference map analysis revealed a previously undetected influence of circadian rhythms on immune organization of peripheral organs that was particularly prominent in pulmonary lymphocytes and macrophages. The symptom severity of patients diagnosed with infectious or atopic lung pathologies (i.e., allergies, asthma, and viral pneumonias) fluctuates in a circadian manner (*44*, *45*). These results provide a potential explanation for these trends, as the lung-resident immune compartment undergoes circadian reorganization. This suggests that certain modes of antigen presentation could become exacerbated during different times of the day, or could indicate that nasally applied vaccines or therapeutics might have differing influences on immune function depending on the time of application.

Integrating human data into the reference map

Because immune cell types are well conserved between mice and humans, we analyzed human data overlaid onto the murine reference map (*46*). Mass cytometry data from whole peripheral blood from four healthy human donors was passed through the Scaffold map algorithm. We calculated distance between clusters on the basis of 15 cell surface markers that have similar cell subset expression patterns between humans and mice (Fig. 5, A to C). Differences between the species were apparent, such as the increased frequency of neutrophils and relative scarcity of B cells in human peripheral blood (*47*). However, the similar overlay pattern confirmed a common global structure of immunity. We also generated a map of murine blood using only the same 15 proteins to measure distance from the established landmarks (Fig. 5C). This similarity is not surprising. Gene expression networks in species as widely separated as humans and mice have strong similarities—even to the point of enabling drug screening based on gene network similarities (*48*). The human data were not normalized or differentially transformed in any manner, underscoring the robustness of the mapping approach. Efforts to generate a human-centric reference map may enable more detailed mapping of human immune organization, but these results

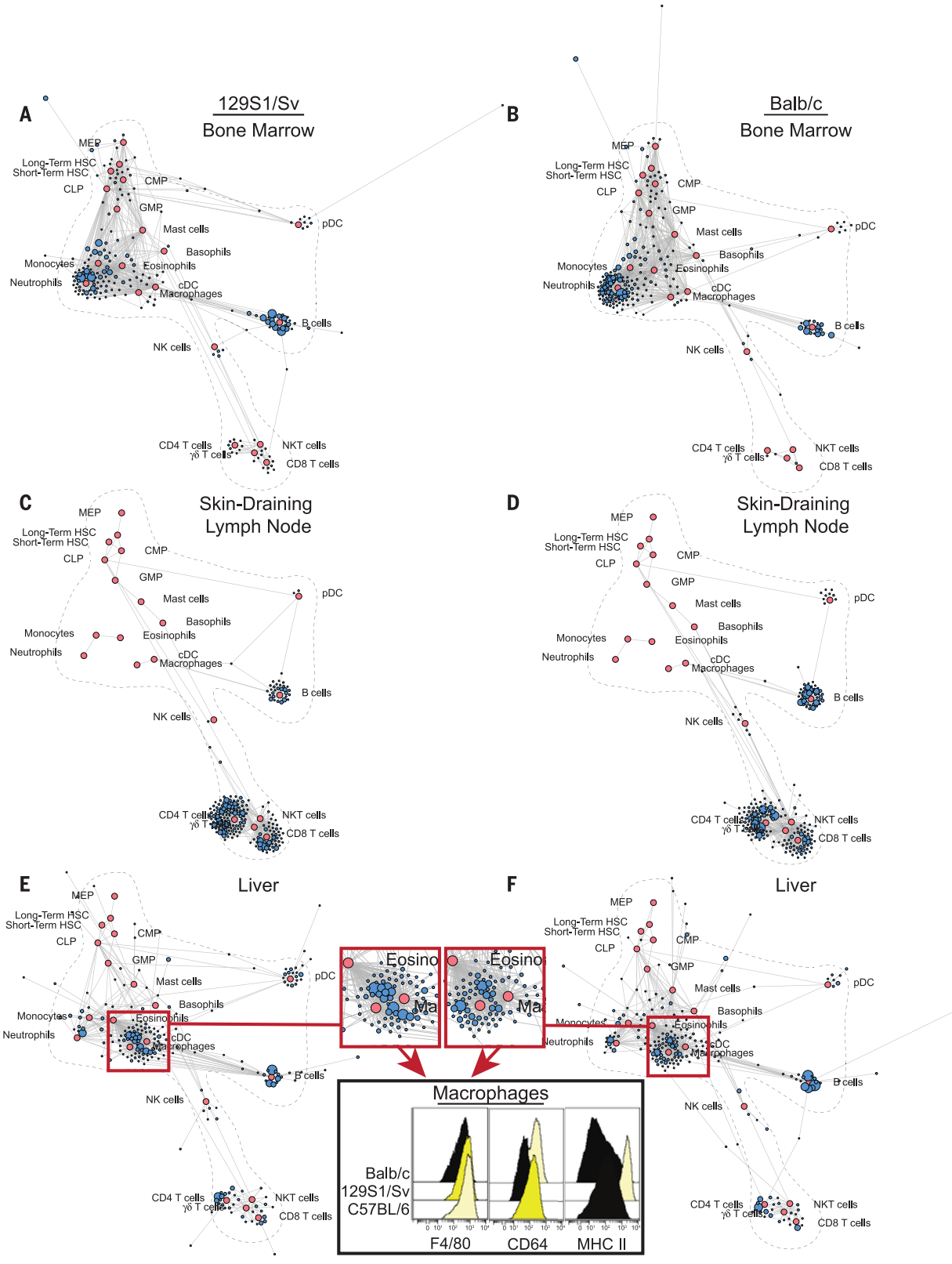


Fig. 3. Immune organization across inbred mouse strains. Scaffold maps for several tissues from 129S1/Sv and Balb/c mice, using C57BL/6 bone marrow as the reference sample to define landmark nodes (red): (**A**) bone marrow from 129S1/Sv mice, (**B**) bone marrow from Balb/c mice, (**C**) SLN from 129S1/Sv mice, (**D**) SLN from Balb/c mice, (**E**) liver from 129S1/Sv mice, (**F**) liver from Balb/c mice (n = 3 for each panel). Histograms of CD64 and MHC II expression on liver macrophages from representative mice of each strain.

demonstrate the feasibility of comparing cellular features across the species barrier.

Mapping archival data

The ability to map data from independent experiments would increase the utility of a reference map, creating a dynamic resource in which knowledge could accrue over time. Therefore, we mapped archival fluorescence-based flow cytometry data onto the reference map (Fig. 5, D to F). We used a previously published data set of bone marrow cells from C57BL/6 mice obtained with eight-color flow cytometry including lineage-specific markers [B220 for B cells, CD11b for myeloid cells, T cell receptor β chain (TCRβ) for T cells, CD4, and CD8 to distinguish the major types of mature T cells] as well as stem cell/progenitor markers [stem cell growth factor receptor (c-Kit), stem cell antigen 1 (Sca-1), and CD150] (*17*). We used only the information contained in these eight dimensions to calculate similarity (Fig. 5E). As a point of reference, we also generated a Scaffold map from the original mass cytometry data of the C57BL/6 bone marrow using these same eight dimensions (Fig. 5F).

Cells from the fluorescence data occupied the major regions of the Scaffold map with frequencies similar to those in the original reference. Moreover, the maps generated from both fluorescence and mass cytometry data using the same eight dimensions exhibited strong similarity, suggesting that the underlying structure of the system remained the primary driver of the layout organization. Cell populations for which no unique markers exist and for which complex combinations of markers define cell types (such as the different myeloid cell subsets) exhibited lower resolution on the map, and as such, they are grouped in the center of several landmark nodes. Thus, although the specific selection of measured features affects the ability to discriminate between similar cell populations, even a few key parameters can drive cell clusters toward cognate known reference cell subsets within the map.

A cross-sectional view of cellular compartments

It would be useful to reveal in detail the local structure of cell subsets that lack preexisting landmarks, so as to enable characterization of similarities and deviations. Having identified distinctions within given cell subsets across anatomical locations, we used unsupervised force-directed graphs (lacking landmark populations) to organize cells of a given cell type (T cells or dendritic cells, for instance) defined by traditional criteria such that differences between them would become apparent (Fig. 6). Each major cell population from every tissue was clustered and mapped together into force-directed graphs, resulting in a phenotypic landscape for that given cell type. As noted, manually defined landmarks were omitted, although they could be defined in subsequent analyses as desired by the user. Cell

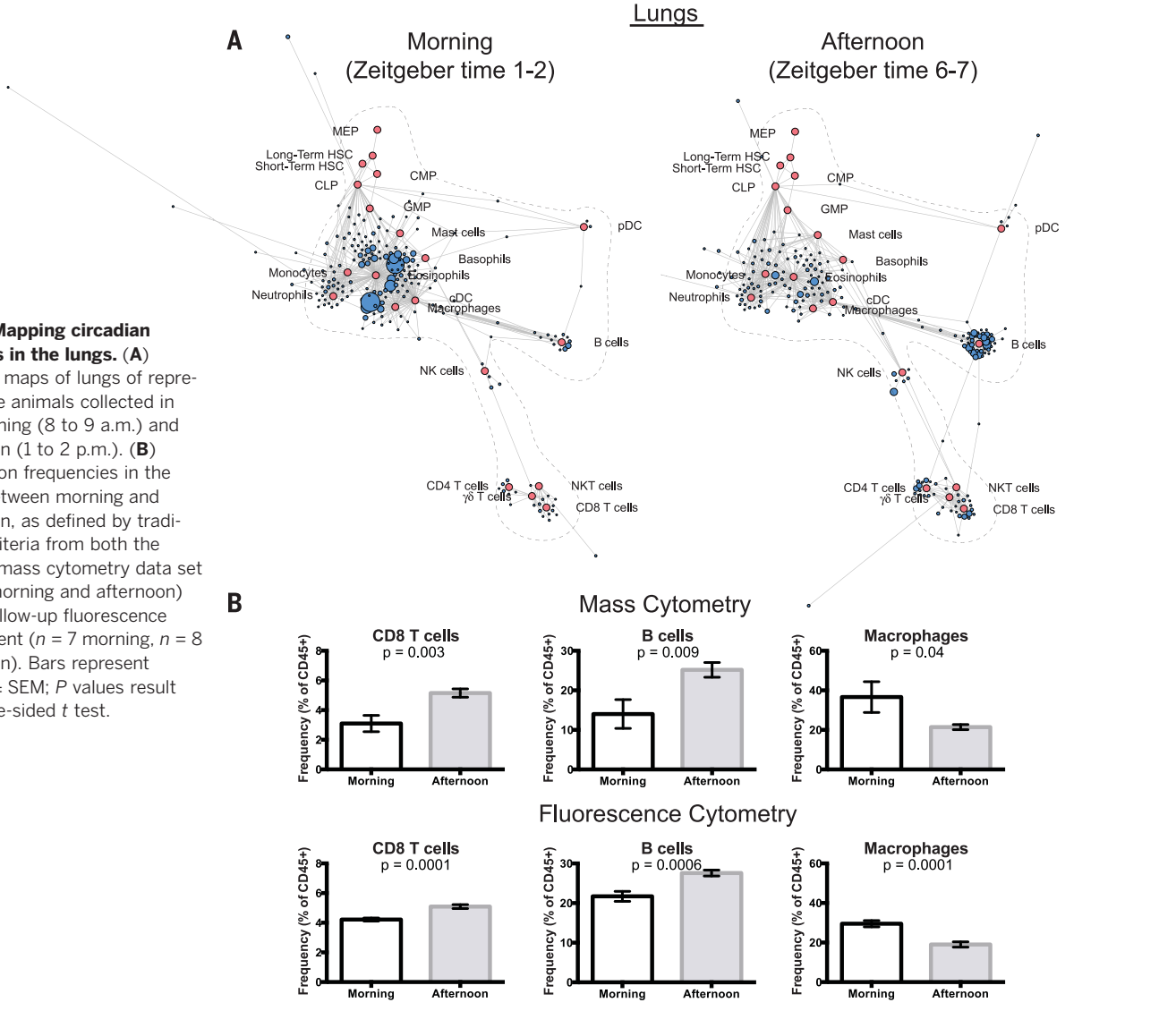


Fig. 4. Mapping circadian changes in the lungs. (**A**) Scaffold maps of lungs of representative animals collected in the morning (8 to 9 a.m.) and afternoon (1 to 2 p.m.). (**B**) Population frequencies in the lungs between morning and afternoon, as defined by traditional criteria from both the original mass cytometry data set (n = 7 morning and afternoon) and a follow-up fluorescence experiment (n = 7 morning, n = 8 afternoon). Bars represent means ± SEM; P values result from one-sided t test.

clusters were colored according to their tissue of origin to reveal how each tissue is represented within the global similarity map for each cell type. Scaling each cluster proportionally to the percentage of total leukocytes represented the relative frequency of cells in each cluster.

We began by examining the landscape of T cells across the body, as T cells are well known to exhibit organ-specific properties. The mapping shows that a large group of cell clusters was exclusively located in the thymus and expressed both CD4 and CD8, characteristic of developmental double-positive (DP) T cells (Fig. 6A, fig. S9, and table S4). The T cell map then showed two predominant branches characterized by CD4 (left) or CD8 expression (right), which were bridged by smaller clusters lacking high expression of either. Some of these cell clusters expressed the γδ TCR (Fig. 6A, inset). Others expressing TCRβ were localized to the gut and

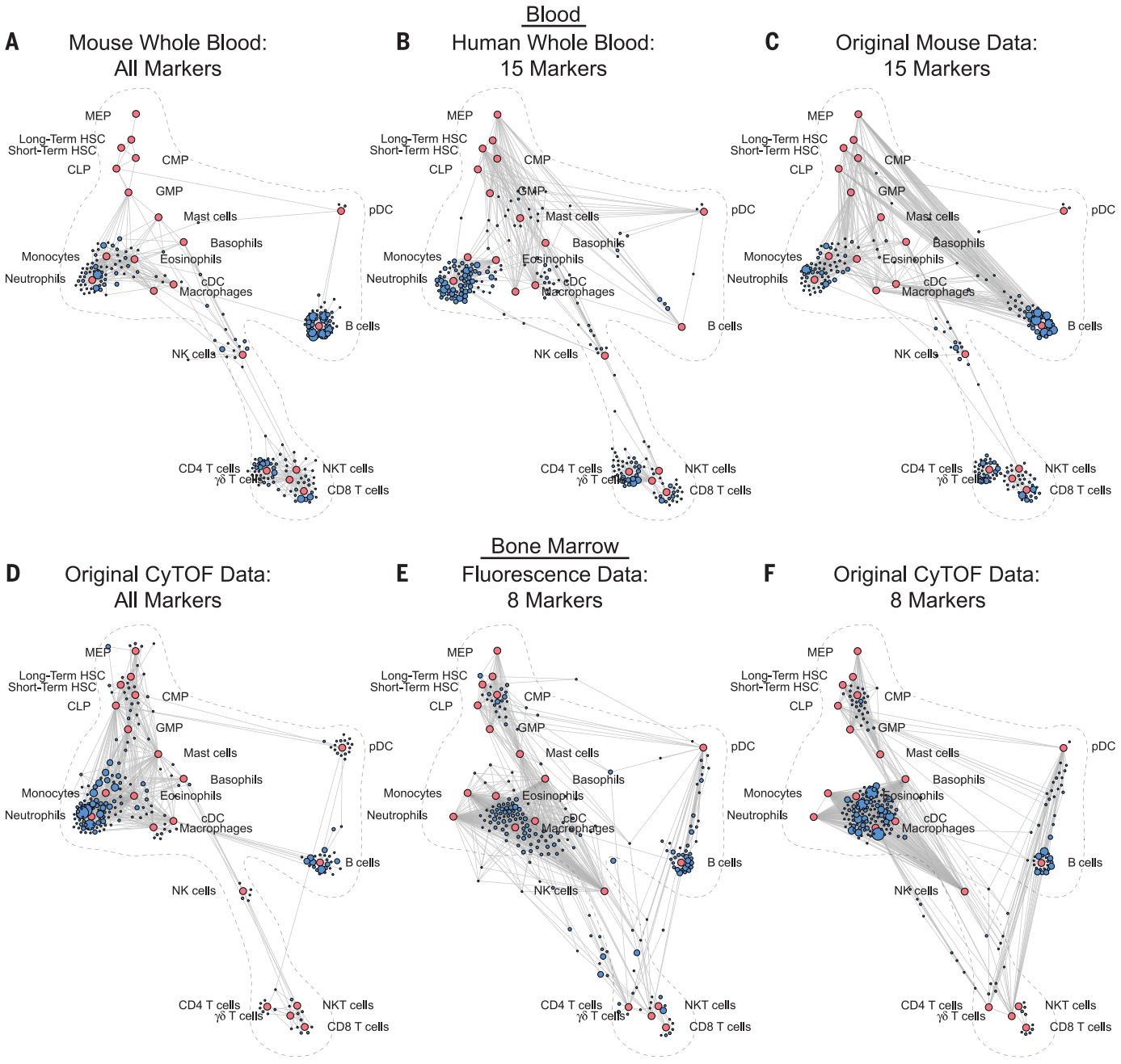


Fig. 5. Mapping human and archival data onto the reference map. (**A**) Original mass cytometry whole-blood Scaffold map from C57BL/6 mice, $n = 14$. (**B**) Scaffold map of human whole blood interrogated by 15-parameter mass cytometry with distance measured using only those 15 dimensions for layout of unsupervised clusters onto the reference. Human parameters were assigned to murine correlate markers with similar cellular distribution, including canonical surface markers used for identification of cell populations by conventional criteria as well as several orthologous proteins, $n = 4$. (**C**) Scaffold map of original murine blood mass cytometry data with distance measured using only the same 15 dimensions for layout of unsupervised clusters onto the reference. (**D**) Original mass cytometry bone marrow Scaffold map from C57BL/6 mice. (**E**) Scaffold map of C57BL/6 bone marrow interrogated by eight-color fluorescence-based flow cytometry from a previously published data set (*17*) with distance measured using only those eight dimensions (B220, CD11b, TCRβ, CD4, CD8, c-Kit, Sca-1, CD150) for layout of unsupervised clusters onto the reference. (**F**) Scaffold map of original mass cytometry data with distance measured using only the same eight dimensions for layout of unsupervised clusters onto the reference.

lungs, likely representing recently described mucosa-associated invariant T (MAIT) cells (fig. S9 and table S4) (*49*). Among the $CD4^+$ and $CD8^+$ T cells expressing the αβ TCR, further divisions were driven by CCR7, CD27, and CD44, which are common markers that distinguish differentiation states (fig. S9 and table S4) (*50*). The tissue distribution of these subsets appeared skewed, with enrichment of effector and memory T cells in the peripheral solid organs. A group of $CD4^+$ αβ T cell clusters expressed CD25 and forkhead box P3 (Foxp3), characteristic of regulatory T cells, and were overrepresented in the gut (fig. S9 and table S4).

Whereas T cells demonstrate a largely bifurcated set of phenotypes with "bridging" cell subsets, the B cell landscape was markedly different, exhibiting a continuum of phenotypes in tissues distributed across the body (Fig. 6B). Although B cells in the bone marrow exhibited a wide range of phenotypes reflecting developmental

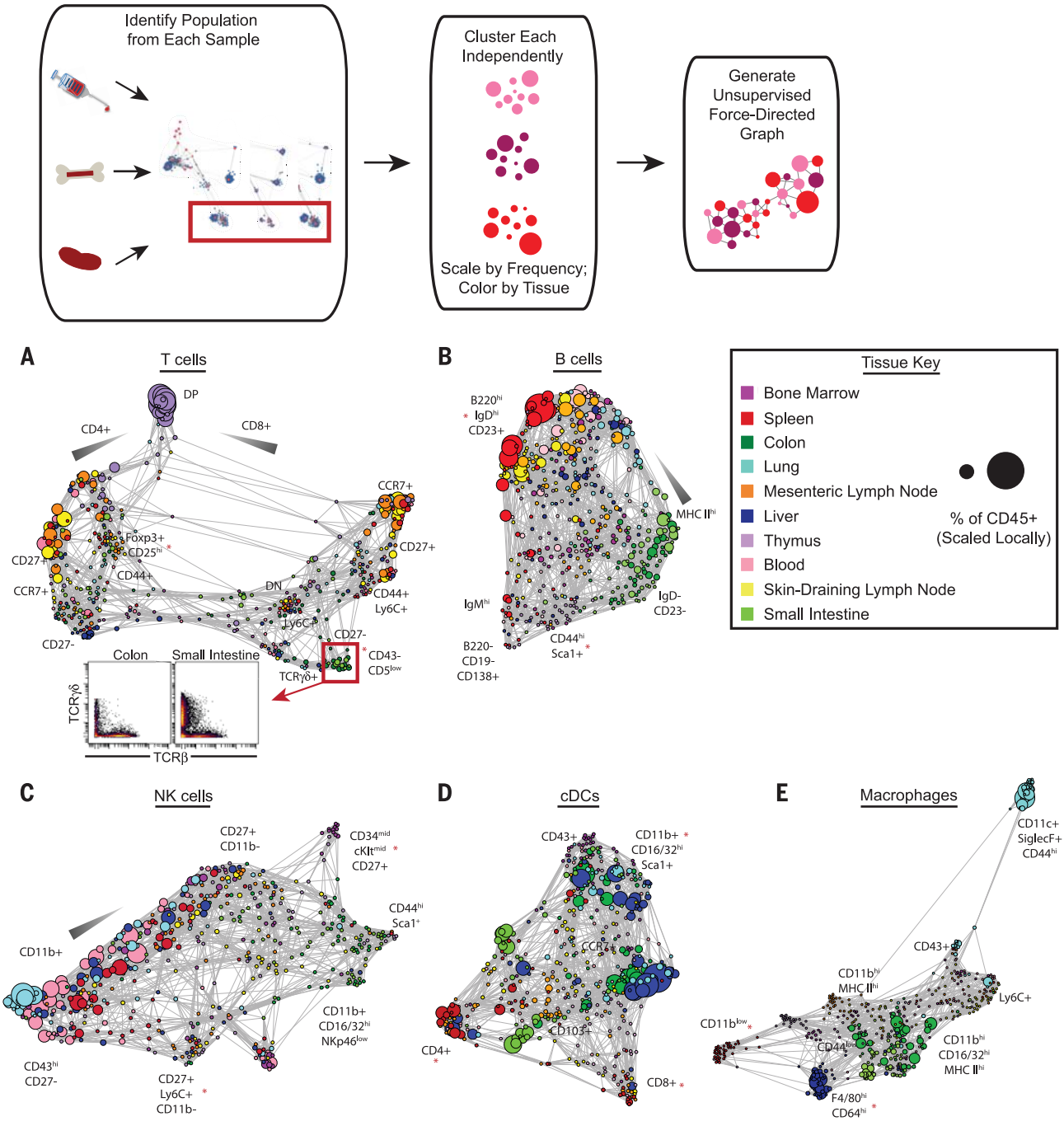


Fig. 6. Defining the landscape of immune cell populations. Population-specific landscapes were generated as follows: Cell populations were manually gated, subjected to unsupervised clustering, and laid out in an unsupervised force-directed graph. Clusters are colored according to tissue of origin and sized by the number of cells in each cluster as a percentage of the total number of leukocytes in the tissue of origin. Each plot is scaled independently. (**A**) T cell landscape including $CD3^+$ cells. Cells comprising T cell clusters from the colon and small intestine falling within the red box are visualized by 2D scatterplot, $n = 14$. (**B**) B cell landscape including $B220^+$ and $CD138^+$ cells, $n = 14$. (**C**) NKT cell landscape including $CD49b^+$ cells, $n = 14$. (**D**) cDC landscape including $CD11c^{hi}$ MHC II^{hi} cells, $n = 14$. (**E**) Macrophage cell landscape including $CD64^+$ $F4/80^+$ cells, $n = 14$. Lineage markers are defined in Materials and Methods.

stages, those in the secondary lymphoid organs expressed higher amounts of B220 and CD19 (a cell surface co-receptor expressed by most mature B cells) with variable expression of the B cell receptor isotypes IgM, IgD, and CD23 [the low-affinity immunoglobulin E (IgE) receptor] (fig. S10 and table S4). The majority in peripheral solid organs exhibited reduced amounts of IgD and CD23 with increased MHC II (fig. S10 and table S4) (*51*). Many thymic B cells exhibited a unique phenotype, characterized by the extracellular matrix receptor CD44 and Sca-1, and mapped near the plasma cells, which express CD138 (fig. S10 and table S4). Thus, the B cell landscape was characterized by a phenotypic continuum with enrichment of specific phenotypes according to tissue of residence.

The NKT cell landscape was predominantly organized by expression of CD11b and CD27, which delineate NKT cell maturation stages (Fig. 6C, fig. S11, and table S4) (*52*). A discrete population of NKT cells expressing higher levels of developmental markers CD34 and cKit (CD117) was found in the bone marrow (fig. S11 and table S4). In the peripheral solid organs, large populations of NKT cells were present in the liver and lung with fewer in the gut. A group of NKT cells with broad tissue distribution expressed Ly6C, which has been associated with NKT cell memory (fig. S11 and table S4) (*53*). These results recapitulate the known landscape of lymphoid cell biology and provide new insights regarding immune organization across the body according to the tissues in which the immune cells reside (table S4).

Definitive statements regarding myeloid phenotypes and their functions remain a matter of interest (*54*, *55*) and occasional contention (*56*). For instance, examining the cDC landscape revealed several subgroups, some of which expressed CD4 or CD8; their expression was mutually exclusive, and these cell types were overrepresented in the secondary lymphoid organs (Fig. 6D). Several of the thymic cDC clusters expressed CD8, a feature characteristic of cross-presenting DCs, which may reflect their need to present intracellular antigens in the context of both MHC I and II to promote T cell tolerance (fig. S12 and table S4) (*57*). Many cDCs in peripheral solid organs and the bone marrow were $CD11b^{+}$ and expressed higher levels of Fcγ receptors (CD16/CD32), which suggests that they may be more sensitive to antibody-mediated activation (fig. S12 and table S4).

The macrophage landscape exhibited distinct segregation by location, consistent with their tissue-specific homeostatic functions and self-renewal (Fig. 6E) (*15*). Relative to macrophages present in the SLN and MLN, which exhibited high expression of the CD11b integrin and MHC II, red-pulp macrophages in the spleen expressed significantly less CD11b (fig. S13 and table S4). The macrophages in the gut exhibited the highest expression of MHC II and Fcγ receptors (CD16/CD32), which might reflect a greater capacity to present antigen to CD4 T cells or sensitivity to activation via antibodies (fig. S13 and table S4). Macrophages in the liver (Kupffer cells) expressed the highest levels of F4/80 and CD64, whereas alveolar macrophages in the lung segregated far away, as judged by their high expression of the CD11c integrin, the Siglec-F lectin, and CD44 (fig. S13 and table S4).

Thus, the force-directed graphical landscapes enabled rapid identification of the features that distinguish each population across the samples of interest, providing a model for characterizing the predominant differences among multiple conditions.

Conclusions

We exploited the increased parameterization afforded by mass cytometry to generate a consolidated, extensible reference map of the murine immune system with single-cell resolution. By assessing the composition and characteristics of immune populations throughout the body, this provides the basis for a systematic model of immune organization. Such an objective necessitated new analytical methods for comparing groups of complex cellular samples. Our visualization algorithm combines unsupervised clustering with cellular landmarks defined by prior knowledge. The resulting Scaffold maps enabled global characterization of the steady-state immune structure from different anatomical locations, genetic backgrounds, circadian time points, and species barriers. When compared to an unsupervised graph across the organismal immune system (fig. S14), the advantages of such a framework become apparent. The incorporation of landmarks assists in the interpretation of the graphical organization. They also provide the reference points for comparing data, enabling the unique features of new, uncharacterized samples to stand out by comparison to a characterized baseline sample. A reference map of this nature will be useful in additional iterations when merged with immunological perturbations such as infection, autoimmune disease, or cancer to identify how altered immune states deviate from the steady state.

Beyond providing an analytical framework to understand immune organization from the unified data set generated here, the approaches we describe can serve as a data repository for collating experimental data from the research community (fig. S15). This would provide several distinct benefits. First, users could mine the data included in these studies to investigate the characteristics and distribution of cell types of interest in a dynamic way. Second, user modification of defined parameters (such as the definition of landmark populations) could provide analyses of immune structure not biased by prior strictures.

Perhaps more urgent to the community at large, mapping of newly created data sets onto a reference structure will assist in global comparisons of archival animal experiments with clinical human data. Investigators can merge newly mapped data to compare cellular features across previously mapped features in the reference landscape. With the implementation of standard regression analysis, the presence or absence of given clinical outcomes due to certain immune configurations might be discerned—much as has been the case with accessible archival gene expression data sets (*9*). In one analysis, the expression of a newly discovered regulatory molecule from ongoing forward genetics efforts (*58*, *59*) could be defined in all immune cell types during health and disease. This could be achieved by measuring such a molecular feature by mass cytometry in addition to the proteins included here and mapping the resulting data. Alternatively, changes in metabolism or cell death programs within the global immune system during chronic inflammation or aging would be revealed, providing knowledge to inform the design of precise therapeutic strategies. Moreover, as the number of measurable parameters on a single-cell basis increases, the framework could easily be updated to reflect more detailed data sets.

Scaffold maps demonstrate the capacity to align data from distinct analysis platforms, including fluorescence-based flow cytometry, or across species of interest, such as the demonstration of mapping human immune data onto a murine framework. As the throughput of other single-cell analysis modalities, such as single-cell RNA sequencing (*60*, *61*), continues to develop, these data could also be incorporated into the map along with other metadata types such as publication records, clinical phenotypes, and other relevant assays analogous to other strategies for data integration (*62*, *63*). Therefore, this core infrastructure forms the basis for a centralized repository in which single-cell data can accrue over time, providing a unified reference map for understanding the organization and behavior of complex cellular systems. Efforts that characterize cellular behavior in this open-source approach will continue to improve upon the initiating reference presented here to reveal the inherent structure in biological networks of immunity for clinical benefit.

REFERENCES AND NOTES

1. H. R. Hulett, W. A. Bonner, J. Barrett, L. A. Herzenberg, Cell sorting: Automated separation of mammalian cells as a function of intracellular fluorescence. *Science* **166**, 747–749 (1969). doi: 10.1126/science.166.3906.747; pmid: 4898615
2. L. A. Herzenberg, L. A. Herzenberg, Toward a layered immune system. *Cell* **59**, 953–954 (1989). doi: 10.1016/0092-8674(89)90748-4; pmid: 2688900
3. S. C. Bendall, G. P. Nolan, M. Roederer, P. K. Chattopadhyay, A deep profiler's guide to cytometry. *Trends Immunol.* **33**, 323–332 (2012). doi: 10.1016/j.it.2012.02.010; pmid: 22476049
4. Y. Mahnke, P. Chattopadhyay, M. Roederer, Publication of optimized multicolor immunofluorescence panels. *Cytometry* **77A**, 814–818 (2010). doi: 10.1002/cyto.a.20916; pmid: 20722004
5. A. Aderem, L. Hood, Immunology in the post-genomic era. *Nat. Immunol.* **2**, 373–375 (2001). pmid: 11323684
6. D. E. Zak, V. C. Tam, A. Aderem, Systems-level analysis of innate immunity. *Annu. Rev. Immunol.* **32**, 547–577 (2014). doi: 10.1146/annurev-immunol-032713-120254; pmid: 24655298
7. T. S. P. Heng, M. W. Painter, The Immunological Genome Project: Networks of gene expression in immune cells. *Nat. Immunol.* **9**, 1091–1094 (2008). pmid: 18800157
8. V. Jojic *et al.*, Identification of transcriptional regulators in the mouse immune system. *Nat. Immunol.* **14**, 633–643 (2013). doi: 10.1038/ni.2587; pmid: 23624555
9. M. Sirota, A. J. Butte, The role of bioinformatics in studying rheumatic and autoimmune disorders. *Nat. Rev. Rheumatol.* **7**, 489–494 (2011). doi: 10.1038/nrrheum.2011.87; pmid: 21691330

10. A. Califano, A. J. Butte, S. Friend, T. Ideker, E. Schadt, Leveraging models of cell regulation and GWAS data in integrative network-based association studies. *Nat. Genet.* **44**, 841–847 (2012). doi: 10.1038/ng.2355; pmid: 22836096
11. Cancer Genome Atlas Research Network *et al*., The Cancer Genome Atlas Pan-Cancer analysis project. *Nat. Genet.* **45**, 1113–1120 (2013). doi: 10.1038/ng.2764; pmid: 24071849
12. M.-S. Kim *et al*., A draft map of the human proteome. *Nature* **509**, 575–581 (2014). doi: 10.1038/nature13302; pmid: 24870542
13. ENCODE Project Consortium, An integrated encyclopedia of DNA elements in the human genome. *Nature* **489**, 57–74 (2012). pmid: 22955616
14. J. Dutkowski *et al*., NeXO Web: The NeXO ontology database and visualization platform. *Nucleic Acids Res.* **42**, D1269–D1274 (2014). doi: 10.1093/nar/gkt1192; pmid: 24271398
15. D. Hashimoto *et al*., Tissue-resident macrophages self-maintain locally throughout adult life with minimal contribution from circulating monocytes. *Immunity* **38**, 792–804 (2013). doi: 10.1016/j.immuni.2013.04.004; pmid: 23601688
16. F. P. Heinzel, M. D. Sadick, B. J. Holaday, R. L. Coffman, R. M. Locksley, Reciprocal expression of interferon gamma or interleukin 4 during the resolution or progression of murine leishmaniasis. Evidence for expansion of distinct helper T cell subsets. *J. Exp. Med.* **169**, 59–72 (1989). doi: 10.1084/jem.169.1.59; pmid: 2521244
17. P. Qiu *et al*., Extracting a cellular hierarchy from high-dimensional cytometry data with SPADE. *Nat. Biotechnol.* **29**, 886–891 (2011). doi: 10.1038/nbt.1991; pmid: 21964415
18. E.-A. D. Amir *et al*., viSNE enables visualization of high dimensional single-cell data and reveals phenotypic heterogeneity of leukemia. *Nat. Biotechnol.* **31**, 545–552 (2013). doi: 10.1038/nbt.2594
19. S. C. Bendall *et al*., Single-cell mass cytometry of differential immune and drug responses across a human hematopoietic continuum. *Science* **332**, 687–696 (2011). doi: 10.1126/science.1198704; pmid: 21551058
20. S. C. Bendall *et al*., Single-cell trajectory detection uncovers progression and regulatory coordination in human B cell development. *Cell* **157**, 714–725 (2014). doi: 10.1016/j.cell.2014.04.005; pmid: 24766814
21. O. Ornatsky *et al*., Highly multiparametric analysis by mass cytometry. *J. Immunol. Methods* **361**, 1–20 (2010). doi: 10.1016/j.jim.2010.07.002; pmid: 20655312
22. X. Lou *et al*., Polymer-based elemental tags for sensitive bioassays. *Angew. Chem. Int. Ed.* **46**, 6111–6114 (2007). doi: 10.1002/anie.200700796; pmid: 17533637
23. M. Vidal, M. E. Cusick, A.-L. Barabási, Interactome networks and human disease. *Cell* **144**, 986–998 (2011). doi: 10.1016/j.cell.2011.02.016; pmid: 21414488
24. O. Rozenblatt-Rosen *et al*., Interpreting cancer genomes using systematic host network perturbations by tumour virus proteins. *Nature* **487**, 491–495 (2012). doi: 10.1038/nature11288; pmid: 22810586
25. K. Basso *et al*., Reverse engineering of regulatory networks in human B cells. *Nat. Genet.* **37**, 382–390 (2005). doi: 10.1038/ng1532; pmid: 15778709
26. K. Wang *et al*., Genome-wide identification of post-translational modulators of transcription factor activity in human B cells. *Nat. Biotechnol.* **27**, 829–837 (2009). doi: 10.1038/nbt.1563; pmid: 19741643
27. H. Carter, M. Hofree, T. Ideker, Genotype to phenotype via network analysis. *Curr. Opin. Genet. Dev.* **23**, 611–621 (2013). doi: 10.1016/j.gde.2013.10.003; pmid: 24238873
28. V. Litvak *et al*., A FOXO3-IRF7 gene regulatory circuit limits inflammatory sequelae of antiviral responses. *Nature* **490**, 421–425 (2012). doi: 10.1038/nature11428; pmid: 22982991
29. N. Aghaeepour *et al*., Critical assessment of automated flow cytometry data analysis techniques. *Nat. Methods* **10**, 228–238 (2013). doi: 10.1038/nmeth.2365; pmid: 23396282
30. T. Ideker, J. Dutkowski, L. Hood, Boosting signal-to-noise in complex biology: Prior knowledge is power. *Cell* **144**, 860–863 (2011). doi: 10.1016/j.cell.2011.03.007; pmid: 21414478
31. J. Dutkowski *et al*., A gene ontology inferred from molecular networks. *Nat. Biotechnol.* **31**, 38–45 (2013). doi: 10.1038/nbt.2463; pmid: 23242164
32. E. R. Zunder, E. Lujan, Y. Goltsev, M. Wernig, G. P. Nolan, A continuous molecular roadmap to iPSC reprogramming through progression analysis of single-cell mass cytometry. *Cell Stem Cell* **16**, 323–337 (2015). doi: 10.1016/j.stem.2015.01.015; pmid: 25748935
33. P. Eades, D. S. Meek, V. G. H. J. Rees, Eds., A heuristic for graph drawing. *Congressus Numerantium* **42**, 149–160 (1984).
34. T. M. Fruchterman, E. M. Reingold, Graph drawing by force-directed placement. *Softw. Pract. Exper.* **21**, 1129–1164 (1991). doi: 10.1002/spe.4380211102
35. B. Bodenmiller *et al*., Multiplexed mass cytometry profiling of cellular states perturbed by small-molecule regulators. *Nat. Biotechnol.* **30**, 858–867 (2012). doi: 10.1038/nbt.2317; pmid: 22902532
36. R. Finck *et al*., Normalization of mass cytometry data with bead standards. *Cytometry* **83A**, 483–494 (2013). doi: 10.1002/cyto.a.22271; pmid: 23512433
37. L. Kaufman, P. J. Rousseeuw, *Finding Groups in Data* (Wiley, New York, 1990).
38. A. A. Itano, M. K. Jenkins, Antigen presentation to naive CD4 T cells in the lymph node. *Nat. Immunol.* **4**, 733–739 (2003). doi: 10.1038/ni957; pmid: 12888794
39. A. C. Kirby, M. C. Coles, P. M. Kaye, Alveolar macrophages transport pathogens to lung draining lymph nodes. *J. Immunol.* **183**, 1983–1989 (2009). doi: 10.4049/jimmunol.0901089; pmid: 19620319
40. D. Movita *et al*., Kupffer cells express a unique combination of phenotypic and functional characteristics compared with splenic and peritoneal macrophages. *J. Leukoc. Biol.* **92**, 723–733 (2012). doi: 10.1189/jlb.1111566; pmid: 22685319
41. A. L. Gavin, E. H. Leiter, P. M. Hogarth, Mouse FcγRI: Identification and functional characterization of five new alleles. *Immunogenetics* **51**, 206–211 (2000). doi: 10.1007/s002510050033; pmid: 10752630
42. C. Scheiermann, Y. Kunisaki, P. S. Frenette, Circadian control of the immune system. *Nat. Rev. Immunol.* **13**, 190–198 (2013). doi: 10.1038/nri3386; pmid: 23391992
43. K. D. Nguyen *et al*., Circadian gene Bmal1 regulates diurnal oscillations of $Ly6C^{hi}$ inflammatory monocytes. *Science* **341**, 1483–1488 (2013). doi: 10.1126/science.1240636; pmid: 23970558
44. M. H. Smolensky, A. Reinberg, G. Labrecque, Twenty-four hour pattern in symptom intensity of viral and allergic rhinitis: Treatment implications. *J. Allergy Clin. Immunol.* **95**, 1084–1096 (1995). doi: 10.1016/S0091-6749(95)70212-1; pmid: 7751526
45. S. E. Panzer, A. M. Dodge, E. A. B. Kelly, N. N. Jarjour, Circadian variation of sputum inflammatory cells in mild asthma. *J. Allergy Clin. Immunol.* **111**, 308–312 (2003). doi: 10.1067/mai.2003.65; pmid: 12589350
46. T. Shay *et al*., Conservation and divergence in the transcriptional programs of the human and mouse immune systems. *Proc. Natl. Acad. Sci. U.S.A.* **110**, 2946–2951 (2013). doi: 10.1073/pnas.1222738110; pmid: 23382184
47. J. Mestas, C. C. Hughes, Of mice and not men: Differences between mouse and human immunology. *J. Immunol.* **172**, 2731–2738 (2004). doi: 10.4049/jimmunol.172.5.2731; pmid: 14978070
48. J. Usary *et al*., Predicting drug responsiveness in human cancers using genetically engineered mice. *Clin. Cancer Res.* **19**, 4889–4899 (2013). doi: 10.1158/1078-0432.CCR-13-0522; pmid: 23780888
49. L. Le Bourhis *et al*., Mucosal-associated invariant T cells: Unconventional development and function. *Trends Immunol.* **32**, 212–218 (2011). doi: 10.1016/j.it.2011.02.005; pmid: 21459674
50. F. Sallusto, J. Geginat, A. Lanzavecchia, Central memory and effector memory T cell subsets: Function, generation, and maintenance. *Annu. Rev. Immunol.* **22**, 745–763 (2004). doi: 10.1146/annurev.immunol.22.012703.104702; pmid: 15032595
51. Y. Shimomura *et al*., A unique B2 B cell subset in the intestine. *J. Exp. Med.* **205**, 1343–1355 (2008).pmid: 18519649
52. L. Chiossone *et al*., Maturation of mouse NK cells is a 4-stage developmental program. *Blood* **113**, 5488–5496 (2009). doi: 10.1182/blood-2008-10-187179; pmid: 19234143
53. J. C. Sun, L. L. Lanier, NK cell development, homeostasis and function: Parallels with $CD8^+$ T cells. *Nat. Rev. Immunol.* **11**, 645–657 (2011). doi: 10.1038/nri3044; pmid: 21869816
54. E. L. Gautier *et al*., Gene-expression profiles and transcriptional regulatory pathways that underlie the identity and diversity of mouse tissue macrophages. *Nat. Immunol.* **13**, 1118–1128 (2012). doi: 10.1038/ni.2419; pmid: 23023392
55. J. C. Miller *et al*., Deciphering the transcriptional network of the dendritic cell lineage. *Nat. Immunol.* **13**, 888–899 (2012). doi: 10.1038/ni.2370; pmid: 22797772
56. F. Geissmann, S. Gordon, D. A. Hume, A. M. Mowat, G. J. Randolph, Unravelling mononuclear phagocyte heterogeneity. *Nat. Rev. Immunol.* **10**, 453–460 (2010). doi: 10.1038/nri2784; pmid: 20467425
57. H. Hadeiba, E. C. Butcher, Thymus-homing dendritic cells in central tolerance. *Eur. J. Immunol.* **43**, 1425–1429 (2013). doi: 10.1002/eji.201243192; pmid: 23616226
58. K. Hoebe *et al*., CD36 is a sensor of diacylglycerides. *Nature* **433**, 523–527 (2005). doi: 10.1038/nature03253; pmid: 15690042
59. B. Beutler, C. C. Goodnow, How host defense is encoded in the mammalian genome. *Mamm. Genome* **22**, 1–5 (2011). doi: 10.1007/s00335-010-9312-4; pmid: 21184083
60. A. K. Shalek *et al*., Single-cell transcriptomics reveals bimodality in expression and splicing in immune cells. *Nature* **498**, 236–240 (2013). doi: 10.1038/nature12172; pmid: 23685454
61. B. Treutlein *et al*., Reconstructing lineage hierarchies of the distal lung epithelium using single-cell RNA-seq. *Nature* **509**, 371–375 (2014). doi: 10.1038/nature13173; pmid: 24739965
62. T. Ideker *et al*., Integrated genomic and proteomic analyses of a systematically perturbed metabolic network. *Science* **292**, 929–934 (2001). doi: 10.1126/science.292.5518.929; pmid: 11340206
63. D. Hwang *et al*., A data integration methodology for systems biology: Experimental verification. *Proc. Natl. Acad. Sci. U.S.A.* **102**, 17302–17307 (2005). doi: 10.1073/pnas.0508649102; pmid: 16301536

ACKNOWLEDGMENTS

All mass cytometry data are accessible at www.cytobank.org/nolanlab/reports and the. R package is available at https://github.com/nolanlab. R. Finck, S. Bendall, and G.P.N. have served as paid consultants of Fluidigm Sciences, the maker of the mass cytometry instrumentation and reagents used for the data collection in this study. We thank J. Kenkel, B. Burt, D.-H. Wang, and M.Ch'ng for their assistance in tissue processing; A.Trejo and A. Jager for mass cytometry quality control and maintenance; B. Gaudilliere and M. Angst for access to human whole blood data; and M. Angelo, C. Loh, N. Reticker-Flynn, and L. Sanman for constructive feedback. Supported by a George D. Smith Stanford graduate fellowship and NIH grant F31CA189331 (M.H.S.); a Stanford Bio-X graduate fellowship and NIH grant T32GM007276 (G.K.F.); CIRM Basic Biology II RB2-01592 and NIH grant NRSA F32 GM093508-01 (E.R.Z.); Damon Runyon Cancer Research Foundation fellowship DRG-2017-09 and NIH grant K99GM104148-01 (S.C.B.); NIH grants 1U19AI100627, 1R01GM109836, and 7500108142, NIAID Bioinformatics Support Contract HHSN272201200028C, PN2EY018228 0158 G KB065, 1R01CA130826, 5U54CA143907NIH, HHSN272200700038C, N01-HV-00242, 41000411217, 5-24927, P01 CA034233-22A1, RFA CA 09-009, RFA CA 09-011, U19 AI057229, U54CA149145, 5R01AI073724, R01CA184968, R33 CA183654, R33 CA183692, 1R01NS089533, 201303028; DOD grants OC110674 and 11491122; Bill and Melinda Gates Foundation grant OPP1113682; CIRM grants DR1-01477 and RB2-01592; FDA grant HHSF223201210194C BAA-12-00118; European Commission grant HEALTH.2010.1.2-1; and the Rachford and Carlota A. Harris endowed professorship (G.P.N.).. P.F.G. is a Howard Hughes Medical Institute Fellow of the Life Sciences Research Foundation.

SUPPLEMENTARY MATERIALS

www.sciencemag.org/content/349/6244/1259425/suppl/DC1
Materials and Methods
Supplementary Text
Figs. S1 to S20
Tables S1 to S4
References (*64*–*68*)

31 July 2014; accepted 28 May 2015
10.1126/science.1259425

RESEARCH ARTICLE

HIV-1 VACCINES

Priming a broadly neutralizing antibody response to HIV-1 using a germline-targeting immunogen

Joseph G. Jardine,[1,2,3]* Takayuki Ota,[1]* Devin Sok,[1,2,3]* Matthias Pauthner,[1,2,3] Daniel W. Kulp,[1,2,3] Oleksandr Kalyuzhniy,[1,2,3] Patrick D. Skog,[1] Theresa C. Thinnes,[1] Deepika Bhullar,[1] Bryan Briney,[1,2,3] Sergey Menis,[1,2,3] Meaghan Jones,[1,2,3] Mike Kubitz,[1,2,3] Skye Spencer,[1,2,3] Yumiko Adachi,[1,2,3] Dennis R. Burton,[1,2,3,4]†‡ William R. Schief,[1,2,3,4]†‡ David Nemazee[1]†‡

A major goal of HIV-1 vaccine research is the design of immunogens capable of inducing broadly neutralizing antibodies (bnAbs) that bind to the viral envelope glycoprotein (Env). Poor binding of Env to unmutated precursors of bnAbs, including those of the VRC01 class, appears to be a major problem for bnAb induction. We engineered an immunogen that binds to VRC01-class bnAb precursors and immunized knock-in mice expressing germline-reverted VRC01 heavy chains. Induced antibodies showed characteristics of VRC01-class bnAbs, including a short CDRL3 (light-chain complementarity-determining region 3) and mutations that favored binding to near-native HIV-1 gp120 constructs. In contrast, native-like immunogens failed to activate VRC01-class precursors. The results suggest that rational epitope design can prime rare B cell precursors for affinity maturation to desired targets.

We lack an effective vaccine against HIV, despite its identification more than 30 years ago. An HIV vaccine most likely will need to elicit antibodies capable of neutralizing the majority of the diverse strains circulating in the population. A minority of HIV-infected individuals eventually develop such broadly neutralizing antibodies (bnAbs), but this generally occurs only after years of protracted viral and antibody coevolution (*1*, *2*). Although they fail to control virus in the individuals themselves, passive transfer of recombinant forms of such bnAbs can prevent infection in animal models (*3*–*8*). Hence, there is an expectation that successful elicitation of bnAbs by vaccination before infection will be protective in humans, and developing such a bnAb-based vaccine is a major research goal.

The CD4 binding site (CD4bs) antibody VRC01 (*9*) and other VRC01-class bnAbs identified in at least seven different donors represent a response with distinguishing features that might be amenable to reproducible vaccine elicitation (*10*–*15*). In particular, VRC01-class bnAbs share a mode of binding that uses the immunoglobulin heavy (H) chain variable (V) gene segment VH1-2*02 to mimic CD4, in contrast to many antibodies that rely on the CDRH3 (complementarity-determining region 3 of the H chain) loop (*10*, *14*, *16*). The VH1-2*02 gene or suitable alternative alleles are present in ~96% of humans (*17*), and these genes are employed frequently, in ~3% of all human antibodies (*18*, *19*), suggesting that the B cell precursors for a VRC01-class response are generally available for vaccine targeting.

However, several key challenges must be met to induce VRC01-class bnAbs. First, as is true for some but not all classes of HIV bnAbs, the predicted germline precursors of VRC01-class bnAbs lack detectable affinity for native HIV envelope glycoproteins (Env) (*10*, *12*, *17*, *20*–*22*). To address this problem, we and others have designed germline-targeting immunogens capable of binding and activating VRC01-class precursor B cells in vitro (*17*, *21*). Whether these immunogens can activate precursors in vivo is an open question. Second, VRC01-class bnAbs carry light (L) chains with unusually short CDRL3s (complementarity-determining region 3 of the L chain) composed of five amino acid residues, typically within a CQQYEFF (*23*) motif (*14*, *16*). The short CDRL3 length is required to avoid clashing with gp120 Env loop D and V5, and amino acids within this motif make specific interactions to stabilize the antibody and to contact gp120 (*10*, *14*, *16*). CDRL3s with this length occur in only 0.6 to 1% of human κ antibodies (figs. S1 and S2) (*14*, *16*) and 0.1% of mouse κ antibodies (fig. S2), and the specific amino acid requirements described above will further reduce the frequency of useful L chains. Therefore, a germline-targeting immunogen must be capable of activating relatively rare VRC01-class precursors in the repertoire. Third, VRC01-class bnAbs, like most other HIV bnAbs, are heavily somatically mutated, as a result of chronic stimulation of B cells by successive HIV variants (*9*, *11*, *12*, *24*). Although engineering approaches can be used to develop less mutated bnAbs (*25*, *26*), it remains clear that vaccine induction of bnAbs will require strategies to induce relatively high mutation levels. This will most likely be achieved by a sequence of different immunogens that successively returns B cells to germinal centers to undergo repeated rounds of affinity maturation (*1*, *10*, *11*, *17*, *21*, *27*–*30*). In this view, each immunogen in the sequence, while naturally inducing antibodies of increasing affinity to itself, must induce maturation in memory B cells that enables weak binding to the next immunogen in the sequence. This challenge is particularly acute for the priming step: The germline-targeting prime must not only activate VRC01-class precursors, it must also induce mutations that enable binding to more native-like boost immunogens that have no detectable affinity for the precursors.

To assess the feasibility of meeting the above challenges with a germline-targeting prime, we constructed a knock-in mouse in which the germline-reverted H chain of VRC01 pairs with native mouse L chains, and we conducted immunization experiments in this mouse with an improved version [eOD-GT8 60-subunit self-assembling nanoparticle (60mer)] of a previously described germline-targeting immunogen (*17*) (see supplementary materials and methods). Responses were interrogated by enzyme-linked immunosorbent assay (ELISA); hybridoma generation; and, most importantly, by antigen-specific B cell sorting to define the pool of memory B cells induced by the immunogens.

VRC01 gH knock-in mice

The true germline precursor is not known for VRC01 or other VRC01-class bnAbs (*31*). In the knock-in mouse, we approximated the true H chain precursor with a VRC01 germline-reverted H chain (VRC01 gH) composed of the VH1-2*02 and IGHJ1*01 genes assigned by JoinSolver (*32*) and supported by recent longitudinal analysis of the VRC01 lineage (*31*), along with the CDRH3 from VRC01 with a single mutation to remove an unpaired cysteine (fig. S3). Though our use of the VRC01 CDRH3 in VRC01 gH (necessary because the germline D gene and V-D and D-J junctions cannot be inferred with confidence) is likely a departure from the (unknown) true germline precursor, the VRC01 CDRH3 plays a relatively minor role in epitope recognition, accounting for only 13.7% of the area buried on the H chain in the VRC01 interaction with gp120 (*10*) or 10.2% of the area buried on germline-reverted VRC01 in its interaction with eOD-GT6 (*17*). Furthermore, the CDRH3 in VRC01 is disulfide-bonded to an affinity-matured cysteine in CDRH1, which may serve to stabilize the antibody conformation and increase affinity for gp120; however, this disulfide is not included in VRC01 gH. Thus, the use of this CDRH3 is unlikely to strongly bias the VRC01 gH mouse toward favorable interactions

[1]Department of Immunology and Microbial Science, The Scripps Research Institute, La Jolla, CA 92037, USA. [2]International AIDS Vaccine Initiative (IAVI) Neutralizing Antibody Center (NAC), The Scripps Research Institute, La Jolla, CA 92037, USA. [3]Center for HIV/AIDS Vaccine Immunology and Immunogen Discovery, The Scripps Research Institute, La Jolla, CA 92037, USA. [4]Ragon Institute of MGH, MIT, and Harvard, Cambridge, MA 02129, USA. *These authors contributed equally to this work. †These authors contributed equally to this work. ‡Corresponding author. E-mail: nemazee@scripps.edu (D.N.); schief@scripps.edu (W.R.S.); burton@scripps.edu (D.R.B.)

Downloaded from www.sciencemag.org on July 10, 2015

with gp120- or eOD-based immunogens, and we believe the VRC01 gH sequence is a reasonable approximation for the true germ line, for the purpose of evaluating germline-targeting immunogens.

Testing for the ability to stimulate VRC01-class precursor B cells could not be carried out directly in wild-type (WT) mice or other small animals, as none are known to have a VH gene with sufficient similarity to the human VH1-02 germline gene (*16*, *17*). To overcome this limitation, we engineered mice to express a VRC01 gH-chain exon under the control of a mouse VH promoter, introduced by gene targeting into the *Igh* locus (fig. S4). This targeting to the physiological locus allows normal regulation of H-chain expression, antibody class switching, and somatic mutation. These VRC01 gH mice have similar frequencies of $CD19^+/B220^+$ B cells as WT littermates (siblings of knock-in mice that lack the knock-in gene by random chance in breeding male heterozygous knock-in mice with WT females) (Fig. 1A). By next-generation sequencing, the VRC01 gH-chain gene was expressed by ~80% of B cells (Fig. 1B and figs. S5 and S6) and was paired with random mouse L chains generated in the course of normal B cell development (fig. S7). The L chains have similar V gene usage and CDRL3 length distributions as those of WT littermates (fig. S8). Thus, VRC01 gH mice carry germline-reverted bnAb precursor B cells at a frequency appropriate for testing of germline-targeting VRC01-class immunogens, including the eOD-GT8 60mer.

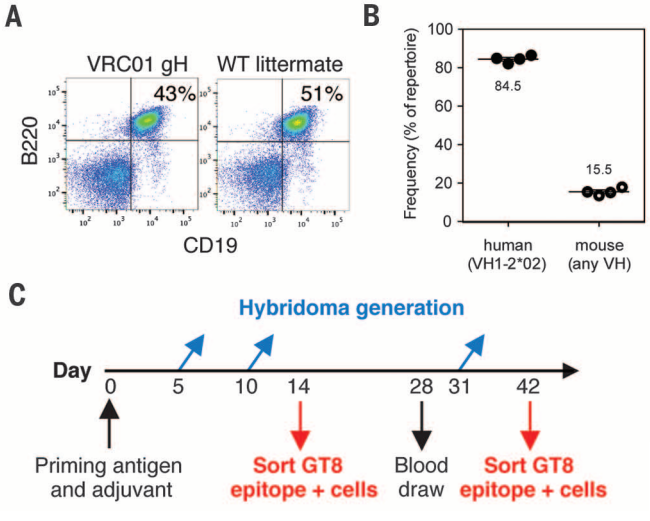
Analysis of antibody responses to different priming immunogens

VRC01 gH mice were immunized with a single injection of eOD-GT8 60mer, a self-assembling nanoparticle composed of an engineered outer domain from HIV gp120 fused to a lumazine synthase protein (fig. S9). To assess whether VRC01-like germline precursors were primed, we followed antibody responses and sequenced antibody genes of eOD-GT8–reactive B cells that were captured as hybridomas or by cell sorting of eOD-GT8–binding immunoglobulin G (IgG) B cells (Fig. 1C and fig. S10). To investigate the effect of multimeric state, we compared responses to 60-subunit nanoparticles (eOD-GT8 60mers) and trimers (eOD-GT8 3mers). To probe for adjuvant effects, antigens were delivered in three different adjuvants: alum, Iscomatrix ["Isco," 40-nm–diameter cagelike structures composed of phospholipids, cholesterol, and saponin that traffic to lymph nodes and can heighten both antibody and T cell responses but contain no known Toll-like receptor (TLR) agonist activity (*33*)], or Sigma Adjuvant system ("Ribi," an oil-in-water emulsion containing synthetic trehalose dicorynomycolate and the TLR4 agonist monophosphoryl lipid A). The alum and Ribi immunizations were given by intraperitoneal injection, and the Isco immunizations were delivered subcutaneously per the manufacturer's recommendations (Fig. 1D). To evaluate whether immunogens bearing an unmodified CD4bs could activate VRC01-like precursors, we tested responses to both the native-like trimer BG505 SOSIP.664 (*34*–*37*) and eOD17 60mers, nanoparticles presenting a native-like and non–germline-targeting CD4bs on an eOD protein similar to eOD-Base (*17*), with all glycosylation sites intact.

The eOD-GT8 60mer challenge elicited a CD4bs response in VRC01 gH mice, as their immune serum IgG bound more strongly to eOD-GT8 than to eOD-GT8-KO, a mutant designed to block germline VRC01 binding [$D^{368}\rightarrow R^{368}$ (D368R), N279A and mutations to restore the N276 glycosylation site] (Fig. 2A and fig. S11). The IgG response of WT mice, in contrast, was mainly to non-CD4bs epitopes. eOD-GT8 immunogens given in all three adjuvants supported a serum IgG response to CD4bs, though eOD-GT8 60mers were stronger than eOD-GT8 3mers, as assessed by an ELISA area-under-the-curve analysis (i.e., area under the eOD-GT8 reactivity curve minus area under the eOD-GT8-KO curve) (Fig. 2B) and by frequencies of IgG^+ memory phenotype B cells that bound eOD-GT8 but not eOD-GT8-KO [$eOD\text{-}GT8^{(+)}/eOD\text{-}GT8\text{-}KO^{(-)}$] identified by cell sorting (Fig. 2C). eOD-GT8 60mers induced lower frequencies of (non-CD4bs) IgG^+ memory phenotype B cells that bound both eOD-GT8 and eOD-GT8-KO [$eOD\text{-}GT8^{(+)}/eOD\text{-}GT8\text{-}KO^{(+)}$], suggestive of an epitope-specific response (fig. S12). Both BG505 SOSIP.664 trimer and eOD17 60mers elicited weak responses by ELISA and antigen-specific B cell frequencies (Fig. 2, B and C).

Selection of L-chain partners by the priming immunogen

Priming of the VRC01-class response was revealed in the sequencing data from sorted B cells and hybridomas. B cell sorting recovered 177 IgG H-L paired sequences from days 14 and 42, 167 of which used the VRC01 knock-in H chain (some were unmutated and others had mutations in either or both of the H or L chains, as discussed below). Additionally, 95 [IgG or immunoglobulin M (IgM)] hybridomas were recovered, all of which used the knock-in H chain. Among IgG B cells, this H chain was paired with κ L-chain partners of highly restricted CDRL3 length and Vκ gene



D

Experimental overview

Immunogen	Multimerization	Adjuvant	VRC01 gH mice (n)	WT mice (n)
eOD-GT8 60mer	Nanoparticle	Alum	11	5
eOD-GT8 60mer	Nanoparticle	Iscomatrix	5	5
eOD-GT8 60mer	Nanoparticle	Ribi	12	5
eOD-GT8 3mer	Trimer	Alum	5	5
eOD-GT8 3mer	Trimer	Ribi	5	5
eOD-17 60mer	Nanoparticle	Alum	5	5
BG505 SOSIP	Trimer	Iscomatrix	5	0
BG505 SOSIP	Trimer	Ribi	5	0

Fig. 1. Generation of VRC01 gH mice and outline of priming experiments. (**A**) Flow cytometry analysis of spleen cells showing B cell frequencies in VRC01 gH mice and WT littermates. (**B**) Next-generation sequencing of splenic cDNA from VRC01 gH mice revealed VH1-2*02 usage compared with mouse VH gene usage. (**C**) Summary of the time course for experiments and analysis. Mice were given a single prime of immunogen in adjuvant and then serum immune responses were evaluated at days 14, 28, and 42 postimmunization. Two of five mice per group were sacrificed for B cell sorting analysis at day 14, and the remaining three of five mice were sacrificed at day 42. In other animals, splenic B cells were collected at days 5, 10, or 31 for hybridoma generation. (**D**) Overview of the immunization groups listed by immunogen (eOD-GT8 60mer, eOD-GT8 3mer, eOD17 60mer, and BG505 SOSIP), multimeric state (nanoparticle or trimer), and adjuvant (Alum, Iscomatrix, or Ribi), along with the number of mice used to test each group. All groups were tested in both VRC01 gH and WT mice, except for BG505 SOSIP, which was tested only in VRC01 gH mice. Five mice per group were used for B cell sorting and/or ELISA, and an additional 13 VRC01 gH mice were employed for hybridoma generation after immunization with eOD-GT8 60mer (6 for Alum, 7 for Ribi).

usage (Fig. 3). Ninety-two percent (154 of 167) of eOD-GT8$^{(+)}$/eOD-GT8-KO$^{(-)}$–sorted IgG B cells using the VRC01 gH had L chains with a CDRL3 length of five amino acids (Fig. 3A and tables S1 and S2), whereas only ~0.1% of naïve (nonimmunized) VRC01 gH B cells or WT mouse B cells had a κ L-chain CDRL3 length of five amino acids (fig. S2). None of the 10 sorted B cells that used an endogenous mouse VH gene contained a five–amino acid CDRL3. Among IgG hybridomas, which were captured as early as day 5 of the response, six of seven hybridomas carried a κ L chain with a five–amino acid CDRL3, each isolated from a different mouse (tables S3 to S6). In contrast, among 88 IgM hybridomas recovered after eOD-GT8 60mer immunization [for which eOD-GT8 affinity was weaker than 100 μM for all but 2 hybridomas, according to surface plasmon resonance (SPR)], only 1 had this CDRL3 signature. This suggests that the initial selection for the unusual CDRL3 length occurred upon class switching. Priming was reproducible, as IgG B cells with five–amino acid CDRL3s were isolated from 20 of 22 mice immunized with eOD-GT8 60mer (14 of 15 mice analyzed by sorting and 6 of 7 mice that produced IgG hybridomas) (table S1). eOD-GT8–binding IgGs preferentially used Vκ genes with a QQY motif at the start of CDRL3 common to mature VRC01-class bnAbs (CQQYEFF) (Fig. 3, B and C, and fig. S13). In contrast, IgM hybridomas used a broad distribution of Vκ and Vλs (table S6), again indicating selection at the class-switch stage. In summary, eOD-GT8 60mer immunization successfully recruited VRC01-like precursors into the T cell–dependent response and promoted the selective IgG class switching of cells carrying desirable L-chain features.

Somatic mutation patterns

A bnAb priming immunogen must not only expand precursor numbers but also promote somatic mutations that allow binding to boosting antigens with closer similarity to HIV Env. We found many somatic mutations among IgG memory phenotype B cells responding to eOD-GT8 60mers and containing a five–amino acid CDRL3, including some L-chain mutations shared with mature VRC01-class antibodies (Fig. 3C). On the L chain, many sequences isolated at day 42 of the response to eOD-GT8 60mer/Ribi achieved a D or E in the VRC01 CQQYEF sequence motif. Sixteen of 47 analyzed IgG memory phenotype B cells had a T-to-G nucleotide mutation in their five–amino acid CDRL3s to introduce a D at position 4 (fig. S14), and several cells had an E at that position.

As the VRC01 gH-chain sequence was known, H-chain mutations were readily identified and could be compared directly to mature VRC01 to identify favorable mutations. To focus exclusively on VRC01-class antibodies, our H chain analysis included only the VH region of Abs that derived from the VRC01 gH chain and contained a five–amino acid CDRL3. Nearly all VRC01-class Abs from day 14 were unmutated. By day 42, however, 53 of 98 VRC01-class Abs contained at least one coding mutation from the starting H-chain sequence (table S7). Among all VRC01-class Abs from days 14 and 42 with at least one coding mutation on the H chain, 55 of 61 contained at least one mutation that is identical to VRC01 (fig. S15), and ≥50% of the mutations in 49 of 61 such Abs were identical to those in one of six VRC01-class bnAbs (12a21, 3BNC60, PGV04, PGV20, VRC-CH31, or VRC01) (Fig. 4A and table S7). In one case, all six coding mutations were identical to mutations found in VRC01-class bnAbs. One particular mutation (H35N) was found in >80% of B cells that had at least one mutation, including cells from 12 different mice and all adjuvant groups (table S2) and including both sorted IgG cells and hybridomas. Examination of the eOD-GT6/GL-VRC01 complex structure [Protein Data Bank identification number (PDB ID): 4jpk] and

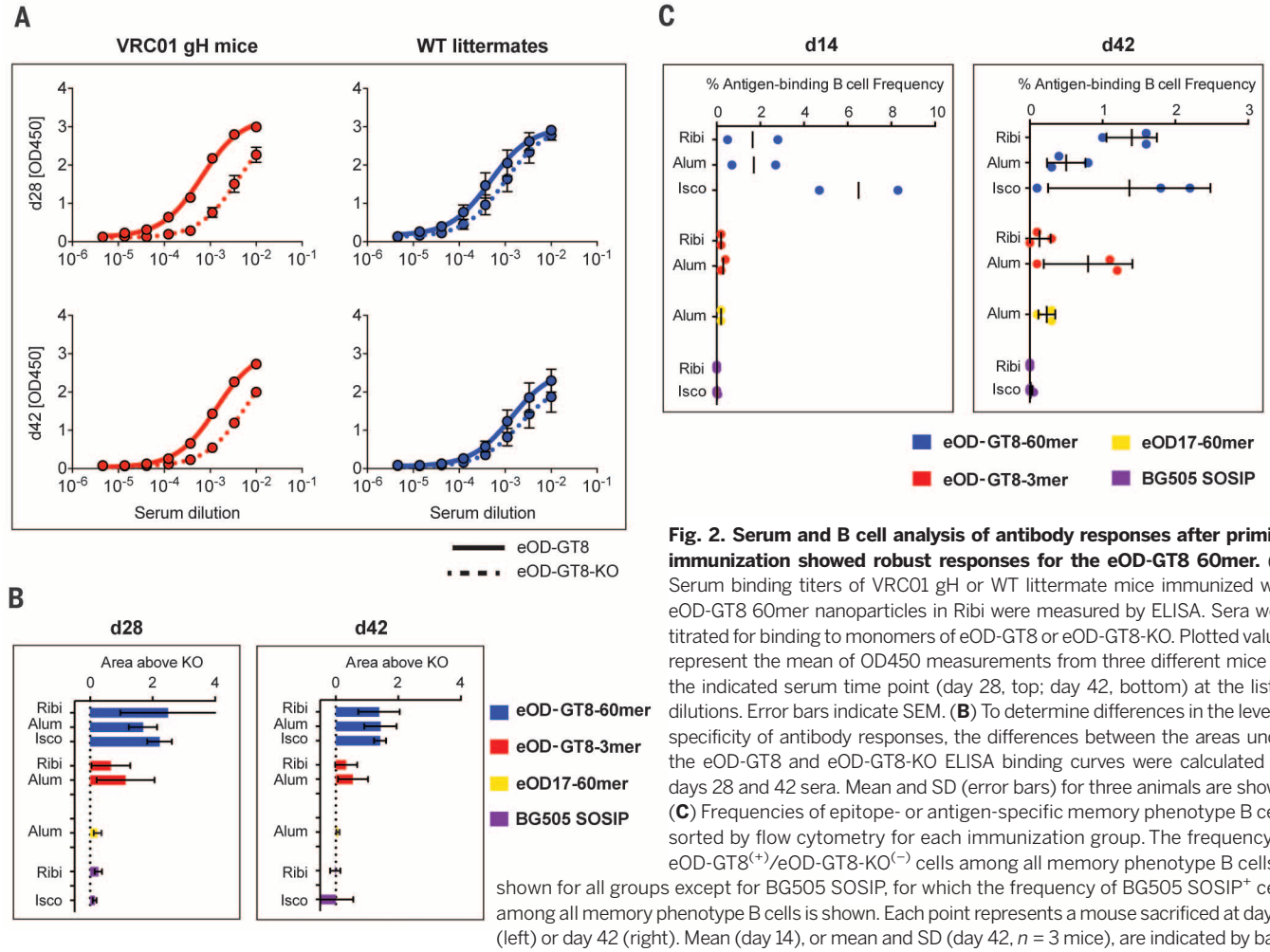


Fig. 2. Serum and B cell analysis of antibody responses after priming immunization showed robust responses for the eOD-GT8 60mer. (**A**) Serum binding titers of VRC01 gH or WT littermate mice immunized with eOD-GT8 60mer nanoparticles in Ribi were measured by ELISA. Sera were titrated for binding to monomers of eOD-GT8 or eOD-GT8-KO. Plotted values represent the mean of OD450 measurements from three different mice for the indicated serum time point (day 28, top; day 42, bottom) at the listed dilutions. Error bars indicate SEM. (**B**) To determine differences in the level of specificity of antibody responses, the differences between the areas under the eOD-GT8 and eOD-GT8-KO ELISA binding curves were calculated for days 28 and 42 sera. Mean and SD (error bars) for three animals are shown. (**C**) Frequencies of epitope- or antigen-specific memory phenotype B cells sorted by flow cytometry for each immunization group. The frequency of eOD-GT8$^{(+)}$/eOD-GT8-KO$^{(-)}$ cells among all memory phenotype B cells is shown for all groups except for BG505 SOSIP, for which the frequency of BG505 SOSIP^{+} cells among all memory phenotype B cells is shown. Each point represents a mouse sacrificed at day 14 (left) or day 42 (right). Mean (day 14), or mean and SD (day 42, n = 3 mice), are indicated by bars.

the gp120/VRC01 complex structure (PDB ID: 3ngb) revealed that the H35N mutation enables a favorable hydrogen bonding interaction with an asparagine on CDRH3 (fig. S16). We also noted differences in mutation levels in different adjuvant groups: Among the day 42 sequences, the percentages of Abs with at least one H-chain coding mutation were 44% (8/18) for alum-immunized mice, 19% (3/16) for Isco-immunized mice, and 67% (42/63) for Ribi-immunized mice (Fig. 4B). Overall, the strong selection of mutations is suggestive of a VRC01-class response, with many mutations identical to those in VRC01-class bnAbs that may help primed cells become cross-reactive to more native-like gp120 molecules. Thus, priming with the eOD-GT8 60mer selected antibody features predicted to improve binding to the CD4bs of Env.

Antibody affinity for the germline-targeting prime and candidate boost immunogens

T cell–dependent immune responses promote somatic hypermutation and selection for B cells with improved affinity for immunogens, but an additional requirement for an effective bnAb HIV priming immunogen is to promote enhanced affinity for the presumed HIV boosting antigen(s). To assess this aspect of the efficacy of eOD-GT8 60mer priming, we expressed 115 H-L paired sequences that used the VRC01 knock-in H chain and contained a five–amino acid CDRL3 from eOD-GT8$^{(+)}$/eOD-GT8-KO$^{(-)}$ IgG memory phenotype–sorted B cells (table S7). We then evaluated their binding to eOD-GT8, eOD-GT8-KO, and candidate boosting antigens by SPR. Of the 115 Abs, 72 contained no H- or L-chain mutations from the germ line. These unmutated Abs bound

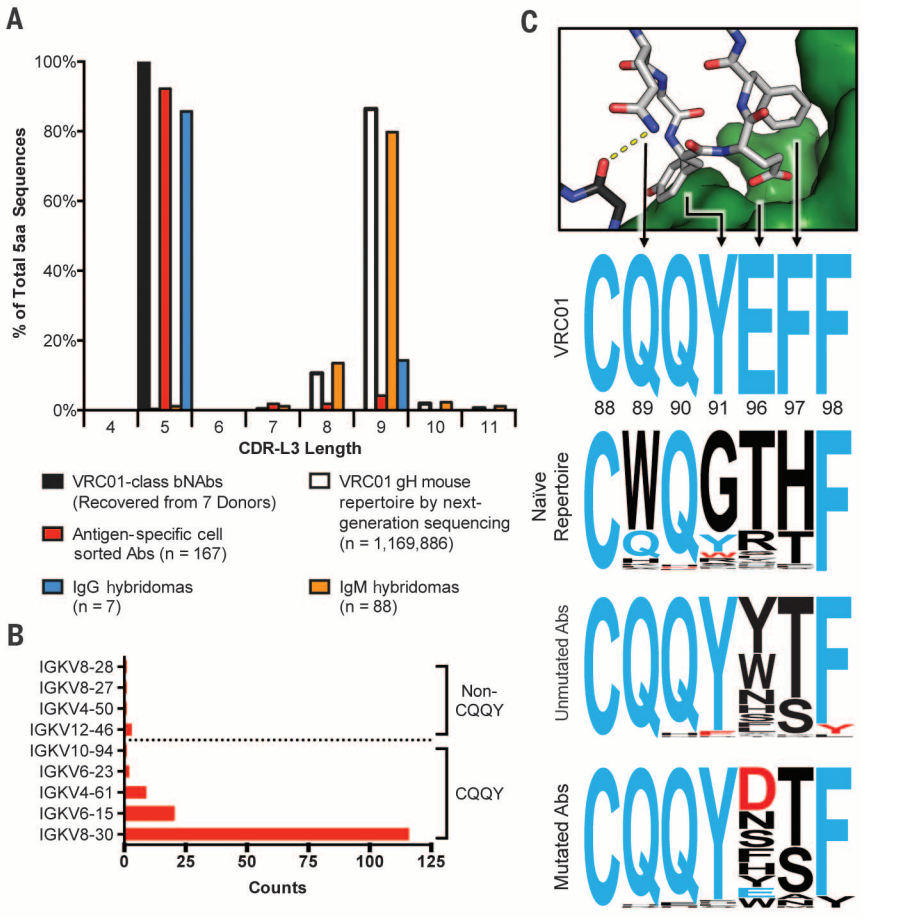


Fig. 3. Priming with eOD-GT8 60mer selects for mouse L chains with VRC01-class features. (**A**) Mouse L chains from sorted antigen-specific IgG^{+} memory phenotype B cells (red) and from hybridomas (blue), as well as mouse L chains from IgM^{+} antigen-specific hybridomas (orange), were sequenced to identify CDRL3 lengths and mutations from germline mouse κ chains. The distribution of CDRL3 lengths is shown in a histogram compared with known VRC01-class antibodies (black) and the naïve (unimmunized) VRC01 gH mouse antibody repertoire (white). This analysis is based on all sequences using the VRC01 gH chain from all mice immunized with eOD-GT8 60mers (from all hybridoma or sorting time points and all adjuvant groups listed in Fig. 1). *n*, number of L-chain sequences from individual sorted cells, hybridomas, or deep sequencing reads, as indicated. (**B**) Gene usage is shown for all Vκ genes in antibodies using the VRC01 gH chain and a five–amino acid CDRL3 recovered by sorting IgG^{+} eOD-GT8^{+}/eOD-GT8-KO$^{(-)}$ memory phenotype B cells at day 14 or 42 from all mice immunized with eOD-GT8 60mers in all adjuvants (table S7). (**C**) Comparison of the VRC01 CDRL3 sequence with sequences of five–amino acid CDRL3s recovered from VRC01 gH mice. Sequences are depicted as sequence logos at the indicated positions, with the size of each letter corresponding to the prevalence of that residue at that position. The "VRC01" sequence logo shows the sequence of the VRC01 CDRL3. The "Naïve Repertoire" sequence logo represents all 1653 sequences with five–amino acid CDRL3 found by deep sequencing of four unimmunized VRC01 gH mice (these sequences amount to 0.14% of all 1,169,886 sequences from those mice). The "Unmutated Abs" and "Mutated Abs" sequence logos represent the sets of unmutated (*n* = 84) or mutated (*n* = 70) antibodies, respectively, using the human VH1-2*02 gene and a five–amino acid CDRL3, isolated from VRC01 gH mice at day 14 or 42 after immunization with eOD-GT8 60mer and Alum, Isco, or Ribi (the red bar at CDRL3 length = 5 in Fig. 3A corresponds to these 154 sequences) (table S7).

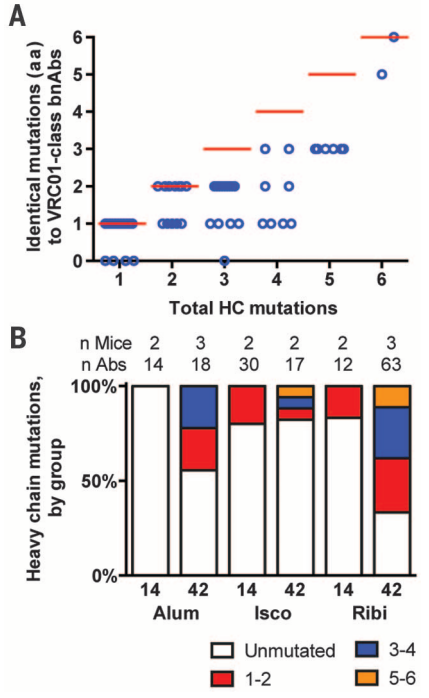


Fig. 4. Priming with eOD-GT8 60mer selects for productive H-chain mutations found in VRC01-class bnAbs. (**A**) A total of 61 mutated H-chain (HC) sequences from day 14 and 42 eOD-GT8 60mer–immunized VRC01 gH-chain mice (table S7) were evaluated for the number of amino acids that match the mutations found in VRC01-class bnAbs (12a12, 3BNC60, PGV04, PGV20, VRC-CH31, and VRC01) compared to total H-chain amino acid mutations from the germ line. Each circle represents a single H-chain sequence that was isolated by antigen-specific memory phenotype B cell sorting. (**B**) The total number of amino acid mutations observed in the H chains of antibodies isolated by antigen-specific memory phenotype B cell sorting is listed by adjuvant (Alum, Isco, or Ribi) for spleen and lymph node samples harvested at 14 or 42 days postpriming immunization. Bar graphs are divided by unmutated (white) versus mutated (colored). The mutated bars are divided into Abs with one or two coding mutations (red), three or four coding mutations (blue), or five or six coding mutations (orange). The number of mice and the number of antibodies used to compute the frequencies in each bar are listed at the top of the graph.

eOD-GT8 with a median dissociation constant (K_D) of 32 nM (Fig. 5, A and B, and table S8). Few mutations were required to promote high affinity—most Abs with more than three coding mutations had an affinity too high to measure accurately (K_D < 16 pM) (Fig. 5A). Confirming epitope specificity, antibodies for which we could measure a K_D for eOD-GT8 showed reduced affinity for eOD-GT8-KO by factors of 36 to 200. We observed intriguing differences among adjuvant groups, with Ribi-immunized mice producing both more Abs (recoverable by sorting) and higher-affinity Abs compared with alum or Isco.

The eOD-GT8 60mer was designed both to prime germline VRC01-class precursors and to select for mutations that confer cross-reactivity to more native-like gp120 (*17*). To test whether the latter was effective, we selected the 29 Abs that bound eOD-GT8 with subnanomolar affinity, as well as eight unmutated variants (with average K_Ds for eOD-GT8), and screened them for binding to more native-like gp120 constructs in both monomer and 60mer form. The Abs with more than three coding mutations not only had improved affinity for eOD-GT8 but in many cases showed affinity for core-e-2CC HxB2 N276D, a conformationally stabilized core gp120 monomer with a near-native CD4bs from strain HxB2 that combines the loop and termini trimming of the "coreE" design (*10*, *14*) with the disulfides and space-fill mutations of the "2CC" design (*38*) but also lacks the N276 glycan. In total, 23 of 29 Abs that bound with high affinity to eOD-GT8 showed detectable binding to core-e-2CC HxB2 N276D (K_D < 100 μM), whereas none of the unmutated Abs did (Fig. 5B and table S8). 60mer nanoparticles of core-e-2CC HxB2 N276D bound to 24 of 29 mutated Abs more strongly than to the monomer by a factor of ~100 due to avidity, but the 60mers also showed no binding to the unmutated Abs. We conclude that priming with eOD-GT8 60mers promotes clonal expansion and facilitates recognition of molecules presenting a near-native CD4bs.

Discussion: The priming problem

A vital goal of rational vaccine design is to understand how to prime naturally subdominant antibody responses in a reproducible manner. Germline-targeting offers one potential strategy to achieve this goal. Here we have used a germline-reverted VRC01 H-chain knock-in mouse model to demonstrate that a germline-targeting immunogen (eOD-GT8 60mer) can activate relatively rare VRC01-class precursors, select productive mutations, and create a pool of memory phenotype B cells that are likely to be susceptible to boosting by more native-like immunogens. In contrast, we found that immunogens bearing a native-like CD4 binding site, including both the eOD17 60mer and the well-ordered BG505 SOSIP.D664 trimer, failed to achieve these goals. These results illustrate the value of an engineered priming immunogen to initiate the development of bnAb lineages by vaccination.

The data in the VRC01 gH mouse model described here have strong potential relevance to human vaccination. Given that (i) VH1-2*02 is expressed in ~80% of B cells in this mouse compared with ~3% of human B cells (*18*, *19*); (ii) the frequency of five–amino acid CDRL3 L chains is 0.1% in VRC01 gH B cells compared with 0.6 to 1% in humans (figs. S1 and S2) (*16*); and (iii) the CDRH3 requirements are modest for VRC01-class bnAbs (*10*, *14*, *16*, *39*) and appear to be minimal for VRC01-class precursors, perhaps requiring a length of 11 to 18 amino acids [75% of human Abs (fig. S17)], it is possible that VRC01-class precursors are less frequent in humans compared with the VRC01 gH mouse by a factor of only ~5 (= 80/3 × 0.1/0.6 × 1/0.75). Even if this estimate is off by an order of magnitude or two due to unknown factors, it is also true that humans have orders of magnitude more B cells than mice, hence more potential targets. Therefore, we believe that this study provides strong support for the idea of human clinical testing of the eOD-GT8 60mer, to assess whether this germline-targeting prime can perform similarly in diverse humans. Moreover, the differences observed with different adjuvants in this mouse model—in serum titers, B cell frequencies, selection of favorable mutations, and generation of high-affinity Abs—indicate that testing different adjuvants should be considered in the design of human clinical experiments probing activation of specific classes of precursor B cells.

Having demonstrated that eOD-GT8 60mer immunization initiates a VRC01-class response in this mouse model, several additional developments are probably needed to induce broad neutralizing activity. The eOD-GT8 60mer contains a modified CD4bs to confer germline reactivity and, as such, is probably not capable of selecting

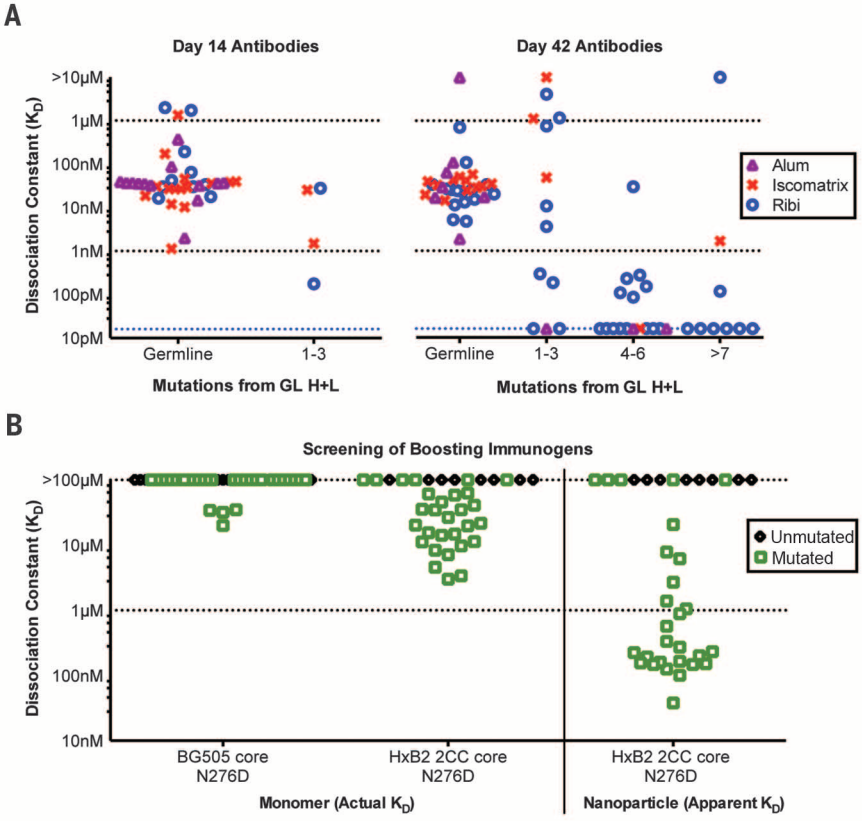


Fig. 5. Binding affinities of eOD-GT8 60mer–elicited antibodies for eOD-GT8 and candidate boost immunogens. (**A**) eOD-GT8 dissociation constants measured by SPR for 115 eOD-GT8 60mer–elicited antibodies isolated by antigen-specific B cell sorting (table S7). Antibodies were captured on the sensor chip, and eOD-GT8 monomer was the analyte. Data are shown for 42 antibodies from day 14 and 73 antibodies from day 42 after immunization of VRC01 gH mice with eOD-GT8 60mer. Each point is colored to indicate the type of adjuvant used (Alum, Iscomatrix, and Ribi) in the immunizations. The scale on the *y* axis spans from the smallest dissociation constant (16 pM) measureable by our SPR instrument (as stated by the manufacturer) to the highest (10 μM) measureable based on the analyte concentration used in the experiment. GL, germ line. (**B**) Dissociation constants measured by SPR between selected eOD-GT8 60mer–elicited antibodies and candidate boost immunogens. Among the 115 Abs in (A), the 29 antibodies with the highest affinity for eOD-GT8 (K_D < 1 nM), along with 8 unmutated antibodies with lower affinity for eOD-GT8, were selected for binding to candidate boosting immunogens (HxB2 core-e 2CC N276D and core BG505 N276D) by SPR. High analyte concentration was used to determine K_Ds up to 100 μM. HxB2 core-e 2CC N276D 60mer nanoparticles were also assayed, with values presented as apparent affinity, due to the avidity between particles and IgG. Mutated antibodies are shown as green squares; unmutated antibodies are shown as black diamonds.

all of the H- and L-chain mutations required for bnAb activity against the native CD4bs. Indeed, no neutralizing activity was detected for any of the 8 eOD-GT8 60mer–induced Abs [all with high affinity (K_D < 1 nM) for eOD-GT8 and low affinity (1 μM < K_D < 100 μM) for core-e-2CC HxB2 N276D] that we tested against a panel of four viruses from clades A and B that included both WT and N276A mutant viruses with increased sensitivity to VRC01-class bnAbs (fig. S18). One design feature of eOD-GT8 is that it lacks the N276 glycan; removal of this glycan is a requirement for germline reactivity (*17*, *21*). However, the N276 glycosylation site is conserved in 94.5% of HIV strains, according to an analysis of 3796 sequences from the Los Alamos HIV database (www.hiv.lanl.gov/). Induction of broad neutralization will probably require one or more boosting immunogens bearing a glycan at N276 so as to select mutations to accommodate that glycan (*17*). On the H chain of VRC01-class bnAbs, mutations in the CDR2, CDR1, FW1, and FW3 are likely required for maximum potency and breadth (*24*, *40*), and native-like Env immunogens will probably be needed to select for these. In sum, boosting with a sequence of increasingly native-like antigens, and potentially including cocktails of different antigens within each boost to mimic the antigenic diversity of the CD4bs, will likely be needed to select the mutations required for VRC01-class bnAb activity. The mouse model presented here, as well as other newly developed VRC01-class knock-in mouse models (*41*), should aid us to test this notion and can be used to identify the antigens and boosting strategies that work best. Of note, we demonstrated here that a single immunization with the eOD-GT8 60mer induces VRC01-class antibodies with modest affinity for the core-e-2CC HxB2 N276D monomer and 60mer, so these molecules represent promising candidates for the first boost. We are thus mapping the first steps in a sequential strategy for the rational induction of bnAbs against HIV.

REFERENCES AND NOTES

1. H. X. Liao *et al.*, *Nature* **496**, 469–476 (2013).
2. N. A. Doria-Rose *et al.*, *Nature* **509**, 55–62 (2014).
3. M. C. Gauduin *et al.*, *Nat. Med.* **3**, 1389–1393 (1997).
4. J. R. Mascola *et al.*, *Nat. Med.* **6**, 207–210 (2000).
5. P. W. Parren *et al.*, *J. Virol.* **75**, 8340–8347 (2001).
6. B. Moldt *et al.*, *Proc. Natl. Acad. Sci. U.S.A.* **109**, 18921–18925 (2012).
7. J. Pietzsch *et al.*, *Proc. Natl. Acad. Sci. U.S.A.* **109**, 15859–15864 (2012).
8. M. Shingai *et al.*, *J. Exp. Med.* **211**, 2061–2074 (2014).
9. X. Wu *et al.*, *Science* **329**, 856–861 (2010).
10. T. Zhou *et al.*, *Science* **329**, 811–817 (2010).
11. X. Wu *et al.*, *Science* **333**, 1593–1602 (2011).
12. J. F. Scheid *et al.*, *Science* **333**, 1633–1637 (2011).
13. M. Bonsignori *et al.*, *J. Virol.* **86**, 4688–4692 (2012).
14. T. Zhou *et al.*, *Immunity* **39**, 245–258 (2013).
15. I. S. Georgiev *et al.*, *Science* **340**, 751–756 (2013).
16. A. P. West Jr., R. Diskin, M. C. Nussenzweig, P. J. Bjorkman, *Proc. Natl. Acad. Sci. U.S.A.* **109**, E2083–E2090 (2012).
17. J. Jardine *et al.*, *Science* **340**, 711–716 (2013).
18. R. Arnaout *et al.*, *PLOS ONE* **6**, e22365 (2011).
19. B. J. DeKosky *et al.*, *Nat. Med.* **21**, 86–91 (2015).
20. S. Hoot *et al.*, *PLOS Pathog.* **9**, e1003106 (2013).
21. A. T. McGuire *et al.*, *J. Exp. Med.* **210**, 655–663 (2013).
22. X. Xiao *et al.*, *Biochem. Biophys. Res. Commun.* **390**, 404–409 (2009).
23. Single-letter abbreviations for the amino acid residues are as follows: A, Ala; C, Cys; D, Asp; E, Glu; F, Phe; G, Gly; H, His; I, Ile; K, Lys; L, Leu; M, Met; N, Asn; P, Pro; Q, Gln; R, Arg; S, Ser; T, Thr; V, Val; W, Trp; and Y, Tyr.
24. J. R. Mascola, B. F. Haynes, *Immunol. Rev.* **254**, 225–244 (2013).
25. I. S. Georgiev *et al.*, *J. Immunol.* **192**, 1100–1106 (2014).
26. D. Sok *et al.*, *PLOS Pathog.* **9**, e1003754 (2013).
27. X. Xiao, W. Chen, Y. Feng, D. S. Dimitrov, *Viruses* **1**, 802–817 (2009).
28. D. S. Dimitrov, *mAbs* **2**, 347–356 (2010).
29. B. F. Haynes, G. Kelsoe, S. C. Harrison, T. B. Kepler, *Nat. Biotechnol.* **30**, 423–433 (2012).
30. F. Klein *et al.*, *Science* **341**, 1199–1204 (2013).
31. X. Wu *et al.*, *Cell* **161**, 470–485 (2015).
32. M. M. Souto-Carneiro, N. S. Longo, D. E. Russ, H. W. Sun, P. E. Lipsky, *J. Immunol.* **172**, 6790–6802 (2004).
33. A. B. Morelli *et al.*, *J. Med. Microbiol.* **61**, 935–943 (2012).
34. R. W. Sanders *et al.*, *PLOS Pathog.* **9**, e1003618 (2013).
35. J. P. Julien *et al.*, *Science* **342**, 1477–1483 (2013).
36. D. Lyumkis *et al.*, *Science* **342**, 1484–1490 (2013).
37. M. Pancera *et al.*, *Nature* **514**, 455–461 (2014).
38. B. Dey *et al.*, *PLOS Pathog.* **5**, e1000445 (2009).
39. R. Diskin *et al.*, *Science* **334**, 1289–1293 (2011).
40. F. Klein *et al.*, *Cell* **153**, 126–138 (2013).
41. P. Dosenovic *et al.*, *Cell* **161**, 1505–1515 (2015).

ACKNOWLEDGMENTS

We thank T. R. Blane, S. Kupriyanov, and G. S. Martin for technical assistance. The data presented in this manuscript are tabulated in the main paper and in the supplementary materials. This work was supported by the IAVI Neutralizing Antibody Consortium and Center (W.R.S. and D.R.B.); the Collaboration for AIDS Vaccine Discovery funding for the IAVI NAC (W.R.S. and D.R.B.); the Ragon Institute of MGH, MIT and Harvard (D.R.B. and W.R.S.); the Helen Hay Whitney Foundation (J.G.J.); and National Institute of Allergy and Infectious Diseases grants R01-AI073148 (D.N.), P01AI081625 (W.R.S.), and CHAVI-ID 1UM1AI100663 (W.R.S. and D.R.B.). IAVI and the Scripps Research Institute are filing a patent relating to the eOD-GT8 immunogens in this manuscript, with inventors J.G.J., D.W.K., S.M., and W.R.S. Materials and information will be provided under a material transfer agreement.

SUPPLEMENTARY MATERIALS

www.sciencemag.org/content/349/6244/156/suppl/DC1
Materials and Methods
Figs. S1 to S18
Tables S1 to S8
References (*42*–*53*)

16 May 2015; accepted 11 June 2015
Published online 18 June 2015;
10.1126/science.aac5894

REPORTS

SOFT ROBOTICS

A 3D-printed, functionally graded soft robot powered by combustion

Nicholas W. Bartlett,[1,2]*† Michael T. Tolley,[3]† Johannes T. B. Overvelde,[1] James C. Weaver,[2] Bobak Mosadegh,[4] Katia Bertoldi,[1] George M. Whitesides,[2,5] Robert J. Wood[1,2]

Roboticists have begun to design biologically inspired robots with soft or partially soft bodies, which have the potential to be more robust and adaptable, and safer for human interaction, than traditional rigid robots. However, key challenges in the design and manufacture of soft robots include the complex fabrication processes and the interfacing of soft and rigid components. We used multimaterial three-dimensional (3D) printing to manufacture a combustion-powered robot whose body transitions from a rigid core to a soft exterior. This stiffness gradient, spanning three orders of magnitude in modulus, enables reliable interfacing between rigid driving components (controller, battery, etc.) and the primarily soft body, and also enhances performance. Powered by the combustion of butane and oxygen, this robot is able to perform untethered jumping.

Robots are typically composed of rigid components to promote high precision and controllability. Frequently constructed from hard metals such as aluminum and steel, these robots require large machining equipment and an intricate assembly process. In contrast, recent work has explored the possibility of creating soft-bodied robots (*1*–*6*) inspired by invertebrates such as cephalopods (*7*–*9*) and insect larvae (*10*), as well as vertebrates, including snakes (*11*) and fish (*12*). The use of compliant materials facilitates the development of biologically inspired robotic systems (*13*) that are more adaptable (*14*), safer (*15*, *16*), and more resilient (*17*) than their fully rigid counterparts.

The design and fabrication of soft robotic systems, however, present significant engineering challenges (*18*, *19*). The bodies of soft robots are typically fabricated in custom-designed molds and require multiple assembly steps (*20*) or lost-wax techniques (*21*) to embed actuation. The molds used to create these soft robots are complex and time-consuming to make, especially for prototype designs that are fabricated in small numbers and are constantly evolving. Additionally, some applications (such as ones

requiring untethered robots) require rigid components to power and control the soft body (*11*, *12*, *17*) or to perform specific tasks. The interfaces between these rigid components and the soft body of the robot are points of recurring failure.

In nature, many animals employ stiffness gradients to join rigid materials and soft structures while minimizing stress concentrations that could lead to failures at rigid/soft interfaces (*22*, *23*). One of the reasons biological systems often outperform engineered systems is that in nature, which employs self-organization for fabrication, added structural complexity comes at a minimal cost. Emerging digital fabrication technologies (such as 3D printing) are beginning to allow designers to move toward this level of structural complexity, albeit at a larger scale and with fewer materials. These technologies can be used to manufacture geometrically intricate designs as efficiently as simple designs with an equivalent amount of material.

[1]School of Engineering and Applied Sciences, Harvard University, Cambridge, MA 02138, USA. [2]Wyss Institute for Biologically Inspired Engineering, Harvard University, Cambridge, MA 02138, USA. [3]Department of Mechanical and Aerospace Engineering, University of California, San Diego, La Jolla, CA 92093, USA. [4]Dalio Institute of Cardiovascular Imaging, Department of Radiology, New York–Presbyterian Hospital and Weill Cornell Medical College, New York, NY 10021, USA. [5]Department of Chemistry and Chemical Biology, Harvard University, Cambridge, MA 02138, USA.
***Corresponding author. E-mail: nbartlett@seas.harvard.edu**
†These authors contributed equally to this work.

We used a multimaterial 3D printer (Connex500, Stratasys) to directly print the functional body of a robot that employs soft material components for actuation, obviating the need for complex molding techniques or assembly (*24*). The robot body is composed primarily of two nested hemispheroids. The flexible bottom hemispheroid features a small depression that provides an initial volume into which oxygen and butane are injected. Ignition of the gases causes a volumetric expansion (*25*, *26*), launching the robot into the air (Fig. 1, A and B). The top hemispheroid has a modulus of elasticity that ranges over three orders of magnitude (from approximately 1 MPa to 1 GPa) through a stepwise gradient of nine different layers, creating a structure that transitions from highly flexible (rubber-like) to fully rigid (thermoplastic-like). In addition to providing a mechanical interface for the rigid control components, the rigid portion of the top hemispheroid also prevents undesired expansion locally and focuses the energy of combustion into the ground, enhancing the jumping efficiency. Pneumatic legs, which use a nested hemi-ellipsoid design similar to that of the main body, surround the central explosive actuator and are used to tilt the body before a jump, controlling the direction of locomotion. This separation of power and control actuators simplifies actuation and gives greater control over direction.

In order to simplify prototyping, we chose a modular design with a rigid core module containing the control components (which are expensive and change infrequently during design iteration of the body), connected through a predefined interface to the body of the robot (Fig. 1C). This modularity enables efficient iteration of the robot body design, as well as rapid replacement in the case of destructive testing. The core module contains a custom circuit board, high-voltage power source, battery, miniature air compressor, butane fuel cell, bank of six solenoid valves, oxygen cartridge, pressure regulator, and an internal network of channels to facilitate interfacing between the components as necessary (fig. S1, A and B). The core module is mechanically attached to the rigid portion of the body with a layer of high-strength mushroom-head fasteners. Otherwise, it interfaces with the body only through four tubes (three pneumatic tubes for the legs and one tube for fuel delivery to the combustion chamber) and two wires (which produce the spark in the combustion chamber).

Characterization of nine 3D-printed materials with a set of mechanical tests informed the design of the 3D-printed rigid/soft robot. We performed qualitative twisting experiments to gain an intuitive understanding of the response of the various materials (Fig. 2A). Mechanical testing on a universal testing machine (Instron 5544, Instron) yielded quantitative values of material properties (supplementary text). This information was used to simulate the operation of the robot using finite element analysis (FEA) software, which allowed us to compare the relative efficiency of jumping robots with different

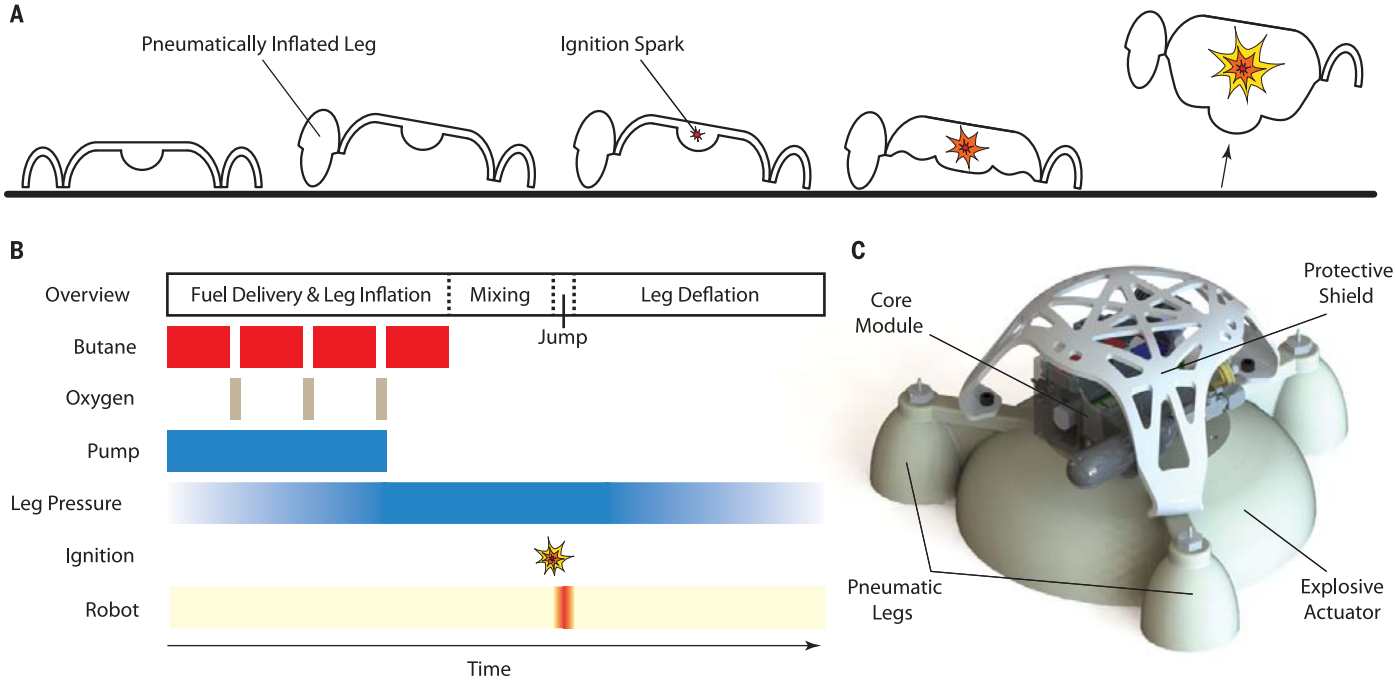


Fig. 1. Robot design and principle of operation. (**A**) To initiate a jump, the robot inflates a subset of its legs to tilt the body in the intended jump direction. Upon combustion, the bottom hemispheroid balloons out, pushing against the ground and propelling the robot into the air. (**B**) The ignition sequence consists of fuel delivery, mixing, and sparking. Butane and oxygen are alternately delivered to the combustion chamber (to promote mixing). After a short delay to promote additional mixing of the fuels, the gaseous mixture is ignited, resulting in combustion. Leg inflation occurs concurrently with fuel delivery, and leg deflation begins shortly after landing. (**C**) Computer-aided design model of the entire robot, consisting of the main explosive actuator surrounded by three pneumatic legs. A rigid core module that contains power and control components sits atop the main body, protected by a semisoft shield.

material distributions. Further simulations allowed us to examine the differences in stress concentrations as a function of material distribution (fig. S2). The results from these studies revealed that, when compared to an abrupt material transition, the incorporation of a graded interface could achieve a 30% reduction in maximum stress upon tensile loading, reaching a value comparable to the maximum stress observed in a soft, single-material model. Although a perfectly smooth gradient from rigid to flexible would have been ideal, the capability of the fabrication technique was limited to a stepwise gradient of at most nine materials. The actuation strategy necessitated a flexible bottom hemispheroid, whereas the off-the-shelf control components required a rigid housing; however, the stiffness distribution of the top hemispheroid was unconstrained. Thus, to determine how the material properties of the top hemispheroid would affect jumping, we simulated three cases: (i) a flexible top with a small rigid portion to mount control hardware, (ii) a top featuring a stiffness gradient from fully flexible to fully rigid, and (iii) a fully rigid top (Fig. 2B and movie S1). Simulations showed that the flexible top was inefficient at directing the energy of combustion into the ground and propelling the robot, suggesting weak jump performance. As expected, the simulated rigid top robot produced the highest ground reaction force, whereas the gradient top robot exhibited a performance between the two extremes.

We carried out additional simulations to investigate the behavior of the three designs during the impact of landing (Fig. 2C and movie S1).

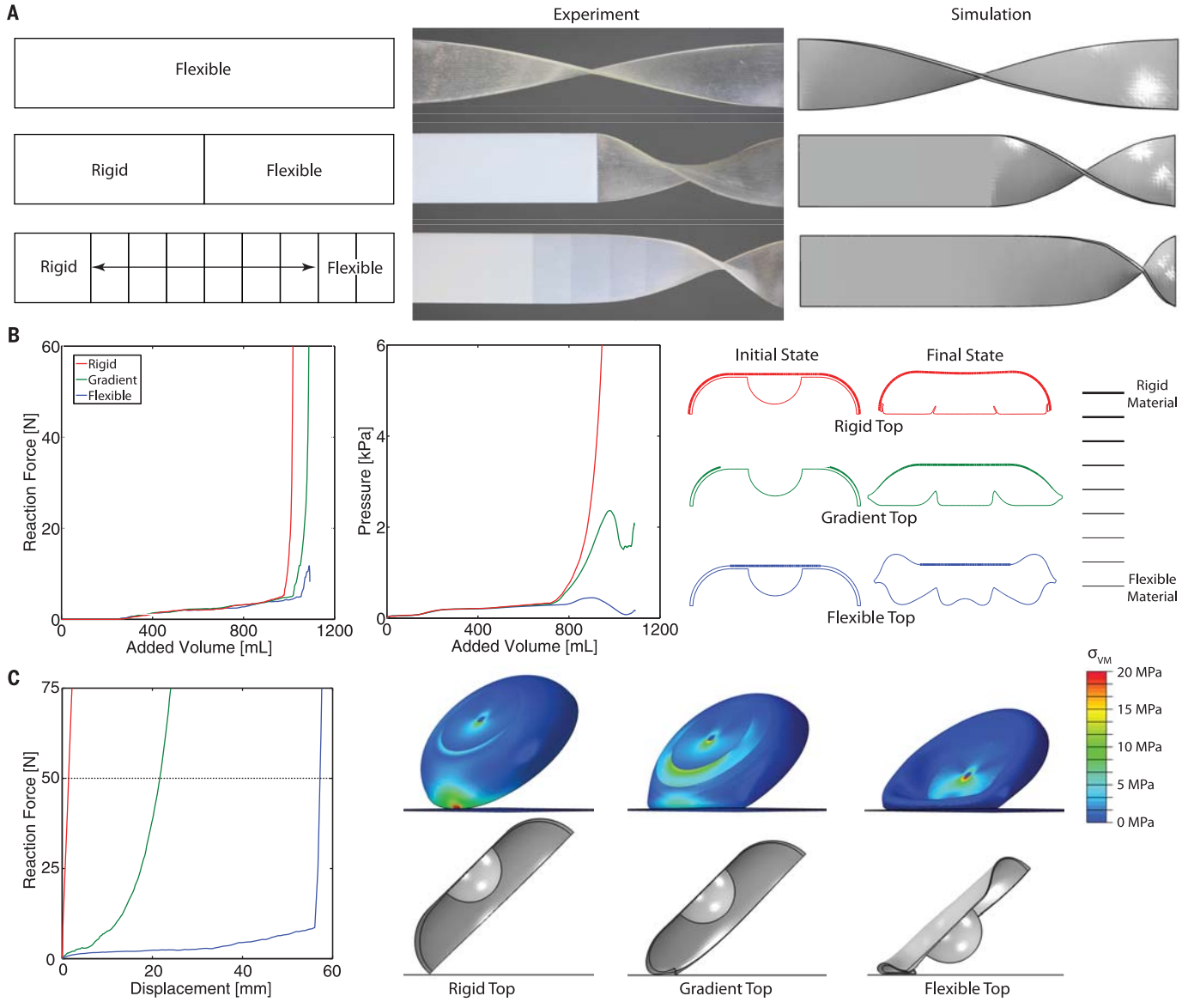


Fig. 2. Material tests and simulation results. (**A**) Qualitative twisting analysis comparing 3D-printed beams that are fully flexible, half rigid and half flexible, or transition gradually from rigid to flexible. These tests were performed to gain an understanding of how these materials respond, as well as to validate the numerical values of the material properties used in simulation. (Left) Material distribution of the beams. (Middle) Beams under torsion. (Right) Simulation of beams under torsion. (**B**) Jumping simulation. (Left) Ground reaction force as internal gases expand. (Middle) Pressure evolution inside the robot body as internal gases expand. (Right) Deformation state of rigid top, gradient top, and flexible top robot bodies at the initial state and the point of maximum simulated gas expansion. Line thicknesses indicate material stiffness. (**C**) Impact simulation. In the simulation, the robot strikes the ground at 45°. This angle was chosen as a particularly extreme loading condition and because it correlated with observations from jumping experiments. (Left) Reaction forces experienced by the three robots upon striking a solid plane under simulated conditions representative of actual testing conditions. (Right) FEA results of rigid top, gradient top, and flexible top robots, compared at 50 N.

The results indicate that the rigid top robot experiences a given reaction force (50 N) at a much smaller deformation than either the gradient or flexible top robots. Immediately upon impact, the rigid top robot experiences an abrupt increase in force, whereas the gradient top robot experiences a more moderate increase. The flexible top robot sees almost no increase, until the small rigid portion strikes the ground, initiating a rapid increase akin to that of the rigid top robot. Integrating the force-displacement curves (up to 50 N), we find that the rigid and flexible top robots only absorb 13 and 73% (respectively) of the impact energy that the gradient top robot absorbs. The increased energy absorbed by the gradient top robot during impact suggests that it will be most successful at distributing the impulse over a longer duration, therefore reducing peak stresses and providing the least violent landing.

By 3D-printing different test cases, we experimentally verified these simulation results. A jumping robot with a completely rigid top was able to jump 1.12 m untethered using 40 ml of butane and 120 ml of oxygen. Identical testing conditions on a gradient top robot produced a jump of 0.25 m. A flexible top robot was deemed impractical to print because of the predictions from FEA. As predicted by the simulations, the gradient top robot was less efficient at jumping. However, the gradient top robot was better able to withstand the impact of landing (Fig. 3A and movie S2). In one test, the body of the rigid top robot shattered upon landing, surviving a total of just five jumps; the gradient top robot survived more than twice that number of jumps and remained operational. Other nearly identical gradient top robots survived over 100 jumps (in 81% of these tests, we removed the core module from the body and delivered the combustion products and ignition sparks through a tether to simplify testing, reducing the system mass to about 50% that of the untethered system). To provide a direct comparison in landing behavior, the gradient top robot was additionally dropped from the maximum height achieved by the rigid top robot and successfully survived 35 falls (supplementary text). The stiffness gradient provides the necessary rigidity to transfer the impulse of combustion to generate effective jumping, and the compliance of the base absorbs and dissipates the energy of the landing impact. By trading the jumping efficiency of the rigid robot for an improved ability to survive landings, the gradient top robot demonstrated a greater overall robustness.

Further testing on the gradient top robot showed high resilience and good performance (Fig. 3B and movie S2). This robot autonomously jumped up to 0.76 m (six body heights) high and demonstrated directional jumping of up to 0.15 m (0.5 body lengths, 20% of jump height) laterally per jump (Fig. 3C and movie S2). Unlike previous combustion-powered soft jumpers that were either tethered (*25*) or achieved only a few untethered jumps due to inconsistent connection of electrical and mechanical components at the interface of the rigid and soft components (*26*), this design allowed for many successful jumps with a single soft robot (21 untethered jumps and 89 tethered jumps). Another jumper design has also shown the ability to perform multiple jumps, can operate on uneven terrain, and can even recover from landing in any orientation (*27*), although at the sacrifice of directional control. In our system, the high energy density of the fuels theoretically allows onboard storage of sufficient fuel for 32 consecutive jumps (supplementary text). The bodies were extremely robust, surviving dozens of jumps before they became unusable. The monolithic design has no sliding parts or traditional joints that can be fouled or obstructed by debris or rough terrain, and the nested design requires minimal deformation for actuation. As with previous jumping soft robots powered by combustion (*25*–*27*), and untethered systems exposed to direct flames (*17*), we did not observe significant damage to the soft (or rigid) body materials due to the brief

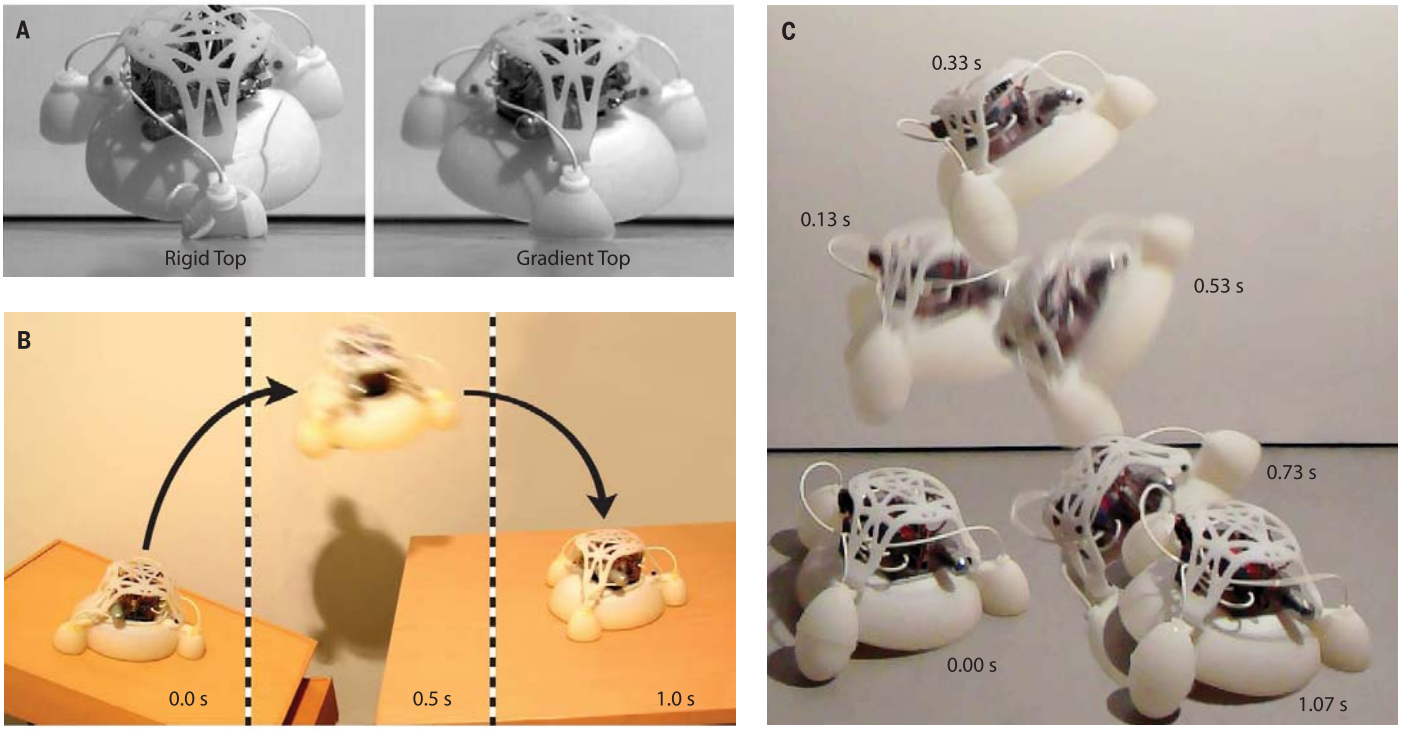


Fig. 3. Experimental testing results. (**A**) Frames shortly after the moment of ground contact from movie S2 (Impact Comparison). Identical testing conditions were used to analyze the difference in landing between a robot with a rigid top and one with a gradient top. Because the rigid top robot jumped higher under combustion-powered testing, the gradient top robot was dropped from the maximum height achieved by the rigid top robot for a direct comparison. (Left) The rigid top robot fractures upon impact. (Right) The gradient top robot is able to absorb the impact and survive the fall. (**B**) Frames from movie S2 (Jump onto Table) at various times. The robot performs a targeted jump off of an angled surface onto a table. (Left) As the robot prepares for the jump, oxygen and butane are delivered into the combustion chamber. (Middle) Upon ignition of the fuel, the robot is propelled into the air. (Right) After jumping across a gap, the robot lands on a table. (**C**) Frames from movie S2 (Directional Jump) at various times during a directional jump. The robot pitches backward during the jump, providing a soft landing on the inflated legs. Upon impact with the ground, the robot pitches forward and returns to its pre-jump stance.

exposure to elevated combustion temperatures and flames.

The fabrication of soft robots using multimaterial 3D printing has numerous advantages over traditional molding techniques. This strategy promotes high-throughput prototyping by enabling rapid design iteration with no additional cost for increased morphological complexity. By allowing designers greater freedom, 3D printing also facilitates the implementation of good robotic design principles, such as modularity and the separation of power and control actuators. Beyond soft robotics specifically, the ability to print a single structure composed of multiple materials enables investigation into mechanically complex designs, without the drawbacks of complicated assembly or inconsistent manufacturing repeatability. One such design is a modulus gradient that eases the transition from soft to rigid components through stress reduction at the interface of materials mismatched in compliance. Although the materials available to this fabrication strategy are currently limited and perhaps best suited to the fabrication of prototype devices, future development of materials compatible with 3D printing will only enhance the relevance of this approach.

REFERENCES AND NOTES

1. D. Rus, M. T. Tolley, *Nature* **521**, 467–475 (2015).
2. D. Trivedi, C. D. Rahn, W. M. Kier, I. D. Walker, *Appl. Bionics Biomech.* **5**, 99–117 (2008).
3. R. Pfeifer, M. Lungarella, F. Iida, *Commun. ACM* **55**, 76 (2012).
4. S. Kim, C. Laschi, B. Trimmer, *Trends Biotechnol.* **31**, 287–294 (2013).
5. C. Majidi, *Soft Robotics* **1**, 5–11 (2014).
6. C. Laschi, M. Cianchetti, *Front. Bioeng. Biotechnol.* **2**, 1–5 (2014).
7. W. McMahan *et al.*, in *Proceedings of the 2006 IEEE International Conference on Robotics and Automation*, 15 to 18 May 2006, Orlando, FL, pp. 2336–2341.
8. R. F. Shepherd *et al.*, *Proc. Natl. Acad. Sci. U.S.A.* **108**, 20400–20403 (2011).
9. C. Laschi *et al.*, *Adv. Robot.* **26**, 709–727 (2012).
10. H.-T. Lin, G. G. Leisk, B. Trimmer, *Bioinspir. Biomim.* **6**, 026007 (2011).
11. C. D. Onal, D. Rus, *Bioinspir. Biomim.* **8**, 026003 (2013).
12. A. D. Marchese, C. D. Onal, D. Rus, *Soft Robotics* **1**, 75–87 (2014).
13. R. Pfeifer, M. Lungarella, F. Iida, *Science* **318**, 1088–1093 (2007).
14. K. Suzumori, S. Iikura, H. Tanaka, *Control Syst. IEEE* **12**, 21–27 (1992).
15. Y.-L. Park *et al.*, *Bioinspir. Biomim.* **9**, 016007 (2014).
16. P. Polygerinos, Z. Wang, K. C. Galloway, R. J. Wood, C. J. Walsh, *Robot. Auton. Syst.*; available at www.sciencedirect.com/science/article/pii/S0921889014001729.
17. M. T. Tolley *et al.*, *Soft Robotics* **1**, 213–223 (2014).
18. H. Lipson, *Soft Robotics* **1**, 21–27 (2014).
19. K.-J. Cho *et al.*, *Int. J. Precision Eng. Manuf.* **10**, 171–181 (2009).
20. F. Ilievski, A. D. Mazzeo, R. F. Shepherd, X. Chen, G. M. Whitesides, *Angew. Chem.* **123**, 1930–1935 (2011).
21. E. Steltz, A. Mozeika, N. Rodenberg, E. Brown, H. M. Jaeger, in *Proceedings of the 2009 IEEE/RSJ International Conference on Intelligent Robots and Systems*, 10 to 15 October 2009, St. Louis, MO, pp. 5672–5677.
22. T. J. Roberts, E. Azizi, *J. Exp. Biol.* **214**, 353–361 (2011).
23. A. Miserez, T. Schneberk, C. Sun, F. W. Zok, J. H. Waite, *Science* **319**, 1816–1819 (2008).
24. Materials and methods are available as supplementary materials on *Science* Online.
25. R. F. Shepherd *et al.*, *Angew. Chem.* **125**, 2964–2968 (2013).
26. M. T. Tolley *et al.*, in *Proceedings of the 2014 IEEE/RSJ International Conference on Intelligent Robots and Systems*, 14 to 18 September 2014, Chicago, IL, pp. 561–566.
27. M. Loepfe, C. M. Schumacher, U. B. Lustenberger, W. J. Stark, *Soft Robotics* **2**, 33–41 (2015).

ACKNOWLEDGMENTS

This material is based on work supported by NSF under award number DMR-1420570; the Wyss Institute for Biologically Inspired Research; and an Army Research Office, National Defense Science and Engineering Graduate (NDSEG) fellowship. Any opinions, findings, conclusions, or recommendations expressed in this material are those of the authors and do not necessarily reflect those of the funding organizations.

SUPPLEMENTARY MATERIALS

www.sciencemag.org/content/349/6244/161/suppl/DC1
Materials and Methods
Supplementary Text
Figs. S1 and S2
Table S1
References (*28*, *29*)
Movies S1 and S2

27 February 2015; accepted 11 June 2015
10.1126/science.aab0129

APPLIED PHYSICS

Mid-infrared plasmonic biosensing with graphene

Daniel Rodrigo,[1] Odeta Limaj,[1] Davide Janner,[2] Dordaneh Etezadi,[1] F. Javier García de Abajo,[2,3] Valerio Pruneri,[2,3] Hatice Altug[1]*

Infrared spectroscopy is the technique of choice for chemical identification of biomolecules through their vibrational fingerprints. However, infrared light interacts poorly with nanometric-size molecules. We exploit the unique electro-optical properties of graphene to demonstrate a high-sensitivity tunable plasmonic biosensor for chemically specific label-free detection of protein monolayers. The plasmon resonance of nanostructured graphene is dynamically tuned to selectively probe the protein at different frequencies and extract its complex refractive index. Additionally, the extreme spatial light confinement in graphene—up to two orders of magnitude higher than in metals—produces an unprecedentedly high overlap with nanometric biomolecules, enabling superior sensitivity in the detection of their refractive index and vibrational fingerprints. The combination of tunable spectral selectivity and enhanced sensitivity of graphene opens exciting prospects for biosensing.

Graphene has the potential to reshape the landscape of photonics and optoelectronics owing to its exceptional optical and electrical properties (*1*–*3*). In particular, its infrared (IR) response is characterized by long-lived collective electron oscillations (plasmons) that can be dynamically tuned by electrostatic gating, in contrast to conventional plasmonic materials such as noble metals (*4*–*10*). Furthermore, the electromagnetic fields of graphene IR plasmons display unprecedented spatial confinement, making them extremely attractive for enhanced light-matter interactions and integrated mid-IR photonics (*11*–*14*). Specifically, biosensing is an area in which graphene tunability and IR light localization offer great opportunities.

The mid-IR range is particularly well suited for biosensing, as it encompasses the molecular vibrations that uniquely identify the biochemical building blocks of life, such as proteins, lipids, and DNA (*15*). IR absorption spectroscopy is a powerful technique that provides exquisite biochemical information in a nondestructive label-free fashion by accessing these vibrational fingerprints. Nevertheless, vibrational absorption signals are prohibitively weak because of the large mismatch between mid-IR wavelengths (2 to 6 μm) and biomolecular dimensions (<10 nm). To overcome this limitation, high sensitivity can be achieved by exploiting the strong optical near fields in the vicinity of resonant metallic nanostructures (*16*–*18*); however, this comes at the expense of a reduced spectral bandwidth and is ultimately limited by the relatively poor field confinement of metals in the mid-IR (*19*).

Here, we report a graphene-based tunable mid-IR biosensor and demonstrate its potential for quantitative protein detection and chemical-specific molecular identification. Our device (Fig. 1A) consists of a graphene layer synthesized by chemical vapor deposition and transferred to a 280-nm-thick native silica oxide of a silicon substrate. Graphene nanoribbon arrays (width W = 20 to 60 nm and period $P \approx 2W$) are then patterned using electron beam lithography and oxygen plasma etching (*20*). A scanning electron microscope image and an atomic force microscope profile for typical samples are shown in Fig. 1, B and C. We apply an electrostatic field across the SiO_2 layer through a bias voltage (V_g)

[1]Institute of BioEngineering, École Polytechnique Fédérale de Lausanne, CH-1015 Lausanne, Switzerland. [2]Institut de Ciències Fotòniques, Mediterranean Technology Park, 08860 Castelldefels (Barcelona), Spain. [3]Institució Catalana de Recerca i Estudis Avançats, 08010 Barcelona, Spain.
*Corresponding author. E-mail: hatice.altug@epfl.ch

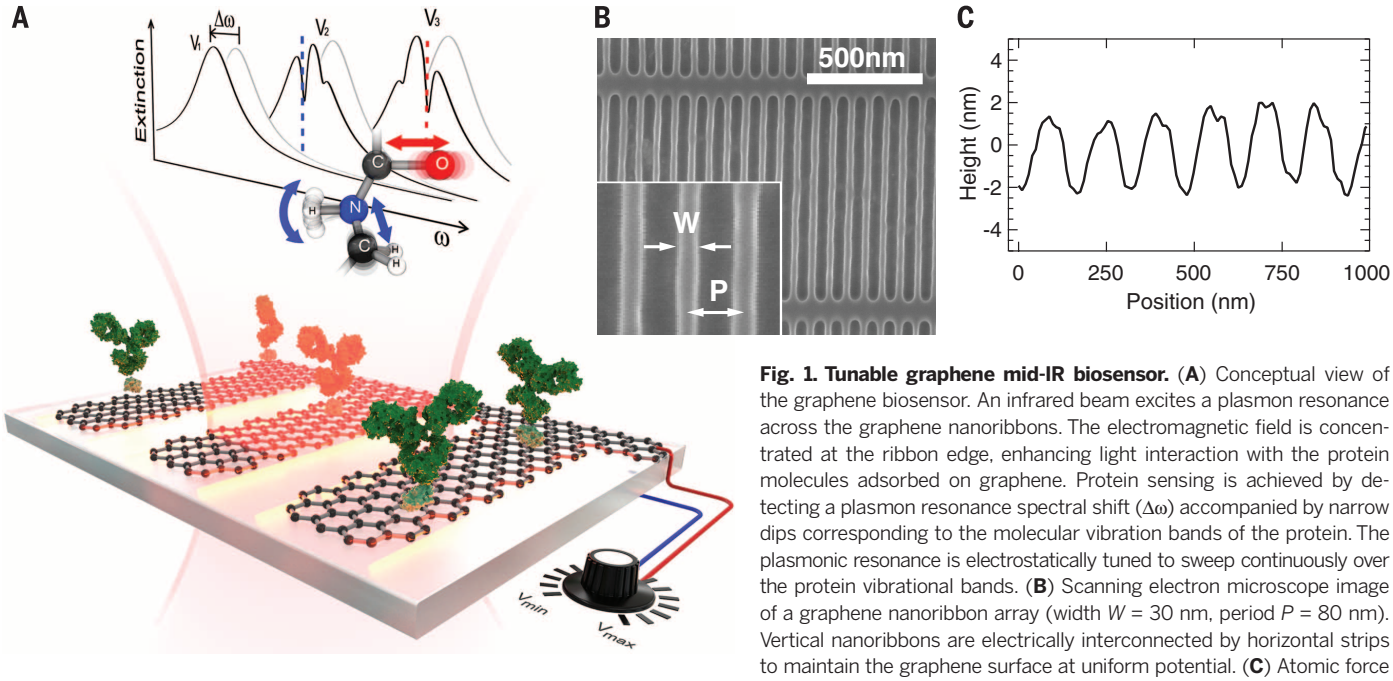


Fig. 1. Tunable graphene mid-IR biosensor. (**A**) Conceptual view of the graphene biosensor. An infrared beam excites a plasmon resonance across the graphene nanoribbons. The electromagnetic field is concentrated at the ribbon edge, enhancing light interaction with the protein molecules adsorbed on graphene. Protein sensing is achieved by detecting a plasmon resonance spectral shift ($\Delta\omega$) accompanied by narrow dips corresponding to the molecular vibration bands of the protein. The plasmonic resonance is electrostatically tuned to sweep continuously over the protein vibrational bands. (**B**) Scanning electron microscope image of a graphene nanoribbon array (width W = 30 nm, period P = 80 nm). Vertical nanoribbons are electrically interconnected by horizontal strips to maintain the graphene surface at uniform potential. (**C**) Atomic force microscope cross section of a graphene nanoribbon array.

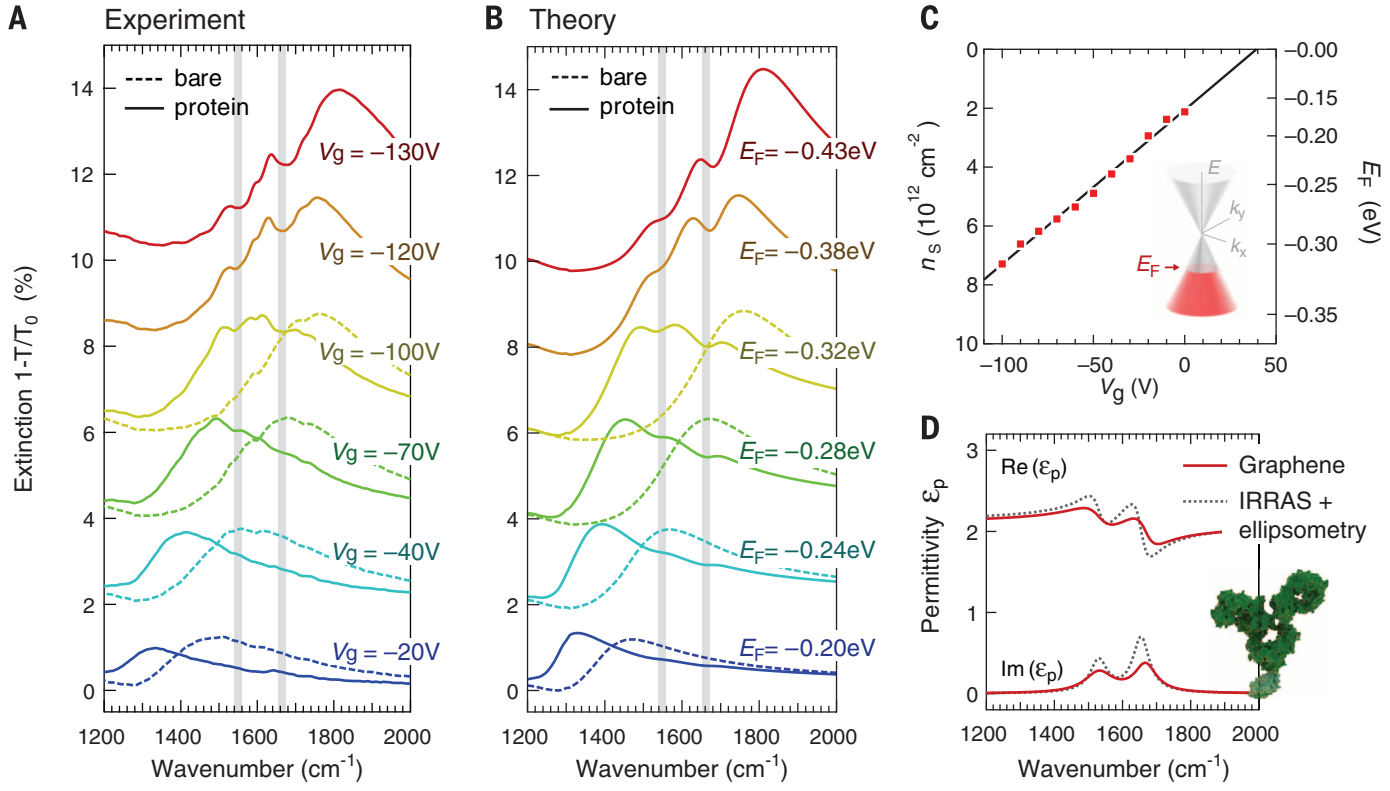


Fig. 2. Mid-IR spectrum of the graphene biosensor. (**A**) Extinction spectra of the graphene nanoribbon array (W = 30 nm, P = 80 nm) for bias voltages V_g from −20 V to −130 V before (dashed curves) and after (solid curves) protein bilayer formation. Extinction is calculated as the relative difference in transmission between regions with (T) and without (T_0) graphene nanoribbons. Gray vertical strips indicate amide I and II vibrational bands of the protein. (**B**) Analytic calculation of the extinction spectra after fitting graphene and protein parameters to reproduce experimental data. (**C**) Graphene carrier density (n_s) and Fermi energy (E_F) extracted from experimental IR extinction spectra of the bare graphene nanoribbon array at different applied bias voltages V_g. (**D**) Permittivity of the protein bilayer extracted from the analytic fit to the experimental IR spectra (solid red curves) of the graphene biosensor compared to the permittivity extracted from IRRAS and ellipsometry measurements (dashed black curves). Upper and lower curves show the real and imaginary components, respectively.

that is varied between 0 and 120 V to dynamically control the Fermi level (E_F) of graphene. Extinction spectra of the device are acquired using Fourier transform infrared (FTIR) spectroscopy for the incident electric field polarized perpendicular to the nanoribbons. Figure 2A shows the extinction for a nanoribbon array with W = 30 nm, P = 80 nm, and different values of V_g (dashed curves). A prominent resonance is observed, which is associated with localized surface plasmons (LSPs) polarized across the nanoribbons. By changing V_g, the resonance frequency is tuned continuously from 1450 cm^{-1} to above 1800 cm^{-1}. The ribbon width W = 30 nm is chosen so that the frequency tuning range sweeps across the target vibrational fingerprints (fig. S1).

We sought to detect protein molecules, the primary material of life enabling most of the critical biological functions. The main vibrational fingerprints of proteins are amide I and II bands (1660 and 1550 cm^{-1}), which are primarily associated with the C=O stretch and N-H bend modes in the amide functional group. For demonstration of protein detection, we used recombinant protein A/G and goat anti-mouse immunoglobulin G (IgG). Incubation of A/G on the sensor surface allows the formation of a protein monolayer by physisorption, which is then used to bind IgG antibodies and form a well-defined protein bilayer (*20*). The extinction spectra of the sensor are presented in Fig. 2A before and after protein bilayer formation, showing radical changes upon protein immobilization. The first observed prominent effect is a red shift of the plasmonic resonance as a consequence of the change in the refractive index at the sensor surface. Despite the nanometric thickness of the protein bilayer, we detected frequency shifts exceeding 200 cm^{-1}. The second prominent effect is the emergence of two spectral dips at 1660 cm^{-1} and 1550 cm^{-1} that are almost undetectable when they are far from the plasmonic resonance (e.g., for V_g = −20 V) and become progressively more intense with increasing spectral overlap (e.g., for V_g = −130 V). Their spectral positions coincide with the amide I and II bands, respectively, unambiguously revealing the presence of the protein compounds in a chemically specific manner. The decrease in extinction induced by the vibrational modes is the result of resonant coupling between plasmons and molecular vibrations (*21*).

To extract quantitative information on the protein optical parameters, we use an analytical model of the IR response of the graphene nanoribbon array (*22*). We model graphene in the electrostatic limit (W, P << λ) under the assumption that the ribbon response is dominated by the lowest-order transversal mode. The model involves a detailed account of the protein layer; however, a reasonable agreement is obtained in the limit of a thick protein layer. The transmission coefficient of the structure then reduces to

$$t = t_0 + \frac{i4\pi^2\alpha^{eff}(\omega)(1+r_0)t_0}{n_2 P\lambda} \quad (1)$$

where

$$\alpha^{eff}(\omega) = \frac{0.894W^2}{\frac{A}{n_1^2+n_2^2} - \frac{i\omega W}{\sigma(\omega)}} \quad (2)$$

is an effective graphene-ribbon polarizability that takes into account the complex refractive indices of the silica substrate n_2 (*23*) and the material immediately above the ribbons n_1, while the coefficient A is a function of P/W (in particular, A = 28.0 for P/W = 2.67). Here, t_0 and r_0 are the transmission and reflection coefficients of the interface between media 1 and 2 in the absence of graphene. The response of the latter enters through its frequency-dependent surface conductivity σ(ω), which we model in the local random-phase approximation (*11*). Finally, we compute the ratio of transmission in regions with and without graphene as $|t/t_0|^2$, which is the magnitude measured in the experiments.

We first used the analytic model to extract the graphene parameters from experimental IR spectra for bare nanoribbons (i.e., with n_1 = 1). The calculated spectra are reported in Fig. 2B (dashed curves) for the extracted relaxation time (τ = 15 fs) and

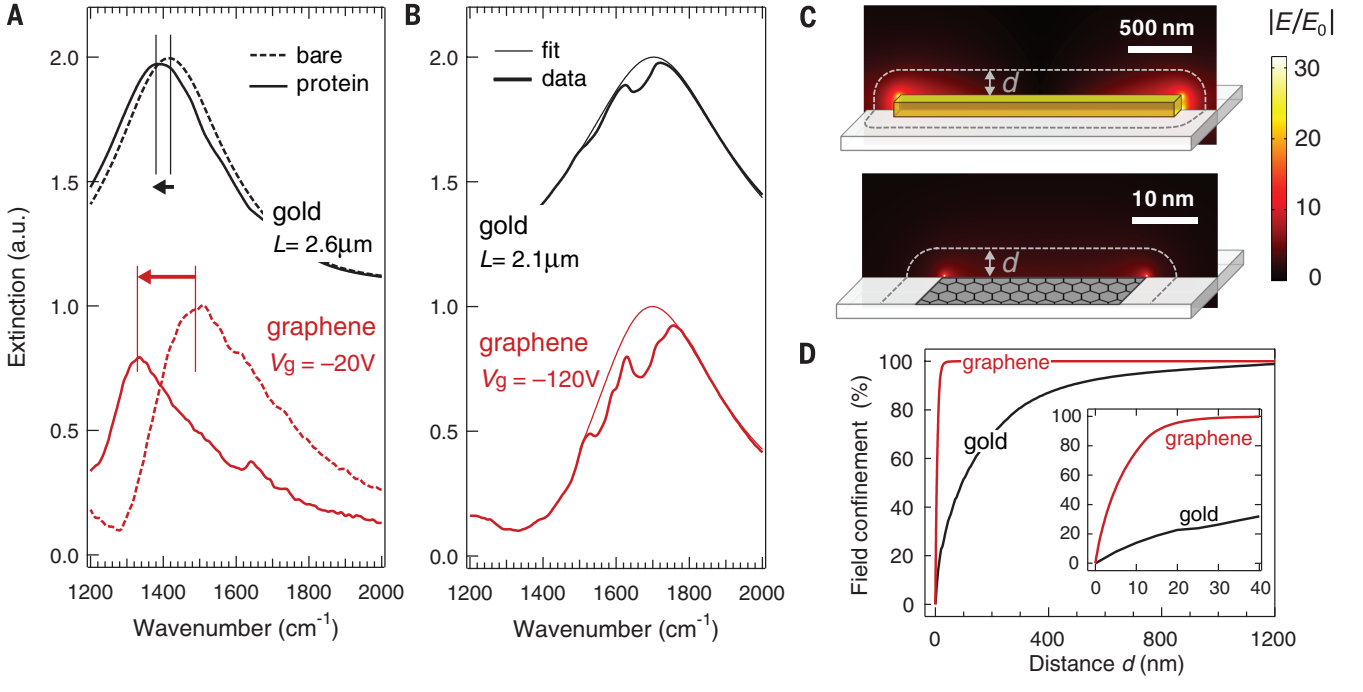


Fig. 3. Graphene versus gold. (**A**) Extinction spectra of graphene and gold nanoantenna arrays before (dashed curves) and after (solid curves) protein bilayer formation for plasmonic resonance peak away from the molecular vibration bands. The gold antennas have dimensions 2.6 μm × 0.2 μm × 0.1 μm while the graphene is biased to V_g = −20 V. The spectral shift of the plasmonic resonance (indicated by horizontal arrows) shows the refractive index sensitivity of the biosensors. (**B**) Extinction spectra of graphene and gold biosensors after protein formation (thick curves) and fitting (thin curves) for plasmon peak overlapping with the molecular vibration bands. The gold antennas have dimensions 2.1 μm × 0.2 μm × 0.1 μm and the graphene gate voltage is V_g = −120 V. The intensity of the spectral features at amide I and II bands (1660 to 1550 cm^{-1}) indicates the SEIRA sensitivity of the biosensors. (**C**) Near-field enhancement distribution $|E/E_0|$ in the plasmonic sensors operating at 1600 cm^{-1} resonance frequency. (**D**) Percentage of space-integrated near-field intensity confined within a volume extending a distance d outside the nanoantenna. Inset shows a zoom-in for d between 0 and 40 nm.

Fermi energies (E_F = −0.17 to −0.43 eV). We observe that the carrier density ($n_s \sim E_F^2$) changes linearly with V_g (Fig. 2C) and graphene has an intrinsic doping E_{F0} = −0.17 eV produced by charge transfer from the silica. Next, the analytic model is used to retrieve the protein permittivity from experimental results by adjusting a Lorentzian permittivity

$$\varepsilon_p(\omega) = n_1^2 = n_\infty^2 + \sum_{k=1}^{2} \frac{S_k^2}{\omega_k^2 - \omega^2 - i\omega\gamma_k} \quad (3)$$

Good agreement is observed between experimental and calculated spectra (Fig. 2B) for the protein Lorentzian parameters upon least-squares fitting. The extracted permittivity has a nondispersive term n_∞^2 = 2.08 and shows two absorption peaks at 1668 and 1532 cm^{-1}, matching the amide I and II bands, respectively (Fig. 2D). The fitted permittivity is also in good agreement with independent protein permittivity measurements from ellipsometry for n_∞^2 and IR reflection absorption spectroscopy (IRRAS) for S_k, ω_k, and γ_k (*20*). There is, however, a small discrepancy, which we attribute to a slight overestimate of plasmon-protein coupling in the theoretical model. These results indicate that the proposed graphene biosensor combines refractive index sensing, so far a prerogative of visible plasmonic sensors, with the unique chemical specificity of mid-IR spectroscopy, together with the extra degree of freedom enabled by the graphene electro-optical tunability.

The characteristics of our graphene biosensor become more evident by comparing its spectral response to that of a state-of-the-art metallic localized surface plasmon resonance (LSPR) sensor composed of a gold dipole-antenna array (Fig. 3). Both devices are first operated in a spectral range free of protein vibrational modes by setting graphene at V_g = −20 V and designing a gold dipole length L = 2.6 μm (Fig. 3A). Upon protein immobilization, we detect a resonance shift of 160 cm^{-1} for graphene, which is approximately 6 times the 27 cm^{-1} shift obtained with gold. Next, the operation spectrum is moved toward the protein amide I and II bands by setting graphene at V_g = −120 V and using a different gold sensor with L = 2.1 μm (Fig. 3B). Clearly, dynamic tunability of graphene is one of its main advantages over gold for surface-enhanced IR absorption (SEIRA), enabling sensing over a broad spectrum with a single device. In addition, for the SEIRA signal corresponding to the amide I band, the graphene sensor features a signal modulation of 27%, which is almost 3 times that observed with the gold sensor (11%).

The large spectral shifts and absorption signals confirm the unprecedented sensitivity of our graphene biosensor to the complex refractive index of the target molecule. For similar IR-frequency plasmons, the graphene atomic thickness leads to a higher confinement, resulting in a much larger spatial overlap between the mid-IR plasmonic field and the analyte. Figure 3C shows the near-field distribution of LSPR modes in graphene nanoribbons and gold dipole arrays calculated with a finite-element method. The field hotspots are located at the endpoints of the gold dipole and along the edges of the graphene nanoribbon. By computing the percentage of near-field intensity confined within a given distance d from the structure (Fig. 3D), we observe that 90% of the mode energy is confined within 15 nm from the graphene surface, whereas the same percentage is spread over a distance 500 nm away from the gold surface, thus confirming the tighter field confinement of graphene in the mid-IR. As the biosensing signal comes only from the field inside the target volume, we also calculate the field overlap with an 8-nm-thick protein bilayer, which is 29% for graphene versus only 4% for gold. The near-field intensity overlap can be experimentally extracted as the ratio of the relative resonance shift ($\Delta\omega/\omega$) and the permittivity variation ($\varepsilon_p - \varepsilon_{air}$) (*24*). This estimate yields 26% and 5% field overlap for graphene and gold, in good agreement with simulations (see above). These results demonstrate the ability of graphene to provide stronger light-protein interactions beyond state-of-the-art metallic plasmonic sensors; further improvement in the graphene quality should lead to even better sensitivity and spectral resolution.

REFERENCES AND NOTES

1. A. N. Grigorenko, M. Polini, K. S. Novoselov, *Nat. Photonics* **6**, 749–758 (2012).
2. F. J. García de Abajo, *Science* **339**, 917–918 (2013).
3. A. Vakil, N. Engheta, *Science* **332**, 1291–1294 (2011).
4. M. Jablan, H. Buljan, M. Soljacic, *Phys. Rev. B* **80**, 245435 (2009).
5. L. Ju *et al.*, *Nat. Nanotechnol.* **6**, 630–634 (2011).
6. H. Yan *et al.*, *Nat. Photonics* **7**, 394–399 (2013).
7. A. Woessner *et al.*, *Nat. Mater.* **14**, 421–425 (2015).
8. Z. Fang *et al.*, *ACS Nano* **7**, 2388–2395 (2013).
9. V. W. Brar *et al.*, *Nano Lett.* **13**, 2541–2547 (2013).
10. Z. Fei *et al.*, *Nature* **487**, 82–85 (2012).
11. F. H. L. Koppens *et al.*, *Nano Lett.* **11**, 3370–3377 (2011).
12. B. Vasić *et al. J. Appl. Phys.* **113**, 013110 (2013).
13. Y. Li *et al.*, *Nano Lett.* **14**, 1573–1577 (2014).
14. P. Li *et al.*, *Nano Lett.* **14**, 4400–4405 (2014).
15. P. R. Griffiths, J. A. De Haseth, *Fourier Transform Infrared Spectrometry* (Wiley, New York, 2007).
16. F. Neubrech *et al.*, *Phys. Rev. Lett.* **101**, 157403 (2008).
17. R. Adato, H. Altug, *Nat. Commun.* **4**, 2154 (2013).
18. C. Wu *et al.*, *Nat. Mater.* **11**, 69–75 (2012).
19. Y. Zhong *et al.*, *J. Nanophotonics* **9**, 093791 (2015).
20. See supplementary materials on *Science* Online.
21. R. Adato *et al.*, *Nano Lett.* **13**, 2584–2591 (2013).
22. F. J. García de Abajo, *ACS Photonics* **1**, 135–152 (2014).
23. E. D. Palik, *Handbook of Optical Constants of Solids* (Academic Press, New York, 1998).
24. J. D. Joannopoulos *et al.*, *Photonic Crystals: Molding the Flow of Light* (Princeton Univ. Press, Princeton, NJ, 2011).

ACKNOWLEDGMENTS

Supported by European Commission grants FP7-IEF-2013-625673-GRYPHON, Graphene Flagship CNECT-ICT-604391, and FP7-ICT-2013-613024-GRASP; the Spanish Ministry of Economy and Competitiveness (MINECO) "Fondo Europeo de Desarrollo Regional" (FEDER) through grant TEC2013-46168-R; NATO's Public Diplomacy Division in the framework of "Science for Peace"; European Union's Horizon 2020 research and innovation program under grant agreement No 644956; the Swiss National Science Foundation through project 133583; and Fundació Privada Cellex, the Severo Ochoa Program, and the Ramon y Cajal fellowship program. We also acknowledge École Polytechnique Fédérale de Lausanne and Center of MicroNano Technology for financial support and nanofabrication. This paper is dedicated to the memory of our friend and colleague, Julien Perruisseau-Carrier.

SUPPLEMENTARY MATERIALS

www.sciencemag.org/content/349/6244/165/suppl/DC1
Materials and Methods
Supplementary Text
Figs. S1 to S3
Reference (*25*, *26*)

11 April 2015; accepted 4 June 2015
10.1126/science.aab2051

GALAXY EVOLUTION

An over-massive black hole in a typical star-forming galaxy, 2 billion years after the Big Bang

Benny Trakhtenbrot,[1]* C. Megan Urry,[2,3,4] Francesca Civano,[3,5] David J. Rosario,[6] Martin Elvis,[5] Kevin Schawinski,[1] Hyewon Suh,[5,7] Angela Bongiorno,[8] Brooke D. Simmons[9]

Supermassive black holes (SMBHs) and their host galaxies are generally thought to coevolve, so that the SMBH achieves up to about 0.2 to 0.5% of the host galaxy mass in the present day. The radiation emitted from the growing SMBH is expected to affect star formation throughout the host galaxy. The relevance of this scenario at early cosmic epochs is not yet established. We present spectroscopic observations of a galaxy at redshift z = 3.328, which hosts an actively accreting, extremely massive BH, in its final stages of growth. The SMBH mass is roughly one-tenth the mass of the entire host galaxy, suggesting that it has grown much more efficiently than the host, contrary to models of synchronized coevolution. The host galaxy is forming stars at an intense rate, despite the presence of a SMBH-driven gas outflow.

Several lines of observational evidence, spanning a wide range of cosmic epochs, have led to a commonly accepted picture wherein supermassive black holes (SMBHs, $M_{BH} > 10^6\,M_\odot$; $M_\odot$ is the solar mass) coevolve with their host galaxies (*1*–*4*). Moreover, energy- and/or momentum-driven "feedback" from accreting SMBHs (Active Galactic Nuclei; AGN) is thought to quench star formation in the host galaxy (*5*). To directly test the relevance of such scenarios at

Downloaded from www.sciencemag.org on July 10, 2015

early cosmic epochs (high redshifts, z) requires the most basic properties of SMBHs and their hosts, including masses and growth rates, to be observed. Several observational studies found that at $z \leq 2$ (more than 3.3 billion years after the Big Bang), the typical BH-to-stellar mass ratio, M_{BH}/M_*, increases toward higher redshifts (*6*–*8*), suggesting that some SMBHs were able to gather mass more efficiently, or faster, than the stellar populations in their hosts. To date, measurements of M_{BH} at earlier epochs ($z > 2$) have only been conducted for small samples of extremely luminous objects [$L_{AGN} > 10^{46}$ erg s^{-1}; (*9*–*12*)] representing a rare subset of all accreting SMBHs, with number densities on the order of 1 to 10 per Gpc^3 [i.e., $\sim 10^{-9}$ to 10^{-8} Mpc^{-3}; (*13*)]. Moreover, the high AGN luminosities in such sources overwhelm the host galaxy emission and prohibit a reliable determination of M_*, and therefore of M_{BH}/M_*. We initiated an observational campaign aimed at estimating M_{BH} in x-ray–selected, unobscured $z \sim 3$ to 4 AGN within the Cosmic Evolution Survey field [COSMOS; (*14*)]. Such sources have lower AGN luminosities and are more abundant than the aforementioned luminous sources by factors of 100 to 1000 [e.g., (*13*, *15*)] and thus form a more representative subset of the general AGN population. Moreover, the fainter AGN luminosities and rich multiwavelength coverage of AGN within the COSMOS field enable reliable measurements of the mass and growth rate of the stellar populations in the host galaxies (M_* and star-formation rate, SFR).

CID–947 is an x-ray–selected, unobscured AGN at $z = 3.328$, detected in both *XMM-Newton* and *Chandra* x-ray imaging data of the COSMOS field [see fig. S4 and sections S2 and S4 in the supplementary materials (*16*)]. We obtained a near-infrared (IR) *K*-band spectrum of CID–947 using the MOSFIRE instrument at the W. M. Keck telescope, which at $z = 3.328$ covers the hydrogen Hβ broad emission line (see details in section S1 in the supplementary materials). The calibrated spectrum shows a very broad Hβ emission line, among other features (Fig. 1). Our spectral analysis indicates that the monochromatic AGN luminosity at rest-frame 5100 Å is $L_{5100} = 3.58^{+0.07}_{-0.08} \times 10^{45}$ ergs^{-1}. The typical line-of-sight velocity [i.e., the full-width at half-maximum of the line] is $11,330^{+800}_{-870}$ kms^{-1} (see section S1.2 in the supplementary materials). By combining this line width with the observed L_{5100} and relying on an empirically calibrated estimator for M_{BH}, based on the virial motion of ionized gas near the SMBH (*17*), we obtain $M_{BH} = 6.9^{+0.8}_{-1.2} \times 10^9 M_\odot$. All the reported measurement-related uncertainties are derived by a series of simulations and represent the 16th and 84th quantiles of the resulting distributions. These simulations indicate a SMBH mass larger than 3.6×10^9 $M_\odot$ at the 99% confidence level (see sections S1.2 and S3 in the supplementary materials for more details). Determinations of M_{BH} from single-epoch spectra of the Hβ emission line are known to also be affected by significant systematic uncertainties, of up to ~0.3 to 0.4 dex. For a detailed discussion of some of the systematics and related issues, see section S3 in the supplementary materials. This high M_{BH} is comparable with some of the most massive BHs known to date in the local universe (*18*) or with the masses of the biggest BHs in the much rarer, more luminous AGN at $z \sim 2$ to 4 [e.g., (*9*)]. The bolometric luminosity of CID–947 is in the range $L_{bol} \simeq (1.1 \text{ to } 2.2) \times 10^{46}$ erg s^{-1}, estimated either from the observed optical luminosity or the multiwavelength spectral energy distribution. Combined with the measured M_{BH}, we derive a normalized accretion rate of $L/L_{Edd} \simeq 0.01$ to 0.02. This value is lower, by at least an order of magnitude, than the accretion rates of known SMBHs at $z \sim 3.5$ [e.g., (*9*, *10*)]. Further assuming a standard radiative efficiency of 10%, we obtain an *e*-folding time scale for the SMBH mass of at least 2.1×10^9 years (Gy) (see section S3 in the supplementary materials), which is longer than the age of the universe at $z = 3.328$. By contrast, even the most extreme models for the emergence of "seed" BHs predict masses no larger than $M_{seed} \sim 10^6$ $M_\odot$ at $z \sim 10$ to 20 [e.g., (*19*)]. Therefore, the SMBH powering CID–947 had to grow at much higher accretion rates and at a high duty cycle in the past, to account for the high observed M_{BH} only 1.7 Gy after $z \simeq 20$. CID–947 could have evolved from a parent population similar to the fast-growing SMBHs observed in $z \gtrsim 5$ quasars, which have $L/L_{Edd} \sim 0.5$ to 1 and $M_{BH} \simeq 10^9$ $M_\odot$ [e.g., (*11*, *12*)]. The requirement for a high accretion rate in the very recent past is supported by the clear presence of a high-velocity outflow of ionized gas, observed in the rest-frame ultraviolet spectrum of the source (fig. S4). The broad absorption features of C IV λ1549 and Si IV λ1400 have maximal velocities of $v_{max} \simeq$ 12,000 km s^{-1}. Assuming that this outflow is driven by radiation pressure, these velocities require accretion rates of $L/L_{Edd} \gtrsim 0.1$, as recently as 10^5 to 10^6 years before the observed epoch (see section S4 in the supplementary materials). We conclude that the SMBH powering CID–947 is in the final stages of growth and that we are witnessing the shut-down of accretion onto one of the most massive BHs known to date.

The rich collection of ancillary COSMOS multiwavelength data available for CID–947 enables us to study the basic properties of its host galaxy (see details in section S2 in the supplementary materials). A previously published analysis of the observed spectral energy distribution of the emission from the source reveals an appreciable stellar emission component, originating from $5.6^{+2.8}_{-0.4} \times 10^{10} M_\odot$ in stars (*20*). Our own analysis provides a yet lower stellar mass, of $M_* = 4.4^{+0.4}_{-0.5} \times 10^{10} M_\odot$. However, we focus on

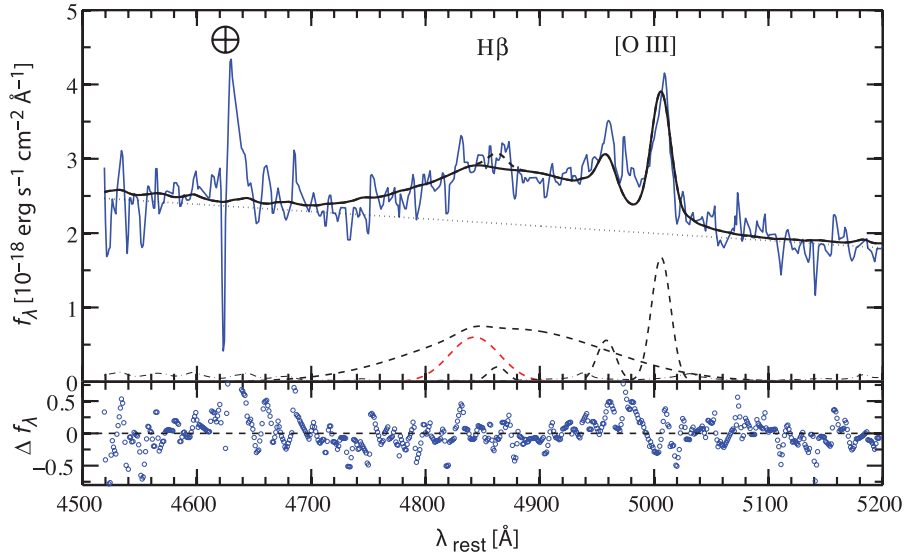


Fig. 1. The observed Keck/MOSFIRE spectrum and best-fit model for the Hβ emission complex of CID–947. The data are modeled with a linear continuum (dotted), a broadened iron template (dot-dashed), and a combination of broad and narrow Gaussians (dashed), which correspond to the Hβ and [O III] emission lines (see section S1.2 in the supplementary materials for details regarding the spectral modeling). The broad component of Hβ has a full width at half maximum of FWHM(Hβ) = 11330 km s^{-1}, which results in $M_{BH} = 6.9 \times 10^9$ $M_\odot$ and $M_{BH}/M_* = 1/8$. The red dashed line illustrates an alternative scenario, in which the SMBH mass derived from the Hβ line width would result in $M_{BH}/M_* = 1/100$ [i.e., FWHM(Hβ) = 3218 km s^{-1}], clearly at odds with the data. The spike at $\lambda_{rest} \simeq 4640$ Å is due to a sky feature. The bottom panel shows the residuals of the best-fit model.

[1]Department of Physics, Institute for Astronomy, ETH Zurich, Wolfgang-Pauli-Strasse 27, Zurich 8093, Switzerland. [2]Department of Physics, Yale University, Post Office Box 208120, New Haven, CT 06520-8120, USA. [3]Yale Center for Astronomy and Astrophysics, 260 Whitney Avenue, New Haven, CT 06520-8121, USA. [4]Department of Astronomy, Yale University, Post Office Box 208101, New Haven, CT 06520-8101, USA. [5]Harvard-Smithsonian Center for Astrophysics, 60 Garden Street, Cambridge, MA 02138, USA. [6]Max-Planck-Institut für Extraterrestrische Physik (MPE), Postfach 1312, 85741 Garching, Germany. [7]Institute for Astronomy, University of Hawaii, 2680 Woodlawn Drive, Honolulu, HI 96822, USA. [8]INAF-Osservatorio Astronomico di Roma, Via di Frascati 33, I-00040 Monteporzio Catone, Rome, Italy. [9]Oxford Astrophysics, Denys Wilkinson Building, Keble Road, Oxford OX1 3RH, UK.
***Corresponding author. E-mail: benny.trakhtenbrot@phys.ethz.ch**

the previously determined, higher stellar mass, as a conservative estimate. The source is also detected at far-IR and (sub)millimeter wavelengths, which allows us to constrain the SFR in the host galaxy to about 400 $M_\odot$ year^{-1}. The stellar mass of the host galaxy is consistent with the typical value for star-forming galaxies at $z \sim 3$ to 4 [i.e., the "break" in the mass function of galaxies; (*21*)]. Similarly, the combination of M_* and SFR is consistent with the typical values observed at $z \sim 3$ to 4, which appear to follow the so-called main sequence of star-forming galaxies (*22*). Thus, the host galaxy of CID–947 is a typical star-forming galaxy for its redshift, representing a population with a number density of about 5×10^{-5} Mpc^{-3} [e.g., (*21*)]. This suggests that neither the intense, ionizing radiation that emerged during the fast SMBH growth, nor the AGN-driven outflow, have quenched star formation in the host galaxy. The relatively high stellar mass and SFR of the host galaxy further suggest that it is unlikely that the AGN affected the host in yet earlier epochs. That is, even in this case of extreme SMBH growth, there is no sign of AGN-driven suppression of star formation in the host.

Our analysis indicates that the BH-to-stellar mass ratio for CID–947 is $M_{BH}/M_* \simeq 1/8$. In comparison, most local (dormant) high-mass BHs typically have $M_{BH}/M_* \sim 1/700$ to 1/500 [see Fig. 2 and, e.g., (*4*, *23*)]. The M_{BH}/M_* value that we find for CID–947 is thus far higher than typically observed in high-mass systems in the local universe, by at least an order of magnitude and more probably by a factor of about 50. The only local system with a comparably extreme mass ratio is the galaxy NGC 1277, which was reported to have $M_{BH}/M_* \simeq 1/7$ [with $M_{BH} = 1.7 \times 10^{10}\ M_\odot \simeq 2.5 \times M_{BH}$(CID–947); see (*24*), but also (*25*)]. At earlier epochs (still $z < 2$), the general trend is for M_{BH}/M_* to increase slightly with redshift, but typically not beyond $M_{BH}/M_* \sim 1/100$ (see Fig. 3). Only a few systems with reliable estimates of M_{BH} show M_{BH}/M_* reaching as high as 1/30 [e.g., (*6*–*8*)].

Given the high masses of both the SMBH and stellar population in CID–947, we expect this system to retain an extreme M_{BH}/M_* throughout its evolution, from $z = 3.328$ to the present-day universe. Because the M_{BH} that we find is already comparable to the most massive BHs known, it is unlikely that the SMBH will experience any further appreciable growth (i.e., beyond $M_{BH} \simeq 10^{10}\ M_\odot$). Indeed, if the SMBH accretes at the observed rate through $z = 2$, it will reach the extreme value of $\sim 10^{10}\ M_\odot$, and by $z = 1$ it will have a final mass of $\sim 2.5 \times 10^{10}\ M_\odot$. As for the host galaxy, we can constrain its subsequent growth following several different assumptions. First, if one simply assumes that the galaxy will become as massive as the most massive galaxies in the local universe [$M_* \simeq 10^{12}\ M_\odot$; (*26*)], then the implied final mass ratio is on the order of $M_{BH}/M_* \sim 1/100$. Alternatively, we consider more realistic scenarios for the future growth of the stellar population, relying on the observed mass (M_*) and growth rate (SFR). Our calculations involve different scenarios for the decay of star formation in the galaxy (see section S5 in the supplementary materials) and predict final stellar masses in the range $M_*(z = 0) \simeq (2 \text{ to } 7) \times 10^{11}\ M_\odot$, which is about an order of magnitude higher than the observed mass at $z = 3.328$. The

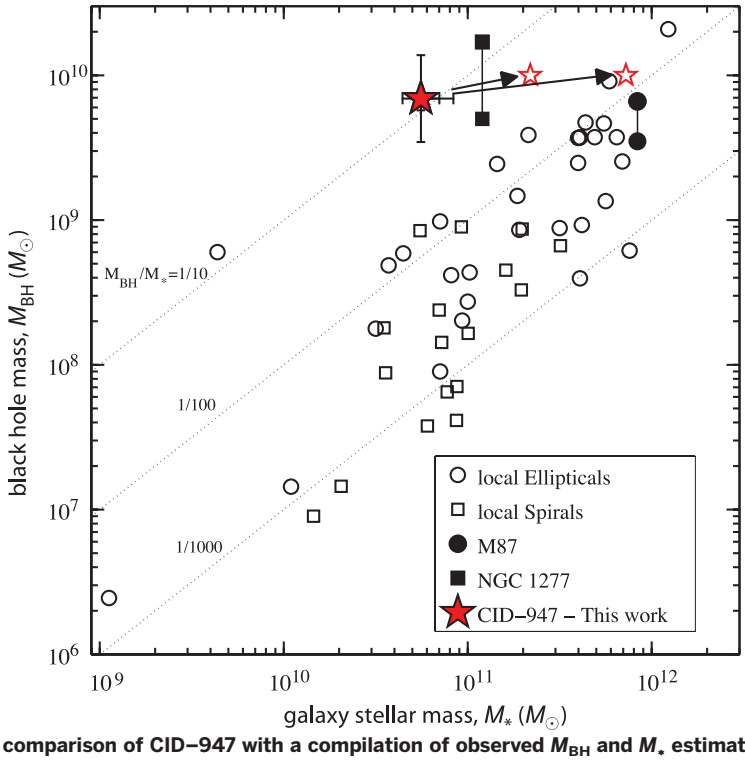


Fig. 2. A comparison of CID–947 with a compilation of observed M_{BH} and M_* estimates in the local universe [adapted from (*4*), assuming the tabulated bulge-to-total fractions]. CID–947 (red star) has a very high BH-to-stellar mass ratio of $M_{BH}/M_* \simeq 1/10$. The asymmetric error bars shown on M_{BH} and M_* represent measurement-related uncertainties, while the symmetric ones demonstrate systematic uncertainties of 0.3 dex (on M_{BH}) and 0.1 dex (on M_*). The masses inferred for subsequent growth scenarios are highlighted as empty red stars. The CID–947 system is expected to evolve only mildly in M_{BH} (perhaps to $\sim 10^{10}\ M_\odot$), but M_* should grow to at least $2 \times 10^{11}\ M_\odot$, and possibly to as much as $\sim 7 \times 10^{11}\ M_\odot$, by $z = 0$. The local galaxies NGC 1277 and M87, which could be considered as descendants of systems like CID–947, are highlighted as filled symbols [(*25*) and (*27*), respectively]. Some studies suggest these galaxies to have somewhat higher M_{BH}, and therefore relatively high mass ratios, of $M_{BH}/M_* = 1/7$ and 1/127, respectively (*24*, *28*).

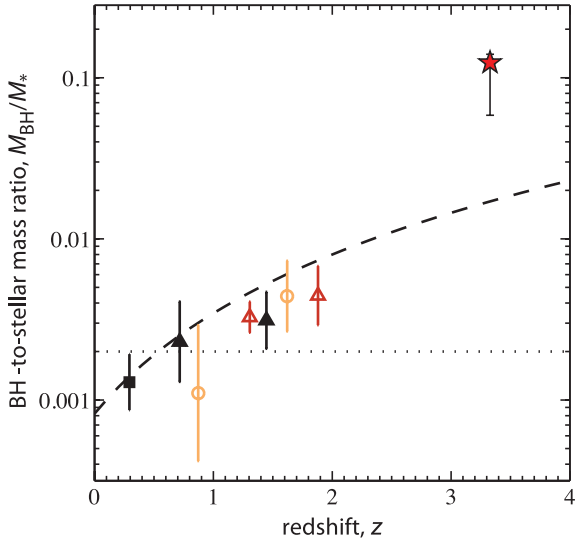


Fig. 3. The observed cosmic evolution of the BH-to-stellar mass ratio, M_{BH}/M_*, and its extrapolation beyond $z \sim 2$. CID–947 (red star) has $M_{BH}/M_* = 1/8$ at $z \simeq 3.3$, which is higher by a factor of at least ~50 than the typical value in local, inactive galaxies (at most, $M_{BH}/M_* \sim 1/500$; dotted line). The error bars shown for CID–947 represent only the measurement-related uncertainties, propagating the uncertainties on M_{BH} and on M_*. The different data points at $z < 2$ represent typical (median) values for several samples with M_{BH}/M_* estimates, with uncertainties representing the scatter within each sample [filled symbols, open circles, and open triangles represent samples from (*7*), (*29*), and (*6*), respectively; adapted from (*7*)]. Even compared to the extrapolation of the evolutionary trend supported by these lower-redshift data, $M_{BH}/M_* \sim (z + 1)^2$ [dashed line, scaled as in (*30*)], CID–947 has a significantly higher M_{BH}/M_*.

inferred final mass ratio is $M_{BH}/M_* \sim 1/50$. This growth can only occur if star formation continues for a relatively long period (≥1 Gy) and at a high rate (>50 $M_\odot$ year^{-1}). This would require the presence of a substantial reservoir, or the accretion, of cold gas, which, however, could not increase the SMBH mass by much. Finally, in the most extreme scenario, the star formation shuts down almost immediately (i.e., due to the AGN-driven outflow), and the system remains "frozen" at $M_{BH}/M_* \sim 1/10$ throughout cosmic time. If the SMBH does indeed grow further (i.e., beyond 10^{10} $M_\odot$), this would imply yet higher M_{BH}/M_*. Thus, the inferred final BH-to-stellar mass ratio for CID–947 is, in the most extreme scenarios, about $M_{BH}/M_* \sim 1/100$, and probably much higher (see Fig. 2).

CID–947 therefore represents a progenitor of the most extreme, high-mass systems in the local universe, like NGC 1277. Such systems are not detected in large numbers, perhaps due to observational selection biases. The above considerations indicate that the local relics of systems like CID–947 are galaxies with at least $M_* \sim 5 \times 10^{11}$ $M_\odot$. Such systems are predominantly quiescent (i.e., with low star-formation rates, SFR ≪ 1 $M_\odot$ year^{-1}) and relatively rare in the local universe, with typical number densities on the order of ~10^{-5} Mpc^{-3} (*26*). We conclude that CID–947 provides direct evidence that at least some of the most massive BHs, with $M_{BH} \gtrsim 10^{10}$ $M_\odot$, already in place just 2 Gy after the Big Bang, did not shut down star formation in their host galaxies. The host galaxies may experience appreciable mass growth in later epochs, without much further black hole growth, resulting in very high stellar masses but still relatively high M_{BH}/M_*. Lower-mass systems may follow markedly different coevolutionary paths. However, systems with M_{BH}/M_* as high as in CID–947 may be not as rare as previously thought, as they can be consistently observed among populations with number densities on the order of ~10^{-5} Mpc^{-3}, both at $z > 3$ and in the local universe, and not just among the rarest, most luminous quasars.

REFERENCES AND NOTES

1. L. Ferrarese, D. Merritt, *Astrophys. J.* **539**, L9–L12 (2000).
2. K. Gebhardt *et al.*, *Astrophys. J.* **539**, L13–L16 (2000).
3. X. Z. Zheng *et al.*, *Astrophys. J.* **707**, 1566–1577 (2009).
4. J. Kormendy, L. C. Ho, *Annu. Rev. Astron. Astrophys.* **51**, 511–653 (2013).
5. A. C. Fabian, *Annu. Rev. Astron. Astrophys.* **50**, 455–489 (2012).
6. A. Merloni *et al.*, *Astrophys. J.* **708**, 137–157 (2010).
7. R. Decarli *et al.*, *Mon. Not. R. Astron. Soc.* **402**, 2453–2461 (2010).
8. V. N. Bennert, M. W. Auger, T. Treu, J.-H. Woo, M. A. Malkan, *Astrophys. J.* **742**, 107 (2011).
9. O. Shemmer *et al.*, *Astrophys. J.* **614**, 547–557 (2004).
10. H. Netzer, P. Lira, B. Trakhtenbrot, O. Shemmer, I. Cury, *Astrophys. J.* **671**, 1256–1263 (2007).
11. G. De Rosa *et al.*, *Astrophys. J.* **739**, 56 (2011).
12. B. Trakhtenbrot, H. Netzer, P. Lira, O. Shemmer, *Astrophys. J.* **730**, 7 (2011).
13. D. Masters *et al.*, *Astrophys. J.* **755**, 169 (2012).
14. N. Z. Scoville *et al.*, *Astrophys. J. Suppl. Ser.* **172**, 1–8 (2007).
15. F. Civano *et al.*, *Astrophys. J.* **741**, 91 (2011).
16. Data and methods, supplementary text, figures and tables are available on *Science* Online.
17. Y. Shen, *Bull. Astron. Soc. Ind.* **41**, 61 (2013).
18. N. J. McConnell *et al.*, *Astrophys. J.* **756**, 179 (2012).
19. M. Volonteri, *Astron. Astrophys. Rev.* **18**, 279–315 (2010).
20. A. Bongiorno *et al.*, *Mon. Not. R. Astron. Soc.* **427**, 3103–3133 (2012).
21. O. Ilbert *et al.*, *Astron. Astrophys.* **556**, A55 (2013).
22. J. S. Speagle, C. L. Steinhardt, P. L. Capak, J. D. Silverman, *Astrophys. J. Suppl. Ser.* **214**, 15 (2014).
23. N. Häring, H. Rix, *Astrophys. J.* **604**, L89 (2004).
24. R. C. E. van den Bosch *et al.*, *Nature* **491**, 729–731 (2012).
25. E. Emsellem, *Mon. Not. R. Astron. Soc.* **433**, 1862–1870 (2013).
26. I. K. Baldry *et al.*, *Mon. Not. R. Astron. Soc.* **421**, 621 (2012).
27. J. L. Walsh, A. J. Barth, L. C. Ho, M. Sarzi, *Astrophys. J.* **770**, 86 (2013).
28. K. Gebhardt *et al.*, *Astrophys. J.* **729**, 119 (2011).
29. C. Y. Peng *et al.*, *Astrophys. J.* **649**, 616 (2006).
30. R. J. McLure, M. J. Jarvis, T. A. Targett, J. S. Dunlop, P. N. Best, *Mon. Not. R. Astron. Soc.* **368**, 1395–1403 (2006).

ACKNOWLEDGMENTS

The new MOSFIRE data presented herein were obtained at the W. M. Keck Observatory, which is operated as a scientific partnership among the California Institute of Technology, the University of California, and the National Aeronautics and Space Administration. The Observatory was made possible by the generous financial support of the W. M. Keck Foundation. We thank M. Kassis and the rest of the staff at the W. M. Keck observatories at Waimea, HI, for their support during the observing run. We recognize and acknowledge the very significant cultural role and reverence that the summit of Mauna Kea has always had within the indigenous Hawaiian community. We are most fortunate to have the opportunity to conduct observations from this mountain. Some of the analysis presented here is based on data products from observations made with European Southern Observatory (ESO) Telescopes at the La Silla Paranal Observatory under ESO program ID 179.A-2005 and on data products produced by TERAPIX and the Cambridge Astronomy Survey Unit on behalf of the UltraVISTA consortium. We are grateful to A. Faisst and M. Onodera for their assistance with the acquisition and reduction of the MOSFIRE data. We thank S. Tacchella, J. Woo, and W. Hartley for their assistance with some of the evolutionary calculations. K.S. gratefully acknowledges support from Swiss National Science Foundation Professorship grant PP00P2 138979/1. F.C. acknowledges financial support by the NASA grant GO3-14150C. M.E. acknowledges financial support by the NASA Chandra grant GO2-13127X. B.T. is a Zwicky Fellow at the ETH Zurich.

SUPPLEMENTARY MATERIALS

www.sciencemag.org/content/349/6244/168/suppl/DC1
Data, Methods, and Supplementary Text S1 to S4
Figs. S1 to S4
Table S1
References (*31*–*81*)

10 December 2014; accepted 29 May 2015
10.1126/science.aaa4506

ANIMAL PHYSIOLOGY

Exceptionally low daily energy expenditure in the bamboo-eating giant panda

Yonggang Nie,[1]* John R. Speakman,[2,3]* Qi Wu,[1]* Chenglin Zhang,[4] Yibo Hu,[1] Maohua Xia,[4] Li Yan,[1] Catherine Hambly,[3] Lu Wang,[2] Wei Wei,[1] Jinguo Zhang,[4] Fuwen Wei[1]†

The carnivoran giant panda has a specialized bamboo diet, to which its alimentary tract is poorly adapted. Measurements of daily energy expenditure across five captive and three wild pandas averaged 5.2 megajoules (MJ)/day, only 37.7% of the predicted value (13.8 MJ/day). For the wild pandas, the mean was 6.2 MJ/day, or 45% of the mammalian expectation. Pandas achieve this exceptionally low expenditure in part by reduced sizes of several vital organs and low physical activity. In addition, circulating levels of thyroid hormones thyroxine (T_4) and triiodothyronine (T_3) averaged 46.9 and 64%, respectively, of the levels expected for a eutherian mammal of comparable size. A giant panda–unique mutation in the *DUOX2* gene, critical for thyroid hormone synthesis, might explain these low thyroid hormone levels. A combination of morphological, behavioral, physiological, and genetic adaptations, leading to low energy expenditure, likely enables giant pandas to survive on a bamboo diet.

The giant panda (*Ailuropoda melanoleuca*) is an enigmatic, critically endangered bear endemic to China. Its diet is made up almost exclusively of bamboo, but it retains a short carnivoran alimentary tract and, consequently, has very low digestive efficiency (*1*–*3*). Therefore, the giant panda must feed for a large part of each day and consume large quantities of food relative to its body mass (*1*, *4*). This has led to speculation that giant pandas must also have low metabolic rates to achieve a daily energy balance (*1*). We report the first measurements of daily energy expenditure (DEE) of captive and free-living giant pandas, measured using the doubly labeled water (DLW) method (*5*) (see supplementary materials and methods). We validated these measurements using estimates of net energy assimilation and matched them with morphological, behavioral, physiological, and genetic data. We measured the DEE of five captive and three free-living pandas (supplementary text S1, tables S1.3 and S1.4). Across the captive individuals, the body mass averaged 91.1 kg and DEE averaged 4.6 ± 0.9 MJ/day (±SEM) (n = 5 animals). In the wild, the equivalent values were

[1]Key Laboratory of Animal Ecology and Conservation Biology, Institute of Zoology, Chinese Academy of Sciences, Beijing, China. [2]State Key Laboratory of Molecular Developmental Biology, Institute of Genetics and Developmental Biology, Chinese Academy of Sciences, Beijing, China. [3]Institute of Biological and Environmental Sciences, University of Aberdeen, Aberdeen, Scotland, UK. [4]Beijing Key Laboratory of Captive Wildlife Technologies, Beijing Zoo, Beijing, China.
*These authors contributed equally to this work.
†Corresponding author. E-mail: weifw@ioz.ac.cn

92.6 kg and 6.2 ± 1.5 MJ/day (n = 3 animals). There was a significant effect of body mass on DEE (regression $P < 0.001$; coefficient of determination r^2 = 83.8%) but no significant difference between captive and wild animals (P = 0.081) (Fig. 1A). The pooled estimate was 5.2 ± 0.7 MJ/day (n = 8 animals). We validated these estimates by comparing the DEE by DLW to the net energy assimilation (NEA) estimated from individual measures of assimilation efficiency, multiplied by the daily fecal production, measured in three captive pandas almost daily for 11 months (n = 961 animal days). Assimilation efficiency varied between 11.1 and 20.5% (supplementary text S2), comparable to previous estimates in captive pandas (7.4 to 38.9%) (*2*, *6*, *7*). Daily NEA (megajoules per day) varied over the year, being higher in the winter months (Fig. 1B). Consequently, there was a significant negative relationship between NEA and the average daily shade temperature (Fig. 1C) [regression: $F_{1,37}$ = 197.9, $P < 0.001$]. Across all measurements, the average NEA was 7.0 ± 2.1 MJ/day (±SD). A prior estimate of NEA for giant pandas in captivity was 4.2 MJ/day (*7*), slightly lower than our measured value, probably because it was made at a higher ambient temperature. Excepting a single value, the DEE data were within the standard deviations of the NEA data. We used the fitted equation between NEA and ambient temperature to predict the expected NEA on the days the DLW method was used. The measured DEE averaged 77.0 ± 7.3% (±SD) of the predicted NEA (absolute mean discrepancy 1.6 ± 0.49 MJ/day). This discrepancy exists because NEA values do not account for energy in urine, which is high because of the role of panda urine in scent marking (*8*). Combining the water turnover from the DLW estimates with the water loss in feces indicated that pandas may produce maximally 5.0 liters of urine daily (supplementary text S2). Linking this estimate with direct measurements of urine solid matter and energy content suggests that pandas may maximally eliminate 2.1 MJ/day in urine, not significantly different from the mean discrepancy between the NEA and DEE estimates (t test: t = 2.02, P = 0.136).

The DEE by DLW was only 37.7% of the expectation (45% for the field data) for a terrestrial mammal on the basis of body mass (Fig. 1D) (*9*). These values are substantially lower than those for other mammals considered to have low DEE, such as the koala (*Phascolarctos cinerus*) at 69% and the echidna (*Tachyglossus aculeatus*) at 66% of the expected value. Additionally, for the pooled DLW estimate, our values were almost equal to that of the three-toed sloth (*Bradypus variegatus*) at 36% of the prediction. The lowest reported primate DEE is for the ring-tailed lemur (*Lemur catta*) at 52% of expected (*10*). Only two other mammals have relative DEE values that are considerably lower than those of the giant panda: the Australian rock rat (*Zyzomys argurus*) (21% of the predicted level) (*11*) and the desert golden mole (*Eremitalpa namibensis*) (26% of expected) (*12*). However, it is unclear whether these small animals were using torpor during the measurements. Otherwise, the measurements for the giant panda are among the lowest, relative to body mass, ever made for a nontorpid mammal. In fact, DEE in the giant panda (and sloth) is closer to the expectations for a 92-kg reptile (4.9 MJ/day) (*13*) than for a terrestrial mammal.

Animals may achieve low rates of metabolism via behavioral, morphological, and physiological adaptations. Low metabolic rates may be achieved by relaxing homeothermy (*14*). However, giant panda body temperatures indicate that they do not engage in either daily torpor or hibernation (*15*). Presumably, giant pandas can sustain a high body temperature, despite their low DEE, because they have a deep pelage able to trap their meager body heat (*1*). Supporting this hypothesis, measurements of lateral surface temperatures of giant pandas are significantly lower than those of

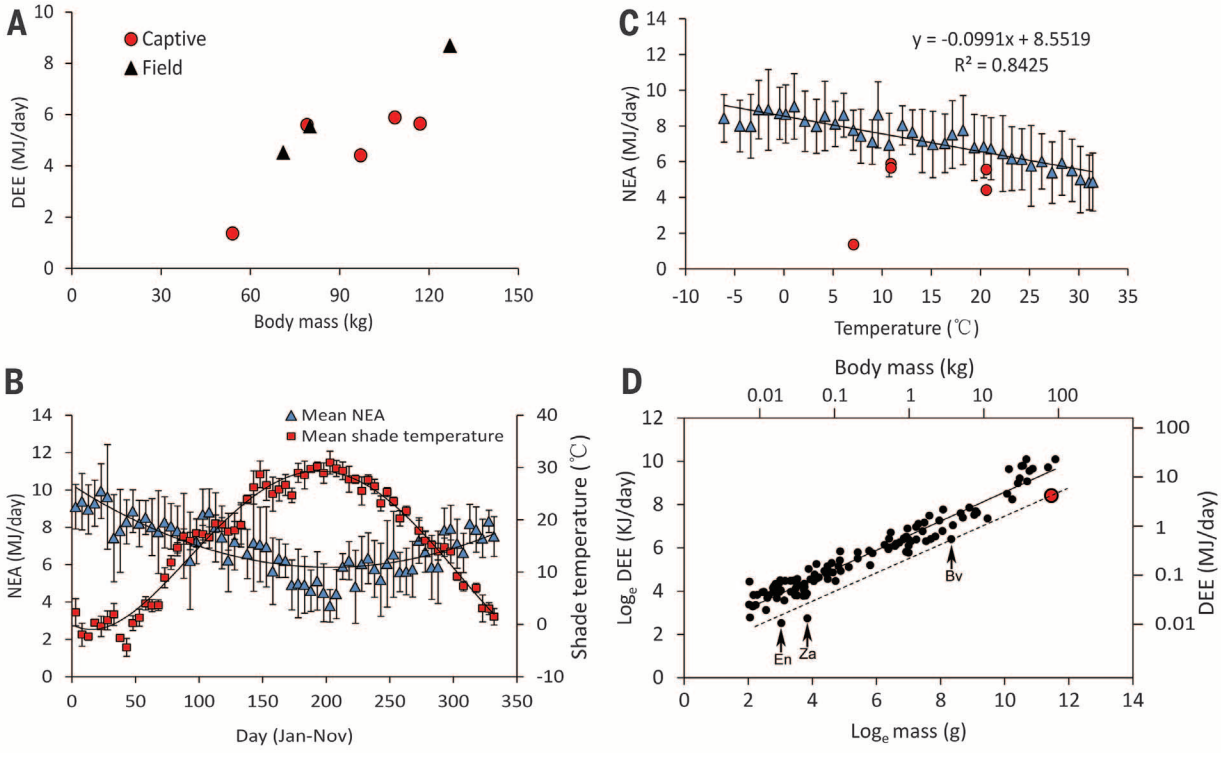


Fig. 1. Daily energy demands of the giant panda. (**A**) Daily energy expenditure (DEE) (megajoules per day) using the DLW method for eight pandas in relation to body mass (kilograms). Captive animals (n = 5) are represented by red circles and wild animals (n = 3) by black triangles. (**B**) Net energy assimilation (NEA) (megajoules per day) averaged across three captive pandas estimated from assimilation efficiency and daily fecal production and plotted against day of year (1 January = 1). Air temperatures (red squares) are also shown (mean ± SD). (**C**) NEA (megajoules per day) plotted against ambient temperature (blue triangles with SD) and DEE (megajoules per day) of five captive individuals by DLW (red circles). (**D**) DEE by DLW of terrestrial mammals [log$_e$ field metabolic rate (FMR) (kilojoules per day)] plotted against body mass [log$_e$ mass (grams)]. Each point represents a different species [data from (*9*) and (*10*)]. The solid line is the equation log$_e$ (FMR in kilojoules per day) = 1.871 + 0.67[log$_e$ mass (grams)] [from (*9*)]. The giant panda is represented by the red data point. The dotted line is equal to 37% of the prediction equation. Some other animals with low metabolism are indicated. Bv, *B. variegatus* (three-toed sloth); En, *E. namibensis* (desert golden mole); Za, *Z. argurus* (Australian rock rat).

zebras (*Equus quagga*), dairy cattle (*Bos taurus*), and domestic dogs (*Canis familiaris*) (Fig. 2).

Animals may also reduce DEE by minimizing the time spent in and intensity of physical activity. We measured the activity of captive pandas by direct observation and in the wild using GPS loggers and direct observation. In captivity, the animals spent 33% of their time being physically active; in the wild, 49% of their time was devoted to physical activity. These findings are similar to those reported previously (*16*). Pandas in the wild were more active than those in captivity (*t* test: $t = -3.93$, $P = 0.017$) (Fig. 3A). Compared with other bears, pandas had lower levels of activity (*1*, *17*). In the wild, both the foraging movement speed (15.5 m/hour) and the mean movement speed (26.9 m/hour) were very low (Fig. 3B).

For larger terrestrial mammals, the dominant component of the daily energy budget is the resting metabolic rate (*9*). Resting metabolism is derived from the summed metabolic

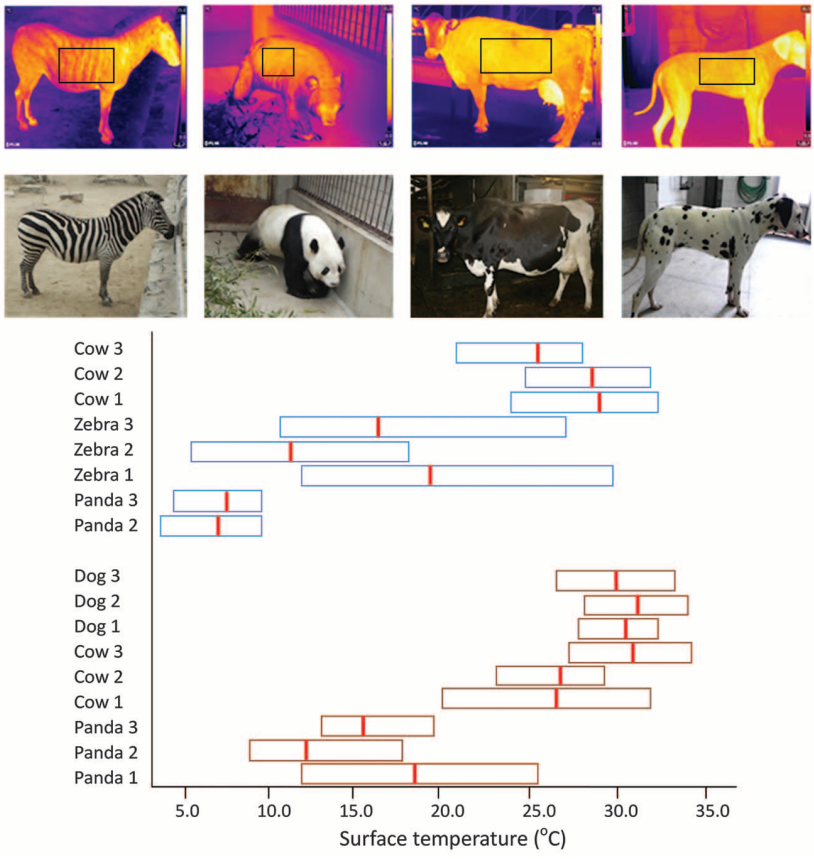


Fig. 2. Surface temperatures of giant pandas, zebras, Holstein cows, and Dalmatian dogs at ambient air temperatures of ~4°C (blue boxes) and 10°C (brown boxes). The pictures show representative thermal images (top) and normal images (bottom). The plot underneath shows the analysis of lateral surface temperatures. Boxes represent the range of surface temperatures (minimum to maximum). Mean values are denoted by the red bars. (See supplementary materials for more details.)

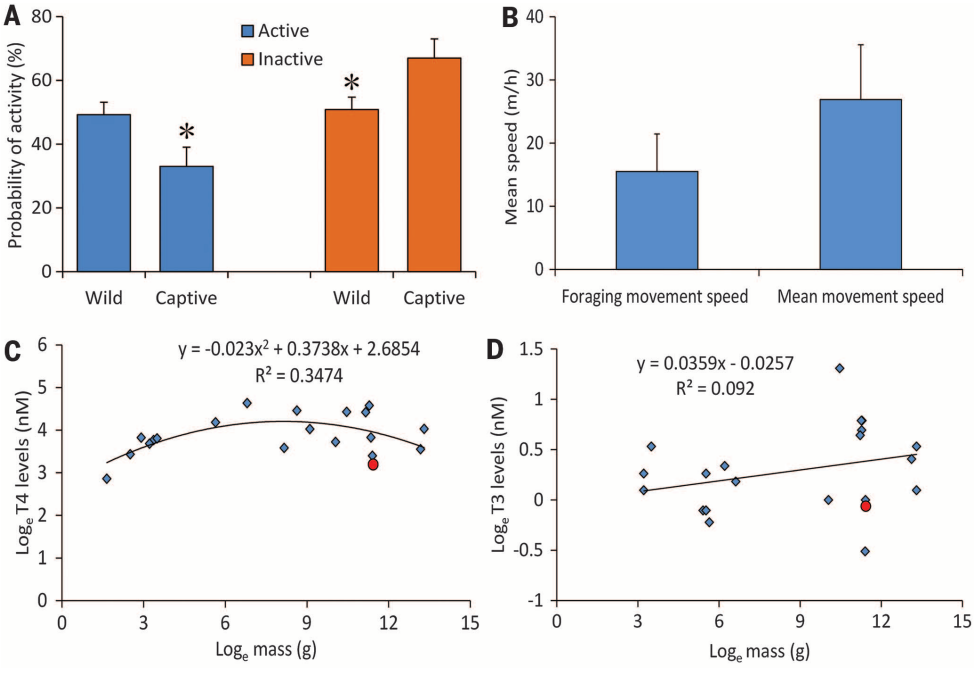


Fig. 3. Physical activity and thyroid hormone levels. (**A**) Physical activity levels in wild and captive pandas (mean ± SD). Asterisks indicate $P < 0.05$ (*t* test). (**B**) Movement speed when foraging and mean movement speed (mean ± SD) over the whole year in wild pandas. Thyroid hormone levels for (**C**) T_4 and (**D**) T_3 in eutherian mammals (blue diamonds) [data from (*28*)]. Each data point represents a different species. The fitted curves show the best-fit polynomial relationships with the associated equations in the respective panels. The giant panda is represented by the red data points.

rates of the body components (*18*). Some organs such as the liver, brain, kidneys, and heart contribute disproportionally to the total (*19*). We used literature autopsy data to assess whether pandas have relatively small organ sizes (supplementary text S3, table S3). Giant pandas have relatively small brains, livers, and kidneys (respectively, 82.5, 62.8, and 74.5% of expectation) compared with other eutherian mammals. These reduced organ sizes probably contribute to their low energy demands. Resting metabolic rate is also strongly influenced by several hormones, particularly the thyroid hormones (*20*) thyroxine (T_4) and triiodothyrioine (T_3). In the same captive animals in which we measured DEE, total T_4 averaged 24.44 ± 1.17 nM (±SEM), and total T_3 averaged 0.94 ± 0.05 nM, similar to previous giant panda measurements (*21*). The T_4 level was 46.9%, and T_3 64.0%, of the expectation for a eutherian mammal of the same body mass (Fig. 3, C and D). These measurements were lower than in hibernating black bears (*Ursus americanus*) (*22*). In Fig. 3D, the data point lower than that for the panda is representative of the gray seal (*Halichoerus grypus*); gray seals are believed to have low T_3 levels to facilitate metabolic suppression during diving. Pandas clearly have low levels of both T_4 and T_3, which may be instrumental in their exceptionally low metabolism.

We compared the panda genome with the genomes of five other carnivorans, mouse, and human. We did not find any notable mutations in the promoter regions and exons or introns of the 182 genes listed in the Kyoto Encyclopedia of Genes and Genomes as linked to the thyroid hormone synthesis and thyroid signaling pathways, with one exception. A unique variation was found in the dual oxidase 2 (*DUOX2*) gene in the panda, which is homologous to the *DUOX2* gene in humans. *DUOX2* encodes a transmembrane protein that catalyzes the conversion of water to hydrogen peroxide, which is used in the final step of T_4 and T_3 synthesis. The giant panda *DUOX2* gene contains a single substitution of C to T in the 16th exon, which causes a premature stop codon (TGA) (Fig. 4). This mutation is also observed in transcriptome data, suggesting that the transcript of *DUOX2* would not be translated into a complete protein. In humans and mice, loss-of-function mutations in *DUOX2* lead to hypothyroidism (*23*–*25*).

Although the metabolic rates of the giant panda are exceptionally low, we do not suggest that they are entirely separate from other eutherian mammals. Other folivorous animals, like the three-toed sloth, also have very low DEEs, and this is probably true of several other species, such as the frugivorous binturong (*Arctictis binturong*) and the folivorous red panda (*Ailurus fulgens*), both of which have very low basal rates of metabolism (*26*). Rather, the giant panda represents one end of a spectrum of metabolic rates where the dominant ultimate factors may be the quality and quantity of the food they exploit (*27*).

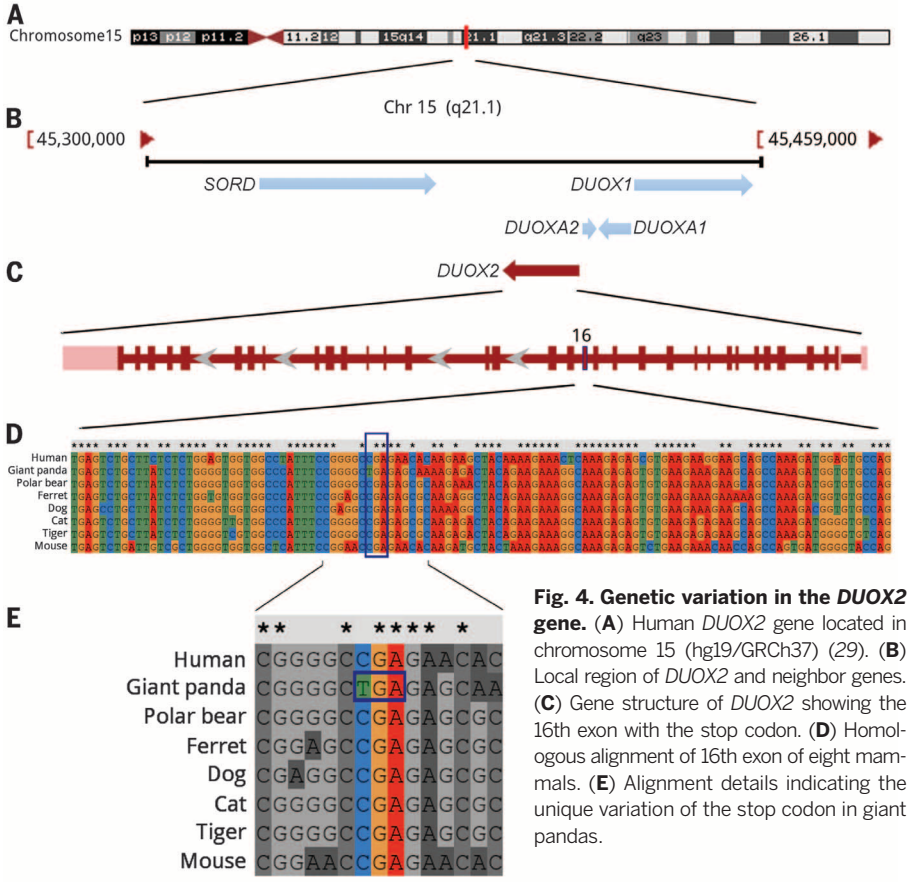


Fig. 4. Genetic variation in the *DUOX2* gene. (**A**) Human *DUOX2* gene located in chromosome 15 (hg19/GRCh37) (*29*). (**B**) Local region of *DUOX2* and neighbor genes. (**C**) Gene structure of *DUOX2* showing the 16th exon with the stop codon. (**D**) Homologous alignment of 16th exon of eight mammals. (**E**) Alignment details indicating the unique variation of the stop codon in giant pandas.

Giant pandas have exceptionally low DEE, which may facilitate survival on their diet of bamboo. A suite of behavioral, morphological, and physiological factors—including low physical activity levels and reduced sizes of some high metabolism organs—probably contribute to the low energy expenditure. Additionally, levels of the thyroid hormones are about half of the expected amounts. This may be linked, in part, to mutations in the panda genome in the *DUOX2* gene, which catalyzes a key step in T_4 and T_3 synthesis.

REFERENCES AND NOTES

1. G. B. Schaller, J. C. Hu, W. S. Pan, J. Zhu, *The Giant Panda of Wolong* (Univ. of Chicago Press, Chicago, 1985).
2. E. S. Dierenfeld, H. F. Hintz, J. B. Robertson, P. J. Van Soest, O. T. Oftedal, *J. Nutr.* **112**, 636–641 (1982).
3. F. Wei *et al.*, *Mol. Biol. Evol.* **32**, 4–12 (2015).
4. W. S. Pan, Z. Lv, X. J. Zhu, D. J. Wang, H. Wang, Y. Long, D. L. Fu, X. Zhou, *A Chance for Lasting Survival*, W. J. McShea, R. B. Harris, D. L. Garshelis, D. J. Wang, Eds. (Smithsonian Institution Scholarly Press, Washington, DC, 2014).
5. P. J. Butler, J. A. Green, I. L. Boyd, J. R. Speakman, *Funct. Ecol.* **18**, 168–183 (2004).
6. S. A. Mainka, G. Zhao, M. Li, *J. Zoo Wildl. Med.* **20**, 39–44 (1989).
7. T. G. Finley *et al.*, *Zoo Biol.* **30**, 121–133 (2011).
8. Y. G. Nie *et al.*, *Anim. Behav.* **84**, 39–44 (2012).
9. J. R. Speakman, E. Król, *J. Anim. Ecol.* **79**, 726–746 (2010).
10. H. Pontzer *et al.*, *Proc. Natl. Acad. Sci. U.S.A.* **111**, 1433–1437 (2014).
11. S. D. Bradshaw, K. D. Morris, C. R. Dickman, P. C. Withers, D. Murphy, *Aust. J. Zool.* **42**, 29–41 (1994).
12. M. Scantlebury, M. K. Oosthuizen, J. R. Speakman, C. R. Jackson, N. C. Bennett, *Physiol. Behav.* **84**, 739–745 (2005).
13. K. A. Nagy, I. A. Girard, T. K. Brown, *Annu. Rev. Nutr.* **19**, 247–277 (1999).
14. F. Geiser, *Annu. Rev. Physiol.* **66**, 239–274 (2004).
15. Y. C. Cheng, Y. H. Cheng, *Chin. J. Wildlife* **4**, 46–47 (1983).
16. M. A. Owen, N. M. Czekala, R. R. Swaisgood, K. Steinman, D. G. Lindburg, *Ursus* **16**, 208–221 (2005).
17. A. G. MacHutchon, *Ursus* **12**, 189–198 (2001).
18. Z. Wang, T. P. O'Connor, S. Heshka, S. B. Heymsfield, *J. Nutr.* **131**, 2967–2970 (2001).
19. M. Elia, in *1st Clintec International Horizons Conference on Energy Metabolism: Tissue Determinants and Cellular Corollaries*, J. M. Kinney, H. N. Tucker, Eds (Raven, New York, 1992), pp. 19–59.
20. J. E. Silva, *Physiol. Rev.* **86**, 435–464 (2006).
21. Z. H. Zhang, F. W. Wei, *Giant Panda Ex-situ Conservation: Theory and Practice* (Sciences Press, Beijing, 2006).
22. T. E. Tomasi, E. C. Hellgren, T. J. Tucker, *Gen. Comp. Endocrinol.* **109**, 192–199 (1998).
23. J. C. Moreno *et al.*, *N. Engl. J. Med.* **347**, 95–102 (2002).
24. N. Pfarr *et al.*, *Clin. Endocrinol.* **65**, 810–815 (2006).
25. K. R. Johnson *et al.*, *Mol. Endocrinol.* **21**, 1593–1602 (2007).
26. B. K. McNab, *Acta Zool. Sinica* **51**, 535–545 (2005).
27. B. K. McNab, *Extreme Measures: The Ecological Energetic of Birds and Mammals* (Univ. of Chicago Press, Chicago, 2012).
28. A. J. Hulbert, *Biol. Rev. Camb. Philos. Soc.* **75**, 519–631 (2000).
29. W. J. Kent *et al.*, *Genome Res.* **12**, 996–1006 (2002).

ACKNOWLEDGMENTS

We thank X. Wang, Y. Jin, W. Zhou, T. Pu, X. Wang, L. Shan, S. Ma, W. Du, Z. Tan, M. Wang, X. Zheng, H. Han, D. Wang, and T. Ma for help with the data collection and P. Thompson for technical assistance with the isotope analysis. We also thank the Foping Nature Reserve and Beijing Zoo for their assistance on this study. This work was supported jointly and equally by the Key Project of National Natural Science Foundation of China (grant 31230011) and the Strategic Priority Research Program of the Chinese Academy of Sciences (grant XDB13030000). The thermal image camera used for the dairy cow images was on loan from the UK Engineering and Physical Sciences Research Council equipment loan pool. The physiological and other data are presented in the supplementary materials. The genetic data have been deposited in the National Center for Biotechnology Information database with accession number KT000656.

SUPPLEMENTARY MATERIALS

www.sciencemag.org/content/349/6244/171/suppl/DC1
Materials and Methods
Supplementary Text
Fig. S1
Tables S1 to S3
References (*30*–*51*)

31 March 2015; accepted 3 June 2015
10.1126/science.aab2413

WATER RESOURCES

Hydrologic connectivity constrains partitioning of global terrestrial water fluxes

Stephen P. Good,[1,2]* David Noone,[3] Gabriel Bowen[1,4]

Continental precipitation not routed to the oceans as runoff returns to the atmosphere as evapotranspiration. Partitioning this evapotranspiration flux into interception, transpiration, soil evaporation, and surface water evaporation is difficult using traditional hydrological methods, yet critical for understanding the water cycle and linked ecological processes. We combined two large-scale flux-partitioning approaches to quantify evapotranspiration subcomponents and the hydrologic connectivity of bound, plant-available soil waters with more mobile surface waters. Globally, transpiration is 64 ± 13% (mean ± 1 standard deviation) of evapotranspiration, and 65 ± 26% of evaporation originates from soils and not surface waters. We estimate that 38 ± 28% of surface water is derived from the plant-accessed soil water pool. This limited connectivity between soil and surface waters fundamentally structures the physical and biogeochemical interactions of water transiting through catchments.

Continental precipitation is routed through soils, plants, and streams on its return to the oceans or atmosphere. This hydrologic routing within catchments determines peak and baseflow stream discharge, plant productivity, and surface water quality. Over the long term, changes in water storage are minimal, and precipitation entering catchments exits as either runoff or evapotranspiration (*1*). Further partitioning evapotranspiration flux into evaporation and transpiration subcomponents is essential for understanding links between ecologic and hydrologic systems, because biologic water use is inexorably coupled with ecosystem productivity (*2*).

At plot scales, transpiration and evaporation fluxes can be directly measured by hydrometric devices such as lysimeters, leaf cuvettes, and sap flow probes, yet these techniques remain difficult to implement at watershed, regional, or continental scales (*3*–*6*). The classic hydrologic paradigm of translatory flow links these fluxes and posits that infiltration entering the soil column, where it may be used by vegetation, displaces previously held water deeper into the profile and eventually into streams (*7*). Observed preferential flow paths at hillslope scales (*8*, *9*) and geochemical evidence (*10*, *11*) point to the possibility that soil water used by plants remains separated from water rapidly passing though soils and into open channels. If this hydrologic separation is established as a generalized phenomena across catchments, models may require a more complex representation of water movement and associated soil biogeochemistry (*12*).

[1]Department of Geology and Geophysics, University of Utah, Salt Lake City, UT, USA. [2]Department of Biological and Ecological Engineering, Oregon State University, Corvallis, OR, USA. [3]College of Earth, Ocean and Atmospheric Sciences, Oregon State University, Corvallis, OR, USA. [4]Global Change and Sustainability Center, University of Utah, Salt Lake City, UT, USA.
*Corresponding author. E-mail: stephen.good@oregonstate.edu

Two distinct stable isotope techniques have emerged as solutions for flux partitioning at regional to global scales (*5*). Both approaches leverage differences between the ratio of heavy to light isotopes of water (e.g, D/H) in transpiration, which is often assumed to be unchanged relative to soil source waters (*13*), and evaporation, which is D-depleted relative to source waters because of the lower vapor pressure and diffusivity of the rare isotopologue (*14*). Runoff-based techniques use differences in the isotope ratios of precipitation inputs and outflowing runoff from hydrologic basins to partition evapotranspiration, with larger differences indicating more evaporation from surface waters (*3*, *15*, *16*). Evapotranspiration-based techniques involve directly measuring the isotopic ratio of upward vapor flux over a region and comparing it to estimated values for the evaporation and transpiration flux end members (*17*–*19*). Though useful, both approaches suffer from key deficiencies. Runoff techniques are unable to consider partial evaporation of soil waters before plant uptake if the remaining water is not discharged to surface waters (*20*, *21*). In contrast, evapotranspiration techniques provide information only within the measurement's flux footprint, and results are difficult to extrapolate across regions of heterogeneous surface cover or to areas with open surface water, which typically lie beyond the footprint of conventional flux-monitoring stations.

We established a unified framework for hydrologic partitioning that reconciles runoff and

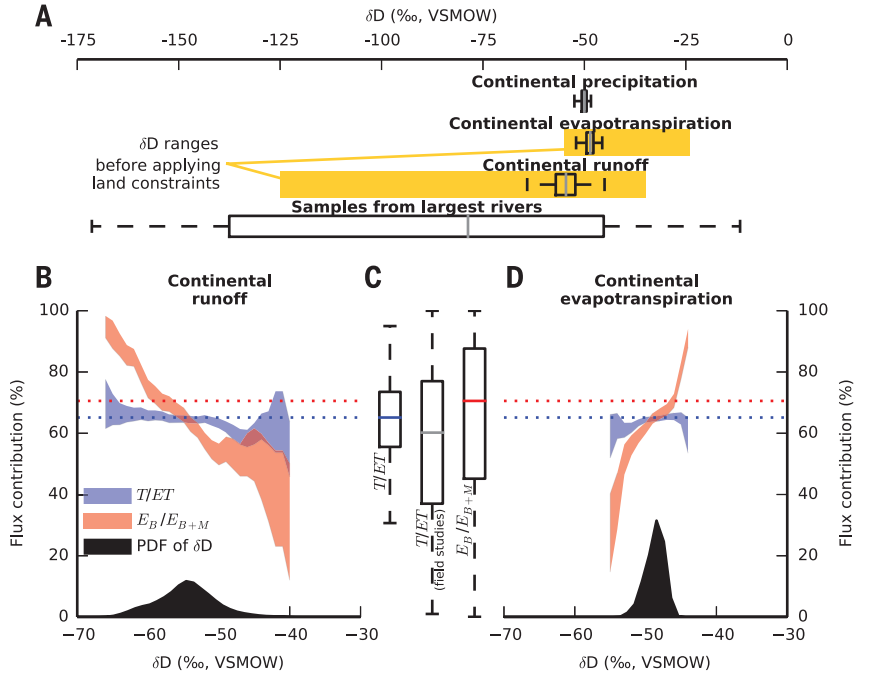


Fig. 1. Continental hydrologic partitioning constrained by the global D/H ratios. (**A**) Estimated global precipitation, evapotranspiration, and runoff δD values compared with values from 23 of the 200 largest rivers (*23*). Box plots depict median, 25th, and 75th percentiles of simulations, whereas yellow boxes depict the range based only on an ocean and atmosphere mass balance. Isotope values are reported in δ notation, where $\delta D = R/R_{VSMOW} - 1$, with R the D/H isotope ratio (VSMOW, Vienna standard mean ocean water). (**B**) Relationship between runoff δD and the transpired fraction of evapotranspiration, T/ET (blue); the fraction of evaporation (E) from soils, E_B/E_{B+M} (red) (B, bound waters; M, mobile waters); and a kernel density estimate, PDF of δD, of the distribution global runoff (black). Red and blue shaded areas show mean values, smoothed with a 5‰ moving window, ± 2 SE; and dotted lines show median percentages across all simulations. (**C**) Box plot of T/ET from this study, T/ET from field studies (*4*), and E_B/E_{B+M} from this study. (**D**) The same as (B) for continental evapotranspiration δD values.

Downloaded from www.sciencemag.org on July 10, 2015

evapotranspiration isotope approaches by quantifying the connectivity between soil matrix waters and mobile surface waters. This "hydrologic connectivity" is formally defined as the fraction of mobile surface water derived from bound waters (water that resides in the soil matrix and is available to support plant transpiration) as opposed to mobile waters (water that rapidly bypasses soils via preferential flow paths and does not mix with bound waters) (*22*). In a fully connected system, consistent with the translatory flow paradigm, water accessible to plants and subjected to soil evaporation also moves into streams. In a disconnected system characterized by preferential flow, soil waters do not interact with surface waters, and therefore water entering streams and rivers has an isotopic composition equivalent to that of rainfall. This theoretical framework can be applied, using established models for isotopic fractionation and data on isotopic inputs (precipitation) and outputs (runoff and evapotranspiration), to constrain the partitioning of hydrologic fluxes into the subcomponents of transpiration, evaporation of bound water in soils, and evaporation from mobile surface waters.

We recently determined the D/H isotope ratios of continental runoff and evapotranspiration (*23*), independent of terrestrial hydrologic partitioning, via an isotopic mass balance of the oceans and atmosphere. This ocean-atmosphere approach used satellite retrievals of marine surface-level D/H isotope ratios in water vapor (*24*) to estimate oceanic evaporation isotope ratios. Combining these with over-ocean precipitation isotope ratios modeled based on monitoring station data (*25*), we calculated the isotope ratios of continental fluxes as the residuals of each isotopologue mass balance. Here, over-land precipitation isotope ratios (*25*) were combined with bulk land-atmosphere water fluxes in gridded simulations of all terrestrial flux subcomponents and their isotope ratios to calculate the global terrestrial water isotope budget (*22*). In determining this budget, the fluxes of soil evaporation, surface water evaporation, and hydrologic connectivity were found so that the isotope ratios of continental runoff and evapotranspiration fluxes were consistent with the ocean-atmosphere mass balance (*23*).

When implementing this framework, constraints on possible runoff, interception, transpiration, and evaporation fluxes within the terrestrial hydrologic cycle (e.g., transpiration may not exceed evapotranspiration) limit the range of continental output flux isotope ratios relative to the previous ocean-atmosphere study (Fig. 1A). For global runoff isotope values, the revised results are within the range of observed large river values (*23*). Few direct observations of evapotranspiration isotope values are available for comparison with our result, and large uncertainties persist in accurately measuring this flux (*5*, *26*). Our simulations show that if the value of global runoff is more D-enriched, less transpiration and more surface water evaporation are required to balance the global isotope budget (Fig. 1B). Conversely, if the isotopic value of global evapotranspiration is more D-enriched, more transpiration and soil evaporation are required to meet observational constraints (Fig. 1D). Overall, the fraction of evaporation occurring in soils is more sensitive to runoff and evapotranspiration composition than is the transpired fraction.

Globally, the transpired fraction of evapotranspiration is estimated to be 56 to 74% (25th to 75th percentiles), with a median of 65% and mean of 64%. A previous estimate of global partitioning (*3*), which did not incorporate the evaporation of bound soil water and its connectivity to mobile water, suggested a value of 80 to 90%. Subsequent critiques and revisions of that study have obtained estimates similar to those reported here, though with greater uncertainty (*6*, *20*). The estimated transpired fraction described here is relatively insensitive to the hydrologic connectivity, which reflects the strong constraint imposed by the high isotope value of global evapotranspiration on the magnitude of this relatively D-enriched flux. We find that the global fraction of evaporation occurring in soils is 45 to 88%, with a median of 71% and a mean of 65%. Based on our simulations, we estimate hydrologic connectivity to be 14 to 59%, with a median of 31% and mean of 38%, which suggests a pervasive disconnect between water bound in soils and water entering streams, although not a complete separation.

Although local runoff D/H ratios in our model are typically larger then local precipitation D/H ratios, the flux weighted D/H ratio of global runoff is smaller than that of global continental precipitation because of spatial patterns in continental precipitation D/H composition and hydrologic routing. Locally, the evaporation of bound soil waters raises the isotope value of transpiration flux because plant roots will withdraw D-enriched soil waters. The positive-skewed distribution of simulation results with a low average hydrologic connectivity reflects the fact that at smaller connectivity values, the flux entering surface waters has decreased D/H ratios because more water is bypassing soils that are D-enriched. Thus, simulations with substantial soil evaporation are consistent with a global evapotranspiration flux that is enriched in D relative to precipitation, and simulations with low connectivity are consistent with a global runoff flux that is more depleted in D than precipitation. In contrast to the transpired fraction, the bound-water evaporation percentage is weakly correlated with connectivity (Fig. 2).

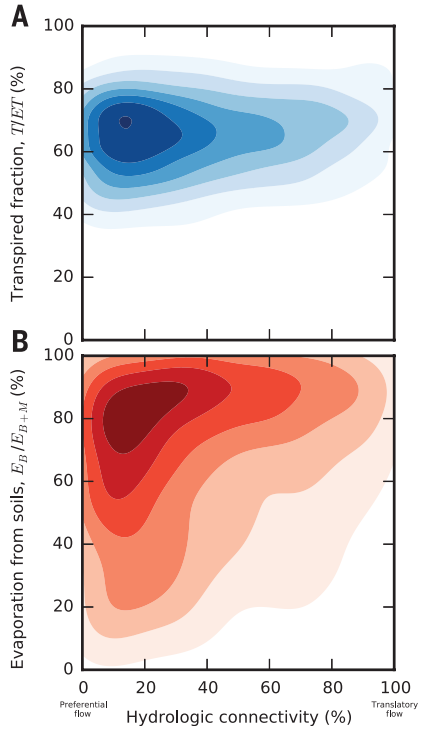


Fig. 2. Relationship between hydrologic connectivity and hydrologic partitioning. This is a bivaraite kernel density plot showing the distribution of results from Monte Carlo simulations of D/H ratios in the continental water cycle, with darker shaded areas more likely. (**A**) The transpired fraction of total evapotranspiration, *T*/*ET* and (**B**) the fraction of soil and surface water evaporation that occurs from soils, E_B/E_{B+M}.

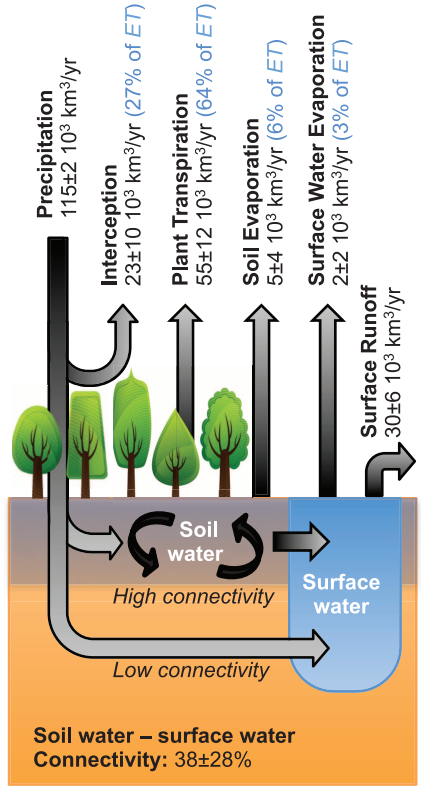


Fig. 3. Partitioned continental hydrologic fluxes. Terrestrial precipitation (annual mean ± 1 SD) not intercepted by vegetation mixes into soils or flows into surface waters. Soil water is withdrawn by plant roots via transpiration, subjected to evaporation, and leaks into the surface water. Of the flux entering the surface waters, our results suggest that 38% is derived from the soils, with the remainder being consistent with precipitation routed directly via preferential flow paths. Surface water that does not evaporate returns to the ocean as runoff.

This suggests predictive limits of our approach, in that more-connected systems with more soil evaporation and less-connected systems with less soil evaporation will produce similar continental output flux isotope ratios.

The terrestrial hydrologic partitioning estimated here corresponds to a total transpiration of 55,000 ± 12,000 km^3 per year (mean ± 1 SD), a total soil evaporation of 5000 ± 4000 km^3 per year, and a total surface water evaporation of 2000 ± 2000 km^3 per year, assuming an interception of 23,000 ± 10,000 km^3 per year (*27*) and a continental precipitation of 115,000 ± 2000 km^3 per year (*28*) (Fig. 3). The transpired fraction determined here is consistent with previous meta-analyses (Fig. 1C) and places an observational constraint on transpiration estimates from global Earth system models, which range between 38 and 80% (*4*–*6*, *29*). The fraction of total evapotranspiration flux occurring from surface waters, 2.9%, is also consistent with values from global Earth system models, which range from 2 to 4% when reported (*29*). Globally, tropical forests provide the bulk of continental transpiration, although these regions contribute modest amounts of soil and surface water evaporation as well.

Transpiration fluxes form the primary link between the water and carbon cycles, with water lost from plant stomata during carbon assimilation (i.e., plant water use efficiency) being a critical factor determining ecosystem function and productivity. Although we estimate that plant transpiration is a majority of the evapotranspiration flux, our results demonstrate that previous partitioning approaches may overestimate the contribution of transpiration, because they do not consider evaporation from multiple catchment water pools and their connectivity. Furthermore, isotopic partitioning approaches are sensitive to bulk flux estimates and their uncertainties, as well as assumptions about interception rates, with larger interception isotopically indistinguishable from increased transpiration because both fluxes are often assumed to be unfractionated relative to their source waters (*6*, *20*). Because a majority of evaporation occurs from soils and not open waters, more knowledge is needed of the role of ecosystem structure and microclimate in determining sub-canopy evaporation rates.

Finally, the partial hydrologic disconnect between bound and mobile waters, which our estimates suggest is substantial and pervasive at the global scale, has implications for prediction and monitoring of both water quantity and quality within streams and rivers. The hydrologic and hydrochemical properties of surface water systems are strongly influenced by physical flow paths within the near surface, and the low connectivity found here suggests, for example, that stream biogeochemistry may be less sensitive to soil zone processes than it would be if hydrologic connectivity were higher. Although we determined a single average connectivity value, connectivity varies with geography and in time as preferential flow paths are activated and deactivated throughout the year (*30*). Indeed, the relation between the connectivity metric and soil-water transit time distributions is likely to be complex. Given the ubiquitous nature of both water quantity and water quality issues affecting watersheds worldwide, an improved understanding of hydrologic connectivity at variety of temporal and spatial scales is essential.

REFERENCES AND NOTES

1. T. H. Syed, J. S. Famiglietti, D. P. Chambers, J. K. Willis, K. Hilburn, *Proc. Natl. Acad. Sci. U.S.A.* **107**, 17916–17921 (2010).
2. B. D. Newman *et al.*, *Water Resour. Res.* **42**, W06302 (2006).
3. S. Jasechko *et al.*, *Nature* **496**, 347–350 (2013).
4. L. Wang, S. P. Good, K. K. Caylor, *Geophys. Res. Lett.* **41**, 6753–6757 (2014).
5. S. J. Sutanto *et al.*, *Hydrol. Earth Syst. Sci. Discuss.* **11**, 2583–2612 (2014).
6. W. H. Schlesinger, S. Jasechko, *Agric. For. Meteorol.* **189-190**, 115–117 (2014).
7. J. J. McDonnell, *Wiley Interdiscip. Rev. Water* **1**, 323–329 (2014).
8. M. Stieglitz *et al.*, *Global Biogeochem. Cycles* **17**, 1105 (2003).
9. M. Weiler, J. J. McDonnell, *Water Resour. Res.* **43**, W03403 (2007).
10. J. R. Brooks, H. R. Barnard, R. Coulombe, J. J. McDonnell, *Nat. Geosci.* **3**, 100–104 (2009).
11. G. R. Goldsmith *et al.*, *Ecohydrology* **5**, 779–790 (2012).
12. F. M. Phillips, *Nat. Geosci.* **3**, 77–78 (2010).
13. G. Dongmann, H. W. Nürnberg, H. Förstel, K. Wagener, *Radiat. Environ. Biophys.* **11**, 41–52 (1974).
14. H. Craig, L. I. Gordon, in *Stable Isotopes in Oceanographic Studies and Paleotemperatures*, E. Tongiori, Ed. (Consiglio Nazionale Delle Richerche Laboratorio Di Gelogica Nucleare, Pisa, Italy, 1965), pp. 9–130.
15. J. J. Gibson, T. W. D. Edwards, *Global Biogeochem. Cycles* **16**, 10-1–10-14 (2002).
16. J. R. Brooks *et al.*, *Limnol. Oceanogr.* **59**, 2150–2165 (2014).
17. X. F. Wang, D. Yakir, *Hydrol. Processes* **14**, 1407–1421 (2000).
18. E. A. Yepez *et al.*, *Agric. For. Meteorol.* **132**, 359–376 (2005).
19. S. P. Good *et al.*, *Water Resour. Res.* **50**, 1410–1432 (2014).
20. A. M. J. Coenders-Gerrits *et al.*, *Nature* **506**, E1–E2 (2014).
21. D. R. Schlaepfer *et al.*, *Ecosphere* **5**, art61 (2014).
22. Materials and methods are available as supplementary materials on *Science* Online.
23. S. P. Good, D. Noone, N. Kurita, M. Benetti, G. J. Bowen, *Geophys. Res. Lett.* 10.1002/2015GL064117 (2015).
24. J. Worden *et al.*, *Atmos. Meas. Tech.* **5**, 397–411 (2012).
25. G. J. Bowen, J. Revenaugh, *Water Resour. Res.* **39**, 1–13 (2003).
26. S. P. Good, K. Soderberg, L. Wang, K. K. Caylor, *J. Geophys. Res.* **117**, D15301 (2012).
27. D. Wang, G. Wang, E. N. Anagnostou, *J. Hydrol. (Amst.)* **347**, 308–318 (2007).
28. R. F. Adler *et al.*, *J. Hydrometeorol.* **4**, 1147–1167 (2003).
29. L. Wang-Erlandsson, R. J. Van Der Ent, L. J. Gordon, H. H. G. Savenije, *Earth Syst. Dyn.* **5**, 441–469 (2014).
30. I. Heidbüchel, P. A. Troch, S. W. Lyon, M. Weiler, *Water Resour. Res.* **48**, W06520 (2012).

ACKNOWLEDGMENTS

This project was funded by the NSF Macrosystems Biology program, grant EF-01241286, and the U.S. Department of Defense. D.N. acknowledges the support of the NSF Climate and Large Scale Dynamic program as part of a Faculty Early Career Development award (AGS-0955841). Support and resources from the Center for High Performance Computing at the University of Utah are also gratefully acknowledged. Bulk flux data used in this study are available online from NASA (http://precip.gsfc.nasa.gov/, http://gmao.gsfc.nasa.gov/merra/) and the Woods Hole Oceanographic Institute (http://oaflux.whoi.edu/). Global surface vapor isotope data are available as supplementary information in (*23*). The model code and input data files used in this study are available at http://waterisotopes.org.

SUPPLEMENTARY MATERIALS

www.sciencemag.org/content/349/6244/175/suppl/DC1
Materials and Methods
Figs. S1 to S3
References (*31*–*37*)

7 January 2015; accepted 2 June 2015
10.1126/science.aaa5931

CLIMATE CHANGE

Climate change impacts on bumblebees converge across continents

Jeremy T. Kerr,[1]* Alana Pindar,[1] Paul Galpern,[2] Laurence Packer,[3] Simon G. Potts,[4] Stuart M. Roberts,[4] Pierre Rasmont,[5] Oliver Schweiger,[6] Sheila R. Colla,[7] Leif L. Richardson,[8] David L. Wagner,[9] Lawrence F. Gall,[10] Derek S. Sikes,[11] Alberto Pantoja[12]†

For many species, geographical ranges are expanding toward the poles in response to climate change, while remaining stable along range edges nearest the equator. Using long-term observations across Europe and North America over 110 years, we tested for climate change–related range shifts in bumblebee species across the full extents of their latitudinal and thermal limits and movements along elevation gradients. We found cross-continentally consistent trends in failures to track warming through time at species' northern range limits, range losses from southern range limits, and shifts to higher elevations among southern species. These effects are independent of changing land uses or pesticide applications and underscore the need to test for climate impacts at both leading and trailing latitudinal and thermal limits for species.

Biological effects of climate change threaten many species (*1*), necessitating advances in techniques to assess their vulnerabilities (*2*). In addition to shifts in the timing of species' life cycles, warming has caused range expansion toward the poles and higher elevations (*3*–*6*). Climate impacts could cause losses from parts of species' trailing range margins (*7*), but those losses are infrequently observed (*4*). Such responses depend on species' traits, such as

heat or cold tolerance, that reflect shared evolutionary history and climatic origins (e.g., tropical or temperate) of taxa (*8*, *9*). Climate change can interact with other threats, like land-use intensification, to alter species' responses to emerging conditions (*10*). Such global changes can alter or erode ecological services provided by the affected species (*11*). Few species assemblages contribute more to these services than bumblebees (*Bombus*), many of which are declining (*12*, *13*). No study has yet evaluated climate change impacts across the latitudinal and thermal limits of such a large species assemblage spanning two continents.

[1]Department of Biology, University of Ottawa, Ottawa, ON, Canada, K1N6N5. [2]Faculty of Environmental Design, University of Calgary, Calgary, Alberta, Canada. [3]Department of Biology, York University, Toronto, Ontario, Canada. [4]School of Agriculture, Policy and Development, The University of Reading, Reading, UK. [5]Department of Zoology, Université de Mons, Mons, Belgium. [6]Department of Community Ecology, Helmholtz Centre for Environmental Research, Halle, Germany. [7]Wildlife Preservation Canada, Guelph, Ontario, Canada. [8]Gund Institute, University of Vermont, Burlington, VT, USA. [9]Department of Ecology and Evolutionary Biology, University of Connecticut, Storrs, CT, USA. [10]Peabody Museum of Natural History, Entomology Division, Yale University, New Haven, CT, USA. [11]University of Alaska Museum, University of Alaska Fairbanks, Fairbanks, AK, USA. [12]United States Department of Agriculture, Agricultural Research Service, Subarctic Agricultural Research Unit, Fairbanks, AK, USA.
***Corresponding author. E-mail: jkerr@uottawa.ca** †Present address: United Nations Food and Agriculture Organization, Santiago, Chile.

We assembled a database of ~423,000 georeferenced observations for 67 European and North American bumblebee species (fig. S1 and tables S1 and S2). Species observations were gathered from the Global Biodiversity Information Facility (171,479 North American and 192,039 European records) (*14*), *Bumblebees of North America* (*15*) (153,023 records), and the Status and Trends of European Pollinators Collaborative Project (237,586 records). We measured differences in species' northern and southern range limits, the warmest or coolest temperatures occupied, and their mean elevations in three periods (1975 to 1986, 1987 to 1998, and 1999 to 2010) (figs. S2 to S4) relative to a baseline period (1901 to 1974) (*16*). We investigated whether land use affected these results. Finally, we used high-resolution pesticide application data available in the United States after 1991 to investigate whether total pesticide or neonicotinoid applications accounted for changes in bumblebee species' range or thermal limits (table S3). Tests used phylogenetic generalized least-squares models (PGLS), using a phylogenetic tree constructed from nuclear and mitochondrial markers (*17*), and accounted for differences in sampling intensity between time periods (Table 1).

If species expanded their northern range limits to track recent warming, their ranges should show positive (northward) latitudinal shifts, but cool thermal limits should be stable through time. In contrast to expectations and responses known from other taxa (*4*), there has been no change in the northern limits of bumblebee distributions in North America or Europe (Fig. 1A). Despite substantial warming (~ +2.5°C), bumblebee species have also failed to track warming along their cool thermal limits on both continents (Fig. 1B and Table 1). These failures to track climate change occur in parallel in regions that differ in their intensities of human land use (e.g., Canada and northern Europe), which had no direct or interaction-based effect in any statistical model (Table 1).

If bumblebee species climate responses resemble most terrestrial ectotherm taxa (*4*), their southern range limits should have remained stable with increasing temperatures along species' warm thermal limits. However, bumblebee species' range losses from their historical southern limits have been pronounced in both Europe and North America, with losses growing to ~300 km in southern areas on both continents (Fig. 1C). Throughout North America, species also experienced range losses from the warmest areas they historically occupied, while European species' range losses extend across the warmest regions (where mean temperatures exceed ~15°C) (Fig. 1D). These responses showed a significant phylogenetic signal, with closely related bumblebee species showing increasingly similar range shifts from southern and warm thermal limits (Table 1). As with failures to expand northward or into cooler areas, land-use changes do not relate to range losses from bumblebee species' southern or warm thermal limits.

Table 1. PGLS models showing climate change and interactive effects on North American and European bumblebees. Changes in latitude (km north of equator), thermal (°C), or elevation (m) variables observed by 1999 to 2010 for each species (relative to the 1901 to 1974 baseline period) are regressed against predictors listed on the left. Models reported in each column were selected using AIC, which can include statistically nonsignificant variables. Sample sizes in each time period (median *n* per species = 536) were tested but excluded using AIC. Variable coefficients are given, with SEs in parentheses. A dash indicates that this variable was not part of the AIC-selected model. Ordinary least squares (OLS) regression summary statistics (adjusted R^2) are provided to enable comparison with PGLS results; OLS coefficients are similar.

Predictors	Latitude		Thermal		Elevation
	Northern	Southern	Cool	Warm	
Intercept	−268.3 (614.7)	657.8 (150.4)	2.436 (0.5)	657.8 (150.4)	1075 (340.7)
Latitudinal or thermal limit (1901–1974)	0.04 (0.08)	−0.12 (0.04)	−0.009 (0.05)	0.19 (0.1)	–
Mean latitude (1999–2010)	–	–	–	–	−0.21 (0.07)
Covariates					
Continent	1158 (1039)	–	–	10.59 (2.24)	384.5 (504.1)
Δ Crop land (1999–2010)	−4.25 (7.68)	–	–	–	–
Δ Pasture (1999–2010)	−43.1 (60.71)	–	–	–	–
Interactions with continent					
Thermal or latitudinal limits (1901–1974)	−0.12 (0.14)	–	–	−0.47 (0.12)	–
Δ Crop land (1999–2010)	−9.38 (41.73)	–	–	–	–
Δ Pasture (1999–2010)	74.95 (74.35)	–	–	–	–
Mean latitude (1999–2010)	–	–	–	–	−0.03 (0.1)
Models of trait evolution					
AIC (Independent)	915.5	863.2	291.3	274.5	863.6
AIC (Brownian motion)	962.4	897.4	339.3	293.9	916.4
AIC (Ornstein-Uhlenbeck)	917.5	861.8	293.3	264.9	865.4
AIC (Pagel)	915.3	862.2	293.1	273	860.8
Pagel's λ	−0.15	0.49	0.04	0.64	−0.1
Equivalent OLS regression summary statistics					
Adjusted R^2	0.15	0.14	−0.01	0.30	0.28

Species with southern geographical ranges retreated to higher elevations across Europe and North America (Table 1 and Fig. 2), consistent with observations of range losses from their southern range limits. Elevation shifts are larger in Europe [i.e., Akaike's information criterion (AIC)–based model selection includes a small continental effect; intercept for Europe, 1459 m (366 SE); North America, 1074 m (340 SE) (Fig. 2)]. Europe's mountainous areas are oriented predominantly east-west, potentially inducing more pronounced upslope shifts. Mean elevations of observations for southern species have risen ~300 m since 1974. Observed shifts along elevation gradients vary considerably among species (*3*) but follow a coherent geographical pattern. Mean elevations among northern species in Europe and North America shifted lower. Over recent decades, alpine tree lines have advanced upslope in response to human activities, geomorphological factors, and warming (*18*), potentially overtaking nesting, overwintering, and forage habitats in historically open areas. High-elevation habitat changes could contribute to generalist pollinator declines in mountainous areas (*19*), particularly among bumblebee species whose ranges have not expanded from their cold thermal limits.

In addition to land-use changes, we investigated whether pesticide use affected shifts in thermal and latitudinal range limits among bumblebees. Spatially detailed, annual pesticide measurements, including neonicotinoid insecticides, were available for the United States after 1991. Neither total pesticide nor neonicotinoid applications there relate to observed shifts in bumblebee species' historical ranges or thermal limits (table S1). Neonicotinoid effects known from individual and colony levels certainly contribute to pollinator declines and could degrade local pollination services. Neonicotinoid effects on bumblebees have been demonstrated experimentally using field-realistic treatments (*20*). These locally important effects do not "scale up" to explain cross-continental shifts along bumblebee species' thermal or latitudinal limits. The timing of climate change–related shifts among bumblebee species underscores this observation: Range losses from species' southern limits and failures to track warming conditions began before widespread use of neonicotinoid pesticides (figs. S2 and S3).

Regional analyses suggest that latitudinal range shifts toward the poles are accelerating in most species groups (*3*), while their trailing range margins remain relatively stable (*4*). Assemblages showing pronounced northward range expansions and limited southern-range losses, like butterflies, originated and diversified in tropical climates and retain ancestral tolerances to warmer conditions (*21*). Those species' warming-related extinction risks in temperate environments are low (*8*) but increase toward warmer areas where climatic conditions resemble those under which they evolved (*7*, *22*). Drawing on comprehensive range data, bumblebee species show opposite range responses across continents relative to most terrestrial assemblages (*4*): rapid losses from the south and lagging range expansions in the north. Mechanisms leading to observed lags in range responses at species' northern or cool thermal limits require urgent evaluation. Colonization of previously unoccupied areas and maintenance of new populations strongly affect whether species track shifting climatic conditions (*23*), capacities that appear insufficient among bumblebees. Observed losses from species' southern or warm boundaries in Europe and North America, and associated phylogenetic signals, are consistent with ancestral limitations of bumblebees' warm thermal tolerances and evolutionary origins in cool Palearctic conditions (*24*). Warming-related extreme events cause bumblebee population losses (*25*) by imposing demands for energetically costly behavioral thermoregulation, even at high latitudes and elevations (*26*). Such effects are not yet observed for European bumblebees in cooler regions, where species generally experience temperatures exceeding those observed historically within their ranges (Fig. 1D) (*10*). Range losses there will likely accelerate without mitigation from climatic refugia (*27*).

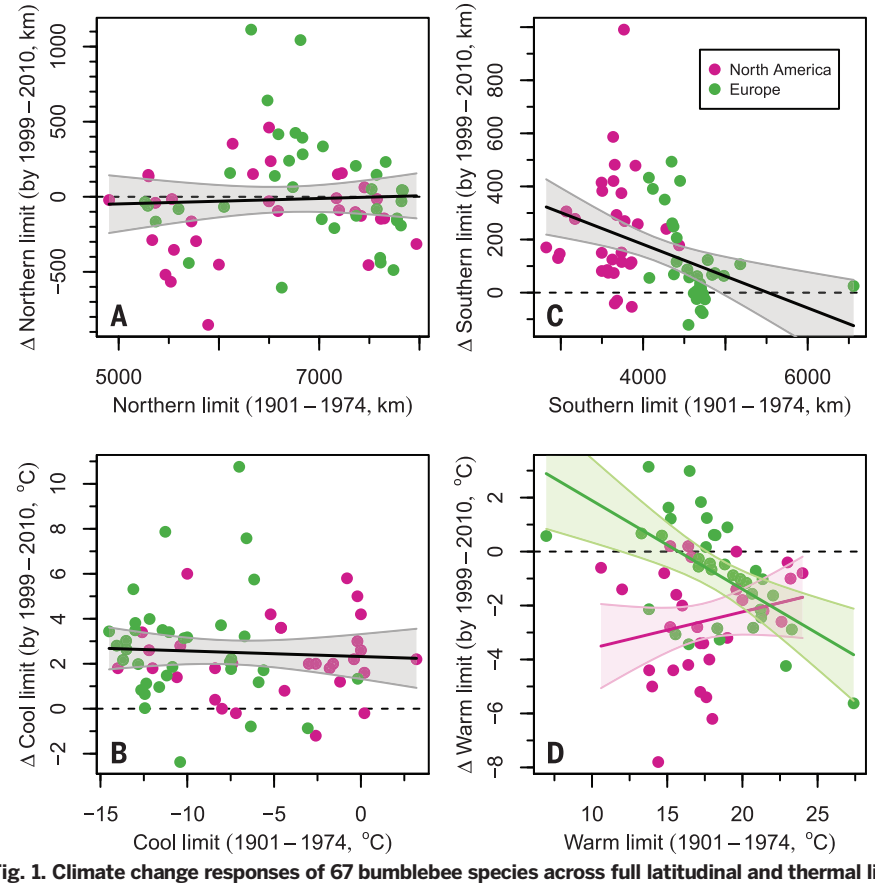


Fig. 1. Climate change responses of 67 bumblebee species across full latitudinal and thermal limits in Europe and North America. For each measurement, the *y* axis shows differences in the latitude of species' range limits [(**A**) Northern, (**C**) Southern] or thermal limits [(**B**) Cool; (**D**) Warm], respectively, by 1999 to 2010 relative to baseline conditions for 1901 to 1974. Each point represents the mean of five observations at the latitudinal or thermal limits for one bumblebee species (green circles for Europe and pink for North America). Null expectations (dashed lines) are for no temporal change in latitudinal or thermal limits. Range expansions from species' historical northern limits (A) are indicated by positive values, and positive values indicate range losses from species' southern limits (B). Temperature changes show whether bumblebee species are tracking differences along their thermal limits through time (no change), falling behind (positive values), or retreating more rapidly than mean conditions detect (negative values). Confidence bands (95%) for regression models (i.e., with and without continent + interaction against latitudinal or thermal change terms) with the lowest AIC are shown.

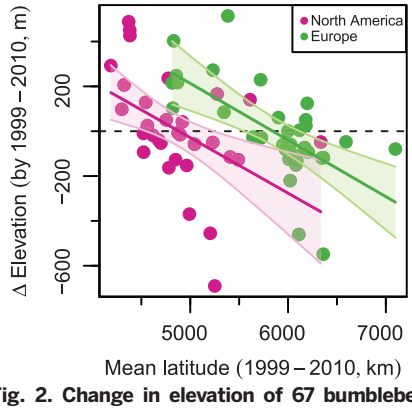


Fig. 2. Change in elevation of 67 bumblebee species by 1999 to 2010 relative to their mean latitude. Elevations are calculated using mean elevations across species observations. The slopes are similar between continents (according to regression and PGLS analyses). The confidence bands (95%) of regression slopes are shown.

Climate change appears to contribute distinctively, and consistently, to accumulating range compression among bumblebee species across continents. Experimental relocation of bumblebee colonies into new areas could mitigate these range losses. Assessments of climate change on species' ranges need to account for observations across the full extent of species' latitudinal and thermal limits and explicitly test for interactions with other global change drivers.

REFERENCES AND NOTES

1. C. D. Thomas *et al.*, *Nature* **427**, 145–148 (2004).
2. M. Pacifici *et al.*, *Nat. Clim. Change* **5**, 215–224 (2015).
3. I. C. Chen, J. K. Hill, R. Ohlemüller, D. B. Roy, C. D. Thomas, *Science* **333**, 1024–1026 (2011).
4. J. M. Sunday, A. E. Bates, N. K. Dulvy, *Nat. Clim. Change* **2**, 686–690 (2012).
5. J. M. Herrera, E. F. Ploquin, J. Rodríguez-Pérez, J. R. Obeso, M. B. Araújo, *J. Biogeogr.* **41**, 700–712 (2014).
6. E. F. Ploquin, J. M. Herrera, J. R. Obeso, *Oecologia* **173**, 1649–1660 (2013).
7. B. Sinervo *et al.*, *Science* **328**, 894–899 (2010).
8. M. B. Araújo *et al.*, *Ecol. Lett.* **16**, 1206–1219 (2013).
9. V. Kellermann *et al.*, *Proc. Natl. Acad. Sci. U.S.A.* **109**, 16228–16233 (2012).
10. V. Devictor *et al.*, *Nat. Clim. Change* **2**, 121–124 (2012).
11. D. Goulson, E. Nicholls, C. Botías, E. L. Rotheray, *Science* **347**, 1255957 (2015).
12. S. A. Cameron *et al.*, *Proc. Natl. Acad. Sci. U.S.A.* **108**, 662–667 (2011).
13. I. Bartomeus *et al.*, *Proc. Natl. Acad. Sci. U.S.A.* **110**, 4656–4660 (2013).
14. GBIF, *GBIF Metadata Profile, Reference Guide,* Contributed by E. O Tuama, K. Braak (Global Biodiversity Information Facility, Copenhagen, 2011).
15. P. H. Williams, R. W. Thorp, L. L. Richardson, S. R. Colla, *Bumble Bees of North America: An Identification Guide* (Princeton Univ. Press, New York, 2014).
16. Materials and methods are available as supplementary materials on *Science* Online.
17. S. A. Cameron, H. M. Hines, P. H. Williams, *Biol. J. Linn. Soc. Lond.* **91**, 161–188 (2007).
18. J. Gehrig-Fasel, A. Guisan, N. E. Zimmermann, *J. Veg. Sci.* **18**, 571–582 (2007).
19. M. L. Forister *et al.*, *Proc. Natl. Acad. Sci. U.S.A.* **107**, 2088–2092 (2010).
20. P. R. Whitehorn, S. O'Connor, F. L. Wackers, D. Goulson, *Science* **336**, 351–352 (2012).
21. T. S. Romdal, M. B. Araújo, C. Rahbek, *Glob. Ecol. Biogeogr.* **22**, 344–350 (2013).
22. C. A. Deutsch *et al.*, *Proc. Natl. Acad. Sci. U.S.A.* **105**, 6668–6672 (2008).
23. S. J. Leroux *et al.*, *Ecol. Appl.* **23**, 815–828 (2013).
24. H. M. Hines, *Syst. Biol.* **57**, 58–75 (2008).
25. P. Rasmont, S. Iserbyt, *Ann. Soc. Entomol. Fr.* **48**, 275–280 (2012).
26. J. M. Sunday *et al.*, *Proc. Natl. Acad. Sci. U.S.A.* **111**, 5610–5615 (2014).
27. K. J. Willis, S. A. Bhagwat, *Science* **326**, 806–807 (2009).

ACKNOWLEDGMENTS

This research was funded by the Natural Sciences and Engineering Research Council of Canada strategic network (CANPOLIN: Canadian Pollination Initiative) and Discovery Grant support and University of Ottawa Research Chair in Macroecology and Conservation to J.T.K. We are grateful to anonymous reviewers whose comments improved this paper and to P. Williams for advice and perspectives during development of the research. All data and supporting scripts are available from Dryad Digital Repository: doi:10.5061/dryad.gf774.

SUPPLEMENTARY MATERIALS

www.sciencemag.org/content/349/6244/177/suppl/DC1
Materials and Methods
Supplementary Text
Supplementary Acknowledgments
Figs. S1 to S4
Tables S1 to S3
References (*28*–*55*)

15 January 2015; accepted 21 May 2015
10.1126/science.aaa7031

PLACE CELLS

Autoassociative dynamics in the generation of sequences of hippocampal place cells

Brad E. Pfeiffer* and David J. Foster†

Neuronal circuits produce self-sustaining sequences of activity patterns, but the precise mechanisms remain unknown. Here we provide evidence for autoassociative dynamics in sequence generation. During sharp-wave ripple (SWR) events, hippocampal neurons express sequenced reactivations, which we show are composed of discrete attractors. Each attractor corresponds to a single location, the representation of which sharpens over the course of several milliseconds, as the reactivation focuses at that location. Subsequently, the reactivation transitions rapidly to a spatially discontiguous location. This alternation between sharpening and transition occurs repeatedly within individual SWRs and is locked to the slow-gamma (25 to 50 hertz) rhythm. These findings support theoretical notions of neural network function and reveal a fundamental discretization in the retrieval of memory in the hippocampus, together with a function for gamma oscillations in the control of attractor dynamics.

In the well-known Hopfield model, a network of recurrently excitable neurons stores discrete memories as stable activity patterns (attractors) to which partial patterns are guaranteed to converge, based on synaptic weights reflecting correlations between neurons in the same pattern ("autoassociation") (*1*). Sequences of patterns can also be stored, based on weights reflecting correlations between different patterns ("heteroassociation"), but are generally unsustainable because any noise leads to divergence in subsequent patterns. A solution is to combine fast autoassociation for each pattern with slower heteroassociation for successive patterns, allowing each pattern to be corrected via attractor network dynamics before transitioning to the next pattern in the sequence (*2*, *3*). This process should result in "jumpy" sequences that sharpen individual pattern representations before transitioning to successive patterns; however, direct evidence is lacking, due largely to the difficulty of obtaining data from very large ensembles of neurons expressing internally generated sequences recorded at the time resolution of neuronal dynamics.

Hippocampal SWR-associated place-cell sequences (*4*–*10*), often termed "replay," are a unique experimental model in which neurons with well-defined receptive fields are activated outside those receptive fields and in specific temporal sequences corresponding to physical trajectories through space, all while the animal is stationary, and thus in the absence of corresponding sequences of stimuli or behaviors. We recently developed methods to record simultaneously from very large numbers of hippocampal neurons (up to 263) with place fields in a single environment (*10*), and we applied these recording techniques to examine the fine structure of SWR-associated place-cell sequences to investigate the underlying mechanisms of this form of memory expression and explore the circuit-level dynamics of an attractor system in vivo.

We recorded bilateral ensemble activity from dorsal hippocampal neurons (figs. S1 and S2) of five rat subjects across multiple recording sessions as they explored open arenas or linear tracks (Fig. 1, A, B, G, and H). We obtained simultaneous recordings from large populations of hippocampal neurons in each recording session (80 to 263 units per session; mean ± SEM = 159.2 ± 11.8 units per session), allowing us to accurately decode spatial information from the hippocampal ensemble activity patterns using a memory-less, uniform-prior Bayesian decoding algorithm (fig. S3) (*5*, *10*). We identified SWRs that encoded temporally compressed spatial trajectories through the current environment (Fig. 1, C to F and I to L, and fig. S4) (*10*), which we term "trajectory events" rather than "replay" to reflect the observation that SWRs do not always represent a perfect replay of immediately prior behavior but instead reflect a more broad array of spatial paths (*8*–*10*). Across all sessions in the open field and linear track, we identified 815 and 564 SWR events, respectively, that met our criteria to be classified as trajectory events.

Consistent with prior reports (*5*), trajectory events displayed average velocities in a relatively narrow range (Fig. 2A); however, when we examined trajectory events on a finer time scale, we observed discontinuous trajectories, alternating between immobility (in which consecutive decoding frames represented the same location) and rapid movement (in which consecutive frames represented a sequential path of unique positions; fig.

Solomon H. Snyder Department of Neuroscience, Johns Hopkins University School of Medicine, Baltimore, MD, USA.
*Present address: Department of Neuroscience, University of Texas Southwestern Medical Center, Dallas, TX, USA.
†Corresponding author. E-mail: david.foster@jhu.edu

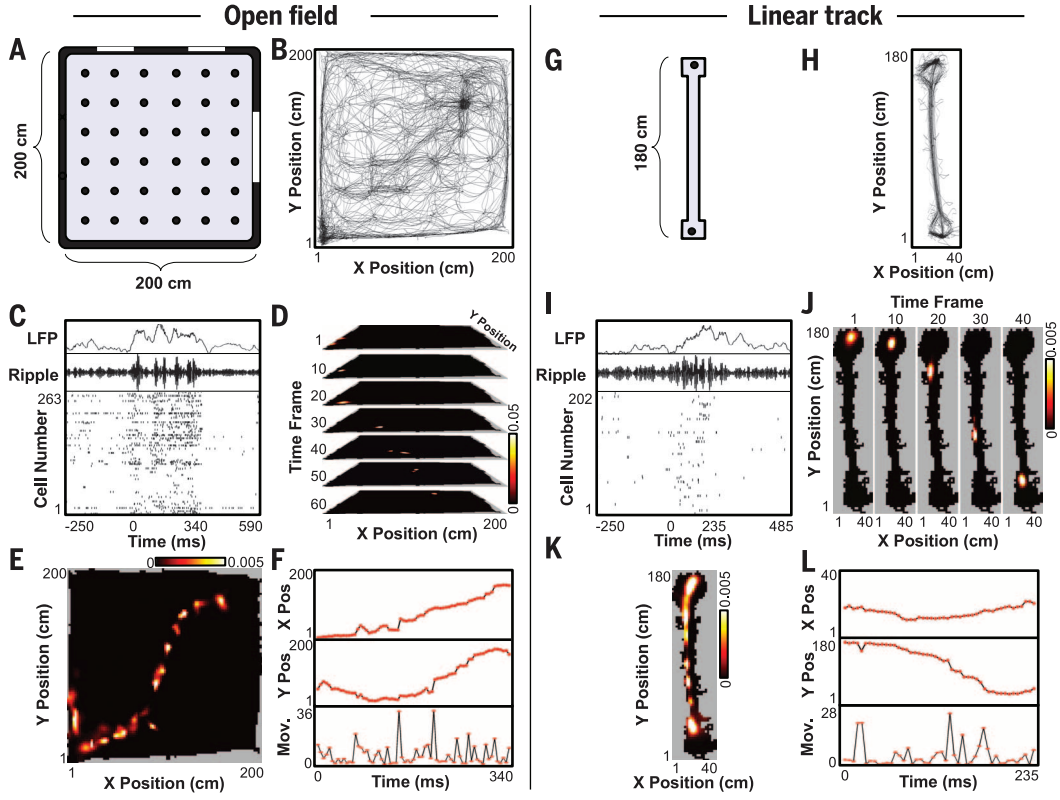


Fig. 1. Open arena and linear track trajectory events. (**A**) Schematic diagram of the open field (circles indicate reward wells). (**B**) Behavioral trajectory for rat 1 throughout an entire recording session. (**C**) Wideband (top) and ripple-filtered (middle) local field potential (LFP), and raster plot of simultaneously recorded neurons (bottom) for a representative SWR in the open arena ± 250 ms. (**D**) Decoded position (Bayesian posterior probability) for evenly distributed time frames throughout the SWR event in (C). Note that individual frames display a tight, spatially restricted representation. (**E**) Mean decoded position across all time frames for the event in (C). Despite spatially localized representations in each individual window (D), the entire SWR encodes a trajectory that crosses the environment. (**F**) Location (in centimeters) and sequence of the encoded trajectory in the *x* (top) and *y* axis (middle) and movement (in centimeters) between each frame (bottom). (**G** to **L**) As in (A) to (F), for representative linear track session and trajectory event.

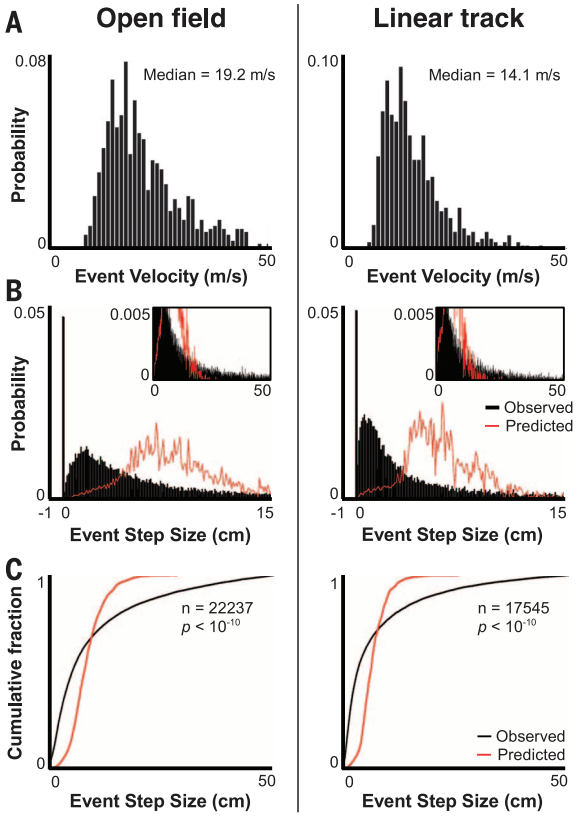


Fig. 2. Movement during trajectory events. Quantification of movement and velocities for trajectories encoded by SWRs during open field (left) and linear track (right) exploration. (**A**) Probability histogram (1 m/s bins) of average trajectory event velocities (total distance covered/total event duration). (**B** and **C**) Probability histogram (B) (0.1-cm bins) and cumulative distribution (C) of step sizes for all trajectory events. Predicted step sizes (red) based on evenly spaced steps. Inset: zoomed *y* axis and expanded *x* axis. Observed versus predicted populations significantly different (Wilcoxon rank-sum test, $P < 10^{-10}$ for both open field and linear track sessions); cumulative distributions significantly different (two-sample Kolmogorov-Smirnov test).

S4). We calculated for each event the step size per frame that would be necessary to encode a smooth trajectory and compared these predicted step sizes to the actual step sizes observed within trajectory events (Fig. 2, B and C). Observed step sizes significantly differed from predicted, with a larger number of very short steps and a longer tail of larger steps (Fig. 2, B and C). The large peak observed at zero arose from consecutive frames in which the spike pattern did not change; eliminating this peak did not affect significance (Wilcoxon rank-sum test, $P < 10^{-10}$ for both open field and linear track sessions). The observation of alternating immobility and movement in trajectory events was observed in two different environments with distinct behavioral requirements and was consistent across a range of decoding criteria, including decoding window size and degree of temporal smoothing (figs. S5 to S9). These data suggest that during SWR-based memory expression, information is not presented in a temporally continuous stream, but is expressed in discrete, temporally separated units. In addition, we observed no effect of trajectory proportion (e.g., start, middle, end) on stepwise movement (fig. S10), indicating that temporal segmentation is present throughout the entirety of a trajectory event and is likely an inherent characteristic of information flow during hippocampal reactivation.

To explore mechanisms underlying the discontinuous flow of information within SWRs, we measured the relative timing of movement and

immobility during trajectory events. We observed that an average stationary epoch lasted 24.1 ± 0.38 ms (n = 3364) in open field sessions and 16.7 ± 0.25 ms (n = 3011) in linear track sessions, whereas epochs of movement had an average duration of 7.9 ± 0.09 ms (n = 3324) and 11.2 ± 0.18 ms (n = 3060) in the open field and linear track sessions, respectively. Thus, on average, repeating cycles of immobility and movement occurred at roughly 30 to 40 Hz, prompting us to examine the correlation between information expression in hippocampal reactivation events and the slow-gamma rhythm, a prominent 25- to 50-Hz oscillation that originates in hippocampal area CA3, one synapse upstream from our recording location (*11*, *12*). Consistent with prior reports (*13*), we noted a transient increase in slow-gamma power during trajectory events (fig. S11). In addition, we observed that both excitatory spiking and movement during trajectory events were phase-locked with the slow-gamma rhythm (Fig. 3, A to C and F to H, and fig. S12). Intriguingly, the preferred phase of movement opposed that of neural activity (Fig. 3, D and I). Accordingly, step size was negatively correlated with spike count during trajectory events (fig. S13), and the total number of spikes across two consecutive decoding windows predicted the resulting step size (Fig. 3, E and J). Furthermore, we observed a phase-dependent correlation between movement and the sharpness of decoded position (fig. S14). These results were replicated with multiple decoding criteria and different degrees of temporal smoothing (figs. S15 to S18), suggesting that the correlation of movement with gamma phase was not dependent on the data-binning procedure. Together, these data indicate that the temporal segmentation of trajectory events is governed by slow-gamma oscillations and that during phases of high neuronal activity within the gamma cycle, spatial representation in the hippocampus is often focused on a single location, whereas during phases of low neuronal activity, the spatial representation is more likely to move to adjacent locations.

It might be hypothesized that systematic variation in the measurement process, or in spike number, could account for the correlation between movement and slow-gamma phase. We asked whether it was possible to observe smooth trajectories whose movement was uncorrelated with gamma phase using the data that we had collected and our analysis methods. Without altering place fields or the precise timing of individual spikes (thereby preserving the correlation of individual spikes to the phase of slow gamma and preserving phase-dependent changes in population firing rate), we created nonrandom shuffles of the cell identities of individual spikes during trajectory events to generate trajectories that followed the same path as the original trajectory event, but progressed smoothly rather than discontinuously through space (fig. S19). The step sizes of these evened trajectory events were not statistically different from ideally smooth step sizes (Fig. 4, A, B, D, and E, and fig. S20). Whereas the correlation of spike activity to slow-gamma rhythm was preserved, the relationship between step size and slow-gamma phase was abolished (Fig. 4, C and F, and fig. S20). We further tested whether our observation of discontinuous movement in trajectory events was a result of poor place-field distribution or inherent noise in neural activity. We simulated trajectory event activity associated with the occupancy of different positions as Poisson spiking based on cells' place fields and the spike rates typically observed during the short time bins used to decode actual trajectory events. We observed that all locations in the arena could be decoded accurately (fig. S21, A and B) and that evenly stepped sequences of positions produced step-size distributions that were significantly

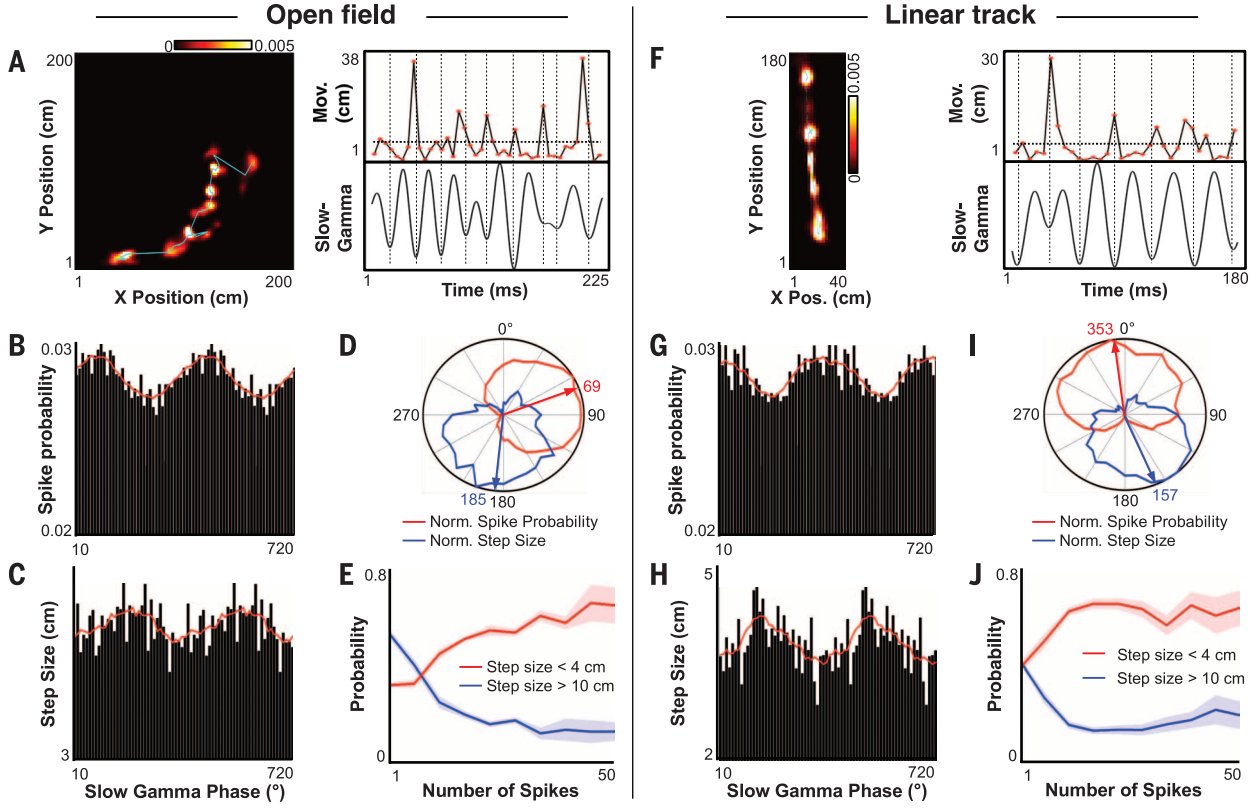


Fig. 3. Correlation between movement, firing rate, and slow-gamma phase. (**A**) Mean posterior probabilities (left, cyan line indicates temporal sequence), movement (top right), and slow-gamma oscillation (bottom right) for a representative trajectory event. Troughs (180° phase) in the gamma trace indicated with dashed lines. (**B** and **C**) For all open field sessions, across-session average spike probability (B) and step size (C) as a function of slow-gamma phase (bin size = 10°) for all trajectory events. Red line indicates running box average (box size = 8 bins). Circular correlation Monte-Carlo P value (50,000 shuffles of gamma phase): spike probability $P < 2.00 \times 10^{-5}$; step size $P = 4.40 \times 10^{-4}$). (**D**) Normalized contour plots and circular weighted mean (arrow) for box-average spike probability (red) and step size (blue) as a function of slow-gamma phase. (**E**) Mean ± SEM probability of observing a step size greater than 10 cm (blue) or less than 4 cm (red) as a function of spike count. (**F** to **J**) As in (A) to (E), for linear track events. (G and H) Monte-Carlo P value: spike probability $P < 2.00 \times 10^{-5}$; step size $P < 2.00 \times 10^{-5}$.

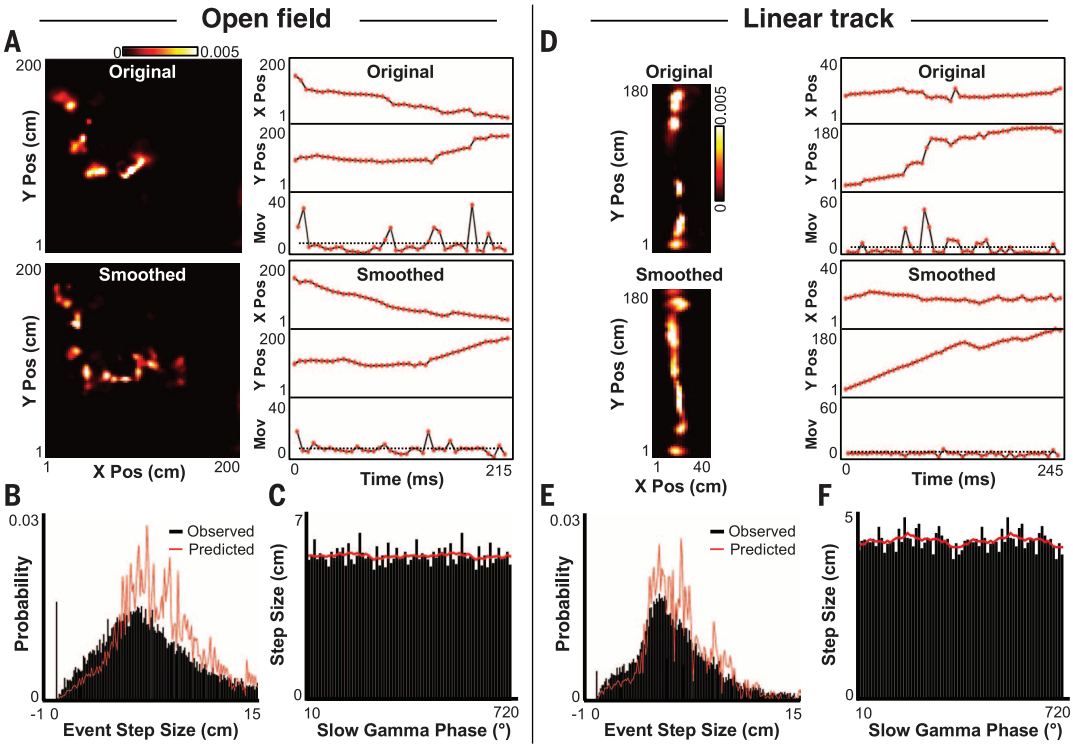


Fig. 4. Forced decorrelation of movement and slow-gamma phase. (**A**) Representative trajectory event before (top) and after (bottom) spike ID shuffles to smooth the encoded path (fig. S19). (**B**) Probability histogram of step sizes across all smoothed open field trajectory events. Predicted step sizes (red) based on evenly spaced steps (Fig. 2B). The population of observed step sizes in the smoothed trajectory events not different from predicted (Wilcoxon rank sum test, $P = 0.385$). (**C**) Across-session average step size as a function of slow-gamma phase (bin size = 10°) for all open field smoothed trajectory events. Red line indicates running box average (box size = 8 bins). No circular correlation observed between smoothed step size and slow-gamma phase (50,000 shuffles of gamma phase, Monte-Carlo P value = 0.632). (**D** to **F**) As in (A) to (C), for linear track sessions. (E) Wilcoxon rank sum test, $P = 0.862$. (F) Monte-Carlo P value = 0.105.

more smooth than actual trajectory events (fig. S21C). Thus, the observation of slow-gamma–locked, discontinuous movement was not a trivial result of our decoding methodology, spike-phase locking, phase-dependent oscillations in population-level firing rate, place-cell sampling, or place-field coverage.

Prior work has demonstrated that slow-gamma power and synchrony across hippocampal areas CA3 and CA1 are transiently increased during both SWRs and memory-dependent tasks (*13*–*15*), indicating that these oscillations play a prominent role in memory consolidation and recall processes. Although CA1 recordings cannot conclusively demonstrate the source of observed slow-gamma rhythm (*16*), it is thought to originate in CA3 (*11*, *12*), a region with a large number of recurrent excitatory connections (*17*). Several studies are consistent with the notion that this recurrence supports an autoassociative network involved in the mnemonic process of pattern completion (*18*, *19*). It is recognized that unbounded attractor dynamics in such a network can lead to runaway excitatory activity (*20*). Our data suggest a solution to this problem, in which attractor strength oscillates at the slow-gamma frequency between high levels of activity [focusing neural representation on a "unit" of information (*21*), such as a single location in space] and low levels of activity (weakening the attractor dynamics to allow transition to a different unit). Our data support the generalization to the SWR state of a model of sequence generation during hippocampal theta, in which a heteroassociative network is identified with connectivity between dentate gyrus and CA3, and an autoassociative network with recurrent synapses within CA3 (*22*). Our data further suggest that these processes alternate in time during trajectory-depicting SWR events and that slow-gamma oscillations may govern switching between them. In this way, slow-gamma rhythm may correspond to the passage of information around a multiregional hippocampal loop.

More broadly, our findings of temporal segmentation of information on the scale of the gamma oscillation have implications for memory and information-processing mechanisms in other brain regions. Gamma-frequency rhythms are observed throughout the brain (*23*), and alterations in gamma oscillations have been linked with several human neuropathies (*24*). Our data are consistent with a growing body of literature implicating gamma oscillations in general memory functions (*14*, *25*–*28*). Furthermore, like hippocampal area CA3, many cortical brain regions contain extensive recurrent excitatory connections (*29*). Rhythmic oscillations are believed to mediate communication and information processing between brain regions by synchronizing local circuitry with remote inputs (*30*); our data point to an additional role in allowing neuronal architectures to focus representation while avoiding excess positive feedback.

REFERENCES AND NOTES

1. J. J. Hopfield, *Proc. Natl. Acad. Sci. U.S.A.* **79**, 2554–2558 (1982).
2. D. Kleinfeld, *Proc. Natl. Acad. Sci. U.S.A.* **83**, 9469–9473 (1986).
3. H. Sompolinsky, I. Kanter, *Phys. Rev. Lett.* **57**, 2861–2864 (1986).
4. J. O'Neill, T. J. Senior, K. Allen, J. R. Huxter, J. Csicsvari, *Nat. Neurosci.* **11**, 209–215 (2008).
5. T. J. Davidson, F. Kloosterman, M. A. Wilson, *Neuron* **63**, 497–507 (2009).
6. S. P. Jadhav, C. Kemere, P. W. German, L. M. Frank, *Science* **336**, 1454–1458 (2012).
7. G. Buzsáki, *Brain Res.* **398**, 242–252 (1986).
8. M. P. Karlsson, L. M. Frank, *Nat. Neurosci.* **12**, 913–918 (2009).
9. A. S. Gupta, M. A. A. van der Meer, D. S. Touretzky, A. D. Redish, *Neuron* **65**, 695–705 (2010).
10. B. E. Pfeiffer, D. J. Foster, *Nature* **497**, 74–79 (2013).
11. J. Csicsvari, B. Jamieson, K. D. Wise, G. Buzsaki, *Neuron* **37**, 311–322 (2003).
12. L. L. Colgin *et al.*, *Nature* **462**, 353–357 (2009).
13. M. F. Carr, M. P. Karlsson, L. M. Frank, *Neuron* **75**, 700–713 (2012).
14. S. M. Montgomery, G. Buzsáki, *Proc. Natl. Acad. Sci. U.S.A.* **104**, 14495–14500 (2007).
15. A. Johnson, A. D. Redish, *J. Neurosci.* **27**, 12176–12189 (2007).
16. G. Buzsáki, E. W. Schomburg, *Nat. Neurosci.* **18**, 484–489 (2015).
17. X.-G. Li, P. Somogyi, A. Ylinen, G. Buzsáki, *J. Comp. Neurol.* **339**, 181–208 (1994).
18. K. Nakazawa *et al.*, *Neuron* **38**, 305–315 (2003).
19. A. E. Gold, R. P. Kesner, *Hippocampus* **15**, 808–814 (2005).
20. M. E. Hasselmo, E. Schnell, E. Barkai, *J. Neurosci.* **15**, 5249–5262 (1995).
21. J. E. Lisman, M. A. Idiart, *Science* **267**, 1512–1515 (1995).
22. J. E. Lisman, L. M. Talamini, A. Raffone, *Neural Netw.* **18**, 1191–1201 (2005).
23. P. Fries, *Annu. Rev. Neurosci.* **32**, 209–224 (2009).
24. P. J. Uhlhaas, W. Singer, *Neuron* **52**, 155–168 (2006).
25. K. W. Bieri, K. N. Bobbitt, L. L. Colgin, *Neuron* **82**, 670–681 (2014).
26. K. M. Igarashi, L. Lu, L. L. Colgin, M.-B. Moser, E. I. Moser, *Nature* **510**, 143–147 (2014).
27. R. T. Canolty *et al.*, *Science* **313**, 1626–1628 (2006).
28. P. R. Shirvalkar, P. R. Rapp, M. L. Shapiro, *Proc. Natl. Acad. Sci. U.S.A.* **107**, 7054–7059 (2010).
29. R. J. Douglas, K. A. Martin, *Annu. Rev. Neurosci.* **27**, 419–451 (2004).
30. J. Lisman, *Hippocampus* **15**, 913–922 (2005).

ACKNOWLEDGMENTS

We thank K. Zhang for discussion. This work was supported by the National Institute for Mental Health (D.J.F.). The data described in this manuscript are stored in the laboratory of D.J.F. in the Department of Neuroscience, Johns Hopkins University.

SUPPLEMENTARY MATERIALS

www.sciencemag.org/content/349/6244/180/suppl/DC1
Materials and Methods
Figs. S1 to S22

20 February 2015; accepted 21 May 2015
10.1126/science.aaa9633

NEURONAL MODELING

Single-trial spike trains in parietal cortex reveal discrete steps during decision-making

Kenneth W. Latimer,[1,2] Jacob L. Yates,[1,2] Miriam L. R. Meister,[2,3] Alexander C. Huk,[1,2,4,5] Jonathan W. Pillow[1,2,5,6]*

Neurons in the macaque lateral intraparietal (LIP) area exhibit firing rates that appear to ramp upward or downward during decision-making. These ramps are commonly assumed to reflect the gradual accumulation of evidence toward a decision threshold. However, the ramping in trial-averaged responses could instead arise from instantaneous jumps at different times on different trials. We examined single-trial responses in LIP using statistical methods for fitting and comparing latent dynamical spike-train models. We compared models with latent spike rates governed by either continuous diffusion-to-bound dynamics or discrete "stepping" dynamics. Roughly three-quarters of the choice-selective neurons we recorded were better described by the stepping model. Moreover, the inferred steps carried more information about the animal's choice than spike counts.

Ramping responses have been observed in a variety of brain areas during decision-making and have been widely interpreted as the neural implementation of evidence accumulation for forming decisions (*1*–*7*). However, ramping can only be observed by averaging together responses from many trials (and, often, many neurons), which obscures the dynamics governing responses on single trials. In particular, a discrete "stepping" process (*8*, *9*), in which the spike rate jumps stochastically from one rate to another at some time during each trial, can also create the appearance of ramping (*10*, *11*). Although decision-making at the behavioral level is well described as an accumulation process (*12*, *13*), whether the brain computes decisions through a direct neural correlate (ramping) or a discrete implementation (stepping) remains a central, unresolved question in systems neuroscience.

We used advanced statistical methods to identify the single-trial dynamics governing spike trains in the lateral intraparietal (LIP) area of macaques performing a well-studied motion-discrimination task (Fig. 1A) (*3*, *14*). We formulated two spike-train models with stochastic latent dynamics governing the spike rate: one defined by continuous ramping dynamics and the other by discrete stepping dynamics (see the supplementary methods for mathematical details). In the ramping model, also known as "diffusion-to-bound," the spike rate evolves according to a Gaussian random walk with linear drift (Fig. 1B). The slope of drift depends on the strength of sensory evidence, and each trial's trajectory continues until hitting an absorbing upper bound. Alternatively, in the stepping model, the latent spike rate jumps instantaneously from an initial "undecided" state to one of two discrete decision states during the trial (Fig. 1C). The probability of stepping up or stepping down and the timing of the step are determined by the strength of sensory evidence. For both models, we assumed that spiking follows an inhomogeneous Poisson process given the time-varying spike rate.

Both latent variable models are "doubly stochastic" in the sense that the probability of an observed spike train given the sensory stimulus depends on both the noisy trajectory of the latent spike rate and the Poisson variability in the spiking process. Fitting such latent variable models requires integrating over all latent trajectories consistent with the observed spike trains, which is not analytically tractable. We therefore

[1]Center for Perceptual Systems, The University of Texas at Austin, Austin, TX 78712, USA. [2]Institute for Neuroscience, The University of Texas at Austin, Austin, TX 78712, USA. [3]Department of Physiology and Biophysics, University of Washington, Seattle, WA 98195, USA. [4]Department of Neuroscience, The University of Texas at Austin, Austin, TX 78712, USA. [5]Department of Psychology, The University of Texas at Austin, Austin, TX 78712, USA. [6]Princeton Neuroscience Institute and Department of Psychology, Princeton University, Princeton, NJ 08544, USA.
*Corresponding author. E-mail: pillow@princeton.edu

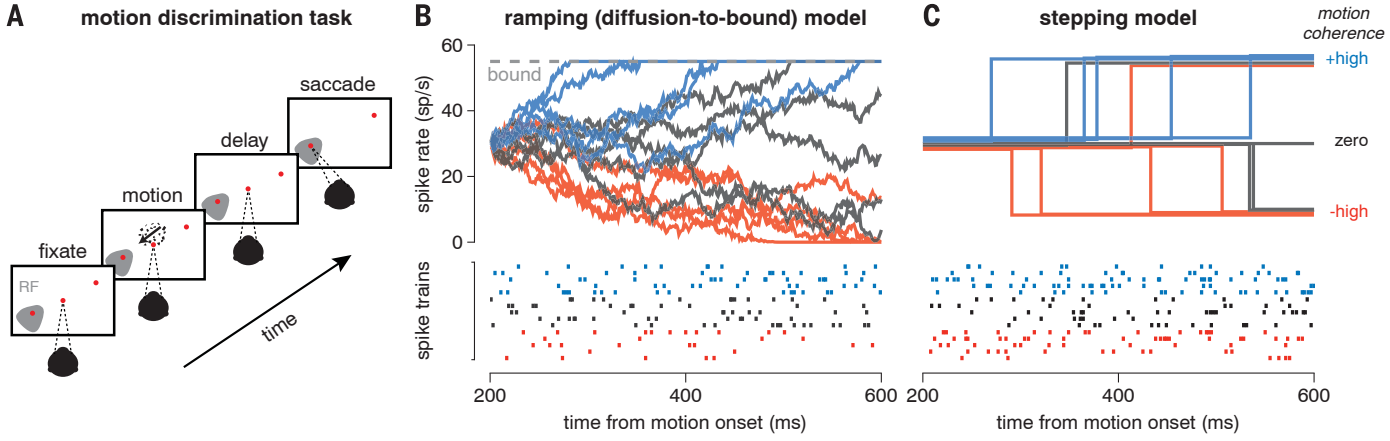


Fig. 1. Motion discrimination task and spike-train models. (**A**) Schematic of moving-dot direction-discrimination task. The monkey views and discriminates the net direction of a motion stimulus of variable motion strength and duration and indicates its choice by making a saccade to one of two choice targets 500 ms after motion offset. One choice target is in the response field of the neuron under study (RF, shaded patch on left); the other is outside it. (**B**) Ramping (diffusion-to-bound) model. Spike rate trajectories (solid traces) were sampled from a diffusion-to-bound process for each of three motion coherences (strong positive, zero, and strong negative). The model parameters include an initial spike rate, a slope for each coherence, noise variance, and an upper bound. We do not include a lower bound, consistent with the competing integrator (race) model of LIP (*5*). Spike trains (below) obey an inhomogeneous Poisson process for each spike rate trajectory. (**C**) Discrete stepping model. Spike rate trajectories (above) begin at an initial rate and jump up or down at a random time during each trial, and spike trains (below) once again follow a Poisson process, given the latent rate. The step times take a negative binomial distribution, which resembles the time-to-bound distribution under a diffusion model. Parameters include the spike rates for the three discrete states and two parameters governing the distribution over step timing and direction for each motion coherence. Both models were fit using the spike trains and coherences for each neuron, without access to the animal's choices.

Downloaded from www.sciencemag.org on July 10, 2015

developed sampling-based Markov chain Monte Carlo methods, which provide samples from the posterior distribution over model parameters and allow us to perform Bayesian model comparison.

We focused on a population of 40 neurons with highly choice-selective responses that exhibited ramping in their average responses (*14*), typically increasing during trials in which the monkey eventually chose the target inside the response field (RF) of the neuron and decreasing when the monkey chose the target outside the RF. We fit each neuron with both ramping and stepping models, using the spike-train data from 200 ms after motion onset (*15*) until 200 ms after motion offset (300 ms before the monkey received the "go" signal). Figure 2A shows the raster of spike trains from an example LIP neuron plotted in two different ways: first, aligned to the time of motion stimulus onset (left); and second, aligned to the step time inferred under the stepping model (right). The traditional raster and peristimulus time histogram (PSTH) at left show that the average response ramps upward or downward depending on choice, as expected. The step-aligned raster at right, however, shows that these data are also consistent with discrete steplike transitions with variable timing across trials. Additional panels show the distribution of step times inferred under the model (Fig. 2B), and the dependence of step direction (up or down) on the motion signal (Fig. 2C). Discrete steps in the instantaneous spike rate could thus plausibly underlie the gradual ramping activity seen in stimulus-aligned and averaged LIP spike responses.

We applied the same analysis to the full set of LIP neurons and observed similar structure in step-aligned rasters (figs. S13 to S15). Figure 3A shows population-averaged PSTHs computed from stimulus-aligned (left) and step-aligned responses, sorted by motion strength (middle), or motion strength and step direction (right). The middle and right plots show that spike rate is effectively constant when spike trains are aligned to the inferred step time on each trial. The multiple step heights observed in the middle plot result from the fact that the proportion of up and down steps varies with motion strength. The right plot confirms that the firing rate, once conditioned on stepping up or down, is

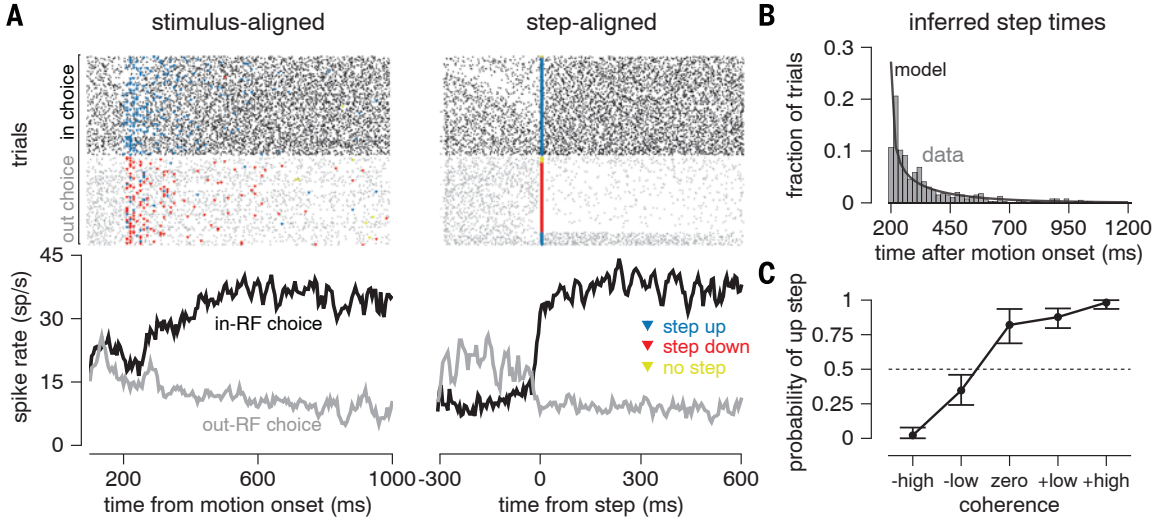


Fig. 2. Model-based analysis of spike responses from an example LIP neuron. (**A**) Spike rasters sorted by the monkey's choice in or out of the RF of the neuron under study (black, in-RF; gray, out-RF) and their associated averages (PSTHs, below). (Left) Conventional stimulus-aligned rasters with each trial aligned to the time of motion onset exhibit commonly observed ramping in the PSTH. Blue and red triangles indicate the inferred time of an up or down step on each trial under the fitted stepping model. Yellow triangles indicate that no step was found during the trial and are placed at the end of the trial segment we analyzed (200 ms after motion offset). (Right) The same spike trains aligned to the inferred step time for each trial. The estimated step direction of the neuron does not always match the animal's decision on each trial. (**B**) The distribution of inferred step times shown in (A) (histogram) and the distribution over step times under the fitted parameters (black trace). (**C**) The probability of an up step for each coherence level. Error bars, 95% CIs.

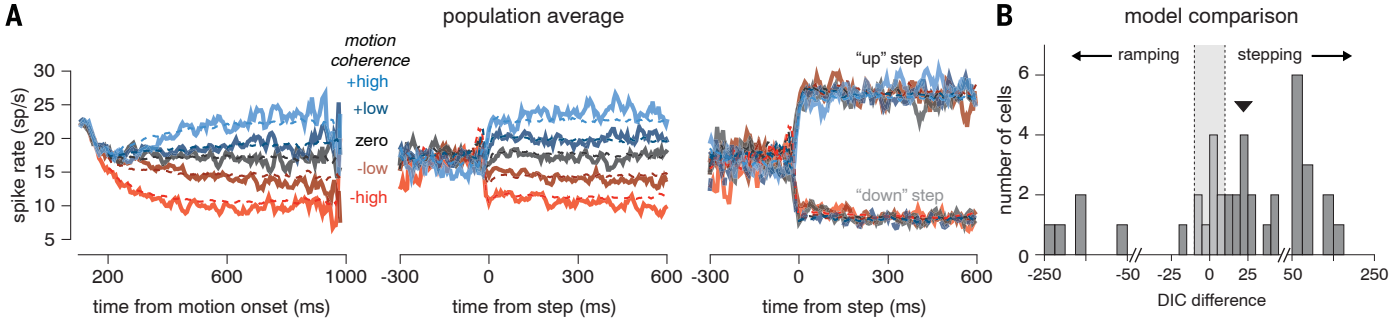


Fig. 3. Stepping model captures LIP responses. (**A**) Population average PSTH sorted by motion coherence computed from spike trains: (Left) Aligned to motion onset and sorted by motion strength. (Middle) Aligned to step times inferred under the stepping model and sorted by motion strength. (Right) Aligned to step times and sorted by both motion strength and inferred step direction. Simulated results from the stepping model (dashed lines) provide a close match to the real data under all types of alignment and conditioning. (**B**) Quantitative model comparison using DIC reveals a superior fit of the stepping model over the ramping model for the majority of cells (31 out of 40). A DIC difference greater than ±10 (gray region) is commonly regarded as providing strong support for one model over the other (*22*). We found substantially more cells with strong evidence for stepping over ramping (25 cells versus 6 cells; median DIC difference = 22.1; sign test $P < 0.001$).

independent of motion strength. Furthermore, simulated spike responses, based on the fitted stepping models, resemble the real data under both kinds of alignment (dashed traces).

Although these analyses provide a visually compelling illustration of the plausibility of stepping dynamics in LIP, they do not by themselves definitively rule out the ramping model (see fig. S16). Using our latent variable models, we can formally address this issue using statistical model comparison. Both models give a probability distribution over spike trains, and the model that better represents the data should place more probability mass over the observed spike trains. We compared the model fits using the deviance information criterion (DIC) (*16*), which integrates over the entire posterior distribution of model parameters given the data, thereby taking into account the uncertainty in the model fit as well as the number of parameters in each model.

The stepping model provided a superior account of LIP responses for 78% (31 out of 40) of the cells compared to the ramping model (Fig. 3B). The stepping model therefore not only accounts for the ramplike activity observed in averaged LIP responses, but its qualitative ability to reveal step times is bolstered by quantitative superiority in accounting for the statistical structure of spike trains for a majority of LIP neurons. The superiority was supported not just by DIC but also by other model comparison metrics, such as Bayes factors (fig. S1).

We subsequently examined how well the two models account for the time-varying mean and the variance of neural responses. Figure 4A shows the comparison for the mean responses (top row) and variance (bottom row) for the data (left column), stepping model (middle column), and ramping model (right column). Although the models were fit to predict the spike responses on each trial, as opposed to these summary statistics, both models did an acceptable job of accounting for the mean response [fraction of variance in the PSTHs explained: stepping R^2 = 0.94, 95% credible interval (CI) (0.90, 0.94); ramping R^2 = 0.78, 95% CI (0.71, 0.79)]. This is consistent with the long-standing difficulty in distinguishing between these two mechanisms. However, the stepping model provided a more accurate fit to the variance of neural responses [stepping R^2 = 0.40, 95% CI (0.09, 0.45); ramping R^2 = −0.49, 95% CI (−0.86, −0.27)]. In particular, the stepping model captured the decreasing variance observed in trials with strong negative motion much better than the ramping model. (A similar result held for estimates of variance of the underlying spike rate; see fig. S21).

Finally, the stepping model provides a platform for neural decoding, because the posterior distribution over the step can be used for reading out decisions from the spikes on a single trial. We first quantified decoding performance using choice probability (CP), a popular metric for quantifying the relationship between choice and spike counts. Aligned to motion onset, CP grows roughly linearly with time (Fig. 4B, left). However, the CP relative to the inferred step times (Fig. 4B, right) was consistent with an abrupt emergence of choice-related activity. We then compared classical CP with a model-based CP measure, which assumed that the direction of the neuron's step predicted the animal's choice. We reiterate that the model was fit to the spike trains without access to the animal's choices. The model-based CP was on average greater than classical CP, indicating that the states estimated under the stepping model were more informative about the animal's choice than raw spike counts (Fig. 4C).

In conclusion, we have developed tractable, principled methods for fitting and comparing statistical models of single-neuron spike trains in which spike rates are governed by a latent stochastic process. We have applied these methods to determine the dynamics underlying neural activity in area LIP. Although neurons in this area have been largely assumed to exhibit ramping dynamics, reflecting the temporal accumulation of evidence posited by models of decision-making, statistical model comparison supports an alternative hypothesis: LIP responses were better described by randomly timed, discrete steps between underlying states. [In a supplementary analysis, we examined data from a response-time version of the dots task and found results consistent with the fixed duration version; this initial comparison will be strengthened by extending the models to account for overlapping decision and motor events and application to larger data sets (figs. S23 to S25) (*17*)]. In addition to accounting better for the dynamics of the mean firing rates, only the stepping model accounts accurately for

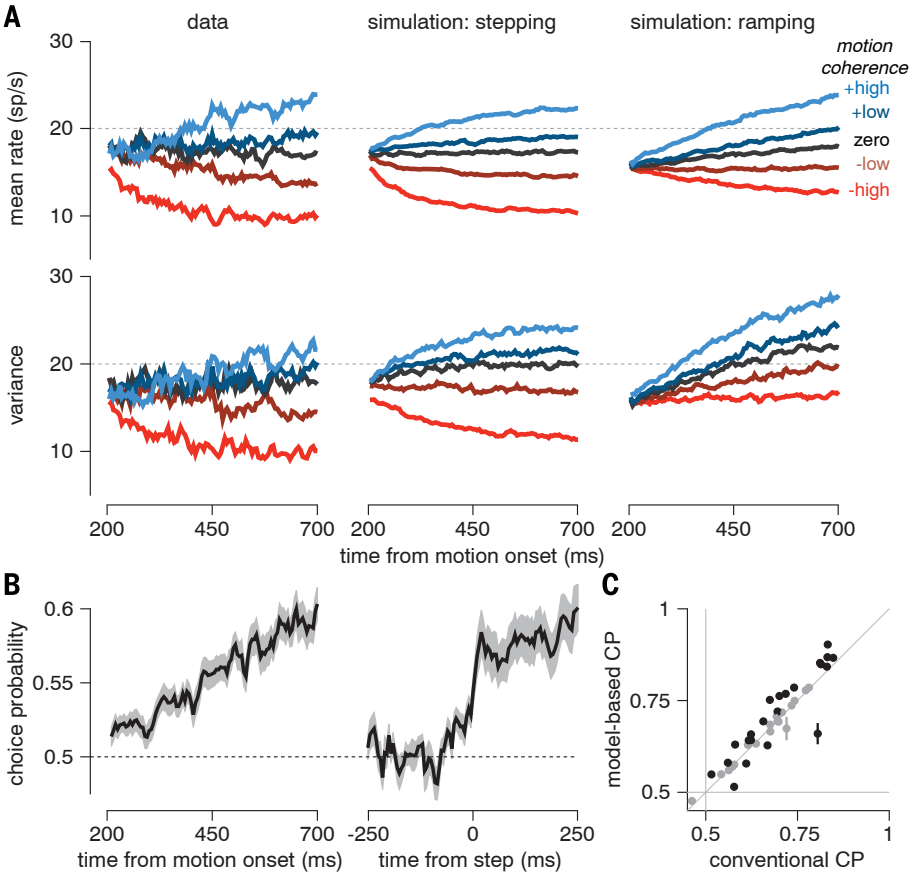


Fig. 4. Stepping model better explains variance of responses and can be used to decode choices. (**A**) Comparison of model fits to average population activity, sorted by stimulus strength. Motion coherence and direction are indicated by color (blue, in-RF; red, out-RF). Average spike rate (top) and spike count variance (bottom) for the population aligned to motion onset. The data (left) and simulations from the stepping model (center) and the diffusion-to-bound model (right) fits to all 40 cells are shown. Spike rates and variances were calculated with a 25-ms sliding window. (**B**) Population average CP aligned to stimulus onset (left) and average CP aligned to estimated step times (right). Gray region indicates mean ± 1 SEM. CPs were calculated with a sliding 25-ms window. Conventional alignment suggests a ramp in choice selectivity, and the model-based alignment indicates a rapid transition. (**C**) Conventional CP based on spike counts using responses 200 to 700 ms after motion onset versus model-based CP using the probability of stepping to the up state by the end of the same period. Model-based CP is greater than conventional CP in the population (Wilcoxon signed rank test; $P < 0.05$). Stepping models were fit using 10-fold cross-validation. Error bars show mean ± 1 SE of CPs, as computed on each training data set. Black points indicate cells with significant differences between model-based and conventional CP (Student's *t* test; $P < 0.05$), and gray indicates that differences were not significant.

the variance of neural responses. Finally, the estimation of single-trial step times provides a novel view of choice-related activity, revealing that choice-correlated fluctuations in response are also dominated by discrete steplike dynamics.

Although these results challenge the canonical perspective of LIP dynamics during decision-making, the approach facilitates new avenues of investigation. Our analyses suggest that accumulation may be implemented by stochastic steps, but simultaneous recordings of multiple neurons will be required to investigate whether population activity ramps or discretely transitions between states on single trials (*8*); population-level ramping could still be implemented via step times that vary across neurons, even on the same trial. Fortunately, the statistical techniques reported here are scalable to simultaneously recorded samples of multiple neurons, and newer recording techniques are starting to yield these multineuron data sets (*18*–*21*). It is also possible that single neurons with ramping dynamics implement evidence integration elsewhere in the brain and that LIP neurons are postdecisional or premotor indicators of the binary result of this computation. More generally, we believe that these techniques will have broad applicability for identifying and interpreting the latent factors governing multineuron spike responses, allowing for principled tests of the dynamics governing cognitive computations in many brain areas.

REFERENCES AND NOTES

1. M. E. Mazurek, J. D. Roitman, J. Ditterich, M. N. Shadlen, *Cereb. Cortex* **13**, 1257–1269 (2003).
2. J. I. Gold, M. N. Shadlen, *Annu. Rev. Neurosci.* **30**, 535–574 (2007).
3. R. Kiani, T. D. Hanks, M. N. Shadlen, *J. Neurosci.* **28**, 3017–3029 (2008).
4. R. Kiani, M. N. Shadlen, *Science* **324**, 759–764 (2009).
5. M. N. Shadlen, R. Kiani, *Neuron* **80**, 791–806 (2013).
6. M. N. Shadlen, W. T. Newsome, *Proc. Natl. Acad. of Sci.* **93**, 628–633 (1996).
7. T. D. Hanks *et al*., *Nature* **520**, 220–223 (2015).
8. P. Miller, D. B. Katz, *J. Neurosci.* **30**, 2559–2570 (2010).
9. D. Durstewitz, G. Deco, *Eur. J. Neurosci.* **27**, 217–227 (2008).
10. M. S. Goldman, *Encyclopedia of Computational Neuroscience*, D. Jaeger, R. Jung, Eds. (Springer, New York, 2015), pp. 1177–1182.
11. A. K. Churchland *et al*., *Neuron* **69**, 818–831 (2011).
12. R. Ratcliff, J. N. Rouder, *Psychol. Sci.* **9**, 347–356 (1998).
13. B. W. Brunton, M. M. Botvinick, C. D. Brody, *Science* **340**, 95–98 (2013).
14. M. L. R. Meister, J. A. Hennig, A. C. Huk, *J. Neurosci.* **33**, 2254–2267 (2013).
15. A. K. Churchland, R. Kiani, M. N. Shadlen, *Nat. Neurosci.* **11**, 693–702 (2008).
16. D. J. Spiegelhalter, N. G. Best, B. P. Carlin, A. van der Linde, *J. R. Stat. Soc. Series B Stat. Methodol.* **64**, 583–639 (2002).
17. J. D. Roitman, M. N. Shadlen, *J. Neurosci.* **22**, 9475–9489 (2002).
18. I. H. Stevenson, K. P. Kording, *Nat. Neurosci.* **14**, 139–142 (2011).
19. A. Bollimunta, D. Totten, J. Ditterich, *J. Neurosci.* **32**, 12684–12701 (2012).
20. R. Kiani, C. J. Cueva, J. B. Reppas, W. T. Newsome, *Curr. Biol.* **24**, 1542–1547 (2014).
21. M. T. Kaufman, M. M. Churchland, S. I. Ryu, K. V. Shenoy, *eLife* **4**, e04677 (2015).
22. K. P. Burnham, D. R. Anderson, *Model Selection and Multimodel Inference: A Practical Information-Theoretic Approach* (Springer Science & Business Media, New York, 2002).

ACKNOWLEDGMENTS

We thank I. Memming Park and C. Carvalho for constructive discussions and J. Roitman and M. Shadlen for public sharing of data. This research was supported by grants from the National Eye Institute (EY017366 to A.C.H.) and the National Institute of Mental Health (MH099611 to J.W.P. and A.C.H.), by the Sloan Foundation (J.W.P.), McKnight Foundation (J.W.P.), a National Science Foundation CAREER award (IIS-1150186 to J.W.P.), and the National Institutes of Health under Ruth L. Kirschstein National Research Service Awards T32DA018926 from the National Institute on Drug Abuse and T32EY021462 from the National Eye Institute. All behavioral and electrophysiological data are presented in (*14*) and are archived at the Center for Perceptual Systems, The University of Texas at Austin.

SUPPLEMENTARY MATERIALS

www.sciencemag.org/content/349/6244/184/suppl/DC1
Materials and Methods
Supplementary Text
Figs. S1 to S25
Tables S1 and S2
References (*23*–*33*)

1 December 2014; accepted 10 June 2015
10.1126/science.aaa4056

PROTEIN STRUCTURE

Crystal structure of a mycobacterial Insig homolog provides insight into how these sensors monitor sterol levels

Ruobing Ren,[1,2,3]* Xinhui Zhou,[1,2,3]* Yuan He,[1,2,3] Meng Ke,[1,2,3] Jianping Wu,[1,2,3] Xiaohui Liu,[4] Chuangye Yan,[1,2,3] Yixuan Wu,[1,2,3] Xin Gong,[1,2,3] Xiaoguang Lei,[4] S. Frank Yan,[5] Arun Radhakrishnan,[6] Nieng Yan[1,2,3]†

Insulin-induced gene 1 (Insig-1) and Insig-2 are endoplasmic reticulum membrane–embedded sterol sensors that regulate the cellular accumulation of sterols. Despite their physiological importance, the structural information on Insigs remains limited. Here we report the high-resolution structures of MvINS, an Insig homolog from *Mycobacterium vanbaalenii*. MvINS exists as a homotrimer. Each protomer comprises six transmembrane segments (TMs), with TM3 and TM4 contributing to homotrimerization. The six TMs enclose a V-shaped cavity that can accommodate a diacylglycerol molecule. A homology-based structural model of human Insig-2, together with biochemical characterizations, suggest that the central cavity of Insig-2 accommodates 25-hydroxycholesterol, whereas TM3 and TM4 engage in Scap binding. These analyses provide an important framework for further functional and mechanistic understanding of Insig proteins and the sterol regulatory element–binding protein pathway.

Cholesterol homeostasis is essential for human physiology. Aberrant accumulation of sterols contributes to the initiation and progression of atherosclerosis that can lead to heart attack and stroke (*1*). Cellular sterol levels are monitored by several membrane-embedded proteins, including insulin-induced gene 1 (Insig-1) and Insig-2, which are essential components of the sterol regulatory element–binding protein (SREBP) pathway that controls cellular lipid homeostasis through a feedback inhibition mechanism (*2*–*5*).

SREBPs are a family of membrane-anchored transcription factors that activate genes encoding low-density lipoprotein receptor and enzymes for sterol synthesis (*6*–*8*). SREBP forms a stable complex with SREBP cleavage-activating protein (Scap) through their respective C domains (*9*–*13*). The complex is anchored on the endoplasmic reticulum (ER) through interactions between the membranous domain of Scap and Insig-1/-2 in a sterol-dependent manner (*14*, *15*). Upon cholesterol deprivation, Scap dissociates from Insig-1/-2 and associates with COPII, which translocates the SREBP-Scap complex from the ER to the Golgi (*16*, *17*). In the lumen of the Golgi, SREBP is cleaved by the membrane-anchored site-1 protease (S1P) and then by the intramembrane site-2 protease (S2P) (*18*, *19*), allowing its soluble N-terminal transcription factor domain to enter the nucleus for gene activation (*20*–*23*).

Insig-1/-2 negatively regulate the cellular accumulation of sterols, mainly through two distinct mechanisms. First, upon binding to 25-hydroxycholesterol (25HC), Insig-1/-2 inhibit the exit of the SREBP-Scap complex from the ER, hence preventing transcriptional activation of genes for cholesterol synthesis and uptake (*24*). Second, during sterol repletion, Insig-1 recruits the protein degradation machinery to quickly

[1]State Key Laboratory of Membrane Biology, Tsinghua University, Beijing 100084, China. [2]Center for Structural Biology, School of Life Sciences, School of Medicine, Tsinghua University, Beijing 100084, China. [3]Tsinghua-Peking Center for Life Sciences, Tsinghua University, Beijing 100084, China. [4]National Institute of Biological Sciences, Beijing 102206, China. [5]Molecular Design and Chemical Biology, Therapeutic Modalities, Roche Pharma Research and Early Development, Roche Innovation Center Shanghai, Shanghai 201203, China. [6]Department of Molecular Genetics, University of Texas Southwestern Medical Center, Dallas, TX 75390-9046, USA.
*These authors contributed equally to this work. **†Corresponding author. E-mail: nyan@tsinghua.edu.cn**

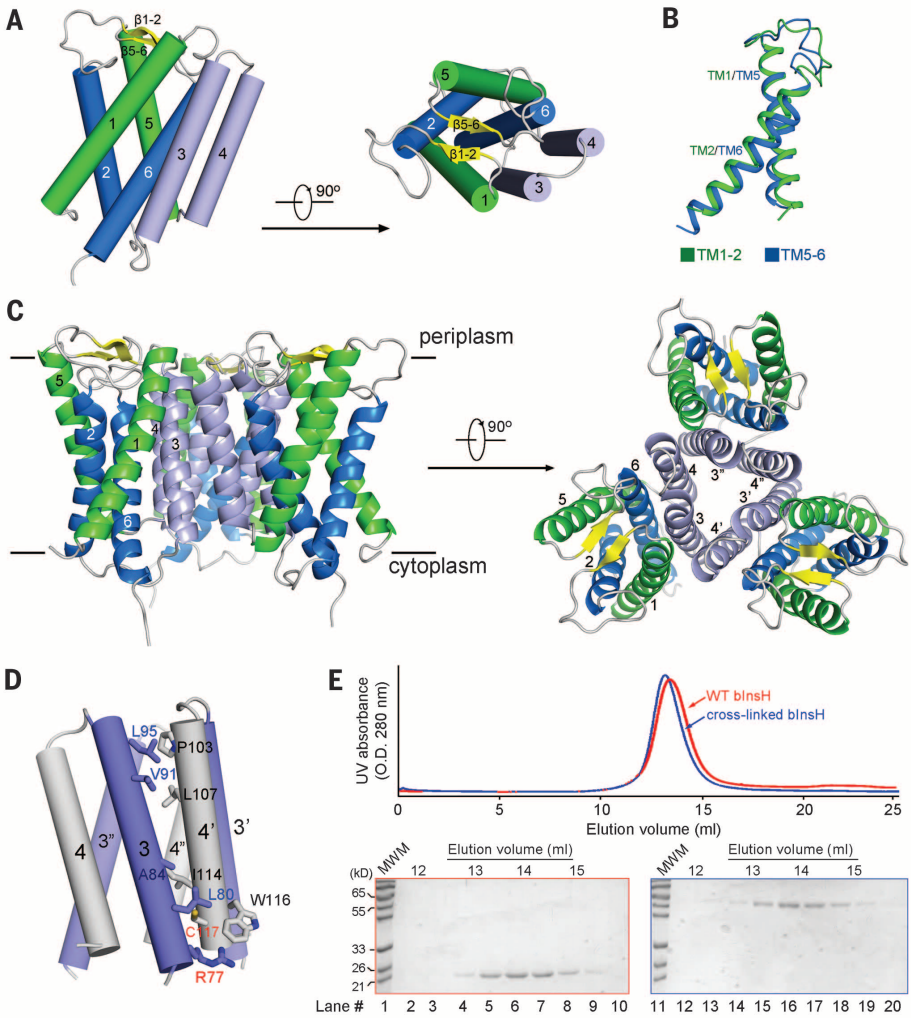


Fig. 1. The crystal structure of MvINS, a mycobacterial homolog of mammalian Insig proteins. (**A**) The overall structure of an MvINS monomer. Two perpendicular views are shown. It reveals a novel fold that may be shared by all Insig proteins. (**B**) TM1/TM2 can be superimposed to TM5/TM6. (**C**) Three adjacent MvINS molecules form a homotrimer in the crystal. The side and periplasmic views of the overall trimer are shown. (**D**) The trimeric interface is mediated exclusively by hydrophobic residues on TM3 and TM4. Arg77 on TM3 was mutated to Cys for disulfide-bond formation with Cys117 on TM4 from the adjacent protomer. Both residues are labeled red. (**E**) MvINS is a trimer in solution. Wild-type and cross-linked MvINS-R77C were subjected to size exclusion chromatography. The peak fractions were applied to SDS–polyacrylamide gel electrophoresis followed by Coomassie blue staining. All structure figures were prepared with PyMol (*37*).

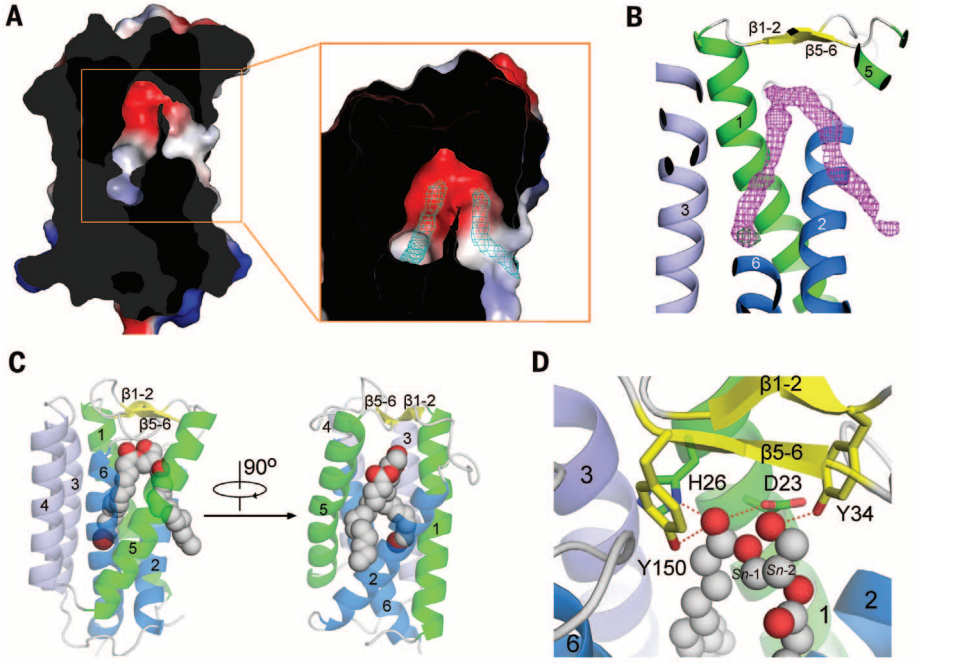


Fig. 2. Each MvINS protomer accommodates one DAG molecule. (**A**) The MvINS protomer encloses a V-shaped cavity. Shown here is a cut-through view of the surface electrostatic potential (calculated in PyMol). The 2Fo-Fc electron density map, contoured at 1σ, is shown as cyan mesh in the inset. (**B**) Electron density for the bound DAG molecule. The 2Fo-Fc electron density for the bromine-derived DAG molecule, shown in magenta mesh, is contoured at 0.8σ. The anomalous signal for Br, shown as green mesh, is contoured at 3.5σ. (**C**) Overall structure of MvINS bound to DAG. The bromine (colored dark red)–derived DAG is shown in gray spheres. (**D**) Coordination of DAG by polar residues in MvINS. The residues that are hydrogen-bonded to DAG are shown in sticks. Hydrogen bonds are represented by red dashed lines.

destruct the rate-limiting 3-hydroxy-3-methylglutaryl-coenzyme A (HMG-CoA) reductase, blocking cholesterol synthesis (*4*, *25*, *26*).

The major players of the SREBP pathway have been identified for over a decade; however, the only structural information on membrane proteins of this pathway came from an archaeal ortholog of S2P (*27*). No bacterial homologs have been identified for SREBP, Scap, or HMG-CoA reductase. Here we report the high-resolution crystal structures of a mycobacterial homolog of Insig proteins. Guided by a homologous structural model of human Insig-2, a number of residues that may contribute to Scap association and 25HC binding were identified and biochemically confirmed.

Using human Insig-1 or -2 as a query, BLAST searches against sequenced bacterial genomes led to the identification of one protein from *Mycobacterium vanbaalenii PYR-1*. This protein, which we named MvINS, shares sequence identities of 23 and 26% with Insig-1 and -2, respectively (fig. S1), and sequence similarity of 40% with both proteins. Using MvINS as a query, six other proteins, all from mycobacteria, were identified (fig. S2A).

Crystals of MvINS in space group *R3* appeared in several conditions under different detergents and diffracted x-rays beyond 2.0 Å resolution. The initial phases were derived from mercury-based single-wavelength anomalous dispersion (Hg-SAD) (fig. S3A). The final atomic model of MvINS was refined to 1.9 Å resolution (Fig. 1A, fig. S3B, and table S1). Consistent with the topological prediction for Insig-1/-2 (*24*, *28*), MvINS comprises six transmembrane segments (TMs), with both the N- and C-termini located on the cytosolic side of the membrane. Given the level of sequence conservation, it is likely that all Insig proteins exhibit the same fold as MvINS.

TM1 and -2, and TM5 and -6, each cross at the middle and are connected by a long segment. The four TMs together form a helical bundle that is tilted counterclockwise (Fig. 1A). The connecting sequences between TM1 and TM2 form a short β strand, which with the corresponding strand β5-6, caps the cavity enclosed by the helical bundle on the periplasmic side. TM1/TM2 and TM5/TM6 display an internal pseudo twofold symmetry around an axis that is perpendicular to the membrane plane and superimpose with root mean square deviation of 1.49 Å over 60 Cα atoms (Fig. 1B and fig. S2B). As found for the corresponding segments in human Insig-2, the N- and C-terminal fragments corresponding to TM1/TM2 and TM5/TM6 share considerable sequence similarity (fig. S2C).

There is one MvINS molecule in each asymmetric unit. Examination of the crystal lattice reveals a homotrimeric assembly involving three neighboring symmetry-related molecules (Fig. 1C and fig. S4A). The trimeric interface is mediated exclusively through van der Waals interactions between TM3 of one protomer and TM4 of the adjacent protomer (Fig. 1C, 1D). To examine whether MvINS indeed exists as a homotrimer in solution, we employed a disulfide bond–mediated cross-linking strategy.

Structural analysis showed that Arg77 on TM3 of one protomer and Cys117 on TM4 of the adjacent protomer are both on the cytoplasmic end of the helix with their Cα atoms 5.7 Å apart, ideal targets for disulfide-bond formation (Fig. 1D). We generated a MvINS variant (MvINS-R77C) with the mutation R77C and two additional cysteines mutated to alanine (C109A/C127A). Upon induction of disulfide-bond formation, MvINS formed a stable homotrimer (fig. S4B). The fully cross-linked MvINS-R77C and wild-type MvINS were eluted at almost identical volumes on size exclusion chromatography (Fig. 1E). Structural characterizations confirmed that MvINS-R77C shows the same trimer conformation as the wild type (fig. S4C and table S2).

Within each MvINS protomer, an extended cavity is formed by TM1/2/5/6 below the periplasmic β strands (Fig. 2A and fig. S5A). Modeling shows that a diacylglycerol (DAG) molecule with two

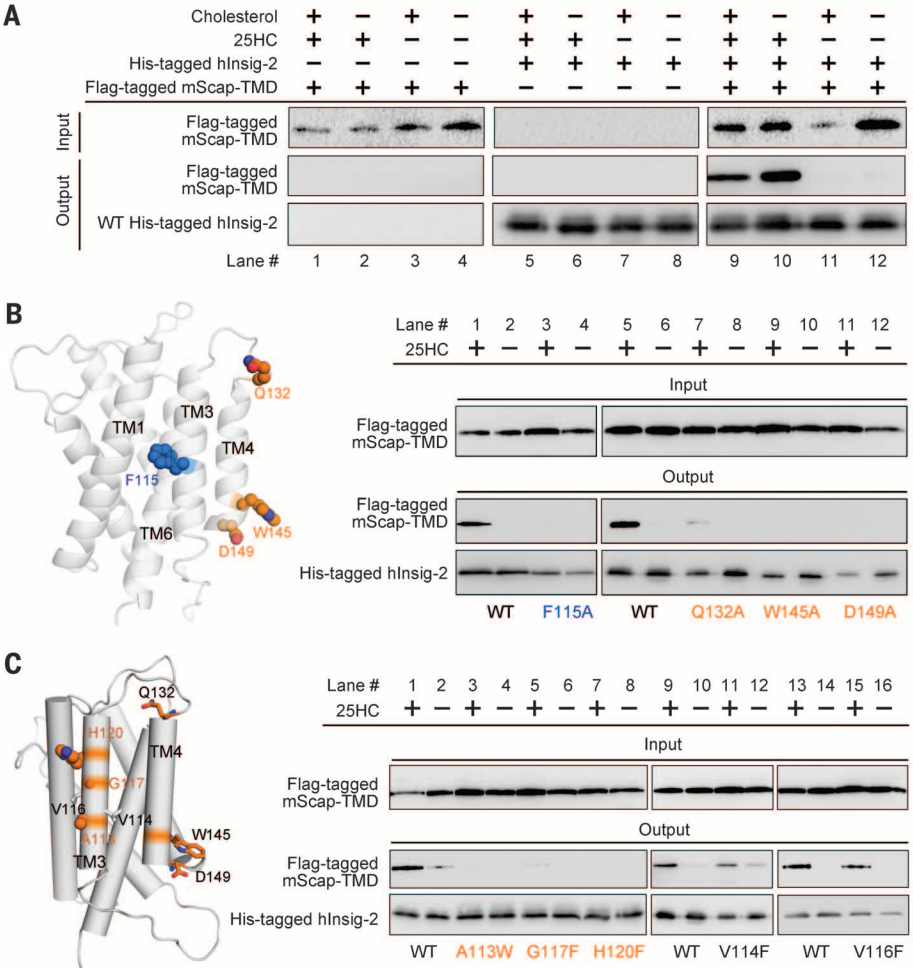


Fig. 3. Structure-guided identification of functional residues in human Insig-2. (**A**) The recombinantly expressed human Insig-2 interacts with the transmembrane domain of mouse Scap (mScap-TMD) in a 25HC-dependent manner. The recombinant proteins of Insig-2 and mScap-TMD were overexpressed in baculovirus-infected Sf-9 cells. (**B**) Examination of the previously identified functional residues using the insect cell assay system. Consistent with the previous report (*24*), single point mutations F115A, Q132Q, W145A, and D149A led to loss of Scap binding even in the presence of 25HC. (**C**) Identification of additional Insig-2 residues that are involved in the 25HC-dependent Scap binding. The three residues Ala113/Gly117/His120 are outward-facing residues on TM3. Single point mutations of these residues led to diminished Scap binding even in the presence of 25HC. In contrast, substitution of Val114 and Val116 with Phe retained complex formation with Scap. Shown here are representative results of at least three repeating experiments.

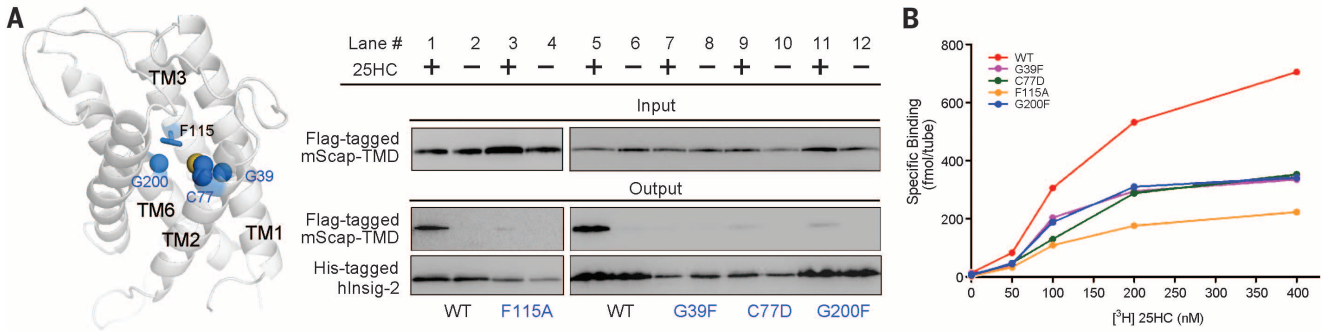


Fig. 4. Identification of residues involved in 25HC binding based on the homologous model of Insig-2. (**A**) Identification of Insig-2 pocket residues that may contribute to 25HC binding. The pocket residues that are in the vicinity of Phe115 were analyzed. Single point mutations G39F, C77D, or G200F resulted in compromised mScap-TMD binding in the presence of 25HC. These three residues and Phe115 are positioned at a similar height within the central pocket of the structural model of Insig-2. (**B**) The measurement of direct binding between [^{3}H]25HC and indicated Insig-2 variants. The experiments were performed following the identical protocol as reported previously (*24*). The data points represent the average of duplicate assays.

14-carbon aliphatic tails can be fitted into the V-shaped cavity. In the structure of MvINS extracted with *n*-dodecyl-*N*,*N*-dimethylamine-*N*-oxide (LDAO), two elongated strips of electron density filling two arms of the V-shaped cavity became clearly visible after most amino acids were modeled (Fig. 2A, inset). These densities probably represent aliphatic lipid or detergent molecules and occupy the DAG-binding site in the course of MvINS overexpression and/or purification.

To investigate whether MvINS can accommodate a DAG molecule, we synthesized a bromine-derived DAG, where the end methyl group of the *Sn*-1 fatty acyl chain is substituted by a bromine (Br) atom, and co-crystallized it with MvINS purified in Cymal-7. The structure was determined at 2.1 Å resolution (table S2). The V-shaped electron density, together with the Br anomalous signal, unambiguously confirmed the presence of DAG in the cavity (Fig. 2B).

The head group and the *Sn*-1 tail are coordinated by residues from TM1/2/3/6 and the periplasmic β strands, whereas the *Sn*-2 tail extends into the lipid bilayer through the cleft between TM2 and TM5 (Fig. 2C). The polar head of the DAG molecule is coordinated through hydrogen bonds by four residues close to the periplasmic side: Asp23 and His26 on TM1, Tyr34 on β1-2, and Tyr150 on β5-6 (Fig. 2D and fig. S2A). The completely buried *Sn*-1 aliphatic tail is surrounded by hydrophobic residues mainly from TM6 and, to a lesser extent, from TM1/2/3 (fig. S5B). The partially bound *Sn*-2 aliphatic chain, on the other hand, is loosely coordinated by a few amino acids, mainly from TM2/5 (fig. S5C).

On the basis of MvINS structure and the sequence similarity between MvINS and human Insig proteins (fig. S1), we generated a three-dimensional structural model for the transmembrane domain of Insig-1/-2 using the program MOE (*29*). As human Insig-1 and Insig-2 share 85% sequence identity at the transmembrane region, we focus here on the structural model of Insig-2 (fig. S6, A and B). The boundaries of the TMs are largely consistent with the prediction derived from biochemical analysis (*24*, *28*), with some minor shifts. One notable difference concerns the beginning of TM2. In the homologous Insig-2 model, TM2 begins at Ser69, which adds seven extra amino acids to the extended linker sequence preceding TM2, as compared to the previous prediction (*24*) (fig. S6A). TM1/2/3/5/6 exhibit approximately 30% identity and 50% similarity between MvINS and Insig-2 (fig. S1). The degree of sequence similarity is probably sufficient for structural modeling of invariant and conserved residues on these five TMs (*30*–*33*).

In Insig-2, Phe115 is critical for the specific recognition of 25HC (*24*). Phe115 is located on the cavity-facing side of TM3 in the homologous model of Insig-2 (fig. S6C), suggesting that the central cavity might provide the accommodation for 25HC. The Insig-2 residues Gln132/Trp145/Asp149 mediate interactions with Scap but are not required for 25HC binding (*24*). All three residues are located on the outside surface of TM4 in the homologous model of Insig-2, suitably positioned to engage other binding partner(s) (fig. S6C). However, the corresponding residues of Gln132 and Trp145 on TM4 of MvINS are involved in homotrimerization, which may exclude its interaction with other proteins. We thus examined the oligomerization states of Insig-2. Size exclusion chromatography is consistent with Insig-2 existing as a monomer in solution; thus, TM4 of Insig-2 may be involved in hetero-oligomerization with Scap (fig. S6D).

To establish the structure-function correlation, we attempted to reconstitute an assay system to examine the oxysterol-regulated interaction between Insig-2 and Scap. A pull-down assay showed 25HC-dependent complex formation between Insig-2 and Scap (Fig. 3A). Insig-2 variants that each carry a single point mutation of F115A, Q132A, W145A, or D149A failed to pull down Scap even in the presence of 25HC (Fig. 3B) (*24*).

Insig-2 variants each containing a single point mutation on TM3 were generated and their interactions with Scap were examined. Replacement of the outward-protruding residues Ala113, Gly117, or His120 by aromatic residues led to complete disruption of complex formation, even in the presence of 25HC. In contrast, substitution of the residues Val114 or Val116, which appear to mediate intramolecular interactions with adjacent TMs, had no effect on Scap association (Fig. 3C). These observations suggest that TM3 and TM4 of Insig-2 contribute to Scap binding.

To identify additional residues for 25HC recognition, we examined the pocket residues (Fig. 4A and fig. S7). Single point mutation of residues adjacent to Phe115, including G39F, C77D, and G200F, led to abolished or markedly decreased complex formation in the presence of 25HC (Fig. 4A). These Insig-2 variants showed decreased affinity with 25HC in the direct binding assay (*24*) (Fig. 4B). Gly39 (TM1), Cys77 (TM2), and Gly200 (TM6) are clustered together with Phe115 (TM3) within the central cavity, enclosing a ring at approximately mid-height across lipid bilayer.

After the discovery of Insig proteins from mammalian cells (*14*, *15*), their homologs have been identified in *Schizosaccharomyces pombe* (*34*), *Saccharomyces cerevisiae* (*35*), and *Aspergillus fumigatus* (*36*). Despite the moderate sequence homology between mammalian and yeast Insig proteins of typically only 20 to 30% identity, they appear to exhibit functional conservation (*35*). Therefore, the structural information reported here for a mycobacterial homolog is consistent with a structural and functional conservation of Insig proteins during evolution (fig. S8). However, no homologs of SREBP, Scap, or HMG-CoA reductase have been found in these mycobacteria, so the physiological function of the bacterial homolog remains a question.

REFERENCES AND NOTES

1. M. S. Brown, J. L. Goldstein, *Science* **232**, 34–47 (1986).
2. M. S. Brown, J. L. Goldstein, *Cell* **89**, 331–340 (1997).
3. W. Shao, P. J. Espenshade, *Cell Metab.* **16**, 414–419 (2012).
4. J. L. Goldstein, R. A. DeBose-Boyd, M. S. Brown, *Cell* **124**, 35–46 (2006).
5. J. L. Goldstein, M. S. Brown, *Cell* **161**, 161–172 (2015).
6. C. Yokoyama *et al.*, *Cell* **75**, 187–197 (1993).

7. X. Hua *et al*., . *Proc. Natl. Acad. Sci. U.S.A.* **90**, 11603–11607 (1993).
8. X. Wang, R. Sato, M. S. Brown, X. Hua, J. L. Goldstein, *Cell* **77**, 53–62 (1994).
9. X. Hua, A. Nohturfft, J. L. Goldstein, M. S. Brown, *Cell* **87**, 415–426 (1996).
10. J. Sakai *et al*., *J. Biol. Chem.* **272**, 20213–20221 (1997).
11. X. Gong *et al*., *Cell Res.* **25**, 401–411 (2015).
12. A. Nohturfft, M. S. Brown, J. L. Goldstein, *J. Biol. Chem.* **273**, 17243–17250 (1998).
13. T. Yang, J. L. Goldstein, M. S. Brown, *J. Biol. Chem.* **275**, 29881–29886 (2000).
14. T. Yang *et al*., *Cell* **110**, 489–500 (2002).
15. D. Yabe, M. S. Brown, J. L. Goldstein, *Proc. Natl. Acad. Sci. U.S.A.* **99**, 12753–12758 (2002).
16. P. J. Espenshade, W. P. Li, D. Yabe, *Proc. Natl. Acad. Sci. U.S.A.* **99**, 11694–11699 (2002).
17. L. P. Sun, L. Li, J. L. Goldstein, M. S. Brown, *J. Biol. Chem.* **280**, 26483–26490 (2005).
18. J. Sakai *et al*., *Mol. Cell* **2**, 505–514 (1998).
19. R. B. Rawson *et al*., *Mol. Cell* **1**, 47–57 (1997).
20. R. B. Rawson, *Nat. Rev. Mol. Cell Biol.* **4**, 631–640 (2003).
21. E. Ikonen, *Nat. Rev. Mol. Cell Biol.* **9**, 125–138 (2008).
22. J. Sakai *et al*., *Cell* **85**, 1037–1046 (1996).
23. M. S. Brown, J. L. Goldstein, *Proc. Natl. Acad. Sci. U.S.A.* **96**, 11041–11048 (1999).
24. A. Radhakrishnan, Y. Ikeda, H. J. Kwon, M. S. Brown, J. L. Goldstein, *Proc. Natl. Acad. Sci. U.S.A.* **104**, 6511–6518 (2007).
25. Y. Jo, R. A. Debose-Boyd, *Crit. Rev. Biochem. Mol. Biol.* **45**, 185–198 (2010).
26. J. S. Burg *et al*., *Cell Metab.* **8**, 522–531 (2008).
27. L. Feng *et al*., *Science* **318**, 1608–1612 (2007).
28. J. D. Feramisco, J. L. Goldstein, M. S. Brown, *J. Biol. Chem.* **279**, 8487–8496 (2004).
29. *Molecular Operating Environment* (*MOE*) (Chemical Computing Group, Montreal, Canada, 2013).
30. D. Deng *et al*., *Nature* **510**, 121–125 (2014).
31. L. Sun *et al*., *Nature* **490**, 361–366 (2012).
32. A. Penmatsa, K. H. Wang, E. Gouaux, *Nature* **503**, 85–90 (2013).
33. A. Yamashita, S. K. Singh, T. Kawate, Y. Jin, E. Gouaux, *Nature* **437**, 215–223 (2005).
34. A. L. Hughes, B. L. Todd, P. J. Espenshade, *Cell* **120**, 831–842 (2005).
35. I. Flury *et al*., *EMBO J.* **24**, 3917–3926 (2005).
36. T. F. Osborne, P. J. Espenshade, *Genes Dev.* **23**, 2578–2591 (2009).
37. W. L. DeLano, The PyMOL Molecular Graphics System, www.pymol.org (2002).

ACKNOWLEDGMENTS

We thank D. Rye, M. Brown, and J. Goldstein (University of Texas Southwestern Medical Center) for their assistance with studies on human Insig-2. We thank J. He, L. Tang, F. Yu, B. Sun, and S. Huang at the Shanghai Synchrotron Radiation Facility (SSRF) and K. Hasegawa and T. Kumasaka at the SPring-8 beamline BL41XU for onsite assistance; and B. Javid for critical discussion. This work was supported by funds from the Ministry of Science and Technology of China (grants 2015CB910101, 2011CB910501, 2014ZX09507003006) and National Natural Science Foundation of China (projects 31130002, 31125009, 91313303, and 20122209). A.R. was supported by the National Institutes of Health (HL-20948), American Heart Association (12SDG12040267), and Welch Foundation (I-1793).The research of N.Y. was supported in part by an International Early Career Scientist grant from the Howard Hughes Medical Institute and an endowed professorship from Bayer Healthcare. The coordinates and structure factors of the MvINS proteins have been deposited in the Protein Data Bank with accession codes 4XU4, 4XU5, and 4XU6. The authors declare no competing financial interests.

SUPPLEMENTARY MATERIALS

www.sciencemag.org/content/349/6244/187/suppl/DC1
Materials and Methods
Supplementary Text
Figs. S1 to S8
Tables S1 and S2
References (*38*–*50*)

12 March 2015; accepted 5 June 2015
10.1126/science.aab1091

HIV-1 ENVELOPE

Effect of the cytoplasmic domain on antigenic characteristics of HIV-1 envelope glycoprotein

Jia Chen,[1,2] James M. Kovacs,[1,2] Hanqin Peng,[1] Sophia Rits-Volloch,[1] Jianming Lu,[3] Donghyun Park,[1] Elise Zablowsky,[4] Michael S. Seaman,[4] Bing Chen[1,2]*

A major goal for HIV-1 vaccine development is the production of an immunogen to mimic native, functional HIV-1 envelope trimeric spikes (Env) on the virion surface. We lack a reliable description of a native, functional trimer, however, because of inherent instability and heterogeneity in most preparations. We describe here two conformationally homogeneous Envs derived from difficult-to-neutralize primary isolates. All their non-neutralizing epitopes are fully concealed and independent of their proteolytic processing. Most broadly neutralizing antibodies (bnAbs) recognize these native trimers. Truncation of their cytoplasmic tail has little effect on membrane fusion, but it diminishes binding to trimer-specific bnAbs while exposing non-neutralizing epitopes. These results yield a more accurate antigenic picture than hitherto possible of a genuinely untriggered and functional HIV-1 Env; they can guide effective vaccine development.

HIV-1 envelope glycoprotein (Env) fuses viral and cell membranes, allowing entry of the virus into host cells to initiate infection. The Env polypeptide chain is produced as a precursor, gp160, which trimerizes to $(gp160)_3$ and then undergoes cleavage into two noncovalently associated fragments: the receptor-binding fragment gp120 and the fusion fragment gp41 (*1*). Three copies each of gp120 and gp41 form the mature envelope spike $(gp120/gp41)_3$, which is the major viral surface antigen and therefore a critical target for vaccine development. Gp120 binds to host primary receptor CD4 and then to coreceptor (e.g., CCR5 or CXCR4), triggering large conformational changes and a cascade of refolding events in gp41 that lead to membrane fusion (*2*, *3*) (fig. S1).

The failure of monomeric gp120 as a vaccine candidate in a large efficacy trial (*4*, *5*) led to the notion that an immunogen mimicking the native, functional envelope trimer would be needed to induce effective, broadly neutralizing antibody (bnAb) responses by vaccination. In particular, bnAbs [except those recognizing the membrane-proximal external region (MPER) (*6*)] were thought to bind only the untriggered, native Env trimer (*7*). Attempts to produce such an Env preparation have met with only limited success (*8*, *9*). Moreover, we lack an accurate standard for a native, functional trimer because most Env preparations, both soluble and membrane-bound, including those on the surface of infectious virions, show considerable structural instability and heterogeneity, leading to conflicting interpretations. For instance, based on virus-capturing assays, some groups conclude that certain "non-neutralizing" (including strain-specific neutralizing) epitopes are exposed on the native, functional Env trimer, whereas others believe that there are both functional and nonfunctional Envs present on the surface of infectious viral particles (*10*–*13*). Furthermore, the uncleaved ectodomain of trimeric $(gp160)_3$, designated gp140, is often considered to mimic the native state of Env. Recombinant gp140 trimers derived from selected strains are stable and homogeneous, with certain desired antigenic properties (*14*–*16*), but we cannot know how closely they resemble functional and untriggered Env spikes without a good native-trimer reference. Are these soluble gp140 trimers—all with certain non-neutralizing epitopes (e.g., V3 loop) exposed—really the best surrogate for a native Env trimer. If not, how can we improve them? Recent work on conformational dynamics of the Env spikes on the virion surface suggests that the native trimer transitions among three distinct prefusion conformations (*17*). If this is true for difficult-to-neutralize clinical isolates, how can the functional trimer limit access to the non-neutralizing epitopes that overlap with the functionally important sites, such as the CD4 binding site and the V3 loop?

We have previously screened many HIV-1 primary isolates and identified two (clade A 92UG037.8 and clade C C97ZA012) that yield stable, homogeneous gp140 trimers (*6*, *14*). The two Envs have about 74% sequence identity. Their divergence, typical for cross-clade comparisons, samples a range of Env diversity. Additional stable, clade-C trimers have since been reported (*18*), but we have not yet detected a clear "stability signature." Our previous immunogenicity studies using either gp120 or gp140 immunogens derived from these two isolates failed to show any autologous

[1]Division of Molecular Medicine, Boston Children's Hospital, Boston, MA 02115, USA. [2]Department of Pediatrics, Harvard Medical School, 3 Blackfan Street, Boston, MA 02115, USA. [3]Codex BioSolutions, Inc., 401 Professional Drive, Gaithersburg, MD 20879, USA. [4]Center for Virology and Vaccine Research, Beth Israel Deaconess Medical Center, 330 Brookline Avenue, Boston, MA 02215, USA.
***Corresponding author. E-mail: bchen@crystal.harvard.edu**

neutralizing antibody responses, although V3-specific antibodies were present in the sera of immunized animals (*19*, *20*). We surmised that the non-neutralizing V3 epitopes must not be exposed on the native Env trimers of these strains, despite their accessibility on the corresponding soluble gp140 trimers (*14*). Indeed, V3 accessibility is the one antigenic characteristic of the stable uncleaved gp140s (*14*) and of the BG505 SOSIP.664 trimer (*15*, *21*, *22*) that does not correlate with neutralization. The V3 loop is only slightly exposed in the disulfide-stabilized SOSIP crystals structure (*21*), but the molecule in solution presumably visits a wider range of conformations when not bound by one or more conformation-specific antibodies, as in crystal and cryogenic electron microscopy structures.

To study the antigenic characteristics of intact, native Env trimers, we generated 293T cell lines stably transfected with either 92UG037.8 or C97ZA012 gp160 (fig. S2). Efficient fusion with TZM.bl cells (*23*), completely blocked by T20 (1 μM) (fig. S3A), showed that there were fully functional envelope trimers on the cell surfaces. About 50% of gp160s were cleaved into gp120 and gp41, both inside the cells and on the cell surfaces (fig. S3B).

We analyzed antibody binding to cell-surface Env by a fluorescence-activated cell sorting (FACS) assay (see table S1 for antibodies used and references) (*24*). Antibody 2G12, which recognizes a glycan-dependent epitope on gp120, bound the cell-surface Env equally well with and without CD4, indicating no significant CD4-induced gp120 shedding (Fig. 1 and fig. S4). CD4 binding site (bs) bnAbs all bound the cell-surface Env tightly, consistent with their neutralization potency; soluble CD4 effectively competed with all of them (Fig. 1, figs. S5A and S6, and table S2). A CD4bs antibody, b6, that does not neutralize the two isolates used here, showed no binding at all, suggesting that its epitope is inaccessible on both cleaved (fusion-competent) $(gp120/gp41)_3$ and uncleaved (not fusion-competent) $(gp160)_3$. Binding of non-neutralizing CD4i (CD4-induced) antibodies 17b and 412d was likewise independent of the cleavage but completely dependent on CD4 engagement. Another non-neutralizing CD4i antibody, A32, failed to bind these Envs under any circumstances. The trimer-specific bnAbs recognized only the native, untriggered Env trimer with high affinity, but not the CD4-bound form (Fig. 1, fig. S5A, and table S2). Another two bnAbs, PGT128 and 10-1074, which target a glycan-dependent epitope in the V3 stem, also bound the native Env but not the CD4-liganded form.

Non-neutralizing epitopes, including V3 loop (3791 and 19b), V2 (2158), gp41 cluster I epitopes (246-D, 240-D, and 7B2), and gp41 cluster II epitopes (1281 and 167-D) were inaccessible on the cell-surface trimer (Fig. 1 and fig. S5A), explaining why these antibodies do not neutralize. Their occlusion was independent of the cleavage between gp120 and gp41, as ~50% of the Env on the cell

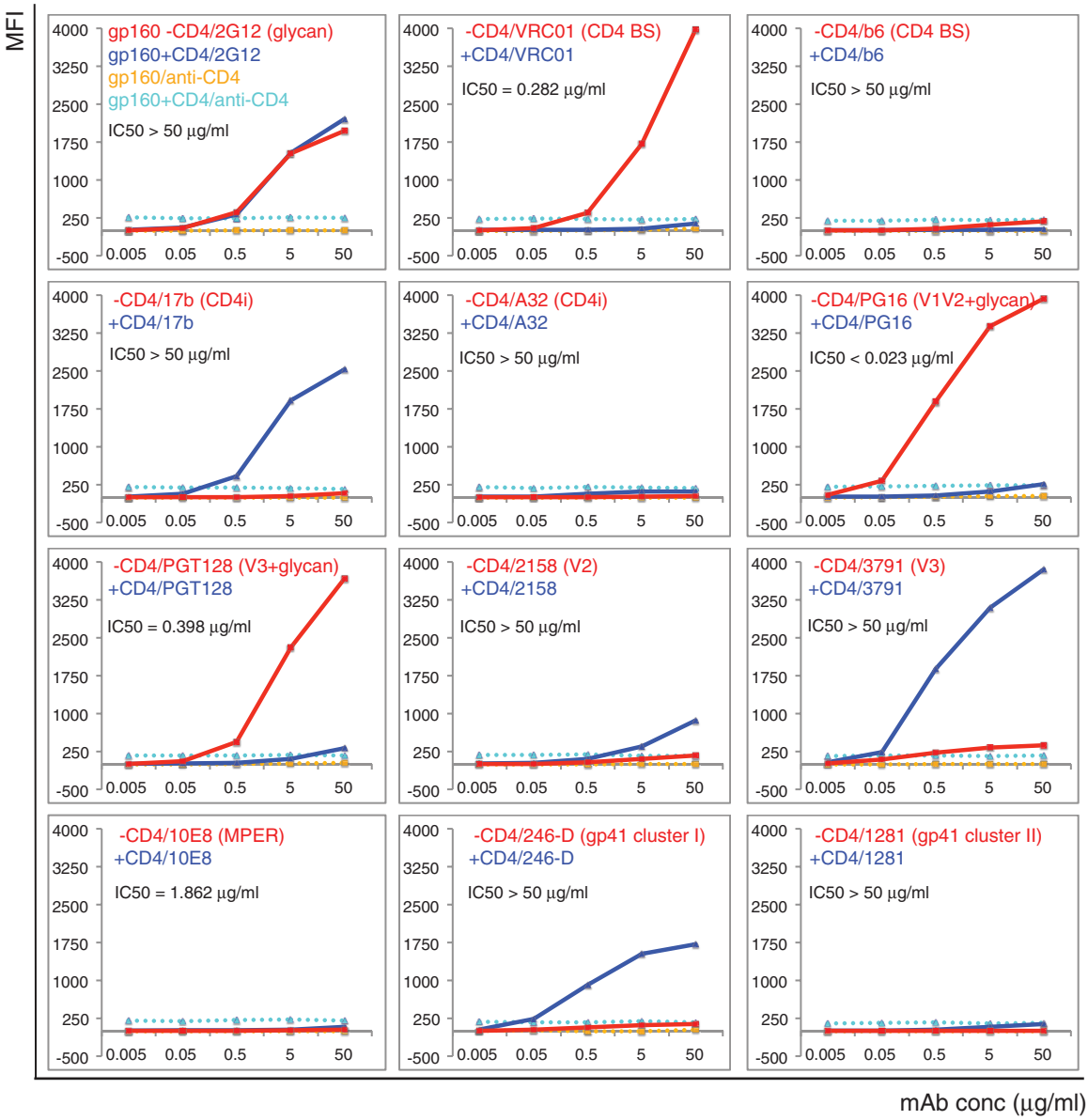


Fig. 1. Antigenic characteristics of the 92UG037.8 Env trimer presented on cell surfaces. Plots of antibody binding to the Env trimer on the 92UG037.8 gp160 cell surfaces in the absence (red) or presence (blue) of soluble CD4. Fluorescent signal for bound CD4 is shown in the presence of CD4 (cyan) or in the absence of CD4 (orange). Antibodies and their epitopes are indicated. The median inhibitory concentration (IC50) values were determined in a luciferase-based virus neutralization assay using 92UG037.8 gp160 and purified antibodies. Unless specified, all antibodies used are Fab fragments. Original flow cytometry histograms are shown in fig. S4. Extensive control experiments were carried out to ensure the binding specificity, and the experiments were repeated at least twice with almost identical results.

surfaces remained uncleaved (fig. S3B). Upon CD4 binding, the V3 loop, the cluster I epitope, and (to a lesser extent) the V2 loop all became accessible. Thus, the antibodies recognizing these epitopes might be better categorized as CD4i antibodies. MPER-directed bnAbs did not bind the Env trimer, consistent with our previous work showing that they target a fusion-intermediate conformation of gp41 (*6*, *25*, *26*). Isolate 92UG037.8 resists neutralization by two antibodies, PGT151 and 152, with epitopes at the gp120-gp41 interface; these antibodies indeed fail to bind native Env trimers (fig. S5A and table S2). Two other interface-directed bnAb (*27*) bound only weakly (fig. S5A). These results are reproducible under different conditions (*28*). In summary, all the Env trimers, cleaved or uncleaved, on the cell surfaces adopted a defined, homogeneous conformation (or small range of conformations) that was recognized by bnAbs only and not by any of the non-neutralizing antibodies tested.

These cell-surface Env trimers have antigenic properties distinct from those of the corresponding gp140 trimers (*14*, *20*), which lack the cytoplasmic tail (CT) and the transmembrane segment (TM). Does the CT influence the antigenicity of the ectodomain? We produced a stable line expressing the 92UG037.8 gp160 with the entire CT deleted (a form designated gp160ΔCT) and replaced by a His tag (fig. S2). This cell line also efficiently fused with TZM.bl cells (fig. S9A). The expression level of gp160ΔCT was much higher than that of intact gp160 (Fig. 2), as reported previously (*29*). As with the gp160 cell line, both cleaved and uncleaved gp160ΔCT trimers were present on the cell surface (fig. S9B), but with a smaller proportion of cleaved molecules; gp160ΔCT without the His tag showed the same extent of cleavage as did intact gp160 (fig. S10).

Binding of 2G12 to gp160ΔCT was unaffected by CD4, indicating no significant CD4-induced gp120 shedding (Fig. 2 and fig. S11). CD4bs bnAbs bound gp160ΔCT as tightly as they did intact gp160, but the non-neutralizing antibody, b6, also bound detectably to gp160ΔCT (Fig. 2 and figs. S12A and S13), suggesting that the CD4 bs is more exposed when the CT is deleted. The CD4i antibodies, 17b and 412d, also showed weak, but detectable, binding to gp160ΔCT, whereas binding by the trimer-specific bnAbs was significantly reduced when normalized by the Env expression level. The non-neutralizing V3 and V2 epitopes were much more exposed and less dependent on CD4 binding for recognition by antibody. In particular, the V3 antibody 3791 blocked cell-cell fusion mediated by gp160ΔCT but not by gp160 (fig. S14), indicating that removal of the CT can expose the V3 loop on a functional (i.e., fusogenic) trimer. PGT128 binding to gp160ΔCT likewise depended less on CD4, and 10-1074 became totally CD4-independent (Fig. 2 and fig. S12A). In addition, although the MPER epitopes and the cluster II epitopes remained inaccessible, the

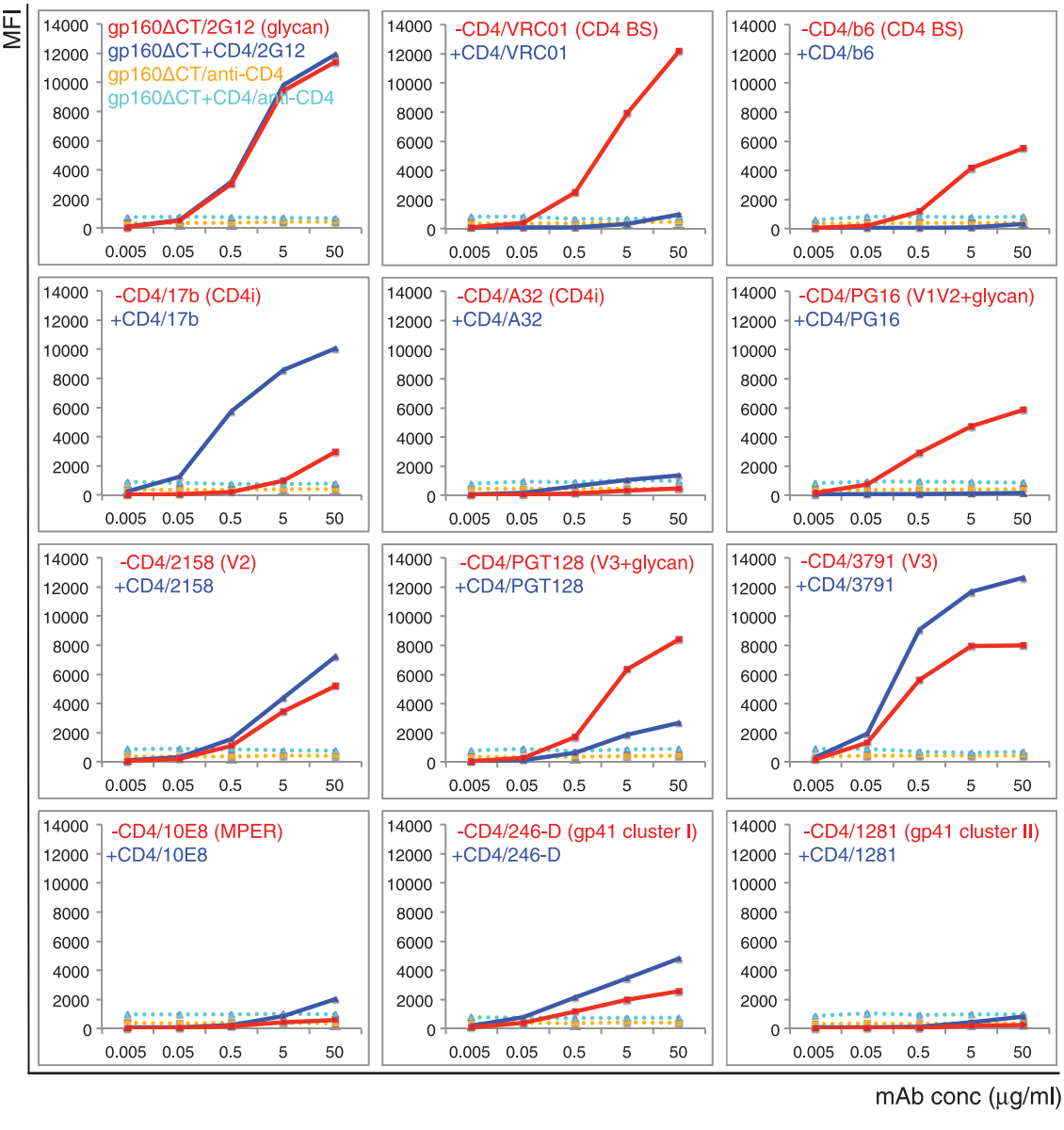


Fig. 2. Antigenic properties of the 92UG037.8 gp160-ΔCT. Plots of antibody binding to the Env trimer on the 92UG037.8 gp160-ΔCT cell surfaces in absence (red) or presence (blue) of soluble CD4. Fluorescent signal for bound CD4 is shown in the presence of CD4 (cyan) or in the absence of CD4 (orange). Antibodies and their epitopes are indicated. Unless specified, all antibodies used are Fab fragments. Original flow cytometry histograms are shown in fig. S11. The experiments were repeated at least twice with almost identical results.

		soluble CD4	gp160	CT120	CT90	CT60	CT30	gp160-dCT	gp140-TMfd	gp140FL20-TM	gp140FL20-TMfd	gp140-GPI
VRC01 (CD4 BS)	-	100	100	100	100	100	100	100	100	100	100	
	+	4	5	11	13	7	8	21	24	26	22	
b6 (CD4 BS)	-	5	12	29	26	29	45	72	72	70	71	
	+	1	2	7	9	3	3	7	8	11	9	
17b (CD4i)	-	2	6	18	13	17	24	41	47	49	16	
	+	64	57	70	65	57	82	58	48	55	30	
A32 (CD4i)	-	1	4	10	11	5	4	13	18	21	12	
	+	3	6	13	14	8	11	15	17	18	15	
PG16 (V1V2+G)	-	99	66	50	56	47	48	5	10	6	3	
	+	7	4	9	12	3	2	3	3	2	2	
2158 (V2)	-	4	16	33	28	35	43	78	64	71	32	
	+	22	23	42	33	38	60	73	61	65	27	
PGT128 (V3+G)	-	92	88	81	90	89	69	61	52	61	49	
	+	8	11	17	17	19	22	35	31	44	29	
3791 (V3)	-	9	27	53	46	50	66	113	127	106	117	
	+	96	94	111	97	87	104	103	87	97	102	
10E8 (MPER)	-	1	4	12	16	4	5	2	2	3	4	
	+	2	7	13	20	7	17	4	4	4	5	
246-D (cluster I)	-	3	9	20	25	20	21	39	32	36	5	
	+	64	37	36	41	44	40	34	34	30	5	
1281 (cluster II)	-	0	2	6	8	2	2	5	2	3	3	
	+	4	3	7	8	5	7	6	4	5	4	
cell-cell fusion		+	+	+	+	+	+	-	-	-	-	

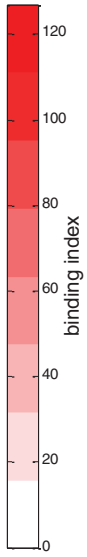


Fig. 3. Effect of the gp41 cytoplasmic tail on antigenic properties of the ectodomain of Env. A tabulated summary of antibody binding to various 92UG037.8 Env constructs, including gp160, gp160-CT120, gp160-CT90, gp160-CT60, gp160-CT30, gp160-ΔCT, gp140-TMfd, gp140FL20-TM, gp140FL20-TMfd, and gp140-GPI. Epitopes targeted by the antibodies include CD4bs, CD4 binding site; CD4i, CD4-induced; V1V2+G, the V1V2 loop and glycans; V3+G, the V loop and glycans; MPER, membrane proximal external region; and gp41, cluster I and cluster II. Binding index is normalized by VRC01 binding to each untriggered Env construct in the absence of CD4, and it is defined as the ratio between the maximum MFI of a given antibody binding and the maximum MFI of VRC01 binding to the same Env construct. Cell-cell fusion capacity of each Env construct was monitored by syncytium formation when mixing Env-expressing cells and TZM-bl cells.

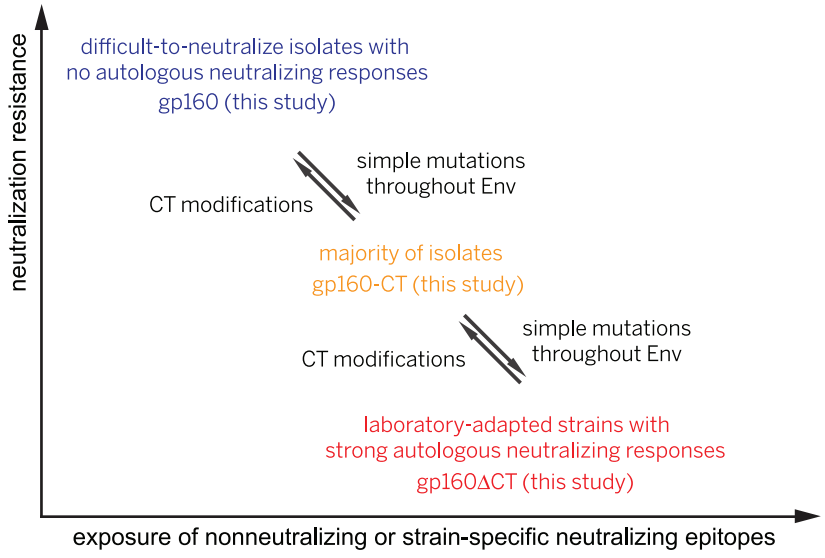


Fig. 4. A proposed relationship among all HIV-1 isolates based on their Env properties. Our gp160 and gp160-ΔCT may represent Envs of the difficult-to-neutralize primary isolates that cannot induce autologous neutralizing antibody responses and the easy-to-neutralize, laboratory-adapted strains that induce strong autologous neutralizing responses, respectively. Other isolates (of intermediate susceptibility to neutralization) may adopt intermediate conformations, like those of our partially truncated gp160-CT constructs. A few mutations can easily convert one form into another, perhaps even within a single patient, and thus an effective vaccine may need to protect against the viruses described in blue.

non-neutralizing cluster I epitopes were exposed even in the absence of CD4. Both His-tagged and nontagged gp160ΔCT constructs had almost identical antigenic profiles despite the different extent of cleavage (figs. S12B and S15), suggesting that the cleavage between gp120 and gp41 does not have a major effect on the trimer antigenicity. Overall, these data indicate that the CT has minimal effect on the membrane fusion function of the Env trimer but that it has an unexpectedly large influence on the antigenic properties of the ectodomain on the other side of the membrane (table S2). Thus, the membrane-fusion capacity of an Env trimer does not depend on strict retention of native antigenic characteristics. The same conclusion can be drawn from comparison of another pair of gp160 and gp160ΔCT, derived from the isolate C97ZA012 (figs. S16A, S16B, S17, and S18).

We constructed four deletion mutants—gp160-CT120, gp160-CT90, gp160-CT60, and gp160-CT30—with gradually decreasing CT lengths (figs. S2 and S10). All these deletion constructs were functional in a cell-cell fusion assay, but shortening the CT led to diminished binding by the trimer-specific bnAbs and increasing exposure of the non-neutralizing epitopes (Fig. 3; fig. S19, A to D; and figs. S20 to S23). Introducing other modifications (*30*) (fig. S2), previously assumed to be "harmless," caused even greater changes in antigenicity. These constructs were all nonfunctional (Fig. 3), and we detected much greater exposure of non-neutralizing epitopes, including those of b6, 17b, A32, 2158, 3971, and 246-D. Binding to the trimer-specific bnAbs, PG16 and PGT145, was completely lost (Fig. 3; fig. S19, E to H; and figs. S24 to S27). The MPER and cluster II epitopes remained concealed even in these nonfunctional Envs.

Our results demonstrate that a native Env trimer can indeed adopt a defined and homogeneous conformational state without contamination by any irrelevant forms of Env (*12*). This native, untriggered conformation seems to be independent of the cleavage between gp120 and gp41. It is particularly surprising that the Env CT has a large effect on the antigenicity of the ectodomain on the other side of the membrane. Various gp160-ΔCT constructs, often with an increased yield, are still widely considered to be faithful substitutes for the full-length gp160, despite published evidence suggesting that the CT may influence epitope exposure (*31*). Our results demonstrate that truncation of the CT affects the antigenic characteristics of the native Env trimer, even in the absence of the matrix protein, but not its fusogenicity. Thus, a "functional" Env may not have a fully "native" antigenic surface (defined by neutralization), because even a fusion-competent Env trimer can expose non-neutralizing epitopes (Fig. 3). Those apparently "harmless" modifications, such as CT deletion—an approach widely used in various vaccine strategies to enhance Env yield and/or stability—can have a strong effect on trimer structure, antigenicity, and potentially immunogenicity.

Strain-specific neutralizing epitopes, such as the V3 loop and the V1V2 loop, are well protected on the native trimer derived from the

hard-to-neutralize strains we have studied, explaining why it is difficult to induce autologous neutralizing antibody responses against such isolates. The antigenic properties of gp160 and gp160-ΔCT may represent, respectively, those of the extreme cases of the difficult-to-neutralize primary isolates that cannot induce autologous neutralizing responses and the easy-to-neutralize, laboratory-adapted strains that induce strong autologous responses, whereas other isolates (of intermediate susceptibility to neutralization) may adopt conformations in between, like those of our partially truncated gp160-CT constructs (Fig. 4). A few mutations within the entire gp160 sequence can convert one form into another, perhaps even within a single patient, just as primary and laboratory-adapted simian HIV or HIV-1 isolates interconvert during in vitro and in vivo passages (*32*, *33*). Interconversion thus allows Envs in a closely related swarm of viruses to sample, at a population level, a much greater dynamic range than previously appreciated (*17*). In an infected individual, immune pressure might drive any particular isolate to evolve into one that is difficult to neutralize and does not induce autologous neutralizing responses (Fig. 4). Such viruses substantially raise the barrier to vaccine development.

In summary, the data presented here paint a more accurate antigenic picture than hitherto available of a genuinely native and functional HIV-1 envelope spike from clinically relevant viruses. They provide an excellent reference for studies on the prefusion conformation of HIV-1 Env trimers and serve as guides for assessing how well potential immunogens mimic a native viral spike.

REFERENCES AND NOTES

1. S. C. Harrison, *Nat. Struct. Mol. Biol.* **15**, 690–698 (2008).
2. D. C. Chan, D. Fass, J. M. Berger, P. S. Kim, *Cell* **89**, 263–273 (1997).
3. W. Weissenhorn, A. Dessen, S. C. Harrison, J. J. Skehel, D. C. Wiley, *Nature* **387**, 426–430 (1997).
4. N. M. Flynn *et al.*, *J. Infect. Dis.* **191**, 654–665 (2005).
5. P. Pitisuttithum *et al.*, *J. Infect. Dis.* **194**, 1661–1671 (2006).
6. G. Frey *et al.*, *Proc. Natl. Acad. Sci. U.S.A.* **105**, 3739–3744 (2008).
7. By "triggered," we mean any of the sequence of conformations that Env adopts after CD4 binding, on the pathway to fusion; by "native," those with antigenic properties fully consistent with antibody neutralization.
8. T. Schiffner, Q. J. Sattentau, L. Dorrell, *Retrovirology* **10**, 72 (2013).
9. L. E. McCoy, R. A. Weiss, *J. Exp. Med.* **210**, 209–223 (2013).
10. P. Liu *et al.*, *J. Virol.* **88**, 5165–5170 (2014).
11. J. York *et al.*, *J. Virol.* **75**, 2741–2752 (2001).
12. P. L. Moore *et al.*, *J. Virol.* **80**, 2515–2528 (2006).
13. T. Tong, E. T. Crooks, K. Osawa, J. M. Binley, *J. Virol.* **86**, 3574–3587 (2012).
14. J. M. Kovacs *et al.*, *Proc. Natl. Acad. Sci. U.S.A.* **111**, 18542–18547 (2014).
15. R. W. Sanders *et al.*, *PLOS Pathog.* **9**, e1003618 (2013).
16. J. Guenaga *et al.*, *PLOS Pathog.* **11**, e1004570 (2015).
17. J. B. Munro *et al.*, *Science* **346**, 759–763 (2014).
18. C. A. Bricault *et al.*, *J. Virol.* **89**, 2507–2519 (2015).
19. J. P. Nkolola *et al.*, *J. Virol.* **84**, 3270–3279 (2010).
20. J. M. Kovacs *et al.*, *Proc. Natl. Acad. Sci. U.S.A.* **109**, 12111–12116 (2012).
21. M. Pancera *et al.*, *Nature* **514**, 455–461 (2014).
22. P. Pugach *et al.*, *J. Virol.* **89**, 3380–3395 (2015).
23. E. J. Platt, K. Wehrly, S. E. Kuhmann, B. Chesebro, D. Kabat, *J. Virol.* **72**, 2855–2864 (1998).
24. In the FACS assay, bound primary antibodies were detected by a fluorescently labeled secondary antibody. Stably transfected cell lines for all Env constructs were necessary for obtaining high-quality data with mostly single sharp peaks in histograms; data that met these criteria gave reliable readings of MFI (mean fluorescence intensity) of a relatively homogeneous cell population (fig. S3C).
25. S. M. Alam *et al.*, *Proc. Natl. Acad. Sci. U.S.A.* **106**, 20234–20239 (2009).
26. J. Chen *et al.*, *J. Virol.* **88**, 1249–1258 (2014).
27. J. Huang *et al.*, *Nature* **515**, 138–142 (2014).
28. We obtained the same results regardless of whether we used a Fab or IgG form of the antibody or a 2-domain or 4-domain soluble CD4 (figs. S5A, S6, S5B, and S7). The antigenic properties of gp160 remained largely the same when the entire experiments were performed at 37°C, except that we saw significant CD4-induced gp120 shedding, as indicated by a lower level of 2G12, 17b, and 3791 binding when CD4 was present and by an increase in 246-D binding (figs. S5C and S8).
29. C. C. LaBranche *et al.*, *J. Virol.* **69**, 5217–5227 (1995).
30. The modifications include replacing TM and CT with a glycosylphosphatidylinositol (GPI) anchor (gp140-GPI), replacing CT with a foldon trimerization tag (gp140-TM-fd), inserting a flexible linker between gp120 and gp41 (gp140-FL20-TM), and adding both the foldon tag and the flexible linker (gp140-FL20-TM-fd).
31. T. G. Edwards *et al.*, *J. Virol.* **76**, 2683–2691 (2002).
32. Y. Ye, Z. H. Si, J. P. Moore, J. Sodroski, *J. Virol.* **74**, 11955–11962 (2000).
33. T. Beaumont *et al.*, *J. Virol.* **75**, 2246–2252 (2001).

ACKNOWLEDGMENTS

We thank S. Harrison, H. Ha, and G. Frey for generous advice and assistance; D. Barouch, B. Haynes, and A. Carfi for critical reading of the manuscript; and the NIH AIDS Reagent Program, Division of AIDS, NIAID, NIH for reagents. The data presented in this manuscript are tabulated in the main paper and in the supplementary materials. This work was supported by NIH grants AI084794 (to B.C. and Dan H. Barouch), GM083680 (to B.C.), AI106488 (to B.C.), Collaboration for AIDS Vaccine Discovery (CAVD) grant OPP1040741 (to Dan H. Barouch from the Bill and Melinda Gates Foundation), and the Center for HIV/AIDS Vaccine Immunology–Immunogen Design AI-100645 (to Barton F. Haynes).

SUPPLEMENTARY MATERIALS

www.sciencemag.org/content/349/6244/191/suppl/DC1
Materials and Methods
Supplementary Text
Figs. S1 to S28
Tables S1 to S2
References (*34*–*75*)

23 February 2015; accepted 8 June 2015
Published online 25 June 2015;
10.1126/science.aaa9804

VESICULAR TRANSPORT

A structure of the COPI coat and the role of coat proteins in membrane vesicle assembly

S. O. Dodonova,[1] P. Diestelkoetter-Bachert,[2] A. von Appen,[1] W. J. H. Hagen,[1] R. Beck,[2] M. Beck,[1] F. Wieland,[2] J. A. G. Briggs[1,3]*

Transport of material within cells is mediated by trafficking vesicles that bud from one cellular compartment and fuse with another. Formation of a trafficking vesicle is driven by membrane coats that localize cargo and polymerize into cages to bend the membrane. Although extensive structural information is available for components of these coats, the heterogeneity of trafficking vesicles has prevented an understanding of how complete membrane coats assemble on the membrane. We combined cryo–electron tomography, subtomogram averaging, and cross-linking mass spectrometry to derive a complete model of the assembled coat protein complex I (COPI) coat involved in traffic between the Golgi and the endoplasmic reticulum. The highly interconnected COPI coat structure contradicted the current "adaptor-and-cage" understanding of coated vesicle formation.

Coat protein complexes I and II (COPI and COPII) and clathrin-coated vesicles mediate transport between different compartments of the cell. COPI mediates retrograde transport, both from the Golgi to the endoplasmic reticulum and within the Golgi (*1*, *2*). Coated vesicles are generally formed in a similar manner (*3*–*5*). In most cases, exchange of guanosine diphosphate for guanosine triphosphate within a small guanosine triphosphatase (GTPase) induces a conformational change that exposes an N-terminal amphipathic helix that inserts into the membrane. The GTPase recruits adaptor proteins, which in turn recruit coat proteins that polymerize to form the outer coat or "cage." This modular approach can allow different adaptor proteins to be used, depending on the cargo being packaged. In the COPI system, where transport can occur independently of the presence of cargo, the adaptor and outer coat are combined in a soluble heteroheptameric complex (called coatomer) that is recruited to the membrane en bloc (*6*). After a coated bud has formed, vesicles are released by a scission reaction before uncoating and fusing with the target membrane.

The three archetypal vesicle coats share aspects of their structural organization. The outer-coat components—clathrin, Sec31 (for COPII), and

[1]Structural and Computational Biology Unit, European Molecular Biology Laboratory (EMBL), Meyerhofstrasse 1, 69117 Heidelberg, Germany. [2]Heidelberg University Biochemistry Center, Heidelberg University, Im Neuenheimer Feld 328, 69120 Heidelberg, Germany. [3]Cell Biology and Biophysics Unit, European Molecular Biology Laboratory, Meyerhofstrasse 1, 69117 Heidelberg, Germany.
***Corresponding author. E-mail: john.briggs@embl.de**

α- and β′-COP (for COPI)—consist of N-terminal β propellers followed by extended α solenoids (7). This "protocoatomer" motif, also found in the nuclear pore, is thought to represent an ancestral module involved in membrane bending (7). Interactions between α solenoids contribute to polymerization of the clathrin and COPII coats to form symmetrical cages whose structures have been solved by cryo–electron microscopy and

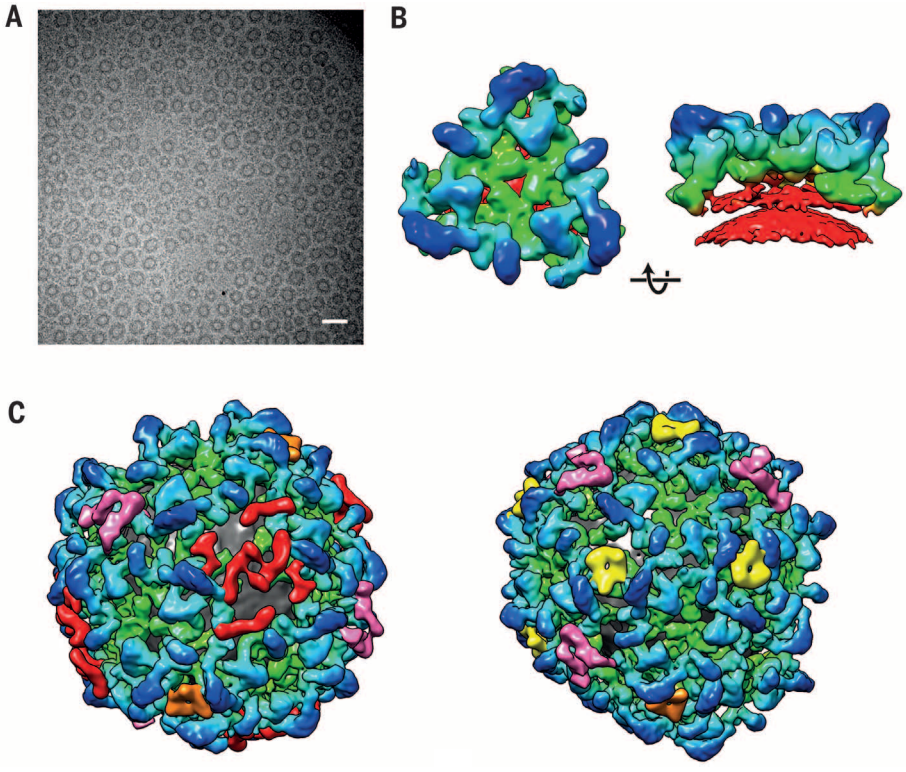


Fig. 1. COPI coat structure. (**A**) Electron micrograph of in vitro–formed COPI-coated vesicles. Scale bar, 100 nm. (**B**) EM reconstruction of the triad at 13 Å resolution, colored from green to blue according to the radial distance from the membrane (red). (**C**) Representations of complete COPI-coated vesicles. The membrane is shown in gray. Densities of intertriad linkages are colored pink (I), orange (II), yellow (III), and red (IV) (fig. S1).

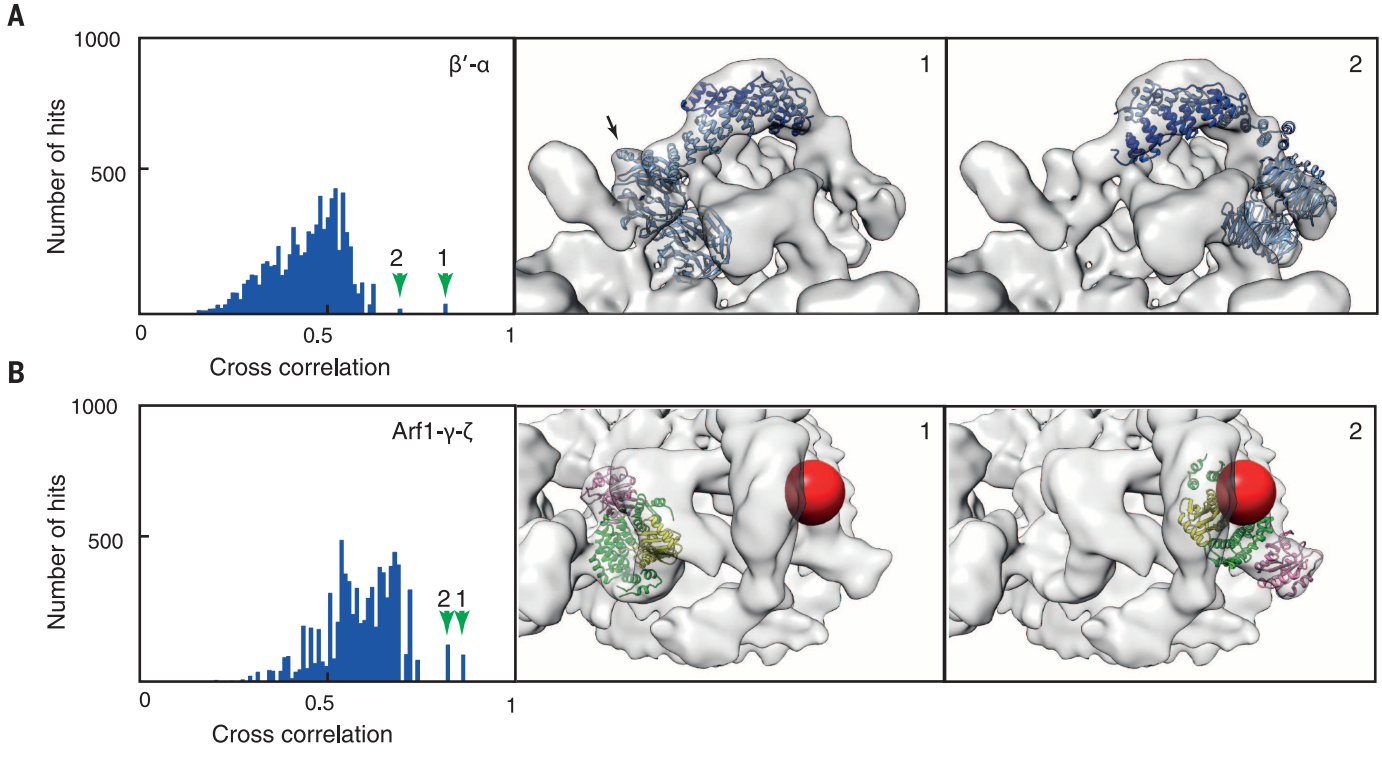


Fig. 2. Global fitting of COPI crystal structures. (**A**) Fitting results for β′-α-COP (PDB ID 3MKQ; β′-COP in light blue, α-COP in dark blue). An additional α helix adjacent to the second β-propeller domain of β′-COP, but absent in α-COP, is marked with black arrow. (**B**) Fitting results for Arf1-γ-ζ-COP (PDB ID 3TJZ; Arf1 in pink, γ-COP in light green, ζ-COP in yellow). Left panels: Histograms of cross-correlation values resulting from 10,000 fitting experiments (Chimera global search). Green arrows mark the highest-scoring fitted positions illustrated in the right panels. Additional density observed when the β-COP N terminus is nanogold-labeled is shown in red (fig. S4).

single-particle analysis (*8*, *9*). In COPI, β′-COP (together with part of α-COP) can be crystallized to form a triskelion-like structure (*10*) that has been proposed to form a polygonal cage. Further similarities between coats are found in the adaptor components: The AP1 and AP2 clathrin adaptors are homologs of the tetrameric subcomplex of COPI, γ-ζ-β-δ-COP (*11*–*13*). These observations make it reasonable to predict that the assembled COPI coat can also be functionally subdivided into adaptor and cage.

Structural biology of heterogeneous membrane-containing systems is challenging. The structures of clathrin and adaptors have not been resolved together on membranes (*14*). Low-resolution structural data have been obtained describing the COPII coat assembled on membranes: The adaptor subunits coat the membrane and are linked flexibly to the outer subunits that form a cage around the membrane (*15*). The structure of the COPI coat on budded coated vesicles has been described at low resolution (*16*). The building block of the coat is a triad of coatomers that are linked together with contacts of variable valence. However, the arrangement of the proteins within the assembled coat remains unclear.

To determine a complete molecular model of the COPI coat, COPI-coated vesicles were produced in vitro by incubating giant unilamellar vesicles with coatomer, the GTPase Arf1, the guanine exchange factor ARNO, and guanosine 5′-*O*-(3′-thiotriphosphate) (*16*). The sample was vitrified by plunge-freezing and imaged by cryo–electron tomography (Fig. 1A). Eighty-two tomograms were collected under conditions optimized for high-resolution structure determination (*17*). To determine the structure of the repeating building block of the coat (the triad), the data set was split into two halves, each of which was independently subjected to subtomogram averaging (*17*). Structures from the two half data sets were compared to determine the resolution and averaged to give a final structure with a resolution of 13 Å (Fig. 1B and fig. S1B) (*18*). A total of 39,558 asymmetric units of the assembled coat from 1265 vesicles and near-complete buds contributed to the final structure.

Subtomogram averaging also determines the positions and orientations of the triads on each vesicle. As previously observed, the triads adopted preferred relative orientations (*16*). Following the approach described in (*16*), we generated reconstructions of the linkages between triads at resolutions between 18 to 23 Å (fig. S1, C to G). By combining these with the structure of the triad, we could visualize the overall arrangement of the coat on individual vesicles (Fig. 1C).

To interpret the reconstruction, we assigned the positions of the individual protein components within the density. Crystal structures are available for ε-COP bound to the C-terminal domain of α-COP (*10*, *19*), β′-COP bound to a part of α-COP (*10*), and for a complex Arf1-γ-ζ-COP (fig. S2) (*12*). At the resolution obtained, global fitting of the crystal structures into the electron microscopy (EM) density allowed us to identify

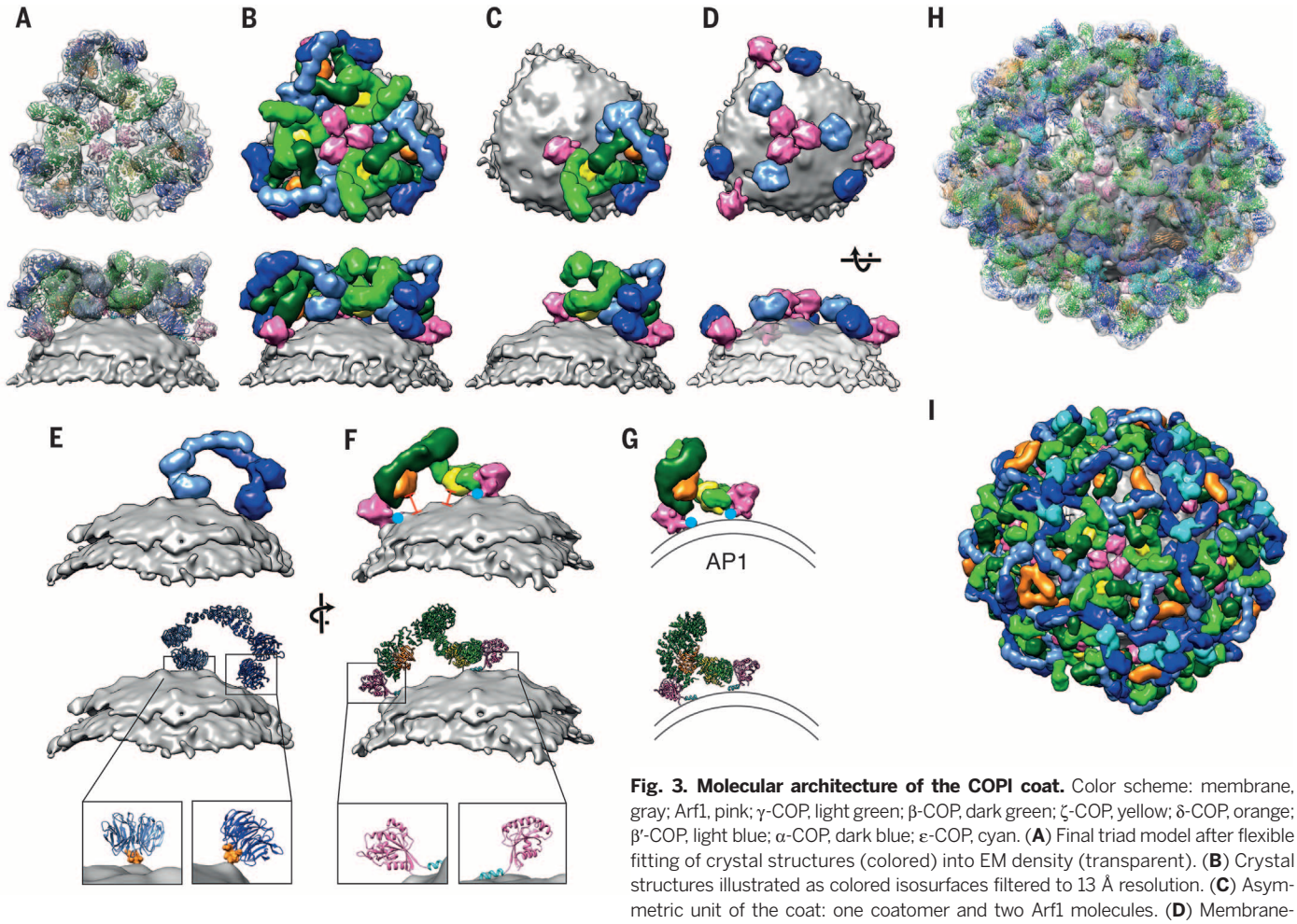


Fig. 3. Molecular architecture of the COPI coat. Color scheme: membrane, gray; Arf1, pink; γ-COP, light green; β-COP, dark green; ζ-COP, yellow; δ-COP, orange; β′-COP, light blue; α-COP, dark blue; ε-COP, cyan. (**A**) Final triad model after flexible fitting of crystal structures (colored) into EM density (transparent). (**B**) Crystal structures illustrated as colored isosurfaces filtered to 13 Å resolution. (**C**) Asymmetric unit of the coat: one coatomer and two Arf1 molecules. (**D**) Membrane-associated domains form a curved surface. Arf1 dimers (*32*) are not observed (fig. S7). (**E**) β′- and α-COP form an archlike dimer. The N-terminal β-propeller domains, containing cargo-binding sites (orange), contact the membrane. (**F**) γ-ζ-β-δ-COP forms a hyper-open archlike dimer. The Arf1 N-termini (illustrative cyan helices) contact the membrane. γ-ζ-COP approaches the membrane closely, whereas its homolog β-δ-COP is further away, which is consistent with the role of γ-COP in binding the cytoplasmic tails of p24 proteins, a function that β-COP lacks (*33*). (**G**) Structure model of an open-form clathrin adaptor for comparison [based on PDB ID 4HMY and the γ-Arf1 interface (PDB ID 3TJZ)]. (**H**) Illustrative model of a complete COPI-coated vesicle showing structures (color) and EM density (transparent). (**I**) Equivalent surface model as in (D).

the possible positions of each structure within the map (Fig. 2 and fig. S3) (*18*). Note that α- and β′-COP are structural homologs (*20*), as are γ-ζ-COP and β-δ-COP (*11*). In these cases, as expected, two positions were identified (Fig. 2) that could be assigned to the correct homolog on the basis of characteristic structural features and labeling experiments (fig. S4) (*18*). Three regions of EM density were not occupied by the core domains of the α-β′-ε-COP or γ-ζ-β-δ-COP subcomplexes (fig. S3C). These densities most likely correspond to the appendage (ear) domains of γ-COP (*21*) and β-COP and the μ-homology domain of δ-COP.

To further validate the arrangement of the core domains determined by fitting and labeling, we applied chemical cross-linking to in vitro–assembled COPI vesicles, followed by digestion and mass spectrometry. Twenty-six pairs of lysine residues were sufficiently close together within the assembled structure to be cross-linked (*22*) (table S1). We then generated multiple alternative structural models for the arrangement of core and appendage domains and measured the separation of the cross-linked lysine pairs in each model (figs. S5 and S6A) (*18*). The model most consistent with the cross-linking data matched the arrangement of core domains determined from fitting and labeling and allowed the appendage domains and δ μ-homology domain to be assigned to the unoccupied densities.

We generated a final structural model (Fig. 3 and movie S1) by placing available crystal structures or homology models of the coat subunits at the positions determined above and performing flexible fitting into the EM density (fig. S6B) (*18*). The structure is consistent with available biochemical data: The curved triad structure positions the Arf1 molecules and cargo binding sites proximal to the membrane (Fig. 3D and fig. S7). Arf1 is accessible for ArfGAP binding (fig. S7D), and binding sites for tethering proteins are on the outside of the coat (fig. S8, A to D). The arrangement of COPI components within the structure suggests that it cannot be functionally subdivided into outer coat and adaptor.

β′- and α-COP interact via the interface described in their x-ray structure [Protein Data Bank identification number (PDB ID) 3MKQ], but they do not assemble triskelions, as previously proposed (*10*, *23*). Instead, the α solenoids of β′- and α-COP form an arch over the γ-ζ-β-δ-COP subcomplex, orienting their N-terminal β propellers such that the K(X)KXX cargo-motif binding sites (K, Lys; X, any amino acid) (*24*, *25*) are optimally positioned against the membrane (Fig. 3E). β′- and α-COP do not form a cage or lattice as in COPII and clathrin coats; instead, they are linked to one another via the γ-ζ-β-δ-COP subcomplexes, forming an interconnected assembly.

The clathrin adaptors AP2 and AP1 have each been crystallized in a closed form (thought to represent the cytoplasmic conformation) and an open form in which cargo binding sites are accessible (thought to represent the membrane-associated conformation) (*26*–*29*). We found the adaptorlike γ-ζ-β-δ-COP subcomplex of COPI (Fig. 3F) to be more extended than either of these conformations; it appears as a "hyper-open" form (compare Fig. 3, F and G). Biochemical experiments point to conformational opening of coatomer by ligand binding (*30*, *31*), suggesting that the transition to the hyper-open form occurs upon membrane association. We speculate that, upon membrane binding, clathrin APs may also transition to a form that is more open than predicted from the available crystal structures. In the hyper-open form, the β- and γ-COP α solenoids form an arch that is bound to the membrane at each end via an interaction of their respective trunk domains with Arf1. This arrangement mimics the arrangement of the α-β′-COP subcomplex (Fig. 3, E and F): Both outer-coat–like and adaptorlike subcomplexes form extended α-solenoid arches linked at each end to the membrane.

The extended α solenoids in the coats of COPI, COPII, and clathrin oligomerize very differently (fig. S9), but in all cases they function as extended spacers that distribute cargo-binding or membrane-bending domains over the curved membrane surface while leaving the surface accessible. We suggest that this, rather than cage formation, is the ancestral function of protocoatomers.

The triads are connected by flexibly attached domains. One set of interactions is formed by the μ-homology domain of δ-COP (fig. S8) and another by ε-COP and the C-terminal domain of α-COP. In some positions, ε-COP forms a homodimeric interface observed in a crystal form (PDB ID 3MKR) (*10*); in other positions, it bridges the C-terminal and core domains of α-COP (fig. S8).

The structural model of the assembled coat is consistent with a model in which local membrane curvature is induced partly by membrane scaffolding by the curved triad structure and partly by insertion of six Arf1 amphipathic helices (*18*) (fig. S7 and movie S2). Linking triads together via flexibly attached domains would propagate this local curvature over larger membrane areas to form buds (fig. S9).

REFERENCES AND NOTES

1. F. Letourneur *et al.*, *Cell* **79**, 1199–1207 (1994).
2. V. Malhotra, T. Serafini, L. Orci, J. C. Shepherd, J. E. Rothman, *Cell* **58**, 329–336 (1989).
3. H. T. McMahon, I. G. Mills, *Curr. Opin. Cell Biol.* **16**, 379–391 (2004).
4. M. Faini, R. Beck, F. T. Wieland, J. A. Briggs, *Trends Cell Biol.* **23**, 279–288 (2013).
5. J. S. Bonifacino, J. Lippincott-Schwartz, *Nat. Rev. Mol. Cell Biol.* **4**, 409–414 (2003).
6. S. Hara-Kuge *et al.*, *J. Cell Biol.* **124**, 883–892 (1994).
7. D. Devos *et al.*, *PLOS Biol.* **2**, e380 (2004).
8. A. J. Noble *et al.*, *Nat. Struct. Mol. Biol.* **20**, 167–173 (2013).
9. A. Fotin *et al.*, *Nature* **432**, 573–579 (2004).
10. C. Lee, J. Goldberg, *Cell* **142**, 123–132 (2010).
11. K. Schledzewski, H. Brinkmann, R. R. Mendel, *J. Mol. Evol.* **48**, 770–778 (1999).
12. X. Yu, M. Breitman, J. Goldberg, *Cell* **148**, 530–542 (2012).
13. W. Yu, J. Lin, C. Jin, B. Xia, *J. Mol. Biol.* **386**, 903–912 (2009).
14. Y. Cheng, W. Boll, T. Kirchhausen, S. C. Harrison, T. Walz, *J. Mol. Biol.* **365**, 892–899 (2007).
15. G. Zanetti *et al.*, *eLife* **2**, e00951 (2013).
16. M. Faini *et al.*, *Science* **336**, 1451–1454 (2012).
17. F. K. Schur, W. J. Hagen, A. de Marco, J. A. Briggs, *J. Struct. Biol.* **184**, 394–400 (2013).
18. Materials and methods are available as supplementary materials on *Science* Online.
19. K.-C. Hsia, A. Hoelz, *Proc. Natl. Acad. Sci. U.S.A.* **107**, 11271–11276 (2010).
20. V. T. Chow, M. K. Sakharkar, D. P. Lim, W. M. Yeo, *Biochem. Genet.* **39**, 201–211 (2001).
21. P. J. Watson, G. Frigerio, B. M. Collins, R. Duden, D. J. Owen, *Traffic* **5**, 79–88 (2004).
22. A. Leitner, T. Walzthoeni, R. Aebersold, *Nat. Protoc.* **9**, 120–137 (2014).
23. A. Spang, *EMBO J.* **32**, 915–916 (2013).
24. W. Ma, J. Goldberg, *EMBO J.* **32**, 926–937 (2013).
25. L. P. Jackson *et al.*, *Dev. Cell* **23**, 1255–1262 (2012).
26. L. P. Jackson *et al.*, *Cell* **141**, 1220–1229 (2010).
27. X. Ren, G. G. Farías, B. J. Canagarajah, J. S. Bonifacino, J. H. Hurley, *Cell* **152**, 755–767 (2013).
28. E. E. Heldwein *et al.*, *Proc. Natl. Acad. Sci. U.S.A.* **101**, 14108–14113 (2004).
29. B. M. Collins, A. J. McCoy, H. M. Kent, P. R. Evans, D. J. Owen, *Cell* **109**, 523–535 (2002).
30. C. Reinhard *et al.*, *Proc. Natl. Acad. Sci. U.S.A.* **96**, 1224–1228 (1999).
31. J. D. Langer *et al.*, *Traffic* **9**, 597–607 (2008).
32. R. Beck *et al.*, *Proc. Natl. Acad. Sci. U.S.A.* **105**, 11731–11736 (2008).
33. L. Zhao, J. B. Helms, J. Brunner, F. T. Wieland, *J. Biol. Chem.* **274**, 14198–14203 (1999).

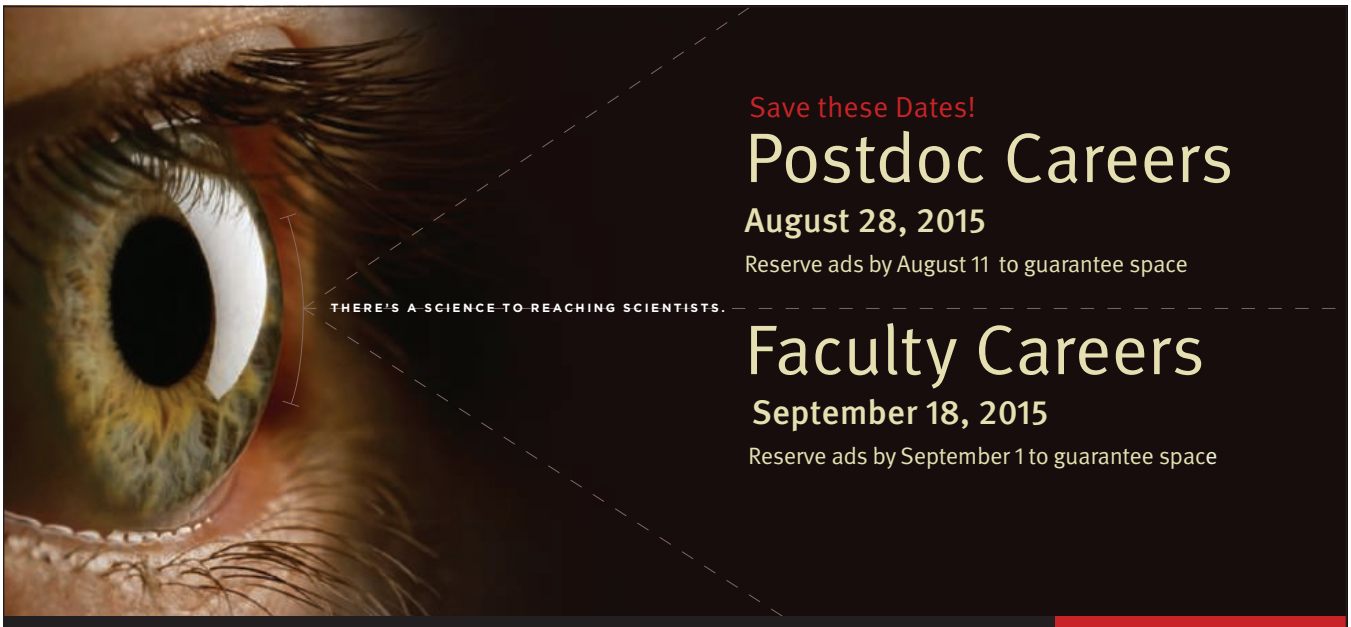
ACKNOWLEDGMENTS

We thank K. Bacia for providing Arf1 protein; M. Schorb and J. Kosinski for technical assistance; and F. Schur, W. Wan, B. Brügger, D. Devos, M. Kozlov, and D. Owen for discussions. This work was technically supported by EMBL IT services and was funded by the Deutsche Forschungsgemeinschaft within SFB638 (A16) to J.A.G.B. and F.W. EM maps and structural models are deposited in the Electron Microscopy Data Bank (accession codes EMD-2985, EMD-2986, EMD-2987, EMD-2988, and EMD-2989) and the Protein Data Bank (PDB IDs 5A1U, 5A1V, 5A1W, 5A1X, and 5A1Y).

SUPPLEMENTARY MATERIALS

www.sciencemag.org/content/349/6244/195/suppl/DC1
Materials and Methods
Figs. S1 to S9
Tables S1 and S2
References (*34*–*68*)
Movies S1 and S2

12 March 2015; accepted 22 May 2015
10.1126/science.aab1121



Two Fantastic Recruiting Opportunities!

POSTDOC CAREERS | August 28, 2015

Be sure to promote your openings to the thousands of scientists who read *Science* to find out about the latest postdoc opportunities.

Reserve space by August 11, 2015.

FACULTY CAREERS | September 18, 2015

Gear up to recruit for the faculty positions at your university with this much anticipated issue that reaches thousands of Ph.D. scientists looking for positions in academia.

Reserve space by September 1, 2015.



Produced by the *Science*/AAAS Custom Publishing Office.

SCIENCECAREERS.ORG

ScienceCareers
FROM THE JOURNAL SCIENCE AAAS

To book your ad: **advertise@sciencecareers.org**

The Americas
202-326-6582

Europe/RoW
+44(0)1223-326500

Japan
+81-3-3219-5777

China/Korea/Singapore/Taiwan
+86-186-0082-9345

"What I do with my Octet HTX time? Climb."

Shave weeks off your lead selection programs.

Broader antibody cross-competition ups your odds of finding the best candidates, but larger epitope binning studies take time. The Octet HTX system lets you use any binning assay format, any size matrix, start a run and get analyzed results the same day or the next day for larger studies. You can also combine multiple experiments into one dataset to easily visualize and cluster antibodies in similar bins or binding groups.

Lucy gets out of the lab more often now to climb. What will you do with your extra time?



fortéBIO®
A Division of **Pall Life Sciences**

PALL Life Sciences

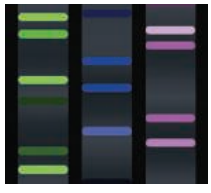
fortebio.com | 888-OCTET-75

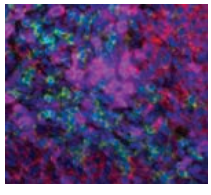
Fast. Accurate. EASY.

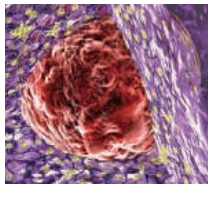
want new technologies?

antibodies
apoptosis
biomarkers
cancer
cytometry
data
diseases
DNA
epigenetics
genomics
immunotherapies
medicine
microbiomics
microfluidics
microscopy
neuroscience
proteomics
sequencing
toxicology
transcriptomics









watch our webinars

Learn about the latest breakthroughs, new technologies, and ground-breaking research in a variety of fields. Our expert speakers explain their quality research to you and answer questions submitted by live viewers.

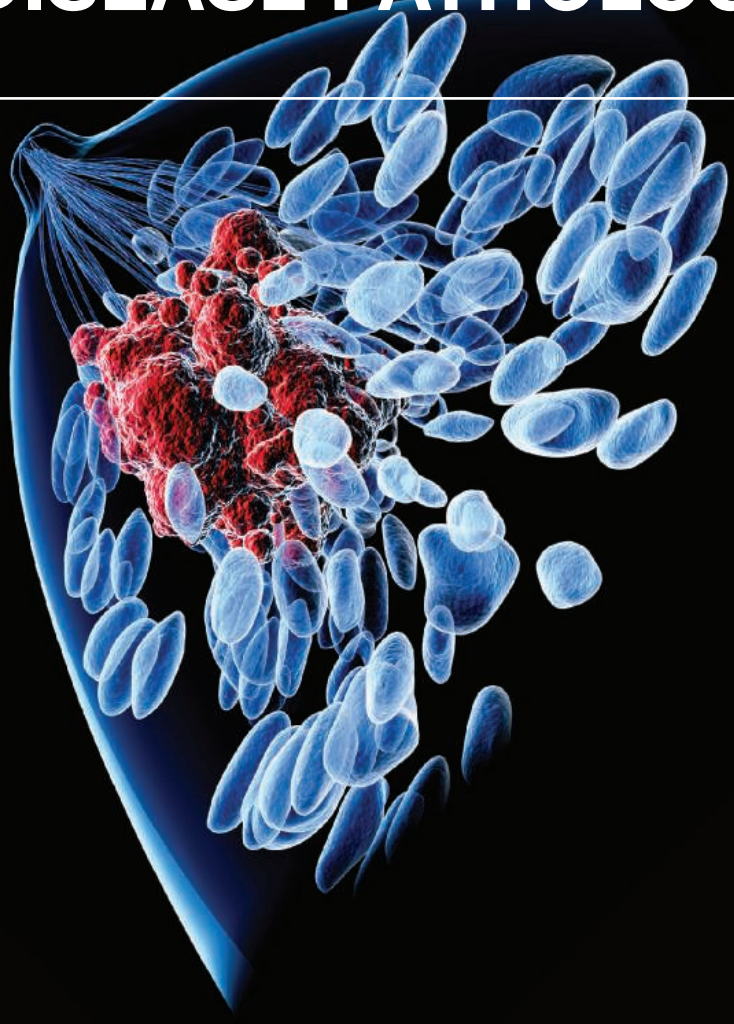
VIEW NOW!
webinar.sciencemag.org

Science
AAAS

Brought to you by the *Science*/AAAS Custom Publishing Office

@SciMagWebinars

DOES YOUR LAB SEEK TO UNDERSTAND MECHANISMS OF DRUG RESISTANCE OR DISEASE PATHOLOGY?



Leslie K. Ferrarelli, "Focus Issue: Refining the War on Cancer", *Sci. Signal.* 7, 318eg2 (2014). Image: Raycat/iStockphoto

Science Signaling | AAAS

CELL SIGNALING IN PHYSIOLOGY AND DISEASE

Find out more about the scope of the journal and submit your research today!
ScienceSignaling.org



Every scientist has a *story*

Read his story at membercentral.aaas.org, the website that takes you to new depths. Connect with others who share your passion.

AAAS MEMBERCENTRAL

Multimode Microplate Reader

A new multimode microplate reader with highly intuitive software delivers automated and versatile functionality to bioscience researchers performing a variety of microplate assays. The Varioskan LUX multimode microplate reader with new SkanIt Software is designed to simplify data acquisition and analysis and accelerate consistency and reliability in assay results. With advancements including integrated smart control technology and automatic dynamic range selection, the Varioskan LUX is designed to simplify setup while optimizing performance to deliver exceptional usability and data reliability. Varioskan LUX is equipped with smart safety controls to help keep research on track. These technologies include automated plate check, built-in shaker speed control, and automatic prime check and position sensors for the built-in dispensers, which are designed to identify and notify the user of potential errors that could compromise research. The SkanIt software monitors and captures measurement data throughout the run to reduce the risk of wasting expensive reagents, samples, and time.

Thermo Fisher Scientific
For info: 800-556-2323
www.thermoscientific.com/varioskanlux

Animal/Xeno-Free Enzymes

Several new grades of Collagenase, recombinant Nucleases DNase I, and RNases A, T1 & T2 and Neutral Protease (Dispase) are now available. All are certified Animal/Xeno-Free (AF) and designed to minimize potential BSE/TSE (prion) and mammalian virus contamination risks associated with bovine and other animal-sourced enzymes for primary and stem cell isolation, bioprocessing, and other biopharm related applications. The use of animal free enzymes eliminates many of the quality and regulatory issues and concerns associated with enzymes commonly purified from animal sources. These new animal/xeno-free plant and fungal sourced proteases products are now available in both research-and bulk-scale quantities. Worthington provides free evaluation samples for qualified customers requiring "contamination-free" enzymes for their critical biomedical applications. All of the Animal/Xeno-Free enzymes meet the required industry documentation from raw material sources through final product release. As well, all enzymes are produced under GMP guidelines in Worthington's ISO 9001 Certified facility.

Worthington Biochemical Corporation
For info: 800-445-9603
www.worthington-biochem.com



Handheld Raman Analyzer

The new Metrohm Instant Raman Analyzer (Mira) brings an increased level of confidence to identification, screening, and confirmation measurements through a unique blend of optical sampling configurations. Mira integrates seamlessly at all phases of the manufacturing process. Eliminating the need for sample transfer and measurement in a separate laboratory setting, Mira brings the analysis to the sample, offering a substantial productivity increase when compared to lab-based analysis. Innovative sampling accessories with built-in system intelligence and search techniques make Mira usable by operators with limited spectroscopy experience. When combined with Orbital Raster Scanning, these sampling improvements provide users with the most repeatable measurements possible. Mira offers the user the choice of two pathways to Raman analysis, providing preassembled industry-specific libraries of compounds, the ability to measure and store user-specific samples for later analysis or a combination of both. An intuitive software package allows assembly of these custom libraries.

Metrohm
For info: 866-638-7646
www.metrohmusa.com

Liquid Handling Syringe Pump

The new Precision Syringe Drive 6 (PSD/6) is a compact, full-height pump for precision dispensing of small to large volumes. The Hamilton PSD/6 is the newest full-height syringe pump to join the Hamilton PSD family, and performs all standard liquid handling functions including dispensing, serial dispensing, and diluting. The PSD/6 offers the largest range of compatible syringes sizes and is the most compact full-height pump available. Enhanced flow stability and increased dispense times make it ideal for applications like flow cytometry and micro fluidics. Designed for simple integration, a variety of mounting configurations are possible for a single unit or a daisy chain of up to 16 pumps. With selectable communication protocols and flexible programming options, every detail of the pump's performance can be adjusted to accommodate even the most challenging applications. The PSD/6 syringe and valve drive movements are optimized to extend the life and time between product maintenance.

Hamilton Company
For info: 800-648-5950
www.hamiltoncompany.com

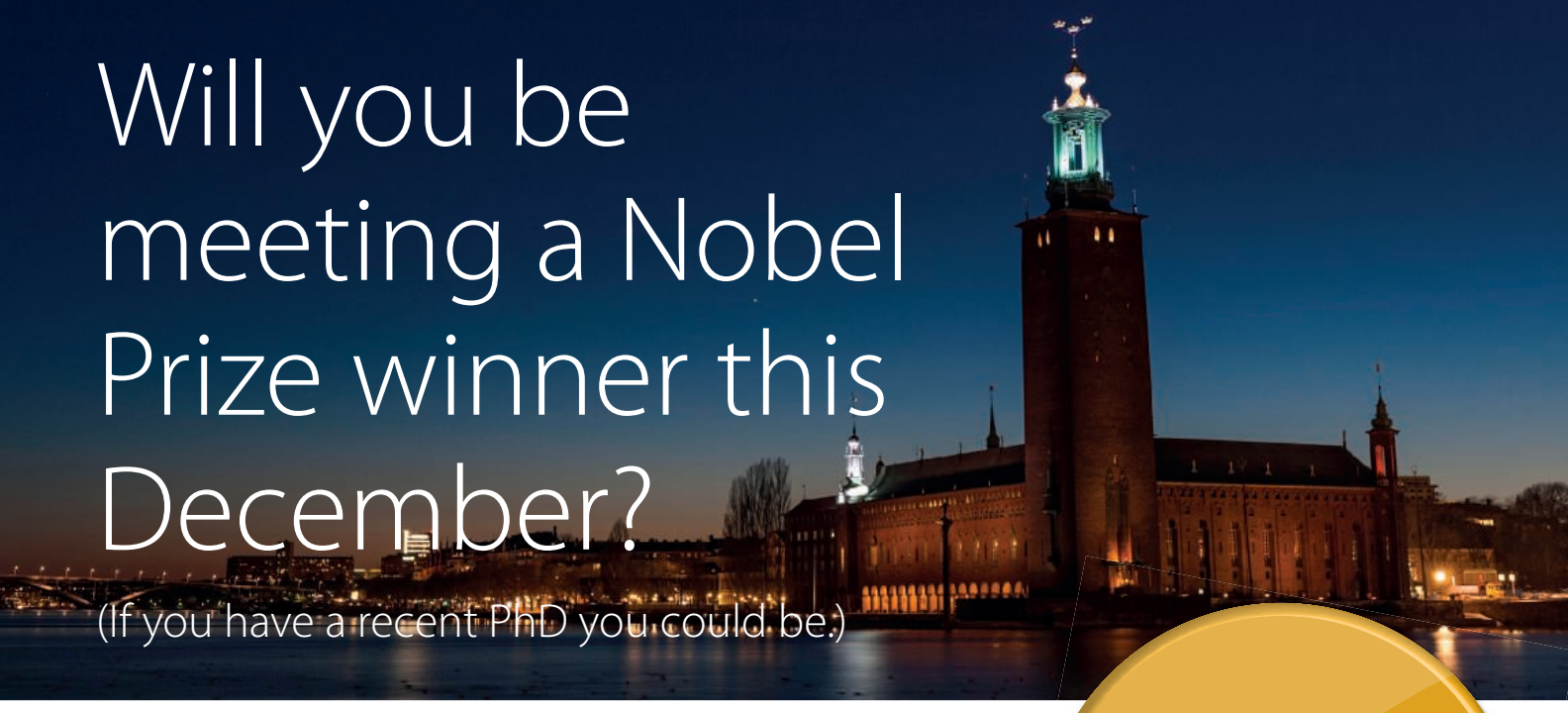
PCR Instrumentation

The IntelliQube is the next generation of high throughput quantitative real-time polymerase chain reaction (qPCR) in Array Tape. The IntelliQube is the first fully automated, high throughput instrument to feature seamless integration of liquid handling, thermal cycling, detection, and data analysis. The IntelliQube supports qPCR, end-point PCR, and isothermal chemistries; allowing labs to realize the benefits of inline automation that are enabled by the innovative Array Tape consumable. Array Tape is a thin polymer strip with serially embossed wells that provides a flexible microplate replacement. The introduction of IntelliQube extends this value to a broader scope of applications and laboratories. With the new 768-well Array Tape format, labs can expect twice the PCR throughput compared to traditional 384-well qPCR instruments while substantially reducing chemistry costs with 1.6 µL reaction volumes. The IntelliQube is compatible with an extensive list of chemistries and fluorogenic probes, and offers five distinct detection channels to enable multiplex reactions.

Douglas Scientific
For info: 320-762-6888
www.douglasscientific.com

Electronically submit your new product description or product literature information! Go to www.sciencemag.org/products/newproducts.dtl for more information.

Newly offered instrumentation, apparatus, and laboratory materials of interest to researchers in all disciplines in academic, industrial, and governmental organizations are featured in this space. Emphasis is given to purpose, chief characteristics, and availability of products and materials. Endorsement by *Science* or AAAS of any products or materials mentioned is not implied. Additional information may be obtained from the manufacturer or supplier.



Will you be meeting a Nobel Prize winner this December?

(If you have a recent PhD you could be.)

Stockholm in the second week of December is a special place. The city is alive with excitement as it welcomes and celebrates the new Nobel Laureates at the annual Nobel Prize ceremony.

If you are a PhD student, you could be here too – meeting a Nobel Laureate and receiving a rather special prize yourself.

The journal *Science* & SciLifeLab have established The *Science* & SciLifeLab Prize for Young Scientists, to recognize and reward excellence in PhD research and support young scientists at the start of their careers. It's about bright minds, bright ideas and bright futures.

Four winners will be selected for this international award. They will have their essays published in the journal *Science* and share a new total of 60,000 USD in prize money. The winners will be awarded in Stockholm, in December, and take part in a unique week of events including meeting leading scientists in their fields.

"The last couple of days have been exhilarating. It has been an experience of a lifetime. Stockholm is a wonderful city and the Award winning ceremony exceeds my wildest dreams."
–Dr. Dan Dominissini, 2014 Prize Winner

Who knows, The *Science* & SciLifeLab Prize for Young Scientists could be a major stepping stone in your career and hopefully one day, during Nobel week, you could be visiting Stockholm in December once again.

Science & SciLifeLab PRIZE FOR YOUNG SCIENTISTS

This prize is made possible with the kind support of the Knut and Alice Wallenberg Foundation. This Foundation grants funding in two main areas; research projects of high scientific potential and individual support of excellent scientists.

The 2015 Prize is now open. The deadline for submissions is August 1, 2015.
Enter today: www.sciencemag.org/scilifelabprize

The 2015 Prize categories are:

- Cell and Molecular Biology
- Ecology and Environment
- Genomics and Proteomics
- Translational Medicine

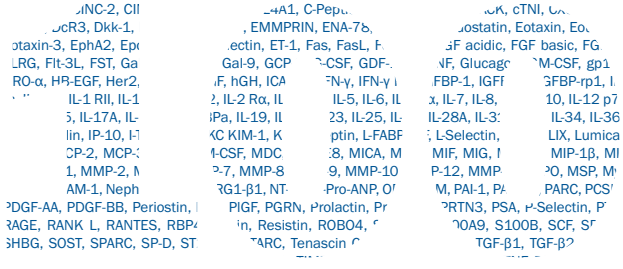
Knut och Alice Wallenbergs Stiftelse

Science AAAS

SciLifeLab

R&D SYSTEMS™
a bio-techne brand

Do You Suffer from **Panel Envy?**



analytes in 1 Luminex® assay.

EXPLORE NOW
rndsystems.com/**100Plex**

#PanelEnvy #100Plex



There's only one Science

Science Careers Advertising

For full advertising details, go to ScienceCareers.org and click For Employers, or call one of our representatives.

Tracy Holmes
Worldwide Associate Director
Science Careers
Phone: +44 (0) 1223 326525

THE AMERICAS

E-mail: advertise@sciencecareers.org

Fax: +1 (202) 289 6742

Tina Burks
Phone: +1 (202) 326 6577

Nancy Toema
Phone: +1 (202) 326 6578

Online Job Posting Questions
Phone: +1 (202) 312 6375

EUROPE / INDIA / AUSTRALIA / NEW ZEALAND / REST OF WORLD

E-mail: ads@science-int.co.uk

Fax: +44 (0) 1223 326532

Sarah Lelarge
Phone: +44 (0) 1223 326527

Kelly Grace
Phone: +44 (0) 1223 326528

Online Job Posting Questions
Phone: +44 (0) 1223 326528

JAPAN

Katsuyoshi Fukamizu (Tokyo)
E-mail: kfukamizu@aaas.org
Phone: +81 3 3219 5777

Hiroyuki Mashiki (Kyoto)
E-mail: hmashiki@aaas.org
Phone: +81 75 823 1109

CHINA / KOREA / SINGAPORE / TAIWAN / THAILAND

Ruolei Wu
Phone: +86 186 0082 9345
E-mail: rwu@aaas.org

All ads submitted for publication must comply with applicable U.S. and non-U.S. laws. *Science* reserves the right to refuse any advertisement at its sole discretion for any reason, including without limitation for offensive language or inappropriate content, and all advertising is subject to publisher approval. *Science* encourages our readers to alert us to any ads that they feel may be discriminatory or offensive.

ScienceCareers
FROM THE JOURNAL SCIENCE AAAS

ScienceCcareers.org



OR ScienceCareers.org

Learn more and conduct your job search the easy way.

- Search thousands of job postings
- Create job alerts based on your criteria
- Get career advice from our Career Forum experts
- Download career advice articles and webinars
- Complete an individual development plan at "myIDP"

Target your job search using relevant resources on **ScienceCareers.org**.

ScienceCareers
FROM THE JOURNAL SCIENCE AAAS

Immunology
UNIVERSITY OF TORONTO

DEPARTMENT OF IMMUNOLOGY TENURE STREAM POSITION
Assistant Professor - 1500674

The Department of Immunology, University of Toronto invites applications for a tenure-stream appointment. The appointment will be at the rank of Assistant Professor and will begin on July 1, 2016, or shortly thereafter.

This new position is part of a continuing program to build on strength in Immunology. Outstanding applicants working in any area of Immunology complementary to our existing faculty www.immunology.utoronto.ca will be considered.

The successful candidate must have a Ph.D. or equivalent degree; postdoctoral experience; and evidence of successful research funding, publications in leading journals, and presentations at academic conferences. The successful candidate will be expected to mount an original, competitive and independently funded research program, and have a commitment to excellence in teaching at the undergraduate, medical and graduate level in Immunology.

Salary will be commensurate with qualifications and experience. The position will be located in the Medical Sciences Building on the downtown St. George campus of the University of Toronto.

All qualified candidates are invited to apply by clicking on the link below. Applications should include a cover letter, curriculum vitae, and a statement outlining current and future research goals. If you have questions about this position, please contact **immunology.search@utoronto.ca**. All application materials should be submitted online.

Submission guidelines can be found at: **http://uoft.me/how-to-apply**. We recommend combining attached documents into one or two files in PDF/MS Word format.

Applicants should also ask three referees to send letters directly to the department via e-mail to **immunology.search@utoronto.ca** by the closing date of **August 28, 2015**.

For information about the Department of Immunology see **http://www.immunology.utoronto.ca**

The University of Toronto is strongly committed to diversity within its community and especially welcomes applications from visible minority group members, women, Aboriginal persons, persons with disabilities, members of sexual minority groups, and others who may contribute to the further diversification of ideas.

All qualified candidates are encouraged to apply; however, Canadians and permanent residents will be given priority.

Institute of Marine and Environmental Technology

Assistant Professor: Fish/Shellfish Immunology

The Institute of Marine and Environmental Technology (IMET) of the University System of Maryland seeks applications for the position of Assistant Professor (tenure-track) working on fish/shellfish immunology. The successful candidate will have a track-record of outstanding research using molecular biology/genetics approaches to study fish and comparative immunity in species that are important to aquaculture and fisheries, or in species that are established animal models (i.e. zebrafish) for immunological studies that are relevant to both fish and human health. Candidates with an interest in practical applications of their fundamental research, including interactions with industry, are encouraged to apply. A demonstrated ability to establish a well-funded research program is expected of the successful candidate. This appointment will be at the University of Maryland Baltimore. The primary focus of the appointee will be on research; teaching at the graduate level is encouraged.

IMET's mission is to study the biology of coastal marine biosystems and ensure their sustainable use, as well as exploit marine-derived systems to improve human health (www.imet.usmd.edu). IMET brings together faculty members from three major USM research institutions - the University of Maryland Baltimore (UMB), the University of Maryland Baltimore County (UMBC), and the University of Maryland Center for Environmental Science (UMCES) - in an integrated state-of-the-art research facility located at Baltimore's Inner Harbor.

A Ph.D. or equivalent terminal degree is required in molecular biology, microbiology, aquatic pathology or related fields and candidates should have postdoctoral experience and a strong publication record. Applicants should send the following in a single PDF file to Russell Hill, Director, IMET; email to imetdirectorsoffice@umces.edu: (1) detailed curriculum vitae, (2) statement of research interests and goals and (3) names and contact details of three to five references. To receive full consideration, application materials should be submitted by **14 August 2015** (the position will be open until filled).

The USM is an Equal Opportunity, Affirmative Action Employer. The University of Maryland, Baltimore is an Equal Opportunity/Affirmative Action Employer. Minorities, women, individuals with disabilities, and protected veterans are encouraged to apply.

UC San Diego

The Department of Pediatrics, Division of Allergy, Immunology and Rheumatology has an open recruitment for a **POSTDOCTORAL POSITION** to be filled as soon as possible.

The candidate should have an M.D. or Ph.D. degree and will be involved in the study of T cells derived from young children exploring antigen presentation, T cell recognition, and T cell linage differentiation.

Interested candidates should send curriculum vitae with three references to **Dr. Alessandra Franco** by **e-mail: alfranco@ucsd.edu**.

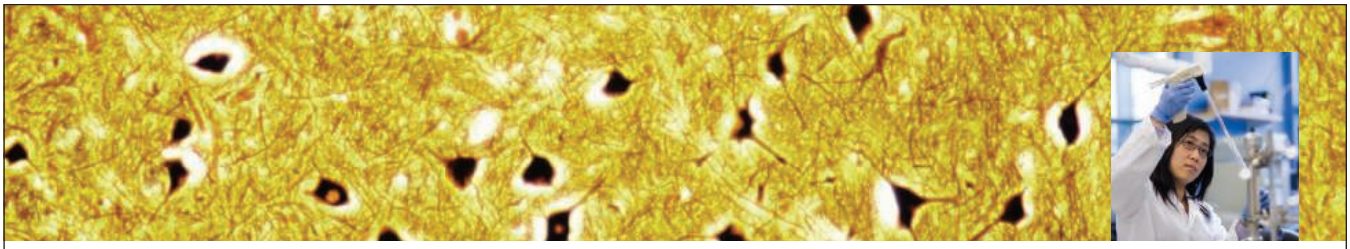
Your career is our cause.

Get help from the experts.

ScienceCareers.org
- Job Postings
- Job Alerts
- Resume/CV Database
- Career Advice
- Career Forum

ScienceCareers
FROM THE JOURNAL SCIENCE AAAS

Post Your Jobs
1 million candidates*
151,000 job applications*
Reach Scientists. Fill Positions.
*Jan–Dec 2014
ScienceCareers
employers.sciencecareers.org



Explore the Amgen Difference

At Our Expanded Facilities in Cambridge and South San Francisco





If you're seeking a career where you can truly make a difference in the lives of others, a career where you can work at the absolute forefront of biotechnology with the top minds in the field, you'll find it at Amgen.

Amgen is committed to unlocking the potential of biology for patients suffering from serious illnesses by discovering, developing, manufacturing and delivering innovative human therapeutics. This approach begins by using tools like advanced human genetics to unravel the complexities of disease and understand the fundamentals ofhuman biology.

Amgen focuses on areas of high unmet medical need and leverages its biologics manufacturing expertise to strive for solutions that improve health outcomes and dramatically improve people's lives. A biotechnology pioneer since 1980, Amgen has grown to be one of the world's leading independent biotechnology companies, has reached millions of patients around the world and is developing a pipeline of medicines with breakaway potential.

Amgen is a biotechnology pioneer with a mission to serve patients. If you're ready for your next step, join us at one of our expanded facilities in **Cambridge, MA** or **South San Francisco, CA.**

AMGEN® 35 YEARS

www.amgen.com/careers

Amgen is an Equal Opportunity employer and will consider all qualified applicants for employment without regard to race, color, religion, sex, sexual orientation, gender identity, national origin, protected veteran status or disability status.

JOB FOCUS: IMMUNOLOGY

UCDAVIS
SCHOOL OF MEDICINE

FACULTY POSITION
Department of Medical Microbiology and Immunology

The Department of Medical Microbiology and Immunology (MMI), School of Medicine, University of California, Davis is engaged in research investigations on human infectious diseases and host immune interactions with pathogens and commensal microbiota. The MMI Department is seeking candidates for one full-time tenure-track academic position at the rank of Assistant or Associate Professor in the tenure track series. Successful candidates must have a Ph.D., and/or M.D. with postdoctoral experience and a record of research publications. Applicants must have active research programs involving human infectious diseases (emphasis on pathogens or resident microbiota or immunology or immunogenomics). Candidates are expected to establish and maintain a strong extramurally funded research program and to actively participate in the academic and service missions of the University. Candidates must possess excellent interpersonal and communication skills and demonstrated ability to work with others in a collegial team atmosphere. Laboratory and office space is available (including BSL2 and BSL3 laboratory space), with state-of-the art facilities, instrumentation, and administrative support. The MMI research and teaching programs intersect with other campus-wide programs and resources in the Schools of Medicine and Veterinary Medicine and Agriculture and Environmental Sciences, Genome Center, MIND Institute, California National Primate Research Center, Center for Comparative Medicine and the Cancer Center. UC Davis is ranked 9th nationally among public universities in research funding. The University's student population is approximately 32,000.

For applicants at the Associate Professor level, a strong track record of teaching at the graduate level, extramural funding and published research is required. For applicants at the Assistant Professor level, a strong record of research publications and potential for obtaining extramural funding are required.For full consideration, applications should be received by **August 31, 2015**; however, the position will remain open until filled through June 30, 2016.Qualified applicants should upload a cover letter, curriculum vitae, statement of research, and 3-5 letters of recommendation online at **https://recruit.ucdavis.edu/apply/JPF00599**.

The University of California, Davis is an Affirmative Action/Equal Opportunity Employer with a strong institutional commitment to the achievement of diversity.

POSITIONS OPEN

Steering Committee of NIPERs - Mohali, Ahmedabad, Guwahati, Hajipur, Hyderabad, Kolkata, & Raebareli under the Chairmanship of Secretary, Department of Pharmaceuticals, Government of India

Advertisement for the Post of Directors of National Institutes of Pharmaceutical Education & Research (NIPERs)-Mohali, Guwahati, Hajipur, Hyderabad & Raebareli (Advt. No. NIPERA/DIR/01/07/2015)

Date of publication: 01.07.2015 Last Date: 31.07.2015

National Institutes of Pharmaceutical Education & Research (NIPERs) under the aegis of Ministry of Chemicals & Fertilizers, Department of Pharmaceuticals are institutions of National Importance created by an Act of Parliament with a mandate to nurture and promote quality and excellence in Pharmaceutical education and research as to create human resource of a higher calibre for the Indian Pharmaceutical Industry, towards making India a global leader in innovation and Drug Discovery while continue to offer leadership in formulations. The NIPERs-Guwahati, Hajipur, Hyderabad, & Raebareli are set up during 2007-08 and are functioning under premier mentor institutions and are being developed as independent institutions soon. The NIPER, S.A.S Nagar (Mohali) is having its own campus.

Now applications are invited for the post of Director of these NIPERs. Details with regard to eligibility, salary, application format, etc are available on websites of Department of Pharmaceuticals, Ministry of Chemicals & Fertilizers **(www.pharmaceuticals.gov.in)** and NIPERs.

The application in prescribed format is required to be sent on or before the last date by hard copy to "The Registrar, NIPER, Ahmedabad c/o B V Patel PERD Centre, SG Highway, Thaltej, Ahmedabad, Gujarat-380054" and electronically to the email id: scsc.niper@gov.in. Email copy is mandatory.

ScienceCareers online @sciencecareers.org



For recruitment in science, there's only one Science



This feature helps postdocs transition from one discipline or department to another. Topics include strategies for making such changes and discussions about the advantages/disadvantages of changing directions.

What makes *Science* the best choice for recruiting?

- Read and respected by 570,400 readers around the globe
- 78% of readers read *Science* more often than any other journal
- Your ad sits on specially labeled pages to draw attention to the ad
- Your ad dollars support AAAS and its programs, which strengthens the global scientific community.

Why choose this postdoc feature for your advertisement?

- Relevant ads in the career section with special postdoc banner
- 67% of our weekly readers are Ph.D.s.

Expand your exposure. Post your print ad online to benefit from:

- Link on the job board homepage directly to postdoc opportunities
- Dedicated landing page for postdoc opportunities.

Post online and your job will be e-mailed to over 13,000 job seekers looking for postdoc positions.

SCIENCECAREERS.ORG

ScienceCareers
FROM THE JOURNAL SCIENCE AAAS

To book your ad: **advertise@sciencecareers.org**

The Americas
202-326-6582

Japan
+81-3-3219-5777

Europe/RoW
+44 (0) 1223-326500

China/Korea/Singapore/Taiwan
+86-186-0082-9345

Cleveland Clinic

Chair, Lerner Research Institute

The Cleveland Clinic, one of the world's most distinguished academic medical centers and ranked by U.S. News & World Report as the No.4 Hospital in America, announces a search for Chair, Lerner Research Institute.

The Lerner Research Institute is home to all of the laboratory-based and translational research at the Cleveland Clinic. Its total research budget in 2014 was $255 million, including $98 million in federal funding. The Institute encompasses 12 departments and has a total of 1,500 employees including 172 principal investigators and 212 postdoctoral fellows contained with 700,000 square feet of laboratory space. Institute faculty published 1442 journal articles in 2014, which described significant discoveries, many in high-impact journals. The faculties are also active in the commercialization of Intellectual property, producing new companies, patents, and licensing agreements each year.

Lerner Research Institute faculty play an important role in teaching and mentoring graduate students and medical students in the Cleveland Clinic Lerner College of Medicine (CCLCM) of CWRU, one of the top-rated medical schools in the United States. Also, in 2014, 180 graduate students worked in the Lerner Research Institute, including 38 in a novel PhD program in Molecular Medicine.

The successful candidate for the position of Chair, Lerner Research Institute will be an internationally recognized scientist with a distinguished career of academic accomplishment within an active biomedical disease-oriented research program and should be eligible for the rank of Professor at CCLCM. Key skills will include superior leadership competency in a multidisciplinary environment, demonstrated collaboration with clinicians, and strength in recruiting and mentoring other outstanding and successful scientists. The position holds an endowed chair and a position on the Board of Governors (Medical Executive Committee) and other executive advisory committees of the Cleveland Clinic.

Interested Candidates should submit a letter of interest, curriculum vitae, and the names of 3 references to: Joseph P. Iannotti MD, PhD, Chair,, Search Committee for Chair, Lerner Research Institute, iannotj@ccf.org Phone: 216-445-5151, www.lerner.ccf.org www.clevelandclinic.org/physicianrecruitment

Equal Employment/Affirmative Action Employer – Min/Fem/Disability/Vet

THE HONG KONG UNIVERSITY OF SCIENCE AND TECHNOLOGY

Director of HKUST Jockey Club Institute for Advanced Study

The University

Founded in 1991, The Hong Kong University of Science and Technology (HKUST) is an international research university dedicated to the advancement of learning and scholarship. The University comprises more than 500 faculty members whose research ranges from science to engineering, business, humanities and social sciences. HKUST has been ranked the No. 1 university in Asia by QS Asian University Rankings in three of the last four years.

The HKUST Jockey Club Institute for Advanced Study (IAS)

IAS is committed to providing an inclusive platform for scholarly interaction among leading scientists and scholars, and represents an important part of the strategic development of HKUST. As an intellectual center integral to the University's academic endeavors and working in close partnership with the Schools and Departments at the University, the Institute spearheads both fundamental and applied research relevant to the region's socio-economic development, nurtures young promising talents to explore their potentials, and raises community interest in the latest scientific and technological discoveries. To realize its vision, mission and goals, IAS recruits top-notch scholars as IAS Professors; invites internationally acclaimed research leaders to visit and interact with the local academic community; and engages outstanding HKUST faculty to lead frontier research projects. Recruitment for the Institute will be supported by a good number of endowed chairs. The Institute organizes and sponsors a wide spectrum of scholarly activities, including programs, workshops, lectures, and is one of the two main sites for the Gordon Research Conference in Asia. Emblematic of the lofty vision and broad inclusiveness of IAS, the iconic 5-storey IAS Lo Ka Chung Building is located atop the Lee Shau Kee Campus commanding a spectacular sea and main campus view.

The Role

Reporting to the President, the IAS Director is responsible for:

- overall direction of the Institute, including planning and overseeing the Institute's academic programs;
- recruitment of IAS Professors and other members;
- management of the Institute's budget;
- building partnerships with local, national and international researchers and education institutions.

The Director is expected to be a top researcher with vision, energy and commitment. University leadership experience that will be relevant to leading the IAS to realize its lofty aims is being looked for. The Director is also expected to assist the President in IAS fundraising effort from time to time.

Terms & Applications/Nominations

The Directorship will be a full-time appointment, normally for an initial term of 5 years which may be renewed for a second term. The appointment will be concurrent with a substantive professorial appointment.

HKUST is being represented by Asianet Consultants (HK) Ltd. for this search. Applications/nominations, together with a full curriculum vitae and the names and addresses of three referees, should be sent to **Mr Peter Liu of Asianet Consultants (HK) Ltd. (by email to hkust-dias@asianetconsultants.com or by post to 702-705 Wilson House, 19-27 Wyndham Street, Central, Hong Kong)**. Review of candidates will begin in September 2015 and continue until the position is filled.

The University is committed to increasing the diversity of its faculty and has a range of family-friendly policies in place.

Additional information about the University and the Institute is available on the websites www.ust.hk and http://ias.ust.hk respectively.

(Information provided by applicants will be used for recruitment and other employment-related purposes.)

UNIVERSITY OF ILLINOIS AT URBANA-CHAMPAIGN
Open Rank Tenured/Tenure-Track Faculty Position
Department of Comparative Biosciences

The Department of Comparative Biosciences at the College of Veterinary Medicine, University of Illinois at Urbana-Champaign invites applications for an open position in reproductive biology at the Assistant, Associate, or Full Professor level. Candidates must possess a Ph.D., or equivalent degree. Candidates currently at the Associate or Full Professor rank with federal funding are especially encouraged to apply. The successful candidate will participate in the professional and graduate curricula and develop research programs which complement existing department and/or campus strengths in reproductive biology, neuroscience, environmental toxicology and cancer biology. Full information about the department is available at http://vetmed.illinois.edu/cb/index.html. The position is a regular, full-time, 9-month, tenured or tenure track appointment, and is available January 2016. Salary and rank will be commensurate with qualifications.

Qualified applicants should apply online at **https://jobs.illinois.edu**. Applications should include a cover letter including a research statement, CV, and contact information for three references. Questions may be directed to **Dr. Jodi A. Flaws**, search committee chair, **jflaws@illinois.edu** or **217-333-7933**.

In order to ensure full consideration, applications must be received by **September 15, 2015**. Applicants may be interviewed before the closing date; however, no hiring decision will be made until after that date.

Illinois is an Equal Opportunity Employer and all qualified applicants will receive consideration for employment without regard to race, religion, color, national origin, sex, age, status as a protected veteran, or status as a qualified individual with a disability. Illinois welcomes individuals with diverse backgrounds, experiences, and ideas who embrace and value diversity and inclusivity (www.inclusiveillinois.illinois.edu).

By **Eleftherios P. Diamandis**

Getting noticed is half the battle

The hiring game starts early. Well before a faculty position even opens, department members and administrators tend to observe the available pool of candidates and shortlist the ones they consider most promising. Savvy candidates work this preselection process to their advantage. Some ways of doing this are obvious: Be an excellent scholar. Publish well. Work hard. Communicate with the public and your peers. But a well-planned, long-range effort to ensure your visibility among those who have hiring responsibilities can be the deciding factor.

Here's how it worked for me. I arrived at the University of Toronto in 1982 as a postdoctoral diploma candidate in clinical biochemistry. Coming from a rather poor country—Greece—was a disadvantage, so I did all I could to adapt to the new environment, fill in my knowledge gaps, and make a good impression with hard work and dedication. When I finished the diploma training in 1984, the chair of the department showed interest in finding a job for me. But I had to go back to Greece first to complete my medical degree. I finished it in 1986.

When I returned to Toronto, I was hired as the director of research and development at a small biotechnology company spun off from the university; I also had an adjunct position in clinical biochemistry at the University of Toronto. I had no special training or experience in business management, but I found myself directing eight Ph.D. scientists, working together to develop a commercial product.

Working at a company was not my first choice, but I gave it everything I had, and the work I did there laid a cornerstone for my future success. I learned to appreciate the difficulties associated with developing and commercializing a system, which we succeeded in doing toward the end of my time there. I learned how to manage people and how to keep them focused on a single task. I met with potential customers and investors and learned how to negotiate and promote products and ideas.

The job was good and challenging, but it was not what I was aiming for in the long term. Meanwhile, a new chair had taken over in the department, and I set out to persuade him to hire me as an academic clinician-scientist.

I worked 16 to 17 hours a day, not just to make progress on the technology but also to publish our results in high-impact journals. How did I manage it? My wife—also a Ph.D. scientist—worked far less than I did; she took on the bulk of the domestic responsibilities. Our children spent many Saturdays and some Sundays playing in the company lobby. We made lunch in the break room microwave.



"I made myself visible by participating in every research seminar."

My colleagues and I managed to publish numerous papers, and I was invited repeatedly to present at national and international conferences. I was able to demonstrate, in the department's annual report, scientific productivity comparable in quantity and quality to the full-time academics in the department. I made sure these activities were noticed.

I made myself visible by participating in every research seminar—not easy, considering the hour-long drive and how busy I was at the company. Each time I entered the lecture room, I made a point of passing in front of the department chair before sitting down. At the end of every seminar, I made sure to ask a carefully crafted question or two.

After 18 months of this, the chair paid me an unexpected visit at the company and invited me to become his deputy in the department and at the teaching hospital. Ten years later, I succeeded him.

Our daughter, by the way, is now a Ph.D. scientist working as a clinical chemist, and our son is in training to become an M.D.-Ph.D. neuropathologist. My wife is a senior scientist at a major teaching hospital.

Making sure you are noticed can give you the edge you need over your silent competition. ■

Eleftherios P. Diamandis is professor and head of clinical biochemistry at the University of Toronto, biochemist-in-chief at University Health Network, and head of clinical biochemistry at Mount Sinai Hospital in Toronto, Canada. For more on life and careers, visit sciencecareers.org. Send your story to SciCareerEditor@aaas.org

ILLUSTRATION: ROBERT NEUBECKER

Downloaded from www.sciencemag.org on July 10, 2015

Published by AAAS